Caracterización de sistemas de fractura mediante la localización relativa de terremotos tectónicos y volcánicos usando métodos clásicos y técnicas de *array*

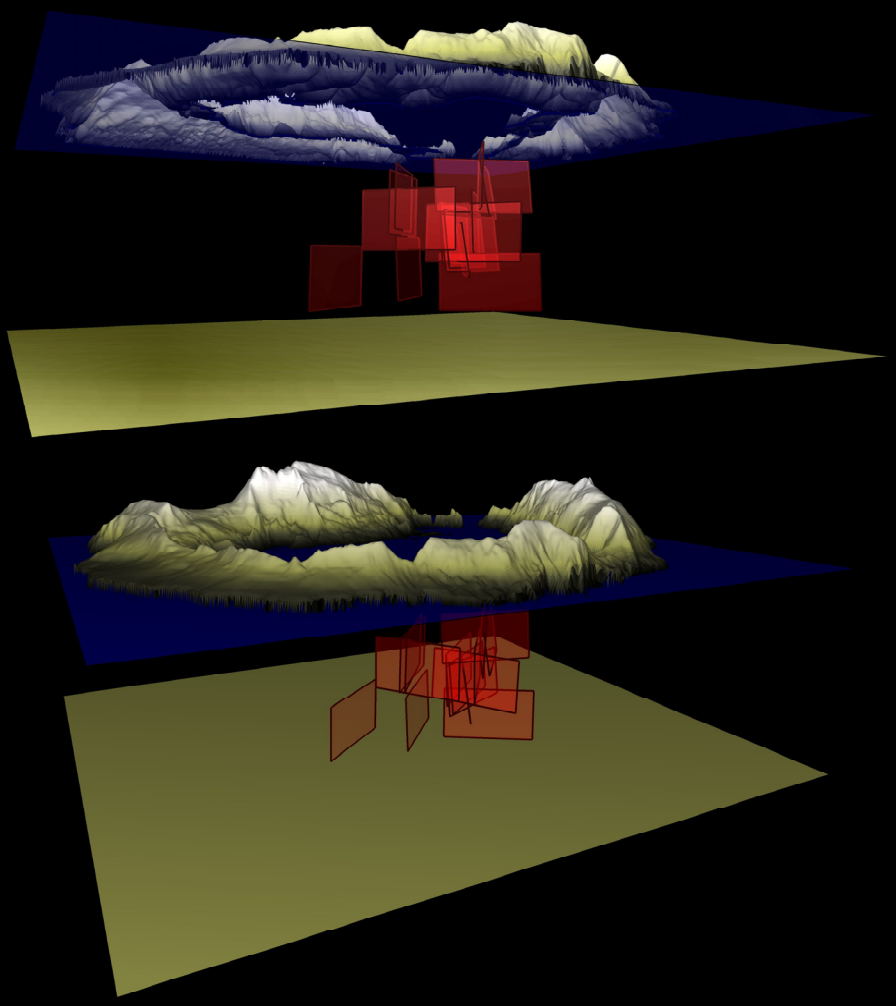

Enrique Carmona Rodríguez

Tesis Doctoral
Universidad de Granada
2009

Instituto Andaluz de Geofísica
y Prevención de Desastres Sísmicos

Departamento de Física Teórica y del Cosmos

Caracterización de sistemas de fractura mediante la localización relativa de terremotos tectónicos y volcánicos con métodos clásicos y técnicas de array

TESIS DOCTORAL

Memoria presentada para optar al Grado de Doctor en Ciencias Físicas por la Universidad de Granada por

Enrique Carmona Rodríguez

DIRECTORES

Dr. Fco. Javier Almendros González

Dr. Jesús M. Ibáñez Godoy

El Doctorando

Enrique Carmona Rodríguez

UNIVERSIDAD DE GRANADA - 2009

.

Editor: Editorial de la Universidad de Granada
Autor: Enrique Carmona Rodríguez
D.L.: GR. 3911-2009
ISBN: 978-84-692-7858-1

Enrique Carmona Rodríguez
Instituto Andaluz de Geofísica
Campus de Cartuja s/n.
Departamento de Física Teórica y del Cosmos
Universidad de Granada
e-mail: ecarmona@iag.ugr.es

A mi familia

AGRADECIMIENTOS

Nunca me imaginé, que después tantos y tantos años para terminar la Tesis, me iba a encontrar escribiendo los agradecimientos en el último suspiro de la noche,…. A mi lado y como siempre, trabajando incluso a estas horas intempestivas, Pepe y Teresa. Uff…como nos acordaremos los tres de esta noche, verdad? Yo para entregar mañana la Tesis y vosotros el informe del Ilustre Poeta. ÁNIMO ¡!.

Llevar tantos años con la Tesis (no diré cuantos, lo siento) lleva consigo conocer a muchísimas personas. Entre todas, unas con granitos de arena y otras con auténticas montañas han contribuido para que termine esta larga aventura.

Quiero agradecer en primer lugar a mis directores. A Jesús por confiar en mí durante muchos, muchos años. Me inició en el mundo de los terremotos y un poco más tarde permitió que me abriera un hueco entre los Volcanes y la Antártida. Sembró la semilla de mi Tesis que como una buena encina mediterránea fue creciendo muy lenta pero firme. Después cogió las riendas Javi, y se echó a cuestas la "Tesis" (espero que tu L5-S1 no se haya quejado mucho). Con su sabiduría y paciencia logró llevar a buen puerto el velero errante de mi Tesis. Pasaste de ser mi compañero y amigo a ser además, mi director de Tesis. Difícil combinación y sin embargo no he notado diferencia alguna. Javi, me harían falta muchas vidas para agradecerte todo lo que has hecho por mi. Gracias de todo corazón.

También quiero agradecer de una forma muy especial, a Pepe y Teresa. Me acogieron en su particular grupo y me enseñaron a mirar con gafas de geofísico lo que tenemos bajo nuestros pies. La frase que más me han dicho estos últimos meses ha sido,…."tú, a tu tesis". Gracias por dejarme trabajar en ella mientras vosotros sacabais adelante un montón de trabajos. Gracias por vuestro apoyo y cariño en todo momento.

Según el trabajo de Abril (2007) donde sugiere que los agradecimientos es lo único que se lee la gente, aprovecharé para decir de qué va mi Tesis,…hala ¡! Pues,..bueno, digamos de forma resumida que en la Tesis hemos trabajado con "familias", familias de terremotos, claro. Así me pasé mucho tiempo contestando cuando me preguntaban que de donde venía,…"pues de ver a mis familias". Luego, matizaba que les daba nombre, elegía su evento maestro y después al resto los localizábamos todo lo mejor que podíamos. Y mas cosas,…, pero si queréis saber más, a leer un poco la tesis, venga.

Las personas, al igual que los terremotos, se pueden agrupar en familias. Y en todo este tiempo tan dilatado que he estado con la Tesis, muchas han sido las familias me han ayudado.

La más destacada y la que ha estado siempre desde el principio ha sido mi *gran familia del IAG*. Tengo que agradecer a Benito su amistad incondicional; a mi tocayo Enrique su eficiencia y afecto; a Merche su simpatía; a Antonio Martos su paciencia; a Jose Manuel su espíritu revolucionario; a Javi Moreno su bondad; a Jaime su veteranía; a Antonio Benítez su naturalidad; a Pepe Morales sus consejos; a Gerardo sus conocimientos; a Paco Carrión su alegría y amistad; a Fede sus puntualizaciones geológicas; a Paco Vidal su ingenio; a Manolo Espinar sus historias andalusíes; a Esquivel su flamenco; a Alfonso sus consejos agrícolas; y a Juande sus saludos matinales. Y a los nuevos becarios Araceli, Guillermo, Rafael y Enrique les deseo que disfruten con la Tesis.

Al igual que ocurre con los terremotos, hay familias dentro de una gran familia. Es el caso de mi *familia de compañeros y amigos del IAG*. A la más bella Flor granaina, porque nunca dudaste de mi Tesis incluso cuando ni yo creía en ella. La Tesis avanzó porque tu sonrisa y tu ánimo estaba siempre presente; a Lorenzo, porque llevas conmigo desde siempre, porque vimos nuestro primer volcán desde el avión aunque luego resultara ser una nube y no el Teide, y por tenerte siempre a mi lado; a Mamen, mi compi del alma, por sentir tu cariño desde todos los rincones de Europa; a la più bella Luisa por hacer soleados todos días del año, *grazie por il tuo affetto*; a Inma, por ayudarme, defenderme, animarme, alentarme, …siempre, siempre, gracias morena; a Dani, por ser el "evento maestro" de esta gran familia y ayudarme en tantas y tantas cosas; al pinche pendejo Mauri por ser mi hermano incluso estando tan lejos; a Rosa, por tener ese corazón tan grande; a Elena, por ser una mujer valiente. Y a mi compi Miguel. Si no fuera porque has leído la Tesis antes que yo y porque sé que me tienes preparada una pregunta para el día de mi lectura, te diría lo que me acuerdo de ti en todo momento, lo mucho que te echo de menos, y la de veces que sueño despierto pensando que algún día te volveré a ver en laboratorio de electrónica del IAG explicándome como funciona el osciloscopio.

A la *famiglia Italiana*. Al personal del Osservatorio Vesuviano. Me acogieron en su regazo con *molto amore* cuando llegué a Napoli. A Francesca *mamma* Bianco, Mario Castellano, Super-Mario La Rocca, Danilo Galluzzo, Marcello Martini, Marco Capello; a Norma Damiano, mi *napoligranaina* preferida; a Lucia Zaccarelli que me enseño a cantar *Bella Ciao*; a Simona que me enseñó *il tramonto* de Stromboli; y por supuesto al gran *direttore d'orchestra*, Edoardo del Pezzo que me dio su apoyo desde mis primeros pasos.

A Gilberto, mi caro maestro, mi ejemplo a seguir. Gracias Gil, tenerte como amigo ha sido de lo más bonito que me ha pasado. A Daria, mi bimba guapa de ojos Mediterráneo por sentirme *felice* a su lado. A Luciano y Enzo, los *grandes ragazzos* del IGNV. A la ciudad de Napoli. A la música de Daniele Sepe.

A mi *familia de bollicaos antárticos.* A Rafa, mi gemelo madrileño,…, Migo, se puede acabar la Tesis ¡ Vamos¡! A Bea, que me vistes dar mis primeros pasos en el Observatorio y que aún estando lejos, siempre me he sentido muy cerca de ti; a mi querida Llanos, mi reina antártica; a Isabelilla por estar siempre ahí; a Juanto por ser como eres; A Alberto Caselli y Gabi, mis hermanos argentinos que me han dado siempre parte de su cariño. A todos los que la Antártida nos embrujó para seguir siendo jóvenes.

A la gran *familia del Museo de Ciencias*. A Alicia García, Ramón Ortiz, Alicia Felpeto, Martita, Mar, Orlandito y mi cariñosa Nieves, por tratarme siempre con ternura. Pero qué primores sois ¡!

A la *familia canaria* con Maria José Blanco y Carmen Romero. A *la familia almeriense* con Antonio Posadas y Paco Luzón. A todos, gracias por ayudarme cuando lo he necesitado.

A la *familia gaditana,*que curiosamente no la encontré en los cálidos carnavales sino en la fría Antártida. Y allí pude comprobar que son simpáticos y "apañaos" hasta fuera de su Cai ¡ Allí encontré a Manolo Berrocoso que me envolvió con su gran corazón antártico. Y conocí a gente estupenda, Alberto, Raúl, Cristina, Salamanca, Eva y Yolanda. Y hasta conocí un extremeño, ahora adoptado por la familia gaditana. Mi querido "sosio" Mariano, el gran *boss* del Tarantar.

Y fue allí, en la Antártida, concretamente en Isla Decepción y Livingston donde se fraguó la *gran familia antártica*. Sería injusto poner a unos y a otros no. Recuerdo con mucho cariño mi primera campaña en el verano austral de 1996, del 2001, del 2002 y la campaña del campamento temporal en el Continente Antártico. Y como no, el año que la Isla Decepción quiso darse a conocer un poco más y sacó su genio en el verano de 1999. Menudo susto. Gracias Isla Decepción por proporcionarnos datos para la Tesis. Gracias a los investigadores y al personal de las dos bases, a los marinos del Hespérides y las Palmas, y al personal del Ejército de Tierra. Conocer a tanta y tanta gente ha sido maravilloso. Para todos, un beso bien grande. Todos los que habéis estado allí, sabéis que tenéis un trocito de mi.

A mi *familia de Física.* A mi "hermano" Joaquín, Juanje, el Marqués y Jesús. A mi Lola, con su "que bonito es el amor", que si no es por ti todavía estaría peleándome con la Cuántica. A la peña Cocoroco.

A mi *familia de amigos de siempre*, que entre la tesis, los bebes y no tener móvil los tengo muy abandonados. A Lourdes, Servando, Jorge, Yolanda y Paqui. Gracias por estar siempre conmigo. Os debo muchas, muchas birras.

A esa *familia* compuesta por los que de corazón se alegran casi como yo de que por fin lea la Tesis. A Carlos Barceló, a Francesca Martini, a Fermín,…

A la *familia Almendros-Muñoz,* y sobre todo y de forma muy especial a Olga. Después de Puri quizás sea la persona que más ganas tenía de que acabara la Tesis. Ha sabido armarse

de paciencia con mis incursiones en su hogar y aguantar que Javi me dedicara muchísimo tiempo. Gracias, primor.

Quiero agradecer a mi *familia de toda la vida.* A mis padres, que desde siempre han estado oyendo la palabra Tesis y conforme pasaban los años muy prudentemente ya no me preguntaban por ella. Gracias por darme vuestro amor. A Mara, que cuidó de nuestros pequeños. A Toté que se que está y estará siempre a mi lado. Haces que me sienta la persona más afortunada del mundo. Gracias hermano.

Y dejo para el final a la familia más especial. Mi *familia del dia al dia.* Ésta se fue construyendo poco a poco. En un regreso antártico encontré una princesa en el desierto Chileno de Atacama. Con los años y con Granada envuelta en un manto blanco llegó una princesita con grandes ojos azules. Y dos años y medio más tarde, con la llegada del otoño apareció un "ángel" para quedarse también. Y formamos una familia ¡! Quiero agradecerte Puri tu paciencia, tu sacrificio y tu amor. Sin ti, esta Tesis hubiese tenido un principio pero no un final. Gracias, princesa. Por cierto, esta noche no me esperes despierta,…ah, que ya te lo imaginabas ¿?

Julia, con las preguntas propias de la edad, ha sido un revulsivo para terminar la Tesis. Con su curiosidad infantil preguntaba siempre que me iba "¿a donde vas Papi?", "a hacer la Tesis" le contestaba; "yo también quiero hacer la Tesis" decía. Y me quedaba un rato pensando," ufff, que me pilla……me tengo que dar prisa".

Me juré a mi mismo que iba a intentar hacer unos agradecimientos escuetos y que la euforia, el cansancio de la noche y la exaltación de la amistad los iba a controlar, pero me temo queno ha sido posible. Ya me lo vaticinaba mi amiga Flor. Lo que si está claro es que es muy tarde y tengo ya que parar aquí. Está a punto de amanecer y todavía me queda insertar algunas páginas. Pero sobre todo voy a dejar de escribir porque tengo la impresión de que va ser la primera vez en la historia de las Tesis Doctorales que los agradecimientos van a ser más largos que la propia Tesis. Así que buenas noches o… buenos días.

Gracias a todos por dejarme alcanzar un sueño. Mi sueño. El Sueño de todos ¡!

(por cierto, qué sueño tengo, zzz…..)

Instituto Andaluz de Geofísica
En Granada, a nueve de octubre de dos mil nueve.

Esta Tesis Doctoral ha sido elaborada gracias a las siguientes Instituciones de las que tuve su respaldo en todo momento,

- Instituto Andaluz de Geofísica. Universidad de Granada.
- Osservatorio Vesuviano. INGV. Napoli (Italia)
- Museo de Ciencias Naturales. Departamento de Volcanología. CSIC.
- Instituto Geográfico Nacional. Centro Geofísico de Canarias.
- Ejército de Tierra – Armada Española
- Istituto Nazionale di Geofisica e Vulcanologia. Pisa (Italia)

y parcialmente financiada por los siguientes proyectos:

- Volcanismo, sismicidad, magnetismo y geodinámica de las Shetland del Sur: Estaciones sísmicas en la BAE (Livingston), CICYT, ANT95-0994-C03-02.
- Sismicidad volcánica, local y regional del área de las Shetland del Sur y Estrecho de Bransfield (Antártida). ANT98-1111.
- Creación de una base de datos sísmicos de la Isla Decepción (Antártida). REN2000-2908-E.
- e-Ruption. A satellite telecommunication and Internet-based seimic monitoring system for volcanic eruption forecasting and risk Management. EU. EVRI-2001-00024.
- TOMODEC. Tomografía sísmica de alta resolución de la Isla Decepción (Antártida) y modelización de la fuente sismo-volcánica. REN2001-3833.
- Sismicidad volcánica del Teide: Tomografía de alta resolución usando datos sísmicos activos y pasivos. TOM-TEIDEVS. CGL2004-05744-C04-01.
- SIS-VOLTEDEC: Monitorización sismo-volcánica, estructura superficial y modelo cortical de la Isla Decepción (Antártida). CGL2005-05789-C03-02/ANT.
- VOLUME. UE, FP6-2004-Global-3-018471

RESUMEN

Uno de los retos de los estudios sismotectónicos de las series sísmicas es encontrar los planos de ruptura responsables de la ocurrencia de los terremotos y relacionar la tectónica local donde tienen lugar las series con la dinámica regional. La elaboración de mapas epicentrales de la serie de forma rutinaria lleva a veces a interpretaciones erróneas de las fallas implicadas en las series sísmicas. Para encontrar los sistemas de fractura activos y poder interpretar de forma fiable las estructuras geológicas locales, es necesario que los terremotos de la serie estén localizados de la manera más precisa que se pueda. Una de las herramientas más utilizadas para este fin es la localización relativa precisa de los hipocentros aprovechando que los terremotos de una serie sísmica se agrupan en familias por la similitud de las formas de onda. Estas localizaciones precisas pueden ajustarse a un plano que se interpreta como el plano de ruptura.

Se han analizado dos series sísmicas en Agrón (Granada) en 1988-1989 e Iznájar (Córdoba) en 1989 y una serie ocurrida en la isla Decepción (Antártida) en 1999. Las dos primeras series se encuentran en o cerca de la Cuenca de Granada y han sido registradas por Red Símica de Andalucía (RSA). La serie de Decepción, ocurrida en un ambiente volcánico, ha sido registrada con antenas sísmicas.

Para las tres series se ha realizado un análisis preliminar que consiste en obtener mapas de localización, estimar la energía implicada, caracterizar su evolución mediante histogramas temporales, y, en el caso de la serie de Decepción, distinguir y estudiar la sismicidad volcánica, con terremotos volcano-tectónicos (VT) e híbridos por un lado y con eventos de largo periodo (LP) y tremor volcánico por otro. En las tres zonas el análisis preliminar de la distribución de terremotos pone de manifiesto la presencia de alineamientos epicentrales aparentes, que quizás indiquen las direcciones de las fallas responsables de la sismicidad. Para resolver esta cuestión se han aplicado distintas técnicas con el objeto de obtener localizaciones hipocentrales precisas de al menos algunos de los terremotos de las series.

Se ha evaluado la similitud de las formas de onda de los terremotos de cada serie utilizando la correlación cruzada y se han agrupado en familias utilizando la técnica de *equivalencia de clases* con umbrales de correlación altos (~0.9). Se han obtenido un total de 5 familias para la serie de Agrón, 154 familias (74 dobletes, 34 tripletes y 46 multipletes) para Iznájar y 48 familias (19 dobletes, 9 tripletes y 20 multipletes) para Decepción.

Se ha elegido un evento maestro para cada familia, y se ha localizado de manera precisa cada uno de sus miembros respecto al evento maestro. Para las series de Agrón e Iznájar, registradas con una red sísmica, se ha empleado el método clásico, basado en determinar con precisión los tiempos de llegada relativos a partir de interpolaciones de la correlación cruzada entre cada terremoto y su correspondiente evento maestro. Para la serie de Decepción, registrada con antenas sísmicas, se ha elaborado un nuevo método que parte de la estimación precisa del vector lentitud aparente relativo de los eventos de las familias respecto a un evento maestro. Estas estimaciones, junto con las diferencias S-P, se utilizan para localizar espacialmente los hipocentros empleando el trazado del rayo. Este método ha sido ampliamente probado para entender su utilidad y asegurar su rendimiento, y promete ser una herramienta interesante para el análisis de eventos sismo-volcánicos registrados en antenas sísmicas.

Las localizaciones precisas de los terremotos de las familias de cada serie sísmica se han ajustado a un plano utilizando mínimos cuadrados. Para la serie de Agrón se han encontrado dos planos N-S, uno E-O, uno NE-SO y otro NO-SE. Para la serie de Iznájar se han obtenido ocho planos con azimut N-S y buzamiento casi vertical; cinco planos NNO-SSE, tres de ellos con poco buzamiento (dos con dirección de buzamiento ENE y uno con dirección OSO); y un plano con dirección E-O muy buzado. Esta información se ha combinado con los mecanismos focales obtenidos de la polaridad de las primeras llegadas de algunos terremotos de las familias para resolver la ambigüedad de los planos nodales y elegir una de las soluciones. Esta combinación ha proporcionado para la serie de Agrón dos soluciones de falla normal con direcciones NO-SE y ENE-OSO, y una tercera solución de salto en dirección sinistra con dirección N-S. Uno de los planos obtenidos y uno de los dos planos conjugados del terremoto principal están de acuerdo con la extensión regional ENE-OSO que actúa en el área. La proximidad observada de fallas con diversa orientación sugiere una fragmentación significativa de la corteza superior en bloques tectónicos pequeños. En la serie de Iznájar, la combinación ha permitido obtener seis soluciones de fallas de salto en dirección sinistra con azimut N-S, y tres soluciones de fallas normales con direcciones NO-SE a NNO-SSE y direcciones opuestas del buzamiento. Las fallas N-S de salto en dirección sinistra dominan en la dislocación, y representarían a la mayoría de las familias analizadas. La coexistencia de los restantes planos (fallas normales puras) sugiere una permutación de los ejes principales de esfuerzo, mayores e intermedios, producida probablemente por la perturbación del esfuerzo local en el transcurso del enjambre.

En la serie de Decepción, la mayoría de los planos calculados con el ajuste de las localizaciones relativas se orientan en dirección NO-SE, y los buzamientos varían entre 41 y 86º. Estas tendencias coinciden con algunos de los sistemas de fallas más importantes de la isla. El resto de azimutes de los planos tienen direcciones entre N120ºO y N170ºO, que también coinciden con otros alineamientos N-S y NE-SO. Las distribuciones de epicentros encontradas en el análisis preliminar y la relocalización muestran dos alineamientos aparentes con dirección NE-SO y ENE-OSO. Estas direcciones no coinciden con la mayoría de las obtenidas de la geometría de los planos de ruptura. Los planos de falla identificados se encuentran localizados en el límite de la cámara magmática situada bajo la bahía. Parece claro que una reactivación de la cámara magmática (en forma de una intrusión magmática profunda) desencadenaría un desequilibrio en la zona, sometida además a un campo de esfuerzos ligado a la tectónica del Estrecho de Bransfield. Los fluidos liberados por el magma podrían interaccionar con las fracturas, dando como resultado una disminución del esfuerzo normal sobre los planos de falla y facilitando el proceso de ruptura que generaría los terremotos volcano-tectónicos registrados.

Las estructuras sismogenéticas implicadas en las tres series no han coincidido del todo con los alineamientos epicentrales aparentes que se observan en la localización preliminar. Del mismo modo, los sistemas de fractura encontrados no coinciden del todo con las direcciones que se esperan a partir de la dinámica regional. Estos resultados ponen de manifiesto que la aplicación de técnicas de localización precisa para el estudio de series sísmicas es fundamental para obtener información sobre las fracturas implicadas y así interpretarlas en el marco de la tectónica local y regional.

ABSTRACT

One of the most challenging tasks of seismo-tectonic analyses of seismic swarms is finding the fracture planes responsible for the occurrence of earthquakes and relating local tectonics with regional dynamics. Preliminary epicentral maps sometimes lead to misinterpretations of the faults involved in the seismic series. In order to find the active fracture systems and obtain reliable interpretations of the local geological structures, the earthquakes must be located as precisely as possible. Among the most used tools for this purpose is the precise relative location of hypocenters, a technique that takes advantage of the waveform similarity displayed by groups of earthquakes within seismic series. The hypocenters obtained using precise locations usually distribute around a plane that can be interpreted as the rupture plane.

We analyzed two seismic swarms that took place in Agrón (Granada, Spain) in 1988-1989 and Iznájar (Córdoba, Spain) in 1989; and a series occurred at Deception Island (Antarctica) in 1999. The first two series are located in or near Granada Basin and have been recorded by the Andalusian Seismic Network (*Red Sismica de Andalucía*, RSA). The latter occurred in a volcanic environment, and has been registered with seismic arrays.

For the three swarms, we have carried out a preliminary analysis to obtain epicentral maps, estimate the energy involved, and understand the series evolution through time plots and histograms. In the case of the Deception swarm, we further identify and study the volcanic seismicity, with volcano-tectonic (VT) earthquakes and hybrids on the one hand, and long-period (LP) events and volcanic tremor on the other. In all three areas, the preliminary analysis of the earthquake distribution shows the presence of apparent epicentral alignments, that perhaps indicate the directions of the faults responsible for the seismicity. To solve this question, we have applied different techniques intended to obtain precise hypocentral locations for at least some of the earthquakes in the series.

We assessed the earthquake waveform similarity in each swarm using cross-correlation, and grouped the earthquakes into clusters or multiplets using the *equivalence of classes* technique with high correlation thresholds (~0.9). We have obtained a total of 5 clusters for the Agrón series; 154 clusters (74 doublets, 34 triplets and 46 multiplets) for the Iznájar series; and 48 clusters (19 doublets, 9 triplets and 20 multiplets) for the Deception Island series.

We have chosen a master event for each cluster. Every cluster member was then precisely located, relative to the master event. For the swarms of Agrón and Iznájar, recorded by a seismic network, we used the classical methodology based on the accurate determination of differential arrival times from interpolations of the cross-correlation function between each earthquake and its corresponding master event. For the swarm of Deception Island, recorded by seismic arrays, we have developed a new method that begins with precise estimates of the relative apparent slowness vectors of the events in relation to their master event. These estimates, along with the S-P delays, are used to spatially locate the hypocenters using a ray tracing procedure. This method has been extensively tested to understand its capabilities and limitations, and we anticipate very interesting results when applied to the analysis of seismo-volcanic events recorded by seismic arrays.

The precise locations of the multiplet earthquakes for each series have been adjusted to a plane using a least-squares fit. For the Agrón swarm we have found two N-S planes, one E-O, one NE-SW, and one NW-SE. For the Iznájar swarm we have obtained eight planes with N-S azimuths and nearly vertical dips; five NNW-SSE planes, three of them with small dips (two with dip directions ENE and one with dip direction WSW); and a subvertical, E-W plane. This information is combined with focal mechanisms calculated for some earthquakes from the polarity of the first motions to solve the ambiguity of the nodal planes and choose one of the solutions. For the Agrón series, this procedure provided two normal fault solutions with NW-SE and ENE-WSW strikes, and a left-lateral, N-S strike-slip fault solution. One of these planes and one of the main earthquake's conjugate planes agree with the ENE-WSW regional extension of the area. The close proximity of faults with different orientations suggests a significant fragmentation of the upper crust into small tectonic blocks. For the Iznájar series, we obtained six left-lateral, N-S strike-slip fault solutions, and three normal fault solutions with NW-SE to NNW-SSE trending faults and opposite dip directions. The N-S, left-lateral strike-slip mechanism is then the dominant dislocation in the Iznájar swarm, accounting for the largest events and the majority of multiplets analyzed. The co-existence of secondary, pure normal faults suggests a permutation of the largest and intermediate principal stresses, which could be produced by local stress perturbations during the course of the swarm.

In the Deceptions Island series, most of the planes calculated by fitting the relative locations are oriented NW-SE, with dips varying between 41 and 86º. These trends coincide

with some of the major fault systems of the Island. The remaining planes have azimuths between N120°W and N170°W, which coincide as well with other alignments N-S and NE-SW. The epicentral distributions found in the preliminary analysis and relocation display two apparent alignments with NE-SW and ENE-WSW directions. These directions do not match most of the fault strikes obtained from the geometry of the rupture planes. The fault planes imaged are located in the boundary of the magma chamber located beneath the bay. A reactivation of the magma chamber (in the form of a deep magma intrusion) would trigger an imbalance in the area, also subjected to a stress field linked to the tectonics of the Bransfield Strait. The fluids released by the magma could interact with the fractures, resulting in a decrease of normal stress on the fault planes and making them prone to the generation of volcano-tectonic earthquakes.

The seismogenetic structures involved in the three swarms do not generally coincide with the apparent epicentral alignments observed in the preliminary locations. Similarly, the fracture systems imaged do not always match the directions expected from regional dynamics. These results show that the application of precise location techniques for the study of seismic series is essential to obtain reliable information on the fractures involved, in order to interpret them in the framework of local and regional tectonics.

LISTADO DE PUBLICACIONES

El trabajo realizado en esta Tesis Doctoral ha permitido la publicación de los siguientes artículos. El orden de los mismos se ha dispuesto en función de su aparición en la presente memoria.

I. Spatial characterization of Agrón, southern Spain, 1988-1989 seismic series (2002). Saccorotti, G., Carmona, E., Ibáñez, J.M., Del Pezzo, E., *Phys. Earth Planet. Inter.,* **129**, 13-29. pág. 105

II. Multiplet focal mechanisms from polarities and relative locations: The Iznájar swarm South Spain. (2009). Carmona. E., Stich, D., Saccorotti, G., Ibáñez, J.M, *Bull. Seismol. Soc. Am.* **Vol. 99**, doi: 10.1785/0120090036 pág. 125

III. The 1998-1999 seismic series at Deception Island volcano, Antarctica (2003). Ibáñez, J.M., Carmona, E., Almendros, J., Saccorotti, G., Del Pezzo, E., Abril, M., Ortiz, R., *J. Volcan. Geotherm. Res.,* **128,** 65-88. pág. 137

IV. Precise determination of the relative wave propagation parameters of similar events using a small-aperture seismic array (2004), Almendros, J., Carmona, E., Ibáñez J.M., *J. Geophys. Res.,* **109,** 285-299. pág. 163

V. Characterization of fracture systems using precise array locations of earthquake multiplets: An example at Deception Island volcano, Antarctica (2009) Carmona, E., Almendros, J., Peña, J.A., Ibáñez, J.M., *Submitted to J. Geophys. Res* pág. 181

Se presenta el listado de otras publicaciones adicionales relacionadas de forma directa con el trabajo de esta Tesis para completar la información sobre las anomalías de velocidad y la sismicidad en la Isla Decepción. Estas publicaciones aparecerán al final de esta memoria como Anexo I y Anexo II. El orden de las mismas sigue la cronología de su publicación.

VI. Slowness anomalies from two dense seismic arrays at Deception Island Volcano, Antarctica. (2001). Saccorotti, G., Almendros, J., Carmona, E., Ibáñez, J.M., Del Pezzo, E. *Bull. Seismol. Soc. Am.,* **91,** 561-571.

VII. The recent seismo-volcanic activity at Deception Island volcano (2003). Ibáñez, J.M., Almendros, J., Carmona, E., Martínez-Arévalo, C., Abril, M., *Deep-Sea Res. II,* **50**, 1611-1629.

Además se enumeran otras publicaciones que se relacionan de forma indirecta con el trabajo de esta Tesis y en las que el autor de la presente memoria ha colaborado. Estas publicaciones no han sido incluidas en este trabajo de Tesis. El orden de las mismas sigue la cronología de su publicación.

VIII. Sismicidad volcánica, (2000). Ibáñez, J.M. y Carmona, E. *Curso Internacional de Volcanología y Geofísica Volcánica.* Astiz, M., García, A. (ed.). 269-282.
En esta publicación se describen los tipos de eventos volcánicos y su origen.

IX. Array analyses of volcanic earthquakes and tremor recorded at Las Cañadas caldera (Tenerife Island, Spain) during the 2004 seismic activation of Teide volcano (2007). Almendros, J., Ibañez, J.M., Carmona, E., Zandomenegui, D. *J. Volcanol. Geotherm. Res.,* **160,** 285-299.
En este trabajo se analiza la aparición de tremor volcánico registrado con arrays sísmicos en el volcán Teide en la activación sísmica de 2004 y la localización de terremotos.

X. Spatial analysis of the La Paca, SE Spain, 2005 seismic series through the relative location of multiplets and principal component analysis (2008). Ocaña, E., Stich, D., Carmona, E., Vidal, F., Bretón, M., Navarro, M., García-Jerez, A., *Phys. Earth Planet. Inter.,* **166,** 117-127.
La metodología empleada para la serie de Agrón (artículo I) se ha utilizado para la serie sísmica de la Paca (Murcia) en 2005 caracterizando los sistema de fractura implicados en la serie.

PREFACIO

El objetivo de esta Tesis es la caracterización de los sistemas de fractura de estructuras geológicas locales, utilizando como base de datos la ocurrencia de terremotos. Cuando muchos terremotos ocurren en un corto espacio de tiempo y en un área pequeña se les considera serie sísmica. Es muy frecuente que en las series sísmicas aparezcan terremotos con formas de onda muy similares. Estos terremotos se pueden localizar de manera precisa lo que nos permitirá determinar los planos de ruptura. La obtención de estos planos nos proporcionará la geometría, y en ocasiones la dinámica, de las fuentes que han generado los terremotos.

En este trabajo se ha estudiado dos áreas. La primera es una zona tectónica como la Depresión de Granada y zonas adyacentes, enmarcada en las Béticas y donde la tectónica regional a veces no coincide con los mecanismos fuente de terremotos locales. La segunda es una zona volcánica, la Isla Decepción, unos de los volcanes más activos de la Antártida y donde la tectónica regional de la zona interfiere en la actividad volcánica. Este estudio se ha realizado a través de tres series sísmicas ocurridas en Agrón (Granada) en el año 1988-89 e Iznájar (Córdoba) en 1998 y en la Isla Decepción en 1999.

Los resultados científicos obtenidos han permitido la publicación de 5 artículos en revistas enmarcadas en el *Science Citation Index*. Por tanto se ha estructurado la presente memoria de Tesis en base a estos trabajos científicos. Esta memoria de Tesis se ha dividido en tres partes. La **primera parte** consiste en un resumen en tres capítulos de los artículos mencionados anteriormente completado con el análisis previo de cada trabajo. La publicación en revistas científicas obliga a unos procesos de revisión que implican un elevado rigor científico de los artículos. Sin embargo el propio formato de las revistas científicas, sobre todo el espacio, obliga a resumir parte del trabajo y a ser muy conciso en la descripción de la motivación, la metodología, el análisis de los datos, etc. En esta primera parte se han añadido una serie de secciones enfocadas a encuadrar coherentemente todo el trabajo realizado.

El *capítulo 1* es una introducción del desarrollo de esta Tesis donde se indica de manera resumida los métodos utilizados y los pasos que se tienen que dar para llegar al objetivo de este trabajo, la caracterización de los planos de ruptura.

En el *capítulo 2* se presentan los resultados obtenidos para las series sísmicas de Agrón (Granada) ocurrida a finales de 1988 e Iznájar (Córdoba) que tuvo lugar en abril de 1998, situadas una en la Cuenca de Granada y otra en su límite más occidental. Estas dos series tienen características particulares que las hacen interesantes. La serie de Agrón ha sido la primera serie registrada con instrumentación digital por parte de la Red Sísmica de Andalucía (RSA). Además está situada en el centro del primer cinturón de la RSA, permitiendo una cobertura azimutal casi ideal. El análisis de esta serie está reflejado en el artículo *"Spatial characterization of Agron, southern Spain, 1988-1989 series"* publicado en la revista *Physics of the Earth and Planetary Interiors* en 2003. La serie de Iznájar, situada al Oeste de la Cuenca de Granada, ha sido la serie reciente en donde se ha registrado el mayor número de terremotos de las ocurridas hasta la fecha no sólo en la Cuenca de Granada sino en todo el Sur de la Península. La situación espacial de la serie respecto a las estaciones sísmicas de la RSA le confiere una mayor dificultad a la hora de realizar el análisis de los datos. El análisis de esta serie de Iznájar queda reflejado en el artículo *"Multiplet focal mechanisms from polarities and relative locations: The Iznajar swarm, South Spain"* aceptado en la revista *Bulletin of the Seismological Society of America* y que será publicado en diciembre de este año 2009.

En el *capítulo 3* se presentan los resultados del análisis en un ambiente volcánico partiendo de una serie sismo-volcánica ocurrida en la Isla Decepción en 1999. Esta serie introduce la diferencia, frente a las dos series anteriores, de que ha sido registrada con *arrays* o antenas sísmicas en una zona volcánica. Eso hace necesario crear nuevas métodos de localización precisa para aplicarlos con esta configuración de instrumentos, puesto que hasta este momento no se disponían de tales técnicas. De esta forma se ha elaborado una nueva herramienta para obtener localizaciones precisas utilizando técnicas de antenas sísmicas y para estimar su posterior ajuste a un plano. Dada la importancia de la utilización de las antenas sísmicas en áreas volcánicas, este nuevo método es un avance significativo en el estudio de la fuente sismovolcánica que nos permite la caracterización de los sistemas de fractura utilizando como única herramienta de registro un solo array sísmico. Este capítulo se basa en los artículos *"The 1998-1999 seismic series at Deception Island volcano, Antarctica"* publicado en la revista *Journal of Volcanology and Geothermal Research* en 2003, donde se analiza la serie mencionada anteriormente; "*Precise determination of the relative wave propagation parameters of similar events using a small-aperture seismic array"* publicado en la revista *Journal of Geophysical Research* en 2004, donde se propone un método (RelSE) para determinar con precisión el vector lentitud aparente relativo de eventos con similar forma de onda registrados en antenas sísmicas; y por último

"*Characterization of fracture systems using precise array locations of earthquake multiplets: An example at Deception Island volcano, Antarctica"* enviado a la revista *Journal of Geophysical Research*, donde se propone un método que, partiendo del método RelSE, permite la caracterización de los sistemas de fractura para terremotos volcano-tectónicos registrados por una antena sísmica.

La **segunda parte** consta de los artículos con el formato original de las revistas en las que han sido o van a ser publicados y que han sido enumerados anteriormente.

En la **tercera parte** se enumeran de forma esquemática las conclusiones de la memoria de esta Tesis junto con trabajos futuros que podrían abordarse después de este trabajo.

Al final de la memoria, como Anexos, se incluyen dos publicaciones que, por su relación directa con este trabajo de Tesis, son un complemento adicional para la comprensión del tercer capítulo de esta memoria. Las dos publicaciones están vinculadas a la Isla Decepción, donde el autor de esta Memoria de Tesis ha estado muy involucrado en varios proyectos de investigación relacionados con la Isla. Uno es el artículo "*Slowness anomalies from two dense seismic arrays at Deception Island Volcano, Antarctica"*, publicada en la revista *Bulletin of the Seismological Society of America,* en 2001, que pone de manifiesto las anomalías de velocidad encontradas en los emplazamientos en las dos antenas sísmicas desplegadas durante la serie de 1999. Y el otro es el artículo "*The recent seismo-volcanic activity at Deception Island volcano"* publicado en 2003 en la revista *Deep-Sea Research II* en un volumen especial sobre la Isla Decepción. En este trabajo se analiza la sismicidad de la Isla Decepción hasta el año de la serie de 1999 y se propone un modelo de fuente para explicar dicha serie.

Las referencias a los artículos en la primera parte de esta tesis se harán entre paréntesis indicando el artículo en números romanos (según el listado de la página xvii), por ejemplo *(art.III)*. Para las figuras obtenidas de los artículos, en el pie de figura se pondrá el número de figura que le corresponda junto con una referencia entre paréntesis a la figura de artículo correspondiente, por ejemplo *Figura 2.3 (art.III fig.4)*.

Algunas palabras inglesas, por no encontrar una traducción satisfactoria, se han dejado en su lenguaje original en modo cursiva. Sin embargo, otras se ha decidido traducirlas al castellano debido a que ya forman parte del lenguaje utilizado en nuestro campo de investigación, como por ejemplo la palabra *array* como "antena" o la palabra *cluster* como "familia", o *multiplet* como "multiplete".

ÍNDICE

PRIMERA PARTE

1. Introducción
2. Caracterización de sistemas de fractura con redes sísmicas
3. Caracterización de sistemas de fractura con antenas sísmicas

1

Introducción

El estudio en detalle de las estructuras geológicas responsables de la actividad sísmica es un reto en el que se está trabajando en los últimos años de manera continuada y cuyos progresos están asociados al avance en la calidad de los datos y a la introducción de nuevas técnicas de análisis. En el caso de pequeñas estructuras, responsables de la actividad local con generación de terremotos de baja magnitud, la complejidad del estudio se incrementa precisamente por la baja energía de estas señales sísmicas. Sin embargo es necesario investigar qué ocurre a nivel local para entender los modelos en un marco tectónico y geodinámico más amplio. En general el problema de la baja energía está siempre presente en regiones volcánicas donde además la ocurrencia de señales sísmicas es variada y de diferente origen, lo que complica el análisis y la interpretación de los datos. En cualquier caso, el estudio deberá basarse en conocer con la mayor precisión posible dónde ocurren estos terremotos y su relación con las estructuras geológicas de la zona.

Una de las herramientas más utilizadas para realizar modelos de sismotectónica local es la determinación de los planos de ruptura implicados en la generación de los terremotos. Para encontrar estos planos y que sean representativos de un área concreta es necesario el uso de un número suficiente de terremotos generados en esa zona. En regiones tectónicas y volcánicas sísmicamente activas, los terremotos suelen agruparse espacial y temporalmente (Torcal, 1998). Cuando estas agrupaciones ocurren en cortos espacios de tiempo (días o

meses) y en áreas locales pequeñas (pocos km^2) se habla de series sísmicas. Mogi (1963) propuso una clasificación de las series en tres tipos en función de la forma de producirse el desarrollo de los terremotos (Udías y Mezcua, 1986):

a. Serie *Tipo I*, el terremoto principal es el primero en ocurrir sin que se produzcan ningunos precursores. Los materiales donde ocurren este tipo de series son muy homogéneos y donde los esfuerzos acumulados no se liberan hasta que se exceden las resistencias de las rocas, produciéndose el terremoto principal.

b. Serie *Tipo II,* aparecen primero los precursores que aumentan rápidamente antes del terremoto principal. Los materiales heterogéneos con distintas resistencias hacen que los esfuerzos acumulados se vayan relajando en forma de terremotos pequeños (precursores) hasta la aparición del terremoto principal.

c. Serie *Tipo III*, la ocurrencia de los terremotos sucede sin un terremoto principal que destaque en magnitud de forma considerable sobre los demás. A este tipo de serie se le llama también enjambre sísmico. Los enjambres ocurren en zonas con materiales muy heterogéneos y con una distribución de esfuerzos poco uniforme y muy concentrada.

El estudio de las series de terremotos tiene mucha importancia para la caracterización de los sistemas de fractura de las zonas en las que han tenido lugar. Nuestra comprensión de la relación entre series y fracturas ha evolucionado desde los primeros estudios. Desde considerarse que las series están asociadas a un solo plano (Richter, 1958), a considerarse que las series se originan en planos distintos que contienen heterogeneidades en forma de asperezas (Kanamori, 1977) y de barreras (Aki 1984), o asociadas estructuras tridimensionales (Bollinger y Langer, 1986; Madariaga *et al.* 1998) e incluso geometrías fractales (Turcotte, 1989; Posadas *et al.* 1996). Todos estos estudios ponen de manifiesto que cuando tiene lugar una serie o enjambre sísmico, no solo se activa a un plano principal sino que pueden aparecer planos secundarios (Michelini y Bolt, 1986; Fehler *et al.* 1987; Posadas, 1991). Generalmente cuando se producen un gran número de microterremotos, éstos se distribuyen espacialmente ensanchando el sistema de fracturas principal activado probablemente por los terremotos de mayor magnitud, provocando una red de fracturas mas pequeñas (Posadas, 1991).

El primer paso que se realiza con la aparición de una serie sísmica es un análisis preliminar para obtener información sobre sus características más generales y globales para responder a preguntas básicas como ¿qué tipo de serie es?, ¿cuantos eventos sísmicos tiene? ¿dónde ha tenido lugar?, ¿qué energía está implicada? Y en el caso de una serie sismo-volcánica ¿qué tipo de eventos sísmicos aparecen? Por regla general estas cuestiones se responden mediante un análisis que suele constar de una localización preliminar (absoluta) de aquellos terremotos que se puedan localizar, un conteo de todos los eventos para estimar

el número total de terremotos implicados en la serie, una caracterización preliminar de la energía implicada a través de gráficas de magnitud frente al tiempo, histogramas del número de terremotos por día para ver la evolución temporal de la serie y mapas epicentrales secuenciales con ventanas temporales para ver la evolución espacial, por si existen desplazamientos de las fuentes sísmicas. Dentro de este análisis preliminar, a veces se utilizan otros métodos para mejorar la localización absoluta de la serie. Por ejemplo tenemos la localización probabilística basada en el teorema de Bayes (Tarantola y Valette, 1982; Moser *et al.* 1992; Wittinher *et al.* 1993; Saccorotti *et al.* 1998), que permite calcular áreas de máxima probabilidad de la localización. Otro método que se puede utilizar es el método de las componentes principales para obtener los buzamientos y azimutes de los planos principales de ruptura (Michelini y Boltz, 1986; Posadas *et al*. 1993). Este método permite caracterizar geométricamente el plano de ruptura buscando los elipsoides que se ajustan de manera óptima a los hipocentros de las familias, escoge los más aplanados y obtiene sus direcciones predominantes. Los planos determinados por estos elipsoides están relacionados con los planos de las fracturas ligadas a los terremotos (Posadas, 1991). Pero estos planos se calculan teniendo en cuenta la cercanía entre sí de los hipocentros, y están sujetos a la necesidad de una correcta localización. Estos análisis rutinarios para las series nos proporcionan una visión de cómo se ha comportado la serie. Todo esto sería un punto de partida para realizar posteriormente un estudio más detallado.

Para la localización espacial y temporal preliminar se pueden usar varias técnicas en función de la instrumentación utilizada. En zonas tectónicas el método más empleado es la localización usando redes sísmicas. En zonas volcánicas, además de la localización con redes se está extendiendo el uso de las antenas sísmicas. La ventaja de las antenas sísmicas consiste en que el muestreo espacio-temporal del campo de onda que realizan nos permite analizar y localizar señales volcánicas caracterizadas por la ausencia de fases claras, como por ejemplo el tremor volcánico o los eventos de largo periodo (LP), además de los microterremotos volcano-tectónicos (VT).

Las técnicas de localización clásicas o con redes sísmicas se llevan a cabo en la mayoría de los centros de registro sísmico. Tienen su origen en los trabajos de Geiger (1912), quien plantea el problema de la localización de los eventos como lineal (cuando en realidad no lo es). Se utilizan métodos iterativos sobre pequeñas variaciones de las localizaciones reales. Las coordenadas hipocentrales junto con el tiempo origen se van modificando iterativamente hasta que hay una solución que satisface las condiciones impuestas. Estas localizaciones son muy sensibles al modelo de velocidad empleado, y la utilización generalizada de los modelos unidimensionales implica no tener en cuenta las variaciones laterales de velocidad.

Las técnicas de localización con antenas sísmicas se utilizan de manera distinta. Las redes símicas tienen distancias entre estaciones de decenas de kilómetros, y se asume que la fuente sísmica se localiza en el interior de la red. Por el contrario, las distancias entre

estaciones de las antenas sísmicas de pequeña apertura (como las empleadas generalmente en zonas volcánicas) son de decenas de metros, y se asume que la fuente es lo suficientemente lejana como para suponer que los frentes de onda incidentes son planos.(Abril e Ibáñez, 2000). Por tanto las técnicas empleadas para localizar se basan en la caracterización del frente de onda que atraviesa la antena sísmica, buscando la máxima coherencia de la señal entre las distintas estaciones. Este análisis nos proporcionará el azimut de donde procede el frente de onda (*back-azimuth)* y la velocidad aparente con que atraviesa la antena sísmica (Figura 1.1). Si estos dos parámetros se combinan con las diferencias de tiempos entre las fases P y S (en caso de que sean terremotos) y se aplica la técnica del trazado del rayo, entonces podremos determinar la posición del foco de estos terremotos.

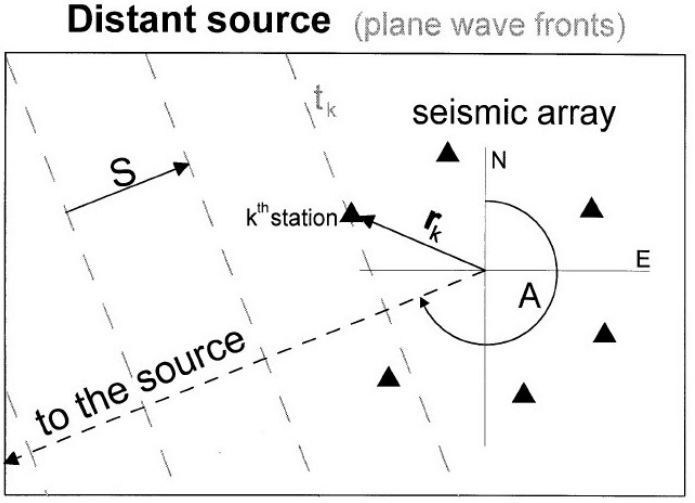

Figura 1.1. Esquema del avance de un frente de onda plano al atravesar una antena sísmica. Los triángulo negros indican la posición de las estaciones, $\mathbf{r}_k$ es el vector de posición de la estación k, A es el *back-azimuth* hacia la fuente y S la lentitud aparente (de Almendros *et al*. 1999)

Es evidente que las localizaciones sísmicas, obtenidas con cualquiera de las técnicas de antenas o redes sísmicas, tienen asociadas un cierto nivel de incertidumbre que se debe a distintos factores. Algunos de estos están relacionados con la metodología empleada. Por ejemplo para las antenas sísmicas hay un error introducido por la aproximación del frente de onda de la señal a un frente plano, la configuración de las estaciones de la antena sísmica, y el espaciado de la malla de lentitud aparente utilizado. Para las redes sísmicas, hay errores que vienen por la incertidumbre en la determinación de las fases, errores en la posición de las estaciones, etc. Además se debe tener en cuenta que en ambos casos (redes y antenas sísmicas) encontramos factores como las heterogeneidades laterales de la estructura de velocidad (que normalmente no se tienen), modelo de velocidad, la presencia de ruido sísmico, efectos de sitio, etc. En general, los intervalos de incertidumbre de las

localizaciones son relativamente grandes, lo que se traduce en localizaciones hipocentrales poco precisas que son útiles para un análisis preliminar pero no para poder relacionar la sismicidad con las posibles estructuras que la originan.

Para intentar localizar de manera más precisa los hipocentros se han desarrollado diferentes técnicas que permiten reducir los efectos de las fuentes de error descritas. Ocaña (2009) realiza un resumen de estas técnicas, entre las que se encuentra la *determinación conjunta de hipocentros* (JHD) (Douglas, 1967; Frohlich, 1979; Pujol, 1988) que reduce los errores del modelo debido a anomalías en velocidad localizadas justo debajo del emplazamiento de la estación. Otro método utilizado es el uso de *términos de estación específicos de la fuente* (SSST) (Richard-Dinger y Shearer, 2000; Lin y Shearer, 2005) que reduce los errores del modelo debidos a anomalías en cualquier parte entre la zona fuente y la estación, calculando un factor correctivo para cada evento, cada fase y cada estación. También se encuentra el *método de la doble diferencia* (DD) (Waldhauser y Ellsworth, 2000, Ruiz *et al*. 2006a,b; Santoyo y Luzón, 2008) que permite localizar simultáneamente eventos de una región minimizando las diferencias de los residuos de los tiempos de viaje para parejas de terremotos a una determinada estación mediante el ajuste del vector diferencia entre sus hipocentros. Sin embargo, la que más se utiliza para localizar de forma precisa los terremotos es la *localización relativa* de unos eventos respecto a otro evento con forma de onda parecida. La localización relativa se ha aplicado en regiones tectónicas y volcánicas. En zonas tectónicas se utiliza principalmente para obtener información sobre el plano de ruptura cuando no se pueden calcular mecanismos focales, por ejemplo para el análisis de series de microterremotos (Deichmann y García-Fernández 1992; Stich *et al*. 2001; Saccorotti *et al*. 2002; Scarfi *et al.* 2003; Massa *et al*. 2006; Ruiz *et al*. 2006; Ocaña *et al*. 2008). Recientemente, se ha aplicado el método de localización relativa para el estudio del tremor no volcánico (Shelly *et al*. 2009). En regiones volcánicas, la localización relativa proporciona información sobre distribución de los hipocentros de los terremotos VT y permite definir con detalle la extensión y la geometría del sistema magmático activo (Fremont y Malone 1987; Gillard *et al.* 1996; Jones, *et al.* 2001; Musumeci *et al*. 2002; Alparone y Gambino, 2003; Brancato y Gresta, 2003; Battaglia *et al*. 2004; Hensh, *et al*. 2008). También se ha aplicado al análisis de los cambios temporales que ocurren en los volcanes como resultado de la dinámica interna y los movimientos de magma (Ratdomopurbo y Poupinet 1995; Snieder y Hagerty 2004; Pandolfi *et al*. 2006; Carmona *et al*. 2008; Martini *et al*. 2009).

Las series sísmicas están caracterizadas a menudo por la ocurrencia de grupos de terremotos con formas de onda similares, que se llaman comúnmente multipletes o familias. (Figura 1.2). Esta similitud se interpreta en base a que los terremotos se originan en el mismo plano de falla con el mismo mecanismo de fuente (Tsujiura 1983; Geller y Muller 1980). Si no se cumpliera esta hipótesis, las diferencias en el mecanismo provocarían variaciones en

las formas de onda. Además, las fuentes deben ser cercanas para que el camino de propagación a través de las heterogeneidades del medio sea el mismo para todos los terremotos (Deichmann y García-Fernández, 1992; Maurer y Deichmann, 1995; Poupinet *et al.* 1996). En caso contrario, habría diferencias importantes en los tiempos S-P, efectos de camino distintos, cambios en el contenido de frecuencias, etc. Según algunos trabajos para el estudio de la coherencia entre las formas de onda, la condición para que los terremotos sean similares es que la distancia entre sus hipocentros sea menor que un cuarto de la longitud de onda dominante (Geller y Mueller, 1980). Pero trabajos más recientes indican que es posible obtener altas similitudes de las forma de onda para distancias hipocentrales de varias veces la longitud de onda (Harris, 1991; Aster y Scott, 1993).

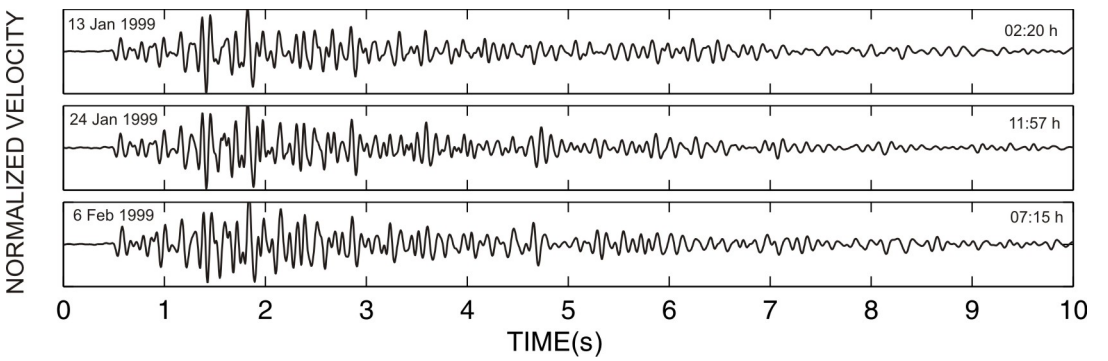

Figura 1.2. Ejemplo de terremotos con formas de onda similares de la serie de la Isla Decepción.

La identificación de terremotos similares se basa en la comparación de los sismogramas registrados en una estación de referencia. Actualmente se han desarrollado distintos tipos de algoritmos, como los "patrones de reconocimiento" (Joswig, 1995), los "patrones sintéticos" (Zhizhin *et al.* 1994), los que utilizan una aproximación fractal (Smalley *et al.* 1987). Pero el que se sigue empleando con más frecuencia es el análisis de la correlación cruzada de las formas de onda entre pares de eventos (p.ej. Mezcua y Rueda, 1994; Shearer, 1997; Stich *et al*. 2001; Kraft *et al*. 2006; Ruiz *et al.* 2006a; Ocaña *et al.* 2008).

Para buscar los eventos con formas de onda similares en las series incluidas en este trabajo de Tesis, se ha utilizado el análisis de la correlación cruzada en el dominio del tiempo. Este análisis se lleva a cabo entre todas las parejas de terremotos, obteniendo como medida de similitud el máximo de la función de correlación cruzada. Se realiza con ventanas de análisis con un mínimo de entre dos y tres ciclos de señal para las fases P y S. Para comparar las formas de onda se suelen utilizar los sismogramas de la estación más cercana a la serie, que suele tener la mejor relación señal-ruido. Este proceso nos proporciona una

estimación de cuánto se parecen las formas de onda, para las dos fases P y S, obteniéndose dos matrices con los máximos de la función de correlación (Figura 1.3)

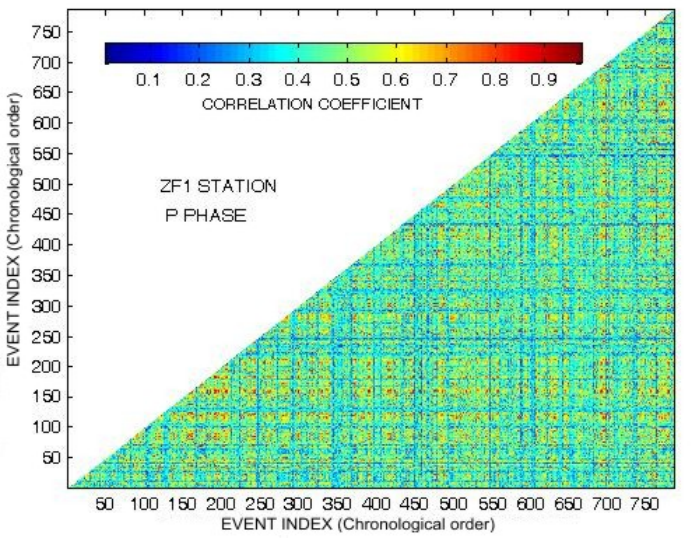

Figura 1.3. Matriz de correlación para la fase P de los terremotos de la serie de Decepción.

Una vez que se tiene una estimación de la similitud de la forma de onda de los terremotos, se procede a agruparlos. Si la serie es pequeña en número de terremotos, se puede hacer de manera visual (Ito, 1985; Augliera *et al.* 1995). Pero si el volumen de terremotos es grande es necesario utilizar algún algoritmo de clasificación. A partir de los resultados de la correlación cruzada, existen varias formas de agrupación, por ejemplo la *agrupación jerárquica* (Kraft *et al.* 2006) donde las agrupaciones se realizan en estructuras en forma de árbol, o el método de *equivalencia de clases* propuesto por Press *et al*. (1988) y adaptado por Aster y Scott (1993) para considerar la conexión entre parejas de eventos que tengan uno de ellos en común. Esta última forma de agrupar los eventos deja los grupos abiertos y se podría dar el caso de que el evento A sea similar al evento B y que B sea similar al evento C pero que A y C no tengan buena similitud de forma de onda, lo que provocaría grandes grupos de eventos conteniendo a otros grupos con mejor similitud en la forma de onda. Para evitar este problema, Maurer y Deichmann (1995) incorporaron una nueva condición de equivalencia para asegurarnos una asociación más robusta y evitar el problema del "evento puente" entre dos pares de terremotos. Además de los dos umbrales de correlación para la onda P y S se introduce un tercer umbral que es el producto escalar normalizado de las filas de la matriz de correlación. De esta forma nos aseguramos que los elementos de una misma familia cumplen entre ellos las condiciones descritas anteriormente,

favoreciendo una buena similitud de la forma de onda entre los eventos de una misma familia (Figura 1.2, 1.4)

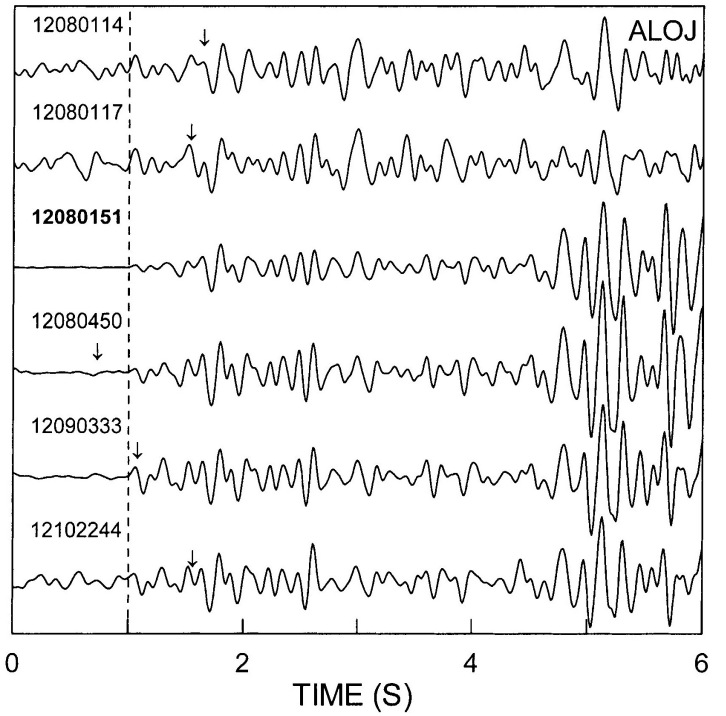

Figura 1.4 *(art. I fig. 8b)* Ejemplo de los sismogramas de una familia de la serie de Agrón para las estación ALOJ. La línea discontinua indica el alineamiento de la onda P de las trazas una vez utilizado el ajuste de tiempos respecto del evento maestro (en negrilla). Las flechas marcan las lecturas visuales sobre el sismograma dado por el análisis preliminar.

Para la búsqueda de familias de las series de Iznájar y Decepción, se ha utilizado el método de equivalencia de clases con los criterios de Maurer y Deichmann (1995) para las fases P y S. Para la serie de Agrón, debido a la falta de claridad en la fase S se tomó solo el umbral de la fase P. En cualquier caso, los umbrales que se han utilizado para los terremotos de las tres series analizadas han sido muy altos del orden de 0.9.

Como ya se ha comentado, la localización preliminar que se realiza a una serie no es suficiente para tener una localización de los hipocentros precisa debido principalmente a los errores sistemáticos que se pueden tener al realizar las lecturas de las fases en terremotos de baja magnitud. La Figura 1.4 muestra un ejemplo comparativo entre las lecturas visuales y las proporcionadas por la correlación. Este problema se puede resolver si dentro de una familia se localizan los terremotos respecto de uno de ellos que tenga una garantía de que tiene fases claras y por tanto su localización absoluta no tiene grandes errores. Esta forma de

localizar los terremotos de una misma familia respecto a un evento pertenecientemente a esa familia se conoce como "localización relativa con evento maestro".

En trabajos de localización relativa donde se han realizado pruebas tomando diferentes eventos maestros se ha podido comprobar que la elección no afecta a los resultados finales, incluso mantienen la orientación espacial de los hipocentros (Lees, 1998). Sin embargo, debido al hecho de localizar el resto de miembros de la familia respecto del evento maestro, es aconsejable que su elección cumpla algunos criterios básicos. Ocaña (2009) hace un resumen de los métodos más empleados para la elección del evento maestro. Por ejemplo se pueden citar la mejor relación señal-ruido (Moriya *et al.* 2003), el que tenga una magnitud intermedia para que sea lo más parecido posible al resto (Delacou *et al.* 2005), el de mayor magnitud (Kraft *et al.* 2006), el que tenga la mayor similitud con respecto el resto de miembros (Scarfi *et al.* 2003), el evento que contenga las llegadas de la fase P más claras (Nishigami, 1987) o aquel que haya sido registrado por el mayor número de estaciones (Ocaña *et al.* 2008).

En el análisis de las series de Agrón e Iznájar, se ha optado por elegir el evento maestro con éste último criterio, aquel que esté registrado en el mayor número de estaciones. De este modo se asegura un mayor número de lecturas y por tanto una localización absoluta del evento maestro aceptable. Para la serie de Decepción, el criterio ha sido escoger aquel terremoto que tenga una mayor relación señal-ruido, asegurándonos una mejor localización absoluta con las técnicas de antenas sísmicas.

Para la localización precisa relativa es necesario estimar las diferencias entre el evento maestro y el resto de los miembros de la familia. Estas diferencias son los tiempos de retraso entre terremotos en cada estación. En el caso de utilizar redes sísmicas estos retrasos se emplean para calcular la posición relativa. En el caso de las antenas sísmicas los retrasos se emplean para calcular el vector lentitud aparente relativo, que posteriormente se utiliza para calcular la posición relativa. En cualquiera de los dos casos, estas diferencias obedecen a las pequeñas diferencias entre la posición hipocentral del evento maestro respecto al terremoto que se compara.

Para estimar las diferencias de tiempos de llegada, se pueden emplear distintas técnicas en el dominio del tiempo o en el dominio de la frecuencia. En el dominio del tiempo se emplea la determinación del máximo de la correlación cruzada (p.ej. Stich *et al*. 2001; Kraft *et al*. 2006; Ruiz *et al.* 2006a; Ocaña *et al.* 2008). En el dominio de la frecuencia, se emplea el cálculo de la pendiente de la fase del espectro cruzado (p. ej. Poupinet *et al*. 1984; Ito, 1985,1990; Fremont y Malone, 1987; Got *et al*. 1994; Lees, 1998). La elección de un método u otro depende del contenido en frecuencias de las señales y la razón señal-ruido. En general, puesto que la coherencia depende de la presencia de ruido y decae más rápidamente para frecuencias más altas, el método del espectro cruzado suministra mejores resultados para las señales de baja frecuencia con relación señal-ruido alta. Por el contrario, el método de la

correlación cruzada es más estable y robusto en situaciones donde las señales tienen mucho ruido (Augliera *et al.* 1995; Cattaneo *et al.* 1997). En este trabajo de Tesis, se ha utilizado la correlación cruzada para estimar las diferencias de tiempo entre el evento maestro y el resto de los miembros, porque las señales registradas de las tres series son de baja magnitud y por tanto su relación señal-ruido es baja.

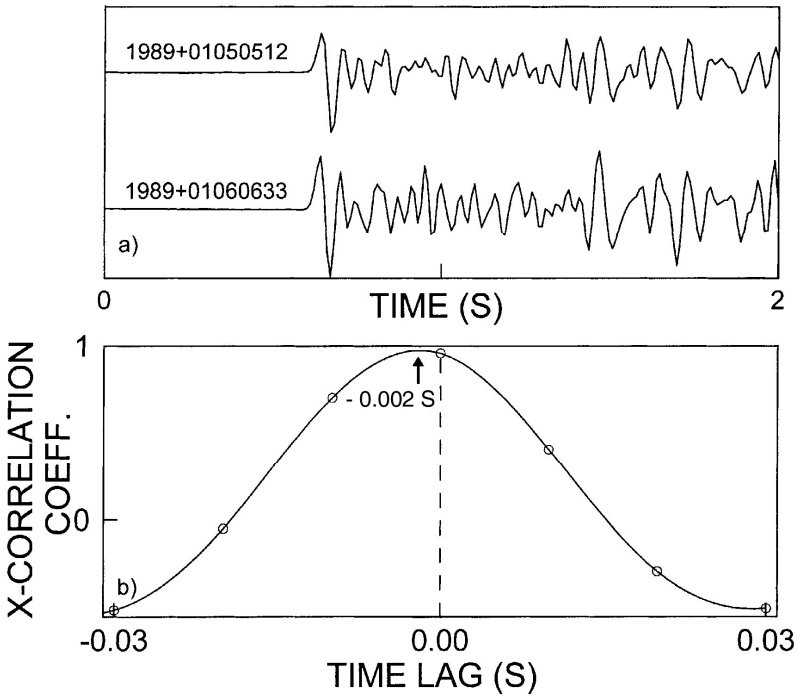

Figura 1.5 *(art. 1 fig.7)*. Ejemplo de la correlación cruzada entre dos terremotos de la serie de Agrón. Los dos eventos se han alineado utilizando la máxima correlación (arriba). Los círculos representan la función de correlación con el intervalo de muestreo de los sismogramas. La línea continua representa la interpolación con *spline* de la función de correlación cruzada. La flecha indica el máximo de la función interpolada.

Para el análisis con redes sísmicas, las diferencias de los tiempos de llegada se calculan correlacionando las formas de onda de las fases P y S del evento maestro con cada uno de los miembros de la familia para cada estación. El parecido de las formas de onda hace que podamos determinar los retrasos con una precisión superior al intervalo de muestreo. Para ello se ha utilizado una función de interpolación (interpolador cúbico *spline)* para aumentar el muestreo (Figura 1.5). Para tener un control de calidad, se elige un umbral mínimo de correlación. Aquellos retrasos entre eventos cuya correlación no superen el umbral se

desestiman para la localización relativa. Al final se obtienen las diferencias de tiempo del evento maestro con el resto de miembros de la familia para cada estación y cada fase P y S en función de la máxima correlación. Basándose en las hipótesis de partida de que la distancia entre hipocentros es pequeña en comparación con la distancia hipocentro-estación, se puede resolver el problema de la localización mediante una aproximación lineal, lo que implica que los rayos de salida fuente-estación del evento maestro y del resto de la familia se consideran paralelos. Este hecho simplifica los cálculos y permite establecer unas ecuaciones que relacionan los tiempos de llegada a las estaciones, los parámetros del terremoto (coordenadas hipocentrales y tiempo origen) y el modelo de velocidad. Para resolver este problema inverso se puede realizar un proceso iterativo que busca el hipocentro dentro de una malla hasta alcanzar una solución óptima que ajuste el modelo y los datos observados. Para la búsqueda de esta solución óptima se pueden minimizar algunos de los estimadores clásicos, como la norma L1 (suma de los residuos absolutos), más estable para residuos grandes, o la norma L2 (suma de los cuadrados de los residuos), más fácil de emplear. Al final se han obtenido unas localizaciones hipocentrales precisas de cada uno de los eventos de las familias respecto al evento maestro.

Para el análisis con antenas sísmicas se busca en primer lugar estimar de manera precisa el vector lentitud aparente. Existen varios métodos para estimar el vector lentitud aparente, por ejemplo la correlación cruzada promedio, *beam-forming*, MUSIC, etc. Todos ellos tratan de ajustar las formas de onda registradas de manera que se correspondan con la llegada de un frente de onda. Sin embargo, los efectos locales hacen que las formas de onda de un mismo terremoto varíen entre estaciones de la misma antena sísmica (Figura 1.6). Esto reduce considerablemente la precisión con la que se pueden medir los retrasos y por tanto aumenta la incertidumbre asociada con la estimación del vector lentitud aparente.

Durante el análisis de la serie sísmica de Decepción, se ha encontrado que los registros de los terremotos de una familia obtenidos en una estación son más parecidos entre sí que los registros de un solo terremoto en las estaciones de la antena sísmica (Figura 1.6). Esta observación es fundamental y sugiere que podemos obtener el retraso entre las llegadas de dos terremotos a una misma estación con más precisión que el retraso entre las llegadas de un terremoto a dos estaciones de la antena sísmica. Partiendo de esta premisa, se ha desarrollado en esta Tesis una técnica que permite localizaciones relativas de microterremotos de forma precisa, basándonos en un método novedoso de estimación precisa del vector lentitud aparente relativo (RelSE) de un terremoto respecto a un evento maestro de la misma familia.

En general, el retraso medido en cada estación entre el evento maestro y el resto de los miembros de cada multiplete se debe a varios factores. El primero es obviamente la diferencia en los tiempos origen de los terremotos. Esta diferencia se puede eliminar alineando las llegadas de la fase P, lo que equivale a suponer que los eventos de cada familia

ocurren simultáneamente en el tiempo. El segundo factor es la propagación de las ondas al atravesar la antena sísmica. La configuración de las estaciones de la antena genera unos retrasos adicionales que en primera aproximación se calculan utilizando el vector lentitud aparente del evento maestro. Esto implica asumir que las fuentes de todos los terremotos de la familia están localizadas en el mismo sitio que la fuente del evento maestro. Los retrasos residuales de una misma fase en cada estación se pueden calcular de manera precisa usando interpolaciones de la correlación cruzada de las formas de onda de los terremotos. Estos retrasos nos permiten determinar el vector lentitud aparente relativo de cada miembro de la familia respecto al vector lentitud aparente del evento maestro.

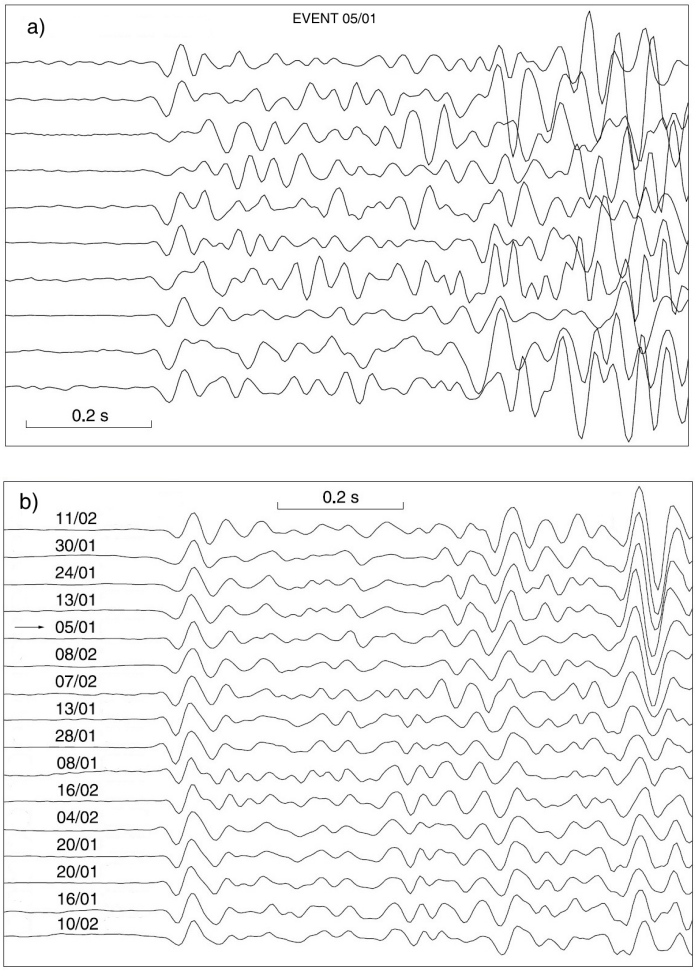

Figura 1.6 *(art. IV fig. 11)*. a) Ejemplo de un terremoto registrado en una antena sísmica para todas las estaciones. b) Ejemplo de los terremotos de una familia para una misma estación de una antena sísmica en el que se encuentra el terremoto de a) marcado con una flecha.

Una vez obtenidos los vectores lentitud aparente relativos correspondientes a la onda P de los terremotos, se suman al vector lentitud aparente del evento maestro para proporcionar la lentitud aparente y los azimutes de propagación de la onda P de los miembros de cada familia. Para la localización espacial se necesitan conocer los tiempos S-P. Los retrasos S-P se pueden estimar con precisión utilizando interpolaciones de la correlación cruzada de las fases P y S del terremoto maestro con el resto de los terremotos de la familia. Así se evitan los errores cometidos por las lecturas visuales. Una vez obtenidos los tiempos S-P precisos y los vectores lentitud aparente precisos, se aplica el trazado del rayo para obtener las localizaciones relativas precisas de los hipocentros para cada familia.

Las localizaciones relativas, tanto con redes como con antenas sísmicas, permiten obtener resultados más precisos que los proporcionados rutinariamente por cualquier red sismológica, llegando incluso a las decenas de metros de precisión frente a los km de incertidumbre. Esta mejora de la precisión hace que en general se observen distribuciones planares de hipocentros que nos permiten obtener información sobre las estructuras sismogenéticas. Si se ajusta un plano a los hipocentros precisos de una misma familia, se obtiene una estimación del azimut y el buzamiento del plano de ruptura común del multiplete.

La determinación del plano de ajuste de un conjunto de hipocentros se puede hacer utilizando técnicas por mínimos cuadrados o por medio de las componentes principales. Para el control de calidad del plano de ajuste, se pueden utilizar varias medidas. Por ejemplo, la dispersión obtenida realizando una serie de simulaciones con el método de Monte Carlo, variando la distribución de los miembros de los multipletes dentro de sus elipsoides de error (Stich *et al.* 2001). Otra forma de estimar la calidad del plano de ajuste es calculando parámetros como el residuo medio (la media de las distancias de los hipocentros al plano), o la planaridad definida como $1-\lambda_3/\ \lambda_2$, donde $\lambda_2>\lambda_3$ son los dos autovalores menores de la matriz de covarianza de la distribución de hipocentros. Un ajuste óptimo debería tener bajo residuo y alta planaridad. Cualquiera de estos métodos de control de la calidad del ajuste nos permitirá estimar qué planos son los que podrán ser considerados como planos de ruptura de cada serie sísmica para su posterior interpretación en el marco tectónico.

El método de localización relativa con redes sísmicas se lleva aplicando mucho tiempo en muchos sitios y está bien demostrada su fiabilidad y robustez. En cambio la novedad del método de localización relativa con antenas sísmicas exige la realización de unas pruebas que aseguren la calidad de los resultados obtenidos para comprobar la robustez tanto del método de estimación del vector lentitud aparente como de la caracterización de los planos de ruptura. Entre otras cosas, se han investigado los efectos de la presencia de ruido y de la configuración de la antena sísmica sobre la resolución del método. También se ha comprobado la influencia del modelo de velocidad empleado para la localización espacial, se ha estimado la influencia de la incertidumbre del vector lentitud aparente del evento maestro

y por último, se ha comprobado cómo influye la elección del evento maestro dentro de una familia. Los resultados de estos test demuestran que el método es muy estable y que permite obtener resultados comparables a los del método con redes.

En este trabajo de Tesis, estas técnicas de localización relativa para caracterizar los planos de ruptura se han aplicado a las series de Agrón e Iznájar en la Cuenca de Granada y a la serie de 1999 en la Isla Decepción (Antártida). Las dos primeras series ocurren en una zona tectónica y se analizan con técnicas clásicas (o de redes sísmicas). Estas series tienen mucho interés por encontrarse muy cercanas a la ciudad de Granada, sede del IAG de la Universidad de Granada. Debido a la existencia de terremotos destructores en la zona y la presencia de terremotos moderados sentidos por la población de Granada y los alrededores, el estudio de estas series para comprender la sismotectónica de la zona es fundamental. La serie de la Isla Decepción fue registrada por antenas sísmicas. Está localizada en una de las mayores zonas volcánicas activas de la Antártida, con erupciones muy recientes, que también es una de las zonas con mayor afluencia de turistas. La Universidad de Granada a través del IAG, lleva quince años monitoreando la actividad sísmica, y durante este tiempo ha sido una de las responsables del control del riesgo volcánico y la puesta en marcha de alertas. Esto hace que el estudio del origen de la reactivación de la Isla durante la serie de 1999 sea fundamental para conocer el estado de la actividad volcánica de Decepción.

Para las tres series se ha realizado un análisis preliminar en el que han localizado los terremotos y estimado la energía estudiando las magnitudes de los terremotos implicados a través de histogramas y del cálculo del parámetro b. Para la serie de Agrón se han aplicado además la localización con técnicas probabilísticas y el análisis de las componentes principales. Estos análisis previos de las series no son suficientes para definir las estructuras sismotectónicas implicadas en cada serie y por tanto es necesario utilizar otros métodos que nos permitan obtener esta información.

Después de este análisis previo se realizó para las tres series una búsqueda de terremotos con forma de onda parecida por medio de la correlación cruzada en el dominio del tiempo para después agrupar los terremotos mediante la técnica de equivalencia de clases (Press *et al.* 1992). Se han obtenido familias de eventos sísmicos para las tres series que nos han permitido aplicar las técnicas de localización relativa respecto a un evento maestro.

Para las series de Agrón e Iznájar se han utilizado técnicas de localización relativa con redes sísmicas. La información que proporcionan las técnicas de localización relativa precisa y su posterior ajuste al plano de ruptura, se pueden complementar con la determinación de los mecanismos focales, a través de la inversión del tensor momento o bien de la polaridad de las primeras llegadas (Brillinger *et al.* 1980, Snoke *et al.* 1984). Estas técnicas se pueden aplicar en aquellos terremotos de una magnitud suficientemente alta que estén registrados por un número suficiente de estaciones con buena cobertura azimutal. Uniendo la información de los planos obtenidos con la localización relativa, las componentes principales

(en el caso de la serie de Agrón) y los mecanismos focales, hemos podido resolver las ambigüedades de los mecanismos de las primeras llegadas, y así obtener información no solo de la dirección (azimut) y buzamiento del plano, sino también de la dirección del vector deslizamiento. Esto ha permitido caracterizar las estructuras implicadas en las dos series e interpretar los resultados enmarcándolos en la tectónica regional.

Para el caso de la serie de la Isla Decepción, las técnicas de localización han sido diferentes a las empleadas con las series tectónicas. Los eventos se registraron con antenas sísmicas y por tanto requieren de una técnica que combine las técnicas clásicas de localización relativa con las técnicas de antenas sísmicas. Se ha desarrollado esta técnica para estimar de manera precisa el vector relativo de un evento de una familia respecto de un evento maestro. Estas estimaciones se combinan con el cálculo de los tiempos S-P entre cada terremoto y su evento maestro, utilizando correlaciones cruzadas interpoladas, para su localización hipocentral con el método del trazado del rayo. Las distribuciones hipocentrales de los miembros de cada familia se han ajustado a un plano, que interpretamos como el plano de ruptura responsable de la generación de los terremotos. Finalmente, interpretamos los resultados en el entorno volcánico y tectónico regional de la Isla Decepción.

2

Caracterización de sistemas de fractura con métodos clásicos en la Cuenca de Granada y zonas adyacentes

2.1. Introducción

La Cuenca de Granada y sus zonas adyacentes han sido objeto de muchos trabajos de geología estructural y geodinámica (Morales *et al.* 1990; Galindo-Zaldívar *et al.* 1999) siempre tomando como base la tectónica regional de las Béticas. Cuando se densifica la red de estaciones sísmicas en la Cuenca de Granada (Alguacil, 2002; Morales *et al.* 2007) y los terremotos se localizan con más precisión, se empiezan a observar diferencias entre los modelos sismológicos y las estructuras geológicas principales, es decir, que la sismicidad de la zona no se corresponde con la tectónica regional de la zona. Esto incitó al estudio de la Cuenca de Granada mediante investigaciones con trabajos sismotectónicos (Ibáñez *et al.* 1990; Morales *et al.* 1993; Peña *et al.* 1993; Morales *et al.* 1996; Muñoz *et al.* 2002; Serrano *et al.* 2002). Por otro lado, los detalles sismogenéticos de cada episodio sísmico son todavía muy poco conocidos, y esto se debe a varias razones. Por ejemplo, la gran mayoría de los terremotos ocurren a una profundidad entre 9 y 16 Km. (Morales *et al*. 1997) y a estas profundidades el estudio de la fuente se hace extremadamente difícil debido a las heterogeneidades de la estructura superficial de la corteza. Otro inconveniente es el bajo nivel de magnitud de la sismicidad en esta zona (Vidal, 1986) que dificulta tanto la localización de hipocentros como el cálculo de los mecanismos focales. La dispersión de los hipocentros debida a los errores de localización hace que sea complicado distinguir con claridad las estructuras implicadas en la generación de la sismicidad. Algunos de estos inconvenientes para conocer las estructuras sismotectónicas se pueden subsanar por medio de técnicas que nos permitan localizar de manera precisa los terremotos.

Para el estudio sismotectónico de una zona es necesario el suficiente número de terremotos para poder aplicar metodologías que nos permitan obtener información sobre la fuente. La Cuenca de Granada y sus zonas adyacentes son muy propensas a la aparición de series de terremotos. Entre las series más recientes e importantes se encuentran la serie de Granada en 1979 (Vidal, 1986), Antequera en 1989 (Posadas *et al*. 1993), Loja en 1985 (Posadas 1991), Agrón en 1988-1989 *(art.I)* e Iznájar en 1998 *(art.II)*. También recientemente hemos tenido micro-series con menos de 50 terremotos en Loja en 2000 (Ocaña, 2009) y en 2003, Zafarraya en 2001 y 2009, y al sur de Granada en 2009 (Figura 2.1). En este trabajo se han utilizado las dos únicas series de la Cuenca de Granada y zonas adyacentes registradas por las estaciones digitales de la Red Sísmica Andaluza (RSA) con un número importante de terremotos (> 300). Éstas han sido la serie de Agrón, Granada (1989) y la serie de Iznájar, Córdoba (1998).

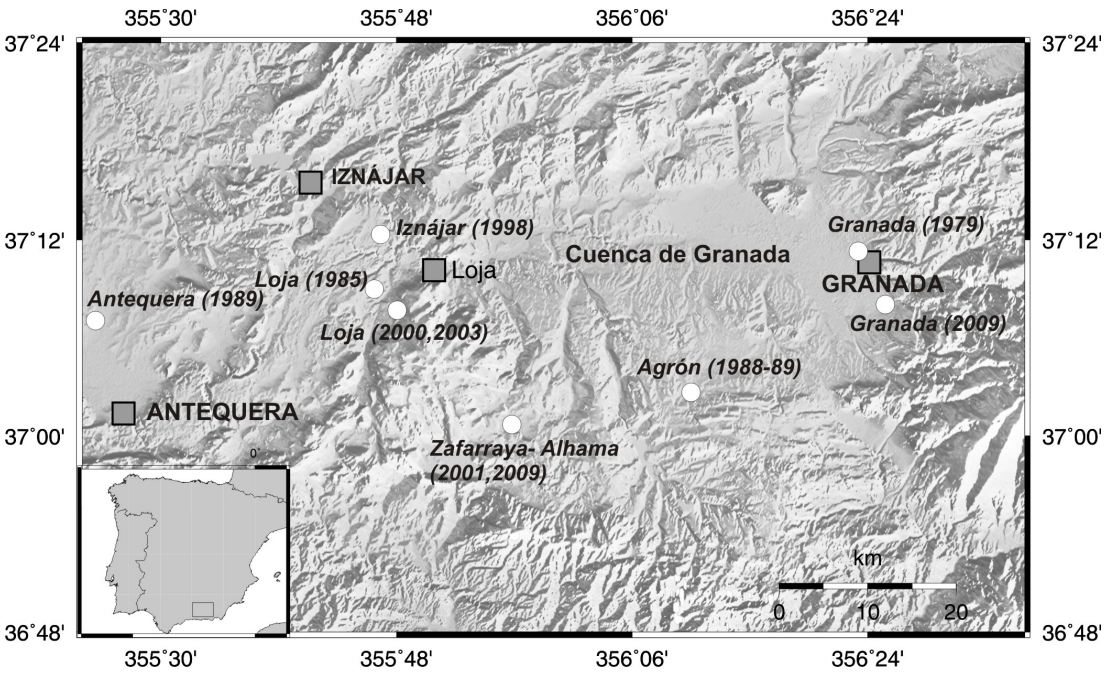

Figura 2.1. Mapa de la Cuenca de Granada y zonas adyacentes con las principales series sísmicas recientes registradas (círculos blancos). Entre paréntesis se muestra el año de ocurrencia.

Los objetivos principales de este capítulo son investigar las evoluciones temporal y espacial de estos terremotos, delinear la localización, fijar las estructuras sismogenéticas principales e investigar su relación con el complejo campo de esfuerzos activo presente en la región. El estudio de estas dos series tiene interés por varios motivos. La serie de Agrón, con un total de 400 terremotos, es la única serie ocurrida en el centro de la Cuenca de Granada y que por tanto se encuentra en el centro de la RSA, lo que la sitúa con una excelente cobertura azimutal. También el hecho de ser la primera serie que se registra con estaciones digitales le confiere ser la primera de una era. La serie de Iznájar es una serie desplazada de la zona central de la RSA, con un elevado número de terremotos (1837 terremotos). Es la mayor serie sísmica reciente de todo el Sur de la Península Ibérica en cuanto a número de terremotos.

Para el análisis de las dos series se ha partido de un catálogo de localizaciones rutinarias realizado por el personal del Instituto Andaluz de Geofísica (IAG) de la Universidad de Granada. Estas localizaciones preliminares se realizan prácticamente en tiempo real durante el transcurso de la serie y son una muy buena estimación provisional para llevar un seguimiento espacio-temporal. Con estos catálogos se han podido tener los primeros mapas epicentrales y establecer una primera visión general de la serie. Pero debido a la gran dispersión de las localizaciones preliminares y a que a veces están incompletas por el gran

número de registros, se ha decidido realizar una relocalización con las mismas técnicas utilizadas por los técnicos del IAG para tener catálogos completos para las dos series y sobre todo para tener una sistematización de las lecturas. Estas nuevas localizaciones han proporcionado unos mapas epicentrales que revelan alineamientos. ¿Indican estos alineamientos las direcciones de las fallas activas responsables de la sismicidad?

En caso de la serie de Iznájar todo indica que la disposición de la serie en la periferia de la RSA provoca un alargamiento en la distribución de los epicentros con dirección EO. Para la serie de Agrón, el asunto no está tan claro porque la serie está situada en el centro de la RSA, garantizando en cierto modo la calidad de las localizaciones. Para esclarecer esta duda se aplica una técnica de localización probabilística basada en el teorema de Bayes (Tarantola y Valette, 1982; Moser *et al.* 1992; Saccorotti *et al.* 1998), aunque los resultados no resuelven la pregunta anterior. Para comprobar si estos alineamientos son o no reales, se recurre al análisis de las componentes principales. Los resultados indican la presencia de varios planos, sin que ningún plano principal coincida con los alineamientos descritos en la relocalización preliminar. Queda claro que para interpretar posibles alineamientos a partir de las localizaciones es necesario que sean lo más precisas que se pueda.

El análisis de las formas de onda de las dos series nos ha proporcionado un conjunto de familias con terremotos muy similares. De esta forma se han podido aplicar las técnicas de localización relativa respecto a un evento maestro descritas en el capítulo 1. Para las dos series, las localizaciones precisas nos han permitido ajustar la distribución de hipocentros de cada familia a un plano. Estos resultados se han combinado con el cálculo de mecanismos focales, resolviendo en algunos casos la ambigüedad nodal de dichos planos y caracterizando algunas estructuras implicadas.

2.2. Marco geológico y tectónico

La Cuenca de Granada se enmarca en la Cordillera Bética, que es el conjunto de montañas que se extienden desde el Golfo de Cádiz hasta las costas meridionales del País Valenciano. Esta cordillera está limitada al N por la Cuenca del Guadalquivir y por el borde meridional del Macizo Ibérico, mientras que en el borde S se localiza el mar de Alborán. Sin embargo, en sentido geológico, se extiende más allá de los límites geográficos, prolongándose hacia el S por debajo del mar de Alborán y hacia el NE por el fondo del Mediterráneo y del promontorio balear hasta la Isla de Mallorca. En esta cordillera se distinguen varios dominios (Serrano, 1999): las Zonas Internas y las Zonas Externas, los materiales del Campo de Gibraltar y las Cuencas Neógenas (Figura 2.2).

Las Zonas Externas están formadas principalmente por materiales mesozoicos y cenozoicos cabalgados y plegados sin metamorfizar, es decir, principalmente rocas sedimentarias que se encuentran localizadas en la zona norte de la Cordillera Bética. Las Zonas Externas tienen dirección predominantemente ENE-OSO y se dividen a su vez en Zona Prebética (sector oriental y central de la Cordillera) y Zona Subbética (sector Sur).

Las Zonas Internas resultan mucho más complejas por su litología y estructura, ya que incluyen materiales sedimentarios y del propio zócalo prealpino, levantados por el plegamiento alpino; además los materiales han sufrido procesos metamórficos y aparecen materiales de origen volcánico. Desde el punto de vista estructural el empuje de Sur a Norte producido por el plegamiento alpino ha hecho que los materiales de las Zonas Internas no sólo se plieguen sino que también se desplacen en esta dirección en forma de mantos de corrimiento. Las Zonas Internas están localizadas en la zona sur de la Cordillera Bética y se dividen en tres grandes complejos: el complejo Maláguide, formado por un zócalo paleozoico (arcillas, cuarcitas y conglomerados) sobre el que se sitúan rocas sedimentarias de edad Mesozoico y Cenozoico; el complejo Alpujárride, formado por tres grandes unidades, unidad inferior (esquistos oscuros y a veces gneises), unidad media (filitas, esquistos con cuarcitas, yeso y rocas ígneas básicas), y unidad superior (dolomías, peridotitas y calizas o mármoles); y el complejo Nevado-Filabre, formado también por rocas metamórficas con unidades en la parte inferior de esquistos oscuros y cuarcitas, unidades de esquistos de colores claros con cuarcitas en la parte media y mármoles en la parte superior (Jabaloy *et al.* 2008).

Las unidades del campo de Gibraltar se encuentran entre las Zonas Internas y las Externas y están formadas por turbiditas, también llamadas depósitos tipo Flysch.

El choque entre las Zonas Internas (Microplaca de Alborán o Mesomediterránea) y Externas (Paleomargen Sudibérico) producido por la Orogenia Alpina durante el Mioceno inferior-medio (entre 23 y 11 Ma) y la convergencia entre las placas Africana e Ibérica, hicieron que la parte central de las Béticas se estructurara en zonas hundidas y levantadas en una serie de cuencas marinas, separadas por importantes islas. Aunque en origen todas las zonas deprimidas estuvieron inundadas por el mar, progresivamente el mar se fue retirando y algunas de ellas pasaron a ser cuencas endorreicas donde desembocaban ríos formándose importantes lagos. Estas zonas se conocen como Cuencas Neógenas. Entre las más importantes de la Cordillera se encuentran la Cuenca del Guadalquivir, que separa la cordillera Bética del Macizo Ibérico, y la del mar de Alborán (la única que permanece sumergida). Además existen pequeñas cuencas neógenas intramontañosas como la de Granada, Guadix-Baza (con alturas de hasta 1200 m), Ronda, Huércal-Overa, Almería y Sorbas.

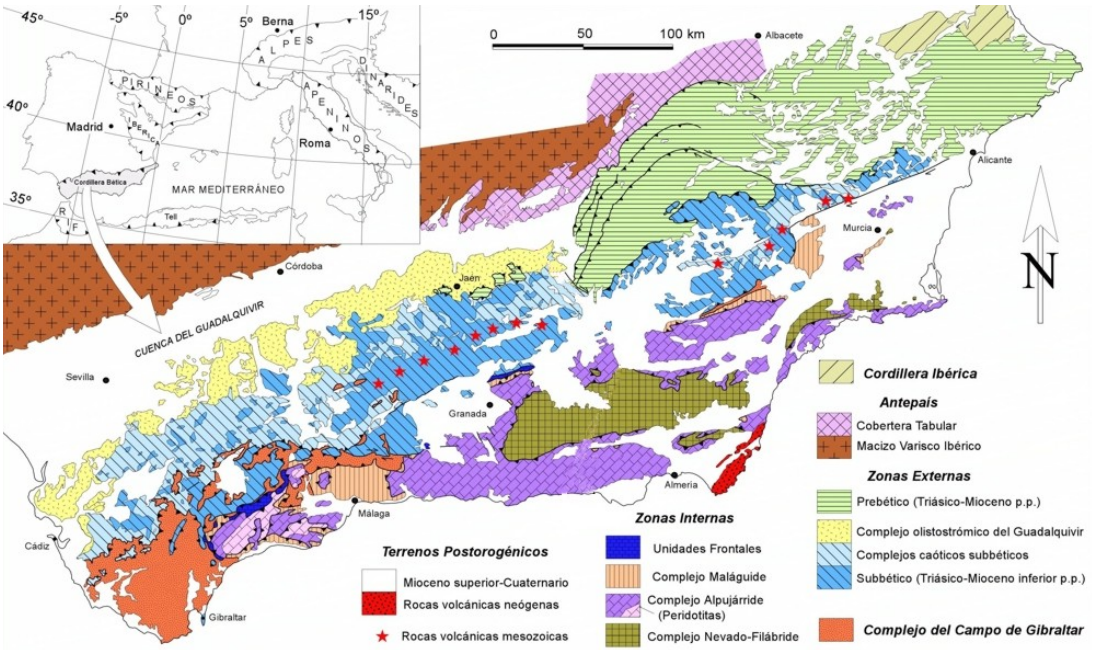

Figura 2.2. Mapa geológico de la Cordillera Bética indicando los diferentes afloramientos de las distintas unidades (Vera, 2004)

Estas cuencas están ligadas con la actividad tectónica regional del conjunto Bético-Rifeño. Existen tres conjuntos importantes de sistemas de fallas en la Cordillera Bética. El primero, con dirección N60-90ºE, tiene a su vez dos subconjuntos de fallas: la de Cádiz-Alicante con dirección N60-70ºE y la de las Alpujarras y la que forma la costa de Málaga a Almería con dirección E-O. Un segundo grupo está distribuido por toda la Cordillera Bética con dirección NO-SE, siendo las mas importantes las de Tíscar, Nerja y la Cuenca de Granada. Y un tercer grupo que tiene dirección NE-SO, comprende dos alineamientos destacados con direcciones N10-20ºE y N40-50ºE. Las más notables son las de Carboneras y Lorca (Henares, 2009).

Nuestro análisis se centra en la Cuenca de Granada, donde tuvo lugar la serie de Agrón, y en una zona adyacente al Oeste de la Cuenca de Granada, límite con las Zonas externas, donde tuvo lugar la serie sísmica de Iznájar.

La Cuenca de Granada se encuentra situada en el sector central de la Cordillera Bética, concretamente sobre el contacto de dirección NE-SW entre las Zonas Externas y las Zonas Internas (Figura 2.3). Geográficamente está limitada al Norte por las sierras Subbéticas de Parapanda, Montefrío y Moclín; al Sur por las Sierras de Tejeda, Alhama y Albuñelas; al

Este por Sierra Nevada y Sierra Arana; al Oeste por la Sierra de Loja. Con una elevación media de 700 metros sobre el nivel del mar (Morales *et al*. 1990), es una de las cuencas neógenas más grandes de la Cordillera Bética. Su extensión es de unos 60 km en dirección E-O y unos 40 km en dirección N-S.

La formación de la Cuenca o Depresión de Granada comenzó en el Mioceno Medio y su individualización se ha ido consiguiendo progresivamente a partir del Mioceno superior hasta la actualidad (Vidal *et al.* 1984). La neotectónica, con los sistemas de fallas N40-50ºO, N10-30ºE y E-O principalmente, ha ido configurando hasta la actualidad esta Cuenca (Vidal, 1986). Ésta ha estado sometida desde el Tortoniense a una elevación que produce estructuras extensionales en la parte superior de la corteza. Esta elevación ayuda la presencia de estructuras de extensión NE-SO más abundantes que las estructuras de compresión NO-SE y por tanto favorecería la permutación entre ambos esfuerzos (Galindo-Zaldívar *et al.* 1999).

Los depósitos aluviales cuaternarios de la Vega de Granada alcanzan hasta los 200-300m de potencia en la zona de más subsidencia. En ellos se encuentra un acuífero importante y que tiene mucha influencia en los daños sísmicos de esta zona de la Vega (Vidal *et al.* 1981).

El interés del estudio de la Cuenca de Granada desde el punto de vista tectónico está en comprender cómo se desarrolla una cuenca neógena extensiva entre límites de placas convergentes (Galindo *et al*. 1999) y su relación con la tectónica regional. Los tres sistemas de fallas más importantes de la Cuenca de Granada y sus zonas aledañas se muestran en la Figura 2.3. En ella se aprecian los sistemas N30-60ºO, que corresponden a las fracturas que atraviesan y delimitan el Macizo Sierra Gorda-Sierra de Loja y que están asociadas con la serie de Loja de 1985 (Vidal, 1986; Posadas, 1991). También se pueden ver con esta dirección los sistemas de fracturas de Pinos Puente-Santa Fé, Gabia, Cuenca del Padul-Valle de Lecrín y sobre todo las estructuras paralelas que pasan por Granada que actúan como fallas normales verticales y son las responsables de la actividad sísmica de Granada y de algunos terremotos destructores, como por ejemplo 1806, 1910, 1956, etc. (Vidal y De Miguel, 1983; Vidal 1986). Otro sistema importante es N70-80ºE que corresponde al accidente Cádiz-Alicante que a su paso por la Cuenca de Granada atraviesa Loja, Huétor Tájar y N de Sierra Elvira. Su desplazamiento es de falla de desgarre dextrorso. Los movimientos de desgarre de estas fallas no han afectado directamente a la formación de la Cuenca de Granada puesto que son anteriores (Sanz de Galdeano, 2001). Y finalmente el tercer gran sistema son las estructuras con dirección E-O. Estos sistemas se sitúan entre las localidades de Padul y Alhama de Granada (Figura 2.3). Son fallas normales con saltos que oscilan entre la decena de metros a los 200 m. Estas fallas son las responsables de la concentración de actividad sísmica de la zona (Sanz de Galdeano, 2001).

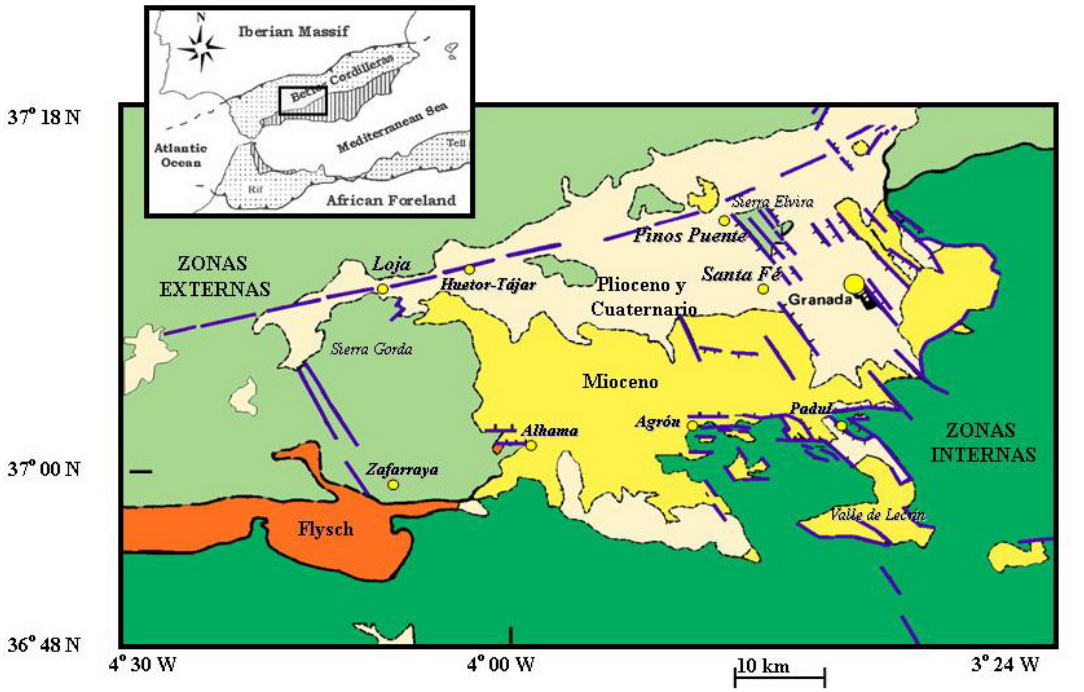

Figura 2.3 Mapa geológico simplificado de la Cuenca de Granada y sus zonas adyacentes con las fallas mas importantes (Modificada de Serrano *et al*. 2002)

2.3. Instrumentación

Los datos utilizados en esta Tesis han sido registrados en la Red Sísmica de Andalucía perteneciente al Instituto Andaluz de Geofísica, de la Universidad de Granada. El IAG gestiona la Red, que en la actualidad consta de sensores de corto periodo, un sensor de largo periodo y sensores de banda ancha. Las estaciones de corto periodo y largo periodo llevan operativas en digital desde finales de 1988, aunque desde al año 1983 se llevaba registrando en soporte analógico (Alguacil, 1986, 2002). La red de banda ancha comenzó su instalación con la estación de Sierra Elvira (SELV) (Buontempo, 2008) en el año 1995, pero no es hasta el año 2000 cuando se densifica la red con un total de 11 estaciones repartidas por toda Andalucía (Mancilla, 2006; Morales *et al*. 2007). Para este trabajo hemos utilizado los datos proporcionados por la red de corto periodo y puntualmente la estación de banda ancha de Sierra Elvira.

Las estaciones de la red de corto periodo están situadas por la provincia de Granada con la idea de tener una buena cobertura para el estudio de la microsismicidad de la Cuenca y sus zonas aledañas. Todos los sensores son verticales, la mayoría Mark L4-C y algunos modelos Ranger SS-1, y todos tienen frecuencia propia de 1 Hz. Las señales producidas por las estaciones son transmitidas vía radio a la central de registro del IAG en Granada (Figura 2.4), digitalizadas y grabadas en ordenadores personales, con una frecuencia de muestreo de 100 muestras por segundo por canal y una resolución de 14 bits (Alguacil, 1986). Los registros tienen un tiempo común proveniente de un receptor GPS que garantiza la sincronización de todas las estaciones con el mismo patrón de tiempo, evitando de esta manera tener que introducir ningún tipo de corrección de tiempo para las estaciones. El sistema de adquisición funciona por disparo con el algoritmo STA/LTA.

Durante la serie de Agrón, estaban operativas como estaciones permanentes las estaciones de corto periodo de ATEJ, APHE, ALOJ, AAPN y ASMO, junto con la estación CRT de largo periodo. Adicionalmente se instalaron por esa época las estaciones portátiles de corto periodo RESI (que pasó a ser estación permanente hasta mediados de 2005), TORR, DILR, HACH y PARA (Figura 2.5). En el transcurso de la serie, se instaló una estación de corto periodo en la misma área epicentral (AGRO), con registro en papel térmico desde el 7 hasta el 15 de Diciembre de 1988. Esta estación no se utilizó para el análisis de la forma de onda pero sí para las lecturas de los tiempos de llegada de la fase P y de las polaridades para el cálculo de los mecanismos focales.

Figura 2.4. Sistema de registro analógico (registro en bandas de papel térmico) y digital (registro en los PC que hacen de sistema de adquisición de datos) de las estaciones de corto periodo y la estación de largo periodo (CRT).

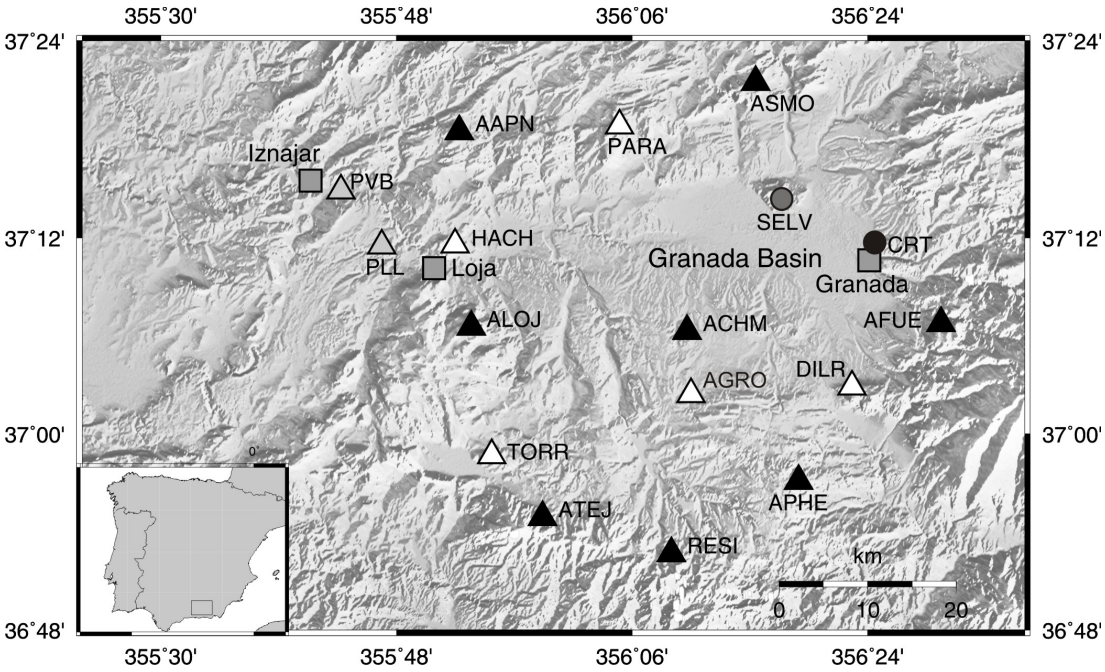

Figura 2.5. Estaciones de la Red del IAG utilizadas en este trabajo. Los triángulos negros corresponden a las estaciones permanentes de corto periodo, el círculo negro a la estación de largo periodo CRT y el círculo gris a la estación SELV de banda ancha. Los triángulos blancos son las portátiles utilizadas para la serie de Agrón y en gris para la serie de Iznájar. Los cuadrados corresponden a las poblaciones más significativas.

Las estaciones operativas durante el transcurso de la serie de Iznájar fueron las estaciones de corto periodo permanentes AAPN, ALOJ, ACHM, AFUE, APHE, ATEJ, ASMO y RESI, junto con la estación de largo periodo CRT. Durante ese tiempo, estaba operativa la primera estación de banda ancha de la RSA (SELV) (Figura 2.5). Además de estas estaciones, durante los días 14 y 15 de abril se desplegaron adicionalmente dos estaciones de corto periodo Mark-L4 de 3 componentes (PLL, PVB) en el área epicentral para mejorar la cobertura azimutal, la resolución en profundidad y la capacidad de detección (Figura 2.6). Cada una de estas estaciones estaba gestionada por un módulo de adquisición de datos de 16 bits. La sincronización y el control del tiempo se realizaban con un receptor GPS, cuya configuración y control se realizaban a través del puerto serie del PC con formato RS-232. La frecuencia de muestreo era de 200 muestras por segundo por canal. Los datos eran grabados por el sistema de adquisición utilizando, al igual que en las estaciones permanentes el algoritmo STA/LTA por disparo.

Figura 2.6. Instalación de la estación portátil PLL para el registro de la serie de Iznájar.

La instalación de estaciones portátiles en la misma área epicentral es de suma importancia cuando se trata de actividad microsísmica. Los eventos de muy baja magnitud apenas se registran en estaciones a decenas de kilómetros de distancia. Además para el caso de la serie de Iznájar, donde en ese momento todas las estaciones de la RSA eran de componente vertical (a excepción de la estación de banda ancha SELV y la estación de largo periodo de CRT), el hecho de disponer de dos estaciones de 3 componentes supuso una gran ventaja para definir el volumen hipocentral de forma más precisa.

2.4. Sismicidad en la Cuenca de Granada y zonas adyacentes

La Cuenca de Granada es una de las zonas con mayor concentración de actividad sísmica de toda la Península Ibérica. Se trata de una actividad mayoritariamente microsísmica, donde la mayoría de los terremotos no superan magnitudes de 5.5. Además apenas alcanzan una profundidad de 20 km, con la excepción de cuatro terremotos profundos con profundidad mayor de 600 km en los años 1954 (Chung, 1976; Buforn *et al*. 1997), 1973, 1990 y 1993 (Vidal, 1986; Henares, 2009) y algunos terremotos de profundidad intermedia (40-80 km). Por tanto la sismicidad en la Cuenca de Granada se puede considerar como moderada y superficial.

Sin embargo, históricamente existen evidencias de por lo menos 20 grandes terremotos desde 1400, produciendo intensidades entre VIII y X (Vidal, 1986; Bretón, 1997). Entre estos terremotos hay que destacar el de Julio de 1431 en Atarfe-Granada con intensidad máxima de IX-X y magnitud estimada de 6.5, el terremoto del 27 de octubre de 1806 con intensidad VIII-IX y magnitud estimada de 5.9, o el conocido como terremoto de Andalucía (de Arenas del Rey) con intensidad máxima de X y una probable magnitud de 6.8.

En la Figura 2.7 se ha representado toda la actividad sísmica registrada por la RSA desde 1988 hasta la actualidad. Aparecen seis zonas donde la concentración de terremotos destaca sobre otras áreas: la zona SE de Granada capital, la zona NO de Granada donde se encuentra la población de Atarfe, la zona más al Oeste de la Cuenca con Loja e Iznájar como poblaciones más importantes, la zona de Alhama-Zafarraya, la zona de Agrón y la zona al SE de Agrón.

La ocurrencia de terremotos en la Depresión de Granada se presenta generalmente en forma de series, como por ejemplo las 21 series históricas entre 1800 y 1960. Entre ellas, las más importantes por el número de terremotos han sido las de Pinos Puente (Granada) entre 1806-1807, con 159 terremotos sentidos, y la de Arenas del Rey (Granada) entre 1884-1886 con 253 terremotos sentidos. La mayoría están gobernadas por las fracturas N40-50ºO (Vidal, 1986). Estas series se pueden considerar enjambres sísmicos de microterremotos (Tipo III según la clasificación de Mogi, 1963) con ausencia de terremotos principales, a excepción del terremoto de 1884. El motivo por el cual la mayoría de las series no vienen precedidas de terremotos principales es probablemente el elevado grado de heterogeneidad de los materiales. Esto provocaría que la acumulación de esfuerzos sea menor y no se generen terremotos de magnitud alta.

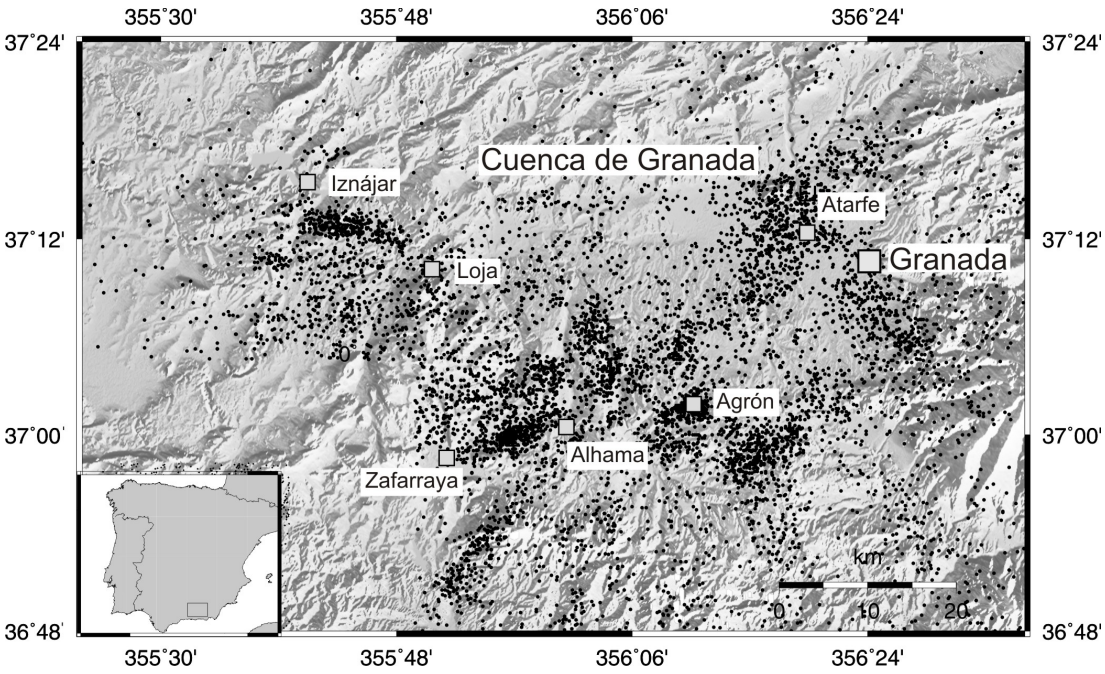

Figura 2.7. Sismicidad de la Cuenca de Granada y zonas adyacentes desde 1988 hasta agosto de 2009.

Entre las series más importantes de los últimos 30 años está la **serie de Granada de 1979** que afectó a toda la Depresión de Granada y áreas vecinas y permaneció activa casi durante un año. El mayor terremoto de esta serie tuvo una magnitud de 4.8, y fueron sentidos por la población más de 55 terremotos. La serie fue la suma de varios episodios, siendo el más destacable el ocurrido durante los meses de julio y agosto. La mayoría de los terremotos fueron superficiales, aunque uno de ellos tuvo una profundidad de 72 km, con mecanismo de falla inversa y un esfuerzo compresivo predominante de dirección E-O (Vidal, 1986).

Otra serie de interés es la **serie de Loja de 1985,** que tuvo lugar en las cercanías de la población de Loja durante el mes de febrero de 1985, con más de 1500 terremotos. El mayor de la serie fue un terremoto de magnitud 3.7, considerándose esta serie también como un enjambre sísmico. Esta serie tuvo lugar en Sierra Gorda (Sierra de Loja) y probablemente el sistema responsable tiene dirección N30-60ºO (Vidal, 1986). Esta fractura corta el macizo y lo limita en su contacto suroriental con la Depresión de Granada (De Miguel, 1976).

Otras series importantes fueron la **serie de Agrón** de 1988 y la **serie de Iznájar** de 1998 que son el objeto de este capítulo, y la **serie de Antequera** de 1989 ocurrida entre el 7-9 de junio de 1989 y compuesta por 158 terremotos con magnitudes entre 2.5 y 3.4. Muchos de estos terremotos fueron sentidos por la población cercana al área epicentral (Posadas, 1993).

Más recientemente (desde el año 2000) se han producido cinco pequeñas series (< 100 microterremotos) destacables. Dos de ellas ocurrieron en las cercanías de Loja, una en octubre de 2000 con un total de 89 eventos localizados en cinco días con magnitudes entre 1.2 y 2.4 (Ocaña, 2009) y otra en febrero de 2003 con 40 terremotos localizados en tres días con magnitudes entre 0.6 y 2.5. Son destacables también las dos microseries de Zafarraya-Alhama en enero-febrero de 2001, con 96 eventos localizados en un mes y magnitudes entre 0.5 y 2.6, y en marzo de 2009 con 46 eventos localizados y magnitudes entre 0.5 y 2.6. Y la más reciente de todas, al Sur de la capital de Granada, comenzó en enero de 2009 y hasta el 30 de junio lleva 35 microterremotos localizados con magnitudes entre 0.8 y 3.1, cuatro de ellos sentidos por la población (web del IAG). Las profundidades medias de los terremotos de estas series se encuentran comprendidas entre los 8-9 km de las series de Granada (2009) y Loja (2000), los 11 km de las series de Zafarraya-Alhama (2001) y Loja (2003) y los 14 km de la serie de Zafarraya-Alhama (2009). Estas profundidades coinciden con los resultados de Morales *et al*. (1997), que afirman que la actividad sísmica en la Cuenca de Granada y zonas limítrofes está mayoritariamente localizada en la Corteza Superior donde la mayoría de los terremotos ocurren en un rango de profundidad entre 9-16 km, y gradualmente van profundizando hasta aproximadamente 25 km en el sector SO.

Han sido varios los terremotos de la Cuenca de Granada a los que se les ha calculado su mecanismo focal. Serrano *et al*. (1996) representaron las direcciones de los ejes P y T obtenidas en el cálculo de mecanismos focales de la Cuenca de Granada y zonas adyacentes. Ponen de manifiesto que para terremotos con magnitud menor de 3.8 existe una dispersión

en los ejes T, que indicaría que el régimen de esfuerzos para estos microterremotos está regido por los esfuerzos locales y no por los regionales. Para el caso de terremotos de mayor magnitud existe una tendencia general en la dirección del eje del mínimo esfuerzo hacia el NNE. Estos autores concluyen que, para la Cuenca de Granada, la extensión en la dirección NNE domina sobre el campo de esfuerzos regionales con compresión NO.

También se ha calculado el tensor momento para algunos terremotos de la Cuenca de Granada (Stich *et al*. 2003). Predominan las fallas de componente normal (Figura 2.8). Entre las conclusiones que se pueden obtener está que la Cuenca de Granada se caracteriza por tener un campo de esfuerzos extensional, con el eje σ_1 casi vertical y un eje σ_2 casi horizontal (Sitch *et al*. 2006). Actualmente, la extensión tiene una dirección N120ºO, paralela a la dirección de estiramiento ENE-OSO dada por el Rift de Alborán (Faccenna *et al*. 2004).

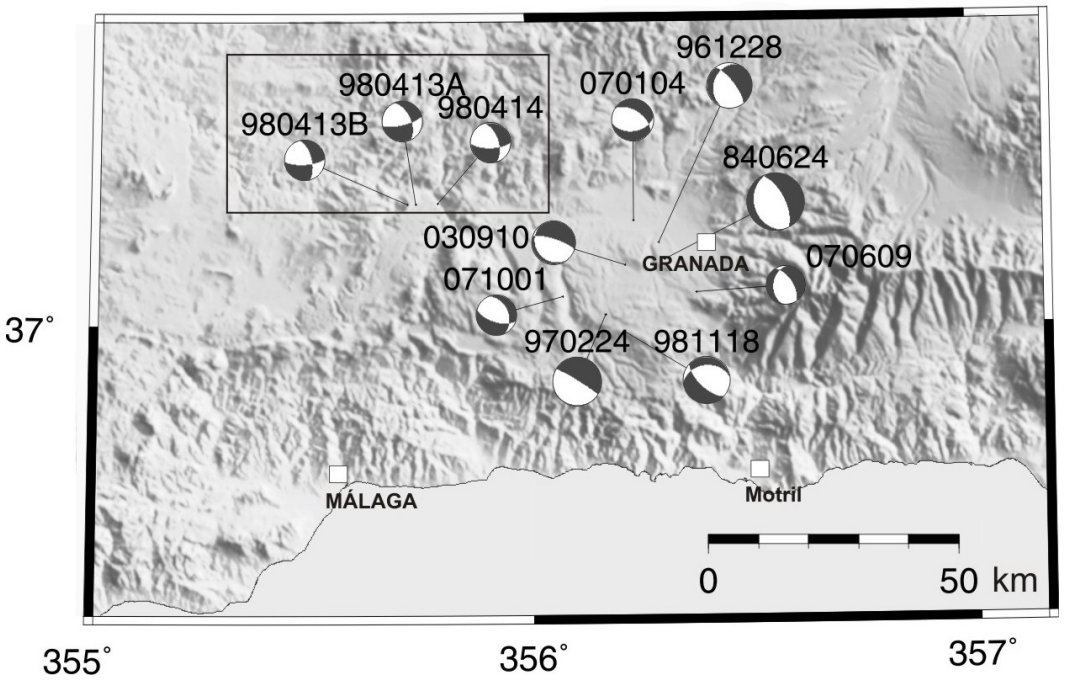

Figura 2.8. Esferas focales obtenidas mediante la inversión del tensor momento para algunos terremotos importantes ocurridos en la Cuenca de Granada y zonas vecinas (D. Stich, comunicación personal). El número indica año (dos dígitos), mes y día. El recuadro muestra los tres terremotos más importantes de la serie de Iznájar.

En la Cuenca de Granada, Galindo-Zaldívar *et al*. (1999) proponen que el estado de esfuerzos en la parte superior de la Cuenca es extensivo con dirección entre N-S y NE-SO. Aunque el estado de esfuerzos es extensivo, encuentran terremotos con régimen compresivo. Eso querría decir que los mecanismos de falla inversa estarían distribuidos entre los mecanismos de falla normal. Estas estructuras serían más abundantes que las de compresión NO-SE. Este complejo sistema desencadenaría la permutación entre los ejes de esfuerzos. Hancock (1985) propone que la permutación de los ejes de esfuerzos es una consecuencia de la deformación frágil de los materiales.

Dado el variado sistema de fracturas en el que se encuentra la Cuenca de Granada y sus zonas aledañas y a raíz de las permutaciones de los ejes de esfuerzos es posible pensar que su estructura está formada por bloques. Estos bloques constituirían un conjunto de estructuras a distintos niveles y limitadas por fracturas que favorecen el movimiento de unos bloques respecto de otros. Esto explicaría la coexistencia de deformaciones en compresión y en extensión en una misma zona, en la que además aparecen fallas de salto en dirección (Morales, 1991).

2.5. Serie de Agrón

2.5.1. Análisis preliminar *(art. I)*

La serie sísmica de Agrón se produjo entre Octubre de 1988 y Abril de 1989 y estuvo compuesta por un total de 400 terremotos registrados por la RSA. El comienzo de la serie fue observado por un incremento de la microsismicidad, el 10 de Noviembre y los días 4 y 5 de Diciembre de 1988, con más de 30 terremotos cada uno de esos días. El terremoto de mayor tamaño de la secuencia ocurrió el 5 de Diciembre de 1988 con una magnitud de 4.0.

Se realizó un análisis preliminar por parte del IAG, obteniendo el primer mapa epicentral de la serie (Figura 2.9a) y las primeras estimaciones de las magnitudes implicadas. Con este catálogo inicial se ha evaluado la secuencia temporal del número de terremotos por día (Figura 2.9b). Lo primero que llama la atención son los dos picos de máxima actividad. Durante el segundo pico tiene lugar cinco terremotos de magnitud mayor de 3, entre ellos el mayor de la serie. Esta característica enmarca la serie en el Tipo III (enjambre sísmico) sin la presencia de un terremoto principal.

Las magnitudes locales fueron determinadas utilizando la duración de la coda, según una escala calculada por De Miguel *et al*. (1988). El catálogo inicial contiene rangos de magnitud

del orden de 0.3 hasta 4.0 (Figura 2.9c). La relación de Gutenberg-Richter mostrada en la Figura 2.9d indica que el catálogo puede muy bien considerarse completo aproximadamente a partir de magnitud 1. La profundidad hipocentral en el catálogo inicial está comprendida entre 5 y 45 km. Esta dispersión en profundidad se debe probablemente al error que se produce en las lecturas de las fases como consecuencia de la pequeña magnitud de la mayoría de los terremotos.

Estas localizaciones rutinarias realizadas por el IAG muestran que una parte de los epicentros se encuentran concentrados en un área de aproximadamente 10x10 km y el resto se encuentran muy dispersos. Esta dispersión viene dada principalmente por la incertidumbre de las localizaciones de los microterremotos. Para tener una sistematización en los tiempos de llegada se han revisado las lecturas y se ha vuelto a localizar la serie con una modificación del programa HYPOELIPSE (Lahr, 1989). Para este análisis se relocalizan aquellos terremotos que han sido registrados por al menos 4 estaciones digitales. El catálogo pasa de tener 400 a tener 125 terremotos. Se ha evaluado la llegada de la onda P para todos los eventos, asignando intervalos de error; no se han leído las llegadas de la onda S por la incertidumbre asociada al hecho de que solo se tienen estaciones de componente vertical. Se ha utilizado un modelo de velocidad que consiste en dos capas con espesores de 10 y 30 km y velocidades de la P de 5.6 y 6.6 km/s, respectivamente, y a partir de esa profundidad se tiene una velocidad para la P de 7.8 km/s. Las profundidades obtenidas se encuentran comprendidas entre 1 y 25 km. El error medio horizontal de la relocalización fue de aproximadamente 1 km. Incluso con estaciones tan cercanas, la incertidumbre en la estimación de la profundidad es demasiado grande, no quedando resuelta la profundidad para varios terremotos.

Una vez obtenido el nuevo catálogo, los epicentros se concentran más claramente, desapareciendo la dispersión del catálogo inicial. En la Figura 2.10 se han mostrado las localizaciones epicentrales para cuatro intervalos de tiempo con el fin de comprender la evolución espacial de la serie. Los primeros eventos del catálogo revisado están concentrados en una región epicentral muy definida. Se pueden observar dos diferentes alineamientos de los epicentros (Figuras 2.10b y c*)*. Para el final de la serie los datos relocalizados comienzan a dispersarse (Figura 2.10d). Estos mapas dan una visión exhaustiva de la distribución de la sismicidad en el plano horizontal, pero queda pendiente el problema de la profundidad de los hipocentros. Por otro lado, surge la pregunta de si esos alineamientos observados en el plano horizontal de la Figura 2.10 reflejan la estructura correspondiente a la dirección de una falla que provoca esos terremotos.

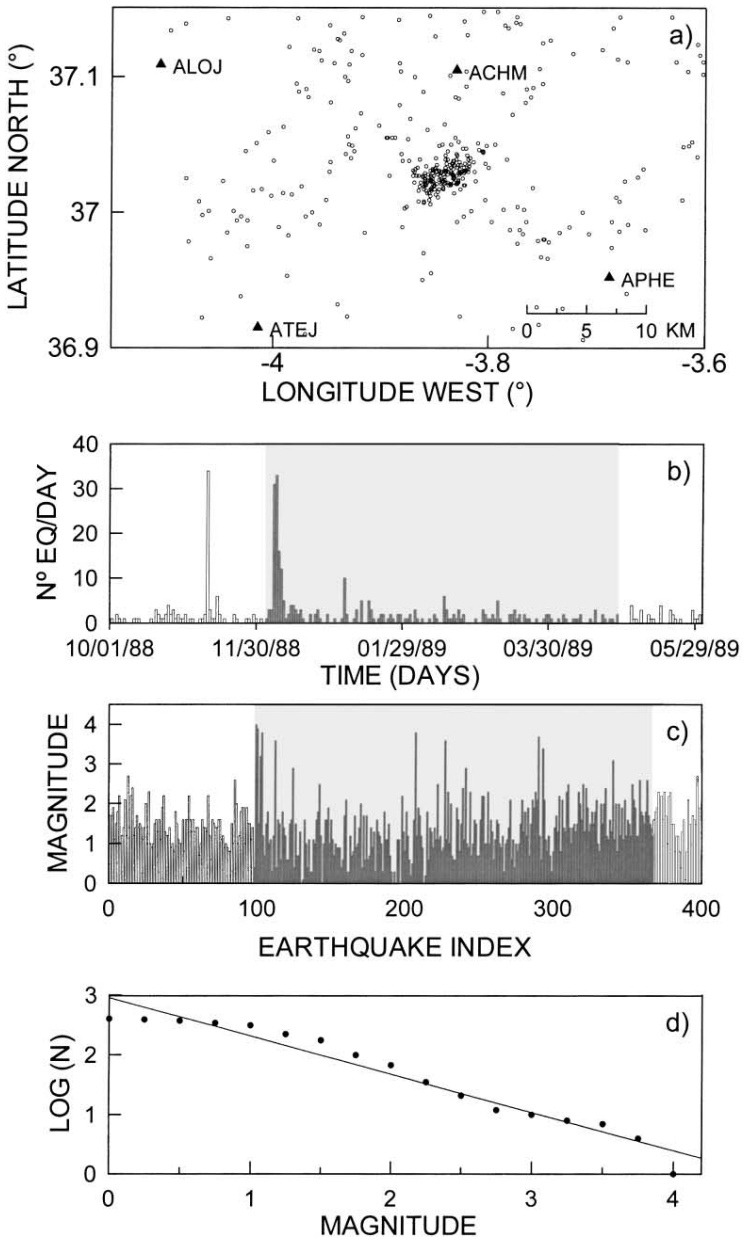

Figura 2.9 *(art. I fig. 2)*. (a) Mapa preliminar de epicentros de la serie de Agrón desde el 1 de Octubre 1988 hasta el 31 de Mayo de 1989 (datos del catálogo del IAG). Los triángulos marcan la posición de las estaciones más cercanas de la RSA a la serie. (b) Histograma que muestra la evolución temporal del número diario de terremotos. La banda gris (desde el 1 de Diciembre de 1988 hasta el 29 de Abril de 1989) indica los datos utilizados para este trabajo. (c) Evolución de la magnitud. La gráfica muestra desde el 1 de Octubre de 1988 hasta el 31 de Mayo de 1989. (d) Relación de Gutenberg-Richter de todos los eventos de la serie. Le corresponde un valor b de 0.63.

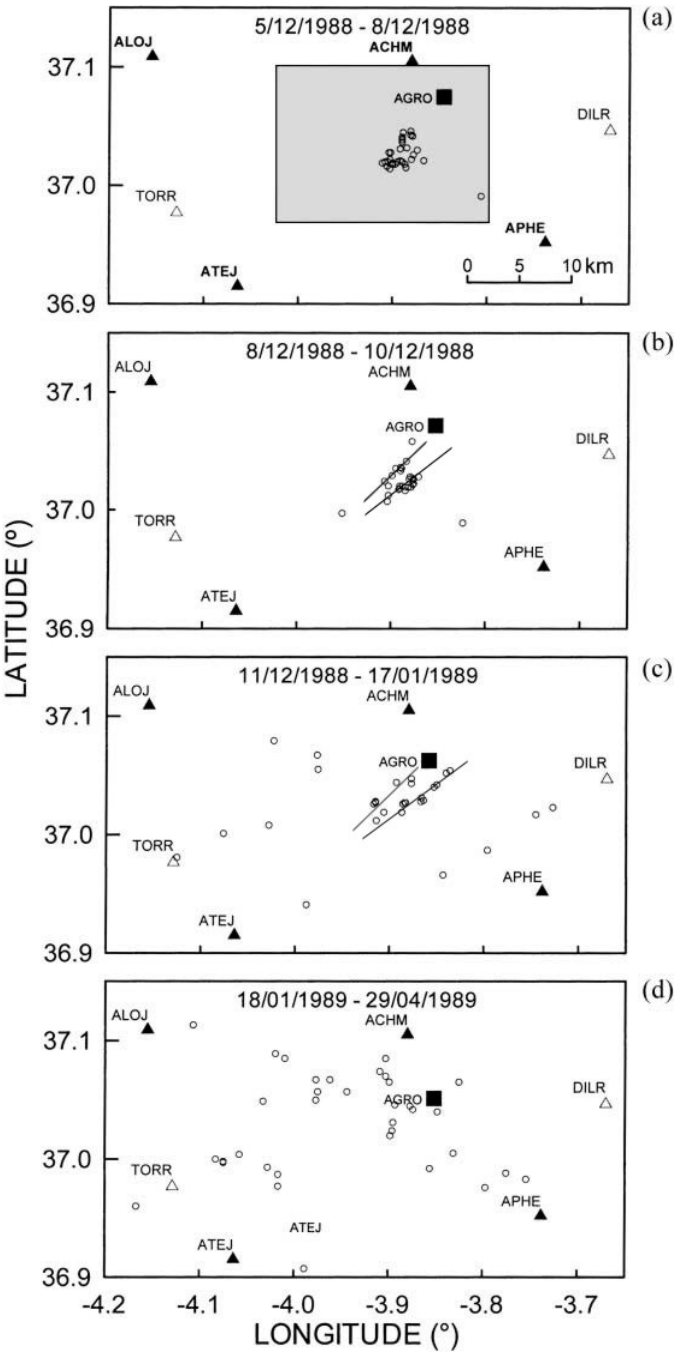

Figura 2.10 *(art. I fig.3).* Relocalización de la serie de Agrón. Cada mapa representa grupos de 30 terremotos consecutivos en el tiempo. El área marcada en el primer mapa muestra el área de estudio de la relocalización probabilística. En las Figuras b y c se han marcado los posibles alineamientos. Los triángulos muestran las estaciones de corto periodo de la RSA permanentes (negro) y las portátiles (blanco). El cuadrado muestra la estación portátil de papel térmico.

2.5.2. Resultados y discusión *(art. I)*

El análisis de la serie sísmica de Agrón se ha realizado según el esquema siguiente. Primero se ha intentado mejorar la estimación de la posición hipocentral de los terremotos utilizando una aproximación probabilística. Después se han calculado los posibles alineamientos utilizando un método estadístico basado en el análisis de las componentes principales (PCA) de los datos hipocentrales. Después se han identificado familias de terremotos similares con la correlación cruzada de las formas de onda digitales. A continuación se han localizado los terremotos de cada familia con respecto a un evento principal utilizando la técnica de localización relativa precisa. Los hipocentros de cada familia se distribuyen siguiendo un plano, que hemos ajustado para obtener los planos de falla activos durante la serie.

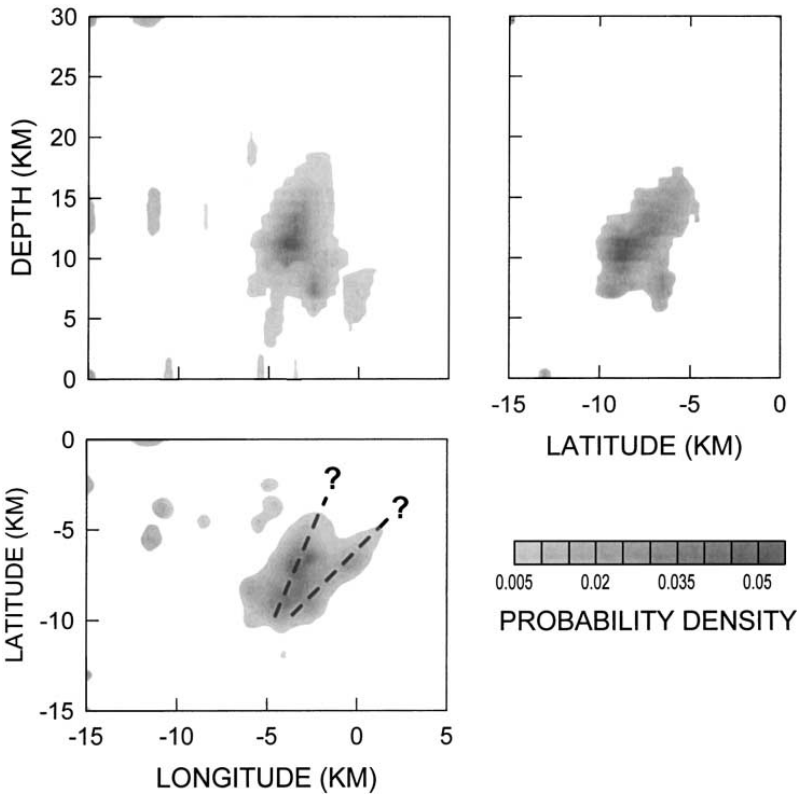

Figura 2.11 *(art.I fig.4)*. Resultados de la localización probabilística de los terremotos proyectada sobre el plano horizontal y los dos planos verticales EW y NS. Aparecen dos cluster con profundidades entre 6-8 km y 10-15 km. En el mapa horizontal se ha dibujado dos posibles alineamientos que coinciden con los del mapa de la Figura 2.9.

Finalmente, se han calculado los mecanismos focales de algunos terremotos de las familias. La interpretación combina las informaciones derivadas del PCA, las soluciones de los mecanismos para las polaridades la onda P, y las localizaciones relativas de alta resolución.

La relocalización probabilística basada en el teorema de Bayes (Tarantola y Valette, 1982; Moser *et al.* 1992; Saccorotti *et al.* 1998) ha permitido definir de una forma más clara las profundidades de las fuentes, mostrando dos agrupamientos principales de hipocentros con profundidades cerca de 6-8 km y 10-15 km. Estos rangos de profundidades mejoran y precisan mejor los hipocentros respecto a las obtenidas del catálogo inicial (5-45 km) y de la relocalización del catálogo inicial (1-25 km). En la proyección NS-EO de la función de probabilidad (Figura 2.11), aparecen vagamente los alineamientos de los epicentros de la relocalización (Figura 2.10). Sin embargo, estos resultados no contribuyen determinar si estos alineamientos se corresponden con las fallas implicadas en la serie.

Se ha utilizado el PCA espacial sobre la serie con los datos de los 125 terremotos relocalizados. En este caso el análisis del conjunto de datos de la serie nos proporciona cinco planos significativos que corresponden posiblemente a cinco planos de falla activos (Figura 2.12). Estos planos tienen direcciones NO-SE, NE-SO y E-O. Parecen estar relacionados con la mayoría de la distribución de la sismicidad, representando dos de ellos la dirección NE-SO del posible doble alineamiento supuestamente reflejado en la Figura 2.10. Sin embargo, estos resultados con el PCA dejan en el aire algunas dudas. ¿Qué ocurre con el resto de planos obtenidos con el PCA que no coinciden con los alineamientos? Y lo que es más importante, el análisis del PCA utiliza localizaciones hipocentrales ¿pero son verdaderamente precisas estas coordenadas focales como para definir sistemas de fractura? Es evidente que se hace necesaria la localización precisa de los terremotos. Para este fin se ha utilizado la localización relativa de alta resolución.

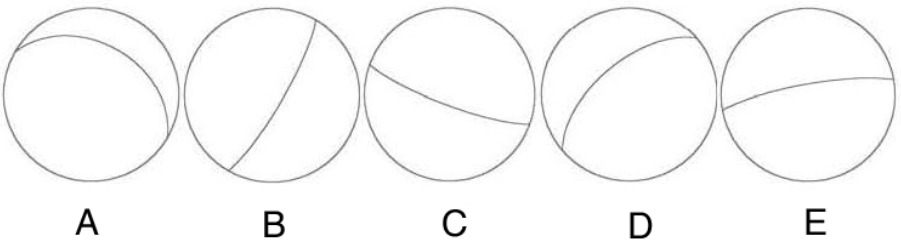

Figura 2.12 *(art.I fig.5c)* Proyecciones estereográficas de los 5 planos principales obtenidos con el método de las componentes principales.

Utilizando la correlación cruzada de la forma de onda, los terremotos de la serie se han agrupado formando cinco familias con coeficientes de correlación de mayores de 0.9 (Figura 2.13). Los terremotos de cada familia se localizaron relativamente respecto a un evento maestro elegido como el terremoto registrado en el mayor número de estaciones. Con un ajuste por mínimos cuadrados se han obtenido las localizaciones precisas del resto de componentes de cada familia. Para cada familia se ha determinado el plano de ruptura que mejor se ajusta a la nube de hipocentros precisos (Figura 2.14). Estos planos se muestran en la Figura 2.15 en representación estereográfica con línea discontinua. Se observa una gran diversidad, con dos planos N-S, uno E-O, uno NE-SO y otro NO-SE. Esta variedad de direcciones en un volumen tan pequeño indica una distribución compleja de esfuerzos y sugiere una distribución de bloques de pequeño tamaño que se han desestabilizado provocando la serie sísmica.

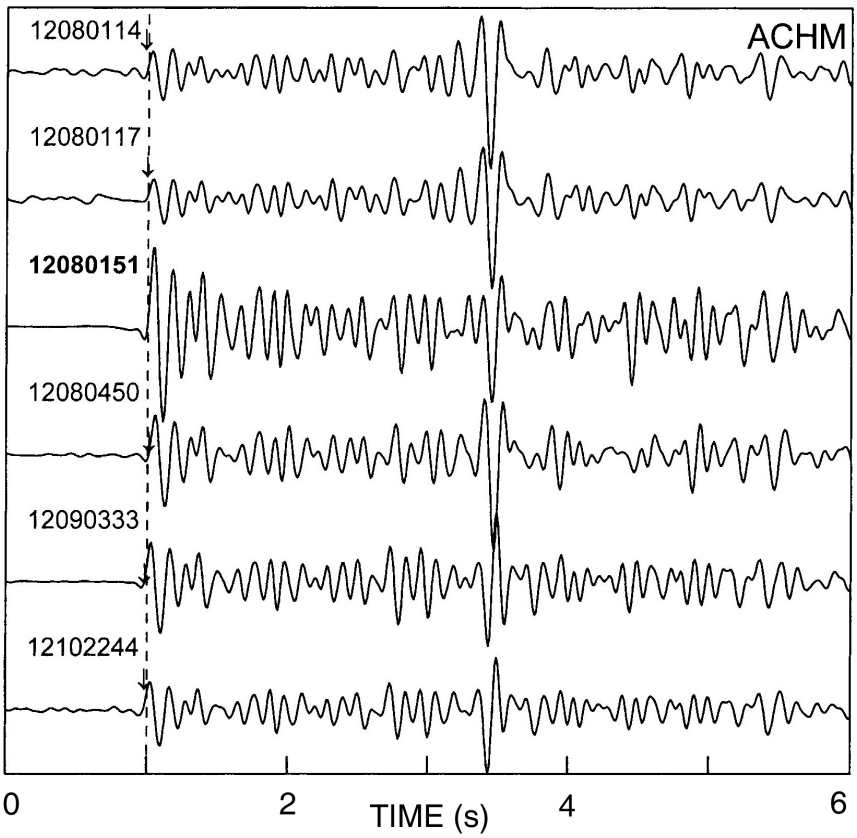

Figura 2.13 *(modificada art.I fig. 8)* Ejemplo de familia de terremotos de la serie de Agrón para la estación ACHM.

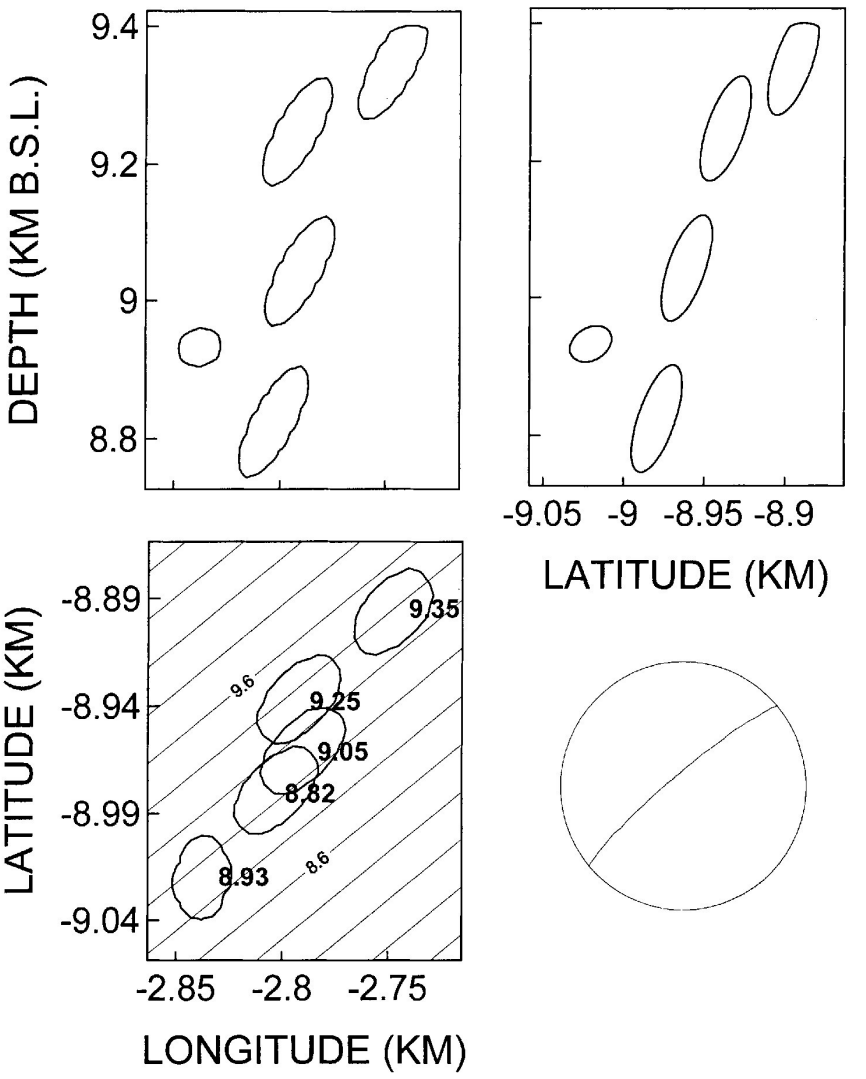

Figura 2.14 *(art.I fig.9)*. Localizaciones relativas para el multiplete II. Se muestran las proyecciones para el plano horizontal y dos planos verticales orientados N-S y E-O. Las elipses muestran el intervalo de confianza del 90% de la localización del hipocentro. Las líneas continuas en la proyección horizontal son isolíneas de profundidad del plano de ajuste con un intervalo de 200m. Se muestra en negrilla para cada localización la profundidad del hipocentro. A la derecha se dibuja la proyección estereográfica del plano de ajuste de este multiplete.

Para completar los resultados se calculan los mecanismos focales de algunos terremotos (Figura 2.15). Tres de los cinco planos obtenidos del PCA espacial se validan con las informaciones proporcionadas por las localizaciones relativas de alta precisión y las soluciones del mecanismo focal con los datos de la polaridad de la onda P.

Lo más interesante se presenta al examinar los resultados que en algunos casos coinciden al utilizar diversas técnicas. Algunos de los planos deducidos a través de los mecanismos focales y de las localizaciones relativas encuentran de hecho una correspondencia con los patrones evidenciados por el PCA espacial, obteniendo un aumento en la robustez de los resultados. Existe parecido entre los planos B y D (Figura 2.12) que corresponden a los multipletes III y II, respectivamente. De la misma manera, se observa una buena correspondencia entre el plano C y uno de los planos conjugados de la solución del mecanismo del terremoto principal, y entre el plano E y los provenientes de la localización relativa del multiplete I. Hay que tener en cuenta el intervalo de incertidumbre (10º) al aplicar el PCA y la dispersión al ajustar el plano de falla de las localizaciones relativas. Estos errores hay que considerarlos a la hora de interpretar los resultados porque afectan en varios grados a los azimutes del plano y sus buzamientos. Se puede concluir que, con la única excepción del plano A, todos los planos de falla derivados del PCA espacial son validados por las localizaciones relativas y las soluciones de los mecanismos focales.

Se ha combinado la información que nos ha suministrado el análisis de componentes principales, la localización relativa y los mecanismos focales para permitirnos representar un sistema de fracturas extremadamente complejo, donde los planos de falla varían enormemente en un volumen focal pequeño. Solamente algunas de estas fallas (por ejemplo la que corresponde al multiplete V y uno de los dos planos conjugados del terremoto principal) están de acuerdo con la extensión regional de ENE-OSO que actúa en el área (Galindo-Zaldívar *et al.* 1999). Sin embargo, como estos últimos autores precisaron, los esfuerzos locales que actúan en la Cuenca de Granada parecen estar caracterizados por una naturaleza alargada del elipsoide de esfuerzos, con el eje σ_1 inclinado hacia SO y los ejes σ_2 y σ_3 casi idénticos. Esta configuración del campo de esfuerzos local podría conducir así a la reactivación de los planos preexistentes de falla, como por ejemplo el sistema de fallas NE-SO representado probablemente por los multipletes II y III. Por otra parte, la proximidad observada de las fallas con diversa orientación sugiere una fragmentación significativa de la corteza superior en bloques tectónicos pequeños. Esto lo propusieron Stich *et al*. (2001) con el estudio de la sismicidad occidental de Almería. Este grado tan grande de fragmentación representa un escenario apropiado para explicar la redistribución compleja del esfuerzo de cizalla después de cada evento, que podría incidir en la reactivación de los planos de falla con orientaciones diferentes al campo de esfuerzos regional.

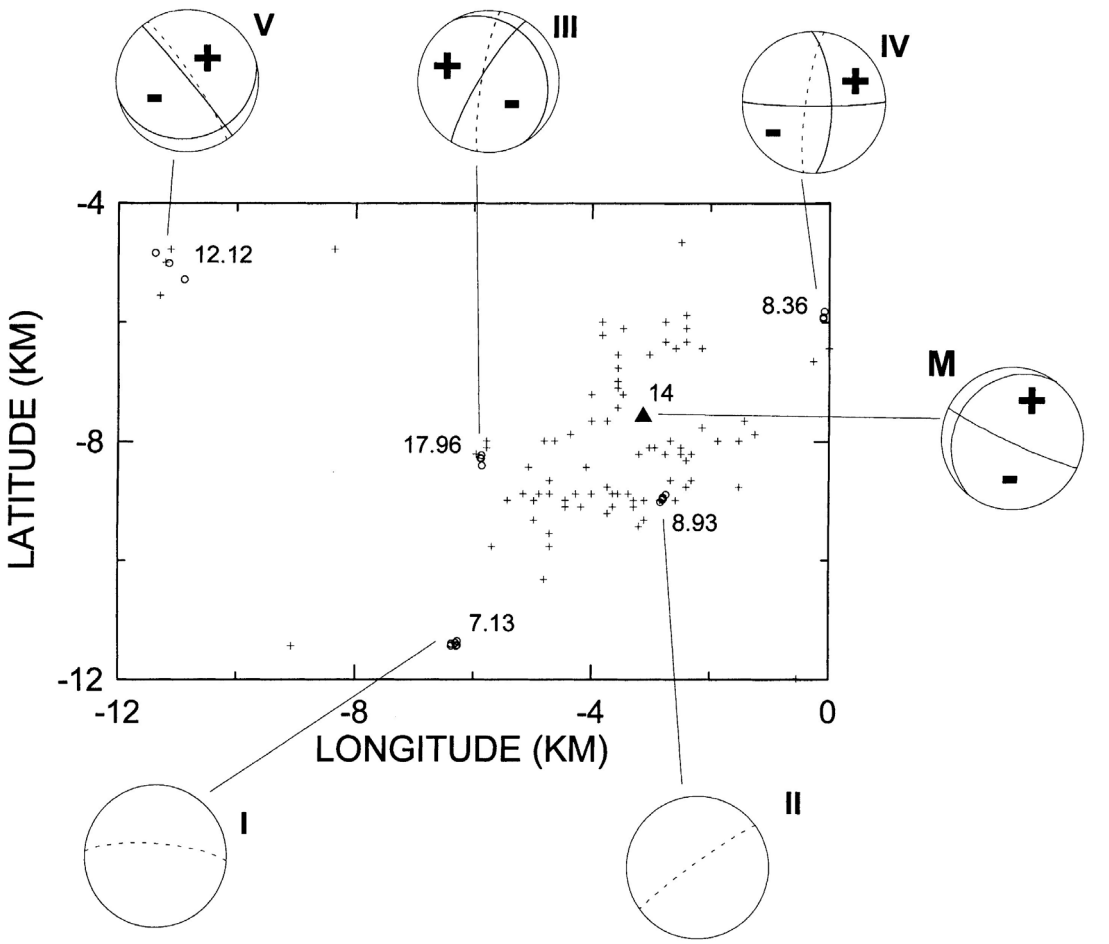

Figura 2.15 *(art.I fig.10)*. Mapa epicentral donde se comparan los mecanismos focales y los planos obtenidos en la localización relativa. Las cruces indican las localizaciones originales y los círculos, los epicentros de la localización relativa. En las proyecciones estereográficas se muestran los planos obtenidos con la localización relativa (líneas discontinuas) y los planos obtenidos de los mecanismos focales con las polaridades de la onda P (líneas continuas). En número romanos se indica el multiplete en orden cronológico. El evento principal de la serie se representa con la letra M. Los números nos muestran la profundidad de cada multiplete.

2.6. Serie de Iznájar

2.6.1. Análisis preliminar *(art. II)*

La serie comenzó la noche del 11 de abril de 1998, en una zona situada a unos 50 km al Oeste de Granada y cercana a las poblaciones de Iznájar y Loja. La serie se desarrolló durante los meses de abril y mayo. Comenzó sin la presencia de ningún terremoto principal. A los dos días se produjeron los terremotos de mayor magnitud (3.8 -3.9), el 13 y 14 de abril. Por tanto se podría catalogar a esta serie como enjambre sísmico (Tipo III). El enjambre de Iznájar de 1998, con más de 1800 eventos registrados entre el 11 de abril y 13 de mayo, es hasta la fecha la serie sísmica reciente más numerosa del Sur de la Península registrada por una red local digital.

El análisis preliminar por parte del IAG permitió localizar aquellos terremotos con magnitudes superiores a 2.5, obteniéndose un primer mapa epicentral de la serie y un catálogo inicial. Para completar el catálogo y contabilizar los terremotos no localizables se ha realizado una cuidadosa inspección visual de los registros en la estación más cercana (AAPN), con la lectura de las fases P y S, junto con la duración de la coda. Se han contabilizado un total de 1837 eventos hasta el 13 de mayo. El histograma de terremotos por día muestra claramente que durante los tres primeros días de la serie tiene lugar más de la mitad del total de terremotos (Figura 2.16a). La magnitud–duración (De Miguel *et al.* 1988) oscila entre 0.6 y 3.9 (Figura 2.16b). La relación de Gutenberg-Richter indica un valor de b relativamente alto, de 1.27, y sugiere que el catálogo es casi completo a partir de magnitud 2 (Figura 2.16c). Los eventos de menor magnitud tan solo son registrados en las estaciones más cercanas, debido principalmente a la baja energía y la distancia epicentral. Además se puede dar el caso de que algunos microterremotos con magnitudes bajas estén solapados en las codas de los eventos anteriores, ya que los terremotos se han detectado aproximadamente cada 3 minutos en los momentos de máxima actividad de la serie.

Con la nueva revisión del catálogo, se ha relocalizado la serie completa con el programa HYPOCENTER (Lienert *et al*. 1995) integrado en el paquete SEISAN (Havskov y Ottemöller, 1999) para aquellos terremotos que han sido registrados en un mínimo de cuatro estaciones. Al final el catálogo revisado queda con un total de 778 sismos. Las localizaciones muestran una importante dispersión y una tendencia E-O (Figura 2.17) que se puede atribuir a la geometría de la red y los grandes errores de la localización de los eventos más pequeños, con un alto nivel de ruido y lecturas de las llegadas con incertidumbres altas en las estaciones más lejanas. Los terremotos mejor localizados se agrupan en torno a 37.21°N, 4.20°O y a 12 km de profundidad.

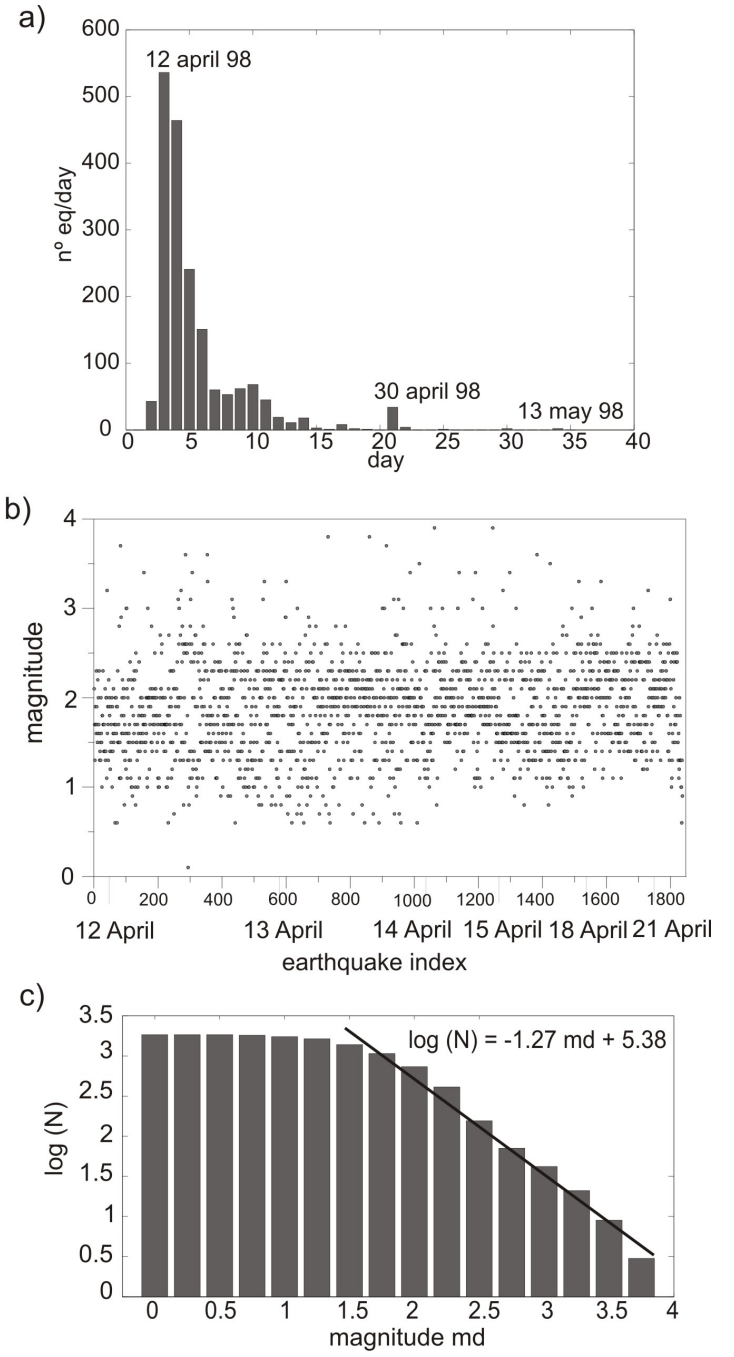

Figura 2.16. a) Evolución temporal del número diario de terremotos. b) Evolución temporal de la magnitud. c) Relación de Gutenberg-Richter del catálogo revisado (1837 terremotos)

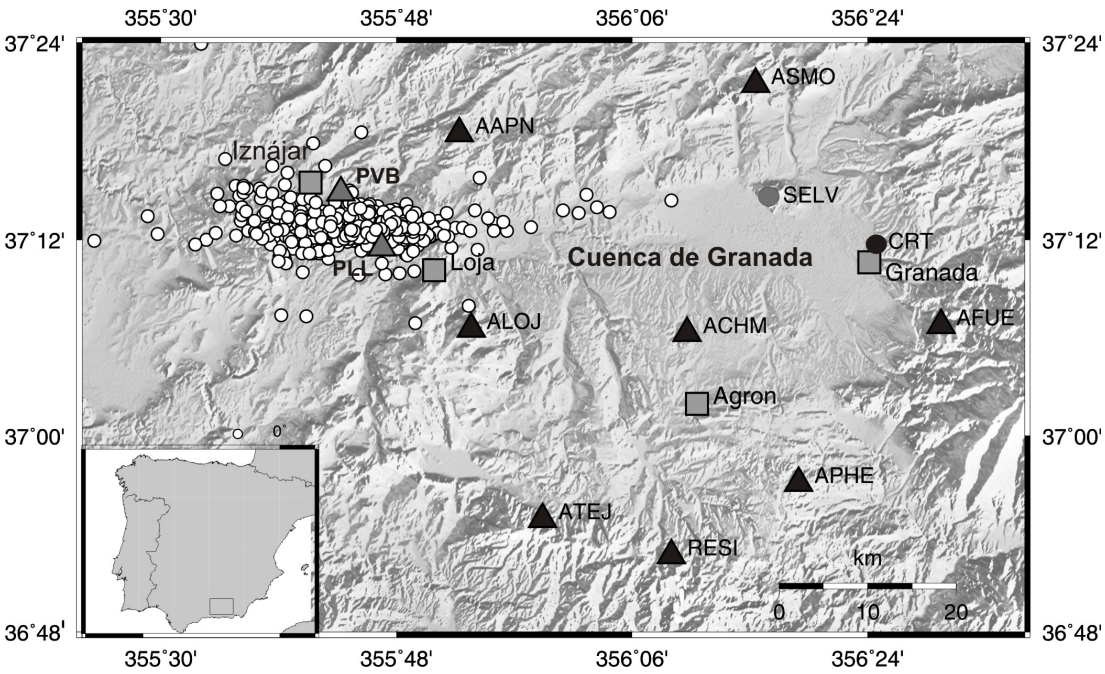

Figura 2.17 *(modificada art.II fig. 1).* Mapa epicentral de la Serie de Iznájar y de las estaciones utilizadas para la localización. Los triángulos negros representan las estaciones permanentes de corto periodo.El círculo negro la estación de largo periodo. El círculo gris la estación de banda ancha. Los triángulos grises las estaciones portátiles instaladas durante la serie. Los cuadrados indican las poblaciones más representativas.

2.6.2. Resultados y discusión *(art. II)*

El análisis de la serie sísmica de Iznájar se ha realizado según el esquema siguiente. Primero se han identificado familias con alta similitud de la forma de onda, por medio de la correlación cruzada. Estas familias se han localizado de forma precisa realizando una localización relativa respecto a un evento maestro. Se han determinado los planos de ajuste de las localizaciones relativas precisas de las familias. Posteriormente se han calculado los mecanismos focales con las polaridades de las primeras llegadas. Y por último se han combinado las localizaciones relativas precisas y los mecanismos focales para resolver la ambigüedad de los planos nodales y caracterizar mejor el mecanismo de las rupturas implicadas.

La correlación cruzada de la forma de onda del conjunto total de terremotos (1837) para la estación más cercana (AAPN) nos ha permitido agrupar 154 familias con alta similitud de la forma de onda (Figura 2.18) con correlaciones para las fases P y S del orden de 0.9. Estas

familias incluyen un total de 596 eventos (32% del catálogo de Iznájar), con 74 dobletes, 34 tripletes y 46 multipletes con 4 a 26 eventos.

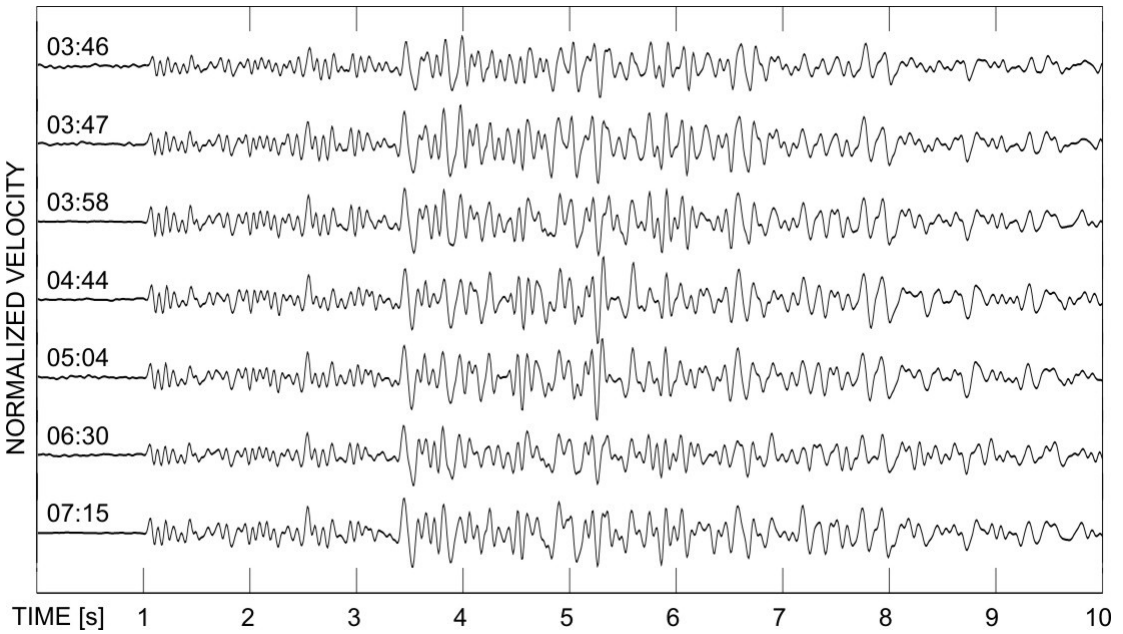

Figura 2.18 *(art.II. fig.5)*. Ejemplo de una familia (114) para la estación AAPN. Los sismogramas son de componente vertical y están filtrados entre 1 y 25 Hz y alineados en la llegada de la onda P.

Se han seleccionado las 13 mejores familias teniendo en cuenta la calidad de la forma de onda y el número de terremotos. Se han calculado las localizaciones relativas de los eventos de las familias respecto a un evento maestro, elegido por su calidad en la forma de onda y por estar registrado en el mayor número de estaciones. Se han obtenido los tiempos de retraso por medio de la correlación cruzada entre los eventos de cada familia con su evento maestro, y se han utilizado para ajustar por mínimos cuadrados la mejor solución hipocentral. Estas localizaciones precisas nos han permitido obtener hipocentros concentrados en apenas 200-300 m (Figura 2.19). A continuación, se ha ajustado la distribución de hipocentros a un plano. Todas las familias se han podido ajustar a una distribución planar e incluso en una de ellas las localizaciones relativas han proporcionado dos planos de ajuste (Figura 2.18, multiplete 72). Para estimar los límites de confianza de estos planos se ha empleado el Método de Montecarlo para 100 simulaciones gaussianas aleatorias. Se han obtenido errores de dispersión entre 4 y 34 metros, que se han traducido en incertidumbres para el azimut del plano y el buzamiento de aproximadamente 20-30º.

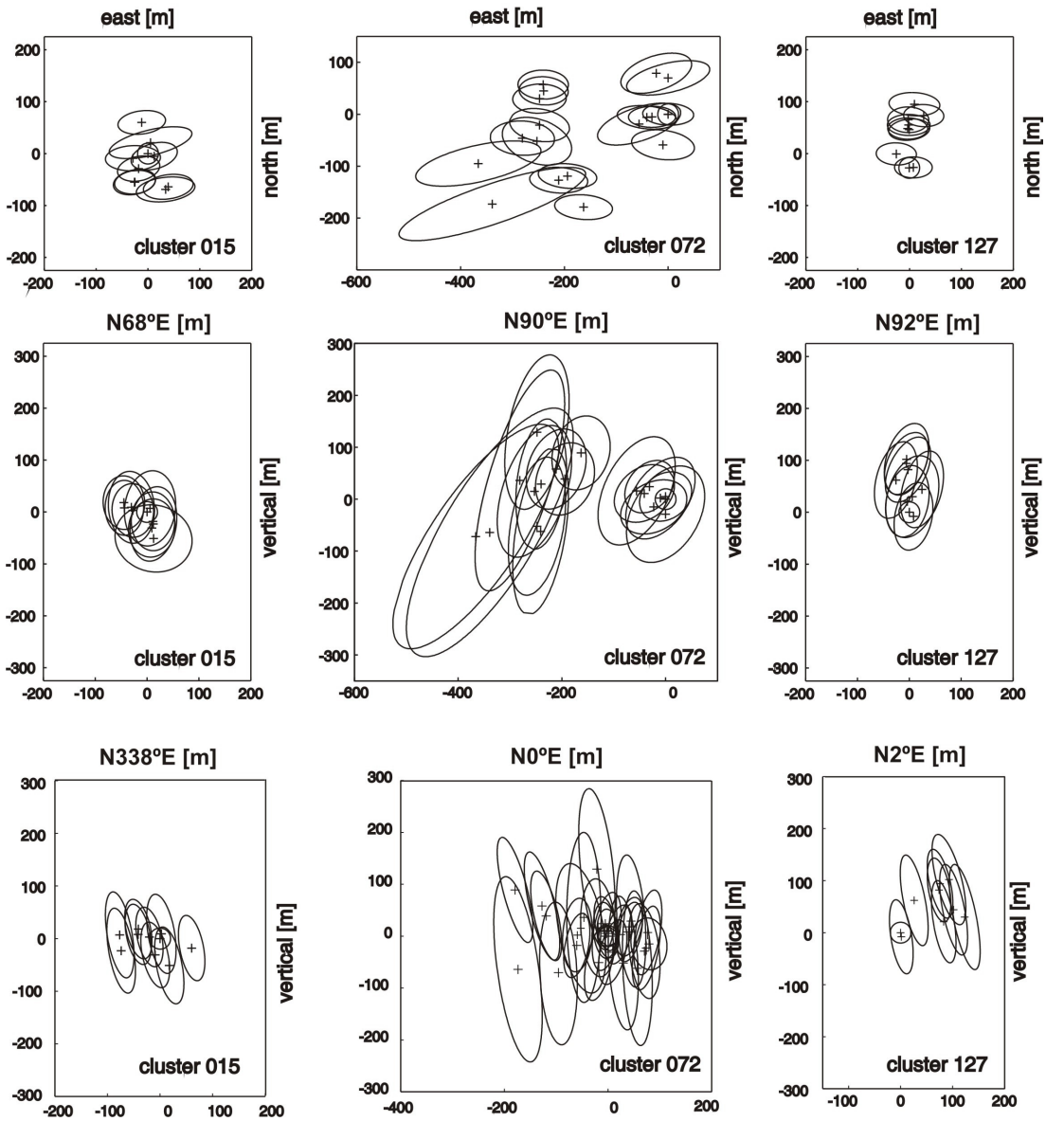

Figura 2.19 *(art.II fig.6)*. Localizaciones relativas y elipsoides de error para los multipletes 15, 72 y 127 para proyecciones horizontales (arriba) y dos proyecciones verticales (medio y abajo).

Se han obtenido ocho planos con azimut N-S y buzamiento casi vertical; cinco planos NNO-SSE, tres de ellos con poco buzamiento (dos con dirección de buzamiento ENE y uno con dirección OSO); y un plano con dirección E-O muy buzado (Figura 2.20).

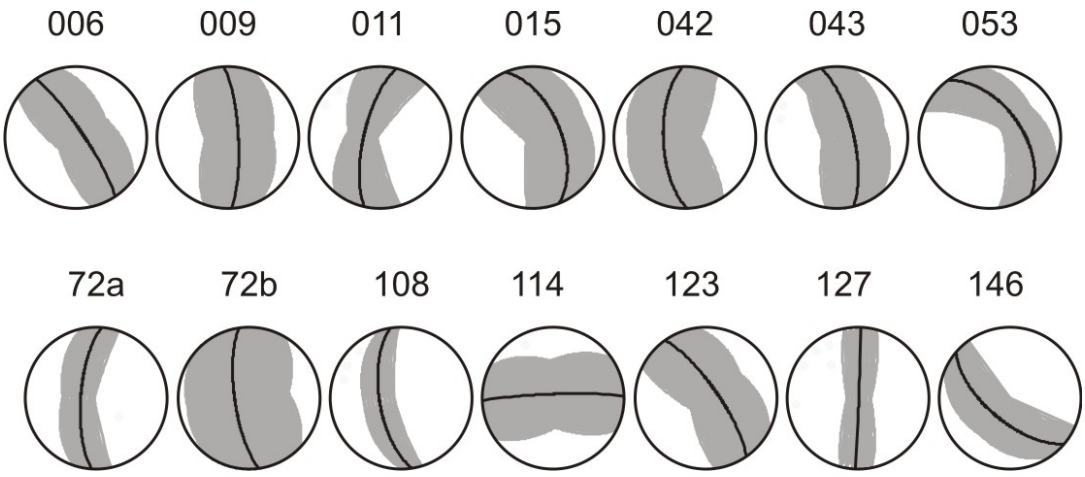

Figura 2.20 (*art.II fig.7a)*. Representación estereográfica de los ajustes a un plano de las localizaciones relativas precisas. El número indica el número de la familia. La banda gris indica el intervalo de incertidumbre del ajuste.

Se han calculado los mecanismos focales para los eventos de las familias a través de la polaridad del primer movimiento. Se ha utilizado la similitud de los sismogramas de las familias para garantizar que la polaridad de la onda P tenga bajo nivel de ruido. Como era de esperar, no se han encontrado discordancias de las polaridades de la onda P para los miembros de una misma familia. De este modo, se han obtenido de 3 a 8 polaridades de la onda P por familia. Con estos datos se ha realizado una búsqueda en un sistema de mallas (FOCMEC, Snoke *et al*. 1984) para probar toda una gama de soluciones de fallas de doble par, con un incremento de 10º en los parámetros de la falla. Las soluciones del mecanismo focal han sido poco restrictivas en parte por el escaso número de polaridades y por la pobre cobertura de la esfera focal. Este conjunto de soluciones no resuelven la ambigüedad de los planos nodales y elegir una solución preferida sería muy arriesgado. Es necesaria la combinación con otro conjunto de soluciones que nos permita resolver esta ambigüedad.

Para resolver este problema, se han utilizado las orientaciones de los planos de ajuste de las localizaciones relativas precisas de las familias combinándolos con el conjunto de soluciones del mecanismo focal (Figura 2.21). Para la mayoría de las familias con 5-8 lecturas de polaridades, la combinación de estos dos conjuntos de soluciones muestra muy poca dispersión, definiendo muy bien el azimut del plano, el buzamiento y el ángulo de la dirección de deslizamiento, y resolviendo por tanto la ambigüedad del plano nodal.

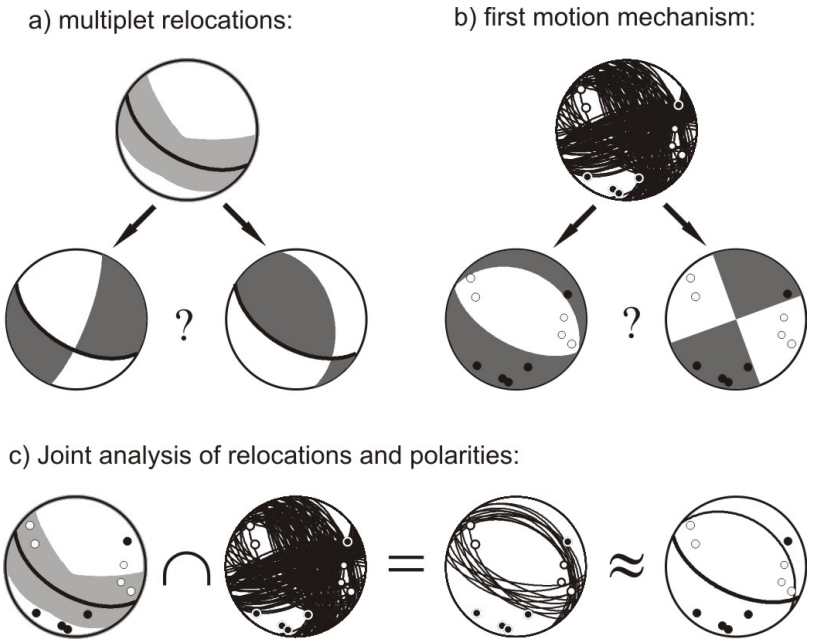

Figura 2.21 (*art. II fig. 3)*. Ejemplo de la combinación de las técnicas de localización relativa y mecanismos focales de las polaridades de las primeras llegadas para una familia de terremotos. (a) La localización relativa de una familia proporciona el azimut y el buzamiento del plano de falla (línea negra) y su incertidumbre asociada (banda gris), pero no resuelve el vector deslizamiento. (b) Los mecanismos focales a través de las polaridades proporcionan el azimut, el buzamiento y el vector deslizamiento, pero puede haber varias soluciones y además no es posible distinguir entre el plano de falla y el plano auxiliar. (c) Combinando ambos resultados se puede resolver la ambigüedad, estimar un mecanismo focal y resolver la simetría del plano nodal.

Los resultados de la combinación de estos métodos para la serie de Iznájar proporcionan un total de nueve soluciones de las catorce posibles (Figura 2.22). Se observan seis soluciones de fallas de salto en dirección sinistras con azimut N-S, y tres soluciones de fallas normales con direcciones NO-SE a NNO-SSE y direcciones opuestas del buzamiento. Para el caso de la familia 72, en la que el método de localización relativa separa los hipocentros en dos planos, se observan dos fallas paralelas de salto en dirección a una distancia de aproximadamente 230 m, lo que indica un alto grado de fracturación en el volumen fuente.

Si comparamos los resultados con los tensores momento calculados para la serie de Iznájar (Stich *et al*. 2003) (Figura 2.8) parecen ligeramente diferentes. Sin embargo la región de confianza de los mecanismos obtenidos por el tensor momento incluye fallas de salto en dirección ~N-S, y se podrían identificar los planos nodales con esta dirección como el plano

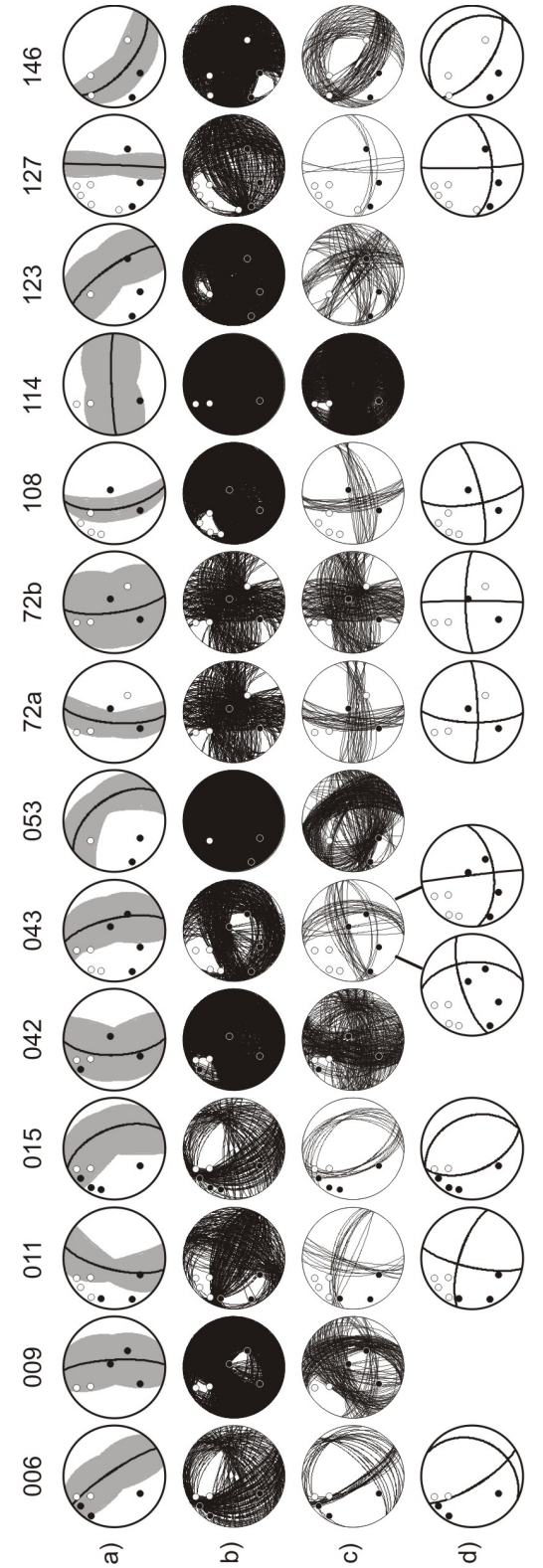

Figura 2.22 (*art. II fig. 7*). Geometría de los multipletes en proyección estereográfica de igual área. (a) Planos de falla de los multipletes(negro)on los errores estándares (bandas grises) y polaridades leídas (círculos blancos para las dilataciones, negros para las compresiones). (b) Soluciones para el mecanismo focal con la rejilla de búsqueda. (c) Intersección de los rangos de soluciones de la fila a y b. (d) Media de las soluciones de los mecanismos focales (cuando la dispersión en c es pequeña). Para el multiplete 43 se muestra dos posibles soluciones.

de falla activo de las soluciones del tensor momento. Las fallas N-S de salto en dirección sinistra dominan en la dislocación del enjambre de Iznájar, y representarían a la mayoría de las familias analizadas. La coexistencia de los restantes planos (fallas normales puras) sugiere una permutación de los ejes principales de esfuerzo, mayores e intermedios, producido probablemente por la perturbación del esfuerzo local en el transcurso del enjambre.

Aunque la localización absoluta de los eventos de las familias no es suficientemente precisa para inferir la relación geométrica de estos elementos estructurales, las fallas de salto en dirección y normales pueden actuar entre sí para compensar el desplazamiento diferencial entre fallas adyacentes. Tales fallas tectónicas delimitadas por bloques se han propuesto anteriormente para explicar la estructura fina en otras series sismotectónicas de la zona (Stich *et al.* 2001), así como a escala regional de las fallas neotectónicas en la Cordillera Bética (Martínez-Díaz y Hernández-Enrile, 2004, Martínez-Martínez *et al.* 2006). El predominio de fallas de salto en dirección hace que esta actividad sea diferente de la sismicidad asociada a la Cuenda de Granada, donde dominan los mecanismos de falla normal y extensión ENE-OSO (por ejemplo, Galindo-Zaldívar *et al.* 1999; Muñoz *et al.* 2002; Stich *et al.* 2006). Existe un patrón similar de distribución de fallas de salto en dirección y fallas normales de terremotos a ~20 km al sureste de la Cuenca de Granada (Martínez-Martínez *et al.* 2006). La profundidad de la serie de Iznájar y las fallas bajo la Cuenca de Granada (concentradas entre 9 y 16 km de profundidad, Morales *et al.* 1997) son similares, a pesar de que el enjambre de Iznájar está a unos 30-40 km de distancia de las principales concentraciones de terremotos, en la parte oriental de la Cuenca.

Debido a las pequeñas dimensiones de las fallas involucradas en los terremotos del enjambre de Iznájar, no podemos especular sobre la importancia de estas fallas en relación con los esfuerzos de la tectónica regional, pero en cualquier caso, nuestros resultados ponen de relieve la alta heterogeneidad de la deformación tectónica en la Cordillera Bética, donde la sismotectónica a diferente escala puede ser controlada por fallas que interaccionan entre sí.

3

Caracterización de sistemas de fractura con técnicas de array en la Isla Decepción

3.1. Introducción

La Isla Decepción es uno de los volcanes más activos de la Antártida y a la vez de los más estudiados a través de distintas disciplinas geofísicas y geológicas. La tectónica regional e incluso la tectónica superficial local de la isla se encuentran muy documentadas (Pelayo y Wiens, 1989; Rey *et al.* 1995; González-Casado *et al.* 1999; Robertson Maurice *et al*. 2003; Fernández-Ibáñez *et al.* 2005; Paredes *et al*. 2006; Maestro *et al*. 2007). Estos estudios han tratado de establecer un nexo de unión entre los procesos geológicos regionales en los que está enmarcada la Isla Decepción y el particular proceso dinámico de la fuente activa del volcán. Pero para intentar comprender el proceso dinámico en el interior del volcán y en cierto modo predecir su comportamiento es necesario la utilización de técnicas geofísicas (análisis de gases, geomagnetismo, deformación, sismología, ...) que proporcionen información de la actividad volcánica reciente.

La sismología volcánica puede mejorar el conocimiento de los procesos dinámicos activos de los volcanes a partir del análisis de las señales sísmicas que se generan. Estas señales nos dan información acerca de numerosos aspectos, como los parámetros de la fuente (posición, evolución espacio-temporal, cuantificación energética, dinámica y geometría, etc.) y las características del medio (estructura de velocidad, atenuación, heterogeneidades, etc.). Los eventos puramente volcánicos, como el tremor volcánico o los eventos de largo periodo (LP) aportan información sobre la dinámica y el mecanismo del transporte de fluidos en el sistema volcánico. Los terremotos volcano-tectónicos (VT) nos permiten conocer la dinámica y la geometría de la ruptura que los ha generado, y por tanto constituyen una herramienta para investigar el estado local de esfuerzos y por consiguiente la fuente sísmica (p.ej. Chouet 1996).

Para caracterizar la sismotectónica de una zona volcánica es necesario un número suficiente de terremotos. Esta actividad sísmica nos la pueden proporcionar las series sísmicas. Desde que se tienen registros sísmicos en Decepción, han tenido lugar dos series sísmicas importantes: una en 1992 con 776 terremotos VT y la serie de 1999 con más de 2000 terremotos VT. La serie de 1992, debido a la escasez de instrumentación desplegada en ese momento, no permitió obtener información sobre las estructuras implicadas, pero sí sobre la evolución energética (Ortiz *et al.* 1997). Para la serie de 1999, la utilización de antenas sísmicas ha permitido realizar un análisis más exhaustivo de la fuente y la tectónica.

La utilización de antenas sísmicas además de las redes convencionales en zonas volcánicas cada vez está más extendida. Las técnicas de antenas sísmicas se han utilizado

para localizar los eventos sísmicos, investigar la evolución temporal de la fuente, analizar el ruido, o conocer los detalles de la estructura local. Se han utilizado en muchos volcanes, como por ejemplo Stromboli (Chouet *et al*. 1997; La Rocca *et al*. 2004), Etna (Saccorotti *et al*. 2004), Vesubio (Saccorotti *et al*. 2001b), Teide (Del Pezzo *et al*. 1997; Almendros *et al*. 2000, 2007), Masaya (Metaxian *et al*. 1997), Arenal (Metaxian *et al*. 2002; Mora *et al*. 2006), Kilauea (Almendros *et al*. 2001a,b), Decepción (Almendros *et al*. 1997, 1999; Ibáñez *et al*. 2000), Copahue (Ibáñez *et al*. 2008), y Colima (Palo *et al*. 2009). Las antenas sísmicas nos proporcionan una estimación del vector lentitud aparente, cuyo módulo representa la inversa de la velocidad aparente con que las ondas atraviesan el medio y cuya dirección indica el azimut con que se propagan. Para obtener una localización espacial, se pueden utilizar fundamentalmente tres técnicas: el método del frente de onda circular, el trazado del rayo, y la localización conjunta con varias antenas sísmicas. El primero se basa en la estimación del radio de curvatura del frente de onda, para lo cual la fuente debe ser cercana a la antena sísmica (Almendros *et al*. 1999). El segundo se basa en el trazado del rayo en un modelo de tierra predefinido. Además de la información sobre el vector lentitud aparente que nos proporciona la antena sísmica, necesitamos conocer los tiempos de llegada de las fases P y S para fijar la distancia a lo largo del rayo, lo cual limita su aplicación a terremotos con fases claras (p.ej. Del Pezzo *et al*. 1997; Almendros *et al*. 2000, 2007; Saccorotti *et al*. 2001b). Finalmente, el tercer método se basa en el uso de varias antenas. Los vectores lentitud aparente estimados por cada array se combinan para determinar la posición espacial de la fuente. Este método es muy potente y flexible, y además se puede aplicar a cualquier tipo de señal, incluyendo las señales puramente volcánicas (Almendros *et al*. 2000, 2001a, b; La Rocca *et al*. 2000, 2008; Metaxian *et al*. 2002).

En este capítulo se presenta el análisis de la serie sísmica ocurrida en Decepción en 1999 con un total de 3643 eventos registrados con antenas sísmicas. Ha sido la más importante desde la última erupción de 1970 hasta la actualidad, de la que se tenga registro instrumental. Este hecho la convierte en una referencia importante para el conocimiento de la fuente volcánica de Decepción y el estudio del riesgo volcánico que supone para las bases antárticas y el turismo que visita la Isla en los meses de verano austral.

Se ha realizado un análisis preliminar que incluye la localización de los eventos con técnicas de antenas sísmicas, el seguimiento de la evolución espacio-temporal de la fuente y una estimación de la energía implicada. La localización de los terremotos VT muestra alineamientos aparentes de los epicentros, pero sugiere la pregunta clave: ¿son estos alineamientos una indicación de las fallas implicadas en la serie?

Las localizaciones que proporcionan las técnicas de antenas sísmicas, al igual que ocurre con las técnicas de localización con redes sísmicas, son suficientes para obtener una estimación de la evolución espacio-temporal de la actividad y lograr mapas hipocentrales de los terremotos. Pero estas localizaciones no permiten la caracterización de las estructuras

implicadas, por la dispersión de los hipocentros. Para este fin es necesario que los terremotos estén localizados de forma precisa para poder interpretar las estructuras con fiabilidad.

Para localizar de forma precisa los terremotos registrados en antenas sísmicas, se ha desarrollado un método que consiste en la combinación de técnicas de antenas sísmicas junto con el procedimiento de localización relativa con "evento maestro". La semejanza de la formas de onda de eventos similares registrados en las estaciones de las antenas sísmicas puede ser utilizada para estimar los parámetros de propagación relativos, es decir, las diferencias de lentitud aparente y de azimut del frente de onda correspondiente a terremotos similares. Una vez obtenidas estas estimaciones se localizan espacialmente los hipocentros de las familias seleccionadas. Cuando las distribuciones de hipocentros observadas se ajustan a un plano (lo que suele ocurrir en el caso de multipletes), podemos interpretar ese plano como el plano de ruptura responsable de la generación de los terremotos.

Este novedoso método se ha aplicado a la serie de Decepción de 1999, obteniendo la caracterización de algunas estructuras implicadas en la serie. Para comprobar la robustez del método, se han realizado una serie de tests que confirman su validez para encontrar planos de ruptura mediante técnicas de antenas sísmicas. Finalmente, se han interpretado los resultados en el entorno volcánico y tectónico regional de la Isla Decepción.

3.2. Marco geológico

La Isla de Decepción se encuentra situada dentro de las Islas Shetland del Sur, a 62º43'S y 60º57'O frente a la Península Antártica. El marco tectónico regional es bastante complejo. En esta zona confluyen varias placas tectónicas (Pelayo y Wiens, 1989; Baraldo y Rinaldi, 2000; Robertson Maurice *et al*. 2003). Por un lado dos placas principales, la Placa Sudamericana y la Placa Antártica. Y por otro lado, tres microplacas, la de Scotia, la de Drake y la de las Shetland del Sur (Figura 3.1). La fosa de las Shetland del Sur sufre un proceso muy lento de subducción *slab roll-back* (Ibáñez *et al.* 1997; Robertson Maurice *et al*. 2003). Este proceso provocó la ruptura y separación entre la microplaca de las Shetland del Sur y la Península Antártica hace 2 millones de años, creándose lo que hoy se conoce como el Rift del Bransfield. Este Rift está formado por tres cuencas extensionales activas con tendencia NE, que provocan el volcanismo de la zona así como fallas normales. La sismicidad regional más superficial (menos de 40 km de profundidad) es compatible con el rift de expansión, mientras que la sismicidad más profunda es coherente con la subducción de la placa del Drake (Pelayo y Wiens, 1989, Ibáñez *et al*. 1997; Robertson Maurice *et al*. 2003).

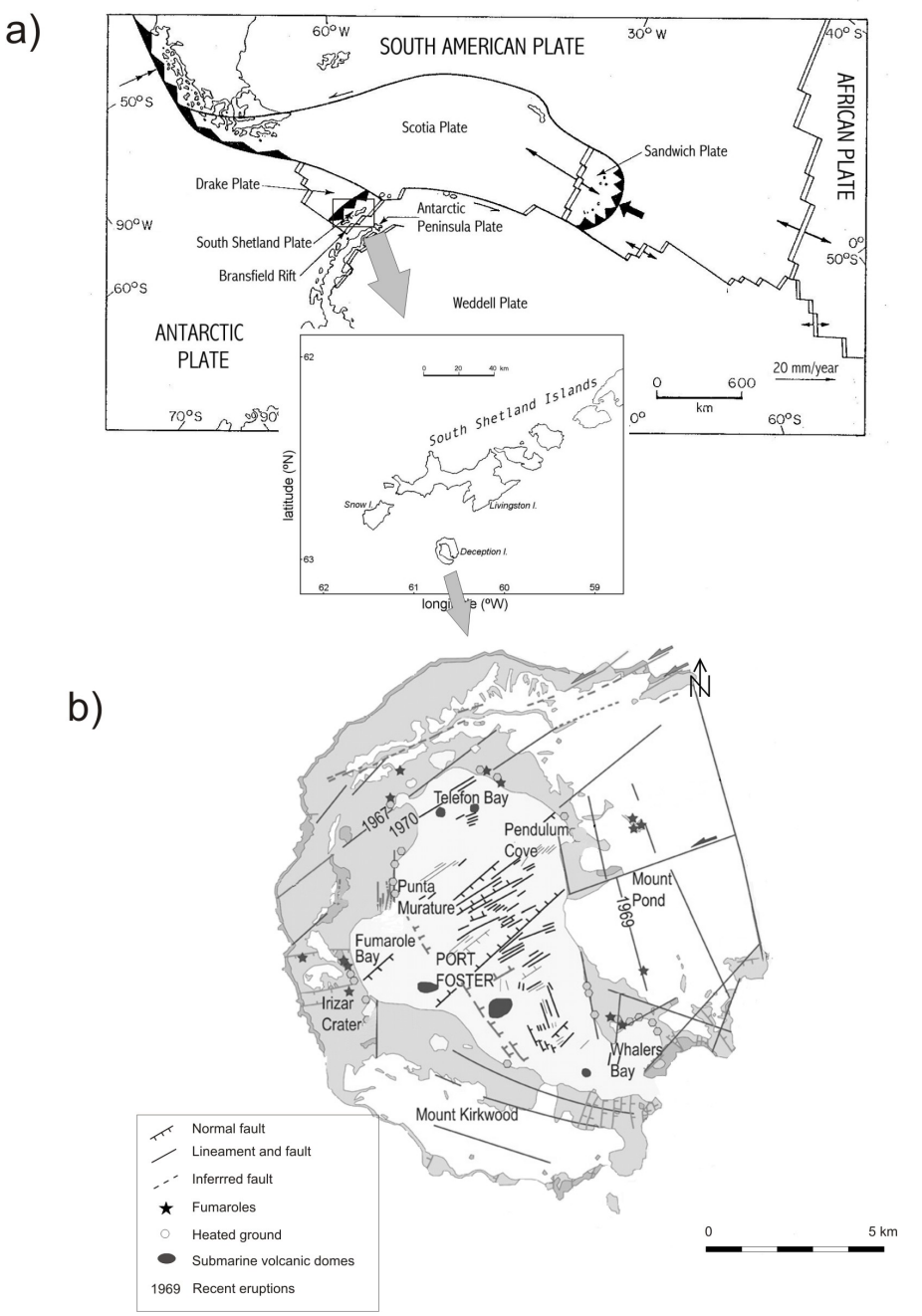

Figura 3.1 (*art.V fig.1)*. (a) Mapa tectónico de la región de Scotia. Dentro se muestra un mapa de la región de las Islas Shetland del Sur. (b) Mapa geológico simplificado de la Isla Decepción (modificado de Maestro *et al*. 2007)

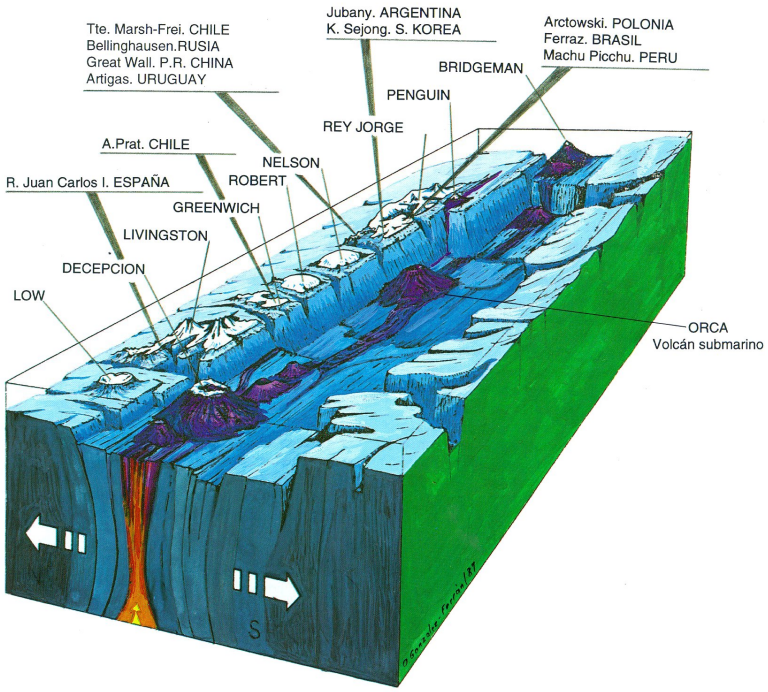

Figura 3.2. Diagrama del Rift del Bransfield en el que se encuentra la cadena volcánica a la que pertenece Decepción (de González-Ferrán, 1995)

La Isla de Decepción está situada en el eje de extensión de la Cuenca Central del Bransfield (Figura 3.2) y es probablemente uno de los volcanes antárticos más activos en la actualidad con erupciones conocidas en 1842, 1912, 1917 y las más recientes durante 1967, 1969 y 1970 (Smellie, 1988). Tiene forma de herradura con su parte interna inundada de agua y con unos 15 kilómetros de diámetro en la zona emergida (Blanco, 1997). El origen de esta forma tan peculiar en herradura tiene varias explicaciones posibles. Una podría ser el colapso de un gran edificio volcánico debido a erupciones grandes, produciéndose una colmatación y provocando fracturas en forma de anillo (González-Ferrán y Katsui, 1970; Baker *et al*. 1975). En trabajos recientes de tomografía sísmica se ha constatado la presencia de una cámara magmática en el centro de la bahía de Decepción (Zandomeneghi *et al*. 2009). Otra posible explicación podría ser que la caldera se formara por una depresión tectónica provocada por movimientos extensivos a lo largo de fallas normales regidas por la tendencia regional extensiva, desestimando la presencia de fallas circulares (Martí *et al*. 1996; Rey *et al*. 1995; González-Casado *et al*. 1999).

Las distintas campañas de sísmica de reflexión, junto con las observaciones de campo, ponen de manifiesto tres grandes sistemas de fallas (Rey *et al*. 1995; Martí *et al*. 1996). El primer gran sistema es coherente con el régimen extensional del Bransfield, con dirección NE-SO, desde Punta Murature hasta Bahía Telefono. Estos alineamientos coinciden con las erupciones de 1967 y 1970. Además, en trabajos de tomografía sísmica se ha encontrado un contraste de velocidad entre la Isla de Decepción y el basamento de las Shetland del Sur, cuya dirección es precisamente NE-SO (Zandomeneghi *et al*. 2009; Ben-Zvi, *et al*. 2009). El segundo sistema, con una orientación aproximadamente E-O coincide con las alineaciones del Mt. Kirkwood, con erupciones freatomagmáticas generadas a partir de estas fisuras, con la erupción de 1842 o incluso algunos cráteres de la erupción de 1970 y con alineamientos de conos submarinos en el interior de la caldera. Y el tercer sistema tiene orientaciones NNO-SSE entre los que se encuentran el alineamiento más característico de Costa Recta (Fernández-Ibáñez *et al*. 2005), el sistema del Mt Pond, fallas subparalelas a lo largo de la zona de Bahía Fumarolas y el glaciar Negro, y las fisuras eruptivas de 1969. Aparte de estos tres sistemas de fallas, diversos autores han constatado la presencia de otros conjuntos de fallas a través de distintas técnicas como las observaciones geológicas en superficie, testificaciones geofísicas, batimetrías, análisis morfológico del modelo digital de elevaciones, lineamientos morfológicos producidos por la actividad volcánica reciente, etc. (Martí *et al*. 1996, González-Casado *et al*. 1999; Paredes *et al*. 2006; Maestro *et al*. 2007; Barclay *et al*. 2009). Estos trabajos ponen de manifiesto la presencia de numerosas fallas con diferentes direcciones.

3.3. Instrumentación

El monitoreo sistemático de la actividad sísmica de la Isla Decepción comienza en los años 50. Una primera etapa se extiende hasta finales de los años 60, cuando se producen las erupciones más recientes. Se ha dejado constancia escrita de que justo antes de las erupciones se produjo un aumento considerable de la actividad sísmica. Después de la erupción de 1970 la Isla no se monitorea hasta el verano austral de 1986 y no se tienen registros sísmicos para ese periodo. La instrumentación desde 1986 hasta 1988 consistía en estaciones verticales analógicas de corto periodo con registro en papel térmico. Entre el periodo comprendido entre 1989 y 1991, los datos eran registrado por una red de estaciones compuesta por cinco estaciones de corto periodo con telemetría vía radio, realizándose los primeros estudios sísmicos de la Isla (Vila *et al*. 1992, 1995). En la campaña 1991-1992 se tenía desplegada una estación de tres componentes de corto periodo cerca de la base argentina, que registró un incremento considerable de actividad (Ortiz *et al*. 1992, 1997;

García *et al*. 1997). Para las campañas de 1992-1993 y 1993-1994 se desplegaron nuevas estaciones símicas entre las bases argentina y española. Entre 1994 y 1999 debido a que con las estaciones desplegadas en anteriores campañas era complicado localizar la actividad volcánica se desplegaron antenas sísmicas para su localización (Almendros *et al*. 1997, 1999; Almendros 1999; Ibáñez *et al*. 2000). A partir de 1998 y hasta la actualidad, la instrumentación sísmica desplegada ha sido variada, con antenas sísmicas, estaciones de registro continuo y estaciones de banda ancha. El monitoreo de la Isla durante todos estos años ha sido durante los meses del verano austral, no obteniéndose registros durante los meses de invierno. En enero de 2008, la instalación de una estación permanente de banda ancha ha podido suministrar datos en continuo durante todo un año (Martínez-Arévalo *et al.* 2009).

La situación geográfica de la Isla de Decepción le confiere una particularidad especial para monitorear la actividad sísmica. La preparación y posterior instalación de las estaciones sísmicas se organiza en "campañas" que coinciden con la estación estival austral (3 meses). Desde el año 1994 hasta la actualidad, el Instituto Andaluz de Geofísica lleva participando en estas campañas antárticas, que se pueden dividir en tres partes: la precampaña, la campaña de campo y la poscampaña.

La precampaña consiste en la organización y la logística necesaria para desplegar en Decepción la instrumentación que se haya decidido instalar. Desde los comienzos de la monitorización de la Isla, la instrumentación utilizada ha ido evolucionando y por tanto ha sido necesario una preparación y puesta a punto particular de la instrumentación para cada campaña. Esta preparación consiste en comprobar el funcionamiento correcto de las estaciones sísmicas y el aprendizaje de las mismas, así como la preparación y embalaje de todo el material para el transporte. La precampaña puede durar unos meses e implica el apoyo de numeroso personal técnico del IAG (electrónicos, informáticos, personal de mantenimiento, personal de administración, etc.) antes de estar todo preparado para el viaje desde el IAG hasta la Antártida.

Las campañas de campo suelen durar 3 meses y consisten en la instalación y mantenimiento de la instrumentación desplegada así como el análisis preliminar "in situ" de la actividad sísmica registrada. La instalación de la instrumentación requiere un esfuerzo por parte de todo el personal técnico de las bases españolas. La orografía de la Isla Decepción requiere la utilización de medios de transporte terrestres y marítimos para llegar a las áreas donde se instalarán las estaciones sísmicas. La instalación de las estaciones suele durar unas semanas dependiendo siempre de las condiciones climatológicas. Una vez desplegadas, el mantenimiento se realiza prácticamente a diario y consiste en el cambio de baterías para el consumo de los sistemas de registro. Los datos sísmicos registrados se procesan en la base (Figura 3.3) realizando un análisis preliminar que permite establecer un control de la actividad sísmica del volcán. La campaña finaliza con el cierre de las bases españolas y

consiste en la desinstalación de las estaciones y su posterior embalaje para el regreso a España.

Figura 3.3. En la foto de la izquierda se muestra el mantenimiento de una estación sísmica durante la campaña de 1998-1999. A la derecha, trabajos de gabinete dentro de la base antártica española.

La post-campaña consiste en dos partes, por un lado la recepción del material y revisión del mismo y por otro, el análisis más exhaustivo de los datos registrados en esa campaña de campo, para finalmente emitir un informe al Comité Polar Español con las incidencias, actividad sísmica y resultados de la campaña.

Figura 3.4 Instalación de una antena sísmica en Bahía Fumarolas. En el margen inferior izquierdo de la foto izquierda se observa el sistema de adquisición de datos junto con el PC de registro.

Durante la campaña antártica 1998-1999 se instalaron dos antenas sísmicas. Cada una de ellas estaba gestionada por dos módulos de adquisición de datos de ocho canales y 16 bits. La sincronización y el control del tiempo, fundamental en una antena sísmica, se realizaba con un receptor GPS, cuya configuración y control se realizaban a través del puerto serie del PC con formato RS-232. La frecuencia de muestreo era de 200 muestras por segundo por canal. Los datos eran grabados por el sistema de adquisición utilizando el algoritmo STA/LTA por disparo. Para la antena sísmica situada en la zona denominada Playa de Obsidianas los 16 canales se correspondían con una estación de tres componentes y 13 estaciones de componente vertical, todos con sensores Mark L28 de 4.5 Hz con respuesta extendida a 1 Hz. Por su parte, la antena sísmica situada en la zona de Fumarolas, (Figura 3.4), estaba compuesta por 7 sensores verticales Mark L28, también con respuesta extendida a 1 Hz, y 3 estaciones de 3 componentes con sensores Mark L4C con 1 Hz de frecuencia propia. También se contaba con una estación de registro en continuo, compuesta por un sensor de tres componentes Mark L4C de 1Hz de frecuencia propia junto con un sistema de adquisición de 16 bits. Estaba situada en las cercanías de la Base Antártica Española (Figura 3.5)

Figura 3.5. Imagen panorámica del estado actual de la base española “Gabriel de Castilla” (cortesía de Rosa Martín)

La idea de utilizar las dos antenas sísmicas era tratar de comparar la actividad en las distintas zonas y a su vez utilizar la técnica de localización cruzada mediante antenas múltiples (La Rocca *et al.* 2000; Almendros *et al*. 2000). Esto no fue posible, debido a que la estructura superficial de velocidad bajo las dos antenas era muy diferente, afectando a la estimación del vector lentitud aparente de los eventos registrados por ambas antenas. Debido al sistema tan complejo en el que se encuentra situada la antena sísmica de Obsidianas (Saccorotti *et al.* 2001a; Luzón *et al*. 2009) se decidió utilizar para nuestro trabajo los datos registrados en la antena sísmica de Fumarolas. Esta antena sísmica estaba desplegada en las proximidades del sistema fumarólico de Bahía Fumarolas, aproximadamente a 500 m NNE de la Base argentina. Tenía una apertura aproximada de 240 m, con forma geométrica

compuesta por dos semicírculos concéntricos de radio 120 m y 60 m. El espaciado angular entre estaciones fue aproximadamente de 45º para el semicírculo externo y de 60º para el semicírculo interno (Figura 3.6).

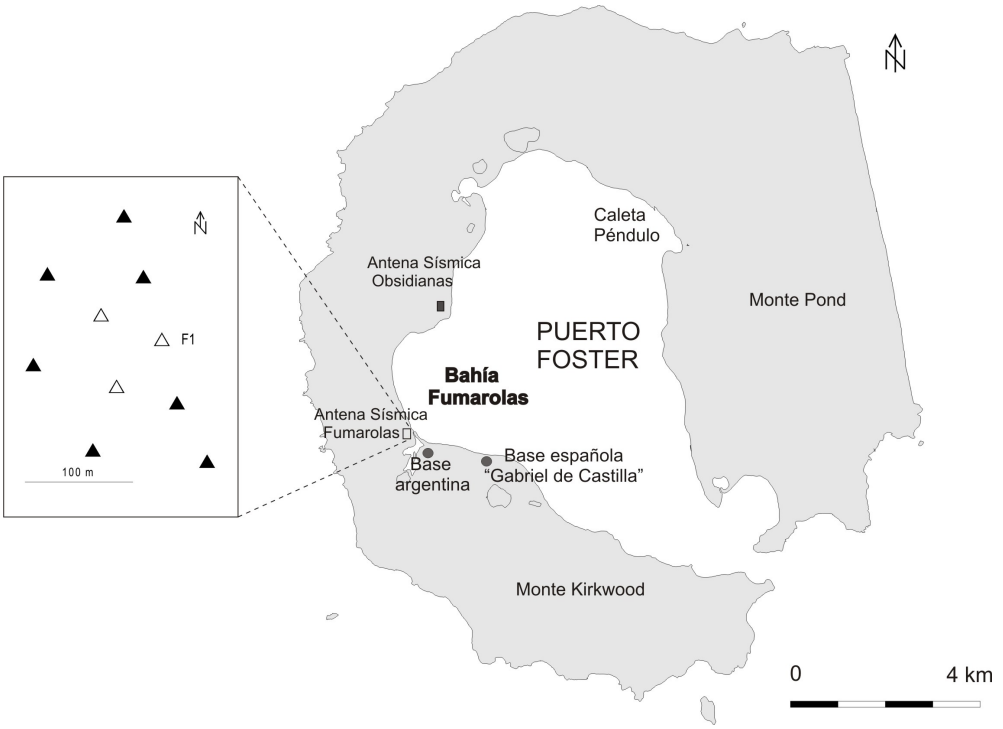

Figura 3.6. Mapa de Decepción con la instrumentación instalada durante la campaña 1998-1999. Se muestra la configuración de la antena sísmica de Fumarolas. Los triángulos negros son estaciones verticales. Los triángulos blancos son estaciones de tres componentes. En un cuadrado gris se muestra la situación de la antena de Obsidianas y con círculos la situación de las bases española y argentina.

3.4. Sismicidad en la Isla Decepción

La actividad sísmica que se registra en Decepción se puede dividir principalmente en tres grupos: terremotos volcano-tectónicos (VT), eventos de lago periodo (LP), incluyendo en este tipo el tremor volcánico, y eventos híbridos (Figura 3.7).

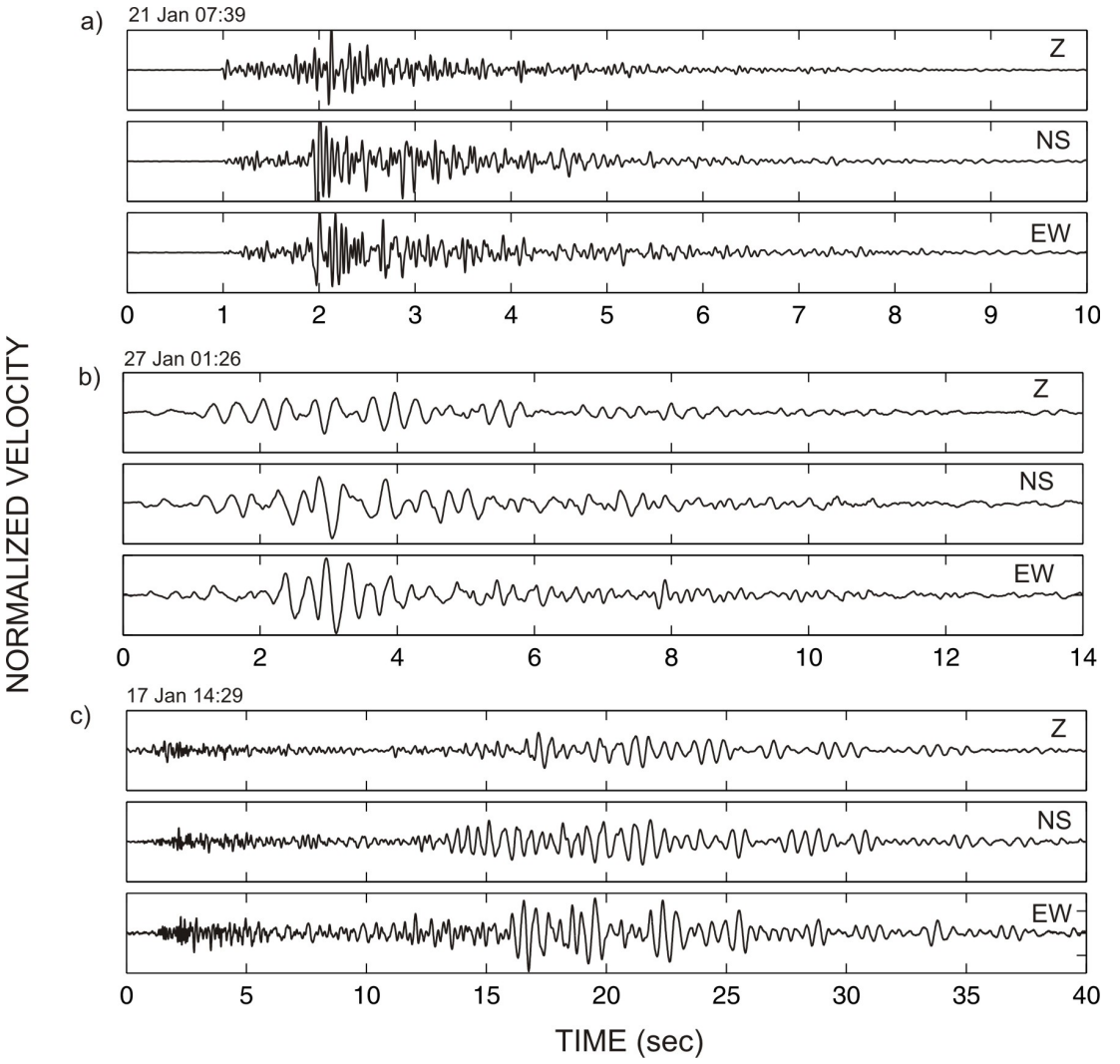

Figura 3.7. Ejemplos de eventos sísmicos registrados durante la serie de 1999. a) Terremoto VT. b) Evento LP. c) Híbrido. En los tres ejemplos se muestran los sismogramas de las 3 componentes.

Los terremotos VT son terremotos locales generados en el edificio volcánico y que por las dimensiones de la estructura volcánica de la Isla suelen ser de baja magnitud y tener tiempos S-P menores de 4 segundos. Tienen un contenido espectral distribuido con energía en un rango amplio de frecuencias, hasta por encima de 30 Hz. Los distintos estudios de la sismicidad VT muestran distintas zonas de ocurrencia. Vila *et al*. (1995) muestran que la actividad de terremotos VT durante el periodo desde 1986 hasta 1991 está localizada por toda la Isla. Ibáñez *et al*. (2000) y Almendros (1999) localizan los terremotos durante el periodo 1994-1998 a lo largo de un sistema de fractura NE-SO, cerca de la base española. Los terremotos VT suelen ser superficiales y de baja magnitud, aunque existe constancia de

terremotos de magnitud 3.5 en el interior de la Isla. El origen de los terremotos VT está relacionado con los sistemas de fractura del edificio volcánico y su generación puede ser debida a los cambios en la distribución de esfuerzos locales (volcánicos) o regionales.

La sismicidad de largo periodo está caracterizada por un contenido en frecuencias casi monocromático. Entre este tipo de sismicidad se encuentran los eventos LP y el tremor volcánico. Los eventos LP tienen poca duración (menos de 60 s) y contenido espectral que va desde 1 hasta 10 Hz. Tienen una llegada poco impulsiva que hace complicada su localización. La fuente que genera este tipo de eventos está relacionada con la resonancia de fluidos dentro de las cavidades (Chouet, 1996). El tremor volcánico está caracterizado por una señal monocromática similar a los LP, pero de larga duración (desde minutos hasta horas y días). Los modelos de generación del tremor volcánico están basados en desgasificaciones, fluctuaciones de gases, resonancia de conductos, etc. (Chouet, 1992; Julian 1994). En algunos estudios se ha puesto de manifiesto que el origen de los eventos LP y el tremor volcánico es el mismo (Almendros *et al*, 1997, 2001b).

Los eventos híbridos son señales que contienen una parte generada por un mecanismo de doble-par y otra parte generada por la resonancia de los fluidos. Están caracterizados por llegadas de altas frecuencias, similares a las de los terremotos VT y unas llegadas más tardías de fases monocromáticas de baja frecuencia similares a los eventos LP. El origen de las bajas frecuencias es el mismo que para los eventos LP, con la diferencia de que en los híbridos esa resonancia de fluidos la provoca el proceso de ruptura de las fallas implicadas.

Desde el comienzo del monitoreo en Decepción, el nivel de actividad sísmica registrado ha sido variado. Desde periodos donde la actividad ha sido muy baja hasta campañas donde el número de eventos ha estado muy por encima del resto (campañas 91-92 y 98-99), hasta el punto de considerarlas series sísmicas. El patrón de ocurrencia sísmica de las series de 1992 y de 1999 ha sido muy parecido. Hasta 1992 domina la sismicidad LP frente a los terremotos VT. Después de la serie de terremotos VT de 1992 vuelven a dominar los LP hasta la llegada de la crisis de 1999. En el año 1992 se contabilizaron 766 terremotos VT en un período de dos meses, con terremotos sentidos, enjambres de eventos de largo periodo y episodios de tremor volcánico, en algunos momentos sentido (Ortiz *et al.* 1997). Durante los años 1993 a 1998, la actividad volvió a los parámetros normales con unos períodos más activos que otros. El segundo episodio importante de reactivación de la actividad volcánica tuvo lugar durante la campaña de 1998-1999, con un total de 3643 eventos. En la campaña siguiente (1999-2000) se registraron varias decenas de eventos VT. Algunos de ellos estaban localizados en la misma zona epicentral que los terremotos de enero y febrero de 1999. Estos terremotos pueden responder a la activación de los mismos sistemas de fractura. En el resto de campañas hasta febrero de 2009 aparecen algunos episodios de eventos LP y tremor volcánico y algunos terremotos VT, aunque el nivel de actividad sísmica es en general mucho más bajo.

3.5. Serie de 1999 de Isla Decepción

3.5.1. Análisis preliminar *(art. III)*

La serie sísmica comenzó a finales de diciembre de 1998, obteniéndose registros hasta abril de 1999. A partir de esta fecha, la llegada del invierno impidió obtener más datos por lo que desconocemos el final real de la serie.

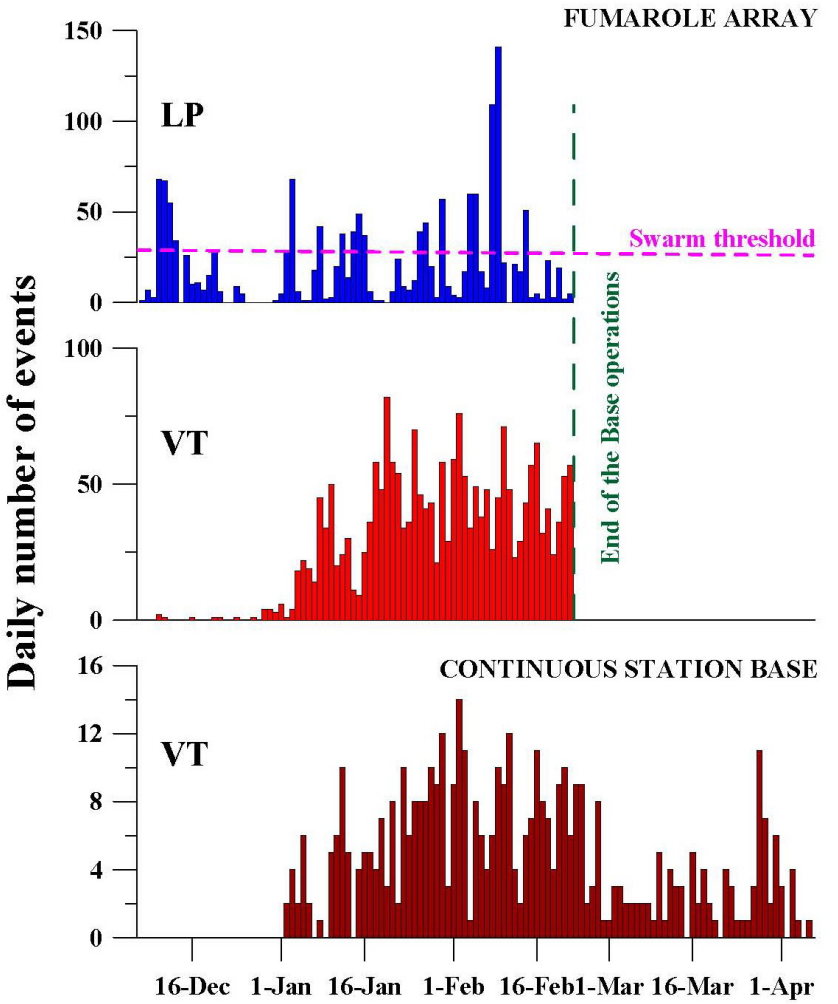

Figura 3.8 *(art. III fig. 6)*. Histograma del número de eventos LP y VT por día detectados en la antena sísmica de Fumarolas y la estación de continuo de la base "Gabriel de Castilla".

Las antenas sísmicas estuvieron registrando desde el comienzo de la serie hasta finales de febrero de 1999 (Figura 3.8). Registraron un total de 3643 eventos de los cuales 2072 fueron terremotos VT, 1556 fueron eventos LP y 15 fueron eventos híbridos. También se dieron algunos episodios de tremor volcánico.

La magnitud momento de los terremotos varía entre -0.8 y 3.4. Los dos terremotos más grandes de la serie, con magnitudes de 2.8 y 3.4, ocurrieron el 11 y 20 de enero de 1999, respectivamente, y fueron sentidos por el personal de la base "Gabriel de Castilla". Las magnitudes de los terremotos VT han permitido que se siga la evolución de la energía de la serie sísmica, estimando también el momento sísmico acumulativo (Figura 3.9). A excepción de los dos terremotos grandes, la energía relajada en función del tiempo es más o menos constante.

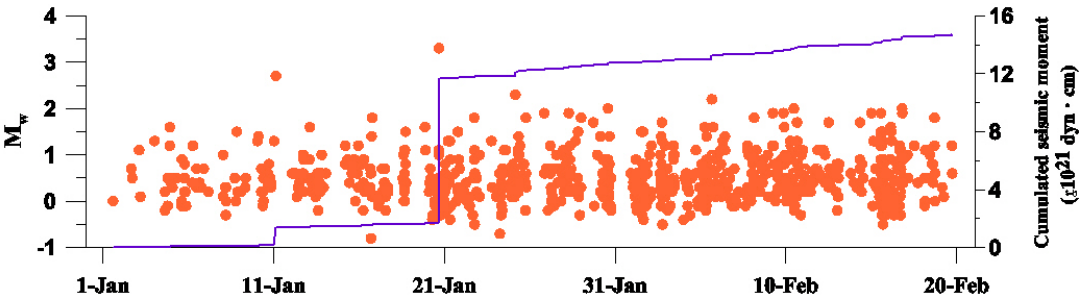

Figura 3.9 (*art. III fig. 14)*. Magnitud de los terremotos (eje izquierdo) frente al tiempo (enero-febrero 1999). La línea continua representa el momento sísmico acumulativo (eje derecho)

También se calcularon los valores de la caída de esfuerzos a partir de la magnitud obteniéndose valores bajos entre 0.1 y 4 bar. Se estimaron tamaños de la fuente del orden de 10-100m. Estos resultados nos dan una idea del pequeño tamaño que podrían tener las fracturas implicadas en el proceso de generación de la serie.

Los terremotos VT se localizaron usando el método de la *correlación cruzada promedio* (Frankel *et al.* 1991) para estimar el vector lentitud aparente de las primeras llegadas de la onda P. Se realizó para tres bandas de frecuencia. Posteriormente se estimaron visualmente las diferencias S-P y se utilizó la técnica del trazado del rayo con un modelo de velocidad obtenido combinando otros trabajos anteriores (Ibáñez *et al.* 2000; Saccorotti *et al.* 2001a). En total se obtuvieron 863 terremotos localizados. Para el análisis de los eventos LP y de los episodios de tremor volcánico se utilizaron dos bandas de frecuencia, obteniéndose lentitudes aparentes y azimutes diferentes a los obtenidos para los VT (Figura 3.10). Estos resultados coinciden con trabajos anteriores en distintas campañas (Ibáñez *et al*. 2000) y hacen pensar que la actividad de largo periodo es de origen hidrotermal y no guarda relación con la serie VT de 1999. También se analizaron 9 eventos híbridos, obteniéndose resultados

similares a los obtenidos para los eventos VT, lo que indica la presencia de fluidos en la zona de ocurrencia de los eventos VT.

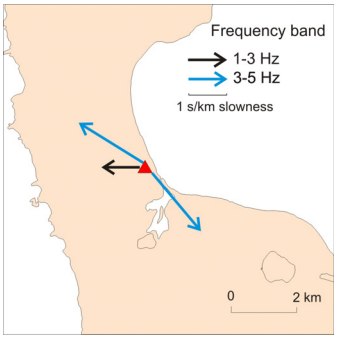

Figura 3.10. Promedio de los vectores lentitud aparente estimados para los eventos LP y el tremor para las bandas de frecuencia 1-3 Hz (flecha negra) y 3-5 Hz (flecha azul). La longitud de la flecha indica el valor de la lentitud aparente, y su dirección el azimut hacia la fuente.

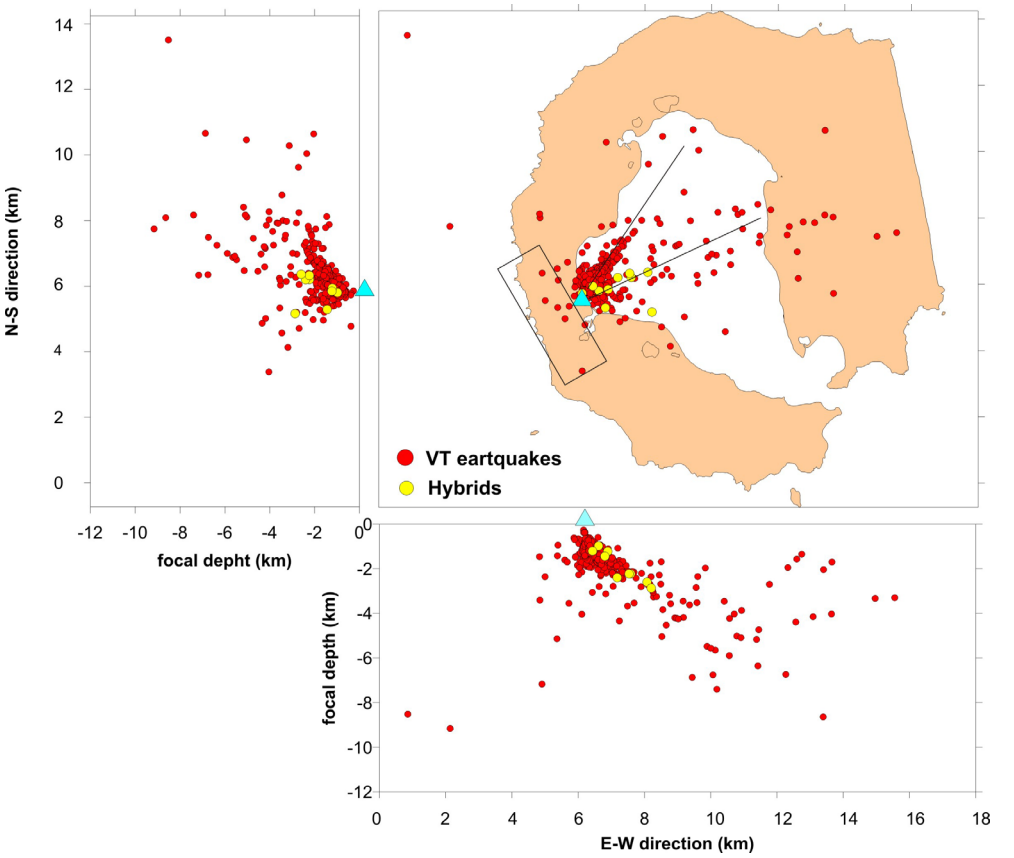

Figura 3.11 (modificada *art III fig.12)*. Localización hipocentral de los terremotos VT (círculos rojos) y eventos híbridos (círculos amarillos). En el recuadro se marca la probable región fuente de la sismicidad LP. Las líneas continuas marcan los posibles alineamientos.

La localización muestra que la inmensa mayoría de los eventos VT se encuentran muy cercanos a la antena sísmica y a profundidades en torno a los 2 km. Se pueden apreciar dos posibles alineamientos, uno con dirección N45ºE, con profundidades focales entre 1 y 4 kilómetros y un segundo, más disperso, que se extiende N80ºE (Figura 3.10).

En la Figura 3.11 se observa que la sismicidad está concentrada cerca del array. Podemos investigar si esta nube de datos podría ser producto del umbral de detección de los instrumentos sísmicos. Para comprobarlo, se dibuja la magnitud momento (Mw) frente a la profundidad focal y la distancia epicentral (Figura 3.12). Se puede ver que todos los terremotos con magnitudes más pequeñas, hasta 0.8, están concentrados en los primeros dos kilómetros de profundidad focal y de distancia epicentral. Para eventos más distantes, la magnitud mínima detectada es alrededor de 1.0. Esto implica que pudo haber sismicidad de baja magnitud localizada a más de 2 kilómetros del array que no pudo detectarse.

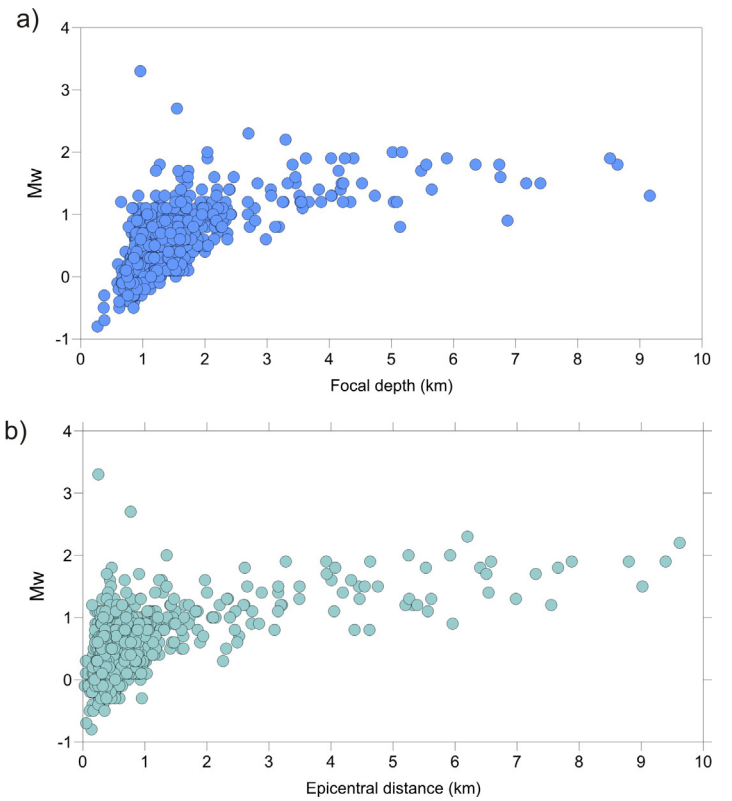

Figura 3.12 *(art. III fig. 16a)*. (a) Gráfica de la magnitud momento de los terremotos VT frente a la profundidad focal y (b) la distancia epicentral.

Estas localizaciones han permitido realizar un primer análisis de la serie obteniendo una valoración preliminar de la serie. Sin embargo, surge la pregunta que se planteaba en el capítulo anterior ¿Estos alineamientos de los epicentros se corresponden con las estructuras tectónicas implicadas? Aparentemente estas direcciones (Figura 3.1) se corresponden con fallas observadas en otros trabajos (Rey *et al.* 1995). Pero ¿son estas fallas las responsables de la serie? De nuevo es necesaria la localización precisa de los hipocentros para valorar e interpretar estos alineamientos y relacionarlos con las fallas que han generado la serie sísmica.

3.5.2. Método RelSE y caracterización de fracturas *(art. IV y V)*

Para localizar de forma precisa los terremotos registrados en antenas sísmicas se necesita estimar de forma precisa los parámetros que nos proporcionan las técnicas de localización de antenas sísmicas. Estos parámetros son las componentes del vector lentitud aparente del frente de onda que atraviesa las distintas estaciones de la antena sísmica. Aprovechando la similitud de la forma de onda que tienen los terremotos de una serie sísmica que se agrupan en familias, se pueden estimar de forma precisa sus vectores lentitud aparente relativos.

En este trabajo de Tesis, se ha desarrollado un método denominado RelSE que nos proporciona una estimación precisa del vector lentitud aparente relativo de cada uno de los eventos de una familia respecto al vector lentitud aparente absoluto del evento maestro. La innovación que introduce el método RelSE se basa en lo siguiente. La diferencia de tiempos de llegada de un frente de onda de un evento n a dos estaciones i,j está dada por

$$\Delta t_{ij}^{n} = \Delta \mathbf{r}_{ij} \cdot \mathbf{s}_{n} \qquad (1)$$

donde $\Delta \mathbf{r}_{ij}$ representa la posición de la estación j respecto a la estación i, y $\mathbf{s}_{n}$ es el vector lentitud aparente con el que se propaga el frente de onda (Figura 3.13). Las técnicas clásicas de antenas sísmicas comparan las formas de onda entre las estaciones de la antena. La precisión de esta estimación depende de nuestra capacidad para determinar los retrasos con precisión. El problema es que, en muchos casos, estos retrasos no se pueden estimar con demasiada precisión, ya que debido a efectos locales las formas de onda varían de un punto a otro de la antena sísmica (Figura 3.14).

Supongamos ahora las llegadas al array de una misma fase producida por dos terremotos m y n (Figura 3.13). La diferencia entre los retrasos en dos estaciones i y j de la antena sísmica vendrá dada por la ecuación

$$\Delta t_{ij}^{n} - \Delta t_{ij}^{m} = \Delta \mathbf{r}_{ij} \cdot \Delta \mathbf{s}_{mn} \qquad (2)$$

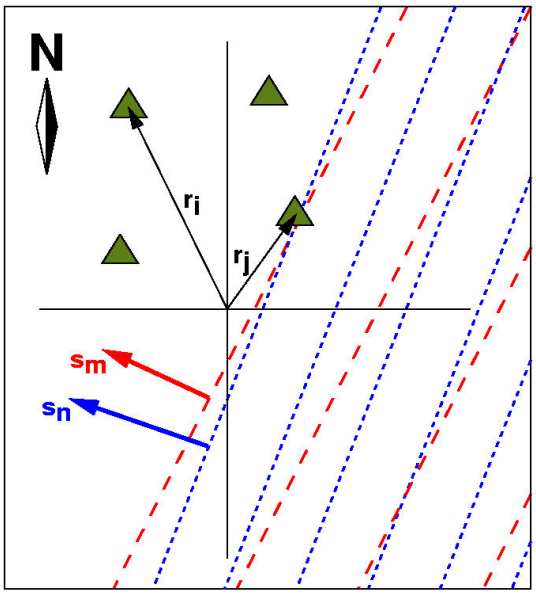

Figura 3.13 *(art. V fig. 1)*. Esquema de situación de dos frentes de onda caracterizados por sus vectores lentitud aparente (**s_m y s_n**) que atraviesan una antena sísmica con sus correspondientes estaciones (triángulos).

donde $\Delta\mathbf{s}_{mn} = \mathbf{s}_n - \mathbf{s}_m$ es la diferencia entre el vector lentitud aparente correspondiente a los dos terremotos. Esta diferencia de retrasos se puede expresar también

$$\Delta t_{ij}^{n} - \Delta t_{ij}^{m} = \Delta t_{j}^{mn} - \Delta t_{i}^{mn} \qquad (3)$$

donde Δt_i^{mn} representan el retraso entre las entre los tiempos de llegada de una fase del terremoto n y de la misma fase del terremoto m a la estación i del array. Combinando las ecuaciones (2) y (3), llegamos a la expresión:

$$\Delta t_{j}^{mn} - \Delta t_{i}^{mn} = \Delta\mathbf{r}_{ij} \cdot \Delta\mathbf{s}_{mn} \qquad (4)$$

Puede parecer que esta expresión no aporta nada al problema, respecto a la ecuación (2). Sin embargo, en el caso de familias de terremotos registradas en un array sísmico, las diferencias Δt_i^{mn} se pueden calcular con mucha más precisión que las diferencias Δt_{ij}^{n}. Es decir, podemos obtener el retraso entre las llegadas de dos terremotos a una misma estación con más precisión que el retraso entre las llegadas de un terremoto a dos estaciones del array. Esto es una consecuencia de que las formas de onda son muy parecidas entre terremotos de una familia (Figura 3.14)

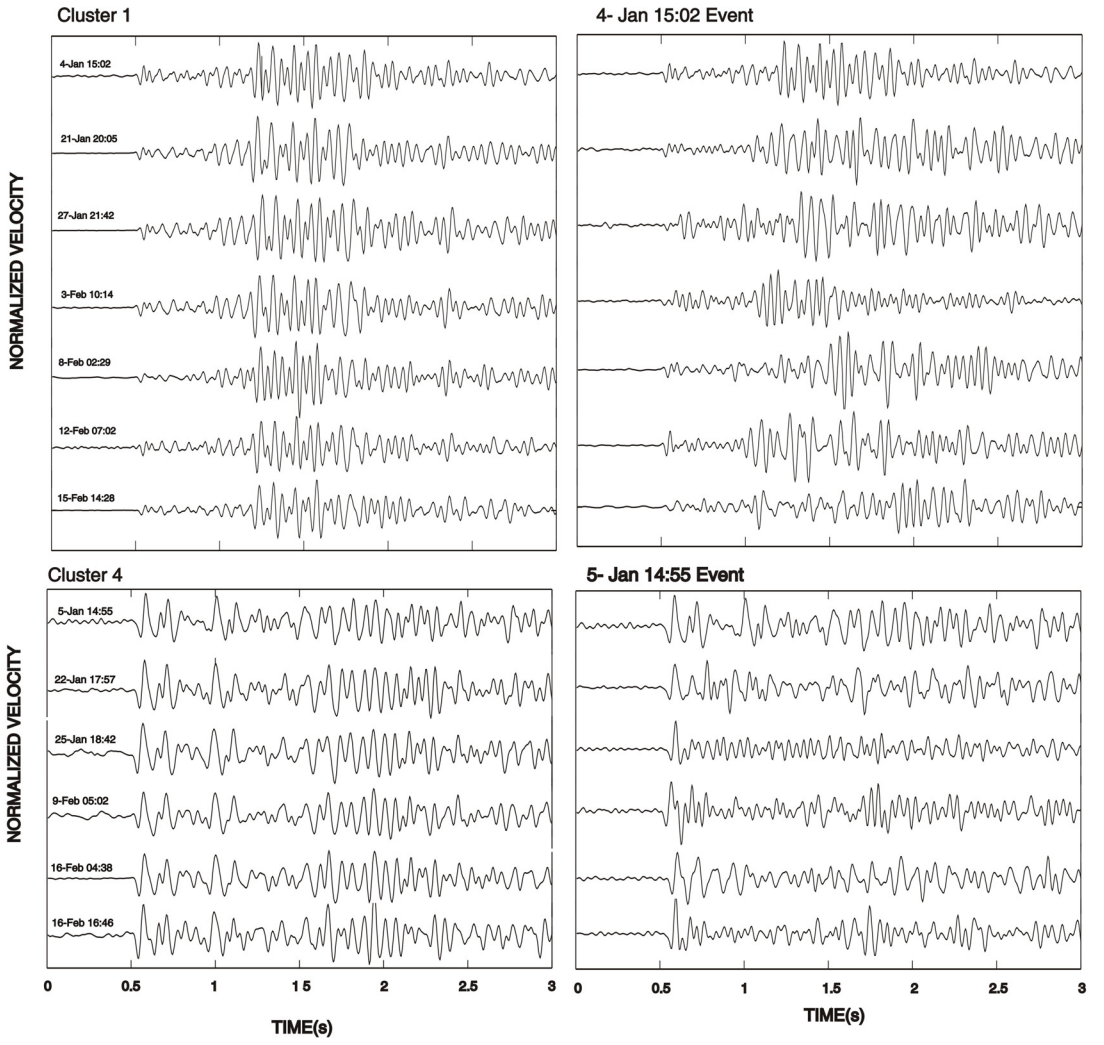

Figura 3.14 *(modificada art. V fig. 5)*. Izquierda: Sismogramas de dos familias (1 y 4) registradas en la misma estación vertical. Derecha: Sismogramas de un evento de cada familia en algunas estaciones verticales de la antena sísmica.

El método RelSE hace uso de la ecuación (4) para permitir la determinación precisa del vector lentitud aparente relativo para familias de terremotos con formas de onda similares registradas en una antena sísmica. Para ello, se define una función que representa la inversa del residuo del ajuste por mínimos cuadrados de la medida Δt_j^{mn} - Δt_i^{mn} al plano del frente de onda. Esta función **s** está definida como

$$F_{mn}(\mathbf{s}) = \left(\frac{2}{N(N-1)} \sum_{i=1}^{N-1} \sum_{j=i+1}^{N} \left(\Delta t_j^{mn} - \Delta t_i^{mn} - \Delta \boldsymbol{r}_{ij}.\boldsymbol{s}\right)^2\right)^{-1/2} \quad (5)$$

Se realiza una búsqueda en una malla par encontrar el vector lentitud que maximiza la función $F_{mn}(\mathbf{s})$. Si consideramos uno de los eventos como evento maestro con vector lentitud $\mathbf{s}_m$ y un evento de la misma familia, podremos estimar con precisión su vector lentitud $\mathbf{s}_n$ como

$$\boldsymbol{s}_n = \boldsymbol{s}_m + \Delta \boldsymbol{s}_{mn} \tag{6}$$

Se han realizado pruebas con sismogramas sintéticos con distintos parámetros del vector lentitud aparente relativo, modificando la relación señal-ruido para comprobar los límites de resolución del método RelSE. Hemos obtenido una relación entre el nivel de ruido y el tamaño de la región de incertidumbre en el dominio del vector lentitud aparente. También se ha comprobado el efecto de la apertura de la antena sísmica, que en el rango de tamaño utilizado generalmente en áreas volcánicas (300-500 m) no introduce diferencias significativas. Finalmente, se ha comprobado que la elección del evento maestro que se utiliza como referencia no altera la distribución de vectores lentitud aparente relativos. Estas pruebas demuestran la robustez del método RelSE.

Con estas estimaciones precisas del vector lentitud aparente de todos los miembros de las familias respecto al evento maestro, se localizan espacialmente los hipocentros de los terremotos. Se ha utilizado el método del trazado del rayo combinando la lentitud aparente junto con la diferencias S-P de cada evento. Para seguir con el rigor que requiere la localización precisa, las diferencias del evento maestro respecto a cada uno de los terremotos de cada familia, se evalúan mediante correlación cruzada para las dos fases P y S, obteniendo una diferencia S-P mucho más precisa que las lecturas visuales del análisis preliminar. Eligiendo un modelo de velocidad apropiado se localizan espacialmente los terremotos. Estas localizaciones precisas relativas se ajustan a un plano para cada familia obteniendo los planos de fractura implicados en la serie correspondiente.

La novedad de esta metodología para obtener planos de ruptura a través de localización relativa precisa registrada en antenas sísmicas, que se aplica por primera vez a esta serie de Decepción de 1999, requiere de unos controles que demuestren su calidad.

El primer control ha consistido en comprobar cómo influye el modelo de velocidad en la geometría de planos de fractura. Para ello se han utilizado variaciones del modelo de tierra original calculando para cada uno de ellos las localizaciones relativas y el plano que mejor se ajusta. Al final se han obtenido un conjunto de valores de azimut y buzamiento que difieren poco del ajuste con el modelo de tierra original. La dispersión es mayor en el buzamiento que en el azimut, debido a que la profundidad de los hipocentros está muy afectada por las variaciones de velocidad en el modelo.

En segundo lugar, se ha comprobado la influencia de la estimación del vector lentitud aparente absoluto del evento maestro. De nuevo se han realizado iteraciones aleatorias, pero

modificando en este caso el azimut y la lentitud aparente del evento maestro. Las distribuciones normales utilizadas están centradas en los parámetros del evento maestro. Para variaciones del azimut del evento maestro, encontramos que tanto el azimut como el buzamiento de los planos son estables. Este resultado era de esperar ya que una modificación del azimut del evento maestro implica una rotación de los hipocentros respecto a la antena sísmica sin cambiar sus posiciones relativas. Para el caso de variaciones de la lentitud aparente del evento maestro, encontramos una gran estabilidad en el azimut, pero más dispersión en el buzamiento. Un cambio en la lentitud aparente absoluta provoca que los hipocentros se desplacen en profundidad. Como resultado, se produce un cambio de inclinación del plano de ajuste. Sin embargo el azimut permanece estable, lo que indica que su estimación es robusta. Estos resultados indican que la estructura planar de la distribución de hipocentros se mantiene para variaciones del vector lentitud aparente absoluto del master del orden de su rango de error.

Otra prueba que hemos hecho ha sido comprobar si la elección del evento maestro influye en los resultados. Se ha demostrado que los vectores lentitud aparente relativos no varían al cambiar el evento maestro. La localización absoluta del evento maestro debe ser lo más precisa posible, porque respecto de él se localizarán los eventos restantes de la familia. En general, las estimaciones absolutas de azimut y lentitud aparente para los miembros de una familia son muy parecidas, y varían dentro de unos márgenes relativamente estrechos. Estos valores son del orden del tamaño de la región de incertidumbre asociado a las estimaciones realizadas con el método de correlación cruzada promedio. Por tanto, la elección de un evento maestro distinto equivale a cometer un cierto error en la estimación del vector lentitud aparente absoluto. Se ha demostrado que las soluciones son estables para este caso.

Finalmente, un problema que se podría dar al aplicar este método es que si las diferencias S-P entre los miembros de una familia son muy parecidas, los eventos estarán a la misma distancia de la antena sísmica. Por tanto el azimut del plano de ajuste formará un ángulo de 90º con la dirección hacia la antena. El problema es que esto ocurriría independientemente de las estimaciones de los vectores lentitud aparente relativos. En el caso de la serie de Decepción, se ha comprobado mediante el análisis de las orientaciones de los planos respecto al array y de los parámetros de los ajustes que no se produce este efecto.

3.5.3. Resultados y discusión *(art. V)*

El análisis de la serie de 1999 en la Isla Decepción se ha realizado según el esquema siguiente. Primero se han identificado familias con alta similitud de la forma de onda utilizando la correlación cruzada. Para estas familias se ha elegido el evento maestro y se ha

estimado su vector lentitud aparente con parámetros más finos que los utilizados en el análisis preliminar. Se ha aplicado el método RelSE para estimar de forma precisa el vector lentitud aparente de los terremotos de cada familia relativo al evento maestro. Posteriormente se han calculado las diferencias S-P entre el evento maestro y el resto de miembros de la familia utilizando correlaciones cruzadas. Se han localizado espacialmente los eventos de cada familia utilizando las estimaciones precisas relativas de la lentitud aparente y las diferencias S-P a través del trazado del rayo. Y por último se han determinado los planos de ajuste de las localizaciones relativas precisas de las familias.

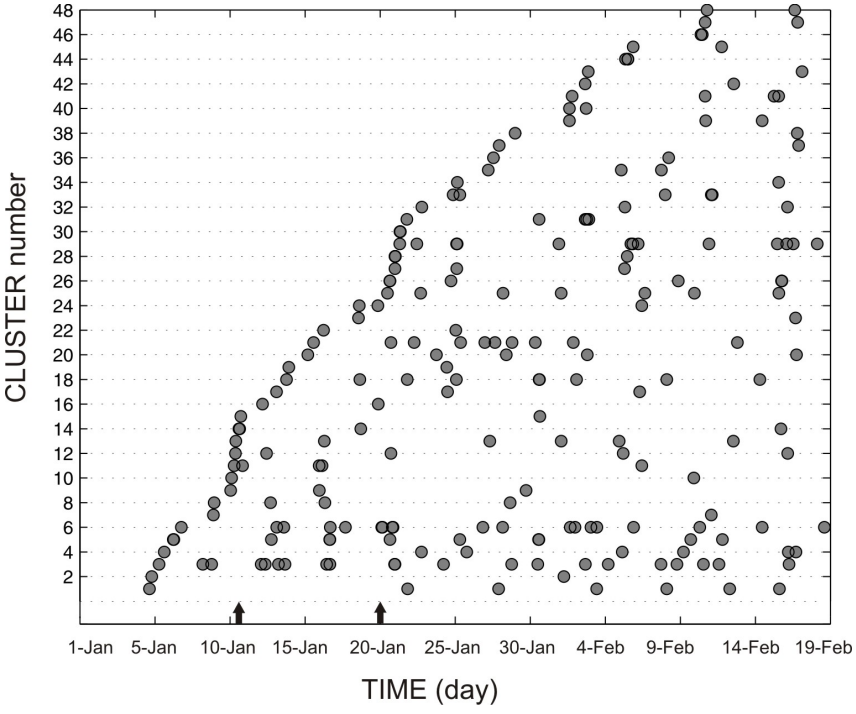

Figura 3.15 *(art. V fig.4)*. Distribución temporal de los terremotos de los 48 multipletes identificados. Cada círculo corresponde a un terremoto. Las flechas en el eje inferior muestran los dos eventos principales de la serie.

La correlación cruzada de la forma de onda de los 863 terremotos localizados en el análisis preliminar ha permitido agrupar 48 familias, entre las que se encuentran 19 dobletes, 9 tripletes y 20 multipletes con 4 o más eventos (Figura 3.15). Los umbrales utilizados han sido de 0.9 de correlación para las fases P y S.

En total, se han agrupado 225 eventos, lo que supone el 26 % del número total de terremotos VT localizados de la serie. Este porcentaje es bastante representativo, teniendo en cuenta la baja magnitud de los eventos de la serie donde la inmensa mayoría se encuentran

en un rango entre 0-1 de magnitud Mw. Las distintas familias seleccionadas tienen formas de onda muy diferentes entre ellas (Figura 3.14), lo que nos sugiere una cierta diversidad del mecanismo de la fuente que las ha generado.

Se ha realizado una reestimación del vector lentitud aparente con el método de correlación cruzada promedio con parámetros más finos que nos permitan asegurar que la estimación se hace exactamente con el mismo segmento de sismograma alrededor de la onda P de los terremotos. Con los resultados obtenidos de este procedimiento, hemos calculado los hipocentros utilizando el trazado del rayo. El modelo elegido para representar el medio es similar al utilizado en el análisis preliminar. Es una combinación de modelos 1D utilizados en otros trabajos. Como base se ha utilizado el descrito por Ibáñez *et al*. (2000), para toda la Isla. Se ha combinado con el calculado por Saccorotti *et al*. (2001a) para las capas más superficiales de Bahía Fumarolas. Para suavizar el modelo y evitar discontinuidades y reflexiones críticas, se calculó un ajuste exponencial.

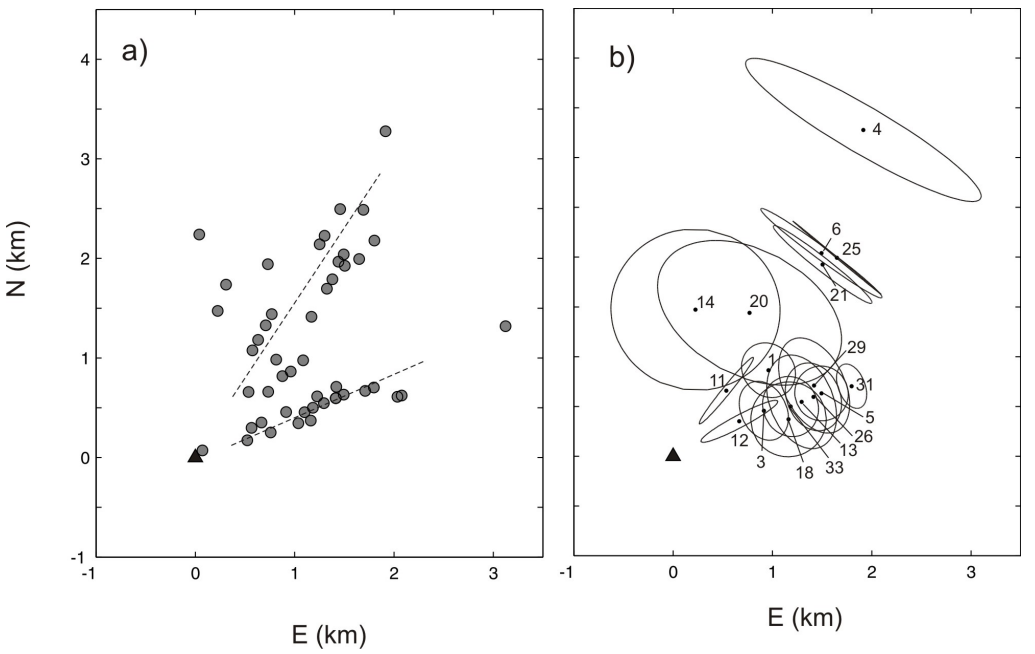

Figura 3.16 *(art. V fig. 6)*. (a) Mapa epicentral de la re-localización de los eventos maestros de los 48 multipletes. Las líneas discontinuas indican dos posibles alineamientos. (b) Elipses de error de las localizaciones del evento maestro de los multipletes analizados. El triángulo negro muestra la localización del array.

La Figura 3.16a muestra la distribución epicentral de los eventos maestros. En ella se pueden apreciar dos alineamientos a N35ºE y N70ºE. Estas direcciones coinciden con los alineamientos de N45ºE y N80ºE hallados en la localización preliminar de la serie. Esto se

podría interpretar como que las familias son una buena representación de toda la serie. La Figura 3.16b muestra la proyección horizontal de las regiones de error para los eventos maestros de las familias con cinco o más elementos.

Se ha aplicado el método RelSE a la onda P de los terremotos. Para elegir la mejor estimación del vector lentitud aparente hemos hecho una media ponderada de los resultados de las ventanas alrededor de la onda P, con residuos bajos (menores de 5 ms). De esta forma se mejora la estabilidad de la estimación final. Del conjunto de familias se han seleccionado 17 con 5 o mas miembros. Para cada familia, hemos seleccionado como evento maestro, el evento con la mejor relación señal-ruido. Se han obtenido los valores del vector lentitud aparente relativo para la onda P de 124 de los 150 terremotos contenidos en 14 de las 17 familias seleccionados. El resto de terremotos (incluidas 3 familias completas) no producen residuos por debajo de 5 ms y por tanto se han descartado.

La aplicación de esta metodología nos lleva a estimar los vectores lentitud aparente de los terremotos de cada familia. Desde el punto de vista relativo estas estimaciones son de alta precisión, es decir, las diferencias de los vectores se conocen con precisión gracias a la técnica RelSE. Sin embargo, sus valores absolutos se basan en estimaciones iniciales de los vectores lentitud aparente del evento maestro, realizadas con el método de correlación cruzada promedio.

Con el fin de medir el tiempo S-P con mayor exactitud, se utilizaron interpolaciones con splines de las funciones de correlación cruzada entre los terremotos y sus correspondientes eventos maestros para las llegadas de las ondas P y S. Esta técnica utiliza la similitud de la forma de onda observada en los terremotos de la familia, y reduce las incertidumbres del picado visual de los sismogramas.

Para las localizaciones espaciales utilizamos el trazado del rayo con el mismo modelo 1D descrito anteriormente. La Figura 3.17 muestra los resultados correspondientes a las 14 familias seleccionadas. Se aprecian cuatro zonas epicentrales. En la zona más cercana a la antena sísmica, están la mayoría de las familias localizadas (familias 1, 3, 5, 11, 13, 18, 29 y 31). Otra de las zonas es frente a Punta Murature que contiene tres familias (6, 21 y 25). Las otras zonas tienen solo una familia: la número 14, localizada la más al Oeste de la zona epicentral; y la número 4 localizada aproximadamente 3 km hacia el NNE de la antena sísmica. Prácticamente todas las familias están situadas en un rango de profundidades muy pequeño, entre los 1.2 y 2 km, a excepción de la familia 14, que se sitúa en un rango de profundidades entre los 2.8 y los 3.2 km.

La mayoría de los eventos de cada familia tienden a distribuirse planarmente. Hay un alargamiento en profundidad, debido a la mayor incertidumbre en profundidad, pero en general definen un plano. Se ha utilizado una técnica de ajuste por mínimos cuadrados para calcular los parámetros del mejor ajuste a un plano de la distribución de hipocentros (Figura

3.18). Se han podido obtener los parámetros de planos de ajuste para las 14 familias seleccionadas. En dos casos (familias 3 y 6), el método ha separado espacialmente dos subgrupos distintos dentro del cluster. La calidad del plano de ajuste incluyendo todos los miembros de la familia era muy baja. Sin embargo, el ajuste del plano de estos subgrupos proporciona un mejor resultado (Figura 3.19). De hecho, hay ligeras variaciones en las formas de onda, que son imperceptible para el algoritmo de detección de las familias. Por tanto, se han subdividido estas familias (3a, 3b; 6a, 6b) y se han obtenido un total de 16 planos.

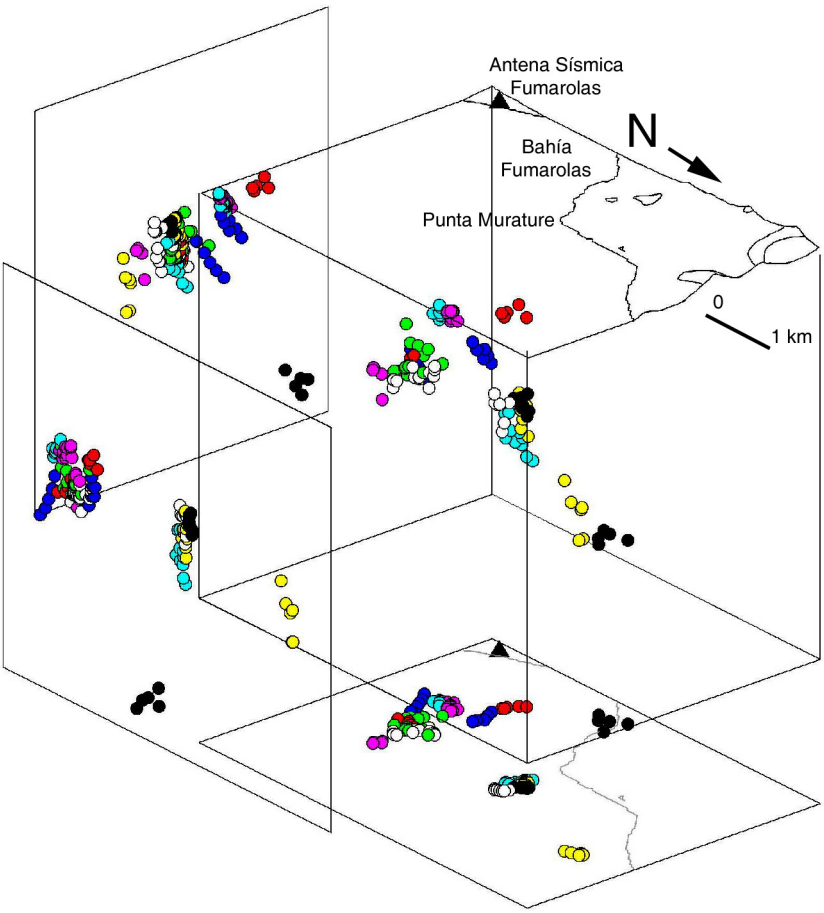

Figura 3.17 *(modificada art. V fig. 7)*. Localizaciones relativas de las fuentes para los 14 multipletes seleccionados. Cada multiplete se ha coloreado para diferenciarse del resto. La Figura muestra proyecciones (horizontal y verticales) de los hipocentros. El triángulo negro muestra la localización de la antena sísmica.

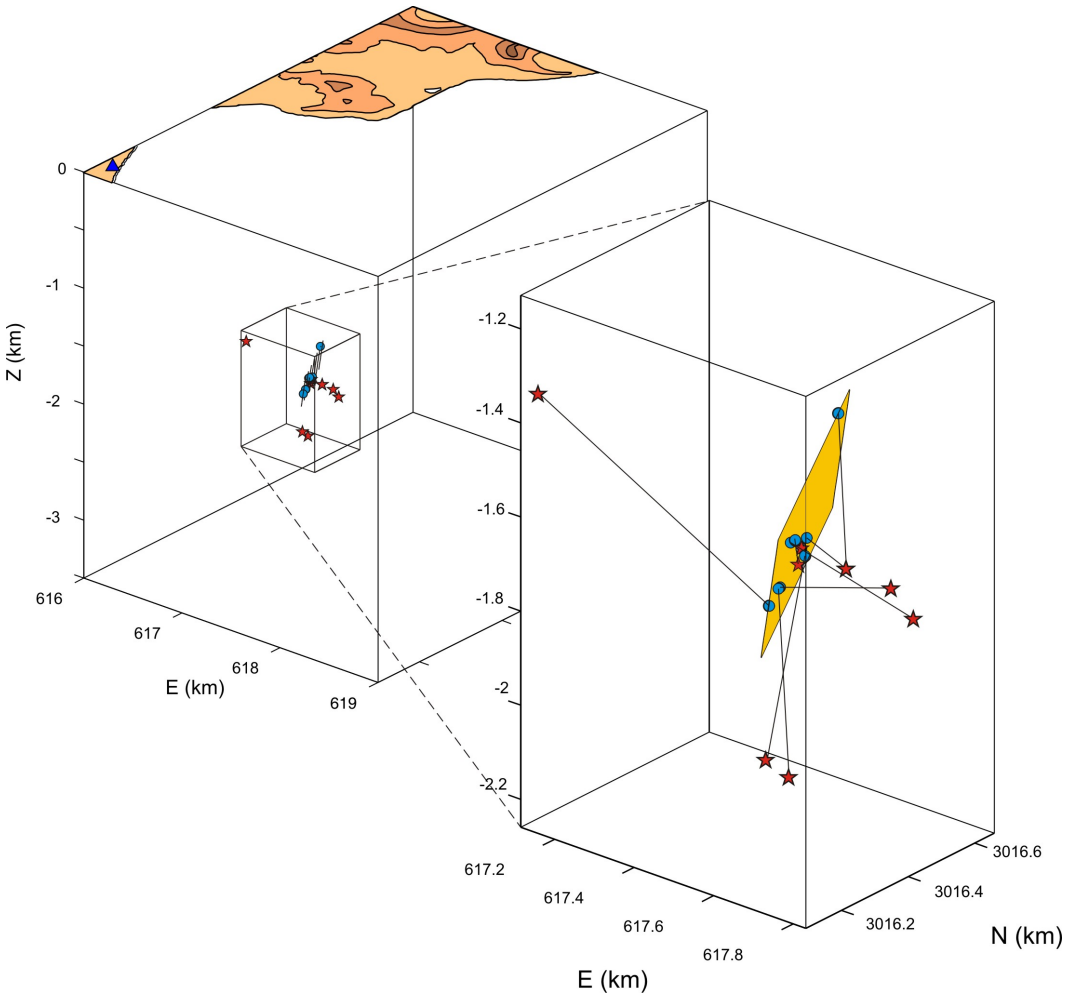

Figura 3.18 *(art. V fig.8)*. Comparación de la localización obtenida con el método de correlación cruzada promedio (estrellas) y el RelSE (círculos). En gris se muestra el plano que mejor ajusta la distribución de hipocentros.

La mayoría de ajustes muestran una planaridad muy elevada, por encima de 0.75. Este umbral es similar al empleado en otros trabajos para definir el rango significativo de la planaridad (Shearer *et al*, 2003). La distancia promedio de los hipocentros al plano de ajuste varía entre 3 y 18 m. Las distancias de las proyecciones de los hipocentros sobre el plano son del orden de centenares de metros, lo que de nuevo da una idea de la forma planar de la distribución.

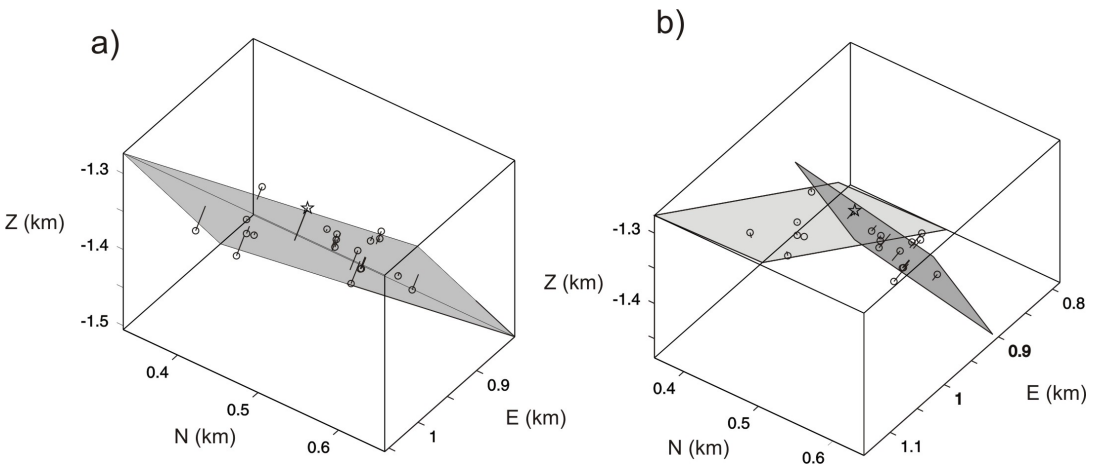

Figura 3.19 *(art. V fig. 9)*. (a) Representación del plano obtenido mediante el ajuste de todos los terremotos del multiplete 3. (b) Los planos obtenidos al separar el multiplete 3 en dos subgrupos.

El azimut del plano varía entre N119ºE y N38ºO, aunque la mayoría de los planos se orientan en dirección NO-SE. Los buzamientos varían entre 41 y 86º. Muchos de ellos son buzamientos elevados, lo que sugiere la presencia de planos subverticales. La Figura 3.20 muestra la situación y la orientación de los planos obtenidos. El rango de colores indica la calidad de los ajustes. La Figura 3.21 muestra histogramas de los valores de azimut y buzamiento de los resultados. También se muestra una representación estereográfica de los 16 planos calculados. Las orientaciones de los planos respecto a la antena sísmica, representadas por el ángulo teta (ángulo que forma el plano de ajuste y la antena sísmica) varían entre 17 y 130º. La mayoría de ajustes tienen un teta diferente de 90º, lo que indica que no se trata de planos con un azimut perpendicular a la línea antena-hipocentro del evento maestro.

La mayoría de los azimutes de estos planos tienen dirección N120-140ºE, es decir NO-SE. Estas tendencias coinciden con algunos de los sistemas de fallas más importantes de Decepción descritos por otros autores. Por ejemplo, Rey *et al*. (1995) presentan tres sistemas de fallas: N160-170Eº fallas de salto en dirección destral, fallas normales de dirección 45-N60ºE y fallas normales N115-120ºE al SE de la Isla. Martí *et al*. (1996) hablan también de tres sistemas de fallas que atraviesan la Isla: NE-SO, NO-SE y N-S. El más importante es NE-SO (Smellie *et al*. 1988). González-Casado *et al*. (1999) establecen también tres sistemas principales de microfracturas: NE-SO, E-O y NO-SE, con buzamientos superiores a los 60º y relacionadas con la extensión NO-SE del estrecho del Bransfield. Estos mismos autores establecen que las fallas con dirección NO-SE representan fallas de transferencia de los sistemas NE-SO. Smellie y López-Martínez (2000) realizaron un mapa geomorfológico de la Isla Decepción donde también aparecen fallas normales NO-SE en la zona de nuestro

estudio. Paredes *et al*. (2006) ponen de manifiesto las direcciones encontradas en la fracturación de la Isla presentando un mapa de morfolineamientos. Realizaron un resumen de todos los trabajos hasta el momento unido a un análisis morfométrico del modelo digital de elevaciones, creando un mapa síntesis de las trazas de las fallas. Las direcciones preferentes fueron NE-SO, N-S y NNO-SSE.

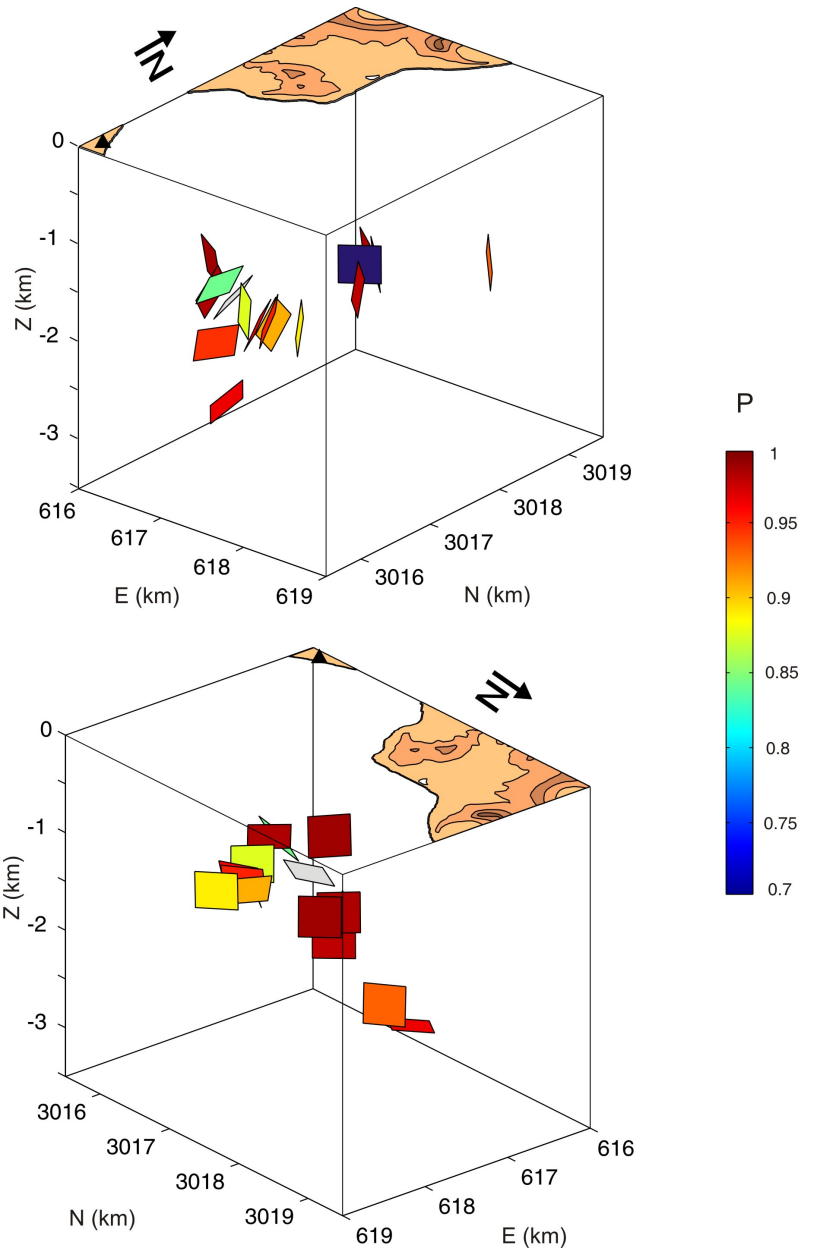

Figura 3.20 *(art. V fig. 10)* .Vista general de los planos de ruptura identificados para los 16 multipletes analizados. Se muestran desde dos perspectivas diferentes. La gama de colores indica la calidad del ajuste en términos de la planaridad. El plano de color gris está por debajo de 0.7.

Para nuestros resultados, la dirección predominante NO-SE coincide con algunos alineamientos descritos por estos autores. El resto de azimutes de los planos tienen direcciones entre N170ºO y N120ºO, que también coinciden con otros alineamientos descritos anteriormente (N-S y NE-SO). Los buzamientos de los planos obtenidos, en su mayoría subverticales, son concordantes con las fallas que se esperan en una zona de extensión (González-Casado *et al*. 1999).

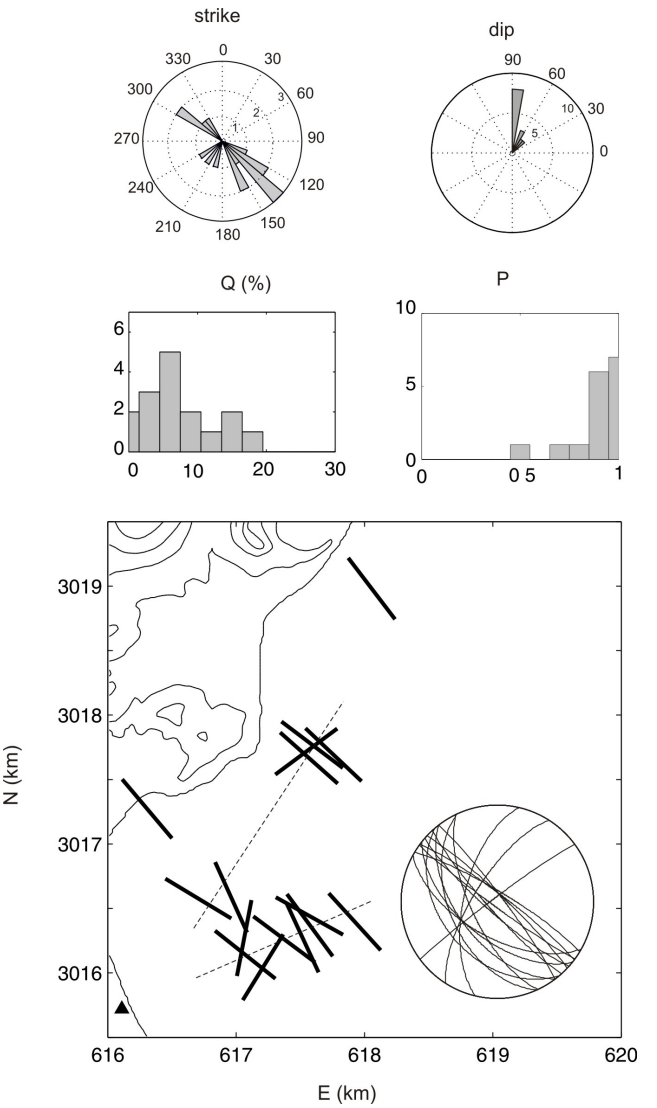

Figura 3.21 *(art. V fig. 11)*. (a) Histograma de azimut y buzamiento y gráficas de los parámetros de calidad del plano de ajuste Q (cociente entre el residuo y la distancia media de las proyecciones de los hipocentros sobre el plano al centro de la distribución; y P (planaridad). (b) Alineamientos de los planos y representación estereográfica de los planos. En línea discontinua se muestran las alineaciones preliminares obtenidas con las localizaciones epicentrales de los eventos maestros.

Las dos distribuciones encontradas en el análisis preliminar y las relocalizaciones muestran dos alineamientos con dirección NE-SO y ENE-OSO. Estas direcciones no tienen nada que ver con las obtenidas en la geometría de los planos de ruptura de la serie (Figura 3.21). La consecuencia es que la interpretación de los mapas de epicentros en términos de alineamientos de fracturas puede estar sesgada y no aportan información real sobre las direcciones de ruptura. El régimen tectónico local solo puede abordarse utilizando información de los mecanismos de la fuente o por el contrario, con la definición de los planos de ruptura utilizando localizaciones relativas precisas.

Hemos encontrado 16 planos de fractura en la zona de Bahía Fumarolas. No hemos podido investigar otras zonas de la Isla, ya que todas las familias seleccionadas ocurren en esta zona. Sin embargo, como se ha visto en el análisis preliminar se pone de manifiesto que la acumulación de epicentros en las cercanías de la antena sísmica es un efecto aparente debido a la baja magnitud de los eventos y a la elevada atenuación del medio bajo Puerto Foster (Vila *et al*. 1995; Martínez-Arévalo *et al*. 2003; Martínez-Arévalo, 2005). Es probable que existan distribuciones de fracturas similares a distancias mayores en la zona N de Puerto Foster, donde se localizan algunos de los terremotos más lejanos de la serie (Figura 3.11).

Se podría interpretar que las direcciones de los planos obtenidos se distribuyen vagamente paralela y perpendicularmente al borde de la caldera en la zona de Fumarolas. Esto podría sugerir la presencia de fallas en forma de anillo que se relacionan con la formación de una caldera de colapso. Sin embargo, la estabilidad de las orientaciones de los planos (Figura 3.20) sugiere una estrecha relación con la tectónica local, tal y como han sugerido otros autores (Martí *et al.* 1996; Rey *et al.* 1995; González-Casado *et al.* 1999).

La presencia de estos planos de ruptura sugiere que se produjo una desestabilización del estado de esfuerzos de la zona provocando la presencia de terremotos VT. ¿Pero qué provocó este desajuste? Se podrían barajar tres hipótesis. La primera podría ser que la generación de los terremotos VT fuera producto de la tectónica regional. La segunda hipótesis es que podría tratarse de un enjambre sísmico producido directamente por el movimiento de magma en la región de la fuente. Y la tercera, la serie sísmica podría ser causada por la acumulación de esfuerzos generada por el levantamiento del área fuente por la inyección de magma en profundidad. Por tanto, la activación de estos planos podría deberse a factores puramente de tectónica regional, puramente volcánicos, o una mezcla de ambos.

Los trabajos de Caselli *et al*. (2004) sobre la geoquímica de los gases en la zona de la Bahía Fumarolas después de la crisis de 1999 ponen de manifiesto el aumento del flujo de SO_2. Este aumento parece estar relacionado con la intrusión de diques a capas superficiales. Este hecho produjo la aparición de depósitos de azufre nativo y sulfuros de hierro en finas capas en los sistemas fumarólicos de la bahía. Los estudios de deformación de la Isla sugieren que la actividad volcánica de Decepción responde a dos alineamientos principales (Fernández-Ros *et al*. 2007). Después de la crisis de 1999 se produce un cambio en el

movimiento de la Isla. Se pasa de una extensión y elevación generalizadas a un proceso compresivo de subsidencia en las zonas N y NO de la Isla (Berrocoso *et al*. 2008). Estos resultados ponen de manifiesto una reactivación volcánica relacionada con la aparición de el enjambre de terremotos VT de 1999.

Lo que sí parece claro es que una reactivación de la cámara magmática de Isla Decepción desencadenaría un desequilibrio en la zona. Esto podría ser la causa de la serie de terremotos VT. En trabajos de tomografía sísmica se obtuvo la imagen de una cámara magmática en la Isla Decepción (Zandomeneghi *et al*. 2009; Ben-Zvi, *et al.* 2009). Esta cámara llega hasta unos 2-4 km de profundidad bajo la bahía interna de Decepción, y está ligeramente desplazada hacia el O y alargada en dirección NO-SE. Estudios de deformación han calculado el origen de la deformación superficial producida tras la crisis de 1999 y la sitúan en el interior de la bahía frente a la playa de Obsidianas (Berrocoso *et al*. 2008). Esta zona coincide con la posición de la cámara determinada por los trabajos de tomografía sísmica. Este hecho indica que la activación de la cámara está relacionada con el origen de la serie. La tomografía sísmica también proporciona velocidades Vp bajas a 2 km de profundidad en la zona de Fumarolas, lo que sugiere un elevado estado de fracturación, coincidente con nuestros resultados. Las fracturas involucradas en la serie están situadas dentro o en los límites de la cámara magmática. Esta área debería ser una zona con rocas a altas temperaturas, lo que provocaría un comportamiento dúctil que dificultaría la generación de terremotos VT. Sin embargo, nuestras observaciones evidencian que el medio es suficientemente rígido como para producir terremotos. Hay constancia de la presencia de terremotos VT dentro de cuerpos de baja velocidad en otros volcanes (Dawson *et al*. 1999, Waite *et al.* 2009). La presencia de magma explicaría también la ocurrencia de eventos híbridos en la misma zona donde se encuentran los terremotos VT. Los fluidos liberados por el magma superficial podrían interaccionar con las fracturas, fundamentalmente relacionadas con la dinámica regional del Bransfield. Este proceso da como resultado una lubricación que disminuye el esfuerzo normal que actúa sobre los planos de falla, facilitando el proceso de ruptura de la propia falla y la generación de terremotos volcano-tectónicos.

4

Referencias

Abril, M. e Ibáñez , J.M. (2000). Uso de antenas sísmicas en ambientes volcánicos. *Curso Internacional de Volcanología y Geofísica Volcánica.* Astiz, M., García, A. (ed.). 269-282.

Aki, K., (1984). Aperities, barriers, characteristic earthquake and strong motion prediction. *J. Geophys. Res.,* **89,** No B7, 5867-5872.

Alguacil, G., (1986). *Los instrumentos de una red telemétrica para microterremotos. La Red Sísmica de la Universidad de Granada.* Tesis Doctoral. Universidad de Granada. 238 pp.

Alguacil, G., (2002). Etapas del desarrollo en la época universitaria del Observatorio de Cartuja. *Centenario del Observatorio de Cartuja, IAG.* Universidad de Granada.

Almendros, J., J.M. Ibáñez, G. Alguacil, E. Del Pezzo, Ortiz, R., (1997). Array tracking of the volcanic tremor source at Deception Island, Antarctica. *Geophys. Res. Lett.,* **24,** 3069-3072.

Almendros, J. (1999). *Análisis de señales sismo-volcánicas mediante técnicas de array.* Tesis Doctoral. Universidad de Granada. 318 pp.

Almendros, J., J.M. Ibáñez, G. Alguacil, Del Pezzo, E., (1999). Array analysis using circular wavefront geometry: An application to locate the nearby seismo-volcanic source. *Geophys. J. Int.*, **136,** 159-170.

Almendros, J., Ibáñez, J.M., Alguacil, G., Morales, J., del Pezzo, E., La Rocca, M., Ortiz, R., Araña, V., Blanco, M.J. (2000). A double seismic antenna experiment at teide Volcano: Existence of local seismicity and lack of evidences of volcanic tremor. *J. Volcanol. Geotherm. Res.* **103,** 439-462.

Almendros, J., Chouet, B., and Dawson, P., (2001a). Spatial extent of a hydrothermal system at Kilauea Volcano, Hawaii, determined from array analyses of shallow long-period seismicity-1.Method, J. *Geophys. Res.,* **106** (B7), 13,565-13,580.

Almendros, J., Chouet, B., and Dawson, P., (2001b). Spatial extent of a hydrothermal system at Kilauea Volcano, Hawaii, determined from array analyses of shallow long-period seismicity: 2. Results, *J. Geophys. Res.,* **106** (B7), 13,581-13,597.

Almendros, J., Ibañez, J.M., Carmona, E., Zandomeneghi, D., (2007). Array analyses of volcanic earthquakes and tremor recorded at Las Cañadas caldera (Tenerife Island, Spain) during the 2004 seismic activation of Teide volcano. *J. Volcanol. Geotherm. Res.,* **160,** 285-299.

Alparone, S. y Gambino, S., (2003). High precision locations of multiplets on south-eastern flank of Mt. Etna (Italy), reconstruction of fault plane geometry. *Phys. Earth Planet. Int.,* **135**, 281-289.

Aster, R.C. y Scott, J., (1993). Comprehensive characterization of waveform similarity in microearthquake datasets. *Bull. Seismol. Soc. Am.* **4**, pp. 1307–1314.

Augliera, P., Cattaneo, M., Eva, C., (1995). Seismic multiplets analysis and its implication in seismotectonics. *Tectonophysics,* **248**, 219-234.

Baker, P.E., I. McReath, M.R. Harvey, M.J. Roobol and T.G. Davis, (1975). The Geology of the South Shetland Islands: V. Volcanic evolution of Deception Island, *British Antarctic Survey Scientific Reports,* **78**, 81.

Baraldo A., y Rinaldi, C.A., (2000). Stratigraphy and structure of Deception Island, south Shetland Island, Antarctica. *J. South Am. Sciences.* **13,** 785-796.

Barclay, A.H., Wilcock, W.S.D., Ibáñez, J.M., (2009). Bathymetric constraints on the tectonic and volcanic evolution of Deception Island Volcano, South Shetland Islands. *Antartic Science,* **21** (2), 153-167.

Battaglia, J., Thurber, C.H., Got, J., Rowe, C.A., White, R.A., (2004). Precise relocation of earthquakes following the 15 June 1991 eruption of Mount Pinatubo (Philippines). *J. Geophys. Res.***, 109,** doi:10.1029/2003JB002959.

Ben-Zvi, T., Wilcock, W.S.D., Barclay, A., Zandomeneghi, D., Ibáñez, J.M., Almendros, J., (2009). The P-wave velocity structure of Deception Island, Antartica, from two-dimensional seismic tomography. *J. Volc. Geoth. Res.,* **180,** 67-80.

Berrocoso, M., Fernández-Ros, A., Ramírez, M.A., Salamanca, J.M., Torrecillas, C., Pérez-Peña, A., Páez, R., García-García, A., Jiménez-Teja, Y., García-García, F., Soto, R., Gárate, J., Martín-Dávila, J., Sánchez-Arzola, A., de Gil, A., Fernández-Prada, J.A., Jigena, B., (2008). Geodetic Research on Deception Island and its Environment (South Shetland Islands, Bransfield Sea and Antartic Peninsula During Spannish Antarctic Campaigns (1987-2007). *Geodetic and Geophysical Observations in Antartica,* A. Capra, R. Dietrich (eds.), 97-123.

Blanco, I., (1997). *Análisis e interpretación de las anomalías magnéticas de tres calderas volcánicas: Decepción (Shetland del Sur, Antártida), Furnas (San Miguel, Azores) y las Cañadas del Teide (Tenerife, Canarias).* Tesis Doctoral. Universidad Complutense de Madrid, 250 pp.

Bollinger, G.A. y Langer, C.J., (1986). A note on the geometric configuration of seismogenic zones. *Eastern Section. Seismological Society of America.* Earthquakes Notes. Vol **57,** Nº2.

Brancato, A. y Gresta, S., (2003). High precision relocation of microearthquakes at Mt. Etna (1991-1993 eruption onset), a tool for better understanding the volcano seismicity. *J. Volcanol. Geotherm. Res.* **124.** 219-239.

Bretón, M., (1997). *Los terremotos en la Edad Media y sus efectos en el patrimonio histórico (siglos IX-XVI). Precisiones sobre sismicidad histórica.* Tesis Doctoral. Universidad de Granada, 745 pp.

Brillinger, D., Udías A., Bolt, B.A., (1980). A probability model for regional focal mechanism solutions. *Bull. Soc. Seism. Am.* **70,** 149-170.

Buontempo, 2008. *Seismic anisotropy in the Iberian Peninsula.* Tesis doctoral. Universidad de Granada. 227 pp.

Buforn, E., Coca, P., Udías, A., Lasa, C., (1997). Source mechanism of intermediate and deep earthquake in southern Spain. *Journal of Seismology,* **1,** 113-130.

Carmona, E., Martini, F., Ibanez, J.M., (2007). Families of events and seismic velocity changes during the 1998–99 seismic series at Deception Island volcano. *Eos Trans. AGU* **88** (52) Fall Meet. Suppl.

Caselli, A. T., Santos-Afonso M., Agusto., M. R. (2004). Gases fumarólicos de la isla Decepción (Shetland del Sur, Antártida): variaciones químicas y depósitos vinculados a la crisis sísmica de 1999, *Rev Asoc. Geol. Arg.*, **59**, 291-302.

Cattaneo, M., Augliera, P., Spallarossa, D., Eva, C., (1997). Reconstruction of seismogenetic structures by multiplet analysis: an example of western Liguria, Italy. *Bull. Seismol. Soc. Am.* **4**, pp. 971–986.

Chouet, B., (1992). A seismic model for the source of long-period events and harmonic tremor, in *Volcanic Seismology* (IAVCEI Proceedings in Volcanology 3), Aki, K., Gasparini, P. and Scarpa, R. (ed.), Springer-Verlag, 133-156.

Chouet, B., (1996). Long-Period volcano seismicity: Its source and use in eruption monitoring, *Nature*, **380**, 309-316.

Chouet, B., G. Saccorotti, M. Martini, P. Dawson, G. De Luca, G. Milana, Scarpa, R., (1997). Source and path effects in the wave fields of tremor and explosions at Stromboli Volcano, Italy, *J. Geophys. Res.,* **102,** 15129-15150.

Chung, W.-Y. and Kanamori, H., (1976). Source process and tectonic implications of the Spanish deep-focus earthquake of March 29, 1954. *Phys. Earth Planet. Int.* **13**, pp. 85–98.

Dawson, P.B., Chouet, B.A., Okubo, P.B., Villaseñor, A., Benz, H.A., (1999). Three-dimensional velocity structure of the Kilauea caldera, Hawaii. *Geophys. Res. Lett.,* **26,** 2805-2808.

Deichmann, N. y Garcia-Fernandez, M., (1992). Rupture geometry from high-precision relative hypocenter locations of microearthquake clusters. *Geophys. J. Int.* **110**, pp. 501–517.

Delacou, B., Deichmann, N., sue, C., Thouvenot, F., Champagnac, J.D., Burkhard, M., (2005). Active strike-slip faulting in the Chablais (NW Alps) from earthquake focal mechanism and relative locations. *Eclogae Geol. Helv.,* **98,** 189-199.

De Miguel, F., (1976). La ocurrencia temporal de terremotos en la Península Ibérica y áreas adyacentes. *II Asam. Nac. Geod. y Geof***.** (I), 609-618.

De Miguel, F., Alguacil, G., Vidal, F., (1988). Una escala de magnitud a partir de la duración para terremotos del sur de España. *Rev. de Geofísica* **44**, 75–86.

Del Pezzo, E., La Rocca, M., Ibanez, J. M., (1997). Observations of high-frequency scattered waves using dense array*s* at Teide volcano, *Bull. Seism. Soc. Am.,* **87**, 1637-1647.

Douglas, A. (1967). Joint epicentre determination. *Nature,* **215,** 47-48.

Faccenna, C., Piromallo, C., Crespo-Blanc, A., Jolivet, L., Rossetti, F., (2004). Lateral slab deformation and the origin of the western Mediterranean arcs. *Tectonics,* **23,** TC1012, doi:10.1029/2002TC001488.

Fehler, M., House, L., Kaieda, H., (1987). Determining planes along which earthquakes occur: method and application to earthquakes accompanying hydraulic fracturing. *J. Geophys. Res.,* **92,** B9, 9407-9414.

Fernández Ros, A., Berrocoso, M., and Ramirez, M.E., (2007), Volcanic deformation models for Deception Island (South Shetland Islands, Antarctica). *USGS* OF-2007-1047, Extended Abstract 094.

Fernandez-Ibáñez, F., Pérez-López, R., Martínez-Díaz, J.J., Paredes, C., Giner-Robles, J.L., Caselli, A., Ibáñez, J., (2005). Costa Recta Beach, Deception Island, West Antarctica: a retreated scarp of a submarine fault? *Antartic Science,* **17,** 418-426.

Frankel, A., Hough, S., Friberg, P., Busby, R., (1991). Observations of Loma Prieta aftershocks from a dense array in Sunnyvale, California. *Bull. Seism. Soc. Am.* **81,** 1900-1922.

Fremont, M.J. y Malone, S.D., (1987). High precision relative locations of earthquakes at Mount St. Helens, Washington. *J. Geophys. Res.* **92**, pp. 10223–10236.

Frohlich, C. (1979). An efficient method for joint hypocenter determination for large groups of earthquakes. *Computer & Geosciences,* **5,** 387-389.

Galindo-Zaldívar, J., Jabaloy, A., Serrano, I., Morales, J., González-Lodeiro, F. and Torcal, F., (1999). Recent and present-day stresses in the Granada Basin (Betic Cordilleras): example of a late Miocene-present-day extensional basin in a convergent plate boundary. *Tectonics* **18**, pp. 686–702.

García, A., Blanco, I., Torta, J.M., Astiz, M., Ibáñez, J.M., Ortiz, R., (1997). A search for the volcanomagnetic signal at Deception volcano (South Shetland Island, Antarctica). *Annali de Geofisica,* **40,** 319-327.

Geiger, L., (1912). Probability method for the determination of earthquake epicentres from the arrival time only. *Bull. St. Louis Univ.,* **8,** 60-71.

Geller, R.J. and Mueller, C.S., (1980), Four similar earthquakes in Central California. *Geophys. Res. Lett,* **7,** 821-824.

Gillard, D., Rubin, A.M., and Okubo, P., (1996). Highly concentrated seismicity caused by deformation of Kilauea's deep magma system. *Nature,* **384,** 343-346.

González-Casado, J.M., López-Martínez, J., Giner, J., Durán, J.J., Gumiel, P., (1999). Análisis de la microfracturación en la isla Decepción, Antártida occidental. *Geogaceta,* **26,** 27-30.

González-Ferrán, O. y Katsui, Y., (1970). Estudio integral del volcanismo cenozoico superior de las Islas Shetland del Sur, Antártida. *Instituto Antártico Chileno Ser. Cient.,* **1,** 123-174.

González-Ferrán, O. (1995) *Volcanes de Chile,* Instituto Geofráfico Militar Chileno.

Got, J.L., Frechet, J. , Klein, F.W., (1994). Deep fault plane geometry inferred from multiplet relative relocation beneath the south flank of Kilauea. *J. Geophys. Res.* **99**, pp. 15375–15386.

Hancock, P.L., (1985). Brittle microtectonics: Principles and practice, *J. Struct. Geol.,* **7**, 437-457.

Harris, D.B., (1991). A wave-form correlation method for identifying quarry explosions. *Bull. Seismol. Soc. Am.,* **81,** 2395-2418.

Havskov J., y Ottemöller, L., (1999). SEISAN earthquake analysis software. *Seismologiacl Research letters,* **70,** 532-534.

Havskov J., J.A. Peña, J.M. Ibáñez, L. Ottemöller and C. Martínez-Arévalo, (2003). Magnitude scales for very local earthquakes. Application for Deception Island volcano (Antarctica). *J. Volc. Geoth. Res.,* **128**, 115-133.

Henares, J., (2009). *Caracterización multifractal de la sismotectónica de la Cordillera Bética.* Tesis Doctoral. Universidad de Granada. 200 pp.

Hensch, M., Riedel, C, Reinhardt, J., Dahm, T., (2008). Hypocenter migration of fluid-induced earthquake swarms in the Tjörnes Fracture Zone (North Iceland). *Tectonophysics,* **447,** 80-94.

Ibáñez, J.M., Del Pezzo, E., De Miguel, F., Herraiz, M., Alguacil, G., Morales, J., (1990). Depth-dependent seismic attenuation in the Granada zone (Southern Spain). *Bull. Seismol. Soc. Am.,* **80**, 1232-1244.

Ibáñez, J.M., Morales, J., Alguacil, G., Almendros, J., Ortiz, R., Del Pezzo, E., (1997). Intermediate-focus earthquakes under South Shetland Islands (Antarctica), **24,** *Geophys. Res. Lett.,* 531-534.

Ibáñez, J. M., Del Pezzo, E., Almendros, J., La Rocca, M., Alguacil, G., Ortiz, R., García, A. (2000). Seismovolcanic signals at Deception Island volcano, Antarctica: wavefield analysis and source modeling, *J. Geophys. Res.* **105,** 13905–13931.

Ibáñez, J.M., Del Pezzo, E., Bengoa, C., Caselli, A., Badi, G., Almendros, J., (2008). Volcanic tremor and local earthquakes at Copahue volcanic complex, Southern Andes, Argentina. *J. Volcan. Geotherm. Res.,* **174,** 284-294.

Ito, A., (1985). High-resolution relative-hypocenters of similar earthquakes by the cross-spectral analysis method. *J. Phys. Earth* **33**, pp. 279–294.

Ito, A. (1990). Earthquake swarm activity revealed from high-resolution relative hypocenters; clustering of microearthquakes, Tectonophysics, 175, 47– 66.

Jabaloy, A., Galindo-Zaldíval, J., Sanz de Galdeano, C., (2008). Guía Geológica. Serie Granada. *Guías de la Naturaleza.* Ed. Diputación de Granada.

Jones, J.P., Thurber, C.H., Lutter, W.J. (2001). High-precision location of pr-eruption seismicity at Mount Pinatubo, Philippines, 30 May-3 June, 1991. *Phys. Earth Planet. Intern.,* **123,** 21-232.

Joswig, M., (1995). Automated classification of local earthquake data in the BUG samall array. *Geophys. J. Int.*, **120,** 262-286.

Julian, B.R., (1994). Volcanic tremor: nonlinear excitation by fluid flow, Journ. Geophys. Res., 99, 11859-11877.

Kanamori, H., (1977). The energy release in great earthquakes. Jour. Geophys. Res., 82, 2981-2987.

Kraft, T., Wassermann, J., Igel., H., (2006). High-precision relocation and focal mechanisms of the 2002 rain-triggered earthquake swarms at Mt Hochstaufen, SE Germany. *Geophys. J. Int.*, **167** 1513-1528.

La Rocca, M., Petrosino, S., Saccorotti, G., Simini, M., Ibáñez, J.M., Almendros, J., Del Pezzo, E., (2000). Location of the source and shallow velocity model deduced from the explosion quakes recorded by two seismic antennas at Stromboli Volcano. *Phys. Chem. Earth,* **25**, 731-735.

La Rocca, M., Saccorotti, G., Del Pezzo, E., Ibáñez, J.M., (2004). Probabilistic source location of explosion quakes at Stromboli volcano estimated with double array data. *J. Volcan. Geotherm. Res.***, 131,** 123-142.

Lahr, J.C., (1989). HYPOELLIPSE (Version 2.0): A Computer Program for Determining Local Earthquake Hypocentral Parameters, Magnitude and First Motion Pattern. US Geological Survey Open-File Report 89–116, 92 pp.

Lees, J. (1998), Multiplet analysis at Coso geothermal, *Bull. Seismol. Soc. Am.*, **88**, 1127–1143.

Lienert, B.R., Berg, E., Frazer L.N., (1986). HYPOCENTER- An earthquake location method using centered, scaled, and adaptively damped least-squares. *Bull. Seismol. Soc. Am.*, **76,** 771-783.

Lin, G. y Shearer, P. (2005). Test of relative earthquake location techniques using synthetic data. *J. Geophys. Res.,* **110,** B04304, doi:10.1029/2004JB003380.

Luzón, F., Almendros, J., García-Jerez, A., (2009). Shallow structure of Deception Island volcano, Antarctica, using the two station spatial autocorrelation method on a dense set of seismic arrays. *Submitted to Geophysical Journal International.*

Madariaga, R., Olsen, K., Archuleta, R., (1998). Modeling Dynamic Rupture in a 3D Earthquake Fault Model. *Bull. Seismol. Soc. Am.*, **88**, 1182-1197.

Maestro, A., Somoza, L., Rey, J., Martínez-Frías, J., López-Martínez, J., (2007). Active tectonics, fault patterns, and stress field of Deception Island: A response to oblique convergente between the Pacific and Antarctic plates. *J. South Am. Earth Sciences,* **23,** 256-268.

Mancilla, F., (2006). *Leyes de escalado del movimiento sísmico del suelo en el Sur de España.* Tesis Doctoral. Universidad de Granada. 166 pp.

Martí, J., Vila, J.,Rey, J., (1996). Deception Island (Bransfield Strait, Antarctica): an example of volcanic caldera developed by extensional tectonics. *J. Geological. Soc. London.* **110,** 253-265.

Martínez-Arévalo, C., Bianco, F., Ibáñez, J.M., Del Pezzo, E., (2003). Shallow seismic attenuation and shear-wave splitting in the short period range of Deception Island Volcano (Antarctica). *J. Volcan. Geotherm. Res.,* **128**, 89-113.

Martínez-Arévalo, C. (2005). *Estructura superficial de atenuación para ondas sísmicas directas, P y S, en ambientes volcánicos. Aplicación al volcán Isla Decepción (Antártida) y al volcán Etna (Italia).* Tesis Doctoral. Universidad de Granada. 337 pp.

Martínez-Arévalo, C., Mancilla, F., Almendros, J., Aznarte, J.L., Alguacil, G., (2009). Preliminary results of receiver function analyses at three sites across the Bransfield Strait. Antarctica., *EGU General Assembly 2009,* Geophysical Research Abstract, Vol. 11, EGU2009-13362-1,

Martínez-Díaz, J.J. y Hernández-Enrile, J.L., (2004). Neotectonics and morphotectonics of the southern Almeria region (Betic Cordillera-Spain) kinematics implications, *Int. J. Earth. Sci.* **93**, 189-206.

Martínez-Martínez, J.M., Booth-Rea, G., Azañon, J.M., Torcal, F. (2006). Active transfer zone linking a segmented extensional system (Betics, southern Spain): Insight into heterogeneous extension driven by edge delamination, *Tectonophysics* **422**, 159-173.

Martínez-Solares, J.M., (2003). Sismicidad histórica de la Península Ibérica. *Física de la tierra,* **15**, 13-28.

Martini, F., Bean, C., Saccorotti, G., Viveiros, F., Wallenstein, N., (2009). Seasonal cycles of seismic velocity variations detected using coda wave interferometry at Fogo volcano, Azores, during 2003-2004. *J. Volcan. Geotherm. Res.,* **181,** 231-46.

Massa, M., Eva, E., Spallarossa, D., Eva, C., (2006). Detection of earthquake clusters on the basis of waveform similarity, an application in the monferrato region (Piedmont, Italy). *J. Seim.,* **10,** 1-22.

Maurer, H. y Deichmann, N., (1995). Microearthquake cluster detection based on waveform similarities, with an application to the western Swiss Alps. *Geophys. J. Int.* **123**, pp. 588–600.

Metaxian, J.P., Lesage, P., Dorel, J., (1997). Permanent tremor of Masaya volcano, Nicaragua: wave field analysis and source location. *J. Geophys. Res. ,***102,** 22529-22545.

Metaxian, J.P., Lesage, P.,Valette, B., (2002). Locating sources of volcanic tremor and emergent events by seismic triangulation: Application to Arenal volcano, Costa Rica. *J. Geophys. Res. Solid Earth.* **107***,* doi:10.1029/2001JB000559.

Mezcua, J., Rueda, J., (1994). Earthquake relative location based on waveform similarity, Tectonophysics, 233, 253– 263.

Michelini, A. y Bolt, B.A., (1986). Application of the principal parameters method to the Coalinga, California, aftershocks sequence. *Bull. Seismol. Soc. Am.* **76**, pp. 409–420.

Mogi, K., (1963). Some discussions on aftershocks, foreshocks and earthquakes swarm – the fracture of a semi finite body caused by an inner stress origin and its relation to the earthquake phenomena. *Bull. Earthquake Res. Inst.,* **41,** 615-658.

Mora, M.M., Lesage, P., Valette, B., Alvarado, G.E., Leandro, C., Métaxian, J.P., Dorel, J., (2006). Shallow velocity structure and seismic site effects at Arenal volcano, Costa Rica. *J. Volcan. Geotherm. Res.,* **152,** 121-139.

Morales, J., Vidal, F., De Miguel, F., Alguacil, G., Posadas, A.M., Ibáñez, J.M., Guzmán, A., Guirao, J.M. (1990). Basement structure of the Granada basin, Betic Cordilleras, Southern Spain. *Tectonophysics,* **177**, 337-348.

Morales, J., (1991).*Caracterización de la respuesta sísmica local en las cuencas de Granada (España) y Ciudad Guzmán (México) mediante el análisis espectral de microterremotos y terremotos*. Tesis Doctoral. Universidad de Granada. 275 pp.

Morales, J., Seo, K., Samano, T., Peña, J.A., Ibáñez, J.M., Vidal, F., (993) Site Response on Seismic Motion in the Granada Basin (Southern Spain) Based on Microtremor Measurements. *J. Phys. Earth.,* **41,** 221-238.

Morales, J., Singh, S.K., Ordaz, M., (1996). Analysis of the Granada (Spain) earthquake of 24 June, 1984 (M=5) with emphasis on seismic hazard in the Granada Basin. *Tectonophysics,* **257,** 253-263.

Morales, J., Serrano, I., Vidal, F., Torcal, F., (1997). The depth of the earthquake activity in the Central Betics (southern Spain). *Geophys. Res. Lett.* **24**, pp. 3289–3292.

Morales, J., Alguacil, G., Martos, A., Martín, J.B. **(**2007). The Instituto Andaluz de Geofisica- Universidad de Granada seismic network in Southern Spain. *Orfeus Newsletter,* 7 (2).

Moriya, H., Niitsuma, H., Baria, R., (2003). Multiplet-clustering análisis reveals structural details within the seismic cloud at the Soultz geothermal field, France. , *Bull. Soc. Seism. Am.,* **93,** 6563-6572.

Moser, T.J., van Eck, T., Nolet, G., (1992). Hypocenter determination in strongly heterogeneous earth models using the shortest path method. *J. Geophys. Res.* **97**, pp. 6563–6572.

Muñoz, D., Cisternas, A., Udías, A., Mezcua, J., Sanz de Galseano, C., Morales, J., Sánchez-Venero, M., Haessler, H., Ibáñez, J.M., Buforn, E., Pascual, G., Rivera, L., (2002). Microseismicity ant tectonic in the Granada Basin (Sapin). *Tectonophysics,* **356,** 233-252.

Musumeci, C., Gresta, S., Malone, D., (2002). Magma system recharge of Mount St. Helens from precise relative hypocenter location microearthquakes. *J. Geophys. Res.,* **107,** doi: 10.1029/2001JB000629.

Nishigami, K., (1987). Clustering structure and fracture process of microearthquake sequences, *J. Physics Earth,* **35,** 425-448.

Ocaña, E., Stich, D., Carmona, E., Vidal, F., Bretón, M., Navarro, M., García-Jerez, A., (2008). Spatial analysis of the La Paca, SE Spain, 2005 seismic series through the relative location of multiplets and principal component analysis. *Phys. Earth Planet. Intern.,* **166,** 117-127

Ocaña, E., (2009). *Análisis especial de la actividad sísmica del Sur de España.* Tesis Doctoral. Universidad de Granada. 299 pp.

Ortiz, R., Vila, J., García, A., González-Camacho, J., Diez-Gil, J-L., Aparicio, A., Soto, R., Viramonte, J.R., Risso, C., Petrinovic, I., (1992). Geophysical fextures of Deception Island, in Recent Progress in Antartic Earth Science, *Terra Scientific publishing Company, Tokyo,* 143-152.

Ortiz, R., Garcia, A., Aparicio, A., Blanco, I., Felpeto, A., Del Rey, R., Villegas, M.T., Ibáñez, J.M., Morales, J., Del Pezzo, E., Olmedillas, J.C., Atiz, M., Vila, J., Ramos, M., Viramonte, J.G., Risso, C., Caselli, A., (1997). Monitoring of the volcanic activity of Deception Island, South Shetland Island, Antarctica (1986-1995). *The Antarctic Region: geological Evolution and Process.* 1071-1076.

Palo, M., Ibáñez, J.M., Cisneros, M., Bretón, M., Del Pezzo, E., Ocaña, E., Orozco-Rojas, J., Posadas, A.M., (2009). Analysis of the seimic wavefield properties of volcanic explosions at Volcán de Colima, México: insights into the source mechanism. *Geophys. J. Int.,* 2009, **177,** 1383-1398.

Pandolfi, D., Bean, C.J., Saccorotti, G., (2006). Coda wave interferometric detection of seismic velocity changes associated with the 1999 M=3.6 event at Mt. Vesuvius. *Geophys. Res. Lett.,* **33,** doi: 10.1029/2005GL025355.

Paredes, C., Pérez-López, R., giner-Robles, J.L., de la Vega, R., García-García, A., Gumiel, P., (2006). Distribución especial y zonificación tectónica de los morfolineamientos en la Isla Decepción (Shetland del Sur, Antártida). *Geogaceta.* **39,** 75-78.

Pelayo, A.M. y D.A. Wiens, (1989). Seismotectonics and relative plate motions in the Scotia Sea region, *Journal of Geophysical Research,* **94** (B6), 7293-7320.

Peña, J.A., Vidal, f., Posadas, A.M., Morales, J., Alguacil, G., De Miguel, F., Ibáñez, J.M., Remacho, M.D., López-Linares, A., (1993). Space clustering properties of the Betic-Alborán earthquakes in the period 1962-989. *Tectonophysics***, 221,** 125-134.

Posadas, A.M., 1991. *Análisis espacio-temporal de series sísmicas. Aplicación a las Béticas centrales*. Tesis Doctoral. Universidad de Granada.

Posadas, A.M., Vidal, F., De Miguel, F., Peña, J.A., Alguacil, G., Ibáñez, J.M., Morales, J., (1993). Spatial–temporal analysis of a seismic swarm using the principal component analysis. The Antequera swarm (Spain). *J. Geophys. Res.* **98**, pp. 1923–1932.

Posadas, A.M., Vidal, F., Benjumea, B., Lorenzo, F., (1996). *Fractales en sismología.* Sismología aplicada. A.M. Posadas, F. Vidal, J. de Martín (eds.) Universidad de Almería, 9-41.

Poupinet, G., Ellsworth, W.L., Frechet, J., (1984). Monitoring velocity variations in the crust using earthquakes doublets: an application to the Calaveras fault, California. *J. Geophys. Res.* **89**, pp. 5719–5731.

Poupinet, G., Ratdomopurbo, A., Coutant, O., (1996). On the use of earthquake multiplets to study fractures and the temporal evolution of an active volcano, *Ann. Geofis.,* 39, 253– 264.

Press, W.H., Flannery, B.P., Teukolsky, S.A., Vetterling, W.T., (1988). Numerical recipes (Fortran version). The Art of Scientific Computing *Cambridge University Press,* Cambridge.

Press, W.H., Teukolsky, S.A., Vetterling, W.T., Flannery, B.P., (1992). Numerical Recipes:, 2nd Edition. *Cambridge University Press,* Cambridge, UK.

Pujol, J., (1988). Comments on the jpint determination of hypocenters and station corrections. *Bull. Soc. Seism. Am.,* **78,** 1179-1189.

Ratdomopurbo, A., y Poupinet, G. (1995). Monitoring a temporal change of seismicity velocity in a volcano, application to the 1992 eruption of Mt. Merapi (Indonesia). *Geophys. Res. Lett.,* **22,** 775-778.

Rey, J., Somoza, L., Martínez-Frías, J., (1995). Tectonic, volcanic, and hydrothermal event sequence on Deception Island (Antarctica). *Geo-Marine Lett.,* **15,** 1-8.

Richards-Dinger, K.B. y Shearer, P.M., (2000). Earthquake locations in southern California obtained using source-specific station terms. *J. Geophys. Res.,***105,** 10939-10960.

Richter, C.F., (1958). *Elementary seismology.* W.H. Freeman, S. Francisco. California.

Robertson Maurice, S.D., Wiens D.A., Shore P.J., Vera E., Dorman L.M., (2003). Seismicity and tectonics of the South Shetland Islands and Bransfield Strait from a regional broadband seismograph deployment.., *J. Geophys. Res.,* **108,** 10.029/2003JB002416.

Ruiz, M., Gaspà, O., Gallart, J., Díaz, J., Pulgar, J.A., García-Sansegundo, J., López-Fernández, C., Gonzalez-Cortina, J.M., (2006a). Aftershocks series monitoring of the September 18, 2004 M=4.6 earthquake at the western Pyrenees: A case of reservoir-triggered seismicity ? *Tectonophysics,* **424,** 223-243.

Ruiz, M., Díaz, J., Gallart, J., Pulgar, J.A., González-Cortina, J.M., López, C., (2006b). Seismotectonic constraints at the western edge of the Pyrenees: aftershock series monitoring of the 2002 February 21, 4.1 Lg earthquake. *Geophys. J. Int.*, **166** 238–252

Saccorotti, G., Chouet, B., Martini, M., Scarpa, R., (1998). Bayesian Statistics Applied to the Location of the Source of Explosions at Stromboli Volcano, Italy. *Bull. Seismol. Soc. Am.,* **88,** 1099-1111.

Saccorotti, G., Almendros, J., Carmona, E., Ibáñez, J.M., Del Pezzo, E., (2001a). Slowness anomalies from two dense seismic arrays at Deception Island Volcano, Antarctica. *Bull. Seismol. Soc. Am.,* **91,** 561-571.

Saccorotti, G., Maresca, R., Del Pezzo, E., (2001b). Array analyses of seismic noise at Mt. Vesuvius Volcano, Italy. *J. Volcan. Geotherm. Res.*, **110,** 79-100.

Saccorotti, G., Carmona, E., Ibáñez, J.M., and Del Pezzo, E., (2002). Spatial characterization of Agron, southern Sapin, 1988-1989 seismic series. *Phys. Earth Planet. Intern.,* **129,** 13-29.

Saccorotti, G., Zuccarello, L., Del Pezzo, E., Ibañez, J.M., Gresta, S., (2004). Quantitative analysis of the tremor wavefield at Etna Volcano, Italy. *J. Volcan. Geotherm. Res.,* **136**, 223-245.

Santoyo, M.A. y Luzón, F., (2008). Stress relations in three recent seimic in the Murcia region, southeastern Spain. *Tectonophysics,* **457,** 86-95.

Sanz de Galdeano, C., (2001). Inserción de la Cuenca de Granada en la evolución geotectónica de la Cordillera Bética. *La Cuenca de Granada. Estructura, Tectónica activa, Sismicidad, Geomorfología y dataciones existentes.* Sanz de Galdeano, C., Peláez Montilla, J.A. y López Garrido, A.C. (ed.) CSIC-Universidad de Granada, 143-147.

Scarfi, L. Langer, H.,Gresta, S., (2003). High-precision relative locations of two microearthquakes clusters in Southeastern Sicily, Italy. *Bull. Seismol. Soc. Am.,* **93,** 1479-1497.

Serrano, I., Morales, J., Vidal, F., (1996). Mecanismos focales en la cuenca de Granada. *Libro Homenaje al Profesor Fernando de Miguel Martínez,* F. Vida, M. Espinar y J.A. Esquivel (eds.) Universidad de Granada. 619-641.

Serrano, I., (1999). *Distribución espacial de la sismicidad en las Cordilleras Béticas-Mar de Alborán.* Tesis Doctoral. Universidad de Granada, 225 pp.

Serrano, I., Zhao, D., Morales, J., (2002). 3-D crustal structure of the extensional Granada Basin in the convergent boundary between the Eurasin and African plates. *Tectonophysics*, **344,** 61-79.

Shearer, P.M., (1997). Improving local earthquake locations using the L1 norm and waveform cross correlation: application to the Whittier Narrows, California, aftershock sequence. *J. Geophys. Res.* **102**, pp. 8269–8283.

Shearer, P.M., Hardebeck, J.L., Astiz, L., Richards-Dinger, K.,B., (2003). Analysis of similar event clusters in aftershocks of the 1994 Northridge, California, earthquake. *J. Geophys. Res.,* **108,** doi:10.1029/2001/JB000685.

Shelly, D.R., Ellsworth, W.L., Ryberg, T., Haberland, C., Fuis, G.S., Murphy, J., Nadeau, R.M., Bürgmann, R., (2009). Precise location of Andreas Fault tremors near Cholame, California using seismometer clusters: Slip on the deep extension of the fault?. *Geophys. Res. Lett.,* **36,** doi: 10.1029/2008GL036367.

Smalley, R.F., Chatelain, J.L., Turcotte, D.L., Prevot, R., (1987). A fractal approach to the clustering of earthquake-applications to the seismicity of the New Hebrides. *Bull. Seismol. Soc. Am*., **77,** 1386-1381.

Smellie, J.L., (1988). Recent observations on the volcanic history of Deception Island, South Shetland Islands. *Br. Antarct. Surv. Bull.,* **81,** 83-85.

Smellie, J.L., y López-Martínez, J., (2000). Geological map of Deception Island. BAS GEOMAP Series, Sheet 6-A. 1:25,000. British Antartic Survey, Cambridge.

Snieder, R., y Hagerty, M., (2004). Monitoring change in volcanic interiors using coda wave interferometry: Application to Arenal Volcano, Costa Rica. *Geophys. Res. Lett.,* **31,** doi: 10.1029/2004GL019670.

Snoke, J. A., Munsey, J. W., Teague, A. G., Bollinger, G. A., (1984). A program for focal mechanism determination by combined use of polarity and SV-P amplitude ratio data. *Earthquake notes,* **55,** p15.

Stich, D., Alguacil, G., Morales, J., (2001). The relative location of multiplets in the vicinity of the Western Almeria (southern Spain) earthquake series of 1993–94. *Geophys. J. Int.*, **146,** 801-812.

Stich, D., Ammon, C.J., Morales, J., (2003). Moment tensor solutions for small and moderate earthquakes in the Ibero-Maghreb region. *J. Geophys. Res*. **108**, 2148, doi10.1029/2002JB002057.

Stich, D., Serpelloni, E., Mancilla, F., Morales, J., (2006). Kinematics of the Iberia-Maghreb plate contact from seismic moment tensors and GPS observations, *Tectonophysics*, **426**, 295–317.

Tarantola, A. y Valette, B., (1982). Inverse problems─quest for information. *J. Geophys.* **50**, 159–170.

Torcal, F., (1998). *Simulación probabilística, energética y temporal, de series sísmicas. Tesis Doctoral.* Universidad de Granada. 239 pp.

Tsujiura, M., (1983). Characteristics frequencies for earthquake families and their tectonic implications, evidences from earthquake swarm in the Kanto District, Japan. *Pure Appl. Geophys.,* **4,** 573-600.

Turcotte, D.L., (1989). Fractals in Geology and Geophysics. *Pure Appl. Geophys.* **131,** 171-196.

Udías, A., y Mézcua, J., (1986). *Fundamentos de Geofísica*. Ed. Alhambra Universidad, 419 pp.

Vera, J.A., (2004). *Geología de España*. Madrid, Sociedad Geológica de España, Instituto geológico y Minero de España.

Vidal, F., De Miguel, F., Alguacil, G., Guirao, J.M., (1981). Características de la secuencia sísmica granadina del año 1979. *Com. IV Asam. Nal. De Ged. y Geof. Zaragoza 1981*, Tall. Inst. Geog. Nal. **Vol I**, 423-438.

Vidal, F., y De Miguel, F., (1983). Datos macrosísmicos de los terremotos sentidos en la Depresión de Granada, durante el año 1979. *Publ. Obs. Univ. de Cartuja,* report 3, pp 77.

Vidal, F., De Miguel, F., Sanz de Galdeano, C., (1984). Neotectónica y sismicidad de la Depresión de Granada. Energía Nuclear, N. 149-150, 267-275.

Vidal, F., (1986). *Sismotectónica de la región Béticas-Mar de Alborán.* Tesis Doctoral. Universidad de Granada. 450 pp.

Vila, J., Martí, J., Ortiz, R., García, A., Correig, A. M., (1992). Volcanic tremors at Deception island (South Shetland Islands, Antartica). *J. Volcanol. Geotherm. Res.,* **53,** 89-102.

Vila, J., Correig, A.M., Martí, J., (1995). Attenuation and source parameters at Deception Island (South Shetland Island, Antartica). *Pageoph.* **144,** 229-250.

Waite, G.P.y Moran, S.C., (2009). Vp Structure of Mount St. Helens, Washington, USA, imaged with local earthquake tomography, *J. Volcanol. Geotherm. Res.,* **182,** 113-122.

Waldhauser, F. y Ellsworth, W.L. (2000). Fault structure and mechanisms of the Hayward fault, California, from double-difference earthquake locations. *J. Geophys. Res*., **107**(B3), doi, 10.1029/2000JB000084.

Wittlinger, G., Herquel, G., Nakache, T., (1993). Earthquake location in strongly heterogeneous media. *Geophys. J. Int.* **115**, pp. 759–777.

Zandomeneghi, D., Barclay, A., Almendros, J., Ibáñez, J. M., Wilcock, W. S. D., Ben-Zvi, T., (2009). The crustal structure of Deception Island Volcano from P-wave seismic tomography: tectonic and volcanic implications. *J. Geophys. Res.* 114, B06310, doi:10.1029/2008JB006119.

Zhizhin, M., Cvishiani, A., Rouland, D., Bonnin, J., Mohammadioun, B., (1994). Identification of a Geological Region for Earthquakes Using Syntactic Pattern Recognition of Seismograms. *Natural Hazards.* **10,** 139-147.

SEGUNDA PARTE

I. *Spatial characterization of Agron, southern Spain, 1988-1989 seismic series.*

II. *Multiplet focal mechanisms from polarities and relative locations: The Iznajar swarm South Spain*

III. *The 1998-1999 seismic series at Deception Island volcano, Antarctica.*

IV. *Precise determination of the relative wave propagation parameters of similar events using a small-aperture seismic array.*

V. *Characterization of fracture systems using precise array locations of earthquake multiplets: An example at Deception Island volcano, Antarctica*

I. Spatial characterization of Agron, southern Spain, 1988-1989 seismic series

ELSEVIER

Physics of the Earth and Planetary Interiors 129 (2002) 13–29

PHYSICS OF THE EARTH AND PLANETARY INTERIORS

www.elsevier.com/locate/pepi

Spatial characterization of Agron, southern Spain, 1988–1989 seismic series

G. Saccorotti [a,*], E. Carmona [b], J.M. Ibàñez [b], E. Del Pezzo [a]

[a] *Istituto Nazionale di Geofisica e Vulcanologia, Sez. Napoli (Osservatorio Vesuviano), Via Diocleziano 328, 80124 Napoli, Italy*
[b] *Instituto Andaluz de Geofisica, Universidad de Granada, Campus de Cartuja, 18071 Granada, Spain*

Received 6 December 2000; accepted 27 April 2001

Abstract

During November 1988 to April 1989, a seismic swarm of about 400 earthquakes of magnitude between 0.4 and 4.0 occurred near the village of Agron, Andalusia, southern Spain. The pattern of the energy release versus time clearly shows that the dataset is representative of a seismic swarm, where it is not observable a typical mainshock–aftershock sequence. Basing on the Gutenberg–Richter relationship the catalogue is considered complete down to a magnitude of 1. We revise the dataset by selecting those digital data which were recorded by at least four stations. The revised dataset is relocated using a probabilistic approach based on a Bayesian formalism. The epicenters are barely aligned along two main structures trending NNE–SSW, NW–SE and WNW–ESE, respectively. The focii depth is confined in the 5–20 km interval. Application of a clustering technique based on the principal component analysis (PCA) of the local rupture ellipsoids depicts a spatial clustering of the seismicity according to five main planes, of which only one coincides with the horizontal alignment of epicenters. Cross-correlation among waveforms allows to individuate five different groups of similar events (multiplets). High-resolution estimate of time differences among events belonging to the same multiplet and least-squares adjustment of arrival times allow for precise relative locations, from which we derive the corresponding rupture planes. Focal mechanisms are calculated for three of the five multiplets: for these cases, the planes obtained from the relative locations are coincident with one of the fault plane solutions. The results are consistent with those previously inferred from PCA, and indicate a high variability in the spatial setting of fault planes over a short distance range. These observations are consistent with a fragmentation of the upper crust into small (2–4 km) tectonic blocks, and indicate an heterogenous stress regime, with different stresses acting simultaneously in adjacent areas.

Keywords: Seismic series; Granada Basin; Principal component analysis; Relative location

1. Introduction

The Granada Basin (southern Spain), is an outcrop of Neogene to quaternary sedimentary rocks lying over the NE–SW trending contact between the external and internal zones of the Betic Cordilleras, in correspondence of the diffuse boundary between the lithospheric plates of Eurasia and Africa (Buforn et al., 1988; Galindo-Zaldivar et al., 1999). This and neighboring areas form the region with the highest rate of seismic and microseismic activity in the entire Iberian Peninsula. Since instrumental data are available, these earthquakes have never exceeded magnitudes m_b of 5.5, with the only exception of the deep ($z = 640$ km), $M_w = 7.8$ shock occurred in 1954 (Chung and Kanamori, 1976). Nevertheless, historical

* Corresponding author. Tel.: +39-81-6108-327; fax: +39-81-6108-351.
E-mail address: gilberto@ov.ingv.it (G. Saccorotti).

0031-9201/02/$ – see front matter
PII: S0031-9201(01)00203-5

records bring evidences for the occurrence of at least 20 larger earthquakes which, since 1500, produced intensities ranging from VIII to X (Vidal, 1986). This recognized seismic hazard prompts for a major effort aimed at solving the details of the main seismogenetic structures, in turn investigating their relationships with the complex stresses acting in the region.

The present-day seismicity is mainly characterized by seismic series unassociated with a principal earthquake. An example is the 1979 series (Vidal, 1986) which affected the whole basin and adjoining areas and lasted almost a year. The larger shock from this series had a magnitude $m_d = 4.8$, and 55 more earthquakes were largely felt by the population. Earthquakes also occur as seismic swarms, in which a great number of micro-earthquakes (over thousands) concentrates in a very short period (days or weeks) and in specific areas of a few square kilometers. For example, during February 1985 more than 1500 earthquakes occurred in proximity of the village of Loja (see Fig. 1a), with local magnitudes ranging up to 3.9. From late 1988 to early 1989 a seismic swarm composed by about 400 earthquakes with magnitudes between 0.4 and 4.0 occurred close to the village of Agron. Further examples are the Antequera swarm (June 1989) composed of 158 earthquakes with magnitude between 2.5 and 3.4 (Posadas et al., 1993), and the Iznajar swarm, with more than 2500 earthquakes recorded during a 10-day-long period in April 1998. This activity is mainly located in the upper crust: in the central area of the Betic Cordillera most of the earthquakes occur in the 9–16 km depth range, and gradually deepen to about 25 km moving toward the southwestern sector (Morales et al., 1997).

Recent improvements in regional seismological networks (Alguacil, 1986) have allowed for a better definition in earthquake locations, evidencing a rough correspondence of the seismicity patterns with the main geological structures (Buforn et al., 1988); however, the seismotectonic details of such activity are still poorly known, and this for three reasons. The first, is that most of these earthquakes occur at a typical depth greater than 10 km, thus making the association to the major surface structures extremely difficult. The second is related to the low magnitude range of the seismicity, which prevents from reliable hypocenters and focal mechanisms determination. The third, is that the general spreading of hypocenters

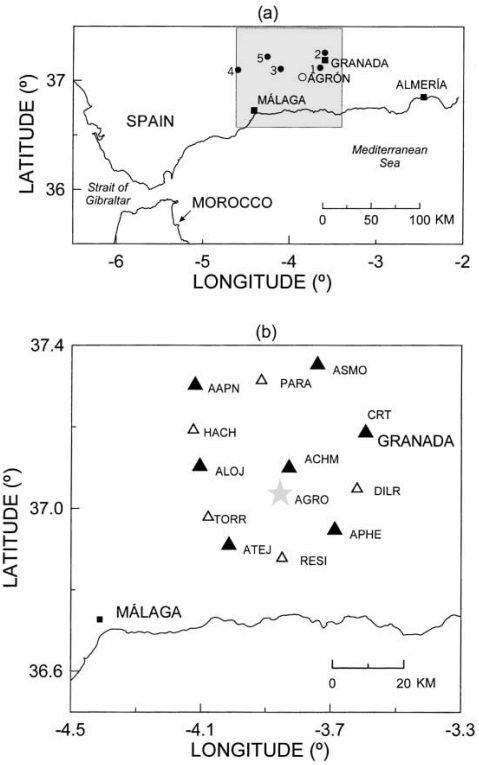

Fig. 1. (a) Map of southern Spain with location of the main cities (filled square); the shaded square bounds the area investigated in this study, which is illustrated in greater detail in (b). Numbered circles mark some of the seismic series occurred in the area: (1) and (2) Granada series; (3) Loja series; (4) Antequera swarm; (5) Iznajar series. (b) Location map of the seismic stations used in the study. Filled and empty triangles mark stations from the permanent and portable seismic networks, respectively. The star marks the zone where most of the earthquakes from the Agron series occurred, and where a mobile station recording on smoked paper drum was deployed shortly after the onset of the series.

observed in most of the episodes hinders the recognition of well-defined patterns or alignments which can be used to solve the ambiguity between the main and auxiliary plane of focal mechanism solutions.

This study is part of an effort aimed at a detailed revision of the recent seismicity occurred in the Granada Basin. The main goals of this research are to investigate the spatial and temporal patterns of these earthquakes, to delineate location and setting of the main

seismogenetic structures, and to investigate their relationship to the complex stress field presently acting in the region. For our analysis we select the dataset collected during the 1988–1989 Agron seismic series, as it is the first for which a good coverage of digital stations is available. Moreover, this series is characterized by a broad interval of magnitudes, representative of a large variety of source sizes.

The paper is organized as follows: first, we introduce the Agron seismic series, and describe the procedures for relocating a selected subset of the original catalogue. This new dataset is then used for application of a non-linear location procedure, aimed at a better definition of the spatial setting of hypocenters. A clustering technique based on analysis of the local rupture ellipsoid is then applied to evidence the main planes along which earthquakes occurred. Cross-correlation analysis of waveforms evidences the presence of five groups of similar events (multiplets), which are used for application of high-resolution, relative location techniques. Results from these investigations are used to constrain focal mechanism data, and to solve the details of some lineaments along which earthquakes occurred. These findings are eventually interpreted and discussed in light of the available informations about the tectonic stresses acting in the area.

2. Data, instruments, and relocation procedures

The data used in this study are from a permanent, telemetered seismic network (Red Sismica de Andalucia, RSA) and some additional portable, digital stations which were installed some months before the onset of the series (Fig. 1b). The *Instituto Andaluz de Geofisica* (IAG) at the University of Granada operated both the permanent and the mobile networks. Signals from either the permanent and mobile stations were radio transmitted to the central IAG monitoring station in Granada, and then recorded by two PC-based modules storing data at 100 samples/s per channel with a dynamic range of 14 bits (Alguacil, 1986); both the recorders used a common time base, provided via synchronization to the DCF77 radio-transmitted clock signal. All the sensors consisted of vertical, Mark Products L4C geophones with natural frequency of 1 Hz. Both the digital seismic networks operated continuously since the end of November 1988. Previously, data from the permanent stations were recorded only on thermic paper drums. From 7 to 15 December 1988, an additional portable station recording on smoked paper was installed on the epicentral area (station AGRO of Fig. 1).

The Agron seismic series is composed by about 400 shocks which occurred between October 1988 and April 1989 (Fig. 2a). The beginning of the series was marked by a sudden increase of the micro-seismicity ($M_L < 2.5$), with a peak value on 10 November 1988 (Fig. 2b); the main shock of the sequence occurred on 5 December 1988 with a magnitude of 4.0 (Fig. 2c). All the earthquakes of the series occurred inside the seismic networks; the local magnitudes were determined using the coda duration relationship established by De Miguel et al. (1988). The pattern of the energy release as evidenced from magnitude–time relationship (Fig. 2c) clearly shows that the dataset is representative of a seismic swarm, where it is not observable a typical mainshock–aftershock sequence. The initial catalogue from the routine operation of the IAG observatory depicted magnitudes ranging from 0.3 to 4; basing on the Gutenberg–Richter relationship depicted in Fig. 2d, this catalogue may be considered complete down to magnitudes of about 1. The hypocentral depths in the original catalogue ranged from 5 to 45 km; however, this scatter has probably to be attributed to the large errors during routine phase reading, as a consequence of the small magnitude of most of the earthquakes.

Our revision of the dataset begun with the selection of those digital data which were recorded by at least four stations; this reduced the catalogue to 125 earthquakes occurred between 5 December 1988 and 29 April 1989. In this procedure, we evaluated the P-wave onset together with its uncertainty interval; we did not read S-wave arrivals because of the possible large uncertainties associated to the fact that only vertical-component recordings were available. This revised set of arrival times was used to relocate the swarm adopting a modified version of the HYPOELLIPSE computer program (Lahr, 1989). We used a velocity model consisting of two layers with thicknesses of 10 and 30 km and P-wave velocities of 5.6 and 6.6 km/s, respectively, underlain by an half-space with a P-wave velocity of 7.8 km/s. The average horizontal error of the relocated earthquakes was of about 1 km; notwithstanding the good station coverage, the

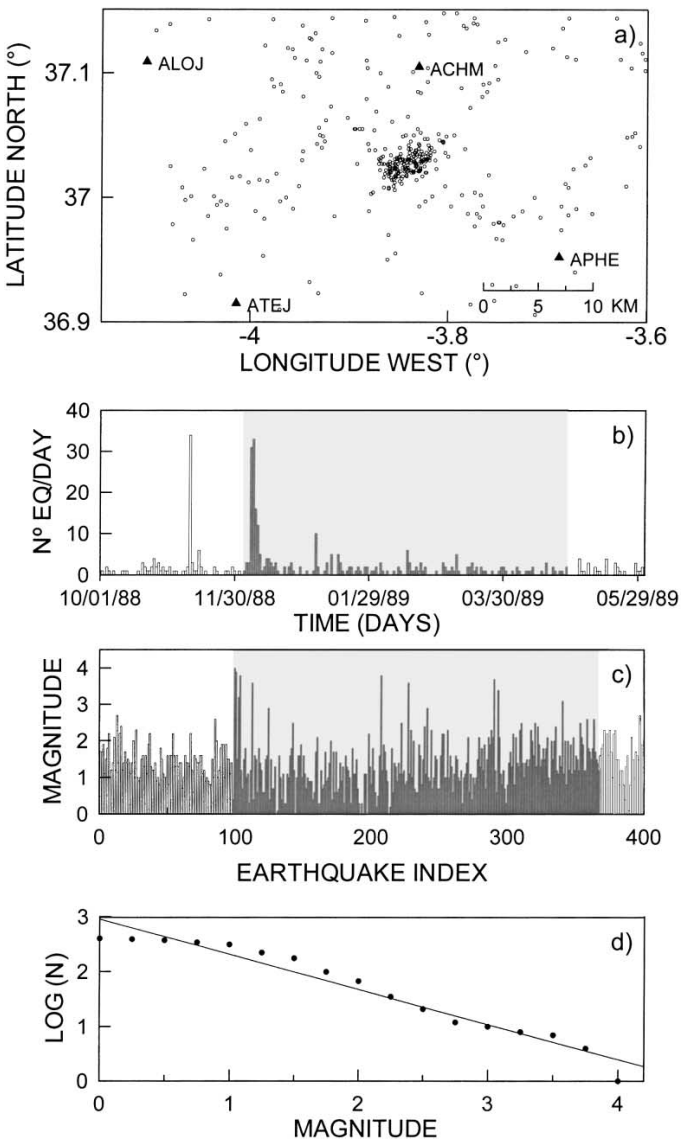

Fig. 2. (a) Map of preliminary epicenters of the Agron seismic series from 1 October 1988, through 31 May 1989 (data from the IAG catalogue). Triangles mark some stations from the Andalusian Seismic Network, which are plotted as reference. (b) Bar plot showing the temporal evolution of the daily number of earthquakes. The shaded region (from 5 December 1988, through 29 April 1989) bounds the dataset analyzed in this study. (c) Evolution of the magnitudes during the series. The horizontal axis represents the earthquake index in chronological order. The selection goes from 1 October 1988, through 31 May 1989. The shaded region bounds the catalogue used for this study. (d) Gutenberg–Richter relationship derived considering all the events depicted in (a). The corresponding *b*-value is 0.63.

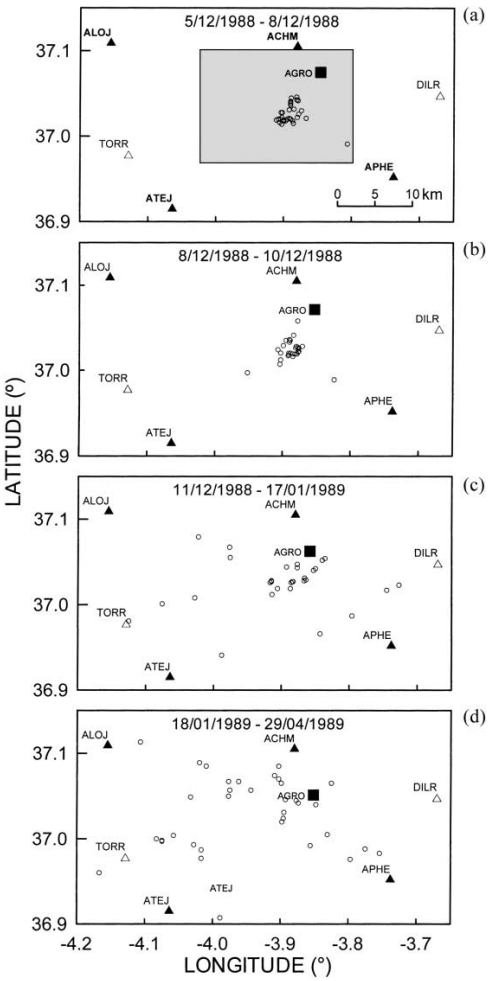

Fig. 3. Temporal evolution of the Agron series. Each map represents consecutive groups of 30 epicenters extracted from the revised catalogue. The shaded area in the upper panel bounds the region investigated for the probabilistic relocation of earthquakes.

uncertainty in depth estimates remained quite large, and for several earthquakes the depth coordinate was completely unresolved.

In Fig. 3 we show the revised epicentral location for four consecutive time intervals. The earlier events of our revised catalogue are tightly clustered in a narrow epicentral region (Fig. 3a); as the series evolves, two different alignment of epicenters are visible (Fig. 3b and c). The second half of our revised dataset is characterized by a spreading of the epicenters, which are now scattered over a much broader area (Fig. 3d). These maps give an exhaustive view about the distribution of the seismicity on the horizontal planes, but the problem of the depth of the seismogenetic structure/s remains pending. Moreover, another question arises: are the alignments observed in the horizontal plane of Fig. 3b and c true, or they rather reflect some effect induced by the network geometry on the relocation procedure? As a first attempt to address these issues, we use the set of revised arrival times to non-linearly solve the hypocentral location problem, which is the object of the next section.

2.1. Probabilistic location

Our approach to the probabilistic location of the Agron earthquakes is based on the method first proposed by Tarantola and Valette (1982), and successively used by Moser et al. (1992) and Wittlinger et al. (1993). The basic relationship used to evaluate the spatial probability density function (PdF) of the hypocenters is Eq. (8) of Tarantola and Valette (1982):

$$\sigma(\boldsymbol{x}_0) \propto \rho(\boldsymbol{x}_0) \exp[-0.5[(\hat{\boldsymbol{t}}^{\mathrm{obs}} - \boldsymbol{h}(\boldsymbol{x}_0, \boldsymbol{x}))^{\mathrm{T}} \times (\boldsymbol{C}^{\mathrm{D}} + \boldsymbol{C}^{\mathrm{M}})^{-1}(\hat{\boldsymbol{t}}^{\mathrm{obs}} - \boldsymbol{h}(\boldsymbol{x}_0, \boldsymbol{x}))]] \quad (1)$$

where $\boldsymbol{x}$ and $\boldsymbol{x}_0$ represent the station and hypocenter coordinates, respectively, $\rho(\boldsymbol{x}_0)$ is an arbitrary a priori PdF containing all the a priori information that we have about the model parameters, $\hat{\boldsymbol{t}}^{\mathrm{obs}}$ the vector of the observed arrival times minus the mean of observed arrival times at the recording stations, $\boldsymbol{h}(\boldsymbol{x}_0, \boldsymbol{x})$ the vector of the theoretical traveltimes minus the mean of the theoretical traveltimes, $\boldsymbol{C}^{\mathrm{D}}$ and $\boldsymbol{C}^{\mathrm{M}}$ are the variance–covariance matrices associated to errors in the phase reading and in the prediction of theoretical traveltimes, respectively. Straightforward computations give the marginal PdFs over the planes defined by the three Cartesian axes:

$$\sigma(x, y) = \int_z \sigma(x, y, z)\,\mathrm{d}z,$$
$$\sigma(x, z) = \int_y \sigma(x, y, z)\,\mathrm{d}y,$$
$$\sigma(y, z) = \int_x \sigma(x, y, z)\,\mathrm{d}x \quad (2)$$

From the maxima of these distributions we obtain the coordinates of the hypocenter. The advantages of this approach over the more classical linearized approach are as follows:

- It fully accounts for errors in both the data and the theory.
- It provides a description of the solution over the entire model space, thus avoiding misleading interpretation as is the case when the misfit function presents multiple minima.
- The solutions derived from each event may be summed, to give an overall distribution of the probability density of seismic events inside a given volume.

Our application of the probabilistic method to the Agron data is mostly aimed at revealing the alignments and depth of hypocenters inside the region of maximum seismicity. We therefore investigate a volume extending 20 km along the NS direction, and 30 km along the EW and depth directions, respectively (see dashed frame in the upper panel of Fig. 3). This volume is then gridded with a constant grid spacing of 0.5 km along the three directions defined by a Cartesian reference system whose x- and y-axis point EW and NS, respectively, and the z-axis is oriented vertically and is positive downward.

For each grid node, theoretical travel times are computed to the different stations of either the permanent and portable networks; this library of travel times is then used to evaluate, for each event, the misfit function and finally the PdF expressed through relationship (1). The diagonal elements C_{ii}^{M} of the model covariance matrix (i.e. the errors in the prediction of the travel times from a given hypocenter to the different stations associated to the scanty knowledge of the velocity structure) are set equal to 0.2 s. Following Tarantola and Valette (1982) and Wittlinger et al. (1993), the off-diagonal elements of the matrix $\boldsymbol{C}^{\mathrm{M}}$ are defined as

$$C_{ij}^{\mathrm{M}} = C_{ii}^{\mathrm{M}} \exp\left(-\frac{d_{ij}^2}{\Delta^2}\right), \quad i \neq j \tag{3}$$

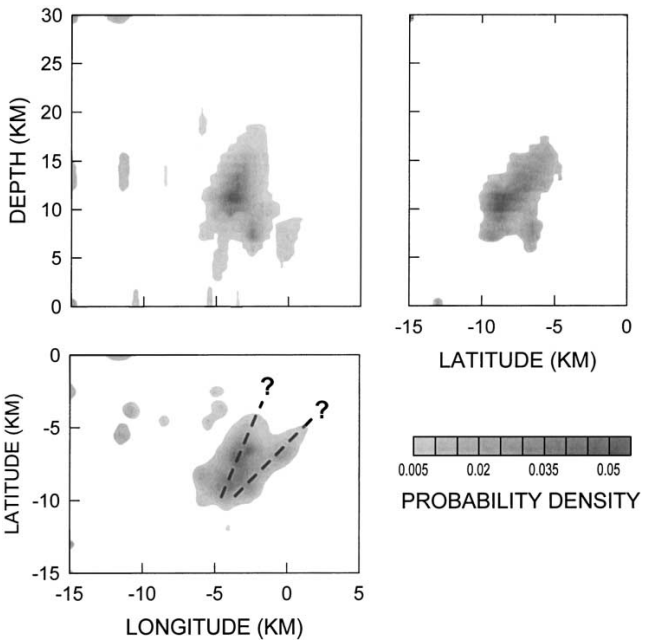

Fig. 4. Marginal probability density functions for earthquake location projected over the horizontal plane and the two vertical planes striking EW and NS, respectively. Two clusters of highest occurrence rate of earthquakes are observed at depths of 6–8 and 10–15 km. The horizontal map depicts two possible alignment of epicenters, as also observed in the maps of Fig. 3.

where d_{ij} is the distance between stations i and j and Δ is the correlation length of the medium, here taken equal to the assumed dominant wavelength (0.5 km). The elements of the (diagonal) matrix $\boldsymbol{C}^{\mathrm{D}}$ are instead taken directly from the phase reading uncertainties.

The results from the above procedure are illustrated in Fig. 4 in form of marginal PdFs projected along the EW–NS plane and the two vertical planes oriented NS and EW. The application of the probabilistic method clearly shows that, in the volume investigated, the whole of the seismicity occurs in the 5–18 km depth interval; however, no significant improvements are obtained in the definition of the two horizontal coordinates of the hypocenters. The two alignment of epicenters are in fact barely visible on the map displaying the marginal PdF projected on the horizontal plane. The problem of exactly determining the planes along which seismicity occurred remain therefore still pending, and is the object of the next two sections.

3. Principal component analysis

In order to retrieve the possible planes along which earthquakes occurred, we examined the spatial distribution of hypocenters using a principal component analysis (PCA). Application of this method begins by forming a series of subgroups of hypocenters. This is achieved by considering, for any given event, all those hypocenters which lie within a sphere of radius D centered on the reference focus. The coordinates of these hypocenters are then used to define a scatter matrix $\boldsymbol{S}$, whose elements are given by Cooley and Lohnes (1971):

$$S_{im} = \frac{1}{K}\sum_{j=1}^{K}(x_{ji} - X_{0i})(x_{jm} - X_{0m}),$$
$$i, m = 1, 2, 3 \tag{4}$$

where j is the earthquake index, and the x's are the Cartesian coordinates of the hypocenter, with the subscripts (i, m) corresponding to longitude, latitude, and depth on taking values of 1, 2 or 3, respectively. The X_0's represent the arithmetic average of the three Cartesian coordinates of the hypocenters, being defined as

$$X_{0m} = \frac{1}{K}\sum_{j=1}^{K} x_{jm}, \quad m = 1, 2, 3 \tag{5}$$

where the index m has the same meaning described above.

Eigenvectors and eigenvalues of the matrix $\boldsymbol{S}$ give the principal axes of an ellipsoid (named the local rupture ellipsoid (LRE) after Michelini and Bolt (1986)) which best fits the original cloud of hypocenters in a least square sense. The relationship between the magnitude of the three eigenvalues thus allows for characterizing the spatial distribution of the seismicity in planar or volumetric patterns. This procedure is quantified through examination of the ratio between the largest and the smallest eigenvalue of each ellipsoid. If this ratio is smaller than 2.5, then the ellipsoid is considered to be predominantly volumetric, and the measurement is rejected. Conversely, when one or two eigenvalues are much greater of the third one, then the ellipsoid is representative of a quasi-planar structure, whose pole is represented by the eigenvector associated to the smaller eigenvalue.

This procedure is iterated over the whole set of hypocenters, and for any accepted ellipsoid, a weight is assigned to that particular quasi-planar volume to evaluate the importance of the subgroup obtained. This weight is quantified through the parameter F, defined as $F = K/N$.

Azimuth and dip of the poles of the quasi-planar ellipsoids are eventually arranged in a multivariate frequency distribution plot, where each azimuth/dip pair has been previously weighted for the corresponding value of F. The peaks of these diagrams thus allow for the identification of the azimuth–dip pairs corresponding to the most representative planes. The main peaks are associated to the dominant fractures activated in the earthquake series, while the minor peaks correspond to secondary fractures accompanying the main ones.

From examination of the frequency distribution of inter-hypocenter spacings, we used a grouping distance D of 3 km. We then applied the spatial PCA to the whole series and to a data subset corresponding to the first 69 earthquakes, for which a clustering of seismicity in a small epicentral area was observed (Fig. 3). Results from this procedure are shown in

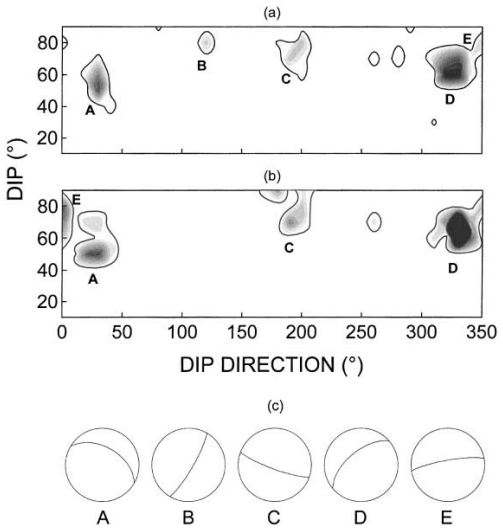

Fig. 5. Frequency distribution of dip and dip directions for planes obtained from eigen-decomposition of the scatter matrix of hypocenters. Each estimate has been weighted for the corresponding F-parameter. The map in (a) is obtained from analysis of the 125 revised earthquakes, and that in (b) from the first 69 of the series. Both the results correspond to an inter-distance D of 3 km. Five trends (named A–E) are identified, of which four (A, C, D and E) are common to the two different dataset. The most significant estimate is associated to plane D, which roughly corresponds to the main alignment observed in the epicentral maps (Figs. 3 and 4). In (c), the five mentioned planes are displayed using lower hemisphere, equal-area stereographic projections.

Fig. 5, which depicts the weighted frequency distribution of the dip direction and dip of the planes inferred from the eigen-decomposition of the RLEs. In the case of the analysis of the whole dataset (Fig. 5a) there are at least five significant planes (named A–E), and therefore five possible active fault planes, whose stereographic projection are displayed in Fig. 5c. Dip direction and dip of these planes are reported in Table 1 . With the only exception of plane B, the same pattern is observed for the analysis of the subset of 69 earthquakes (Fig. 5b). In both the cases, the most significant tendency is that associated to plane D. From examination of the epicentral maps of Figs. 3 and 4, this plane appears to be related to the main distribution of the seismicity, representing a sort of average among the two alignments hypothesized in Fig. 4. More difficult is to interpret the other planes, which apparently do not correspond to any alignment depicted by the hypocentral maps. The consistency and robustness of these findings need therefore to be verified from application of further, more resolutive analyses. This is the object of the next section, where a high-resolution relative location technique is applied to five clusters of similar earthquakes.

Table 1
Dip direction and dip angles of fault planes from PCA

Plane ID	Dip direction (° clockwise from N)	Dip (° from horizontal)
A	30	50
B	120	80
C	190	70
D	320	60
E	350	80

4. Relative locations

Seismic series are often characterized by the occurrence of clusters of similar events, which are commonly referred to as multiplets or families. Conditions for such similarities are fulfilled if all factors contributing to shaping the seismograms (source time function, propagation path, station site and recording instrument) are essentially identical (Maurer and Deichmann, 1995). In this context, source time functions are regarded as similar if the events have a common focal mechanism and similar magnitudes. Identity of the propagation path implies that the hypocenters must be tightly clustered in space, compared to the dimension of the near-source heterogeneities and to the observed wavelength. According to Geller and Muller (1980), such a condition is generally achieved when the hypocenters are spaced by lesser than a quarter of dominating wavelength, even if some more recent works (see Aster and Scott (1993), and references therein) point out that appreciable coherence can exist for inter-hypocenter separation of up to a few times the dominant wavelength. As demonstrated in a pletora of studies, the importance of recognizing the occurrence of these cluster of events principally relies on the fact that the similarities among waveforms allow for a highly consistent determination of

phase onsets, which are in turn used for precise relative hypocenter determination (e.g. Ito, 1985; Fremont and Malone, 1987; Deichmann and Garcia-Fernandez, 1992; Got et al., 1994; Augliera et al., 1995; Cattaneo et al., 1997; Shearer, 1997; Shearer, 1998; Phillips, 2000), other than for measuring temporal changes in seismic velocity (e.g. Poupinet et al., 1984; Haase et al., 1995). In this work, the identification of clusters of similar events is principally aimed at an improvement in event location, in order to put more robust constraints on the location and extent of the main seismotectonic structures activated during the series.

4.1. Searching for earthquake multiplets

In our search for cluster of similar events, we selected seismograms from station ACHM, which recorded all the 125 revised earthquakes. In order to equalize for the effect of different events magnitude, traces were band-pass filtered in the 1–15 Hz frequency band using a zero-phase-shift, three-pole Butterworth Filter. For each seismogram, we then selected a 2 s-long window starting 0.5 s before the onset of the P-wave as picked by during the revision procedure; the starting and ending 10% of these new time series were then tapered with a cosine window, and the normalized cross-correlation among all the independent pairs of signals was finally calculated. The results from this procedure are displayed in form of an upper triangular correlation matrix in Fig. 6, with correlation increasing from lighter to darker colors.

The next problem is obviously that of clustering groups of similar events. Given the high number (7750) of event pairs, we developed an automatic procedure based on the equivalence class (EC) approach described in Press et al. (1992) and applied by Aster and Scott (1993). This procedure identifies groups of elements satisfying a commutative "sameness" condition and assign them to the same family or tree. In our case, the sameness condition is obviously given by a threshold S on the correlation coefficient: that

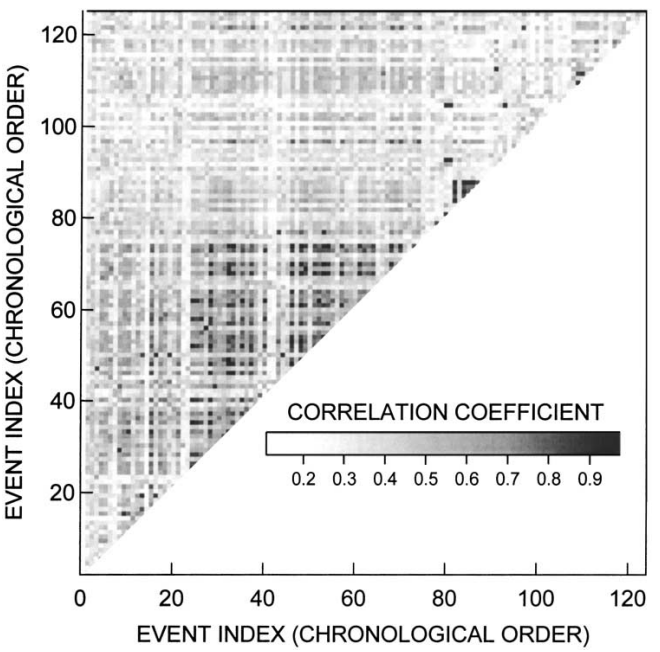

Fig. 6. Correlation matrix of the 125 events recorded at station ACHM and used for identifying clusters of similar events. Gray scale represents the normalized correlation coefficients.

is, a pair of events are grouped in the same family if and only if their correlation coefficient is greater than or equal to S.

A sometimes undesired characteristic of this method relies in the fact that the resulting trees are 'open': in other words, if A is similar to B and B is similar to C, then A, B, and C are assigned to the same group regardless of the similarity between A and C. We partially overcome this feature by considering a value of the threshold S equal to 0.9: this ensures that an high level of similarity is maintained throughout the different elements of the same family. A posteriori manual inspection has confirmed that all the possible pairs of events belonging to the different trees were related by correlation coefficients never lower than 0.8, and thus still significantly similar. On the other side, is also of interest to analyze events whose similarities are spread over a larger interval, in order to use the power of correlation procedures to adjust the arrival times of noisy signals with respect to a well-picked master event (e.g. Shearer, 1997). This procedure allowed for the identification of five different multiplets, where a multiplet is defined as a cluster containing at least three similar earthquakes (Table 2).

Table 2
Attribution of earthquakes to groups of similar events

Multiplet ID	Date	Magnitude
I	1988 + 12080114	1
	1988 + 12080117	1.7
	1988 + 12080151 (M[a])	2.5
	1988 + 12080450	1.6
	1988 + 12080333	1.7
	1988 + 12102244	1.1
II	1988 + 12082048 (M)	1.7
	1988 + 12090846	1.3
	1988 + 12101743	1.1
	1988 + 12152058	1.2
	1988 + 12181808	1.4
III	1989 + 01052024	1.9
	1989 + 01050512	2.4
	1989 + 01052018 (M)	2.9
	1989 + 01052028	1
	1989 + 01060633	2.3
IV	1988 + 12261251 (M)	2.3
	1989 + 01121334	2.1
	1989 + 01241346	2.2
V	1989 + 01162332	1.6
	1989 + 03050022	1.5
	1989 + 03082140 (M)	2.5

[a] M: master event.

4.2. Least squares adjustment of arrival times

Events sharing very similar waveforms allow for a very precise determination in the arrival time differences of the same phase from distinct events at a given station. To that purpose, two main techniques have been used thus far. The cross-spectral analysis method (Poupinet et al., 1984; Ito, 1985; Fremont and Malone, 1987; Got et al., 1994), and the time-domain, cross-correlation approach (Deichmann and Garcia-Fernandez, 1992; Augliera et al., 1995; Cattaneo et al., 1997). In both the approaches, the time- or frequency-domain cross-correlation functions are interpolated thus allowing for a precision in the estimate of the relative delays between pair of signals in the order of a tenth or even hundredth of the original digitization rate. More precisely, for the frequency-domain approach, the phase of the cross-spectrum is least-squares fitted by a linear relationship whose intercept with the y-axis gives the time difference, while in the time-domain the correlation function is interpolated through a polynomial (Deichmann and Garcia-Fernandez, 1992) or a sinc (Augliera et al., 1995) function. We choose a method very similar to the latter one, and interpolate the correlation function using a cubic SP-line interpolator (Press et al., 1992) to estimate the maximum of the cross correlation function with a precision of 1 ms (one-tenth of the original sampling rate; see Fig. 7). We tested the method by considering a real seismogram, and resampling it at a sampling rate of 0.001 s. This trace was contaminated with random (Gaussian) noise, and then duplicated. The two traces were linearly shifted by time intervals ranging between −9 and 9 ms, with steps of 1 ms. The delayed traces were then decimated back to the original sampling rate (100 samples/s), and eventually cross-correlated using the procedure described above. Application of the SP-line interpolator to these traces showed that the method is able to detect time shift of the signal with a resolution of 1/10 the original sampling interval down to a SNR of 8.

We now describe how to use the set of time differences among pairs of similar events to infer the time differences with respect to a master event.

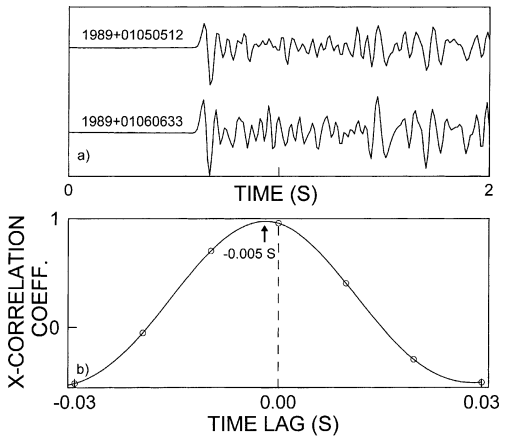

Fig. 7. Cross-correlation function between a pair of seismograms. (a) Two seismograms from multiplet III as recorded at station ACHM and band-pass filtered in the 1–15 Hz frequency band. Date and time identifying the events are reported at the left of each trace. The two recordings are aligned according to the maximum of the discrete cross-correlation function, indicated in (b) by the small circles. The continuous line in (b) represents the cubic SP-line interpolation to the cross-correlation function. The arrow in (b) indicates the maximum of the interpolated cross-correlation function, which allows for retrieving a time shift between the traces smaller than the sampling interval.

Let t_i and t_j be the arrival times of the P-wave of events i and j, as picked (estimated) at a given station of the network. Then, the time difference evaluated after the correlation procedure is:

$$\Delta_{ij} = t_i - t_j + \tau_{ij}$$

where τ_{ij} is the time lag at which the interpolated correlation function takes its maximum value. For a multiplet composed by N events recorded at the kth station, the correlation procedure described above allows for the estimate of the high-precision relative arrival times between all the $N(N-1)/2$ independent event pairs. Our objective is to estimate the time difference of all the events of the multiplet with respect to the sole master event, and in principle only the $N-1$ estimates of Δ_{i1} ($i = 2, \ldots, N$) should be used, where to the master event has arbitrarily assigned the index 1. However, several source of errors affect the correlation estimate: our signal are noisy and band-limited, so that in general $\Delta_{ik} \neq \Delta_{ji} + \Delta_{jk}$. We therefore follow Deichmann and Garcia-Fernandez (1992), and once the multiplet is composed of at least three events, we can express the generic time difference Δ_{ij} ($j > 1, i > j$) as a difference between Δ_{i1} and Δ_{j1}, thus making the system of equations over-determined with respect to these latter quantities.

The system of equations thus takes the form

$$\Delta_{i1}^{\text{true}} - \Delta_{i1}^{\text{est}} = \varepsilon_k,$$
$$i = 2, \ldots, N;\ k = 1, \ldots, N-1 \tag{6}$$

and

$$\Delta_{i1}^{\text{true}} - \Delta_{j1}^{\text{true}} - \Delta_{i1}^{\text{est}} = \varepsilon_k,$$
$$i = 3, \ldots, N;\ j = 2, \ldots, N-1;$$
$$k = N, \ldots, \tfrac{1}{2}N(N-1) \tag{7}$$

Note that this formulation differs from what originally proposed by Deichmann and Garcia-Fernandez (1992), as we do not take into account clock errors: our data were in fact recorded by the same recording system, which insured consistency among the synchronization of the different channels.

The adjustment of differential arrival times according to the L-2 norm is therefore achieved by satisfying the condition

$$\sum_{k=1}^{Np} \varepsilon_k^2 = \min \tag{8}$$

where we have set $Np = N(N-1)/2$.

The system of Eq. (7) is written in matrix notation as

$$\boldsymbol{Gm} - \boldsymbol{d} = \boldsymbol{r} \tag{9}$$

where $\boldsymbol{d}$ and $\boldsymbol{r}$ are vectors of length Np containing the estimates of the differential arrival times and the relative uncertainties, respectively, and $\boldsymbol{G}$ is an auxiliary $Np \times (N-1)$ matrix. As an example, we write out the case for $N = 4$:

$$\begin{pmatrix} 1 & 0 & 0 \\ 0 & 1 & 0 \\ 0 & 0 & 1 \\ -1 & 1 & 0 \\ -1 & 0 & 1 \\ 0 & -1 & 1 \end{pmatrix} \begin{pmatrix} \Delta_{21}^{\text{opt}} \\ \Delta_{31}^{\text{opt}} \\ \Delta_{41}^{\text{opt}} \end{pmatrix} - \begin{pmatrix} \Delta_{21}^{\text{est}} \\ \Delta_{31}^{\text{est}} \\ \Delta_{41}^{\text{est}} \\ \Delta_{32}^{\text{est}} \\ \Delta_{42}^{\text{est}} \\ \Delta_{43}^{\text{est}} \end{pmatrix} = \begin{pmatrix} \varepsilon_1 \\ \varepsilon_2 \\ \varepsilon_3 \\ \varepsilon_4 \\ \varepsilon_5 \\ \varepsilon_6 \end{pmatrix} \tag{10}$$

which, once subjected to the optimization condition (8), is solved using the well-known generalized inverse formulation:

$$\boldsymbol{m} = (\boldsymbol{G}^{\mathrm{T}}\boldsymbol{G})^{-1}\boldsymbol{G}^{\mathrm{T}}\boldsymbol{d} \tag{11}$$

As we wanted to weight the time differences estimated via the cross-correlation approach for the degree of similarities among waveforms, our estimate of the time difference with respect to the master event are obtained from the weighted version of Eq. (11):

$$\boldsymbol{m} = (\boldsymbol{G}^{\mathrm{T}}\boldsymbol{W}\boldsymbol{G})^{-1}\boldsymbol{G}^{\mathrm{T}}\boldsymbol{W}\boldsymbol{d} \tag{12}$$

where $\boldsymbol{W}$ is a matrix containing the normalized correlation coefficients.

To avoid problems associated with large values for the original time picks t_i, times are taken relative to an arbitrary reference time for each event, by subtracting to the estimated P-wave arrival the year, months, days and hours.

The effects from this procedure are illustrated in Fig. 8, where the set of $N = 6$ events belonging to multiplet III and recorded at stations ACHM and ALOJ are aligned to their relative arrival times estimated from application of Eq. (12); the original P-wave picks are also reported for comparison. From a quick examination of the two figures, it is evident that the L-2 adjustment described above allows for a great improvement in the estimate of differential arrival times for low SNRs, as is the case for station ALOJ.

4.3. Relative locations

Our relative location procedure follows a classical master event approach: for each multiplet, the event which has been recorded by the greatest number of stations is selected as the master, and located using a custom location procedure. The arrival times of the slave events, determined as above, are then corrected with the travel time residuals of the master event, and the location procedure iterated over the remaining elements of each multiplet. Both the master and slave events locations are calculated using the same probabilistic approach described above. In solving Eq. (1), we used an iterative grid-search procedure, in which the origin of the grid where the hypocenter is sought is iteratively translated to the minimum misfit node. At each iteration, the grid dimension and the spacing between grid nodes are adjusted consequently. In the final stage of the grid search, this procedure allowed to achieve a nominal resolu-

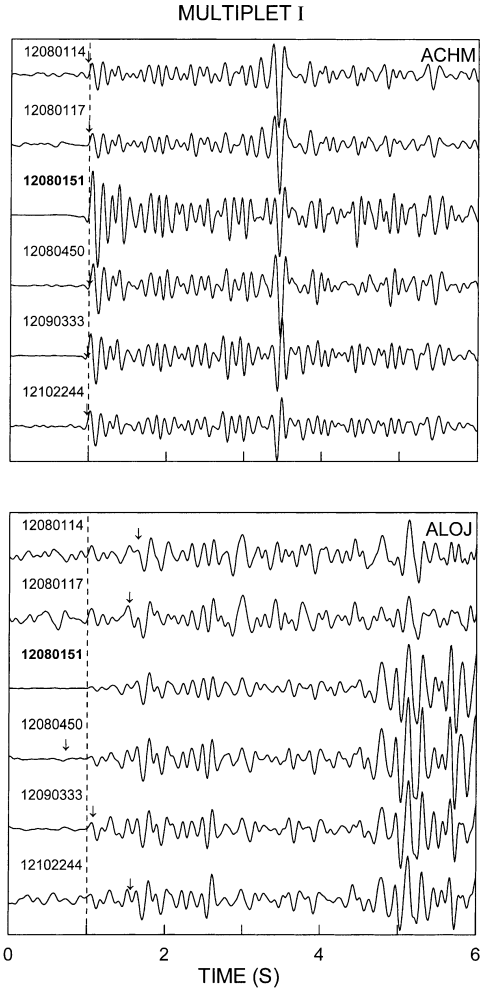

Fig. 8. Wave forms band-pass filtered in the 1–15 Hz frequency band for events belonging to multiplet I (see Table 2) and recorded at stations, ACHM (top) and ALOJ (bottom). Date and time identifying the events are reported at the upper left of each trace; bold labeling indicates the master event. Seismograms are aligned to the P-wave onset of the master event (dashed lines), according to the results from the least-squares adjustment of arrival time. The original time picks are indicated by arrows.

tion of about 3 m with a reasonable computer effort. The weighting scheme describing the errors in the prediction of travel times expressed through Eq. (3) acts selectively over the inversions of the master and slave events, since they were generally recorded by different sets of stations. Since we are only interested in the relative positions of the hypocenters, we set to zero the theoretical error, in order to ensure consistency between the master and slave events locations. We found the absolute location of the master event to differ somehow from the previous locations obtained using a theoretical error in the prediction of travel times of 0.2 s; however, this difference was generally small (a few hundreds of meters), and thus does not affect significantly the reliability of our results. For each family, the maximum-likelihood hypocenters derived from the relative locations are then used to infer a fault plane from a best-fit procedure to focii coordinates.

A sample location for multiplet II is illustrated in Fig. 9 in form of marginal probability density functions projected over the horizontal plane and the two vertical sections oriented EW and NS, respectively. In these maps, contouring indicates the 90% confidence level in the hypocenter coordinates. We note that the errors in hypocenter estimates are in the order of a few tens of meters, in agreement with what observed in most of the above cited studies. However, as a consequence of the non-linear inversion we adopted, the confidence intervals are not necessarily ellipsoidal, but they rather reflect the shape of the error function associated to the relative positioning of hypocenters and recording stations.

PCA described earlier was also applied to the hypocenter data obtained from relative locations. This procedure allowed for retrieving the planes which best fit the hypocenters of individual multiplets, in turn quantifying the degree of planarity of the hypocenter clouds. Details of the planes retrieved from analysis of the five clusters are reported in Table 3, in conjunction to focal mechanism data. The mutual relationships among the eigenvalues of the different LREs listed in Table 3 indicate that, with the only exception of multiplet I, all the remaining hypocenters are arranged according to linear patterns rather than to planar ones. The main (normalized) eigenvalues are in fact two to three orders of magnitude larger than the secondary ones, and the corresponding planes

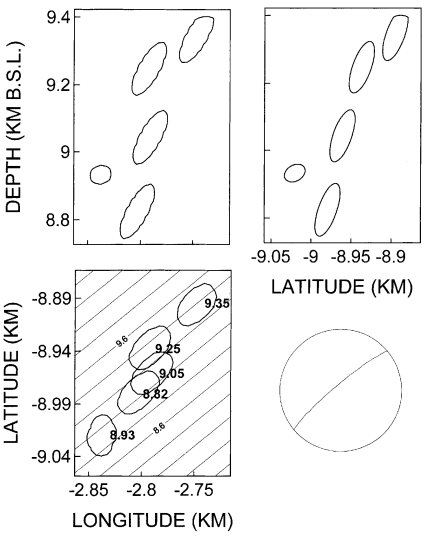

Fig. 9. Relative locations of earthquakes from multiplet II projected on the NS–EW horizontal plane and the two vertical planes oriented NS and EW. The bold contour lines mark the outer contour of the 90% confidence region for hypocenter location. The thin contour lines in the horizontal projection are lines of equal depth for the plane which best fits the hypocenter data; contour interval is 200 m. The stereographic projection (equal area, lower hemisphere) of that plane is shown at the lower right of the plot. Bold numbers on the horizontal projection indicate the depth of the maximum likelihood hypocenters.

depict a quasi-vertical setting. This occurrence could be related to a lack of resolution in the estimates of source depth: buttressing the reliability of our results, however, is the marked agreement among relative location and focal mechanism data, as discussed in the next section.

5. Focal mechanisms

We calculated focal mechanisms for events belonging to multiplets III–V using the classical approach (Reasenberg and Oppenheimer, 1985) based on the minimization of normalized, weighted sum of first-motion polarity discrepancies.

For multiplet III, we calculated a composite focal mechanism using data from four different events (see Table 3), thus obtaining an extremely robust estimate

Table 3
Fault planes from focal mechanisms and relative locations data

Multiplet	Events used for Fault Plane Solution	No. of Polarities	Dip direction and dip from PCA to relative location data (°)	Relative size of LRE eigenvalues			Dip direction and dip from focal mechanisms (°)	
				λ_1	λ_2	λ_3	Main plane	Auxillary plane
–	1988 + 12050512 (mainshock)	10	–	–	–	–	308, 20	205, 85
I	–	–	4, 76	1	0.12	0.03	–	–
II	–	–	310, 82	1	0.05	0.0005	–	–
III	1989 + 01052024	11	279, 82	1	0.05	0.012	301, 80	60, 20
	1989 + 01050512	7						
	1989 + 01052018	8						
	1989 + 01060633	11						
IV	1989 + 01121334	11	278, 81	1	0.06	0	180, 85	88, 70
V	1989 + 03082140	10	56, 83	1	0.004	0	50, 88	165,20

of the fault plane solution. Data for these events resulted to be compatible with two different mechanisms; however, one of the two solutions included a plane which is almost coincident with the fault plane obtained from relative locations, and this is therefore our preferred solution.

This mechanism indicate a sub-vertical, oblique normal fault oriented N–9°E (relative location) or N–31°E (focal mechanism). This plane is also in agreement with those previously obtained by Galindo-Zaldivar et al. (1999) for the same set of events; the slight differences with what measured by these authors may be attributed to the different hypocenter depths, this discrepancies probably owing to the lesser sophisticated location techniques they adopted.

Focal mechanism for multiplet IV was determined using data from a single event, as it was the only member of the cluster for which a sufficient number of polarities was available. As in the previous case, our data are compatible with two distinct mechanisms, and again we select the one for which one of the two possible fault planes corresponds to that derived from relative locations (Table 3). As in the previous case, the fault plane appears to be almost vertical, and oriented roughly NS.

Multiplet V has associated a single mechanism, derived from polarity readings of a single event (Table 3). Again, one of the two focal planes resembles that derived from relative locations, indicating a sub-vertical normal fault oriented approximately N–40°W.

Interesting considerations arise from the joint examination of the results obtained from application of the different techniques. Some of the planes inferred from focal mechanisms and relative locations find in fact correspondence with the patterns evidenced by the spatial PCA, thus allowing for an increase in the robustness of the results obtained from this latter technique. From comparison of Figs. 5 and 10, it is easy to observe the sameness between planes B and D with those corresponding to multiplets III and II, respectively. By the same token, a good correspondence is noted between plane C and one of the two conjugate plane of the fault plane solution of the mainshock, and between planes E and that derived from relative location of multiplet I. In making these considerations, we have to remember the coarse bin size (10°) used in retrieving planes from the PCA, as well as the variability in fault plane setting derived from the relative locations. The plane-fitting to hypocenter data of the identified multiplets is in fact affected by both the intrinsic errors in retrieving hypocenters and the closeness of these latter ones. Thus, experimental errors and resolution limitation imply a variability of several degrees in either the strike and dip of the retrieved planes: bearing this consideration in mind, we may conclude that, with the only exception of plane A, all the fault planes derived from the spatial PCA are

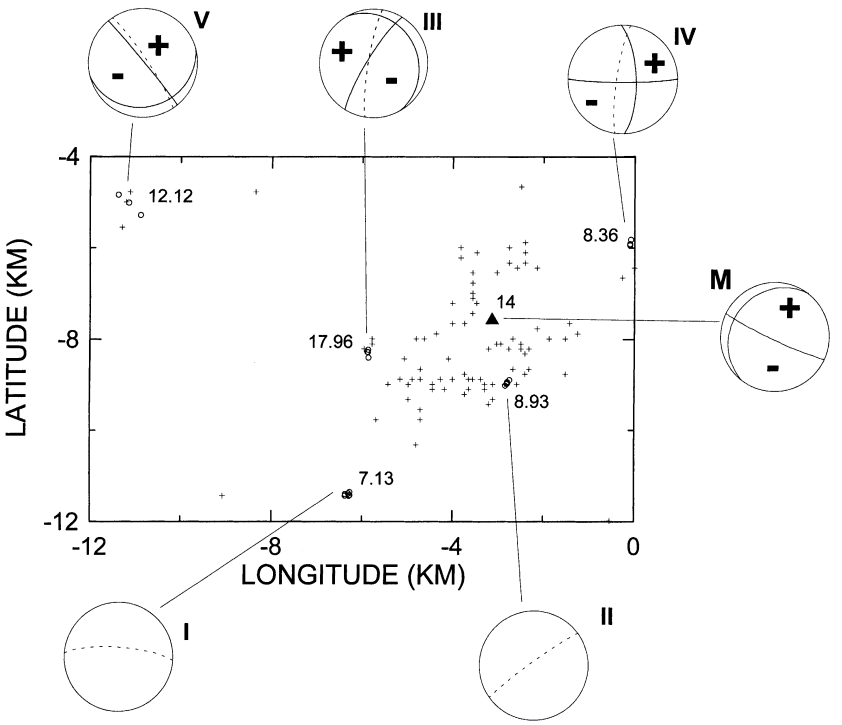

Fig. 10. Epicentral map and focal mechanisms compared to the fault planes obtained from the relative location procedure. Crosses indicate original locations, and circles are epicenters from the relative locations. Equal area, lower-hemisphere stereographic projections display the fault planes from relative locations (dashed lines), and when available, the corresponding focal mechanism from P-wave polarities (continuous lines). The different multiplets are identified by roman numbers aside each projection; note that the numbering is ordered chronologically. The fault-plane solution for the mainshock (black triangle) is reported as well. Numbers in the epicentral map indicate the depth of each cluster. As in Fig. 4, coordinates are taken relative to a point located at 37.1°N and 3.8°W.

validated by the relative locations and fault-plane solutions.

6. Discussion and conclusion

In the present work we analyzed a seismic series occurred in the Granada Basin (Spain) between November 1988, and May 1989. The original catalogue from the IAG observatory in Granada reported about 400 earthquakes with magnitudes ranging between 0.4 and 4.0, and focal depths spread in the 5–45 km depth interval. The analysis of the seismic series has been carried out according to the following scheme:

- Relocation of the earthquakes using a standard linearized location routine applied to digital P-wave arrivals observed at a minimum of four stations.
- Determination of the maximum likelihood hypocentral area using a probabilistic approach.
- Determination of possible active fault planes using a statistical method based on PCA of hypocenter data.
- Identification of cluster of similar earthquakes from cross-correlation of digital waveforms.
- Relative location of similar events using least-squares adjustment of arrival times with respect to a master event.

- Determination of the spatial setting of some of the fault planes activated during the series combining the informations derived from PCAs, fault plane solutions from P-wave polarities, and high-resolution relative locations.

Results from the relocation using the standard procedure allow for a better definition of the source region, showing a cloud of seismicity with two possible sub-parallel alignments striking approximately NE–SW. Epicenters are tightly clustered at the beginning of the series, and spread over a wider region during the final part of the swarm. The focal depths are more defined than in the locations from the original catalogue, and range between 1 and 25 km. These results are consistent with those previously obtained by Morales et al. (1997), who used the Wadati (1933) technique to analyze the seismicity of southern Spain including a subset of the data used in this work.

The probabilistic relocation permits a clearer definition of source depths, showing two main clusters of hypocenters at depths of about 7 and 10–15 km, this latter one being by far the most important. However, these results do not contribute significantly to the determination of the planes along which earthquakes occurred. Further clues are thus obtained from application of the spatial PCA to hypocenter data. Results from this procedure allows for the identification of five possible fault planes, of which only one corresponds to the alignment depicted by the epicenter distribution. However, three of the remaining four planes obtained from the spatial PCA are validated through the informations jointly carried by high-precision relative locations and fault plane solutions from P-wave polarity data.

Taken all together, these results depict an extremely complex picture, where the spatial setting of the fault planes greatly varies over a narrow focal volume. Only a few of these faults (e.g. that corresponding to multiplet V and one of the two conjugate planes of the mainshock) are in agreement with the regional ENE–WSW extension acting in the area (Galindo-Zaldivar et al., 1999). However, as these latter authors pointed out, the present-day stresses locally acting in the Granada Basin seems to be characterized by a prolate nature of the stress ellipsoid, with the σ_1 axis steeply plunging SW and the σ_2 and σ_3 components nearly identical. This configuration of the local stress field could thus lead to the reactivation of pre-existing fault planes, as for instance the NE–SW pliocene fault system probably represented by multiplets II and III. Moreover, the observed closeness of faults with different orientation suggests a significant fragmentation of the upper crust into small (2–4 km) tectonic blocks, as also inferred by Steich et al. (2000) for the western Almeria seismicity (see Fig. 1). This large degree of fragmentation represents an appropriate scenario for explaining the complex redistribution of the shear stress after each event, which could concur in the reactivation of fault planes not favorably oriented with the regional stress field. Given this complexity, the dataset analyzed in this paper make at present impossible any further speculation about the stresses presently acting in the region, a more detailed determination of which is demanded to future studies focused on the analysis of successive, larger datasets (e.g. the 1998 Iznajar series; Fig. 1).

Acknowledgements

Editor J.P. Poirier, Peter Shearer and an anonymous reviewer are greatly acknowledged for the thoughtful comments which significantly helped in improving the quality of the paper. Antonio Posadas provided precious suggestions while carrying out PCA. Gerardo Alguacil, Miguel Abril and Pepe Morales are greatly acknowledged for the assistance given during the development of this work. The study was financed through the projects ANT98-1111 and AMB99-0795-C02-01 under the Spanish Antarctic Program, and ‘Grupo de Investigacion RNM104’ under the Local Government of Andalusia.

References

Alguacil, G., 1986. Los instrumentos de una red telemetrica para microterremotos. La Red Sismica de la Universidad de Granada. PhD Thesis, University of Granada, Granada, Spain.

Aster, R.C., Scott, J., 1993. Comprehensive characterization of waveform similarity in microearthquake datasets. Bull. Seismol. Soc. Am. 4, 1307–1314.

Augliera, P., Cattaneo, M., Eva, C., 1995. Seismic multiplets analysis and its implication in seismotectonics. Tectonophysics 248, 219-234.

Buforn, E., Udias, A., Mezcua, J., 1988. Seismicity and focal mechanism in south Spain. Bull. Seismol. Soc. Am. 6, 2008–2024.

Cattaneo, M., Augliera, P., Spallarossa, D., Eva, C., 1997. Reconstruction of seismogenetic structures by multiplet analysis: an example of western Liguria, Italy. Bull. Seismol. Soc. Am. 4, 971–986.

Chung, W.-Y., Kanamori, H., 1976. Source process and tectonic implications of the Spanish deep-focus earthquake of March 29, 1954. Phys. Earth Planet. Int. 13, 85–98.

Cooley, W.W., Lohnes, P.P., 1971. Multivariate Data Analysis. Wiley, New York.

De Miguel, F., Alguacil, G., Vidal, F., 1988. Una escala de magnitud a partir de la duracion para terremotos del sur de España. Rev. de Geofisica 44, 75–86 (in Spanish).

Deichmann, N., Garcia-Fernandez, M., 1992. Rupture geometry from high-precision relative hypocenter locations of microearthquake clusters. Geophys. J. Int. 110, 501–517.

Fremont, M.J., Malone, S.D., 1987. High precision relative locations of earthquakes at Mount St. Helens, Washington. J. Geophys. Res. 92, 10223–10236.

Galindo-Zaldívar, J., Jabaloy, A., Serrano, I., Morales, J., González-Lodeiro, F., Torcal, F., 1999. Recent and present-day stresses in the Granada Basin (Betic Cordilleras): example of a late Miocene-present-day extensional basin in a convergent plate boundary. Tectonics 18, 686–702.

Geller, R.J., Muller, C.S., 1980. Four similar earthquakes in central California. Geophys. Res. Lett. 7, 821–824.

Got, J.L., Frechet, J., Klein, F.W., 1994. Deep fault plane geometry inferred from multiplet relative relocation beneath the south flank of Kilauea. J. Geophys. Res. 99, 15375–15386.

Haase, J.S., Shearer, P.M., Aster, R.C., 1995. Constraints on temporal variations in velocity near Anza, California, from analysis of similar event pairs. Bull. Seismol. Soc. Am. 1, 194–206.

Ito, A., 1985. High-resolution relative-hypocenters of similar earthquakes by the cross-spectral analysis method. J. Phys. Earth 33, 279–294.

Lahr, J.C., 1989. HYPOELLIPSE (Version 2.0): A Computer Program for Determining Local Earthquake Hypocentral Parameters, Magnitude and First Motion Pattern. US Geological Survey Open-File Report 89–116, 92 pp.

Maurer, H., Deichmann, N., 1995. Microearthquake cluster detection based on waveform similarities, with an application to the western Swiss Alps. Geophys. J. Int. 123, 588–600.

Michelini, A., Bolt, B.A., 1986. Application of the principal parameters method to the Coalinga, California, aftershocks sequence. Bull. Seismol. Soc. Am. 76, 409–420.

Morales, J., Serrano, I., Vidal, F., Torcal, F., 1997. The depth of the earthquake activity in the Central Betics (southern Spain). Geophys. Res. Lett. 24, 3289–3292.

Moser, T.J., van Eck, T., Nolet, G., 1992. Hypocenter determination in strongly heterogeneous earth models using the shortest path method. J. Geophys. Res. 97, 6563–6572.

Phillips, W.S., 2000. Precise Microearthquake locations and fluid flow in the geothermal reservoir at Soultz-sous-Forêts, France. Bull. Seismol. Soc. Am. 90, 212–228.

Posadas, A.M., Vidal, F., De Miguel, F., Peña, J.A., Alguacil, G., Ibáñez, J.M., Morales, J., 1993. Spatial–temporal analysis of a seismic swarm using the principal component analysis. The Antequera swarm (Spain). J. Geophys. Res. 98, 1923–1932.

Poupinet, G., Ellsworth, W.L., Frechet, J., 1984. Monitoring velocity variations in the crust using earthquakes doublets: an application to the Calaveras fault, California. J. Geophys. Res. 89, 5719–5731.

Press, W.H., Teukolsky, S.A., Vetterling, W.T., Flannery, B.P., 1992. Numerical Recipes: The Art of Scientific Computing, 2nd Edition. Cambridge University Press, Cambridge, UK.

Shearer, P.M., 1997. Improving local earthquake locations using the L1 norm and waveform cross correlation: application to the Whittier Narrows, California, aftershock sequence. J. Geophys. Res. 102, 8269–8283.

Shearer, P.M., 1998. Evidence from a cluster of small earthquakes for a fault at 18 km depth beneath Oak Ridge, southern California. Bull. Seismol. Soc. Am. 6, 1327–1336.

Steich, D., Alguacil, G., Morales, J., 2000. The relative location of multiplets in the vicinity of the western Almeria (southern Spain) earthquake series of 1993–94. Geophys. J. Int., submitted for publication.

Tarantola, A., Valette, B., 1982. Inverse problems—quest for information. J. Geophys. 50, 159–170.

Vidal, F., 1986. Sismotectónica de la región Béticas-Mar de Alborán. PhD. Thesis, 450 pp. (in Spanish).

Wadati, K., 1933. On the travel time of earthquake wave. Part II. Geophys. Mag. 7, 101–111.

Wittlinger, G., Herquel, G., Nakache, T., 1993. Earthquake location in strongly heterogeneous media. Geophys. J. Int. 115, 759–777.

II. Multiplet focal mechanisms from polarities and relative locations: The Iznajar swarm South Spain

Bulletin of the Seismological Society of America, Vol. 99, No. 6, pp. –, December 2009, doi: 10.1785/0120090036

Multiplet Focal Mechanisms from Polarities and Relative Locations: The Iznajar Swarm in Southern Spain

by Enrique Carmona, Daniel Stich, Gilberto Saccorotti, and Jesús M. Ibáñez

Abstract In April 1998, a swarm of ~1800 microearthquakes near the village of Iznajar (southern Spain) was recorded at the Granada basin short-period seismic network. Focal mechanisms from local *P*-wave polarities are poorly constrained and cannot characterize the seismotectonics of the series. Here we combine polarity information and multiplet relocation to address this issue. We use waveform cross correlation on *P* and *S* arrivals to identify events with highly similar seismograms, group our detections into multiplet clusters, and invert the cross-correlation time delays to obtain precise relative locations. Relative locations have errors of several 10s to a few 100s of meters horizontally and vertically, and define strike and dip of active fault patches with an accuracy of ~20–30°. We introduce the multiplet fault plane orientations into focal mechanism inversion, now yielding mostly well-constrained solutions, in addition to resolving the nodal plane symmetry. We observe mainly north-south left-lateral strike-slip faulting and a few north-northwest–south-southeast normal faulting solutions, illustrating the kinematic complexity of the swarm, and pointing to a local deformation style different from the nearby Granada basin.

Introduction

The evening of 11 April, 1998, microseismic activity increased abruptly in an area located between the village of Iznajar and the town of Loja, about 50 km west of Granada in southern Spain (Fig. 1). During 12 and 13 April alone, nearly 1000 events can be attributed to this series. The three largest events (M_w 3.5–3.6) occurred in the middle of the series on 13 and 14 April, indicating a clear deviation from a typical foreshock-mainshock-aftershock earthquake sequence and placing this series into the category of seismic swarms. Intense earthquake clustering is common in southern Spain's Betic Cordillera (the westernmost part of the Alpine mountain belt in Europe), especially around the Neogene Granada basin, with seismic swarms, for example, in 1979 (55 felt earthquakes in the Granada basin, $m \leq 4.8$, Vidal, 1986); 1985 (~1500 earthquakes near Loja, $m \leq 3.9$, Posadas, 1991); 1988–1989 (~400 earthquakes near Agron, $m \leq 4.0$, Saccorotti *et al.*, 2002); and 1989 (~160 earthquakes near Antequera, $m \leq 3.4$, Posadas *et al.*, 1993). While seismic activity is mainly concentrated in the eastern part and along the southern limit of the Granada basin, the Iznajar swarm occurred west of the basin (Fig. 1). The 1998 Iznajar swarm with more than 1800 events between 11 April and 13 May is still the largest seismic series recorded by the Granada basin digital local network to date.

For the three largest swarm events, moment tensor mechanisms are available from the inversion of intermediate period waveforms recorded at regional broadband stations (Stich *et al.*, 2003). They show very similar strike-slip mechanisms with a minor normal faulting component and northwest trending *P* axis (Fig. 2). The centroid depths of 12–14 km, obtained by testing different trial depths, are consistent with local network locations. Because of the small magnitudes and the sparse station distribution of the broadband network back in 1998, the moment tensor mechanisms are not tightly constrained (Fig. 2), as indicated by the observation of rather smooth waveform misfit minima during systematic forward modeling for alternative solutions in a grid search scheme (Stich *et al.*, 2003). Other, smaller earthquakes in the Iznajar swarm show high noise content in the intermediate period range where our approximate Earth models may predict regional waveforms appropriately, and are too weak for full waveform moment tensor inversion.

Here we aim at a more comprehensive seismotectonic characterization of the Iznajar swarm through focal mechanism analysis for smaller earthquakes. We recur to the classic approach of double-couple, first-motion focal mechanisms, inferring the geometry of compressive and dilatational quadrants from the back-projection of negative and positive P-wave polarities onto the focal sphere (e.g., Brillinger *et al.*, 1980; Snoke *et al.*, 1984). However, this implies reducing the information content to only 1 bit per station; we will see that first-motion focal mechanisms for the Iznajar swarm are poorly constrained, reflecting the limited amount of reliable polarity readings and an uneven coverage of the focal sphere.

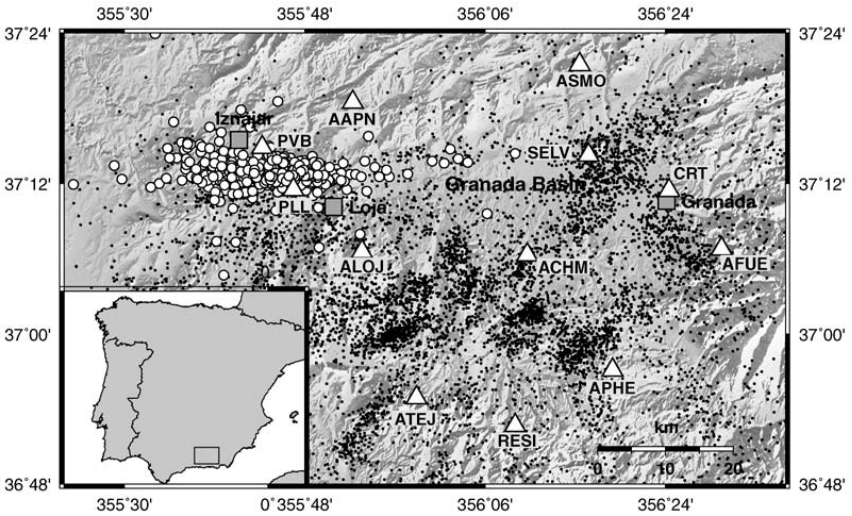

Figure 1. Location map showing single-event locations (circles) for the 1998 Iznajar swarm, background seismicity in the area from 1989 to present (dots, IAG catalog), and permanent and temporary (PLL, PVB) seismic stations used in this article (triangles).

To resolve the notorious ambiguities of first-motion mechanisms, we may invoke additional constraints, such as *S*-wave polarity readings (often difficult to pick reliably on complex regional waveforms) or amplitude ratios among different waves (potentially sensitive to details of the Earth structure involved). In this article, we propose to resolve ambiguities of first-motion mechanisms by using the fault patch orientations inferred from the relative locations of nearby earthquakes to put constraints on strike and dip values in first-motion focal mechanism retrieval. Here we expose the methodology and apply it to the 1998 Iznajar swarm.

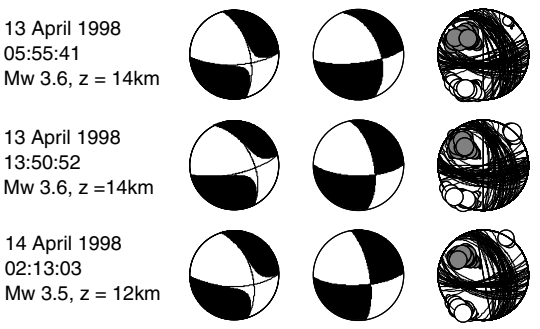

Figure 2. Regional moment tensor solutions for the three largest events of the Iznajar swarm (left column), best least-squares solutions from a systematic double-couple grid search (middle column), and confidence limits estimated from misfit variations for alternative solutions (right column; nodal planes and principal axes for solutions with up to 10% misfit increase are shown; Stich *et al.*, 2003).

Method

Earthquake recordings that show very similar short-period waveforms indicate that the earthquakes sources are closely spaced and have similar radiation patterns. Such events, commonly termed multiplets, are expected to originate from the same fault patch (Geller and Mueller, 1980). Event locations from picked arrival times are usually not accurate enough to resolve the spatial distribution of multiplet earthquakes, but cross-correlation and cross-spectral techniques can do so by exploiting waveform similarity to obtain relative arrival times with high precision (e.g., Ito, 1985; Scherbaum and Wendler, 1986; Pechmann and Thorbjarnardottir, 1990; Deichmann and García-Fernandez, 1992). Here we follow a three-step standard procedure for multiplet relocation (e.g., Stich *et al.*, 2001) consisting in the quantification of waveform similarity through sliding window cross correlation of *P* and *S* arrivals, equivalence class sorting of highly similar events into multiplet clusters, and linear inversion of the interpolated cross-correlation delay times for the relative locations of multiplet earthquakes with respect to a master event. Technical details are discussed in the Multiplet Analysis section.

Assuming that the alignments of relocated multiplet hypocenters define the fault that slips in these earthquakes, we can infer the strike and dip of the active fault patch by fitting a plane to the hypocenter distribution. We assign confidence limits to the fault patch orientation by simulating random dislocation of multiplet events with respect to their individual error ellipsoids. Multiplet relocation techniques have shown their potential to image the seismogenic fine structure responsible for clustered activity in many occasions (e.g., Kraft *et al.*, 2006; Ruiz *et al.*, 2006), but multiplet

relocation in absence of external constraints cannot reveal the slip vector of faulting, thus being unable to fully characterize multiplet kinematics. Here we aim at inferring the direction of the slip vector for multiplet earthquakes from considering available first-motion polarity readings on the multiplet waveforms. On the other hand, first-motion mechanisms are frequently not well-constrained from a limited number of polarity readings. Here we can see the problem from two perspectives; the polarities may not only constrain the slip direction along multiplet planes, but the multiplet focal mechanism determination may also be reduced to a much simpler one: Strike and dip of the fault plane are already known, within certain error bounds; we actually have to estimate only one parameter, the rake angle, and its confidence limits.

To exploit the synergies of first-motion focal mechanism inversion and multiplet relocation, we combine both techniques by intersecting the two sets of solutions. This enables us to estimate strike, dip, and rake of active faulting in cases where waveform or polarity information alone is insufficient, as well as to overcome the ambiguity between fault and auxiliary plane in point source focal mechanisms. In Figure 3 we illustrate the approach for a fictitious multiplet example. In this case we have imaged a fault patch with strike N120° E and dip 55° from relative locations (black plane in Fig. 3a), both angles having fictitious standard errors of 25° (represented by gray bands). First-motion polarities at 10 stations for this multiplet (Fig. 3b) are consistent with a wide range of solutions, including pure normal and pure strike-slip faulting, and cannot constrain the focal mechanism. However, after combining both data, the intersecting set (Fig. 3c) contains only similar solutions; the joint use of relocations and polarities can identify a south-dipping normal fault as the causative structure. This methodology is an extension of an idea proposed by Shearer *et al.* (2003), who resolve ambiguity in first-motion mechanisms by comparing them with the best-fitting plane of cluster relocations, while here we additionally account for the confidence limits of fault orientations from relative location.

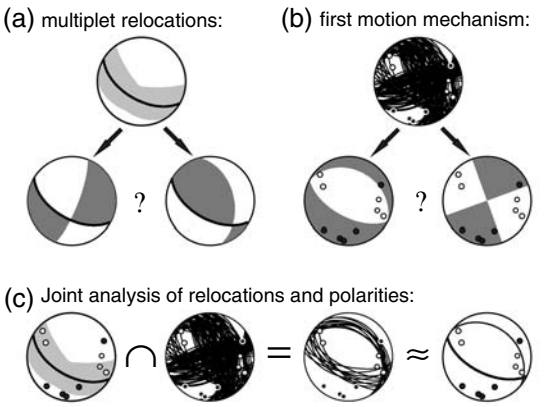

Figure 3. Multiplet focal mechanisms from polarities and relative locations. (a) Relative locations of multiplets provide strike and dip of the fault plane (black) and associated uncertainties (gray), but cannot resolve the rake vector. (b) Polarity focal mechanisms provide strike, dip, and rake, but cannot distinguish between fault and auxiliary plane and are often poorly resolved. (c) Combining these data by intersecting the two sets of solutions, we can reduce ambiguity, estimate a focal mechanism, and resolve the nodal plane symmetry.

Data

The Iznajar swarm was recorded at short epicentral distances by the Instituto Andaluz de Geofisica short-period network, composed of 1 Hz vertical component sensors every ~25 km in and around the Granada basin. In response to the Iznajar swarm, on 14 and 15 April we deployed two additional three-component short-period stations (PLL, PVB) in the epicentral area to improve azimuthal coverage, depth resolution, and detection capability (Fig. 1). However, it turned out that then the activity was already declining; only about one-third of the events were recorded with the full station coverage.

From a careful visual inspection of recordings at the closest stations, we can attribute to this swarm a total of 1837 events until 13 May (Fig. 4). Duration magnitudes (De Miguel *et al.*, 1988) range from 0.6 to 3.9. The magnitude-frequency

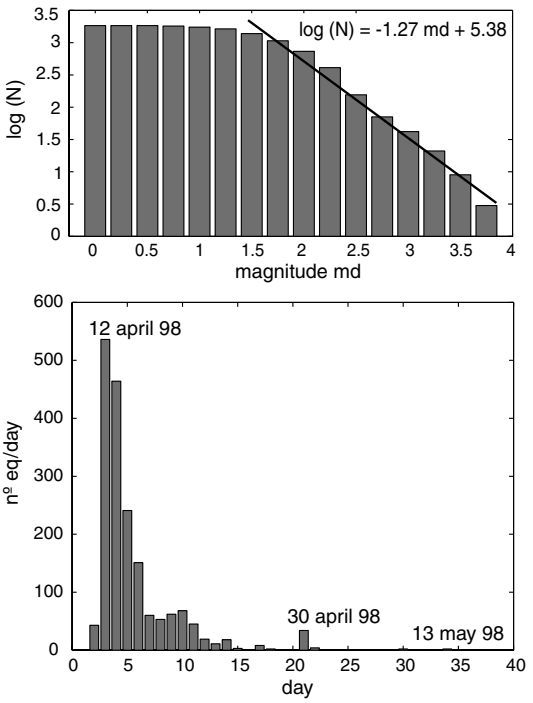

Figure 4. Magnitude-frequency-distribution (top) and temporal distribution (bottom) of 1837 Iznajar events from 11 April to 13 May.

distribution indicates a relatively high b-value of 1.27 and suggests that the catalog is nearly complete down to magnitudes of at least 2. Magnitude 1 events are sometimes detectable at the closest stations, but may be obscured during times of elevated microseismic noise, and may be frequently hidden in the coda of previous events because at the peak of the swarm, earthquakes were detected about every 3 minutes on average. For 778 earthquakes we can obtain single-event locations from P (and S) readings from at least four stations (Fig. 1). The locations show significant scatter and a spurious east-west trend, which can be attributed to the network geometry and large location inaccuracies for the smallest events, with high noise level and few, uncertain arrival picks, while our best locations are tightly clustered around 37.21° N, 4.20° W, and 12 km depth. This average location will be used as a geometrical reference throughout this article, which means we assume that the actual source volume is small compared to single-event location errors.

While we already mentioned that the local seismic network is insufficient to constrain first-motion focal mechanisms, its emplacement and technical characteristics make it well-suited for relative location from cross-correlation delay times. In particular, no clock errors or digitalization delays affect a precise relative timing. Permanent short-period stations transmit via radio to the central recording site in Granada, where the data are digitized with common time base and constant order of channels, while for the autonomously recording portable stations and local broadband station SELV, only relative P-S delay times will be used. Sampling rates of 100 Hz for permanent and 200 Hz for portable stations allow for a high temporal resolution of the cross-correlation maxima. The good station coverage in the epicentral area, with two permanent and two portable stations recording at epicentral distances equal or less than the focal depth, should contribute to a good resolution of relative depths during relocation, allowing for a 3D interpretation of the geometry of active structural elements.

Multiplet Analysis

A close spacing of earthquake sources, typically less than the wavelengths involved, is a condition for the occurrence of highly similar multiplet events suitable for the determination of accurate cross-correlation time delays and precise relative location techniques. We expect to find multiplets among the tightly clustered Iznajar swarm, and evaluate waveform similarity at the nearby permanent station AAPN, providing the best signal-to-noise ratio. Cross-correlation analysis in 1.2 sec P- and S-wave windows was performed for all pairs of 1837 seismograms, band-pass-filtered between 1 and 15 sec. We obtain correlation coefficients up to 0.994 for P waves and up to 0.993 for S waves, confirming the existence of nearly identical earthquakes in the dataset.

We group similar events into multiplet clusters using equivalence class sorting with three thresholds, applied to P-wave correlation, S-wave correlation, and the normalized scalar product of the corresponding rows of the S-wave correlation matrix. The third threshold stabilizes cluster separation by rejecting accidental hits (Maurer and Deichmann, 1995), and was set to 0.6 by trial and error. P-wave arrivals are relatively simple at station AAPN; the P-wave correlation threshold (0.9) is mainly efficient in rejecting events with relevant noise content. S-wave arrivals (threshold 0.8) appear more variable and complex, and permit the assignment of events to clusters with different waveform characteristics. Applying these strict selection criteria, we obtain 154 groups of highly similar earthquake recordings (Fig. 5), including a total of 596 events (32% of the Iznajar catalog). This includes 74 doublets, 34 triplets, and 46 multiplets with 4 to 26 events.

We selected our 13 best multiplets to perform relative centroid location, taking into account waveform quality and the number of earthquakes. We compute multiplet locations relative to a master event, chosen according to waveform quality, by the linear inversion of cross-correlation time delays in a least-squares sense trough the singular value decomposition of the relocation matrix (Press *et al.*, 1989). Correlation peaks are interpolated with splines to obtain a nominal resolution 10 times the original sampling rate. Take-off angles were computed for a 12 km deep source region and a simple velocity model, consisting of a 2 km thick layer ($V_S = 5.4$ km/sec, $V_S = 3.1$ km/sec) over a half-space ($V_P = 6.1$ km/sec, $V_S = 3.5$ km/sec). We obtain closely spaced multiplet distributions with spatial extent of 200–300 m (Fig. 6). We assume standard errors of 5 ms in cross-correlation timing, which is above root mean squares errors of relative locations and can be considered a conservative estimate. Then, the semiaxes of the 68% error ellipsoids of relative locations are usually below 100 m in horizontal and vertical directions. The good depth resolution can be attributed to the availability of recordings at short epicentral distances, corresponding to rays that leave the source region rather vertically.

We estimate the orientation of active fault patches through L1-norm fitting of a plane to the estimated multiplet

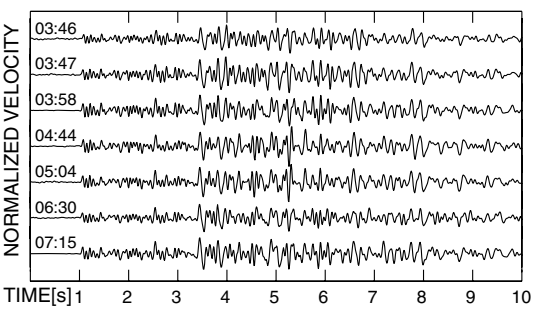

Figure 5. Recordings of multiplet cluster 114 (all events on 14 April) at station AAPN, filtered between 1 and 25 Hz and aligned at the P arrival. Normalized traces show high waveform similarity along the entire seismogram, and very small shifts of S waves, indicating close locations.

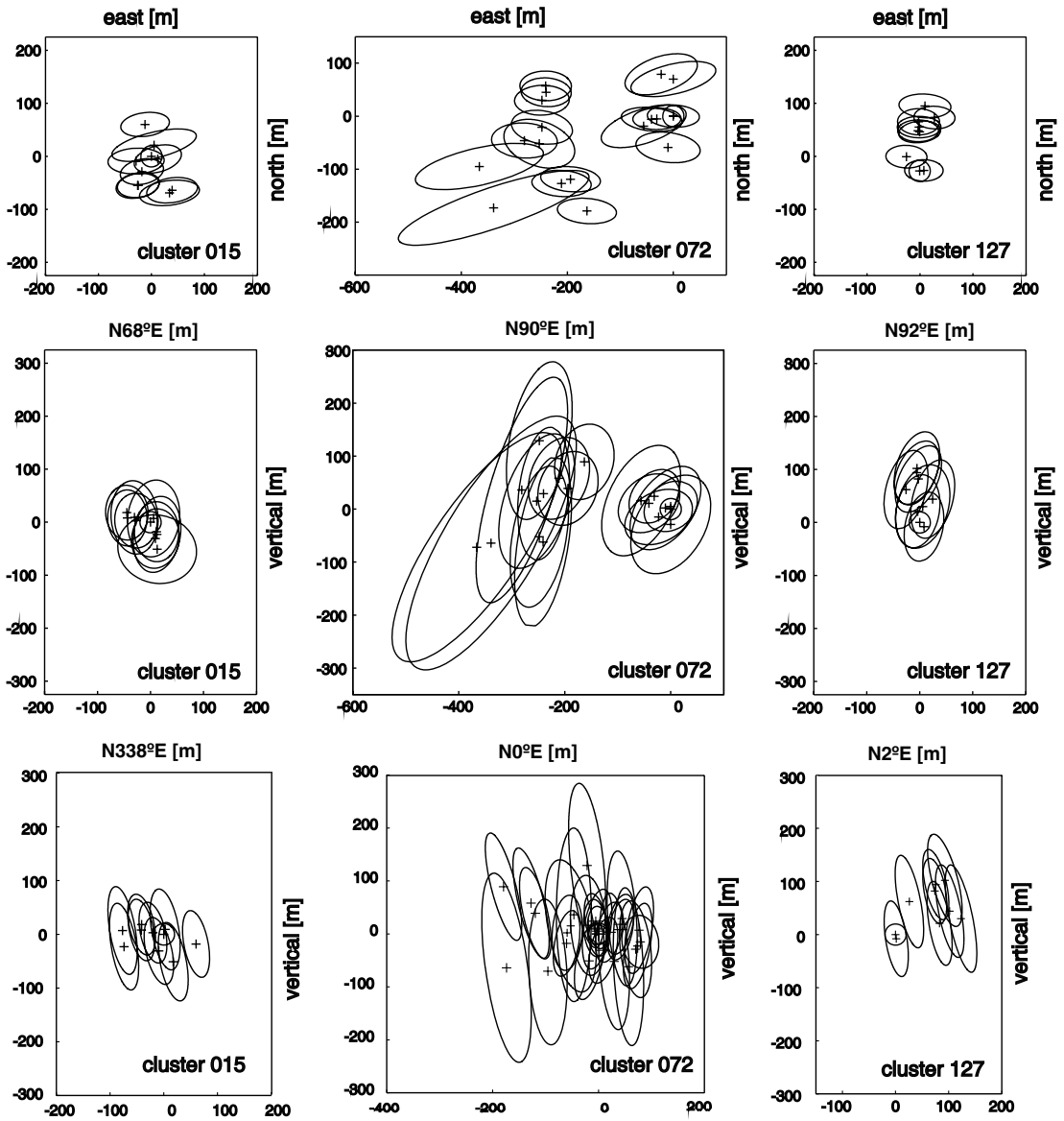

Figure 6. Relative locations and standard error ellipsoids for multiplet clusters 15, 72, and 127. Plan view (top), showing near-linear, ~200–300 m long epicenter alignments with north-northwest–south-southeast to north-south strike, and two nearly parallel alignments for cluster 72. Vertical sections parallel and perpendicular to the strike (middle and bottom rows) show that clusters appear rather planar, and show a good resolution of relative depths, allowing for the 3D interpretation of fault patch geometry.

hypocenter distribution, with the constraint that the fitting plane has to contain individual cluster's baricenters. All multiplets can be represented adequately as planar distributions (or two planar distributions in the case of cluster 72), with L1-norm misfits between 4 m and 34 m. We image eight steep dipping north-south trending planes, five north-north-west–south-southeast planes with shallower dip on average (both, east-northeast and west-southwest dipping), and one steep east-west trending plane (Table 1; Fig. 7). We put confidence limits on fault patch orientation by performing 100 Monte Carlo simulations for random Gaussian perturbations of the multiplet distribution with reference to the one-sigma

Table 1
Summary of Multiplet Cluster Geometry*

Multiplet Clusters			Best-Fitting Plane (L1 Norm)			Polarities and Focal Mechanism			
Cluster	N° EQs	M_{max}	Strike (°)	Dip (°)	Misfit (m)	N° polarities	Strike (°)	Dip (°)	Rake (°)
006	20	2.3	326 ± 17.7	81 ± 15.2	22.57	5	148	75	−114
009	7	2.3	357 ± 23.0	78 ± 37.7	3.62	5	Not available		
011	10	2.6	193 ± 29.3	71 ± 15.0	21.91	7	192	75	−21
015	14	2.7	338 ± 29.2	57 ± 30.1	23.12	6	338	36	−89
042	11	2.6	178 ± 30.2	65 ± 40.4	16.07	5	Not available		
043	11	2.6	347 ± 22.9	71 ± 34.6	4.02	8	356	53	22
			Alternative solution cluster 043:				353	89	−35
053	9	2.3	324 ± 32.4	53 ± 11.8	12.02	3	Not available		
72a	25	2.5	184 ± 15.0	72 ± 9.3	33.74	5	181	73	9
72b			172 ± 37.9	74 ± 56.1	10.68	5	360	87	11
108	11	2.6	171 ± 7.8	65 ± 18.0	8.20	6	171	72	14
114	8	2.5	268 ± 31.9	85 ± 34.8	9.99	3	Not available		
123	11	2.5	325 ± 27.7	76 ± 32.1	12.49	4	Not available		
127	10	3.5	2 ± 13.0	89 ± 12.9	11.40	8	178	86	32
146	33	2.7	130 ± 15.8	64 ± 29.1	27.07	5	126	62	−97

*From left to right, columns give the cluster identification; the number of events contained in each cluster; the maximum duration magnitude, strike, dip, and L1-norm misfit of the best-fitting plane to the relocated events (including error bounds from Monte Carlo simulations); number of first-motion polarity readings; and strike, dip, rake of the focal mechanism from relocations and polarities (where available).

error ellipsoids of the individual relocations (Stich *et al.*, 2001). The standard errors of several 10s of meters translate to inaccuracies in fault patch strike and dip of typically ~20–30°, represented by gray bands in Fig. 7, row (a).

Focal Mechanism Inversion

Multiplet relocation cannot assign rake angles or strain axes orientations to fault patches, thus being unable to fully characterize the kinematics of faulting. Here we attempt to retrieve focal mechanisms for our multiplet events from first-motion polarities at the local network. For our multiplet events, we use the data redundancy in highly similar seismograms to stabilize the retrieval of polarities by analyzing *P*-wave onsets for all available low-noise seismograms in each cluster (Shearer *et al.*, 2003). Consistent with our expectations for planar hypocenter distributions and parallel slip vectors, we do not find clear evidence of opposite polarities of multiplet events at the same station. We use only the most reliable polarity information; in particular, we reject all

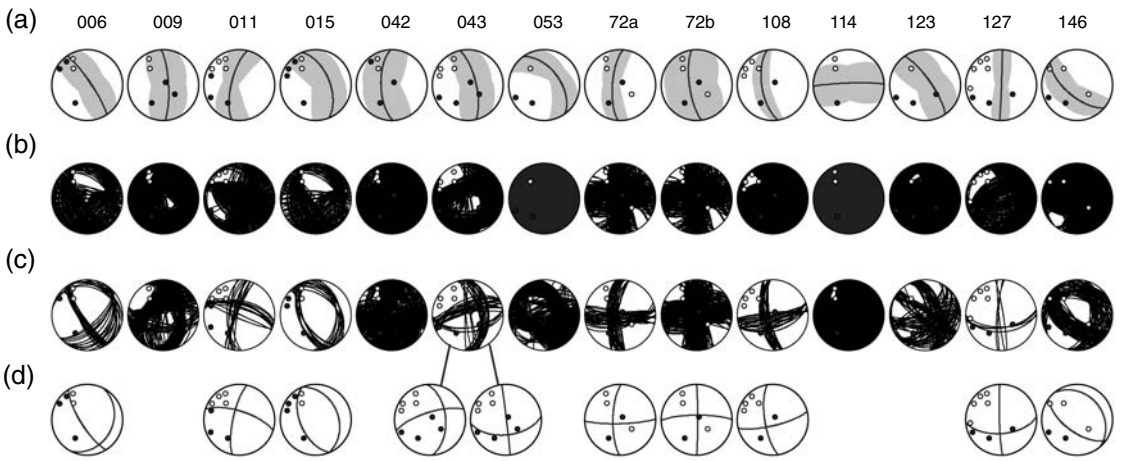

Figure 7. Multiplet geometry in lower hemisphere, equal area projection: (a) Multiplet fault planes (black) with range of standard errors (gray bands) and polarity readings (white dots for dilatation, black dots for compression). (b) Solutions from focal mechanism grid search. (c) Intersection of ranges of solutions from rows (a) and (b). (d) Average focal mechanism solution (when the dispersion in row c is small). For cluster 43, two possible solutions are given.

readings for which we suspect the presence of an emergent arrival hidden in background noise. In this way, three to eight clear *P*-wave polarities per multiplet cluster are obtained.

We use a grid search scheme (program FOCMEC; Snoke *et al.*, 1984) to test the full range of double-couple faulting solutions, with increments of 10°, against the distribution of compressive and dilatational polarities over the focal sphere. No polarity mismatch is permitted in a successful solution because we are conservative at picking and the polarities of the local network are well-documented and tested with teleseismic recordings; portable stations have been checked in the lab before deployment. Nevertheless, the focal mechanism solutions turn out to be completely or largely unconstrained (Fig. 7), reflecting the small number of polarities involved and the rather poor coverage of the focal sphere. Sometimes the sets of solutions indicate a sector where *P* or *T* axes accumulate, but they do not resolve nodal planes and the selection of a preferred solution would be highly ambiguous.

To combine first-motion information with previously determined precise relative locations of multiplets, we search for a set of solutions that is consistent with both the orientation of the multiplet distribution and the picked *P*-wave polarities, which is achieved by intersecting the range of solutions from multiplet analysis (gray bands in Fig. 7, row a) and the set of focal mechanism solutions (Fig. 7, row b). In this way we achieve a significant reduction of ambiguity (Fig. 7, row c) and can interpret focal mechanism for nine multiplet clusters (five to eight polarities), while only five clusters (three to five polarities) remain unconstrained. Our results include six left-lateral north-south trending strike-slip solutions with northwest-southeast *P*-axis orientation, and three normal faulting solutions with north-northwest–south-southeast trending, east-northeast dipping fault plane or northwest-southeast trending, southwest dipping fault plane. We cannot assign a mechanism to our single east-west trending multiplet plane because only three polarity readings have been obtained; but assuming a *T*-axis orientation similar to the other solutions, we think that right-lateral strike slip could be a plausible dislocation style on this plane.

We recall at this point that we use a common location (37.21° N, 4.20° W, 12 km depth) for all multiplet clusters, while actually the Iznajar swarm should be attributed to a finite, small source volume. Takeoff angles are relatively stable at this source depth; multiplet plane orientations do not vary significantly for reasonable changes in cluster location or velocity model, but first-motion mechanisms may be more sensitive because we do not allow polarity mismatches. Variations in source depth tend not to affect the strike-slip mechanisms because the azimuthal distribution of polarities does not change. Lateral location errors have most influence at the closest stations; for example, a shift of 2 km corresponds to an ~10° difference for a ray to a station located on top of the cluster (PLL). Such variations may affect solutions constrained by near-nodal polarities at near-source stations (clusters 43, 72, 108, 127), which might be either slightly more homogeneous or heterogeneous than they appear here, but they are not expected to alter the general picture of coexistence of north-south strike-slip faulting and northwest-southeast normal faulting in the Iznajar swarm.

Discussion

Relative location of multiplet events, for example, from linear inversion of cross-correlation delay times, and focal mechanism analysis for the same events both return information on strike and dip angles of the causative fault patch. These values should coincide for both methods within the respective confidence limits. Additionally, focal mechanism inversion can provide the rake angle of the earthquake slip direction, not available in multiplet relocation, while multiplet relocation may resolve the ambiguity of fault and auxiliary nodal planes inherent to point source focal mechanisms. The comparison between both methods is frequently used to identify the active fault plane in point source mechanisms, especially for small and moderate earthquakes where no surface breakage is observed and regional tectonics cannot resolve the nodal plane ambiguity (e.g., Ocaña *et al.*, 2008). Also, precise relative locations can be used for a consistency check of inverted focal mechanisms, separating plausible solutions from nonplausible solutions, the latter showing too large deviations from the local fault plane orientation (e.g., Kilb and Hardebeck, 2006).

Here we address earthquakes that are too weak to apply waveform inversion, and where available *P*-wave polarities are insufficient to resolve the source geometry, so focal mechanism retrieval is impossible without additional constraints. We use our multiplet relocations for this purpose. To extract a set of solutions that is consistent with both data, we intersect the set of solutions from focal mechanism grid search with the range of multiplet fault plane orientations obtained through Monte Carlo simulations. For clusters with five to eight polarity readings, the intersecting sets show mostly little dispersion, resolving strike, dip, and rake well, and resolving the nodal plane ambiguity. The requirements of having at least five polarity readings as well as multiplet fault patch orientation with an accuracy of ~20–30° are not too difficult to meet in areas where local network data are available, so this strategy could be successful for other seismic swarms and aftershock sequences.

For the Iznajar swarm, we observe six left-lateral north-south strike-slip faulting solutions, as well as three normal faulting solutions with northwest-southeast to north-northwest–south-southeast trending faults and opposite directions of dip. Parallel strike-slip faults with a distance of ~230 m are imaged by cluster 72, indicating a high degree of fracturing in the source volume. Available moment tensor solutions appear slightly different, but are not tightly constrained; their confidence regions (Fig. 2) include ~north-south strike-slip faulting, and we can identify the ~north-south nodal planes of moment tensor solutions as the preferred fault planes. North-south left-lateral strike slip is then the dominant

dislocation in the Iznajar swarm, accounting for the largest events and the majority of analyzed multiplets. The coexistence of secondary, pure normal faulting suggests a permutation of the largest and intermediate principal stresses, which may be introduced by local stress perturbations in the course of the swarm. Although the absolute locations of the multiplet clusters are not sufficiently accurate to infer the geometrical relationship of these structural elements, strike-slip and normal faulting might act upon each other to compensate differential displacement between adjacent fault patches. Such fault-bounded block tectonics have been suggested previously to explain the seismotectonic fine structure in other seismic series in the area (Stich *et al.*, 2001), as well as the regional-scale pattern of neotectonic faults in the Betic Cordillera (Martínez-Díaz and Hernández-Enrile, 2004; Martínez-Martínez *et al.*, 2006).

The predominance of strike-slip faulting makes this activity different from seismicity associated with the nearby Granada basin, where normal faulting mechanisms and east-northeast–west-southwest extension are dominant (Galindo-Zaldívar *et al.*, 1999; Muñoz *et al.*, 2002; Stich *et al.*, 2006). While the depth of the Iznajar swarm and faulting beneath the Granada basin (concentrated between 9 km and 16 km depth; Morales *et al.*, 1997) are similar, the Iznajar swarm is about 30–40 km away from the main concentrations of earthquakes in the eastern part of the basin along its southern limit. Remarkably, a similar pattern of collocated strike-slip and normal faulting earthquakes is also observed ~20 km southeast of the Granada basin (Martínez-Martínez *et al.*, 2006). Because of the small dimensions of faulting involved in the small magnitude earthquakes of the Iznajar swarm, we can hardly speculate about the importance of these strike-slip faults in releasing regional tectonic strain. But, in any case, our results highlight the heterogeneity of tectonic deformation in the Betic Cordillera where seismotectonics at different scales may be controlled by fault interaction.

Data and Resources

We used the seismic catalog and the waveform data base of the Instituto Andaluz de Geofísica (IAG) for this research. Access to these data may be granted by IAG.

Acknowledgments

We are grateful to Peter Shearer and an anonymous reviewer for their valuable comments, to Javier Almendros and Inmaculada Serrano for the discussions, and to Edoardo Del Pezzo for his support. We received financial support through Spanish national projects CGL2008-01830 and CGL2008-01660, and Grupo de Investigación en Geofísica JA RNM-104.

References

Brillinger, D., A. Udías, and B. A. Bolt (1980). A probability model for regional focal mechanism solutions, *Bull. Soc. Seismol. Am.* **70,** 149–170.

Deichmann, N., and M. Garcia-Fernandez (1992). Rupture geometry from high-precision relative hypocenter locations of microearthquake clusters, *Geophys. J. Int.* **110,** 501–517.

De Miguel, F., G. Alguacil, and F. Vidal (1988). Una escala de magnitud a partir de la duración para terremotos del Sur de España, *Revista de Geofísica* **44,** 75–86.

Galindo-Zaldívar, J., A. Jabaloy, I. Serrano, J. Morales, F. González-Lodeiro, and F. Torcal (1999). Recent and present-day stresses in the Granada Basin (Betic Cordilleras): Example of a late Miocene-present-day extensional basin in a convergent plate boundary, *Tectonics* **18,** 686–702.

Geller, R. J., and C. S. Mueller (1980). Four similar earthquakes in Central California, *Geophys. Res. Lett.* **7,** 821–824.

Ito, A. (1985). High resolution relative hypocenters of similar earthquakes by cross-spectral analysis method, *J. Phys. Earth* **33,** 279–294.

Kilb, D., and J. L. Hardebeck (2006). Fault parameter constraints using relocated earthquakes: A validation of first-motion focal-mechanism data, *Bull. Seismol. Soc. Am.* **96,** 1140–1158.

Kraft, T., J. Wassermann, and H. Igel (2006). High-precision relocation and focal mechanisms of the 2002 rain-triggered earthquake swarms at Mt. Hochstaufen, SE Germany, *Geophys. J. Int.* **167,** 1513–1528.

Martínez-Díaz, J. J., and J. L. Hernández-Enrile (2004). Neotectonics and morphotectonics of the southern Almería region (Betic Cordillera-Spain) kinematics implications, *Int. J. Earth. Sci.* **93,** 189–206.

Martínez-Martínez, J. M., G. Booth-Rea, J. M. Azañon, and F. Torcal (2006). Active transfer zone linking a segmented extensional system (Betics, southern Spain): Insight into heterogeneous extension driven by edge delamination, *Tectonophysics* **422,** 159–173.

Maurer, H., and N. Deichmann (1995). Microearthquake cluster detection based on waveform similarities, with an application to the western Swiss Alps, *Geophys. J. Int.* **123,** 588–600.

Morales, J., I. Serrano, F. Vidal, and F. Torcal (1997). The depth of the earthquake activity in the central Betics (southern Spain), *Geophys. Res. Lett.* **24,** 3289–3292.

Muñoz, D., A. Cisternas, A. Udías, J. Mezcua, C. Sanz de Galdeano, J. Morales, M. Sánchez-Venero, H. Haessler, J. Ibañez, E. Buforn, G. Pascal, and L. Rivera (2002). Microseismicity and tectonics in the Granada basin (Spain), *Tectonophysics* **356,** 233–252.

Ocaña, E., D. Stich, E. Carmona, F. Vidal, M. Bretón, M. Navarro, and A. García-Jerez (2008). Spatial analysis of the La Paca, SE Spain, 2005 seismic series through the relative location of multiplets and principal component analysis, *Phys. Earth Planet. Inter.* **166,** 117–127.

Pechmann, J. C., and B. S. Thorbjarnardottir (1990). Waveform analysis of two preshock-mainshock-aftershock sequences in Utah, *Bull. Soc. Seismol. Am.* **80,** 519–550.

Posadas, A. M. (1991). Análisis espacio-temporal de series sísmicas. Aplicación a las Béticas centrales, *Ph.D. Thesis*, University of Granada.

Posadas, A. M., F. Vidal, F. De Miguel, G. Alguacil, J. Peña, J. M. Ibáñez, and J. Morales (1993). Spatial-temporal analysis of a seismic series using the Principal Components Method: The Antequera series, Spain, 1989, *J. Geophys. Res.* **98,** 1923–1932.

Press, W. H., B. P. Flannery, S. A. Teukolsky, and W. T. Vetterling (1989). *Numerical Recipes* Cambridge University Press, New York.

Ruiz, M., J. Díaz, J. Gallart, J. A. Pulgar, J. M. González-Cortina, and C. López (2006). Seismotectonic constraints at the western edge of the Pyrenees: Aftershock series monitoring of the 2002 February 21, 4.1 *Lg* earthquake, *Geophys. J. Int.* **166,** 238–252.

Saccorotti, G., E. Carmona, J. M. Ibáñez, and E. Del Pezzo (2002). Spatial characterization of Agron, southern Spain, 1988–1989 seismic series, *Phys. Earth Planet. Int.* **129,** 13–29.

Scherbaum, F., and J. Wendler (1986). Cross spectral analysis of Swabian Jura (SW Germany) three-component microearthquake recordings, *J. Geophys.* **60,** 157–166.

Shearer, P. M., J. L. Hardebeck, L. Astiz, and K. B. Richards-Dinger (2003). Analysis of similar event clusters in aftershocks of the 1994 Northridge, California, earthquake, *J. Geophys. Res.* **108,** doi 10.1029/2001JB000685.

Snoke, J. A., J. W. Munsey, A. G. Teague, and G. A. Bollinger (1984). A program for focal mechanism determination by combined use of polarity and *SV-P* amplitude ratio data, *Earthquake Notes* **55,** 15.

Stich, D., G. Alguacil, and J. Morales (2001). The relative locations of multiplets in the vicinity of the Western Almeria (southern Spain) earthquake series 1993–1994, *Geophys. J. Int.* **146,** 801–812.

Stich, D., C. J. Ammon, and J. Morales (2003). Moment tensor solutions for small and moderate earthquakes in the Ibero-Maghreb region, *J. Geophys. Res.* **108,** 2148, doi 10.1029/2002JB002057.

Stich, D., E. Serpelloni, F. Mancilla, and J. Morales (2006). Kinematics of the Iberia-Maghreb plate contact from seismic moment tensors and GPS observations, *Tectonophysics* **426,** 295–317.

Vidal, F. (1986). Sismotectónica de la Región Béticas-Mar de Alborán, *Ph.D. Thesis*, University of Granada.

Campus Universitario de Cartuja s/n,
Instituto Andaluz de Geofisica,
Universidad de Granada,
Granada, 18071, Spain

Manuscript received 12 February 2009

III. The 1998-1999 seismic series at Deception Island volcano, Antarctica

Available online at www.sciencedirect.com
SCIENCE DIRECT®
Journal of volcanology and geothermal research
ELSEVIER
Journal of Volcanology and Geothermal Research 128 (2003) 65–88
www.elsevier.com/locate/jvolgeores

The 1998–1999 seismic series at Deception Island volcano, Antarctica

J.M. Ibáñez [a,b,*], E. Carmona [a], J. Almendros [a], G. Saccorotti [c], E. Del Pezzo [c], M. Abril [a], R. Ortiz [d]

[a] *Instituto Andaluz de Geofísica, Universidad de Granada, Campus de Cartuja s/n, 18071 Granada, Spain*
[b] *Departamento de Física Teórica y del Cosmos, Universidad de Granada, Granada, Spain*
[c] *Osservatorio Vesuviano, Istituto Nazionale di Geofísica e Vulcanología, Napels, Italy*
[d] *Departamento de Volcanología, Museo Nacional de Ciencias Naturales–CSIC, Madrid, Spain*

Received 15 May 2002; accepted 10 June 2003

Abstract

During the 1998–1999 Antarctic summer the pattern of seismic activity at Deception Island volcano changed significantly. The change was characterized by the occurrence of an intense swarm of volcano–tectonic (VT) earthquakes. More than 2000 VT earthquakes with S–P times smaller than 4 s were recorded in the period January–February 1999. Pure volcanic events were also detected; especially long-period (LP) events, volcanic tremor and some hybrid events. Seismic monitoring was performed using two short-period small-aperture arrays, among other instruments. Based on their signal-to-noise ratios we selected 863 VT earthquakes, 350 LP events and tremor episodes, and 9 hybrid events for analysis. We estimated apparent slowness and back-azimuth for all events using the Zero Lag Cross-Correlation array technique. Combining this information with S–P times and other indirect evidence, we identified two different source regions. LP seismicity is located less than 1–1.5 km southwest of the Fumarole array site. These events are likely to have a hydrothermal origin. VT earthquakes and hybrid events are located at depths of 0.3–10 km in an area under the bay of Deception Island. The area extends from the Fumarole array to the northeast with epicentral distances that range from 0.5 to 12 km. Most hypocenters are clustered in a small volume of around 8 km^3. The sources of the LP seismicity and the VT earthquakes are spatially distinct, which indicates that they are not produced by the same mechanisms. Moment magnitude analyses of the VT earthquakes provide an average magnitude of 0.5 and very low average stress drop, around 1 bar. A study of first motion of the P-waves suggests that the events in this small source region should have a variety of source mechanisms. This is supported by the existence of families of events with the same waveforms. The occurrence of repeating fracture processes with low stress drop and small fault dimensions can be explained by the lubrication of pre-existing zones of weakness by pressurized fluids. The most probable hypothesis that explains the generation of this seismic series at Deception Island is: a seismic series caused by the stress generated by the uplift of the source area due to a magmatic injection in depth. We favor this hypothesis since it is compatible with the majority of the characteristics of the seismicity and explains the spatial and temporal behavior of the series.

* Corresponding author. Tel.: +34-958248910; Fax: +34-958160907. *E-mail address:* ibanez@iag.ugr.es (J.M. Ibáñez).

0377-0273/03/$ – see front matter © 2003 Elsevier B.V. All rights reserved.
doi:10.1016/S0377-0273(03)00247-6

Keywords: volcanic seismicity; long-period events; volcano-tectonic earthquakes; magma injection; Antarctica

1. Introduction

The seismic activity associated with a volcanic environment is diverse and complex. Several types of seismic signals, with different signatures and frequency content, can be generated within a single volcanic region, and these characteristics are usually not the same for different volcanoes. Recently, however, we have realized that the physics underlying the generation of seismic energy in a volcano is not complex, and relatively simple mechanisms can be invoked to explain the different types of volcano seismicity. Following Chouet (1996), we can distinguish two main classes of source processes in active volcanic areas. The first one consists of the brittle fracture of the medium in response to stress, a purely elastic mechanism that generates the so-called volcano–tectonic (VT) earthquakes. In general, the spectral content of this type of signal is broadband with frequencies up to 50 Hz. The procedure for modelling tectonic earthquakes is well established. With the proper tools, the source parameters for such events can be calculated quickly and accurately. The second class of events requires the presence and movement of fluids with exchange elastic energy with the medium. Most of the theoretical models in use today were developed in the 1980s and 1990s by several authors, for example Crosson and Bame (1985), Chouet (1988, 1992), Dahm (1992), Julian (1994), Nakano et al. (1998), Hellweg (2000) and Neuberg et al. (2000). These models describe the physics of seismic sources when a large amount of fluid is present. In general, these theories describe the source of the seismic radiation as resulting from the trapping of acoustic waves due to the impedance contrast between magmatic/hydrothermal fluids and solid rock. The resulting waveforms and spectra may vary greatly, depending on the shape of the resonating cavity, excitation mechanism, and fluid properties (Kumagai and Chouet, 2000). In any case, they can be described as narrow-band events in contrast to the VT earthquakes, usually with very emergent first motions. We will refer to these signals generated with direct involvement of volcanic fluids generically as pure volcanic signals or long-period (LP) seismicity. They include event types as distinct as volcanic tremor, spasmodic tremor, harmonic tremor, LP events, tornillo events, gas-piston events, and more. In the present work we will distinguish only between LP events and tremor, by means of their short and long durations, respectively. Finally, a third, mixed mechanism sometimes occurs when brittle failure and fluid-driven resonance appear simultaneously in the recordings. This type of seismic signal is called as hybrid and is composed of a VT earthquake followed by a LP signal (Lahr et al., 1994).

The distribution of volcanic seismicity in space and time depends on the type of event and the level of volcanic activity. VT earthquakes have been recorded before, during, and/or after eruptions, but they may occur without eruptions (Benoit and McNutt, 1996) and eruptions may occur without VT earthquakes. Their hypocenters and even the source mechanisms are routinely determined using seismic networks. They are supposed to coincide with the volcanic conduit where magma is moving, and several studies map volcanic conduits using hypocenter locations of VT earthquakes (Klein et al., 1987; Lahr et al., 1994, etc). Pure volcanic signals are more difficult to locate; nevertheless they are more adequate to map the volcanic conduits, since they are generated only in presence of moving fluids (Almendros et al., 2002). Due to the emergent character of the pure volcanic events and their low-frequency content, classical (routine) seismic techniques are almost useless for solving the problem of source location. The study of volcanic seismicity requires the use of new instruments and configurations, in particular dense seismic arrays of seismometers. The analysis may be more complex and time-consuming, but we are able to obtain information about the locations of sources of volcanic signals, properties of the wavefield, and the shallow velocity structure under the array. LP seismicity is usually located at shallow depths (Lahr et al., 1994; Gil Cruz and Chouet, 1997; Ibáñez et al., 2000)

but deep LP events and tremor have been observed as well (Koyanagi et al., 1987). LP seismicity may appear just before eruptions or be associated with hydrothermal activity. Pure volcanic signals have been recorded at most volcanoes. Their significance as precursors to eruptive activity (Chouet, 1996) has been demonstrated by many examples: the 1991 eruption of Mount Pinatubo, Philippines (e.g. Ramos et al., 1999), Mount St. Helens, USA (e.g. Fehler, 1983), Galeras, Colombia (e.g. Narváez et al., 1997), Mount Redoubt, Alaska, USA (e.g. Chouet et al., 1994), and Kilauea, Hawaii, USA (e.g. Ohminato et al., 1998).

In the present work we analyze data recorded at Deception Island volcano, Antarctica, during the 1998–1999 summer field survey. Starting in January 1999, the seismic activity increased suddenly. Before the end of the season we recorded about 1500 VT earthquakes, and a similar number of purely volcanic events. Understanding this seismicity is important because the most recent eruptions at Deception Island was preceded by intense seismic swarms, similar to the series analyzed in this work. We start by classifying the recorded events and studying the temporal evolution of each event type. We use array techniques to estimate back-azimuths and apparent slownesses, and measure the S–P delay to determine hypocenter locations. The temporal and spatial distribution of the hypocenters and the appearance of several different mechanisms in a small source volume will lead us to a hypothesis about the cause of the seismic activity and its implications for the dynamics of the volcano.

2. Instruments and data

2.1. Seismic instruments

During the 1998–1999 Antarctic summer field survey at Deception Island we deployed a Guralp CMG40T broadband sensor, two short-period continuous recording stations, and two seismic arrays. One of the continuous recording stations, with a three-component sensor, was placed near the Spanish base, and the other, with a vertical component sensor, was used as a portable station and deployed in different places around the island.

The first array had an aperture of 320 m and was deployed near Obsidians Hill. It consisted of 13 vertical-component, short-period stations configured as two concentric semicircles with radii of 160 and 80 m, and a three-component sensor at the hub. However, Saccorotti et al. (2001) have documented slowness anomalies in the data recorded at the Obsidians array. Since we are not able to correct for these anomalies we will not use the data from this array. The second array had an aperture of 240 m and was deployed on the southern shore of Fumarole Bay, close to the most active fumarole system on the island. This array had seven vertical-component and three three-component stations, configured in two semicircles with radii of 120 and 60 m (Fig. 1). The seismometers of the external and internal semicircles were spaced at intervals of 45° and 60°, respectively. All instruments were Mark L4C sensors with flat response to 1 Hz. Both arrays were situated on alluvial fans. Each array was equipped with two eight-channel data acquisition systems (DAS). In Saccorotti et al. (2001) there is a complete description of the DAS. The antennas were operative between December 7, 1998, and February 25, 1999, when the Spanish base 'Gabriel de Castilla' closed operations for the season. Due to the high level of seismicity at the end of the field experiment, a permanent seismic station, with a vertical component sensor, was left near the Spanish base at the end of the survey. It operated for two more months. This station recorded at a low sampling rate (25 sps) in order to conserve storage space in the computer.

2.2. Characteristics of the seismicity

All seismic records were inspected visually and classified by their shapes and S–P times as: regional or VT earthquakes, LP events, hybrid events, or volcanic tremor. Regional events are not considered in this study, since they have no relationship to the volcanic activity. Spectra and spectrograms were computed for selected events

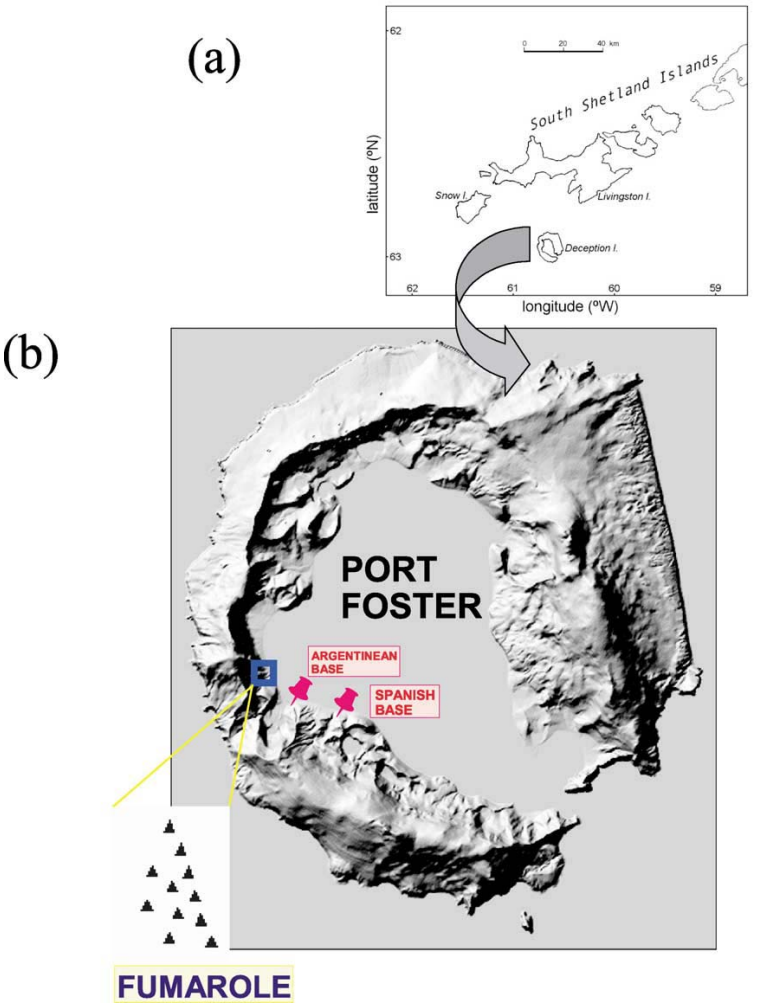

Fig. 1. (a) Map of the South Shetland Islands region, Antarctica, showing the position of Deception Island. (b) Map of Deception Island, showing the location and configuration of the seismic antenna used for the present analysis.

to determine the spectral content of each type of event.

2.2.1. VT earthquakes

Earthquakes with an S–P time less than 4 s are considered to be VT earthquakes. They have a clear P-wave arrival, usually impulsive, and the S-waves are easily identified on the horizontal components (Fig. 2). Their spectra show a very broad spectral content, with energy up to 40 Hz. In the particle motion we clearly see the arrivals of the P-waves and S-waves. Moreover, in the first S-wave onset we detect a sudden change in the horizontal motion. The change from linear to elliptical polarization is related to a delay between the arrivals of the E–W and the N–S components. This may be caused by S-wave splitting, which will be the topic of a future study.

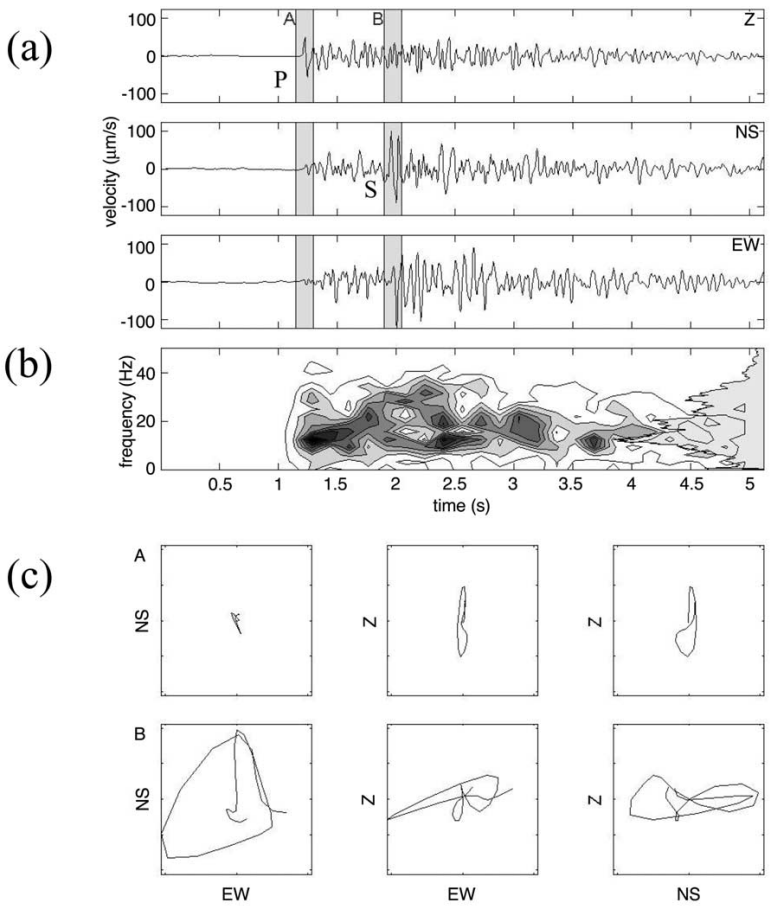

Fig. 2. Example of a VT earthquake recorded at Fumarole array. (a) Seismograms of the three components of the ground motion. The gray areas labelled A and B correspond to the arrival of the P-waves and S-waves, respectively. P and S represent the onset of the P-waves and S-waves over the seismogram, respectively. (b) Spectrogram of the vertical-component seismogram shown in (a). Superimposed at the right edge of the plot is the spectrum of the whole trace. (c) Particle motion diagram corresponding to the windows A and B in (a).

2.2.2. LP events

LP events at Deception Island have spindle-shaped envelopes and durations of a few tens of seconds (Fig. 3). In spectra and spectrograms, these signals are quasi-monochromatic, centered at frequencies between 1 and 6 Hz. The particle motions show that the first onsets might be composed of P-waves. However, suddenly they change to more complex patterns which can be interpreted as mixtures of surface waves (Ibáñez et al., 2000).

2.2.3. Hybrid events

These events begin with a high-frequency phase followed by a monochromatic signal similar to a LP event (Fig. 4). Spectral analysis reveals the different properties of these two distinct phases. The initial high-frequency portion has a broad spectrum, extending up to frequencies of 40 Hz. In contrast, the LP segment is quasi-monochromatic and peaks at low frequencies, around 1–6 Hz.

It is important to point out that some LP

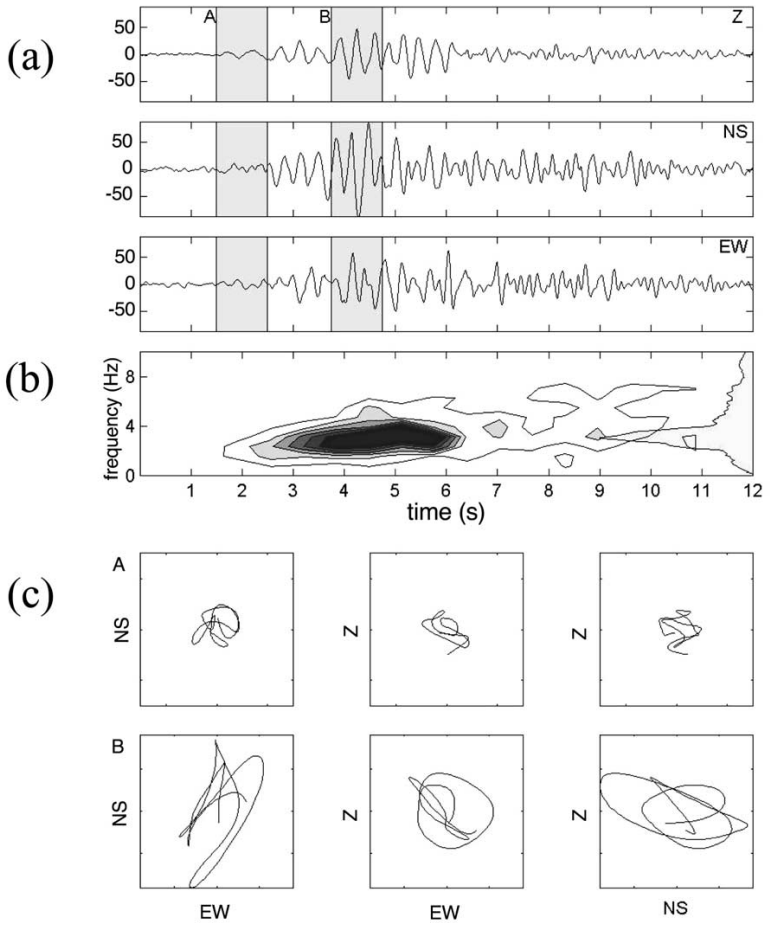

Fig. 3. Example of a LP event recorded at Fumarole array. (a) Seismograms of the three components of the ground motion. The gray areas labelled A and B correspond to the first arrival and the center of the low-frequency wave train, respectively. (b) Spectrogram of the vertical-component seismogram shown in (a). On the right side of the plot we show the spectrum of the whole trace. (c) Particle motion diagrams corresponding to windows A and B in (a).

events have low-energy, high-frequency initial phases, and thus might be confused with hybrid events. The difference is in the source mechanism of these high-frequency waves. For example, Ibáñez et al. (2000) initially used the term *hybrids* for a type of LP events with a strong high-frequency initial phase, due to their spectral properties. However, the definition of Lahr et al. (1994) states that the high-frequency component of a true hybrid is produced by a shear source. This condition is difficult to determine without proper instrumental coverage. In the case of Deception Island, we will confirm the hybrid nature of our signals by their proximity to the hypocenters of VT earthquakes.

2.2.4. *Volcanic tremor*

The presence of volcanic tremor at Deception Island volcano is well known since the first recording of its seismicity in the 1950s. The characteristics of tremor are similar to those observed for the LP events: a narrow spectral peak between

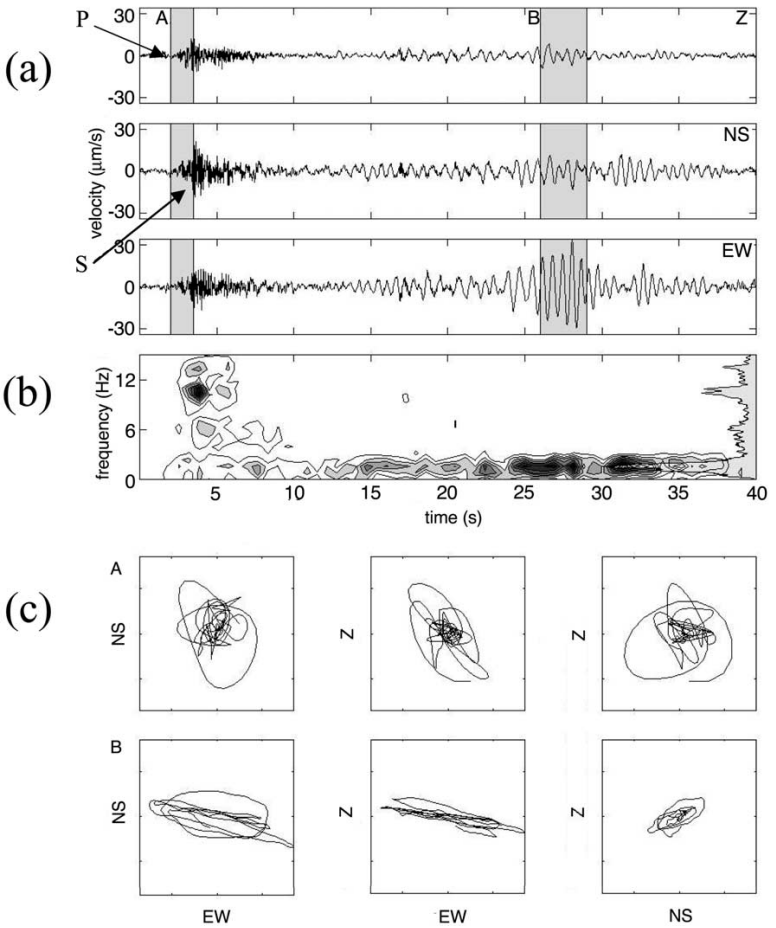

Fig. 4. Example of a hybrid event recorded at Fumarole array. (a) Seismograms of the three components of the ground motion. The gray areas labelled A and B correspond to the first high-frequency arrival and the center of the low-frequency wave train, respectively. P and S represent the onset of the P-waves and S-waves over the seismogram, respectively. (b) Spectrogram of the vertical-component seismogram shown in (a). On the right side of the plot is the spectrum of the whole trace. (c) Particle motion diagram corresponding to the windows A and B in (a).

1 and 3 Hz, and complex particle motion (Fig. 5). The main difference is the long duration of the tremor episodes. They may last for intervals from a few minutes to several days or weeks.

2.3. The evolution of the seismicity in time

The pattern of occurrence is different for the various event types. We counted the daily number of LP events recorded by the Fumarole array and the number of VT events recorded by the array and by the continuous recording station deployed near the Spanish base, in operation until the beginning of April 1999 (Fig. 6).

LP seismicity appears in swarms which last a few days and alternate with rest periods of several days. A total of 1800 LP events were recorded, with peak activity reaching about 150 events per

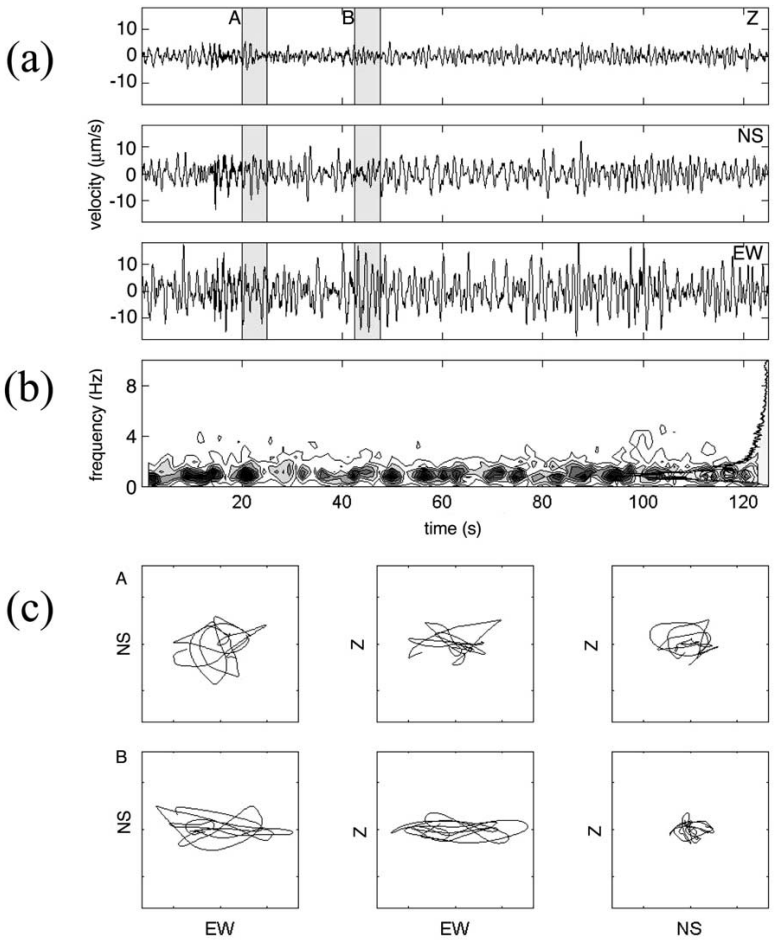

Fig. 5. Example of a tremor episode recorded at the Fumarole array. (a) Seismograms of the three components of ground motion. The gray areas labelled A and B correspond to two samples of waveforms. (b) Spectrogram of the vertical-component seismogram shown in (a). The vertical component is shown for comparison with the traces in previous figures. The right side of the plot shows the spectrum of the whole trace. (c) Particle motion diagram corresponding to the windows A and B in (a).

day. Using a lower limit of 30 events per day to declare a LP swarm (Ibáñez et al., 2000), there were nine swarms distributed randomly throughout the observation interval. This pattern coincides with that previously observed for the LP seismicity on the island (see fig. 4 of Ibáñez et al., 2000). The LP activity in 1998–1999 may therefore be considered normal for the area.

However, the situation is clearly different for VT earthquakes. During December 1998, only 8 VT were recorded. This earthquake occurrence rate is similar to the rate of a few tens of events per season reported by Ibáñez et al. (2000) for previous years. The pattern suddenly changed on January 4, 1999. There was a marked increase in the number of VT earthquakes recorded. The maximum activity was reached around January 20, with the occurrence of 80 VT earthquakes per day. When the field survey ended on February 25, the seismic activity was still high, often with

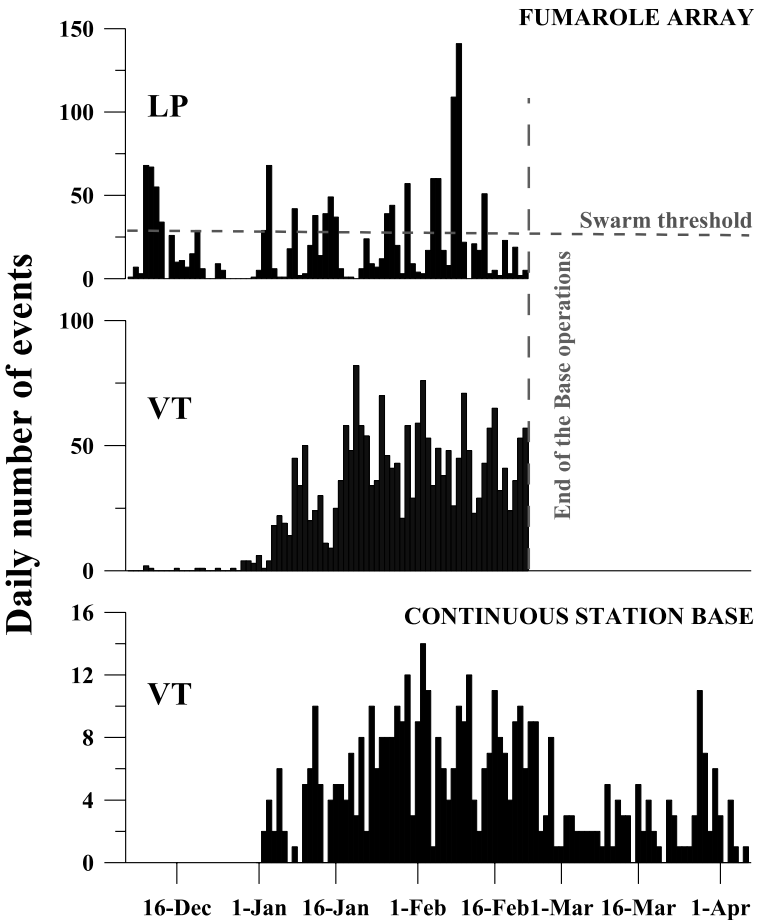

Fig. 6. Histogram of the daily number of LP events and VT earthquakes detected at the Fumarole array and the VT earthquakes recorded at the base continuous station between December 1998 and April 1999.

more than 50 earthquakes per day. At the bottom of Fig. 6, we also show a histogram of the VT earthquakes recorded by the continuous station deployed near the Spanish base, which operated for two more months. The generally lower number of earthquakes recorded by this station suggest that many of the events had magnitudes too low to exceed the detectability threshold at a station located only 2 km further to the south. From Fig. 6, we are not able to determine whether the activity was decreasing or not at the end of the recording period of the base station. The histogram gives no indication of a decrease. The activity may have lasted for some time after the control station stopped working. During the field season more than 3000 VT and LP earthquakes were recorded. Two of them were felt by the staff working on the island, one of them on January 11, at the beginning of the series, and one on January 20. This indicates a qualitative change in the seismic activity compared to the years 1992–1998. There were no reports of felt earthquakes since the 1991–1992 crisis (Ortiz et al., 1997).

About the time at which the first felt earthquake occurred, the properties of the volcanic

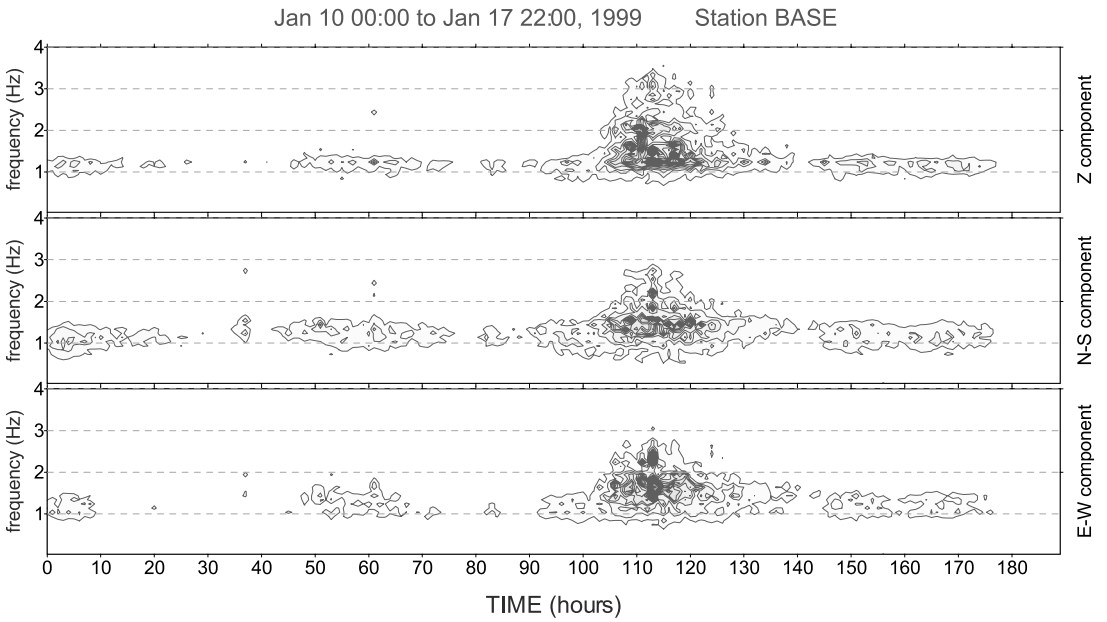

Fig. 7. Spectrogram of the three components of the ground motion recorded at the continuous base station between January 10 and 17, 1999.

tremor changed. Fig. 7 shows spectrograms of 180 h of tremor recorded at the continuous station near the Spanish base. On January 14 a period of 24 h of intense tremor was recorded, with a clear shift in frequency from 1 to 2 Hz. This period of tremor corresponds to a decrease of the number of VT and LP earthquakes in the histogram of Fig. 6. This is probably an artifact due to the reduced sensitivity of the antennas. The increase in the background amplitude affects the STA/LTA triggering algorithm.

Finally, only 15 hybrid events where identified during the field survey, all of them after the start of the VT earthquake series.

3. Array analyses

3.1. The Zero Lag Cross-Correlation method

In the present work we use the Zero Lag Cross-Correlation (ZLCC) technique (Frankel et al., 1991) to estimate the apparent slowness and back-azimuth of incoming wavefronts for successive time windows. Del Pezzo et al. (1997), Almendros et al. (1999) and Ibáñez et al. (2000) have given detailed discussions of the method and error estimation. The method is applied in the time domain and allows us to track the evolution of the source.

The method is based on the search of the apparent slowness vector which best fits the experimental data. It is solved using a grid search over the parameter space. The components of the apparent slowness (S_x, S_y) are allowed to range over an interval broad enough to include the actual solution. We use grid steps ΔS_x and ΔS_y, and for each step calculate the delay times for all stations and the corresponding average cross-correlation of the vertical components. The apparent slowness for which the maximum average cross-correlation (MACC) is reached represents the best fit to the propagation direction and velocity of the wavefront.

The procedure to perform the grid search was as follows. After inspecting the spectra, we se-

Table 1
Parameters used in the ZLCC procedure

Frequency band (Hz)	Length (samples)	Duration (s)	S_{max} (s/km)	ΔS (s/km)
1.0–3.0	300	1.5	4	0.04
3.0–5.0	100	0.5	4	0.04
1.0–4.0	200	1	4	0.04
4.0–8.0	80	0.4	1	0.01
8.0–12.0	60	0.3	1	0.01

lected the most energetic frequency band and filtered the seismograms using a zero-phase, four-pole, Butterworth band-pass filter. LP events and volcanic tremors were filtered in two frequency bands, 1–3 Hz and 3–5 Hz, while hybrids and VT earthquakes are filtered in three bands, 1–4 Hz, 4–8 Hz and 8–12 Hz. We used a moving window with a duration depending on the frequency band selected in order to contain approximately two periods of the signal (Table 1). On the basis of preliminary analyses, we restricted the grid search to adequate apparent slowness ranges which also depended on the frequency band. We selected a grid maximum and spacing of 4 and 0.04 s/km for frequency bands below 5 Hz, and 1 and 0.01 s/km, respectively, for higher frequency bands (Table 1). In each step the analysis window was shifted with 50% overlap, and the ZLCC technique was applied. For VT earthquakes, the analysis was restricted to the interval from the first P-wave to the early coda. For the other signals, the method was applied to the entire seismogram in order to find evidence of possible persistent sources, commonly observed in volcanic areas (e.g. Goldstein and Chouet, 1994).

3.2. LP events and tremor

The ZLCC method was applied to 350 LP events and volcanic tremor episodes recorded at the Fumarole array. We selected two frequency bands, 1–3 Hz and 3–5 Hz. For the 1–3 Hz band the MACC value lies between 0.7 and 0.9. The average apparent slowness is 0.8 s/km and the back-azimuths are stable at about 270°N (Fig. 8). In many cases the pre-event noise of the LP events is also correlated. It has the same apparent slowness and back-azimuth as the LP events but smaller MACC values, between 0.6 and 0.8. In the 3–5-Hz band we observe sporadic arrivals of correlated phases with MACC values greater than 0.7. Quite reasonably the apparent slownesses are higher than those for the 1–3-Hz band, with a peak between 2 and 2.5 s/km. Back-azimuth solutions point into several directions, the most important around 300°N (Fig. 8).

These distributions of apparent slowness and back-azimuth for the LP events and tremor are compatible with those observed by Ibáñez et al. (2000) for the same event types. Ibáñez et al. (2000) found that the LP seismicity at Deception Island during the 1995–1998 surveys was related to hydrothermal interactions between melting snow and ice and shallow hot material. Taking into account the similarity of waveforms and spectra, the coincidence of slowness distributions, and the fact that the main back-azimuth points to the location of glaciers close to the array, we are confident that the source mechanism suggested is applicable to the purely volcanic seismicity analyzed here.

3.3. VT earthquakes

A set of 1500 VT earthquakes recorded at the Fumarole array was selected on the basis of the signal-to-noise ratio of the first P-wave. They were analyzed in three frequency bands, 1–4 Hz, 4–8 Hz and 8–12 Hz. Between 1 and 3 Hz well correlated solutions were always observed, without any peak that could be related to the arrival of the P- or S-waves. For solutions with MACC values greater than 0.7, the distributions of apparent slowness and back-azimuth are very similar to those observed for LP events and tremor (Fig. 9). This suggests that the low-frequency signal, related to the LP events and tremor, is continuous and uncorrelated with the occurrence of earthquakes, which do not have much energy at these frequencies.

The situation changes when we look at solutions in the other two frequency bands. In this case there is only a short interval of well correlated waves with MACC values greater than 0.5. The remaining segments of the interval analyzed only have MACC values lower than 0.25. These

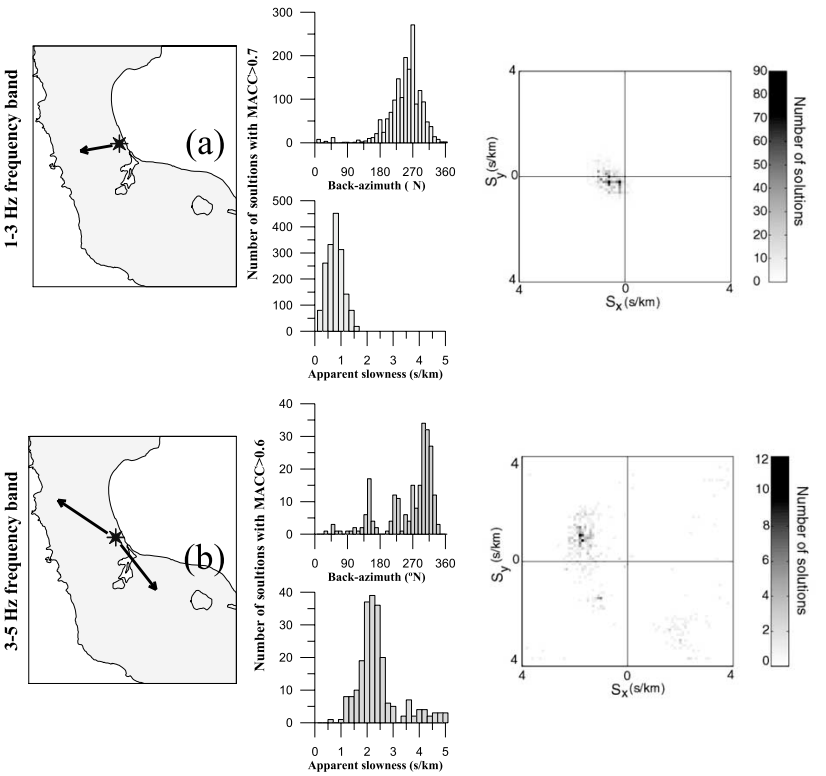

Fig. 8. Results of array analysis for the LP events and tremor in the 1–3-Hz (a) and 3–5-Hz (b) frequency bands. The histograms show the back-azimuths and apparent slownesses for the two frequency bands. The two-dimension plot represent the same values of the histograms with Sx (slowness) on the horizontal axis, Sy in the vertical and the number of solutions as level. Back-azimuth and apparent slowness can be derived easily from them. The arrows on the maps correspond to the apparent slowness vectors deduced from the ZLCC results.

peaks of MACC always coincide with arrivals of the P-wave. Since we use only vertical components, we did not find high MACC values corresponding to any S-wave arrival. Solutions for the 4–8-Hz and 8–12-Hz bands usually coincide and give very similar apparent slownesses and back-azimuths. For each earthquake we selected the apparent slowness and back-azimuth that provide the highest MACC, which corresponds to the P-wave arrival. To avoid low-quality solutions, we impose a MACC threshold of 0.5, which selected 863 earthquakes from the initial set of 1500. Fig. 10 shows histograms of the apparent slowness and back-azimuth for this set of earthquakes. The apparent slowness distribution is centered on 0.3 s/km, which is compatible with the arrival of body waves. The back-azimuth values are completely different from those observed for the LP seismicity. We can distinguish between at least two peaks of back-azimuth at 50 and 90°N, which both point toward Port Foster. Apparently, there is no relationship between the source of VT earthquakes and LP seismicity.

3.4. Hybrid events

From the 15 hybrid events detected, we selected nine for the analysis. They were analyzed in the frequency bands and with the parameters used for the VT earthquakes. In the low-frequency band

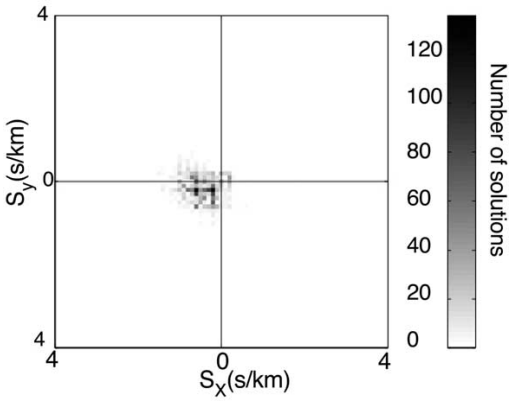

Fig. 9. The two-dimension plots representing the same values of the histograms with Sx (slowness) on the horizontal axis, Sy in the vertical and the number of solutions as level obtained during the analysis of the VT earthquakes in the 1–4-Hz frequency band.

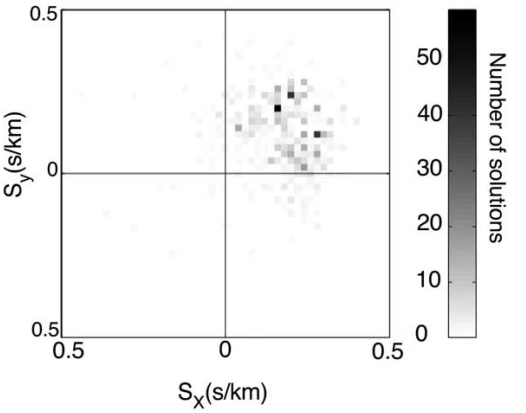

Fig. 10. The two-dimension plots representing the same values of the histograms with Sx (slowness) on the horizontal axis, Sy in the vertical and the number of solutions as level obtained for the P-wave arrival of each VT earthquake. The solutions correspond to the maximum values of MACC obtained in the 4–8-Hz and 8–12-Hz frequency bands.

solutions are usually well correlated, which indicates a stable source. Apparent slownesses are similar to those observed for the LP seismicity, with values centered on 0.6–0.8 s/km (Fig. 11). However, even though the low-frequency part of a hybrid resembles a LP event, the distribution of back-azimuths for hybrids is completely different from that observed for the LP seismicity. They coincide instead with the directions obtained for the high frequency bands in the analysis of the VT earthquakes.

For the high frequency bands, well correlated solutions only appear at the P-wave onset, as in the case of VT earthquakes (see Table 2). Slowness values and back-azimuths are also similar to the solutions obtained for the VT earthquakes, as are the estimates of the S–P delays.

4. Source location

4.1. LP and tremor source

We cannot determine the distance to a source of LP seismicity with a single seismic antenna, unless the distance is small compared to the array aperture and the circular wavefront approximation can be used (Almendros et al., 1999). There is some evidence that the source area could indeed

Table 2
Array solutions for the hybrid events

Date (day-month) 1999	Time (hh:mm) GMT	S–P (s)	Back-azimuth (°N)	Apparent slowness (s/km)	MACC
13-Jan	09:24	0.72	81	0.37	0.90
15-Jan	11:27	0.76	56	0.22	0.86
17-Jan	14:29	0.85	81	0.37	0.85
20-Jan	12:32	0.90	122	0.31	0.73
26-Jan	20:02	1.16	72	0.26	0.84
27-Jan	20:31	1.12	66	0.20	0.93
28-Jan	06:44	1.16	67	0.26	0.84
28-Jan	21:52	1.29	72	0.25	0.95
16-Feb	17:32	1.33	105	0.23	0.78

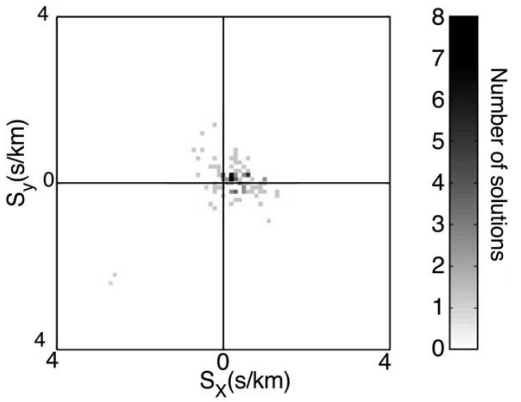

Fig. 11. The two-dimension plots representing the same values of the histograms with Sx (slowness) on the horizontal axis, Sy in the vertical and the number of solutions as level obtained during the analysis of the hybrid events in the 1–4-Hz frequency band.

be very near the array. For example, the LP activity is only recorded by the sensors of the array, and not by nearby seismic stations less than 1.5 km away. In the same way, LP seismicity recorded at the continuously recording station near the Spanish base is not detected at Fumarole array. In both cases the amplitudes of the signals are similar. Using this energetic argument we conclude that the sources of LP events and tremor recorded at the array are less than 1.5 km away.

4.2. VT earthquakes and hybrids

Hypocenter locations of VT earthquakes and hybrids can be determined accurately using the apparent slowness, back-azimuth, and S–P time. The S–P time fixes the distance to the source, the back-azimuth is the direction to the epicenter and the apparent slowness provides the incidence angle. We use inverse ray tracing through a velocity model for Deception Island (Table 3). This model is a combination of the models proposed by Ibáñez et al. (2000) and Saccorotti et al. (2001), and smoothed using a fourth-degree depth-dependent polynomial. In this way, we determine the location for both VT earthquakes and hybrid events given in the hypocentral map in Fig. 12.

Errors in the locations are derived from the errors in the array parameters and the S–P time. Following Del Pezzo et al. (1997), the average errors in the apparent slowness and back-azimuth are ±10% of the measured apparent slowness and ±7° of the back-azimuth, respectively. The average error in the determination of the S–P time is about ±0.05 s. Using these limits to perturb the original apparent slowness, back-azimuth, and S–P time for input to the ray tracing procedure, we delimit a region around the estimated hypocenter giving the error in the location of the source. For example, using average values of 0.8 s/km for the apparent slowness, 90°N for the back-azimuth, and 1.0 s for the S–P delay, we obtain a region of about $0.5\times0.5\times0.5$ km^3. Errors of this size are typical and imply that we should not interpret the detailed structure of the hypocentral distribution shown in Fig. 12, but only its general properties. The choice of velocity model also affects the results. We have tested other models, and conclude that for realistic models the source locations do not differ enough to change our interpretation of the seismicity.

The hypocentral distribution for the VT earthquakes and hybrids shown in Fig. 12 indicates that the seismicity is clustered at a focal depth of around 2 km near the array and toward the northeast. More than 90% of the events are clustered in a volume of around 10 km^3. However, deeper and more distant events have also been located, with focal depths reaching 10 km and epicentral distances up to 18 km. The cluster has two main arms. The first one extends about 3 km N45°E, with focal depths between 1 and 4 km. The second arm is longer but more diffuse, and extends N80°E. In any case the seismicity is all located within the inner bay of Deception Is-

Table 3
Velocity structure for Deception Island

Z (km)	*Vp* (km/s)	*Vp*/*Vs*
0.04	0.9	1.80
1.96	2.30	1.77
6	4.5	1.73
12.0	6.0	1.73
∞	8.0	1.73

Z = layer thickness; *Vp* = P-wave velocity; *Vs* = S-wave velocity.

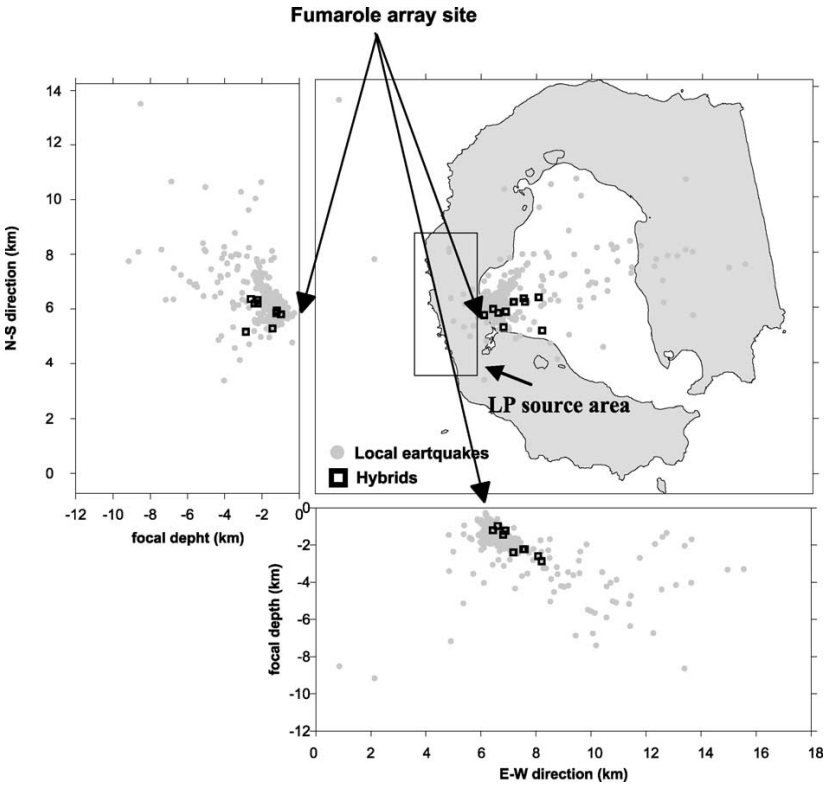

Fig. 12. Hypocentral locations of the VT earthquakes (dots) and hybrid events (squares). The box over Deception Island shows the possible source region for LP seismicity.

land and apparently dips with an angle of about 45°. Hybrid event locations coincide with the cloud of VT earthquake. Most of them are contained in the branch of seismicity extending toward N80°E.

To study the migration of hypocenters with time, we divide the seismic series by time windows, and plot the hypocentral locations in each window separately (Fig. 13). Initially the sources are concentrated in a small region between depths of 1 and 2 km. As time progresses we observe that the source volume increases in size, mainly to greater depths, forming between 1 and 3 km depth and with 2 km of horizontal extension. At the same time the events migrate downward. The deeper and more distant seismicity expressed itself in the larger S–P times, that reached values between 1 and 3 s. The two felt earthquakes were located in the center of the main focal volume.

5. Energetic characterization of the seismic series

In this section we quantify the size of the VT earthquakes. One possible measure is the moment-magnitude scale. The moment-magnitude was defined by Kanamori (1977) as:

$$M_w = 2/3 \log M_o - 6.06 \quad (1)$$

where the moment is measured in Nm.

In this expression M_o corresponds to the seismic moment which can be expressed by:

$$M_o = (\Omega_o / \Psi_{\theta\phi})\ (4\pi\rho v_s^3 R) \quad (2)$$

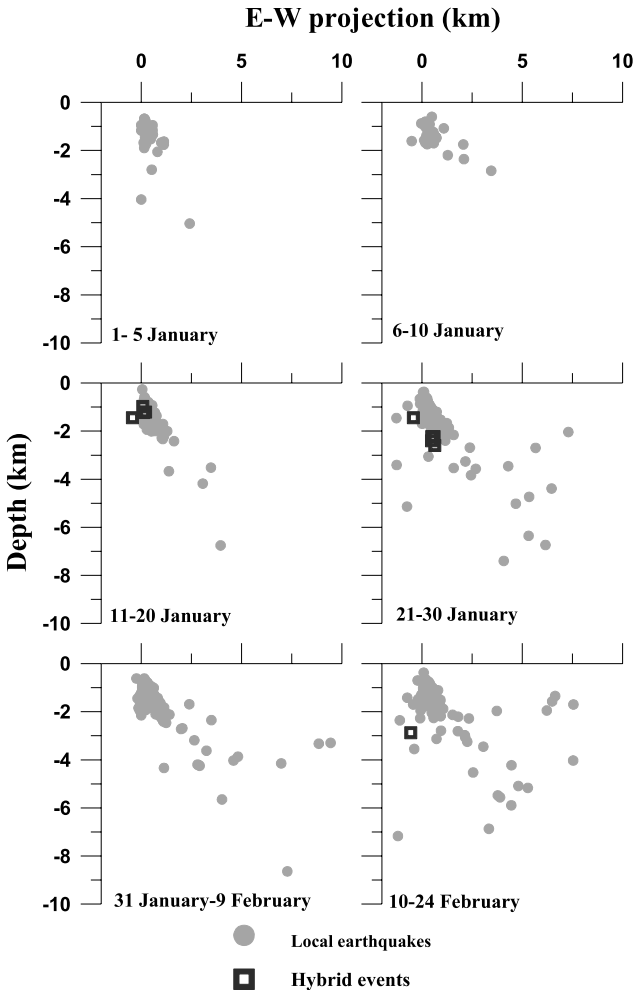

Fig. 13. Evolution of the source locations of the VT earthquakes and hybrid events with time. The panels show hypocentral depth and EW projection during six time intervals.

Ω_o is the spectral level of the attenuation-corrected displacement spectrum which remains flat until the corner frequency f_o; $\Psi_{\theta\phi}$ is a function accounting for the body-wave radiation pattern and the effect of the free surface (we assume a value of 0.85); R is the hypocentral distance; v_s is the S-wave velocity and ρ is the density of the medium.

To estimate Ω_o and f_o we can use both P-waves and S-waves, but it is more correct to use only the S-wave displacement spectrum. As the original Brune model (Brune, 1970) assumed SH-waves, we should use horizontal components for these estimates. The attenuation-corrected spectrum is obtained applying the Q factor to the ground displacement spectrum. The Q factor, the quality factor of the medium, is directly related to seismic attenuation in the region between source and re-

Table 4
Parameters used in the moment-magnitude determination

Hipocentral distance (km)	Q-factor	S-wave velocity (km/s)
<1	50	1
$1<D<1.5$	60	1.2
$1.5<D<2$	80	1.5
$2<D<4$	150	1.8
$D>4$	260	2.5

ceiver. We used frequency-independent Q values obtained as a function of the distance from the study of Martínez-Arévalo et al. (2003), (Table 4).

Other parameters necessary for the estimation of M_o are the density of the medium and body wave velocity. We assume an average density of 2.7 g/cm^3, and velocity values averaged from Table 3 (see Table 4).

The S-wave spectra were calculated using a MATCAD© package. To determine of the spectrum of the ground displacement, we use a 2.56-s window starting at the S-wave onset. We chose data from the three-component station of the Fumarole array which had the best signal-to-noise ratio, and averaged the two horizontal S-wave spectra. The level of the flat part of the spectrum and the corner frequency were determined using a minimization algorithm starting from a initial value for corner frequency, with the frequency decay fixed to -2. From the spectrum we also determine the stress drop, seismic moment, moment magnitude and the probable source radii using two possible hypotheses, Madariaga's model (Madariaga, 1977) and Brune's model (Brune, 1970). We applied this study to most of the VT earthquakes. The biggest ones were excluded because their S-waves were saturated in the recording. For this small data set (6 events) we used the same procedure at a more distant station, the broad-band station located at the Spanish base 'Juan Carlos I' (Livingston Island), 45 km north of Deception Island. In this case we used different parameters to correct the spectra. The S-wave velocity was 3.0 km/s and, because there is no attenuation model for the region, we used Q determined for Granada from Ibáñez et al. (1990), $Q=90$ $(f/f_o)^{0.85}$. For this epicentral distance, the possible error introduced by the uncertainty in the Q value is a second order effect, because the geometrical spreading correction is more important.

The 863 earthquakes span a magnitude range from -0.8 to 3.4. The magnitudes of the VT earthquakes allow us to follow the evolution of the energy of the seismic series, as well as estimate the cumulative seismic moment (Fig. 14). Except for the two earthquakes of magnitude 2.8 and 3.4, the energy release as a function of time is more or less steady. The distribution of magnitudes is nearly the same throughout the series.

The stress drop of the seismic series derived from the magnitude analysis is very low (Fig. 15), with more than 95% of the values concentrated between 0.1 and 4 bar. The corner frequencies range from 40 Hz for the smallest events to 6 Hz for the biggest ones (not including the events which saturated the records). The relationship between corner frequency and magnitude possibly

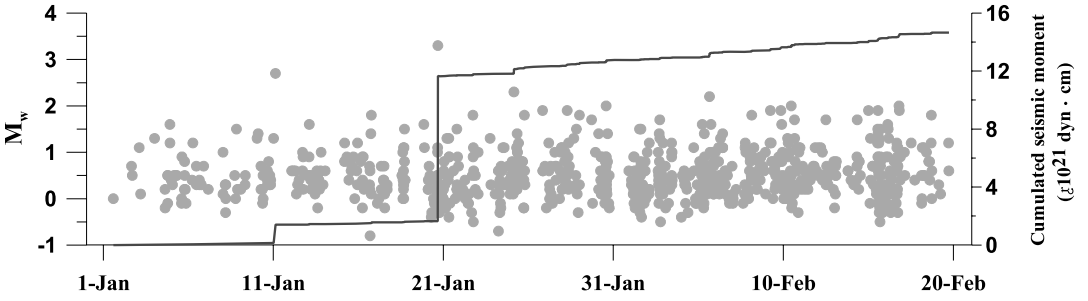

Fig. 14. Earthquake magnitude (left axis) vs. time during January–February, 1999. The solid line represents the cumulative seismic moment (right axis).

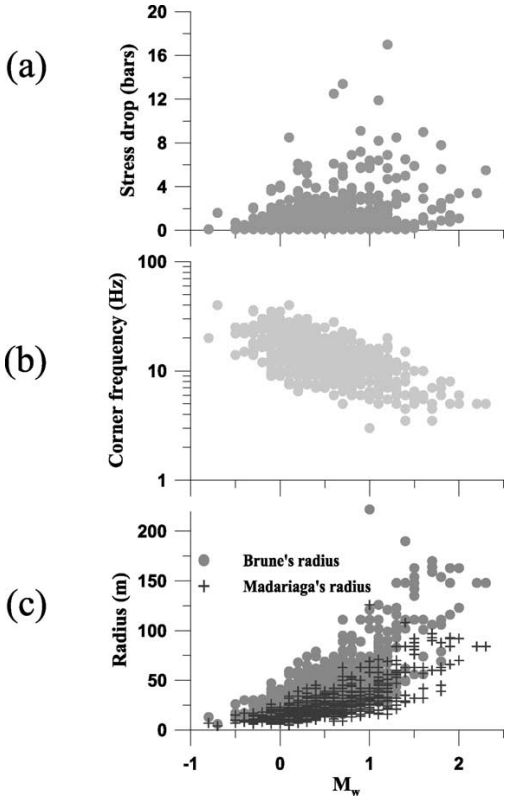

Fig. 15. Stress drop (a), corner frequency (b), and source radius (c) vs. magnitude for the VT earthquakes analyzed.

reflects a scaling law for the series, but the data are too dispersed to obtain a significant fit. The high values of the corner frequencies are consistent with the spectra of the VT earthquakes, which have high signal-to-noise ratios up to frequencies of 50 Hz. The source radii derived from the spectral analysis reveal the small dimensions of the source (Fig. 15). Using Brune's model we found that the source dimensions range from 10 to up to 200 m, with an average of 50 m. In the case of Madariaga's model the dimensions are smaller, ranging from 5 to 120 m, with an average value of 30 m.

In Fig. 12 we observe that the seismicity is clustered close to the array. We can investigate whether this cloud of data could be an artifact due the detection threshold of the seismic instruments. To do this we plot the moment magnitude vs. focal depth and epicentral distance (Fig. 16a). We can see that all earthquakes with magnitudes smaller than about 0.8 are concentrated in the first two km of focal depth and epicentral distance. For more distant events, the minimum magnitude detected is around 1.0. This implies that there might be low-magnitude seismicity located more than 2 km from the array which cannot be detected. Thus, the observed clustering of the seismicity observed in Fig. 12 could be an artifact. The real distribution of seismicity could be quite different. In fact, if we represent only events with magnitudes greater than 1.2, the clustering is reduced and the hypocenter cloud extends clearly to the east and northeast of the array (Fig. 16b).

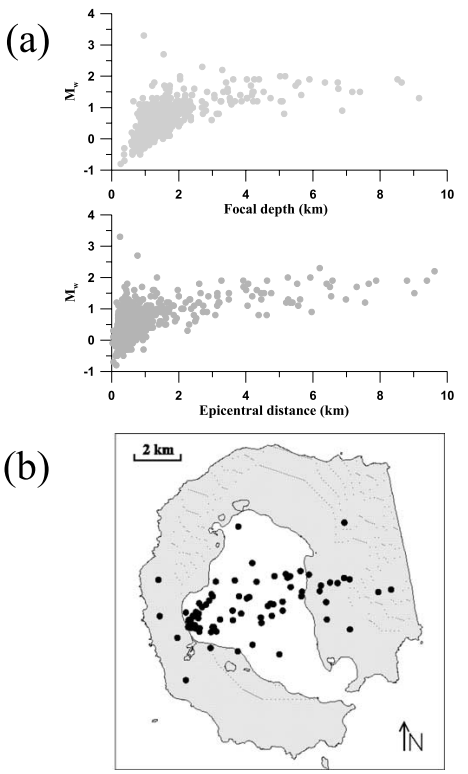

Fig. 16. (a) Plots of the VT earthquake magnitude vs. focal depth and epicentral distance. (b) Epicentral plot for VT earthquakes with magnitudes greater than 1.2.

6. Evidence of different source processes

The source dimensions indicate the small size of the fractures involved in the events of the seismic series. These small fractures are primarily concentrated in a small focal volume, inside of which we detected hundreds of events. Without a seismic network we are not able to estimate the focal mechanisms. However several observations allow us to distinguish at least the presence of many distinct source mechanisms.

Visual analysis of the VT earthquake records reveals clear differences between events which have similar source locations, for example in the direction and shape of the first P-wave motions. Fig. 17 shows two events with similar apparent slownesses, back-azimuths, and S–P times. Although their sources must be located close together, the polarities of the first pulse and whole seismograms are different. This could indicate that the source mechanisms are different. We measured the polarities of the first motion for earthquakes with impulsive arrivals. In Fig. 18 we present the source locations in different time intervals for events with clear up or down first motion directions. There are no obvious spatial or temporal differences between the two distributions.

Another piece of evidence indicating the complexity of the source region is the occurrence of multiplets of events. Several conditions are necessary for the repeated generation of similar earthquakes. Since the path and site effects are essentially the same for earthquakes with nearby hypocenters, the events must have the same source-time function and source mechanism. The presence of multiplets is important because the similarities among waveforms allow phase onsets to be determined with high consistency. This can lead to an improvement in the quality of the hypocentral locations. To identify earthquake multiplets we used the method proposed by Saccorotti et al. (2002) in their study of the Agron series in Southern Spain. In this way we obtained several tens of families, usually with more than 10 events per family. Fig. 19 shows examples of two families. Earthquakes of each family are located within a very small volume. However, they do not appear to correlate in time. There are intervals of several days or weeks between them. During these intervals, events with other source mechanisms often occur in the same source region. The presence of earthquake families in this seismic series is a very interesting topic that will be the subject of a future study.

7. Discussion

7.1. VT earthquakes and hybrids

To understand a fracture process with low stress drop, small dimensions and occurrence of multiplets, we can invoke the role of the fluids. In this framework the release of seismic energy is associated with lubrication of a pre-existing zone of weakness by fluids. Lubrication reduces the friction coefficients and decreases the effective

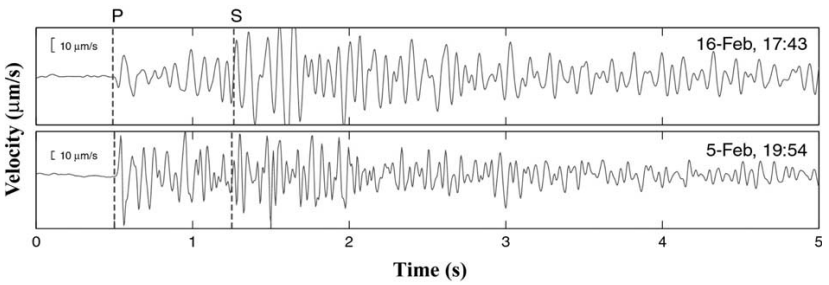

Fig. 17. Vertical-component seismograms of two VT earthquakes with very similar hypocenter locations. The labels P and S show the arrival of the P-waves and S-waves, respectively. The top record has a 'down' first motion, while the bottom record shows a clear 'up' first motion.

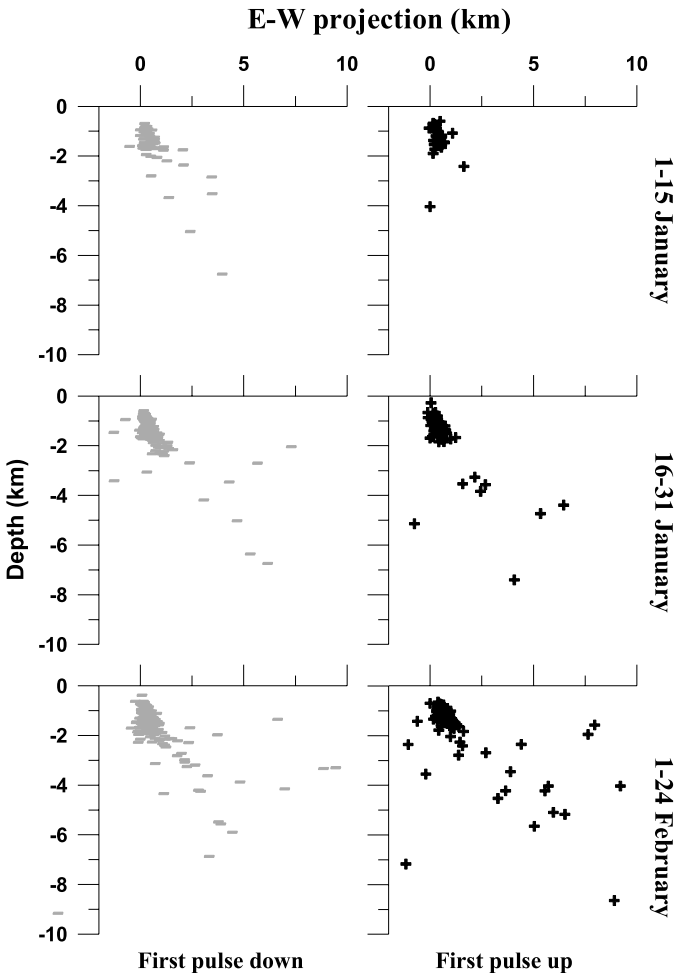

Fig. 18. Hypocentral distributions of VT earthquakes with clear down (left) or up (right) first motions. The top, center, and bottom rows correspond to different time periods.

normal stress over the fault surface. This can in turn trigger the earthquake.

During the seismic series some hybrid events were recorded. We are confident that the hybrids can be considered as true hybrids in the sense of the classification by Lahr et al. (1994): a volcano-tectonic earthquake plus a LP event. There are several observations that support this conclusion. For example, in the high frequency signal we are able to distinguish the arrival of P-waves and S-waves. The array solutions at high frequencies coincide with those obtained for the VT earthquakes. The azimuths of the LP part of the hybrid events point towards the inner bay, as the VT earthquakes do, not to the southeast as do the azimuths of the pure LP events and the tremor. In addition, the hypocenters of the initial earthquake of the hybrid events are located in the same area as the VT earthquakes. We can disregard the fact that the low-frequency wave package may

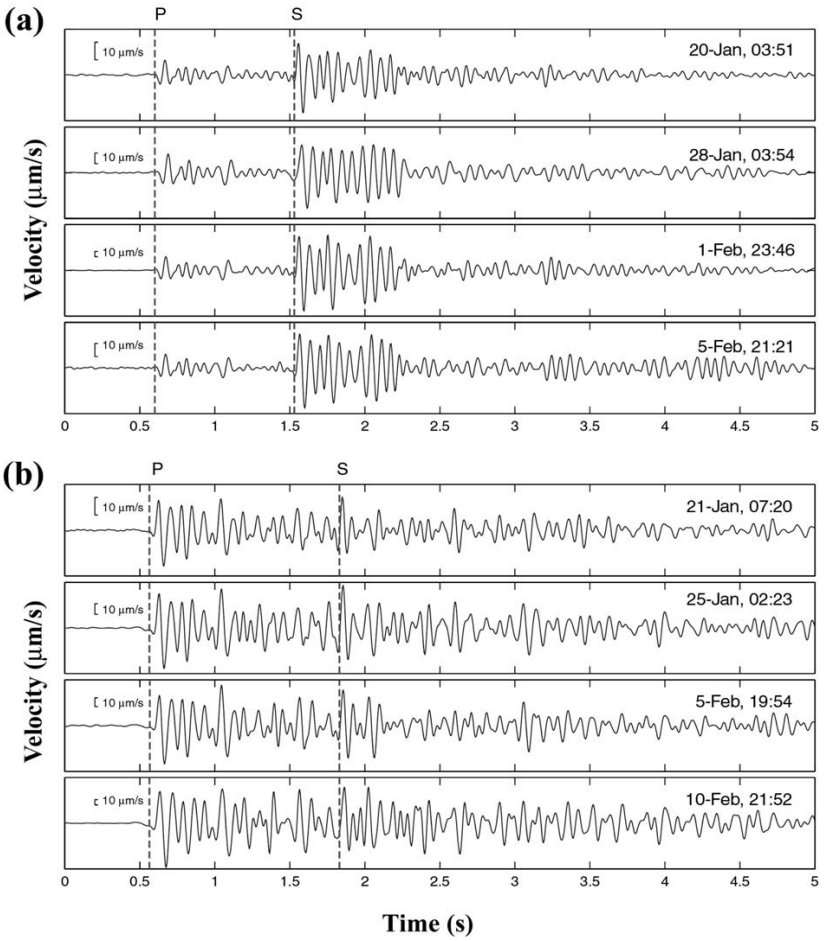

Fig. 19. Examples of two families of VT earthquakes with S–P times of ~0.8 s (a) and 1.3 s (b).

have originated as a path or site effect, because we see earthquakes located very near to the hybrids that do not have this low-frequency train. The occurrence of hybrids during the seismic series is confirmation of the presence of fluids in the source area. These events are evidence that fluids are present in the fracture systems. It is important to point out that the hybrids were detected when the hypocenters of the VT earthquakes began to migrate downwards. This observation is important for understanding the process controlling the seismic series.

7.2. Hypothesis about the origin of the series

Based on the volcanic nature of Deception Island and the well known effects of the regional tectonics on the island (Pelayo and Wiens, 1989), we can imagine three possible scenarios for the source of the stress disturbance producing the series of VT earthquakes. First, these events could be a classical tectonic seismic swarm caused by regional stress. Second, they may be a seismic swarm produced directly by the movement of magma through the source region. Third, the seis-

mic series may be caused by stress generated by the uplift of the source area due to the injection of magma in depth.

We may exclude the first scenario, because the seismic activity is restricted to the inner bay and there are no earthquakes outside the island. If the series were induced by regional stresses, there should be activity along the faults that cross the island (Martí et al., 1996), which we did not detect. Moreover, it is difficult to be convinced that the regional stress field could trigger the seismic series in a single shallow point inside the island. The behavior of the series is not that of a typical main shock–aftershock sequence. The variety of source mechanisms involved in such a small focal volume, the repeated rupture of some fault planes implied by the earthquake multiplets, and the low stress drop, indicate that the source region could be characterized by a complex stress distribution and an asymmetrical pattern of small microfaults. On the other hand, Legrand et al. (2002) have calculated the stress tensor below the Guagua Pichincha volcano (Ecuador) obtaining a single stress tensor but with a mixture of normal faults and strike-slip component faults. These authors have found that the presence of different focal mechanisms could be compatible with a unique stress tensor.

It is unlikely that magmatic fluids are directly involved. If this were the case, we should have observed an upward migration of the hypocenters, following the upward migration of magma. To the contrary, we observed a downward migration of hypocenters. The occurrence of similar events, separated by several days or weeks, is not compatible with this hypothesis. The presence of multiplets reflects that the stress triggering of the earthquakes is nearly constant with time. In contrast, a migration of magma should produce an evolution of the stress field. Further evidence against this hypothesis comes from the separate source areas in which the LP seismicity and the VT earthquake activity are located. The presence of magma at shallow depth and relatively low pressure are usually accompanied by gas, which produces LP and tremor seismicity (e.g. Fehler, 1983; Gil Cruz and Chouet, 1997). The fact that the LP source area and the earthquake hypocentral region do not coincide implies that there is no magma at shallow depth at any time during the series.

Thus, the best model for explaining the origin of the seismic series is the uplift of the Port Foster area by a deep magmatic injection. The presence of a magma reservoir in the Northeast area of Port Foster has been reported by several authors (Blanco, 1997, García et al., 1997). An increase of pressure within the magma reservoir, or the upward displacement of magma, perturbs the stress field in the region over the reservoir. When the stress reaches a threshold value, fracture processes begin, following pre-existing zones of weakness and the series becomes fully active. The absence of visible evidence of a subsequent eruption and the lower level of earthquake activity observed since 1999 lead us to think that the injection of magma stopped before reaching the vicinity of the surface. The uplift hypothesis is compatible with the majority of the observations derived from the present analysis.

We have found that most VT earthquakes were the consequence of small stress drop changes (less than 4 bar) on fractures with an average radius of about 50 m. This fact may be explained by lubrication of the microfaults due to pressurized fluids. The increase of pore pressure in the very shallow crust overlying the magmatic system could have induced the repeated activation of the fracture network. The presence of fluids in the source area not only expedites the fracture processes, but also explains the origin of the hybrids observed. Their low-frequency segments are produced by resonances of fluid-filled cracks. The fluid involved in the lubrication of the microfaults and the generation of hybrid events is probably not magmatic, as explained above, but water embedded in the geological structure. Martini and Giannini (1988) reported the existence of a shallow aquifer near the epicentral area, and a deeper aquifer may be present as well (Martini and Casselli, pers. commun.).

The process described in the present analysis does not seem to be rare at Deception Island. The seismic crisis occurring in 1992 has been described in similar terms (Ortiz et al., 1997). This means that in seven years we observed two vol-

canic crises. If we take into account that there are no permanent stations in the island, and that we are able to make measurements during three months every year (from December to February), then similar intervals of high seismic activity may be occurring more often than we have observed. Deception Island, therefore, seems to be a very active volcano. However, it is also a volcano frequently visited by scientific teams and thousands of tourists, especially during the summer season. In order to reduce the risk associated with volcanic hazards, we must put greater effort into seismic and geophysical monitoring of Deception Island.

Acknowledgements

This work was partially supported by projects ANT98-1111, REN-2000-2897, e-Ruption, and REN-2001-3833. We thank J. A. Peña for his invaluable help in the field work; B. Chouet, J. Morales, G. Alguacil, and C. Martínez-Arévalo for useful comments on the manuscript; Margaret Hellweg for her very useful comments and great grammatical corrections that have improved the paper; Denis Legrand for his valuable comments to the manuscript; the staff and scientists of the Gabriel de Castilla Base; and F. Calexico for his moral support. Logistical support was provided by the Spanish 'Ejército de Tierra' and 'Armada'.

References

Almendros, J., Ibanez, J.M., Alguacil, G., Del Pezzo, E., 1999. Array analysis using circular wavefront geometry: An application to locate the nearby seismo-volcanic source. Geophys. J. Int. 136, 159–170.

Almendros, J., Chouet, B., Dawson, P., Bond, T., 2002. Identifying elements of the plumbing system beneath Kilauea Volcano, Hawaii, from the source locations of very-long-period signals. Geophys. J. Int. 148, 303–312.

Benoit, J.P., McNutt, S.R., 1996. Global volcanic earthquake swarm database and preliminary analysis of volcanic earthquakes swarm duration. Ann. Geofis. 39, 221–229.

Blanco, I., 1997. Análisis e interpretación de las anomalías magnéticas de tres calderas volcánicas: Decepción (Shetland del Sur, Antátida), Furnas (San Miguel, Azores) y las Cañadas del Teide (Tenerife, Canarias). Ph.D. Thesis, Universidad Complutense de Madrid, 250 pp.

Brune, J.N., 1970. Tectonic stress and the spectra of seismic shear waves. J. Geophys. Res. 89, 1132–1146.

Chouet, B., 1988. Resonance of a fluid-driven crack: Radiation properties and implications for the source of long-period events and harmonic tremor. J. Geophys. Res. 93, 4375–4400.

Chouet, B., 1992. A seismic model for the source of long-period events and harmonic tremor. In: Aki, K., Gasparini, P., Scarpa, R. (Eds.), Volcanic Seismology. IAVCEI Proceedings in Volcanology 3, Springer, pp. 133–156.

Chouet, B., 1996. Long-period volcano seismicity: Its source and use in eruption forecasting. Nature 380, 309–316.

Chouet, B.A., Page, R.A., Stephens, C.D., Lahr, J.C., Power, J.A., 1994. Precursory swarms of long-period events at Redoubt Volcano (1989–1990), Alaska: Their origin and use as a forecasting tool. J. Volcanol. Geotherm. Res. 62, 95–135.

Crosson, R.S., Bame, D.A., 1985. A spherical source model for low-frequency volcanic earthquakes. J. Geophys. Res. 90, 10237–10247.

Dahm, T., 1992. Numerical studies of the dynamics of fluid-filled cracks placed in series: A model for inharmonic peaked tremor spectra. In: Aki, K., Gasparini, P., Scarpa, R. (Eds.), Volcanic Seismology. IAVCEI Proceedings in Volcanology 3, Springer, pp. 190–200.

Del Pezzo, E., La Rocca, M., Ibanez, J.M., 1997. Observations of high-frequency scattered waves using dense arrays at Teide volcano. Bull. Seismol. Soc. Am. 87, 1637–1647.

Fehler, M., 1983. Observations of volcanic tremor at Mount St. Helens volcano. J. Geophys. Res. 88, 3476–3484.

Frankel, A., Hough, S., Friberg, P., Busby, R., 1991. Observations of Loma Prieta aftershocks from a dense array in Sunnyvale, California. Bull. Seismol. Soc. Am. 81, 1900–1922.

García, A., Blanco, I., Torta, J.M., Astiz, M.M., Ibáñez, J.M., Ortiz, R., 1997. A search for the volcanomagnetic signal at Deception volcano (South Shetland I. Antarctica). Ann. Geofis. 40, 319–327.

Gil Cruz, F., Chouet, B., 1997. Long-period events, the most characteristic seismicity accompanying the emplacement and extrusion of a lava dome in Galeras volcano, Colombia, in 1991. J. Volcanol. Geotherm. Res. 77, 121–158.

Goldstein, P., Chouet, B., 1994. Array measurements and modeling of sources of shallow volcanic tremor at Kilauea Volcano, Hawaii. J. Geophys. Res. 99, 2637–2652.

Hellweg, M., 2000. Physical model for the source of Lascar's harmonic tremor. J. Volcanol. Geotherm. Res. 101, 183–198.

Ibáñez, J.M., Del Pezzo, E., De Miguel, F., Herraiz, M., Alguacil, G., Morales, J., 1990. Depth dependence seismic attenuation in Granada zone (South Spain). Bull. Seismol. Soc. Am. 80, 1232–1244.

Ibáñez, J.M., Del Pezzo, E., Almendros, J., La Rocca, M., Alguacil, G., Ortíz, R., García, A., 2000. Seismovolcanic signals at Deception Island volcano, Antarctica: Wave field analysis and source modeling. J. Geophys. Res. 105, 13905–13931.

Julian, B.R., 1994. Volcanic tremor: Nonlinear excitation by fluid flow. J. Geophys. Res. 99, 11859–11877.

Kanamori, H., 1977. The energy release in great earthquakes. J. Geophys. Res. 82, 2981–2987.

Klein, F.W., Koyanagi, R.Y., Nakata, J.S., Tanigawa, W.R., 1987. The seismicity of Kilauea's magma system. In: Decker, R.W., Wright, T.L., Stauffer, P.H. (Eds.), Volcanism in Hawaii. US Geol. Surv. Prof. Pap. 1350, pp. 1019–1085.

Koyanagi, R.Y., Chouet, B.A., Aki, K., 1987. Origin of volcanic tremor in Hawaii, Part I. In: Decker R.W., Wright, T.L., Stauffer, P.H. (Eds.), Volcanism in Hawaii. US Geol. Surv. Prof. Pap. 1350, pp. 1221–1257.

Kumagai, H., Chouet, B., 2000. Acoustic properties of a crack containing magmatic or hydrothermal fluids. J. Geophys. Res. 105, 25493–25512.

Lahr, J., Chouet, B., Stephens, C., Power, J., Page, R., 1994. Earthquake classification, location and error analysis in a volcanic environment: Implications for the magmatic system of the 1989–1990 eruptions at Redoubt volcano, Alaska. In: Miller, T., Chouet, B. (Eds.), The 1989–1990 Eruptions of Redoubt Volcano, Alaska. J. Volcanol. Geotherm. Res. 62, 137–151.

Legrand, D., Calahorro, A., Guillier, B., Rivera, L., Ruiz, M., Villagómez, D., Yepes, H., 2002. Stress tensor analysis of the 1998–1999 teconic swarm of northern Quito related to the volcanic swarm of Guagua Pichincha volcano, Ecuador. Tectonophysics 344, 15–36.

Madariaga, R., 1977. High-frequency radiation from crack (stress drop) models of earthquakes faulting. Geophys. J. R. Astron. Soc. 51, 625–652.

Martí, J., Vila, J., Rey, J., 1996. Deception Island (Bransfield Strait, Antarctica): An example of volcanic caldera developed by extensional tectonics. In: McGuire, W., Jones, A., Neuberg, J. (Eds.), Volcano Instability on the Earth and Other Planets. Geol. Soc. Spec. Publ. 110, pp. 253–265.

Martínez-Arévalo, C., Bianco, F., Ibáñez, J.M., Del Pezzo, E., 2003. Shallow seismic attenuation in the short period range of Deception Island volcano (Antarctica). J. Volcanol. Geotherm. Res. 128, this issue (DOI: 10.1016/S0377-0273(03)00248-8.

Martini, M., Giannini, L., 1988. Deception Island (South Shetlands): An area of active volcanism in Antarctica. Mem. Soc. Geol. Ital. 43, 117–122.

Nakano, M., Kumagai, H., Kumazawa, M., Yamaoka, K., Chouet, B., 1998. The excitation and characteristic frequency of the long-period volcanic event: An approach based on an inhomogeneous autoregressive model of a linear dynamic system. J. Geophys. Res. 103, 10031–10046.

Narváez, L., Torres, R.A., Gómez, D.M., Cortés, G.P., Cepeda, H., Stix, J., 1997. 'Tornillo'-type seismic signals at Galeras volcano, Colombia, 1992–1993. J. Volcanol. Geotherm. Res. 77, 159–171.

Neuberg, J., Luckett, R., Baptie, B., Olsen, K., 2000. Models of tremor and low-frequency earthquake swarms on Montserrat. J. Volcanol. Geotherm. Res. 101, 83–114.

Ohminato, T., Chouet, B.A., Dawson, Ph., Kedar, Sh., 1998. Waveform inversion of very long period impulsive signals associated wiht magmatic injection beneath Kilauea Volcano, Hawaii. J. Geophys. Res. 103, 23839–23862.

Ortiz, R., García, A., Aparicio, A., Blanco, I., Felpeto, A., del Rey, R., Villegas, M., Ibáñez, J.M., Morales, J., Del Pezzo, E., Olmedillas, J.C., Astiz, M., Vila, J., Ramos, M., Viramonte, J.G., Risso, C., Caselli, A., 1997. Monitoring of the volcanic activity of Deception Island, South Shetland Islands, Antarctica (1986–1995). In: The Antarctic Region: Geological Evolution and Processes, pp. 1071–1076.

Pelayo, A.M., Wiens, D.A., 1989. Seismotectonics and relative plate motions in the Scotia Sea region. J. Geophys. Res. 94, 7293–7320.

Ramos, E.G., Hamburger, M.W., Pavlis, G.L., Laguerta, E.P., 1999. The low-frequency earthquake swarms at Mount Pinatubo, Philippines: Implications for magma dynamics. J. Volcanol. Geotherm. Res. 92, 295–320.

Saccorotti, G., Almendros, J., Carmona, E., Ibáñez, J.M., Del Pezzo, E., 2001. Slowness anomalies from two dense seismic arrays at Deception Island, Antarctica. Bull. Seismol. Soc. Am. 91, 561–571.

Saccorotti, G., Carmona, E., Ibáñez, J.M., Del Pezzo, E., 2002. Spatial characterization of the Agron, southern Spain, 1988–1989 seismic series. Phys. Earth Planet. Inter. 129, 13–29.

IV. Precise determination of the relative wave propagation parameters of similar events using a small-aperture seismic array

JOURNAL OF GEOPHYSICAL RESEARCH, VOL. 109, B11308, doi:10.1029/2003JB002930, 2004

Precise determination of the relative wave propagation parameters of similar events using a small-aperture seismic array

Javier Almendros, Enrique Carmona, and Jesús Ibáñez
Instituto Andaluz de Geofísica, Universidad de Granada, Granada, Spain

Received 5 December 2003; revised 24 August 2004; accepted 30 August 2004; published 25 November 2004.

[1] We propose a method to determine accurately the relative wave propagation parameters (apparent slowness and propagation azimuth) of a cluster of seismic events with similar waveforms recorded on a seismic array. This relative slowness estimate (RelSE) method is based on precise measurements of the delays among arrivals of different earthquakes to each of the array receivers. Delays are determined using interpolations of the cross-correlation functions of the earthquake waveforms. Accurate relative slowness vectors are estimated using a least squares fit of the observed delays to the delays corresponding to the arrivals of plane wave fronts. We tested the method using both synthetics and real data, in order to understand its resolution capabilities in presence of seismic noise and to assess the uncertainty regions associated with the slowness vector estimates. From these analyses, we establish a procedure to determine the 90% uncertainty regions associated with the estimates of relative slowness vectors. As an example of application of the RelSE method, we analyzed a multiplet composed of 16 similar earthquakes recorded during the 1999 seismic crisis at Deception Island volcano, Antarctica. Using a conventional slowness estimate method produces virtually the same result for every earthquake, because of the large uncertainties. Alternatively, using the RelSE method reduces the uncertainties of the estimates and allows to resolve the detailed distribution of (relative) apparent slowness vectors. Our results show that the slowness vectors are aligned within a narrow, north-south trending band, which represents a clue toward the features of the source region and/or source distribution. We repeated the procedure using different earthquakes as master events. The estimated distribution of slowness vectors is similar in every case, which demonstrates that our results are independent of the choice of reference event. *INDEX TERMS:* 7299 Seismology: General or miscellaneous; 7203 Seismology: Body wave propagation; 7215 Seismology: Earthquake parameters; 7230 Seismology: Seismicity and seismotectonics; 7280 Seismology: Volcano seismology (8419); *KEYWORDS:* seismic arrays, slowness vectors, multiplet analysis, Deception Island volcano

Citation: Almendros, J., E. Carmona, and J. Ibáñez (2004), Precise determination of the relative wave propagation parameters of similar events using a small-aperture seismic array, *J. Geophys. Res.*, *109*, B11308, doi:10.1029/2003JB002930.

1. Introduction

[2] Resemblance among seismic waveforms has been extensively exploited in several fields of seismology. There are essentially two situations in which similar seismograms are likely to be recorded. The first one requires two seismometers deployed at nearby locations; because of the close proximity of the receivers, we expect that any earthquake would yield a couple of highly correlated seismograms. The second one requires the use of a single seismometer and to wait till the Earth produces two quasi-identical earthquakes, something that, surprisingly enough, is not as rare as it sounds. Although these ideas may seem naive, they contain the seeds of two seismological techniques that have advanced very quickly during the past years: the use of seismic arrays and analyses of multiplets.

[3] Seismic arrays are dense, two-dimensional deployments of seismometers intended for recording and analyzing coherent wave fields. Array seismograms look similar because they are recorded at very close receivers. Differences among them consist mainly in phase delays produced by wave propagation. Thus seismic arrays are useful to determine the wave propagation parameters (apparent slowness and azimuth) of signals propagating across the array area. They are particularly appropriate for the analysis of complex wave fields [*Goldstein and Archuleta*, 1987; *Chouet*, 1996a; *Almendros et al.*, 2002a; *Chouet*, 2003]. Applications of seismic arrays for the analysis of wave fields recorded on volcanic areas have been especially numerous and fruitful. They have been used for example to investigate the composition of volcanic tremor [*Ferrazzini*

0148-0227/04/2003JB002930$09.00

et al., 1991; *Saccorotti et al.*, 2001b], to separate and analyze the different components contributing to the wave field [*Del Pezzo et al.*, 1997; *La Rocca et al.*, 2001; *Saccorotti et al.*, 2001b; *Almendros et al.*, 2001b], to separate source and path effects [*Chouet et al.*, 1997; *Saccorotti et al.*, 2001c], to track and locate seismo-volcanic sources [*Goldstein and Chouet*, 1994; *Neuberg et al.*, 1994; *Ibáñez et al.*, 2000; *La Rocca et al.*, 2000; *Almendros et al.*, 2001a], and to study the shallow structure under the array [*Goldstein and Chouet*, 1994; *De Luca et al.*, 1997; *Chouet et al.*, 1998; *Saccorotti et al.*, 2001c].

[4] While the waveform resemblance used by array techniques is circumstantial, and guaranteed only by design (i.e., the close proximity of the seismic receivers), resemblance in multiplet analysis is associated with the occurrence of earthquakes having intrinsically similar characteristics. These groups of similar earthquakes are a common event in all kinds of environments: tectonic, geothermal, volcanic, etc. The main advantage of the enhanced waveform similarity is that we are able to determine very accurately the time delay between the occurrence of two earthquakes. This precise relative timing of multiplet earthquakes can be used to estimate relative locations of clusters of seismic sources [*Got et al.*, 1994; *Phillips*, 2000; *Stich et al.*, 2001; *Saccorotti et al.*, 2002; *Brancato and Gresta*, 2003]. Other applications of precise relative timing include studies of the origin of the coda [*Antolik et al.*, 1996; *Aster et al.*, 1996; *Got and Coutant*, 1997], temporal variations of velocity in tectonic [*Poupinet et al.*, 1984; *Haase et al.*, 1995] or volcanic settings [*Ratdomopurbo and Poupinet*, 1995; *Poupinet et al.*, 1996], and the detailed properties of the inner structure of the Earth [*Song and Richards*, 1996; *Poupinet et al.*, 2000].

[5] In this article we propose a method that benefits from waveform resemblance in both of the senses described above. It is intended to determine very accurately the differences in apparent slowness and propagation azimuth of similar earthquakes, that is, if one of them propagates slightly faster than the others or toward a slightly different direction. The method is based on precise relative timing of earthquake waveforms recorded at the receivers of a seismic array. For a cluster of closely spaced, similar events we can produce precise relative slowness and azimuth estimates, although the average slowness and azimuth of the cluster remains less accurately resolved. The calculation scheme is the same as in relative location methods, only that seismic networks and relative hypocenter locations are substituted by seismic arrays and relative apparent slowness vectors, respectively.

2. Method

2.1. Slowness Estimate Methods

[6] Let us suppose a seismic array composed of N stations at positions $\vec{r}_i$, where $i = 1 \ldots N$. In the plane wave front approximation, the arrival times of a signal propagating across the array are given by

$$t_i^m = t_0^m + \vec{r}_i \cdot \vec{s}_m, \tag{1}$$

where t_0^m is the arrival time of the wave front m to the origin of coordinates, $\vec{r}_i$ is the position of station i, and $\vec{s}_m$ is the apparent slowness vector that characterizes the propagation of the wave fronts. The modulus, S, and direction clockwise from north, A, of the apparent slowness vector correspond to the inverse of the apparent velocity and propagation azimuth of the waves, respectively. The delays among arrivals of a signal characterized by a slowness vector $\vec{s}_m$ to different stations of the seismic array are given by

$$\Delta t_{ij}^m = \Delta \vec{r}_{ij} \cdot \vec{s}_m, \tag{2}$$

where $\Delta t_{ij}^m = t_j^m - t_i^m$ is the difference of arrival times of signal m to stations i and j and $\Delta \vec{r}_{ij} = \vec{r}_j - \vec{r}_i$ represents the relative position of stations i and j.

[7] The comparison of these delays – corresponding to a plane wave – with the delays obtained from the seismic data allows us to estimate the apparent slowness vectors of the recorded signals. This estimate can be done in several ways that lead to a variety of array methods in the time and frequency domains. Although based on very different assumptions and techniques, most methods amount to the calculation of a certain magnitude $F(\vec{s})$ that depends on the apparent slowness vector and quantifies the similarity between the actual wave delays and the plane wave delays given by equation (2). The distribution of F in the slowness vector space is used to estimate the slowness vectors of the recorded wave field, usually by finding the slowness vector $\vec{s}_{\max}$ that provides a maximum of the selected magnitude, $F(\vec{s}_{\max}) = \max\{F(\vec{s})\}$. The shape of the F function on the slowness vector domain is related to the way in which each method deals with noise and gives a measure of the uncertainty of the slowness vector estimate. A narrow peak centered at a particular slowness vector would represent a well-defined solution, while a broad peak means that F is relatively insensitive to changes in the apparent slowness vector, and thus large uncertainties are to be expected.

[8] Several array methods are available in the literature, characterized by different definitions of F. An intuitive example of a magnitude that is able to evaluate the similarity between the actual wave delays and the delays produced by the arrival of a plane wave front is the inverse of the residual of the least squares fit

$$F_{LS}(\vec{s}) = \left(\frac{2}{N(N-1)} \sum_{i=1}^{N-1} \sum_{j=i+1}^{N} \left(\Delta t_{ij}^{measured} - \Delta \vec{r}_{ij} \cdot \vec{s} \right)^2 \right)^{-1/2}. \tag{3}$$

More elaborate methods take advantage of the properties of different functions (both in time and frequency domains) to reduce the uncertainty of the slowness vector estimates and increase the resolution capabilities. For instance, the average cross-correlation (ACC) method [*Del Pezzo et al.*, 1997; *Almendros et al.*, 1999] assumes a function

$$F_{CC}(\vec{s}) = \frac{2}{N(N-1)} \sum_{i=1}^{N-1} \sum_{j=i+1}^{N} CC_{ij} \left(\frac{\Delta \vec{r}_{ij} \cdot \vec{s}}{\Delta T} \right), \tag{4}$$

where CC_{ij} is the normalized cross correlation of traces i and j and ΔT is the sampling interval. The quantity in parenthesis depends on the slowness vector and represents

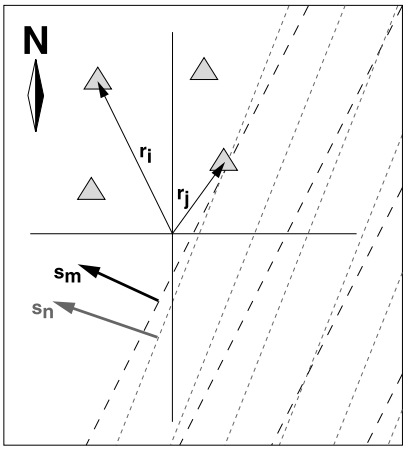

Figure 1. Sketch of the situation addressed by the RelSE method. Two wave fronts characterized by similar slowness vectors $\vec{s}_m$ and $\vec{s}_n$ incide upon a seismic array. The difference of slowness vectors $\vec{s}_n - \vec{s}_m$ can be estimated from the relative wave front delays at the array stations.

the number of samples that the traces are delayed before calculating CC_{ij}. Another example is the multiple signal classification (MUSIC) method [*Schmidt*, 1986; *Goldstein and Archuleta*, 1991]. This method is specifically designed to deal with noise and simultaneous arrivals of several wave fronts. The selected function is in this case

$$F_{MU}(\vec{s}) = \left(\sum_{k=Q+1}^{N} |\vec{a}(\vec{s}) \cdot \vec{v}_k|^2 \right)^{-1}, \qquad (5)$$

where $\vec{a}$ is defined by $a_j = \exp(i2\pi f \vec{r}_j \cdot \vec{s})$, $j = 1 \ldots N$; Q is the number of incoming signals; and $\vec{v}_k$, with $k = Q + 1 \ldots N$, represents a subset of $N - Q$ eigenvectors of the $N \times N$ covariance matrix of the array traces corresponding to small eigenvalues, that are used to define the noise subspace (see *Goldstein and Archuleta* [1991] for details).

[9] In general, high-resolution methods such as MUSIC provide narrower peaks of the $F(\vec{s})$ distributions and better accuracy of the slowness vector estimates. But, depending on the particular situation, different methods might be preferred. In any case, the choice of a method is not the only factor that controls the shape of $F(\vec{s})$. The spatial and temporal samplings of the wave field (array aperture and configuration, sampling interval), characteristics of the seismic signal (frequency content, amount of seismic noise), and presence of local heterogeneities beneath the array site (producing waveform distortions and station delays) impose severe constraints on our capability to obtain precise estimates of slowness vectors from array data. As an example, the typical size of the uncertainty region in the slowness vector domain for a signal with a frequency of a few Hz recorded with good signal-to-noise ratio on a dense seismic array with aperture of a few hundred meters deployed on a volcanic setting is ~0.2 s/km [*Chouet et al.*, 1997, 1998; *Almendros et al.*, 2000, 2001a; *Saccorotti et al.*, 2001a, 2001b].

2.2. RelSE: A Relative Slowness Estimate Method

[10] Uncertainties in the slowness vector estimates obtained with usual array methods are adequate for many applications. However, in the case of earthquake multiplets, we can improve drastically the accuracy of our estimates using a relative approach based on waveform similarity. In the following, we introduce the relative slowness estimate (RelSE) method, that constitutes an application of precise relative timing to data recorded on small-aperture seismic arrays. The key issue which constitutes the motivation for the method proposed is that waveform resemblance among multiplet earthquakes recorded at a single seismometer is generally better than waveform resemblance among seismograms of a single

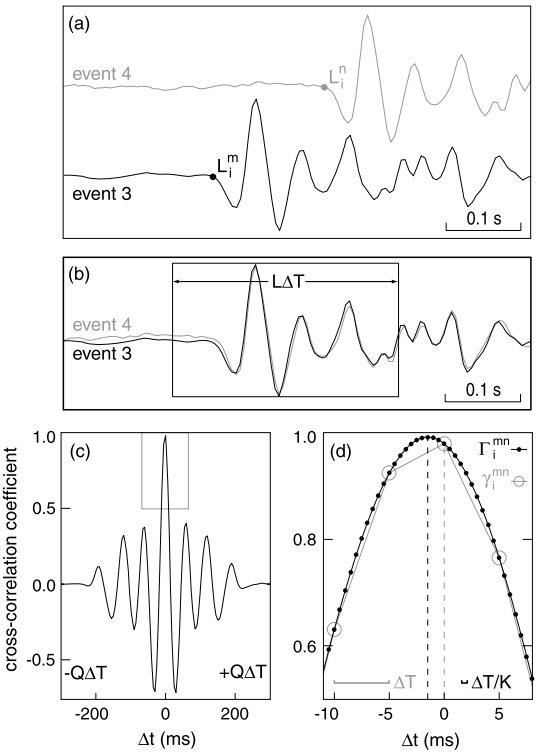

Figure 2. Example of the procedure to determine accurate delays using the interpolation of a CC function. (a) Seismograms of two earthquakes recorded at the same station. The samples labeled L_i^m and L_i^n identify a similar feature, in this case the P wave onset. (b) Seismograms aligned by removing the earthquake and propagation delays. The box represents the analysis window of duration $L\Delta T$. (c) CC function of the two traces, γ_i^{mn}, calculated for lag times between $-Q\Delta T$ and $Q\Delta T$, with $Q = 60$. (d) CC function γ_i^{mn} and its interpolated version Γ_i^{mn}, obtained using $K = 10$ (see text for explanations).

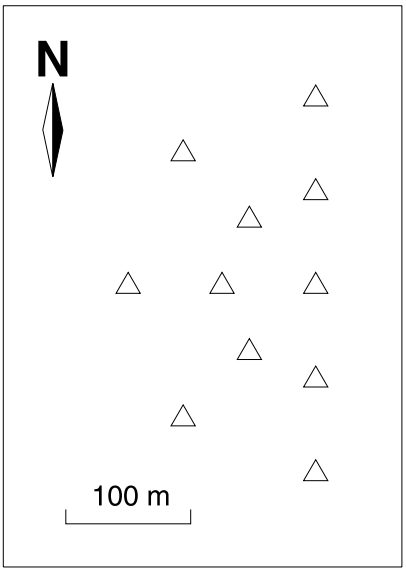

Figure 3. Configuration of the synthetic seismic array used for the tests of the RelSE method.

earthquake recorded at different array receivers, even for small-aperture arrays. Therefore we are able to measure the delay between arrivals of two similar events to the same station with higher accuracy than the delay between arrivals of a single earthquake to different seismic stations.

[11] Let us suppose two wave fronts propagating across a seismic array with slightly different apparent slowness vectors $\vec{s}_m$ and $\vec{s}_n$ (Figure 1). The RelSE method is designed to estimate with high accuracy the difference of slowness vectors $\vec{s}_n - \vec{s}_m$. If the wave fronts are produced by similar earthquakes belonging to a multiplet, we can determine very precisely the delays $\Delta t_i^{mn} = t_i^n - t_i^m$, that represent differences of the arrival times of two earthquakes m and n to the same station i. Estimates of delay times of events with similar waveforms can be achieved with accuracy beyond the sampling interval using two basic approaches. The first one is the cross-spectrum (CS) method, a frequency-domain method that calculates the slope of the phase of the cross spectrum [*Fremont and Malone*, 1987; *Ito*, 1990; *Got et al.*, 1994; *Ratdomopurbo and Poupinet*, 1995; *Poupinet et al.*, 1996; *Got and Coutant*, 1997; *Lees*, 1998]. The second is the cross-correlation (CC) method, that works in the time domain and uses an interpolation of the CC function to determine the delays among wave arrivals [*VanDecar and Crosson*, 1990; *Deichmann and Garcia-Fernandez*, 1992; *Mezcua and Rueda*, 1994; *Shearer*, 1997; *Saccorotti et al.*, 2002]. The choice of an approach depends on the degree of waveform similarity, frequency content of the signals, and signal-to-noise ratio (SNR). In general, since coherency depends critically on the presence of noise and decays faster for higher frequencies, the CS method yields best results for low-frequency signals with high SNR. On the contrary, the CC method is more stable and robust in those situations where signals have relatively low SNR [*Augliera et al.*, 1995; *Cattaneo et al.*, 1997].

[12] The delays Δt_i^{mn} are related to the station positions and apparent slowness vectors of the incident signals by

$$\Delta t_j^{mn} - \Delta t_i^{mn} = \Delta t_{ij}^n - \Delta t_{ij}^m = \Delta \vec{r}_{ij} \cdot \Delta \vec{s}_{mn} \tag{6}$$

where $\Delta \vec{s}_{mn} = \vec{s}_n - \vec{s}_m$ is the difference between the slowness vectors corresponding to the two signals. In order to estimate this difference of slowness vectors, we define for each pair of arriving wave fronts m and n a function similar to equation (3) that represents the inverse of the residual of the least squares fit of the measured $\Delta t_j^{mn} - \Delta t_i^{mn}$ to a plane wave front

$$F_{mn}(\vec{s}) = \left(\frac{2}{N(N-1)} \sum_{i=1}^{N-1} \sum_{j=i+1}^{N} \left(\Delta t_j^{mn} - \Delta t_i^{mn} - \Delta \vec{r}_{ij} \cdot \vec{s} \right)^2 \right)^{-1/2} \tag{7}$$

The best estimate of the difference of slowness vectors of the two signals corresponds to the value of $\vec{s}$ that yields the maximum of this F_{mn} function.

2.3. Implementation of the RelSE Method

[13] The application of the RelSE method to a multiplet of similar events consists of the following three steps.

2.3.1. Slowness Vector of the Master Event

[14] The first step is to calculate an independent estimate of the slowness vector of one of the multiplet members, $\vec{s}_m$,

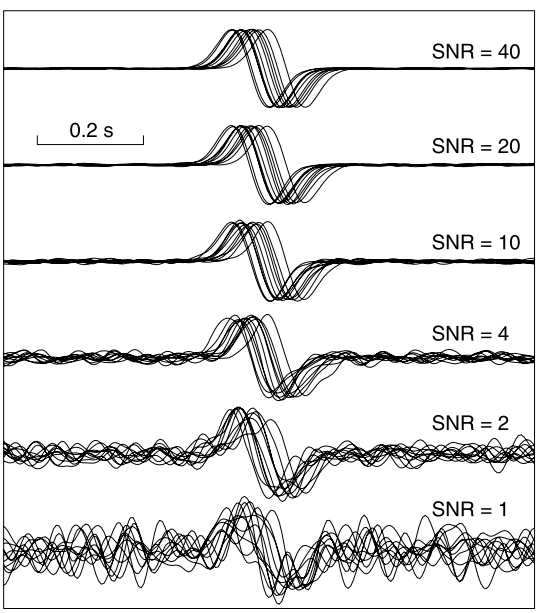

Figure 4. Examples of synthetic seismograms generated to simulate the arrival of a plane wave front characterized by an apparent slowness of 0.25 s/km and azimuth of 30° to the seismic array in Figure 3, for different levels of noise.

which will be used as a master event. For this task, we may use any conventional array technique.

2.3.2. Precise Measurements of Delay Times

[15] The second step is measuring the delay times Δt_i^{mn} between the master event and other multiplet members at every station of the array. Since we are interested just in the delays related to small differences of slowness vectors, we start by removing other effects. First of all, we determine the earthquake delay (ED), which is the time span between the occurrence of the two earthquakes. ED is measured at one of the traces for the master and secondary events by selecting samples L_i^m and L_i^n (Figure 2a) that identify a similar feature in both seismic events, for example the *P* wave onset. Correcting for ED (Figure 2b) means assuming that the earthquakes have occurred simultaneously.

[16] Additional delays for the remaining traces, due to wave propagation across the array, are given in the plane wave front approximation by equation (2). We refer to them as propagation delays (PD). PDs are calculated using the slowness vector of the master event, that for the moment constitutes our best estimate of the slowness vectors of the whole multiplet. Correcting for PD constitutes a procedure named "seismogram alignment" by *Goldstein and Archuleta* [1991]. It represents a translation of the origin in the slowness vector domain, which becomes situated just at the slowness vector of the master event. Therefore the calculated slowness vectors are relative to the master slowness vector.

[17] After correcting for ED and PD, any remaining delays constitute clues toward the relative apparent slowness vector. The precise determination of relative slowness vectors relies upon our ability to measure these residual delays as precisely as possible. In the RelSE method, accurate measurements of delay times are obtained from interpolations of the CC functions of the seismograms corresponding to the master and secondary events. We select an analysis window of length $L\Delta T$ containing the portion of the signal of interest (Figure 2b). CC functions between the master and secondary events at each station, γ_i^{mn}, are then calculated for time lags in a range of $\pm Q$ samples (Figure 2c). Rough estimates of the delays can be obtained from the position of the maxima of these functions, although more accurate values can be obtained by interpolation. Each sampling interval is divided in K intervals. CC values at the K-1 new sampling times are calculated using spline interpolation [*Press et al.*, 1992], keeping the values of the actual samples. This operation produces the interpolated CC functions Γ_i^{mn} (Figure 2d), and effectively means that the CC function, originally defined at $2Q + 1$ samples, is defined now at $2QK + 1$ samples. That is, we multiply by K the sampling frequency. The maxima of these Γ_i^{mn} provide accurate estimates of the delays between the master and secondary events at every station of the seismic array.

2.3.3. Determination of the Maximum of F_{mn}

[18] The third step in the application of the RelSE method consists in using equation (7) with the measured time delays. The differences of delays at two stations are given by

$$\Delta t_j^{mn} - \Delta t_i^{mn} = \left(\mu_j - \mu_i\right)\Delta T/K, \tag{8}$$

where μ_i represents the interpolated sample in which Γ_i^{mn} reaches its maximum. These values are introduced into equation (7) to obtain the distribution of $F_{mn}(\vec{s})$ in the slowness vector domain. The relative slowness vector corresponding to the maximum of F_{mn} is determined by grid search. This vector is our best estimate of the difference of slowness vectors $\Delta\vec{s}_{mn}$. Therefore the slowness vectors of secondary events can be calculated as

$$\vec{s}_n = \vec{s}_m + \Delta\vec{s}_{mn}. \tag{9}$$

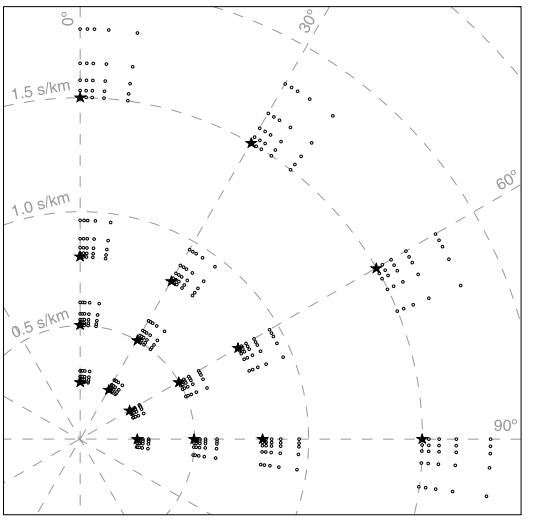

Figure 5. Sketch of the slowness vectors selected for the tests. For each of the 16 groups, the star represents the slowness vector of the master event, $\vec{s}_m$. Dots mark the slowness vectors $\vec{s}_n$ of the 25 events that we compare to the master event using the RelSE method.

3. Tests of the RelSE Method

[19] In order to test the capabilities of the RelSE method, we applied it both to synthetic and real data. In the first case, we generated two sets of similar seismograms W_i^m and W_i^n, $i = 1\ldots N$, corresponding to the arrivals of signals characterized by apparent slowness vectors $\vec{s}_m$ and $\vec{s}_n$, respectively, to the stations of a seismic array. In the second case, real noise was added to a real earthquake recorded at a seismic array. We applied the RelSE procedure to these data and considered the results to understand the resolution performance and to assess the confidence regions associated with the solutions provided.

3.1. Synthetic Environment

[20] Synthetic seismograms were produced for a seismic array composed of 11 receivers distributed in a semicircular configuration with aperture of 300 m (Figure 3). We assumed a sampling interval of 5 ms. The signals are Ricker wavelets defined by

$$X(t,\tau_0) = A\left(\frac{t-\tau_0}{\tau}\right)\exp\left(-\left(\frac{t-\tau_0}{\tau}\right)^2\right) \tag{10}$$

where A is a constant, τ_0 is the delay of the signal from the origin time and τ is a measure of the pulse width. We

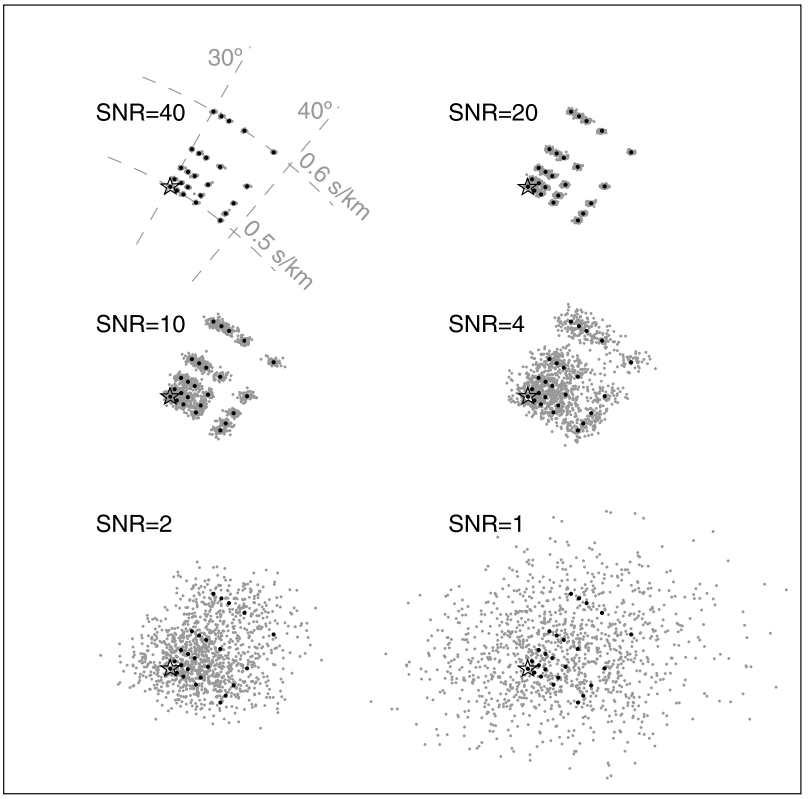

Figure 6. Examples of the results obtained from the relative slowness estimates of similar earthquakes using a master event with S_m = 0.5 s/km and A_m = 30°, for different levels of noise. Solid dots show the theoretical solutions, while grey dots mark estimates obtained by application of the RelSE method to different sets of noisy traces. The star shows the slowness vector of the master event.

selected $A = -\sqrt{2e}$ and τ = 0.05 s for a signal with positive first motion, maximum amplitude equal to unity and duration of about 0.2 s. To simulate a signal characterized by a slowness vector $\vec{s}$, seismograms were delayed by an amount defined by equation (1) for the particular set of propagation parameters assumed. Therefore the initial time τ_0 becomes a function of the apparent slowness vector $\vec{s}$ and the station position $\vec{r}_i$. We selected the central station of the array as the origin of coordinates and set the origin of time at 4 s before the arrival of the signal to the origin. Consequently, the arrival time to station i is given by

$$\tau_i(\vec{s}) \equiv \tau_0(\vec{s}, \vec{r}_i) = \vec{r}_i \cdot \vec{s} + 4 \text{ s}. \tag{11}$$

[21] We added incoherent noise to the traces. The noise samples were generated by filtering random time series of numbers between −1 and 1 in the 0.5–15 Hz band and renormalizing to maximum amplitude 1. Although simplistic, we think this model of seismic noise is appropriate for the present application. After all, we are comparing seismic waveforms recorded at the same station but at different times determined by the occurrence of the multiplet earthquakes. Repeating waveforms might happen in the noise wave field, for example associated with bursts of cultural noise. But there is no reason to think that these repeating waveforms will occur simultaneously with the earthquakes. Nevertheless, we also test the method using real noise and compare the results with those obtained using this simplistic noise model (see section 3.4).

[22] The final seismogram at station i is composed of signal and noise as follows

$$W_i(t, \vec{s}) = X(t, \tau_i(\vec{s})) + \frac{1}{\text{SNR}} \xi(t), \tag{12}$$

where $\xi(t)$ represents a pink noise time series and SNR is the signal-to-noise ratio. Figure 4 shows an example of the seismograms generated at the different stations of the synthetic array for different values of SNR.

3.2. Resolution and Effect of Noise

[23] We performed a series of tests of the RelSE method using two sets of seismograms generated for the synthetic array with different slowness vectors. We selected a grid of 16 slowness vectors $\vec{s}_m$ for the master event, defined by apparent slownesses of S_m = 0.25, 0.5, 0.8, and 1.5 s/km and propagation azimuths of A_m = 0, 30, 60, and 90° (stars in Figure 5). For each slowness vector $\vec{s}_m$ = (S_m, A_m), we

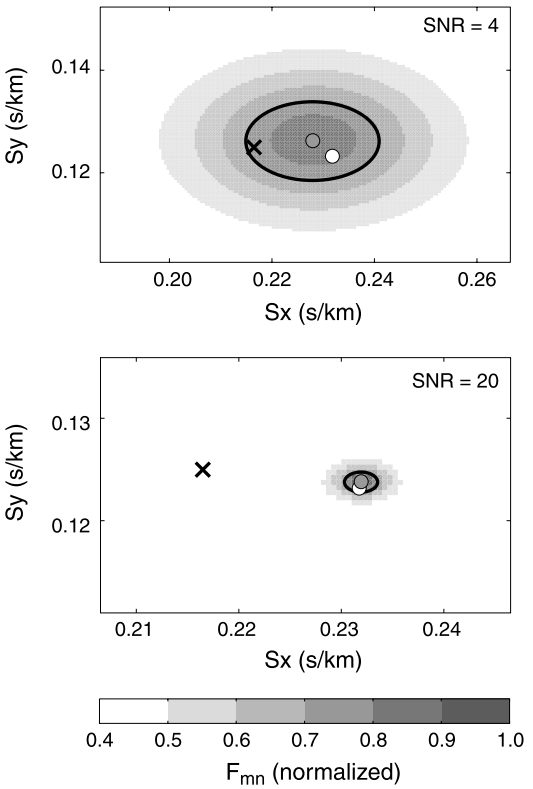

Figure 7. Distribution of F_{mn} in the slowness vector domain for SNRs of (top) 4 and (bottom) 20, showing the maximum used to define the relative slowness vector estimate. In both cases a cross marks the position of the master event slowness vector; an open dot represents the slowness vector of the secondary event; and a shaded dot indicates the position of the maximum of F_{mn} and therefore our best estimate of the slowness vector corresponding to the secondary event.

defined the slowness vectors of the secondary events, $\vec{s}_n = (S_n, A_n)$, using a second grid of 25 slowness vectors. They represent propagation parameters similar to $\vec{s}_m$ and are given by

$$S_n = S_m(1 + dS) \quad , \quad A_n = A_m + dA \tag{13}$$

where dS = 0, 0.02, 0.05, 0.1, and 0.2 and dA = 0, 1, 2, 4, and 8° (dots in Figure 5). We generated seismograms corresponding to the master and secondary events with six different SNRs of 40, 20, 10, 4, 2, and 1. In order to properly represent the random nature of noise, and have a statistically meaningful ensemble, we generated in every case 50 different sets of traces corresponding to the slowness vector $\vec{s}_n$, in which the signal X is exactly the same but with different realizations of ξ (see equation (12)). We applied the RelSE method to a window of 0.3 s centered at the wave arrival at 4 s from the first sample, with the parameters Q = 30 and K = 20 (see section 2.2). The traces were filtered using a weak zero-phase filter in the range 1–25 Hz. In order to optimize the grid search of the maximum of F_{mn}, we defined four slowness domain sizes and grid spacings that were applied successively. Each domain was centered at the provisional maximum obtained with the previous domain, starting at (0, 0) that represents the slowness vector of the master event. In this way, we reduce the computation times and speed up the process. We selected sizes of 4, 1, 0.2, and 0.03 s/km and grid spacings of 0.2, 0.04, 0.008, and 0.0001 s/km, respectively.

[24] This procedure resulted in 6 × 16 × 25 × 50 = 120000 applications of the RelSE method. Figure 6 summarizes part of the results, corresponding to the estimates of the slowness vectors of the secondary events with respect to a master event characterized by slowness of S_m = 0.5 s/km and azimuth of A_m = 30°, for the different SNRs considered. For high SNR, when the waveforms are not significantly altered by the presence of noise, the resolution capabilities of the method are excellent. On the contrary, for signals with low SNR, the waveform similarity is so small (see Figure 4) that the method is not able to provide accurate solutions. In any case, we confirm that our relative approach improves greatly the resolution performance of absolute array methods. For example, for a SNR of 10 we are able to resolve clearly solutions separated just 0.03 s/km in apparent slowness or 2° in azimuth.

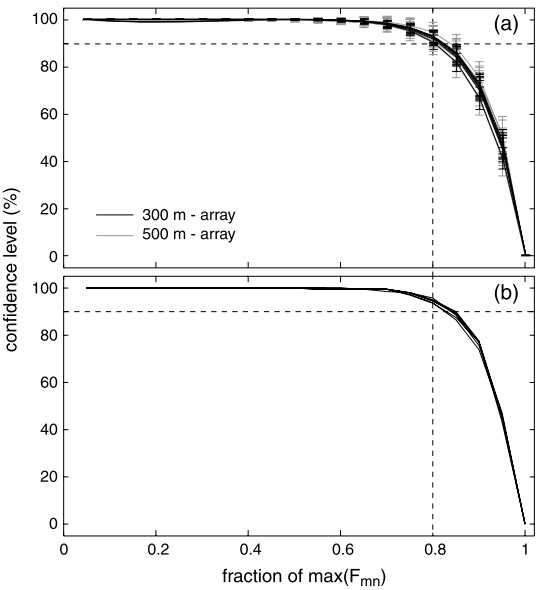

Figure 8. Percentage of slowness vector solutions contained within the isocontours corresponding to different levels of F_{mn} versus the levels that define the isocontours. (a) Results from synthetic tests using arrays with apertures of 300 (black) and 500 m (gray). There is one line for each SNR. The plots are averages of the results for all the slownesses and azimuths considered in the tests. Error bars indicate the standard deviations. (b) Results from the tests performed using real data. There is one line for each SNR.

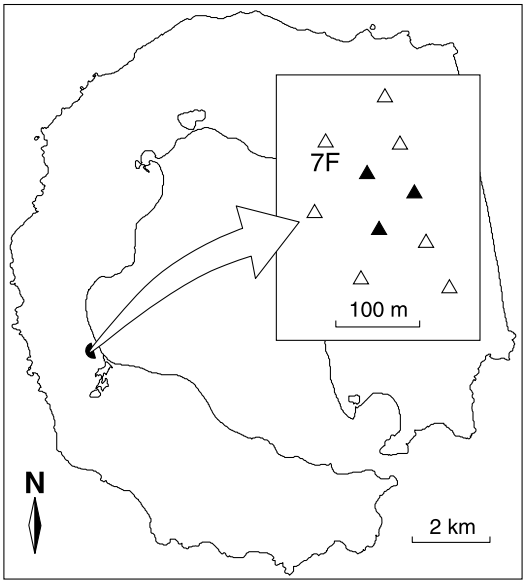

Figure 9. Map of Deception Island volcano, Antarctica, showing the location and configuration of the seismic array operating at Fumarole Bay during the 1999 seismic crisis. Solid triangles represent three-component seismometers, and open triangles are vertical sensors. The label 7F marks the station where the seismograms shown in Figure 10 have been recorded.

[25] The effect of noise and its influence on the resolution capabilities of the RelSE method can be better understood by looking at the shape of $F_{mn}(\vec{s})$. As an example, Figure 7 shows distributions of F_{mn} for events characterized by identical $\vec{s}_m$ and $\vec{s}_n$ but different SNRs. High SNR values yield narrow peaks that provide high slowness resolution, while low SNRs always yield low, broad peaks that are relatively insensitive to changes in slowness.

3.3. Definition of Confidence Limits

[26] The distributions of $F_{mn}(\vec{s})$ produced by the RelSE method not only reveal the best estimates of relative slowness vectors, but also point out the uncertainties of these estimates. The former information is obtained from the position of the maxima in the slowness domain, while the latter can be determined from their shape.

[27] Our tests suggest a direct relationship between the shape of F_{mn} and the magnitude of the estimated errors (i.e., the difference between the real and calculated slowness vectors). Large errors are always related to estimates whose F_{mn} functions display low, broad peaks, while small errors are linked to high, narrow F_{mn} peaks (Figure 7). In order to quantify this idea and assess the confidence limits associated with the relative slowness vector estimates, we investigated the percentage of test solutions for which the true slowness vector was contained within a given isocontour of the corresponding $F_{mn}(\vec{s})$ surface (Figure 8a). If we wish to ensure a reasonable confidence of 90%, we should select a value of 0.80 times the maximum of F_{mn}. Therefore 80% of the maximum F_{mn} constitutes an adequate choice for the assessment of confidence limits in the RelSE method.

[28] To check that this result is not affected by other factors such as the array aperture, we repeated the whole procedure described above for a seismic array with the same configuration as before (Figure 3) but with an aperture of 500 m. The

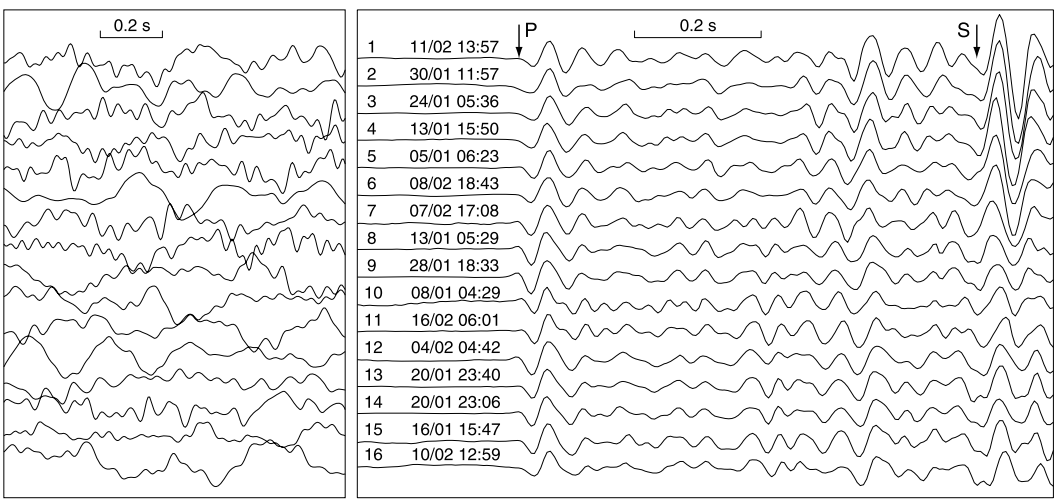

Figure 10. Seismograms of sixteen earthquakes recorded at station 7F of the Fumarole Bay array (see Figure 9) during the 1999 seismic swarm. The left panel shows normalized samples of pre-event noise recorded 2 s before the *P* wave arrival. The right panel shows the earthquake waveforms for 1 s after the *P* wave arrival. The *P* and *S* phases are labeled with arrows. Earthquake numbers refer to Table 1.

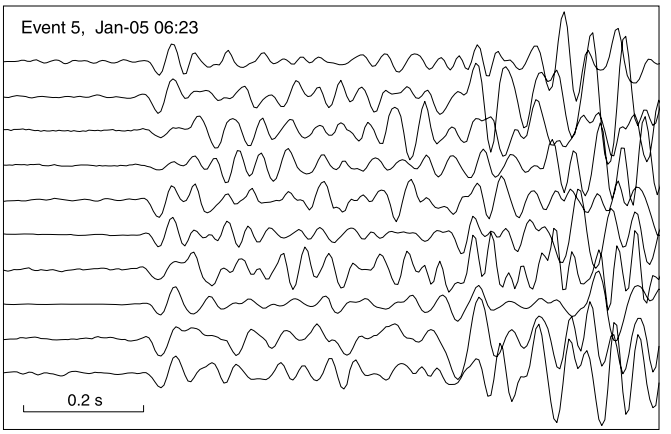

Figure 11. Seismograms corresponding to the earthquake marked as number 5 in Figure 10, recorded at all the sensors of the Fumarole Bay array.

results do not change significantly (Figure 8a), although for small slowness values we found a slight improvement due to the larger times needed to travel across the array.

3.4. Tests With Real Noise

[29] The synthetic signals generated to test the capabilities of the RelSE method may not be a perfect representation of the real wave fields. With this in mind, we proceeded to test the potential of the method with real data. The problem in this case is that there is no way to know what the real slowness vector is, and therefore we are not able to determine the errors. We solved this issue by calculating the slowness vector of an event relative to itself, which should obviously be zero. Any deviation would be an artifact due to the noise content.

[30] We selected the P wave arrival of an earthquake recorded at a seismic array (event 3; see section 4 below for details) and added different amounts of real noise recorded at the same array:

$$S' = S + \alpha \cdot N, \tag{14}$$

where S represents the original signal, N a noise sample, α the amount of extra noise, and S' the modified signal. Since S contains some noise already, the final SNR should be calculated as

$$\mathrm{SNR}' = \frac{S}{N + \alpha N} = \frac{\mathrm{SNR}}{1 + \alpha}. \tag{15}$$

We used α = 0.1, 0.2, 0.4, 1, 2, and 4, which correspond to modified SNRs between 6 and 22, approximately. For each α we repeated the calculations 200 times, using different samples of noise taken from several array records. As before, we investigated the percentage of test solutions for which the area defined by a given $F_{mn}(\vec{s})$ isocontour included the real solution – in this case, the origin of the relative slowness vector domain. We found that this percentage is equivalent to the case of purely synthetic events (Figure 8).

[31] Using these results, we define the error limits in the RelSE method as the region where F_{mn} takes values

Table 1. Estimates of Slowness Vectors for the 16 Events Analyzed Using the Conventional Average Cross-Correlation Approach

Event	Date	P Time	SNR	S_x, s/km	S_y, s/km	S, s/km	A, deg	CC_{max}
1	11 Feb.	1357:58.025	9	−0.20	−0.08	0.215	248	0.72
2	30 Jan.	1157:41.810	10	−0.22	−0.07	0.231	252	0.74
3	24 Jan.	0536:38.170	25	−0.24	−0.12	0.268	243	0.85
4	13 Jan.	1550:33.050	15	−0.26	−0.11	0.282	247	0.82
5	5 Jan.	0623:28.695	20	−0.24	−0.12	0.268	243	0.79
6	8 Feb.	1843:48.165	12	−0.30	−0.12	0.323	248	0.78
7	7 Feb.	1708:19.045	8	−0.30	−0.12	0.323	248	0.76
8	13 Jan.	0529:38.340	7	−0.24	−0.12	0.268	243	0.72
9	28 Jan.	1833:19.215	14	−0.24	−0.12	0.268	243	0.80
10	8 Jan.	0429:39.715	6	−0.27	−0.17	0.319	238	0.63
11	16 Feb.	0602:04.225	12	−0.27	−0.17	0.319	238	0.83
12	4 Feb.	0442:50.750	10	−0.27	−0.17	0.319	238	0.77
13	20 Jan.	2340:49.000	15	−0.24	−0.12	0.268	243	0.86
14	20 Jan.	2306:57.380	16	−0.24	−0.12	0.268	243	0.84
15	16 Jan.	1547:67.265	8	−0.25	−0.12	0.277	244	0.75
16	10 Feb.	1259:17.015	9	−0.24	−0.12	0.268	243	0.79

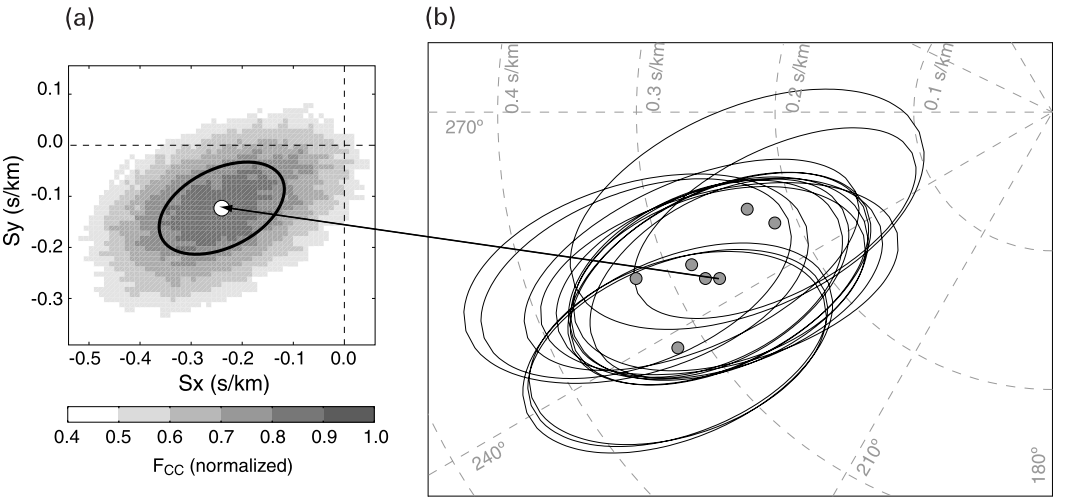

Figure 12. (a) Distribution of the array-average cross correlation in the slowness vector domain, F_{CC}, for event 13. The white dot marks the slowness vector corresponding to the maximum of F_{CC}. The thick line represents the 90% confidence region. (b) Results of the application of the conventional average cross-correlation method for the estimation of the slowness vectors corresponding to the *P* wave of the earthquakes shown in Figure 10. Ellipses indicate the 90% confidence regions. The arrow marks the solution for event 13 shown in Figure 12a.

larger than 80% of its maximum value. This can be expressed as

$$ERR(\vec{s}) = \{\vec{s} \mid F_{mn}(\vec{s}) \geq 0.80 \max(F_{mn})\}. \quad (16)$$

4. Application to Real Data

[32] As an example of the results that the proposed procedure is able to provide, we apply the RelSE method to a selection of data recorded at Deception Island volcano, Antarctica, during the 1999 seismic crisis [*Ibáñez et al.*, 2003a, 2003b]. At that time, a short-period, small-aperture seismic array was operating in Fumarole Bay (Figure 9). The array was composed of 10 seismometers distributed in a semicircular configuration with aperture of ~300 m. The sampling rate was 5 ms. More than 2000 local earthquakes were recorded during a period of two months (January–February). Preliminary locations of 863 earthquakes have been obtained using conventional ACC estimates of the apparent slowness vectors combined with ray-tracing through the velocity model. The distances along the ray paths were determined by the S-P delays [*Ibáñez et al.*, 2003b].

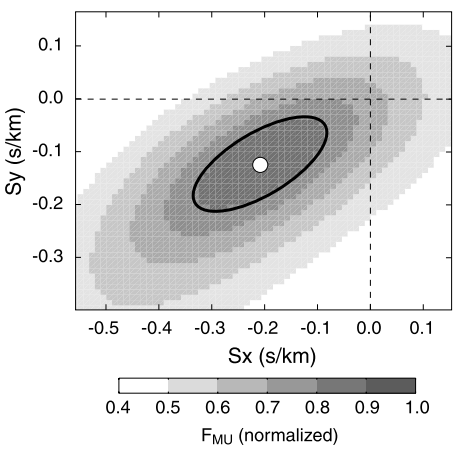

Figure 13. Distribution of the MUSIC power in the slowness vector domain, F_{MU}, for event 13. The open dot marks the slowness vector corresponding to the maximum of F_{MU}. The thick line represents the 90% confidence region.

Table 2. Estimates of Slowness Vectors for the 16 Events Analyzed Using the RelSE Method, Relative to Event 5

Event	S_x, s/km	S_y, s/km	S, s/km	A, deg	F_{max}, ms^{-1}
1	−0.2413	−0.0855	0.25595	250.45	0.40
2	−0.2547	−0.0910	0.27042	250.31	0.78
3	−0.2402	−0.0965	0.25882	248.08	0.75
4	−0.2368	−0.0950	0.25510	248.10	0.75
5	−0.2400	−0.1200	0.26833	243.43	...
6	−0.2538	−0.1017	0.27338	248.13	1.04
7	−0.2736	−0.1321	0.30379	244.20	0.40
8	−0.2412	−0.1406	0.27917	239.73	0.57
9	−0.2510	−0.1425	0.28861	240.38	0.54
10	−0.2507	−0.1583	0.29648	237.70	0.40
11	−0.2554	−0.1717	0.30774	236.06	0.43
12	−0.2543	−0.1508	0.29563	239.30	0.56
13	−0.2324	−0.1426	0.27265	238.43	0.51
14	−0.2446	−0.1453	0.28449	239.26	0.64
15	−0.2344	−0.1428	0.27446	238.62	0.41
16	−0.2487	−0.1582	0.29474	237.51	0.44

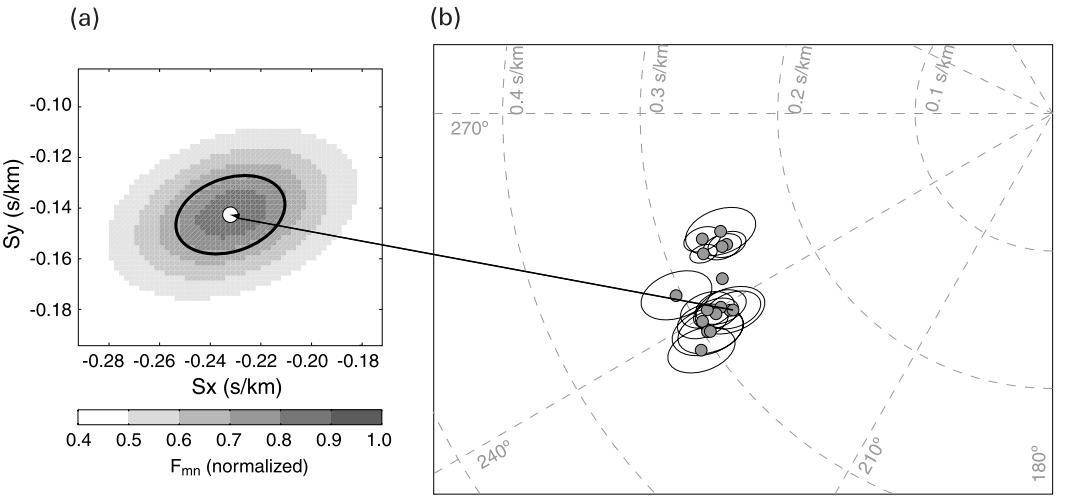

Figure 14. (a) Distribution of F_{mn} in the slowness vector domain for event 13. The open dot marks the slowness vector corresponding to the maximum of F_{mn}. The thick line represents the 90% confidence region. (b) Results of the application of the RelSE method for the estimation of the slowness vectors corresponding to the *P* wave of the earthquakes shown in Figure 10. Ellipses indicate the 90% confidence regions. The master event selected is event number 5 in Figure 10. The arrow marks the solution for event 13 shown in Figure 14a.

[33] For this work, we take advantage of the fact that some of the Deception Island earthquakes display very similar waveforms. Although site effects at a seismic station may induce resembling waveforms for virtually any earthquake, the occurrence of earthquakes with very different waveforms as well [*Ibáñez et al.*, 2003b] ensures that waveform similarity is intrinsically associated with the earthquake source. E. Carmona et al. (Characterization of fracture systems using precise array locations of earthquake multiplets recorded at Deception Island volcano, Antarctica, manuscript in preparation, 2004) grouped the earthquake data set in multiplets using the equivalence-class approach [*Aster and Scott*, 1993; *Maurer and Deichmann*, 1995] and a cross-correlation technique [*Saccorotti et al.*, 2002] that compares both the *P* and *S* waveforms recorded at the central station of the array. We selected one of these groups for the present analysis. The multiplet comprises sixteen members that occur along a time interval of more than a month. Figure 10 shows the corresponding seismograms recorded at one of the array stations. While pre-event noise displays very different waveforms, the similarity among the earthquakes is significant and lasts for several seconds. Conversely, Figure 11 shows the seismograms recorded at every array station for one of the events. Although there is some coherency among the traces, the waveforms are not alike, probably due to distortions produced in local heterogeneities under the array site. These plots illustrate the reason why a relative slowness estimate technique can provide more accurate results than its absolute counterpart, as discussed in section 2.2.

[34] Table 1 and Figure 12 show the results of the conventional ACC method applied to the estimate of the *P* wave slowness and azimuth. We used a slowness grid spacing of 0.01 s/km. Given the dimensions of the seismic

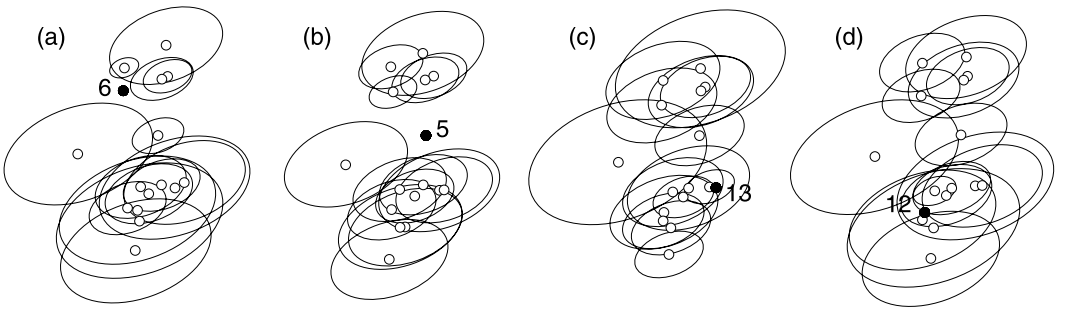

Figure 15. Comparison of the results obtained considering different earthquakes as master event (see Table 1): (a) event 6; (b) event 5; (c) event 13; (d) event 12.

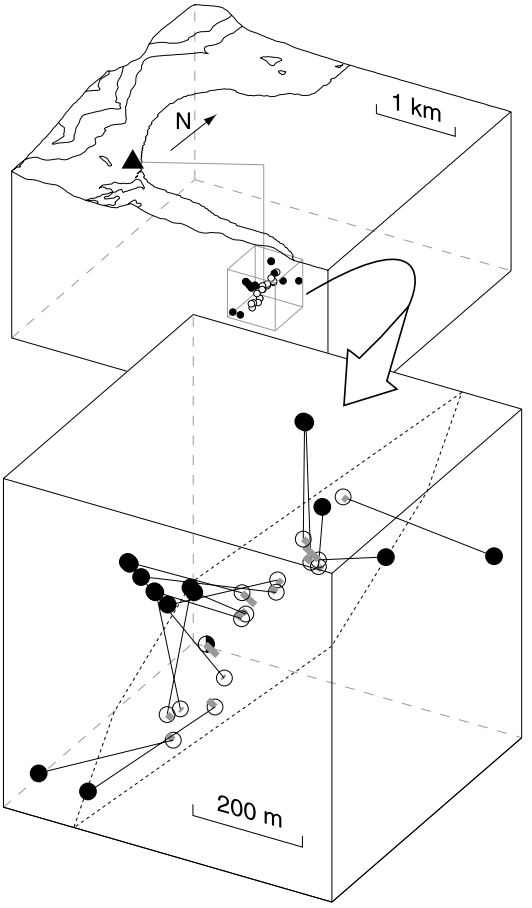

Figure 16. Comparison of ray tracing results using standard ACC (solid dots) and RelSE slowness vector estimates (open circles) for the selected earthquake multiplet. (top) General view of the Fumarole Bay region, showing the position of the seismic array (solid triangle) and the epicentral distance and depth of the source region (gray line). (bottom) Detailed view of the source region. For each earthquake, a black line joins the source locations obtained using the ACC and RelSE methods. For RelSE solutions, thick gray lines show the distance to the best fit plane indicated by the dotted line.

array and the sampling rate involved, a smaller variation in the slowness vector does not produce any change in the CCs and is not perceived by the array. Actually, the optimum grid spacing should be larger, because we have to consider also other effects such as the station density and presence of seismic noise (see, e.g., equation (12) from *Goldstein and Archuleta* [1991]). The absolute slowness vector estimates for the *P* waves of the multiplet events reveal that they propagate with slownesses of 0.22–0.32 s/km and azimuths of 243–252° from north. However, since the error regions are ellipses with approximate dimensions of 0.12 × 0.24 s/km, much larger than the range of variation of the solutions, we should not interpret the estimates in detail, but consider that we obtain basically the same solution for all sixteen events of the multiplet.

[35] For this particular earthquake multiplet, the application of a high-resolution frequency-slowness method such as MUSIC [*Schmidt*, 1986] does not improve significantly the results. The slowness vectors calculated with MUSIC are similar to the slowness vectors obtained with the ACC method and displayed in Figure 12. The exact values are not the same, but the approximate positions of the estimates and sizes of the error regions are alike. As an example, Figure 13 shows a slowness vector estimate performed using the MUSIC algorithm for event 13. Compare this plot with the left panel of Figure 12. In general, for seismograms that display a low level of noise, the results of the MUSIC and ACC methods are usually comparable. Nevertheless, the enhanced resolution capabilities of the MUSIC method are plainly evident when the data exhibit a low signal-to-noise ratio.

[36] We applied the RelSE method to the *P* wave onset of the multiplet earthquakes, using the same parameters as in the synthetic tests. We selected event 5 as master event, and obtained the results displayed in Table 2 and Figure 14. The solutions show apparent slownesses of 0.25–0.31 s/km and azimuths of 236–250°. The sizes of the error ellipses are greatly reduced to an average of about 0.03 × 0.05 s/km, which means that the confidence regions in the relative estimates have areas more than 20 times smaller than the confidence regions in the absolute estimates. We highlight that, although the relative slowness vectors have been accurately determined, the absolute estimates are not precisely known. The relative estimates should be considered as "floating" on the apparent slowness plane, since we still have to consider the uncertainty associated with the absolute estimate of the slowness vector of the master event.

[37] Figure 15 shows the relative slowness vectors obtained using different members of the multiplet as master events. Although there are small differences in the details, the relative positions of the estimated vectors remain the same. The method is robust enough so that the choice of reference event does not affect significantly the results.

5. Discussion

[38] The small sizes of the confidence regions shown in Figure 14 allow us to visualize a structure in the relative slowness vectors of the analyzed multiplet. They are distributed along a north-south trending band in the slowness vector domain, with varying density of solutions. This constitutes a hint toward the spatial distribution of earthquake sources, although the interpretation of detailed slowness vector data in terms of source locations is not trivial. However, if we assume simplifying hypotheses about the medium, such as lateral homogeneity and depth-increasing velocity, we could establish a link between the relative slowness vectors and relative source locations. Taking into account that the delays between the *S* and *P* wave arrivals are similar for all the earthquakes (about 0.7 s), a smaller apparent slowness of the *P* wave implies that the corresponding source location is deeper. Consequently, the features of the slowness vector distribution shown in Figure 14 might be explained if the

earthquakes originate at a fracture system located toward an azimuth of about 60° from the array site and show a southward increase of source depth. Because of the waveform similarity of the multiplet members, this system may indeed be regarded as a single crack dipping approximately to the south, although a more detailed analysis of the *S-P* times and a better knowledge of medium are needed to suggest further conclusions.

[39] Another observation supporting the accuracy of our estimates is that events with nearby slowness vectors show enhanced waveform similarity. For example, events 1–6, characterized by a larger relative amplitude of the *S* wave (Figure 10), are grouped together at the north end of the slowness vector band. The *S* wave amplitude seems to be more sensitive to small differences in source location among the multiplet members.

[40] This simple exercise illustrates that the accurate determination of relative slowness vectors opens up the possibility of performing relative source locations using multiplet data recorded on seismic arrays. Although in this case our reasoning was mostly based on qualitative arguments, quantitative analyses are also feasible. The combination of the RelSE method with an array location technique for a cluster of similar earthquakes would improve the results in two senses. First, the enhanced slowness resolution capabilities of the RelSE method would yield precise estimates of the relative slowness vectors. Therefore the location methods would provide more accurate relative source locations. Second, these array location methods depend on the assumed velocity structure of the medium. The waveform similarity of multiplet earthquakes ensures that most part of the path and site effects will be common. Therefore the uncertainties introduced in the relative locations by our imperfect knowledge of the medium could be reduced, although they remain in the absolute location of the master event.

[41] As an example, we use ray tracing to determine the relative source locations of the earthquake multiplet displayed in Figure 10. The data we need to know are: the apparent slowness vectors of the *P* wave arrivals; measurements of the S-P delay times; and a velocity model for the medium. In order to emphasize the performance of the RelSE method, we use both ACC and RelSE slowness vector estimates (Tables 1 and 2, respectively). The *S-P* times and velocity model are the same used by *Ibáñez et al.* [2003b]. Figure 16 shows the calculated source locations. ACC solutions (solid dots) were already obtained by *Ibáñez et al.* [2003b] in their analyses of the 1999 Deception Island earthquakes. They are contained within a small region northeast of the array site. No clear features are noticeable in this source distribution, most likely due to the large uncertainties associated with the ACC method. In fact, *Ibáñez et al.* [2003b] estimated the uncertainty of their locations in 500 m, larger than the average distance among the solutions given in Figure 16. Therefore the calculated ACC source locations should be basically regarded as coincident in a single position. On the contrary, RelSE solutions (open circles) are characterized by uncertainties of a few tens of meters. They appear in a thin, elongated cluster, defining approximately a plane dipping ~45° toward the southwest. The average distance from the source locations to the best fit plane is lower than 20 m. Although this plot constitutes a preliminary result, it suggests the possibility of using array data to determine precise relative source locations. Moreover, the RelSE method may add a new perspective to the problems for which the standard relative location techniques are useful, for example the determination of fracture geometries from microearthquake data, imaging of brittle regions in volcanoes, etc.

[42] Another potential application of the RelSE method is the analysis of long-period (LP) volcano seismicity. This type of seismicity is characterized by persistency of spectral features and occurrence of seismic events with similar waveforms. These facts have been related to nondestructive sources such as the resonance of cracks and conduits [e.g., *Chouet*, 1996b]. Seismic swarms of LP events with similar waveforms have been recorded at several volcanoes around the world [*Ibáñez et al.*, 2000; *Falsaperla et al.*, 2002]. In many cases, source locations can not be precisely estimated due to emergent onsets and/or unfavorable station distributions. Using seismic arrays allows for the estimates of approximate source locations of the LP seismicity [*Neuberg et al.*, 1994; *Almendros et al.*, 1999; *La Rocca et al.*, 2000; *Chouet*, 2003]. In particular, the source location technique developed by [*Almendros et al.*, 2001b] yields a 3D image of the sources of the seismo-volcanic activity [*Almendros et al.*, 2001a]. The image resolution of the source regions could be greatly improved with the use of the RelSE method.

[43] Although in section 4 we have applied the RelSE method just to the *P* wave onset of the earthquakes, it can be applied to other phases as well. The knowledge of the relative slowness vectors of seismic phases would add geometrical information – about azimuth and incident angles – to the temporal information – about time delays – considered so far in analyses of earthquake multiplets. This extra information could be very useful for a better understanding of the fine details of the Earth structure. Moreover, this method would not necessarily be restricted to conventional phases. Taking advantage of the ability of seismic arrays to detect and characterize any coherent wave front propagating across the array area [e.g., *Almendros et al.*, 2002b], RelSE analyses could comprise virtually the entire seismogram including the coda. Bearing this in mind, we anticipate very interesting applications of the RelSE method to the deterministic study of seismic scattering and coda generation.

[44] **Acknowledgments.** We thank F. Albarede, L. Steck, an anonymous editor, and two anonymous reviewers for their useful comments and suggestions. The data we have used were obtained during a seismic survey under project ANT-1111 of the Spanish Ministry of Science and Technology. We thank all participants in that survey for their help, and the Spanish Navy and Army for providing logistic aid. Partial support for the research was also provided by projects REN2001-3833/ANT and REN2001-2814-C04-04/RIES of the Spanish Ministry of Science and Technology, and by the European Union project EVR1-CT-2001-40021.

References

Almendros, J., J. M. Ibáñez, G. Alguacil, and E. Del Pezzo (1999), Array analysis using circular-wave-front geometry: An application to locate the nearby seismo-volcanic source, *Geophys. J. Int.*, *136*, 159–170.

Almendros, J., J. M. Ibáñez, G. Alguacil, J. Morales, E. Del Pezzo, M. La Rocca, R. Ortiz, V. Araña, and M. J. Blanco (2000), A double seismic

antenna experiment at Teide Volcano: Existence of local seismicity and lack of evidences of volcanic tremor, *J. Volcanol. Geotherm. Res.*, *103*, 439–462.

Almendros, J., B. Chouet, and P. Dawson (2001a), Spatial extent of a hydrothermal system at Kilauea Volcano, Hawaii, determined from array analyses of shallow long-period seismicity: 2. Results, *J. Geophys. Res.*, *106*, 13,581–13,597.

Almendros, J., B. Chouet, and P. Dawson (2001b), Spatial extent of a hydrothermal system at Kilauea Volcano, Hawaii, determined from array analyses of shallow long-period seismicity: 1. Method, *J. Geophys. Res.*, *106*, 13,565–13,580.

Almendros, J., B. Chouet, and P. Dawson (2002a), Array detection of a moving source, *Seismol. Res. Lett.*, *73*, 153–165.

Almendros, J., B. Chouet, P. Dawson, and C. Huber (2002b), Mapping the sources of the seismic wave field at Kilauea volcano, Hawaii, using data recorded on multiple seismic antennas, *Bull. Seismol. Soc. Am.*, *92*, 2333–2351.

Antolik, M., R. M. Nadeau, R. C. Aster, and T. V. McEvilly (1996), Differential analysis of coda Q using similar microearthquakes in seismic gaps, part 2, Application to seismograms recorded by the Parkfield high resolution seismic network, *Bull. Seismol. Soc. Am.*, *86*, 890–910.

Aster, R. C., and J. Scott (1993), Comprehensive characterization of waveform similarity in microearthquake data sets, *Bull. Seismol. Soc. Am.*, *83*, 1307–1314.

Aster, R. C., G. Slad, J. Henton, and M. Antolik (1996), Differential analysis of coda Q using similar microearthquakes in seismic gaps, part 1, Techniques and application to seismograms recorded in the Anza seismic gap, *Bull. Seismol. Soc. Am.*, *86*, 868–889.

Augliera, P., M. Cattaneo, and C. Eva (1995), Seismic multiplet analysis and its implications in seismotectonics, *Tectonophysics*, *248*, 219–234.

Brancato, A., and S. Gresta (2003), High precision relocation of microearthquakes at Mt. Etna (1991–1993 eruption onset): A tool for better understanding the volcano seismicity, *J. Volcanol. Geotherm. Res.*, *124*, 219–239.

Cattaneo, M., P. Augliera, D. Spallarossa, and C. Eva (1997), Reconstruction of seismogenetic structures by multiplet analysis: An example of Western Liguria, Italy, *Bull. Seismol. Soc. Am.*, *87*, 971–986.

Chouet, B. (1996a), New methods and future trends in seismological volcano monitoring, in *Monitoring and Mitigation of Volcano Hazards*, edited by R. Scarpa and R. Tilling, pp. 23–97, Springer-Verlag, New York.

Chouet, B. (1996b), Long-period volcano seismicity: Its source and use in eruption monitoring, *Nature*, *380*, 309–316.

Chouet, B. (2003), Volcano seismology, *Pure Appl. Geophys.*, *160*, 739–788.

Chouet, B., G. Saccorotti, M. Martini, P. Dawson, G. De Luca, G. Milana, and R. Scarpa (1997), Source and path effects in the wave fields of tremor and explosions at Stromboli Volcano, Italy, *J. Geophys. Res.*, *102*, 15,129–15,150.

Chouet, B., G. De Luca, G. Milana, P. Dawson, M. Martini, and R. Scarpa (1998), Shallow velocity structure of Stromboli Volcano, Italy, derived from small-aperture array measurements of Strombolian tremor, *Bull. Seismol. Soc. Am.*, *88*, 653–666.

Deichmann, N., and M. García-Fernández (1992), Rupture geometry from high-precision relative hypocentre locations of microearthquake clusters, *Geophys. J. Int.*, *110*, 501–517.

Del Pezzo, E., J. M. Ibáñez, and M. La Rocca (1997), Observations of high-frequency scattered waves using dense arrays at Teide volcano, *Bull. Seismol. Soc. Am.*, *87*, 1637–1647.

De Luca, G., R. Scarpa, E. Del Pezzo, and M. Simini (1997), Shallow structure of Mt. Vesuvius Volcano, Italy, from seismic array analysis, *Geophys. Res. Lett.*, *24*, 481–484.

Falsaperla, S., E. Privitera, B. Chouet, and P. Dawson (2002), Analysis of long-period events recorded at Mount Etna (Italy) in 1992, and their relationship to eruptive activity, *J. Volcanol. Geotherm. Res.*, *114*, 419–440.

Ferrazzini, V., K. Aki, and B. Chouet (1991), Characteristics of seismic waves composing Hawaiian volcanic tremor and gas-piston events observed by a near-source array, *J. Geophys. Res.*, *96*, 6199–6209.

Frémont, M. J., and S. Malone (1987), High precision relative locations of earthquakes at Mount St. Helens, Washington, *J. Geophys. Res.*, *92*, 10,223–10,236.

Goldstein, P., and R. Archuleta (1987), Array analysis of seismic signals, *Geophys. Res. Lett.*, *14*, 13–16.

Goldstein, P., and R. Archuleta (1991), Deterministic frequency-wavenumber methods and direct measurements of rupture propagation during earthquakes using a dense array: Theory and methods, *J. Geophys. Res.*, *96*, 6173–6185.

Goldstein, P., and B. Chouet (1994), Array measurements and modeling sources of shallow volcanic tremors at Kilauea Volcano, Hawaii, *J. Geophys. Res.*, *99*, 2637–2652.

Got, J. L., and O. Coutant (1997), Anisotropic scattering and travel time delay analysis in Kilauea volcano, Hawaii, earthquake coda waves, *J. Geophys. Res.*, *102*, 8397–8410.

Got, J. L., J. Frechet, and F. W. Klein (1994), Deep fault plane geometry inferred from multiplet relative relocation beneath the south flank of Kilauea, *J. Geophys. Res.*, *99*, 15,375–15,386.

Haase, J. S., P. M. Shearer, and R. C. Aster (1995), Constraints on temporal variations in velocity near Anza, California, from analysis of similar event pairs, *Bull. Seismol. Soc. Am.*, *85*, 194–206.

Ibáñez, J. M., E. Del Pezzo, J. Almendros, M. La Rocca, G. Alguacil, R. Ortiz, and A. García (2000), Seismovolcanic signals at Deception Island volcano, Antarctica: Wavefield analyses and source modeling, *J. Geophys. Res.*, *105*, 13,905–13,931.

Ibáñez, J. M., J. Almendros, E. Carmona, C. Martínez Arévalo, and M. Abril (2003a), The recent seismo-volcanic activity at Deception Island volcano, *Deep-Sea Res., Part II*, *50*, 1611–1629.

Ibáñez, J. M., E. Carmona, J. Almendros, G. Saccorotti, E. Del Pezzo, M. Abril, and R. Ortiz (2003b), The 1998–1999 seismic series at Deception Island volcano, Antarctica, *J. Volcanol. Geotherm. Res.*, *128*, 65–88.

Ito, A. (1990), Earthquake swarm activity revealed from high-resolution relative hypocenters; clustering of microearthquakes, *Tectonophysics*, *175*, 47–66.

La Rocca, M., S. Petrosino, G. Saccorotti, M. Simini, J. M. Ibáñez, J. Almendros, and E. Del Pezzo (2000), Location of the source and shallow velocity model deduced from the explosion quakes recorded by two seismic antennas at Stromboli Volcano, *Phys. Chem. Earth*, *25*, 731–735.

La Rocca, M., E. Del Pezzo, M. Simini, R. Scarpa, and G. De Luca (2001), Array analysis of seismograms from explosive sources: Evidence for surface waves scattered at the main topographical features, *Bull. Seismol. Soc. Am.*, *91*, 219–231.

Lees, J. (1998), Multiplet analysis at Coso geothermal, *Bull. Seismol. Soc. Am.*, *88*, 1127–1143.

Maurer, H., and N. Deichmann (1995), Microearthquake cluster detection based on waveform similarities with an application to the western Swiss Alps, *Geophys. J. Int.*, *123*, 588–600.

Mezcua, J., and J. Rueda (1994), Earthquake relative location based on waveform similarity, *Tectonophysics*, *233*, 253–263.

Neuberg, J., R. Luckett, M. Ripepe, and T. Braun (1994), Highlights from a seismic broadband array on Stromboli volcano, *Geophys. Res. Lett.*, *21*, 749–752.

Phillips, W. S. (2000), Precise microearthquake locations and fluid flow in the geothermal reservoir at Soultz-sous-Forêts, France, *Bull. Seismol. Soc. Am.*, *90*, 212–228.

Poupinet, G., W. L. Ellsworth, and J. Frechet (1984), Monitoring velocity variations in the crust using earthquake doublets: An application to the Calaveras fault, California, *J. Geophys. Res.*, *89*, 5719–5731.

Poupinet, G., A. Ratdomopurbo, and O. Coutant (1996), On the use of earthquake multiplets to study fractures and the temporal evolution of an active volcano, *Ann. Geofis.*, *39*, 253–264.

Poupinet, G., A. Souriau, and O. Coutant (2000), The existence of an inner core super-rotation questioned by teleseismic doublets, *Phys. Earth Planet. Inter.*, *118*, 77–88.

Press, W., B. Flannery, S. Teukolsky, and W. Vetterling (1992), *Numerical Recipes in Fortran: The Art of Scientific Computing*, 2nd ed., Cambridge Univ. Press, New York.

Ratdomopurbo, A., and G. Poupinet (1995), Monitoring a temporal change of seismic velocity in a volcano: Application to the 1992 eruption of Mt. Merapi (Indonesia), *Geophys. Res. Lett.*, *22*, 775–778.

Saccorotti, G., R. Maresca, and E. Del Pezzo (2001a), Array analyses of seismic noise at Mt. Vesuvius volcano, Italy, *J. Volcan. Geotherm. Res.*, *110*, 79–100.

Saccorotti, G., B. Chouet, and P. Dawson (2001b), Wavefield properties of a shallow long-period event and tremor at Kilauea Volcano, Hawaii, *J. Volcanol. Geotherm. Res.*, *109*, 163–189.

Saccorotti, G., J. Almendros, E. Carmona, J. M. Ibáñez, and E. Del Pezzo (2001c), Slowness anomalies from two dense seismic arrays at Deception Island volcano, Antarctica, *Bull. Seismol. Soc. Am.*, *91*, 561–571.

Saccorotti, G., E. Carmona, and J. M. Ibáñez (2002), Spatial characterization of Agron, southern Spain, 1988–1989 seismic series, *Phys. Earth Planet. Inter.*, *129*, 13–29.

Schmidt, R. (1986), Multiple emitter location and signal parameter estimation, *IEEE Trans. Antennas Propag.*, *34*, 276–280.

Shearer, P. M. (1997), Improving local earthquake locations using the L1 norm and waveform cross-correlation: Application to the Whittier

Narrows, California, aftershock sequence, *J. Geophys. Res.*, *102*, 8269–8284.

Song, X., and P. G. Richards (1996), Seismological evidence for differential rotation of the Earth's inner core, *Nature*, *382*, 221–224.

Stich, D., G. Alguacil, and J. Morales (2001), The relative locations of multiplets in the vicinity of the Western Almería (southern Spain) earthquake series of 1993–1994, *Geophys. J. Int.*, *146*, 801–812.

VanDecar, J. C., and R. S. Crosson (1990), Determination of teleseismic relative phase arrival times using multi-channel cross-correlation and least squares, *Bull. Seismol. Soc. Am.*, *80*, 150–169.

J. Almendros, E. Carmona, and J. Ibáñez, Instituto Andaluz de Geofísica, Universidad de Granada, E-18071-Granada, Spain. (alm@iag.ugr.es)

V. Characterization of fracture systems using precise array locations of earthquake multiplets: An example at Deception Island volcano, Antarctica

Characterization of fracture systems using precise array locations of earthquake multiplets: An example at Deception Island volcano, Antarctica

Carmona, E.[(1)], Almendros, J.[(1,2)], Peña, J. A.[(1,3)], Ibáñez, J. M.[(1,2)]

[(1)] Instituto Andaluz de Geofísica, Universidad de Granada, Spain
[(2)] Dpto. de Física Teórica y del Cosmos, Universidad de Granada, Spain
[(3)] Dpto. de Prehistoria y Arqueología, Universidad de Granada, Spain

Submitted to J. Geophys. Res.

Abstract. Volcano-tectonic earthquakes are common seismic events in active volcanic areas. The stress produced by volcanic processes is released through fracturing of the shallow crust. Very often, these earthquakes occur in multiplets with similar waveforms, a fact which indicates common source characteristics. In this work, we introduce a method that uses array techniques to calculate precise relative locations of earthquake multiplets. We use the relative slowness estimate (RelSE) method to determine accurately the apparent slownesses and propagation azimuths of the earthquakes, relative to a selected master event. We also obtain precise estimates of the S-P delays. This information is used to calculate precise relative locations by ray tracing in an Earth model. We applied this method to determine the characteristics of the fractures activated during the 1999 seismic series at the Deception Island volcano, Antarctica. We selected a set of 17 earthquake multiplets, initially located in a small (4x4 km) region a few km NE of the array site. We estimated precise locations for 14 of the clusters. In most cases, hypocenters were distributed in well-defined planar geometries. We found the best-fitting planes, which we interpreted as fractures in the medium. For two clusters, the method spatially separated the earthquakes into two subgroups. Thus we obtained two planes for each of these clusters, resulting in a total of 16 fracture planes. This is the first time that the orientations of fracture planes related to a seismic series have been obtained using a seismic array. We performed several tests to check various aspects in relation to the stability of the method and concluded that the results were robust. The dip angles indicate that the planes are mostly subvertical, while the strike angles clearly show a NW-SE trend for most of the planes and a few planes with NE-SW trends. The geometry and position of these planes suggest that the 1999 seismic series was influenced by regional tectonics, although the origin of the destabilization of the system may be related to the reactivation of a shallow magma chamber.

1. Introduction

The main objective of volcano seismology is to improve our knowledge of active volcanic systems through the analysis of the seismic signals that they generate. These signals contain information about many aspects of the volcano, for example parameters of the seismo-volcanic source (position, geometry, dynamics, energy, spatio-temporal evolution, etc) and characteristics of the medium (velocity structure, attenuation, spatial distribution of heterogeneities, etc). Pure volcanic events such as volcanic tremors and long period (LP) events provide insights into the mechanisms and dynamics of fluid transport within the volcanic system. In addition, volcano-tectonic (VT) events offer us an insight into the dynamics and geometry of brittle fractures in the medium, and thus constitute a powerful means of inves-

tigating the local state of stress produced by volcano dynamics (e.g. Chouet 1996).

Several tools can be used to achieve this objective. In volcanic regions the use of seismic arrays is very common as a complement to conventional seismic networks. The advantage of array techniques is that they provide a space-time sampling of seismic waves as they propagate across the array. These instruments are designed to estimate the apparent slowness vector, whose module represents the inverse of the apparent velocity of the waves and whose direction indicates their propagation azimuth. Arrays allow us to analyze signals characterized by the absence of clear seismic phases, such as volcanic tremors, LP events, earthquake codas, and even seismic noise. They also allow us to analyze low-magnitude VT earthquakes that cannot be recorded properly at distances of more than a few km. These tasks would be difficult using seismic networks, although new methodologies based on seismic amplitudes have recently been developed and applied to source location of LP seismicity (e.g. Battaglia et al. 2005).

Array techniques have been used to locate seismic events, investigate the temporal evolution of the source, analyze the characteristics of seismic noise, and study the details of the local structure. They have been applied at volcanoes such as Stromboli (Chouet et al. 1997; La Rocca et al. 2004), Etna (Saccorotti et al. 2004), Vesuvius (Saccorotti et al. 2001b), Teide (Del Pezzo et al. 1997; Almendros et al. 2000, 2007), Masaya (Metaxian et al. 1997), Arenal (Metaxian et al. 2002; Mora et al. 2006), Kilauea (Almendros et al. 2001a,b), Copahue (Ibáñez et al. 2008), and Colima (Palo et al. 2009). The use of array techniques to obtain spatial locations is based on three different approaches: circular wavefronts; ray-tracing; and joint location with various arrays. The first method is based on the estimate of the radius of curvature of the wavefront, and implicitly assumes nearby sources (Almendros et al. 1999). The second uses ray tracing in a predefined Earth model. In addition to the information on the apparent slowness vector provided by the array, we need to know the arrival times of P and S phases to determine the distance along the seismic ray. This requirement means that the technique can only be applied to earthquakes with clear phases (e.g. Del Pezzo et al. 1997; Almendros et al. 2000, 2007; Saccorotti et al. 2001b). Finally, the third method is based on the use of several arrays. The apparent slowness vectors obtained from each array are combined to determine the spatial position of the source. This method is powerful and flexible, and can be applied to any type of earthquake, including pure volcanic signals (Almendros et al. 2000, 2001a, b; La Rocca et al. 2000, 2008; Metaxian et al. 2002).

In any case, the source locations obtained with either seismic arrays or seismic networks are associated with a degree of uncertainty caused by various factors, some of which are related to the methodology selected. For example, for array analyses there is an error introduced by the approximation of the signals to plane wavefronts, the configuration of stations in the array, the slowness grid size and spacing, etc. For seismic networks, there are errors related to the phase picking, position of the stations, etc. On top of that, in both cases we find the effect of natural factors such as the heterogeneities of the velocity structure (that produce path and site effects), and the presence of seismic noise. The uncertainty intervals are relatively large, which produces generally low-accuracy hypocentral locations.

However, there are methods that in some cases allow us to obtain accurate locations. An example is the relative location of similar earthquakes. This method relies on the observation that seismic series contain earthquakes with very similar waveforms. This similarity is due to the fact that the earthquakes originate along the same fault plane and therefore share similar source mechanisms and hypocenter locations (Tsujiura 1983; Geller and Muller 1980). If these conditions were not met, we would see waveform differences due to the different mechanisms and locations (different P and S waveforms and travel times, distinct path effects, etc). Comparison of the seismograms produces the grouping of earthquakes into clusters characterized by high waveform similarity. Within each cluster, we can take advantage of this similarity to refine the phase picks and perform precise relative locations (Poupinet, et al. 1984; Maurer and Deichman, 1995).

Relative locations using network data have been obtained in tectonic and volcanic regions. In tectonic areas this technique is mainly used to gather information about the plane of rupture when focal mechanisms cannot be calculated, e.g. for the analysis of series of micro-

earthquakes (Deichmann and Garcia-Fernández 1992, Stich et al. 2001; Saccorotti et al. 2002; Scarfi et al. 2003; Massa et al. 2006; Ruiz et al. 2006; Ocaña et al. 2008, Carmona et al. 2009). Recently, relative locations have been used for the study of non-volcanic tremors (Shelly et al. 2009). In volcanic regions, absolute locations of VT earthquakes are particularly complicated be-

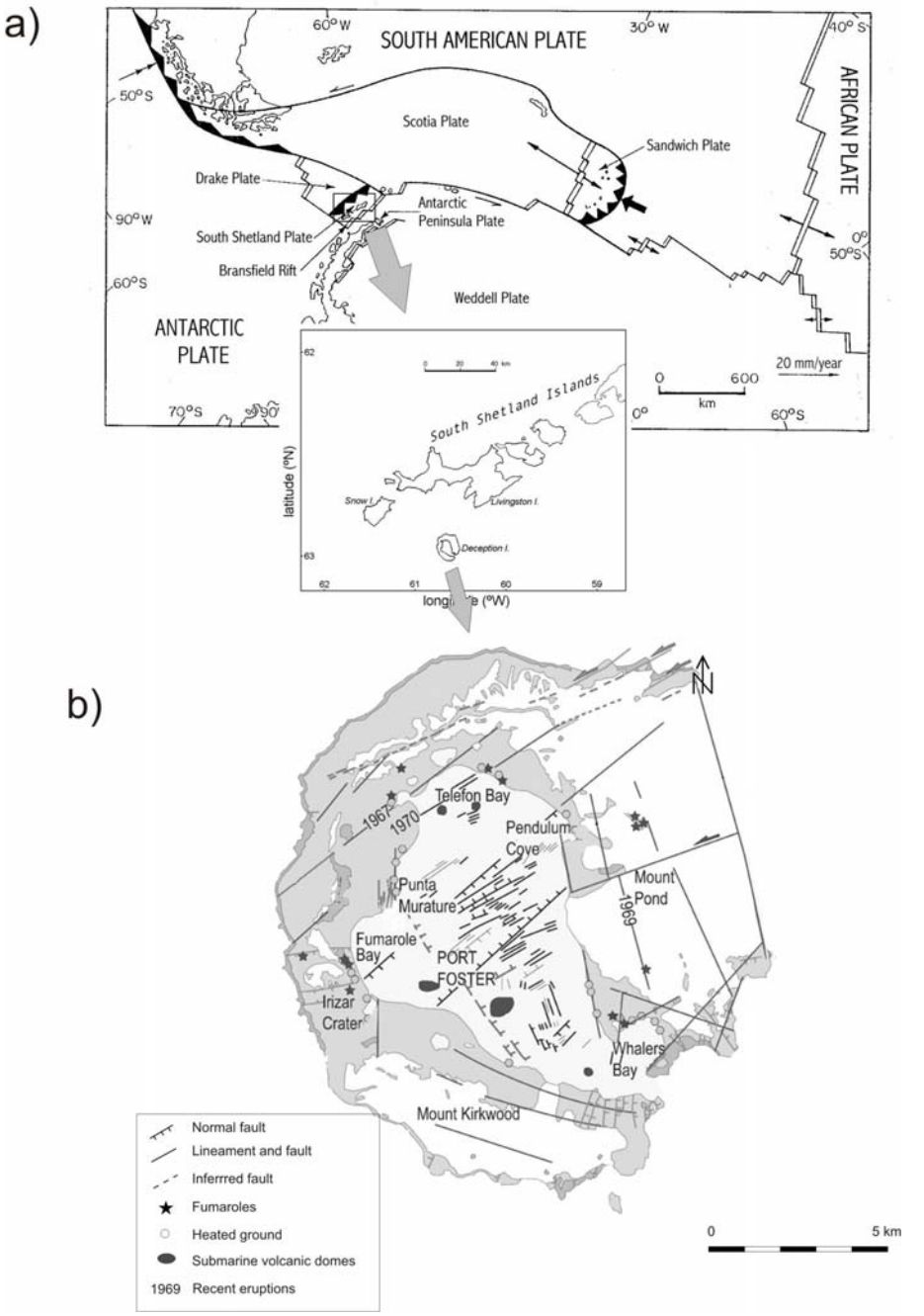

Figure 1. (a) Tectonic map of the Scotia region. The inset shows a map of the South Shetland Islands region. (b) Simplified geological map of Deception Island (modified from Maestro et al. 2004).

cause of the heterogeneity of the environment, the low magnitude of the events, the difficulty of establishing seismic networks with good coverage, etc. The relative location technique provides detailed information on the distribution of hypocenters of VT earthquakes. This enables us to define the extent and the geometry of active magmatic systems (Fremont and Malone 1987; Gillard et al., 1996; Jones, et al., 2001; Musumeci et al. 2002; Alparone and Gambino, 2003; Brancato and Gresta, 2003; Battaglia et al. 2004; Hensh, et al. 2008). It has also been applied to the analysis of temporal changes that occur in volcanoes as a result of internal dynamics and movements of magma (Ratdomopurbo and Poupinet 1995; Snieder and Hagerty 2004; Pandolfi et al. 2006; Carmona et al. 2007; Martini et al. 2009).

In this paper, we combine relative locations and array techniques. We develop a method based on the work of Almendros et al. (2004) that allows for the precise relative locations of microearthquakes recorded by a seismic array. The use of arrays ensures that we could apply the method even to earthquakes that are too small to be analyzed with conventional networks. We analyze a series of VT earthquakes that occurred in Deception Island, Antarctica, in 1999 (Ibáñez et al. 2003b). We compare the waveforms to select clusters of similar earthquakes. We obtain accurate estimates of the relative apparent slowness vectors and S-P delays and spatially locate the earthquake sources. The observed distributions of hypocenters fit to a plane, which we interpret as the rupture plane responsible for the generation of earthquakes. To check the robustness of the method, we perform a series of tests to confirm its validity for finding rupture planes with array techniques. Finally, we discuss the results in the regional tectonic and volcanic environment of Deception Island.

2. Tectonic Setting

Deception Island is one of the South Shetland Islands, lying 62º 43'S and 60° 57'W off the Antarctic Peninsula. Its regional tectonic framework is quite complex due both to its position in the Bransfield Strait, between the Antarctic Peninsula and the South Shetland Islands, and to the converging of several tectonic plates (Pelayo and Wiens 1989; Baraldo and Rinaldi 2000; Robertson-Maurice et al. 2003). These tectonic plates are represented by two major plates, the South American Plate and the Antarctic Plate, and three microplates, the Scotia, the Drake and the South Shetland (Fig. 1).

The South Shetland Islands trench presents a slow slab roll-back subduction process (Ibáñez et al. 1997; Robertson-Maurice et al. 2003) which led to the break-up and separation of the South Shetlands microplate from the Antarctic Peninsula, 2 Ma years ago, creating the well-known Bransfield Rift. In addition to normal faults, this rift also has three active extensional NE trending basins and is related to the volcanic activity in the area. The shallow regional seismicity (above 40 km) is consistent with the expansion of the rift, while the deepest seismicity is consistent with the subduction of the Drake plate (Pelayo and Wiens 1989; Ibáñez et al. 1997; Robertson-Maurice et al. 2003).

Deception Island is located on the extension axis of the Central Bransfield Basin and is probably one of the most active volcanoes in the Antarctic. Several volcanic eruptions have been reported in 1842, 1912, 1917 and more recently in 1967, 1969 and 1970 (e.g. Smellie 1988). The island has a horse-shoe shape with a flooded caldera and its emerged area is about 15 km in diameter. The origin of this peculiar morphology has several possible explanations. It may have been produced by the collapse of a large caldera due to powerful eruptions, which filled up and produced a ring-shaped fracture system (González-Ferrán and Katsui 1970; Baker et al. 1975). Another possible explanation could be that the caldera was formed by a depression caused by extensive tectonic movements along normal faults governed by a regional extensional trend, so ruling out previous findings as to the presence of circular faults (Martí et al. 1996; Rey et al. 1995; González-Casado et al. 1999). Moreover, tomographic models for the region image a high-velocity structure NW of Deception Island. This structure extends NE-SW parallel to the axis of the Bransfield Rift. It has been interpreted as the basement of the South Shetland Islands (Zandomeneghi et al. 2009), which supports the importance of the regional tectonics in the origin and evolution of Deception Island.

Three major fault systems were identified in this zone from field observations and seismic reflection data (Rey et al. 1995; Martí et al. 1996). The first major system is consistent with

the extensional tectonic regime of the Bransfield Strait, with NE-SW direction. These alignments are consistent with the eruptions of 1967 and 1970. The second system presents an approximately EW direction and coincides with various different alignments including the alignments of Mt. Kirkwood, the phreatomagmatic eruptions produced by these fissures and the alignments of submarine cones inside the caldera. The third system is NNW-SSE oriented and its main evidence is in the Costa Recta alignment (Fernández-Ibáñez et al. 2005). Other alignments can be observed in the Mt. Pond system faults, in the subparallel faults present throughout the Fumarole Bay and the Black Glacier, and in the eruptive fissures of 1969. In addition, geological surface observations, geophysical data, bathy-metric information, digital elevation models, morphological evidence of volcanic recent activity, etc, show the presence of a wide variety of fault systems and evidence the complexity of Deception Island (Martí et al. 1996; Gonzalez-Casado et al. 1999; Paredes et al. 2006; Maestro et al. 2007; Barclay et al. 2009).

3. Seismicity of Deception Island

In recent years Deception Island has been monitored from the perspective of several different geophysical disciplines (seismology, geochemistry, geodesy, gravimetry…) in Austral summer surveys. Its recent eruptions, the presence of two Antarctic bases and the arrival of tourism mean that detailed studies of its seismo-volcanic activity and the sources thereof must be performed.

Systematic monitoring of seismic activity in the island began in the 1950's. This first stage ended in the late 60's, when the most recent eruptions occurred. There is written evidence to the effect that there was a considerable increase in seismic activity in the area just before the eruptions. After the 1970 eruption, Deception Island was not monitored again until the Austral summer of 1987. Since then, local volcano-tectonic earthquakes and even some tremor episodes have been recorded. These records, obtained by vertical-component seismometers, enabled the first seismic studies of the island to be carried out (Vila et al. 1992, 1995). In the 1991-92 survey a considerable increase in activity was noted (Ortiz et al. 1997). Between 1994 and 1999 several seismic arrays were deployed in order to locate LP events and volcanic tremors (Almendros et al. 1997, 1999; Ibáñez et al. 2000). Since 1998, a variety of seismic instruments have been used, including seismic arrays, short-period stations and broadband stations. The monitoring of activity has usually been carried out during Austral summers. A permanent broadband station that allows researchers to obtain a continuous record was only deployed in January 2008 (Martínez-Arévalo et al. 2009).

Since the start of the monitoring surveys in Deception Island, the level of seismic activity has been variable. Periods of very low activity were often followed by others of substantially higher activity. Two maxima (in 1992 and 1999, see Ibáñez et al. 2003a) were considered of sufficient importance to be classified as seismic series. The seismic occurrence pattern between these two series was very similar. Until 1992 LP events predominated over VT earthquakes. In the 1992 series 766 VT earthquakes occurred during a two-month period, including some felt events (Ortiz et al., 1997). After this VT series the LP events started predominating over the VTs again. Between 1993 and 1998 seismic activity returned to its normal parameters, with variable activity levels (Ibáñez et al. 2003a). The second remarkable reactivation chapter took place during the 1998-99 survey, when a total of 3643 events were recorded. In both episodes the considerable increase in activity was probably due to a magmatic intrusion that did not reach the surface, causing local tectonic destabilization (Ortiz et al. 1997; Ibáñez et al. 2003a). In the next survey (1999-2000) several dozen VT events were registered, some of which were located in the same epicentral area as the January-February 1999 earthquakes. These events might correspond to the activation of the same fracture systems and could be related to the destabilization caused by the magmatic intrusion that produced the series. Some VT earthquakes, LP events, and volcanic tremor episodes occurred in the other annual surveys until February 2009, although the level of activity has been in general much lower.

4. Instruments

During the 1998-1999 Antarctic survey two seismic arrays were deployed, each of which was composed by two 8-channel, 16-bit data ac-

quisition modules. Every acquisition module was controlled by a notebook PC through its parallel port. Synchronization and management of time, one of the key factors in a seismic array system, was based on GPS receivers, in which the configuration and control was managed through the PC's serial port in RS-232 format. A sampling rate of 200 samples per second was used. Data were recorded in hard disks by the data acquisition systems, using a STA/LTA trigger algorithm. The first seismic array, located in the Obsidianas Beach, was composed of one 3-component and 13 vertical-component stations. All the stations were equipped with 4.5 Hz Mark L28 sensors, whose response was extended electronically to 1 Hz. The second seismic array was composed of 7 vertical Mark L28 sensors (also extended to 1 Hz) and three 3-component stations with 1 Hz Mark L4C sensors. Two continuous recording stations were also deployed, equipped with 3-component Mark L4C seismometers controlled by a 16 bit data acquisition system. They were located in the vicinity of the Spanish Base and in the northern Fumarole Bay area.

The spatial distribution of the sensors in the array systems was originally conceived with two goals in mind. Firstly, we sought to compare the seismic activity in both areas; and secondly we wanted to determine the source position by applying a joint location technique (La Rocca et al. 2000; Almendros et al. 2000). In the end, this second objective proved unfeasible, due to the great difference in the shallow velocity structure under both arrays, which seriously affected the estimates of the slowness vector (Saccorotti et al. 2001b). Taking into account the extremely complex lateral structure beneath the Obsidianas array (Saccorotti et al. 2001a; Luzón et al. 2009), and following Ibáñez et al. (2003b), we decided

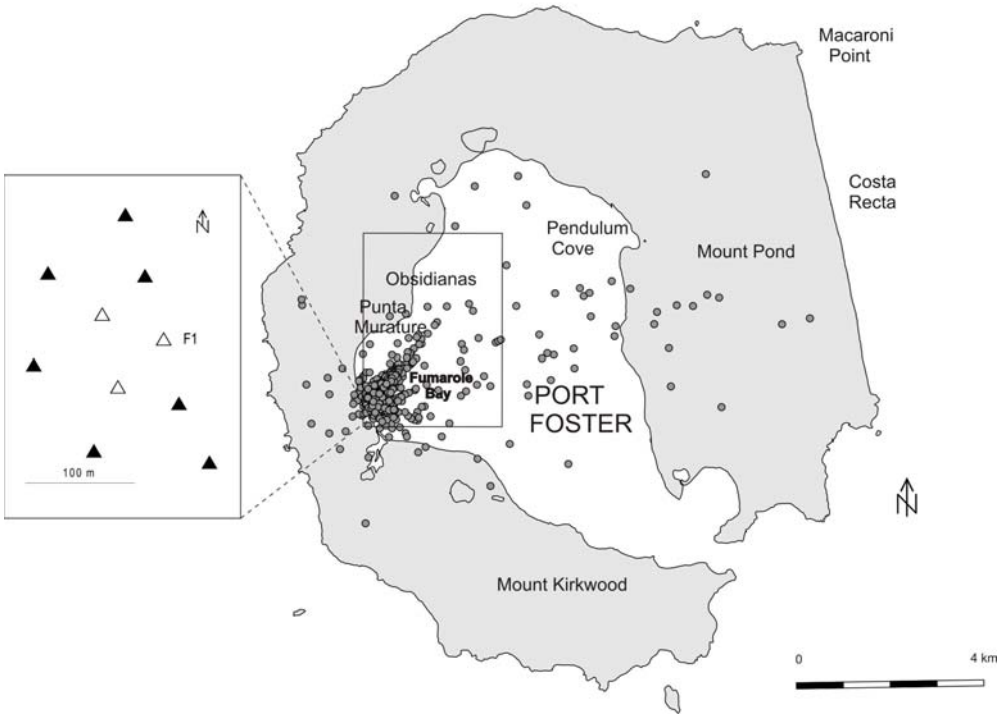

Figure 2. Preliminary epicentral locations of the VT earthquakes of the 1999 seismic series at Deception Island volcano, showing the location and configuration of the seismic antenna used for the present analysis. Black triangles correspond to vertical stations while the open triangles correspond to three-component stations. The box in the epicentral region corresponds to the area zoomed in Figures 7, 8, and 10.

to consider only data recorded in the Fumarole array. This seismic array was deployed in the neighborhood of the fumarolic system of Fumarole Bay, 500 m N-NE from the Argentinean Base. Its shape was approximately a double concentric semicircle, with radii of 60 m and 120 m, thus giving a total aperture of 240 m. The angular separation between stations was approximately 45º in the inner semicircle and 60º in the outer one (see Figure 2).

5. The 1999 seismic series

The 1999 seismic series at Deception Island volcano began in late December 1998. The arrays were recording from the beginning of the series until the end of February 1999. At that point we had to remove the arrays, although other instruments continued recording until April 1999, when the onset of winter prevented us from obtaining more data and finding out exactly when the series really ended (Ibáñez et al. 2003b). The Fumarole array recorded a total of 3643 events of which 2072 were VT earthquakes; 1556 events were LP events; and 15 were hybrids. There were also a few episodes of volcanic tremor. The moment-magnitude of the VT earthquakes ranged between -0.8 and 3.4. The largest earthquakes in this series, with a magnitude of 2.8 and 3.4, occurred on 11 and 20 January 1999 respectively, and were felt by the staff at the "Gabriel de Castilla" Antarctic Station. With the exception of these two large earthquakes, the magnitude distribution and seismic energy release as a function of time is approximately constant throughout the series. The series was characterized by low stress drop values between 0.1 and 4 bar (Havskov et al. 2003). Source sizes were estimated to be in the order of 10-100 m (Ibáñez et al. 2003b). These results indicate that the fractures involved in the process of generating the series were probably quite small.

Ibáñez et al. (2003b) calculated source locations for 863 VT earthquakes. They used the zero-lag cross-correlation (ZLCC) technique (Frankel et al. 1991; Del Pezzo et al. 1997) to estimate the slowness vectors of the P-wave arrivals at three frequency bands. The S-P differences were estimated visually. Subsequently, they obtained the hypocenters using ray tracing. The velocity model was combination of models used by previous authors (Ibáñez et al. 2000; Saccorotti et al. 2001a). Locations show that the majority of these VT events were located very close to the array site and at depths of around 2 km. Two alignments can be inferred, one at a direction of N45°E, with focal depths of between 1 and 4 kilometers and a second, more dispersed, which extends N80°E (Figure 2). Ibáñez et al. (2003b) also analyzed LP events and volcanic tremor episodes, obtaining azimuth and slowness values quite different from those obtained for the VTs. These results indicate that the 1999 LP seismicity is unrelated to the VT series, and agree with previous research in different surveys (Almendros et al. 1997, 1999; Ibáñez et al. 2000) suggesting that the LP seismicity has a hydrothermal origin. We analyzed 9 hybrid events and

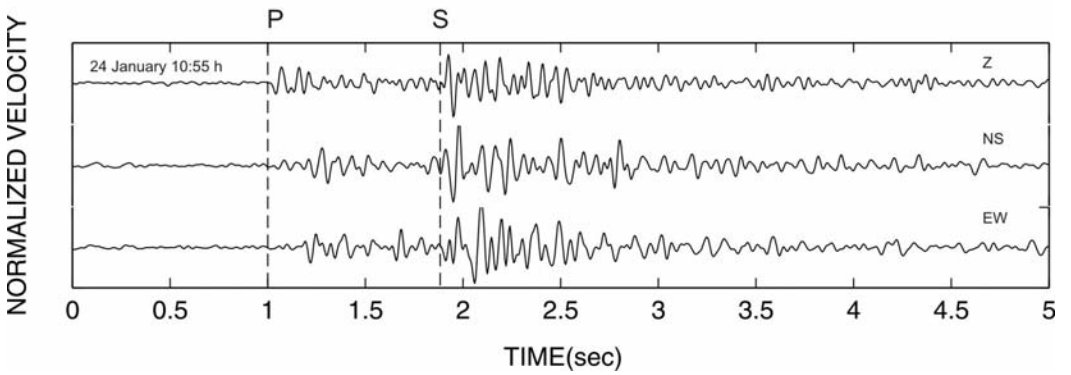

Figure 3. Three-component seismogram for a sample earthquake recorded at station F1 (see Figure 2). The dashed lines correspond to the arrival of the P- and S-waves, respectively. Data has been filtered between 1 and 30 Hz.

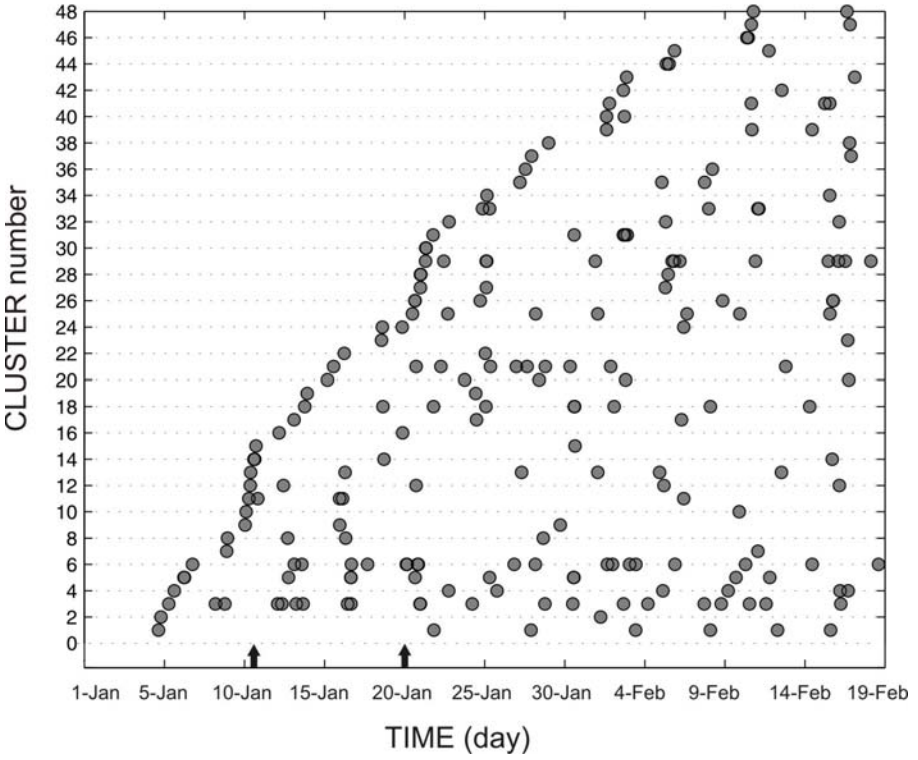

Figure 4. Temporal distribution of the earthquakes included in the 48 multiplets identified. There is a greater concentration of families with more than 5 events in the early days of the series. In the bottom part of the plot, the occurrences of two earthquakes with Mw > 2.8 are indicated with black arrows.

obtained similar results to those obtained for VT events, which indicates the presence of fluids in the VT source area.

Our work is based on the set of VT earthquakes recorded in the Fumaroles array and located by Ibáñez et al. (2003b). These locations allowed the authors to carry out a preliminary analysis of the series. However, the uncertainties of the locations are too large to obtain the planes associated with the earthquake generation processes; hence the need for a method of relative location to calculate the hypocenters with greater precision using array techniques.

6. Search for clusters

The first step in a precise relative location is to try to detect clusters of earthquakes with similar waveforms. We selected the central station of the Fumarole array (Figure 2) to search for these clusters. Figure 3 shows an example of three-component seismogram for a sample VT earthquake. Traces were band-pass filtered between 4 and 15 Hz using a zero-phase, three-pole Butterworth filter. For each trace we selected a window of 120 samples (0.6 seconds), starting 0.1 s before the arrival times picked for the P and S waves. The initial and final 10% of the window were smoothed using a cosine window. We calculated the cross-correlations for the P wave (vertical component) and for the S wave (N-S component) of the 863 located earthquakes. The result was a correlation matrix for the P wave and another for the S wave of all the events located in the series. With the two cross-correlation matrices, we performed a cluster search using the equivalence class technique (Press et al. 1989; Aster and Scott 1993). We used three parameters to define events with a similar waveform: A first threshold for the cross-correlation of the S wave, a second threshold for

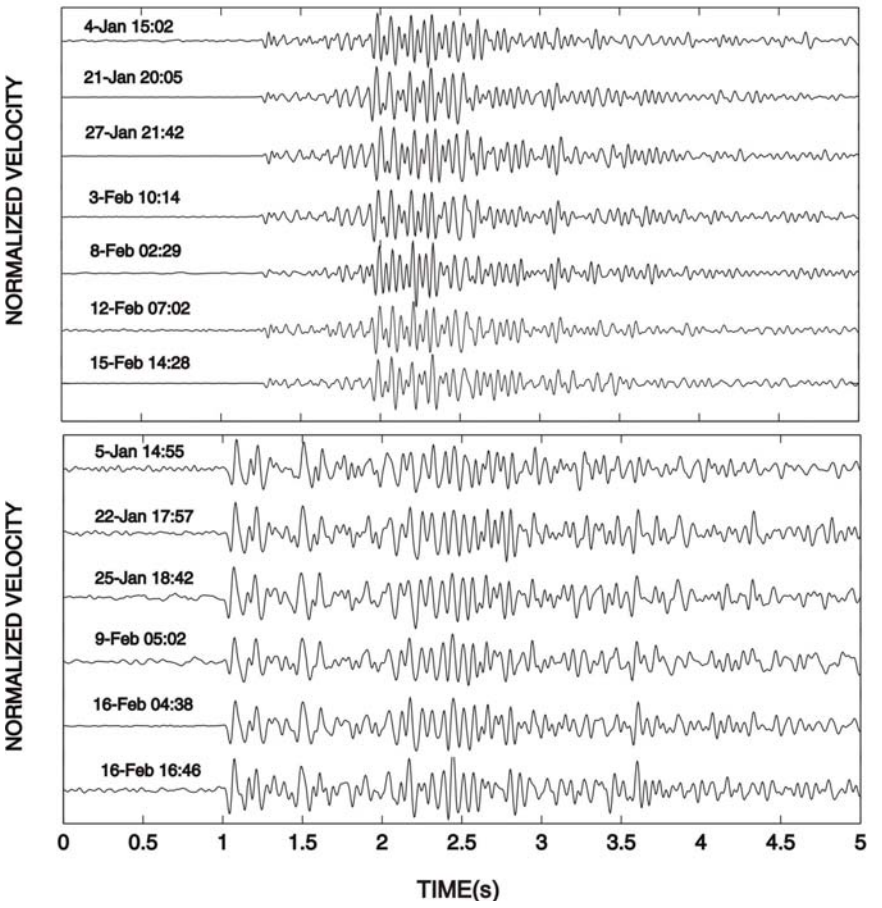

Figure 5. Examples of vertical-component seismograms for two earthquake clusters (1 and 4) recorded at station F1. Data has been filtered between 1 and 30 Hz and aligned at the P-arrival.

the cross-correlation of the P wave, and a third threshold that refers to the standard scalar product of the corresponding rows of the correlation matrix of the S wave. This last threshold was used to ensure that each event had similar correlations within the same family, thus rejecting accidental cases (Maurer and Deichmann 1995). The thresholds used in our work were 0.9 for the correlation of S wave, 0.9 for the P wave and 0.5 for the scalar product of the S wave. These correlation thresholds are quite high, which ensures a very good similarity in the waveforms.

A total of 48 clusters were found, including 19 doublets, 9 triplets, and 20 multiplets with four or more events. The temporal distribution of these clusters (Figure 4) shows that they were not separated in time. The earthquakes within the clusters were distributed along the whole recording period. It can also be seen that there was no time gap in the occurrence of clusters. In total, 225 events were grouped, which represents 26% of the total number of volcano-tectonic events located in the series. This percentage is fairly representative of the series given the low magnitude of the events. The vast majority are in a magnitude range of 0-1 Mw. The clusters present very different waveforms (Figure 5), which suggests a diversity of source mechanisms.

7. Precise relative locations

The occurrence of earthquakes with similar waveforms (multiplets) requires similar source and path effects. Therefore multiplet earthquakes must share similar source locations and mechanisms. Under this assumption, the main differences observed within a multiplet are just phase delays due to the slightly different lengths of the ray paths. These ideas constitute the basis of the master event relative location method.

In our case, the earthquakes were recorded by a seismic array instead of a distributed network. Techniques based on differences of travel times cannot be applied. A seismic array is a tool to estimate the apparent slowness vectors, and thus apparent slowness and azimuth are the parameters that should be used.

Almendros et al. (2004) introduced a technique that combines relative location and array analysis. Their relative slowness estimate (RelSE) method compares the waveforms of similar earthquakes recorded by a seismic array to estimate precisely the differences of apparent slowness and propagation azimuth of wavefronts corresponding to the same phase. This information can be used to produce accurate source locations, as will be shown below.

Among the set of VT clusters found in the 1999 seismic series at Deception Island volcano, we selected 17 clusters with five or more members. For each cluster, we chose the event with the best signal-to-noise ratio as the master event.

Initial source relocations

The preliminary location performed by Ibáñez et al. (2003b) was based on a systematic application of the ZLCC method. They used different filters, analysis windows of 60-80 samples, an overlapping of 50% of the window length, and extended the analysis to the full seismogram from the pre-event noise to the coda. This procedure ensures the fast and automated estimate of a consistent solution, within the uncertainty range, for the apparent slowness vector of the P wave of each VT earthquake.

However, Ibáñez et al. (2003b) do not examine

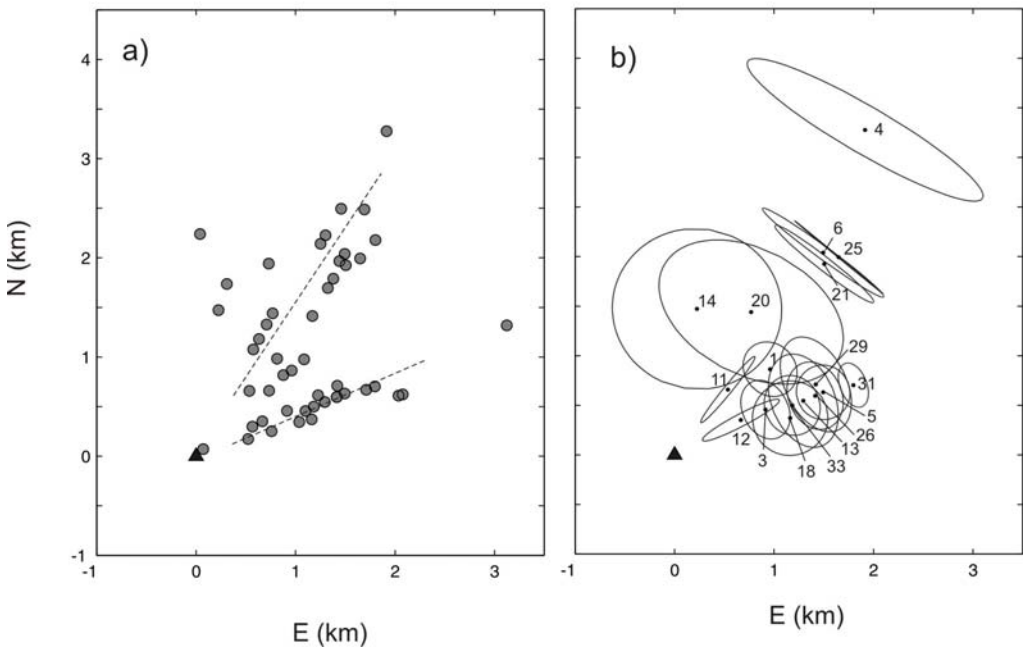

Figure 6. (a) Relocated epicentral map for master events of all clusters of the series. The dashed lines indicate two possible epicenter alignments. (b) Error ellipses of the locations of the master events of the clusters analyzed. The black triangle marks the position of the array.

whether theirs is the best possible estimate. In fact, we observed that the results of Ibáñez et al. (2003b) for the VT clusters displayed a relatively large dispersion, even though the waveforms within each cluster were similar. For this reason, we started our analysis by re-estimating the apparent slowness vectors using the ZLCC method. We fine-tuned the parameters to ensure that the estimates were made using exactly the same segments of seismogram around the P wave arrivals. We selected a filter in the 4-12 Hz band and a window length of 40 samples; increased the overlapping of successive windows to 95% of their length; and reduced the apparent slowness grid interval to 0.01 s/km. We also made a new picking of the P- and S-wave arrivals to estimate the S-P delay.

With the results of this procedure, we calculated hypocenter locations using ray tracing. The model selected to represent the medium is similar to that used by Ibáñez et al. (2003b). It is a combination of 1D Earth models used in previous works. The base was the model described by Ibáñez et al. (2000) for the whole island. This was merged with the model calculated by Saccorotti et al. (2001a) for the shallow layers of Fumarole Bay. To smooth the model and avoid discontinuities and critical reflections, we calculated an exponential fit of the form v(z)=A-B*exp(-z/C), where z is the depth, and A, B, and C are constants. The values obtained for these constants are A=6 km/s, B=5.1 km/s, and C=2.5 km.

Figure 6a shows the epicentral distribution of the master events. The remaining members of the multiplets are located near their master, and have not been plotted so as to ensure greater clarity. We can see two alignments of hypocenters at 35 and 70ºN. These trends coincide approximately with the alignments at 45 and 80ºN found in the preliminary analysis of the series (Ibáñez et al. 2003b). The coincidence suggests that the clusters are a good representation of the whole series. We estimated the location error quantitatively using: (1) the size of the region corresponding to an uncertainty of 90% for each estimate of the apparent slowness vector with the ZLCC method; and (2) the uncertainty associated with the determination of the S-P delays. These parameters provide spatial uncertainty intervals of around 0.5 km in horizontal and 1 km in vertical for most of the master events. These errors are similar to those estimated by Ibáñez et al. (2003b). Figure 6b shows the horizontal projections of the error regions for the master events of the clusters with five or more elements.

Application of the RelSE method

Once we had identified and relocated the VT earthquake clusters, we applied the RelSE method (Almendros et al. 2004). This method uses array data to provide a precise estimate of the relative apparent slowness vectors of the events of the cluster with reference to the absolute apparent slowness vector of a master event. The innovation introduced by the RelSE method relies on the following. The time delay between the arrivals of a wave front from an earthquake n to two array stations i,j is given by:

$$\Delta t_{ij}^{n} = \Delta \mathbf{r}_{ij} \cdot \mathbf{s}_{n} \qquad (1)$$

where $\Delta \mathbf{r}_{ij}$ represents the position vector of the j station from the i station, and $\mathbf{s}_n$ is the apparent slowness vector that characterizes the propagation of the wave front. Classic array techniques are based on the comparison of the seismograms among the array stations. Several methodologies can be used, but in all cases they allow for the calculation of the delays Δt_{ij}^{n} and the estimate of the apparent slowness vector $\mathbf{s}_n$. The accuracy of the estimate depends on our ability to measure accurate time delays. But in many situations the delays cannot be determined precisely, since site effects may produce important waveform variations between the stations of the array.

Let us suppose now that two earthquakes m,n are recorded at the same array. The difference of delays of the same phase at two stations i,j is given by:

$$\Delta t_{ij}^{n} - \Delta t_{ij}^{m} = \Delta \mathbf{r}_{ij} \cdot \Delta \mathbf{s}_{mn} \qquad (2)$$

where $\Delta \mathbf{s}_{mn} = \mathbf{s}_n - \mathbf{s}_m$ is the difference between the apparent slowness vectors corresponding to the earthquakes. This difference of delays can be also written as:

$$\Delta t_{ij}^{n} - \Delta t_{ij}^{m} = \Delta t_{j}^{mn} - \Delta t_{i}^{mn} \qquad (3)$$

where Δt_i^{mn} represents the delay between the arrival times of a phase of earthquake n and the same phase of earthquake m at station i of the array. Combining Equations (2) and (3), we obtain the expression:

$$\Delta t_{j}^{mn} - \Delta t_{i}^{mn} = \Delta \mathbf{r}_{ij} \cdot \Delta \mathbf{s}_{mn} \qquad (4)$$

It may seem that this equation adds nothing to the problem, compared to Eq. (2). However, in the case of clusters of similar earthquakes recorded at a seismic array, the differences Δt_i^{mn} can be determined more accurately than the differences Δt_{ij}^{n}. In other words, we can calculate the delay between the arrivals of two earthquakes to the same station more precisely than the delay between the arrivals of a single earthquake to two array stations. This is a consequence of the improved waveform similarity observed among multiplet earthquakes (see for instance Figure 14 of Almendros et al. 2004).

The RelSE method uses Eq. (4) to determine precisely the relative apparent slowness vector for earthquakes with similar waveforms recorded by a seismic array. We define a function that represents the inverse of the least-square misfit between the measure Δt_j^{mn} - Δt_i^{mn} and a plane wavefront. The best estimate of the relative slowness vector is obtained by maximizing this function.

We apply the RelSE method to the P wave for the selected earthquakes. The parameters we use are based on the results of the tests described by Almendros et al. (2004). We also performed several tests to search for the optimum parameters for our analysis. We filtered the data in the 4-12 Hz band using a two-pole, zero-phase Butterworth filter. These parameters represent a compromise between the needs to reduce undesired noise and to minimize waveform distortion. The duration of the analysis window is 0.2 s (40 samples). This ensures that we use at least 2-3 periods of the signal. Larger windows involve the analysis of larger portions of the P-wave coda, which do not necessarily comply with our hypotheses and generally reduce the level of waveform similarity. In contrast, smaller windows create instability in the slowness vector estimates. The analysis window was shifted along the seismogram, sliding 5 ms (1 sample) each step. We started with a window centered at 60 samples before the P-wave arrival, and analyzed 61 consecutive windows. Almendros et al. 2004 estimated the relative apparent slowness vectors using the window with the minimum misfit. We used a weighted average of the results corresponding to windows around the P-wave arrival with low residuals (below 5 ms). This approach improves the stability of the final estimate.

In this way, we calculated relative apparent slowness vectors for the P-wave arrivals of 124 of the 150 earthquakes contained in 14 of the 17 clusters selected. The remaining earthquakes (including three full clusters) did not produce residuals below 5 ms, and were ruled out. The estimates of the absolute apparent slowness vectors were obtained by adding the absolute apparent slowness vector of the corresponding master event.

Precise spatial locations

The application of the methodology described above provides estimates of the apparent slowness vectors for the earthquakes of each cluster. These estimates are highly accurate in a relative sense, i.e. the differences between the vectors are precisely known thanks to the RelSE technique. Their absolute values, however, are based on the initial estimates of the apparent slowness vectors of the master event performed with the ZLCC method.

The apparent slowness vectors provide the apparent slownesses and propagation azimuths of the P-waves. We need the S-P delays to enable us to apply a ray-tracing procedure and locate the hypocenters. In order to measure the S-P delays with higher accuracy, we again used a relative approach. We performed spline interpolations of the cross-correlation functions between the earthquakes and their corresponding master event for the P- and S-wave arrivals. This technique makes use of the enhanced waveform similarity observed within the VT earthquake clusters, and reduces the uncertainty of the visual picking on the seismograms.

The spatial locations of the hypocenters were obtained from the apparent slowness vectors and S-P delays using a ray-tracing procedure on a 1D model, as described above.

Figure 7 shows the results for the 14 clusters selected. We can see four epicentral areas. The closer area is just 1-2 km away from the array, and contains most of the clusters we analyzed (1, 3, 5, 11, 13, 18, 29, and 31). Another area is located opposite Punta Murature and contains three clusters (6, 21, and 25). The remaining areas contain just one cluster: number 14, located in the W side of the epicentral region; and number 4, located at about 3 km to the N. Most clusters fall within a narrow depth range of between 1.2

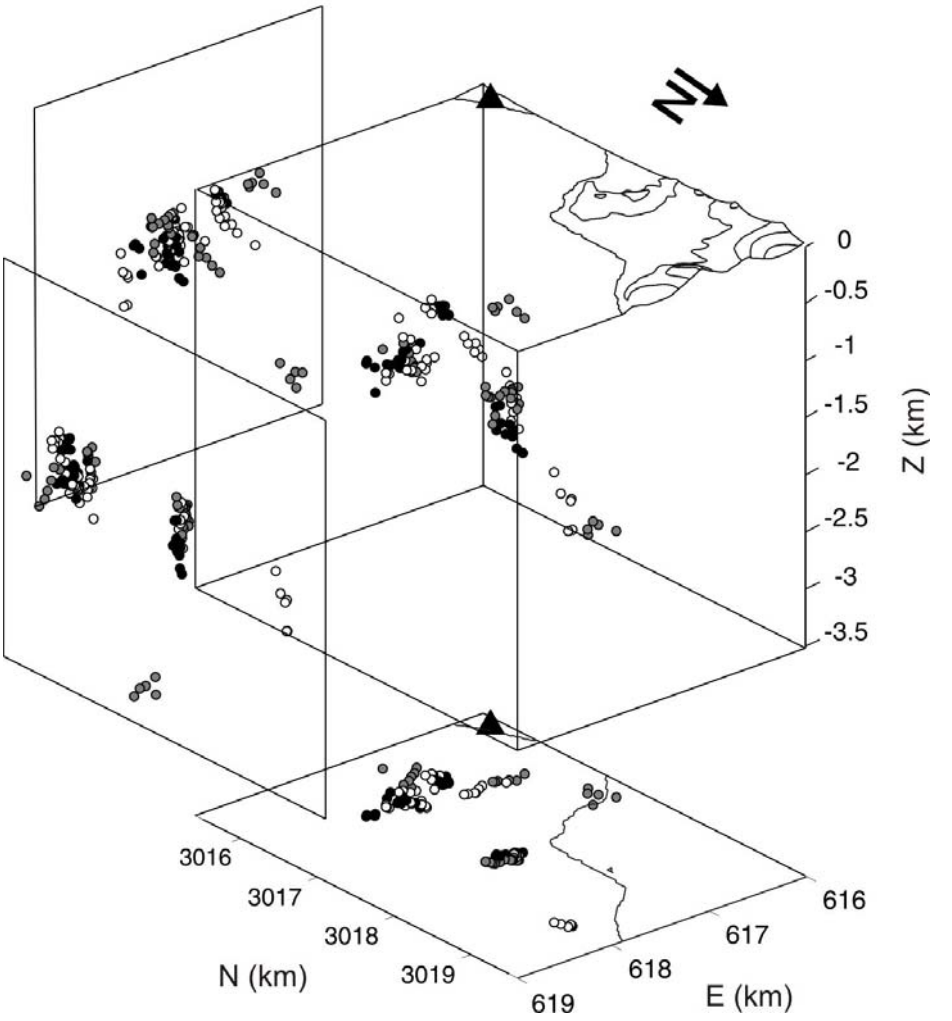

Figure 7. Summary of relative source locations for the 16 clusters selected. Each cluster is shown in a different shade of grey. Side and bottom planes contain vertical and horizontal projections of the hypocenters. The triangle marks the position of the array.

and 2.0 km. Only cluster 14 is deeper and lies between 2.8 and 3.2 km.

Plane fitting

The accuracy of the relative locations enabled us to address the shape of the hypocenter distributions. For most of the clusters, the distributions had a predominantly planar component. They were somewhat elongated in depth, due to the larger sizes of the uncertainty regions, but in general they defined a plane. We used a least-square approach to calculate the parameters of the plane that best fitted the distribution of the hypocenters. The quality of the fit was controlled by three parameters: (1) the misfit R, defined as the average misfit of the hypocenters to the best-fit plane; (2) Q, the ratio of the average misfit R and the average distance of the projections of the hypocenters on the plane to the center of the distribution; and (3) the planarity P, defined as $1-\lambda_3/\lambda_2$, where $\lambda_2>\lambda_3$ are the two smallest eigenvalues of the covariance matrix of the hypocenter

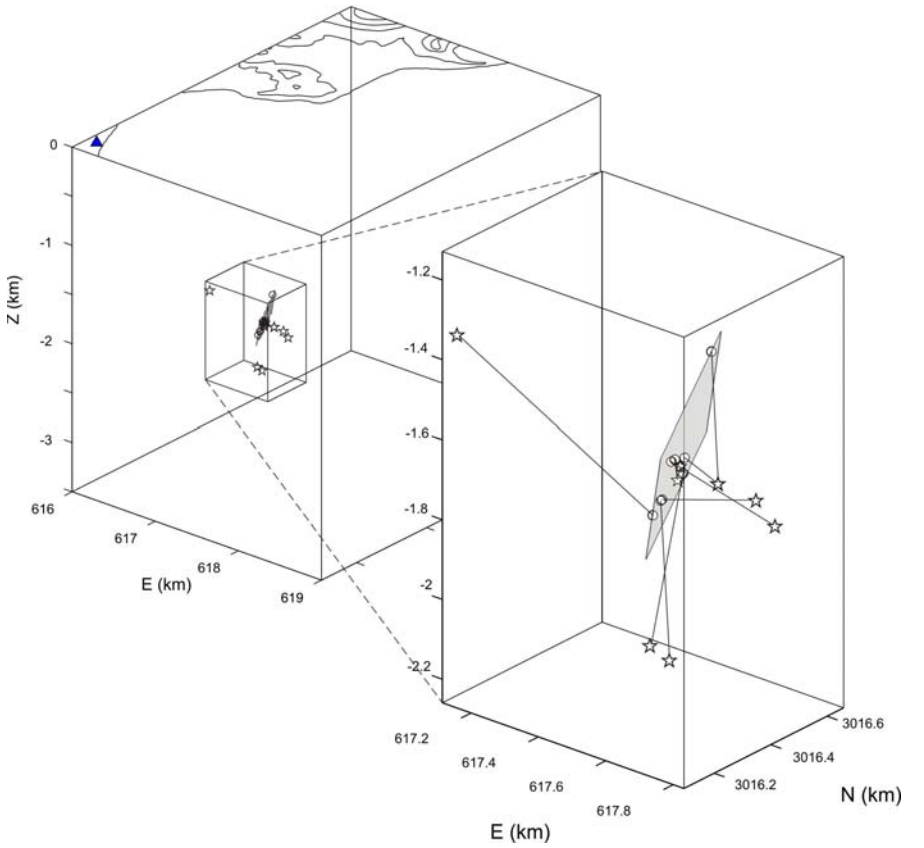

Figure 8. Comparison of source locations obtained using standard ZLCC (stars) and RelSE slowness vector estimates (open circles) for cluster 5. The figure shows a 3D view of the Fumarole Bay area, including the position of the seismic array (solid triangle). In the detailed view of the source region, a black line joins the source locations obtained using the ZLCC and RelSE methods. For the RelSE solutions, we show the best-fit plane in grey.

distribution. Both Q and P are measures of the oblateness of the hypocenter distribution. An optimal fit should have low R, low Q, and high P. Figure 8 shows an example of the results obtained with this procedure for a sample cluster.

We were able to fit planes to the 14 selected clusters. In two cases (clusters 3 and 6) the method discriminated two spatially-distinct subgroups of hypocenters within the cluster. The quality of the plane fit including all members of the cluster was very low. However, the plane fits to these subgroups provided better results (Figure 9). In fact, there were slight variations in the waveforms that were indiscernible to the cluster detection algorithm. We therefore decided to subdivide these clusters (3a, 3b; 6a, 6b) and obtained a total of 16 planes.

Table 1 shows the results of the fit for all the clusters. The table contains: (1) the cluster ID; (2) the number of earthquakes in each cluster and the number of earthquakes used for the fit; (3) measures of the quality of the fit (misfit, Q, and planarity); and (4) the plane orientation (strike and dip) and the angle θ defined as the angle between the plane strike and the line joining the array center and the master event hypocenter. We defined the strike between 0 and 360º, and

earthquake clusters								
cluster ID	Nº eqs	Eqs fit	R (m)	Q (%)	P	strike (ºN)	dip (º)	θ(º)
1	7	6	15.0	10.3	0.47	155	49	107
3a	9	7	3.6	6.4	0.98	129	59	65
3b	13	13	11.1	17.2	0.81	193	62	130
4	7	6	7.9	5.1	0.93	323	85	113
5	11	9	9.7	14.5	0.92	143	56	76
6a	12	12	13.5	13.5	0.75	233	86	17
6b	9	9	3.07	5.3	0.99	307	83	91
11	6	5	3.2	1.1	0.99	301	81	82
13	6	5	9.2	7.0	0.88	126	86	59
14	5	5	12.2	9.0	0.96	140	41	131
18	9	5	2.4	1.5	0.94	212	70	140
21	10	10	4.5	3.4	0.98	132	81	94
25	7	7	3.2	3.3	0.99	313	84	94
26	6	5	3.4	3.7	0.96	155	68	88
29	14	14	18.2	14.3	0.91	119	60	56
31	5	4	5.8	5.3	0.89	138	82	69

Table 1. Summary of multiplet cluster geometry the plane fitting procedure for the 16 selected clusters. Columns give from left to right the cluster ID; the number of events contained in each cluster; the number of events for the plane used in the fit; misfit R of the relative locations to the best-fitting plane; Q; planarity P; strike, dip and θ angle.

measured it in such a way that the dip angle was measured to the right and did not exceed 90º.

Misfits range from 3 to 18 m. The distances on the plane between hypocenter projections are in the order of hundreds of meters, which gives us some idea of the planar shapes of the distributions. This can be also seen from the Q parameter and the planarity. Q is always small,

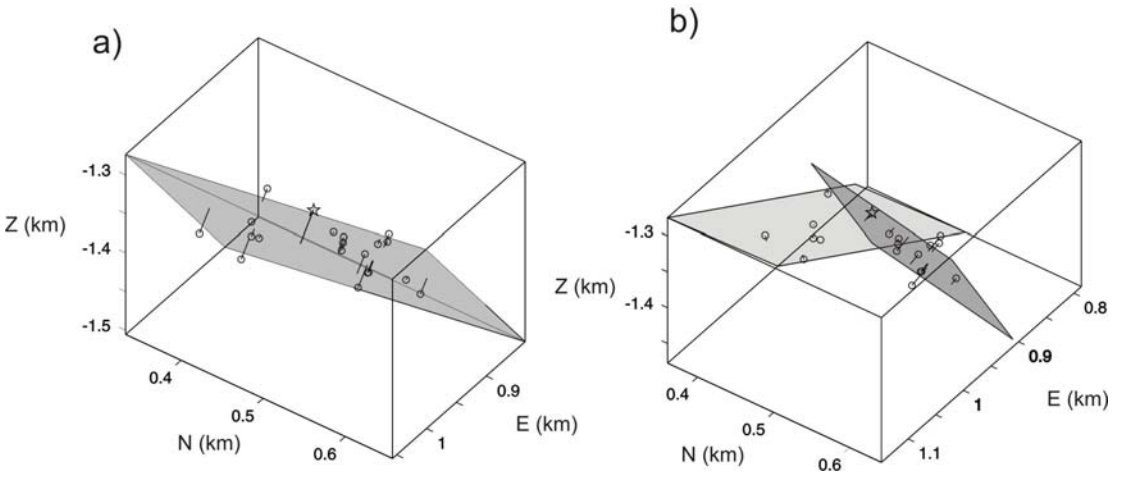

Figure 9. (a) Best-fit plane for cluster 3, using all the earthquakes. (b) Best-fit planes for clusters 3a and 3b, using two spatially distinct subgroups of earthquakes.

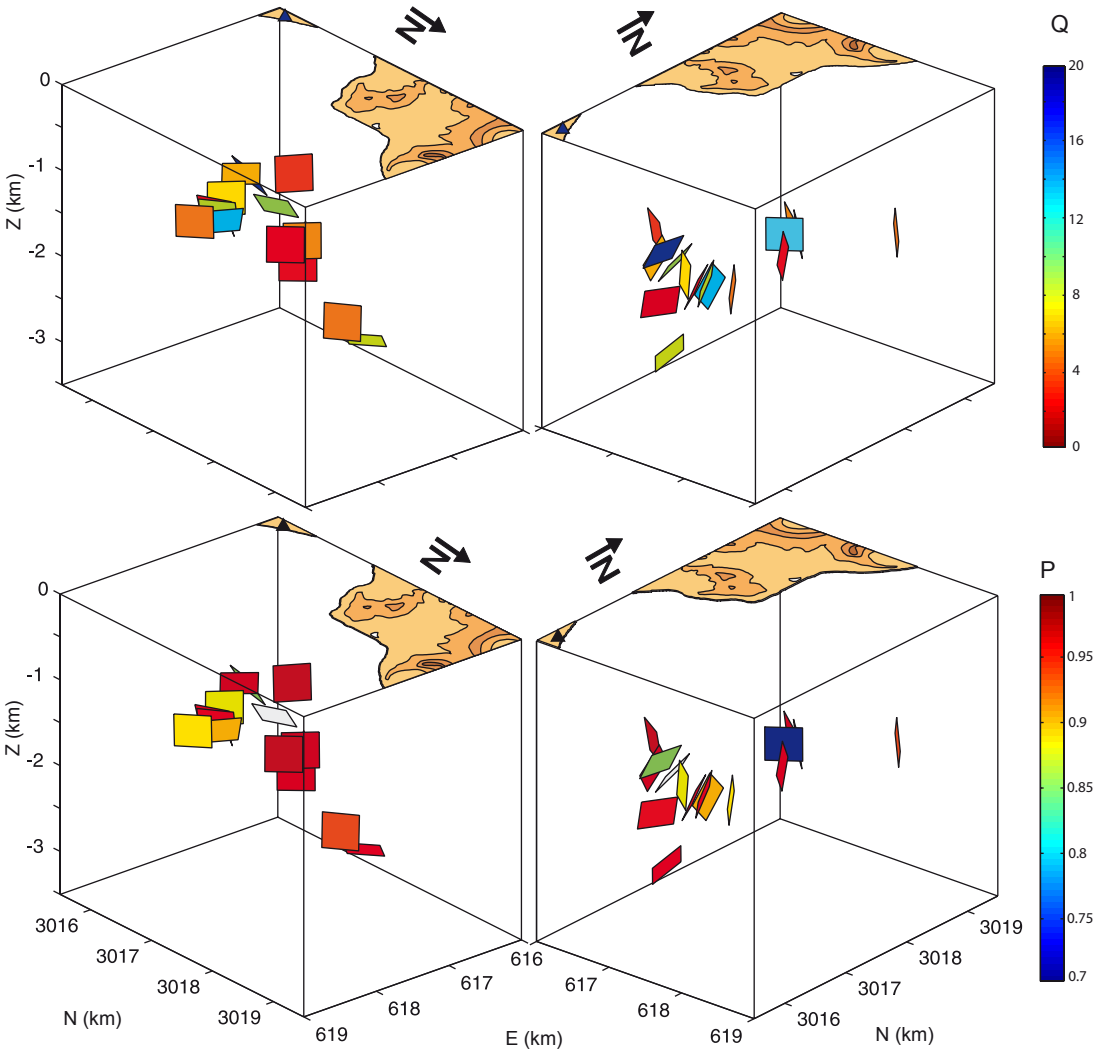

Figure 10. Summary of the best-fitting planes obtained for the 16 clusters. Planes are shown at the corresponding master events locations from two different perspectives. The color scale represents the quality of the fit, in terms of Q (a) and planarity (b). The array position is shown by a triangle. Topography is represented with a contour interval of 50 m.

under 17%. Most distributions have a high planarity above 0.75. This threshold is similar to the limit used in other works to define the significant range of planarity (e.g. Shearer et al. 2003). Strike angles range from 119 to 322ºN, although most planes are oriented NW-SE. Dip angles vary between 41 and 86º. Most of them are large, which suggests the presence of subvertical planes.

Figure 10 shows the location and orientation of the planes found. The color indicates the quality of the fit. Figure 11 shows histograms of the strike and dip angles from Table 1, as well as Q and P. We also show horizontal projections of the strikes and a stereographic representation of the 16 planes. The orientations of the planes with respect to the array (the angles θ) range between 17 and 130º. Most fits are characterized by θ va-

lues different from 90º, which reveals that they are not planes perpendicular to the line array-hypocenter.

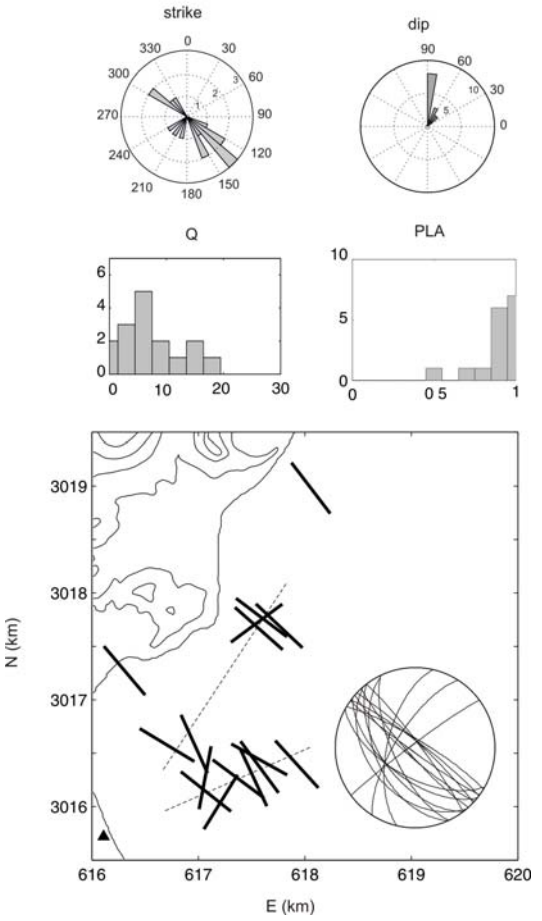

Figure 11. (a) Histograms of strikes, dip angles, Q and planarity of the planes shown in Figure 10. (b) Representation of the strikes of the fracture planes at the corresponding master event epicenters. The alignments of the epicenters obtained from the initial relocations of the series (see Figure 6) are shown as dashed lines. The inset shows a stereographic representation of the planes.

8. Discussion

Validity of the methodology

Relative location methods are among the most commonly used seismological tools for investigating the precise spatial distribution of the earthquake hypocenters. This technique is often used when a sufficient number of earthquakes with similar waveforms have been recorded by a seismic network. In this case we are able to find clusters of earthquakes with similar source locations and mechanisms.

Seismic arrays are often used in volcanic regions. To obtain precise locations from array data, we start with the relative apparent slowness vector estimated method (Almendros et al. 2004). This method allows the precise determination of the differences between the apparent slowness vectors among the members of a cluster. Using these differences, we have developed and applied a methodology to define fracture planes. It is based on ray tracing on a 1D model and the fit of the distribution of hypocenters to a plane. The results provide information on the geometry of the faults implied in the earthquake generation, although they do not address the dynamics of the rupture process.

The seismic series we analyze took place at Deception Island during the austral summer of 1998-1999. VT waveforms were repetitive, which allowed us to search for earthquake clusters. The correlation thresholds used to evaluate the similarity of P and S waveforms were high (~0.9). With these restrictive thresholds we ensured that the earthquakes within a cluster were very similar, so guaranteeing the efficiency of the RelSE method (Almendros et al. 2004). However, we obtained relatively few events per cluster. Only 17 of the 48 clusters contained 5 or more earthquakes.

We obtained fracture planes for 14 clusters. For 12 of these clusters we obtained just one rupture plane, while the other 2 provided two planes each. This result emphasizes the sensitivity of the method, which was able to separate two subgroups of hypocenters spatially within the same cluster. There are small variations in the waveforms (see for example the amplitude of the S wave in Figure 10 of Almendros et al. 2004). These variations have virtually no impact on the cluster selection procedure, but produce different estimates of the relative apparent slowness vectors. This feature has also been observed in the case of relative location methods that use seismic network data (e.g. Carmona et al. 2009).

The quality of the results is related to different factors that may affect the methodology. The

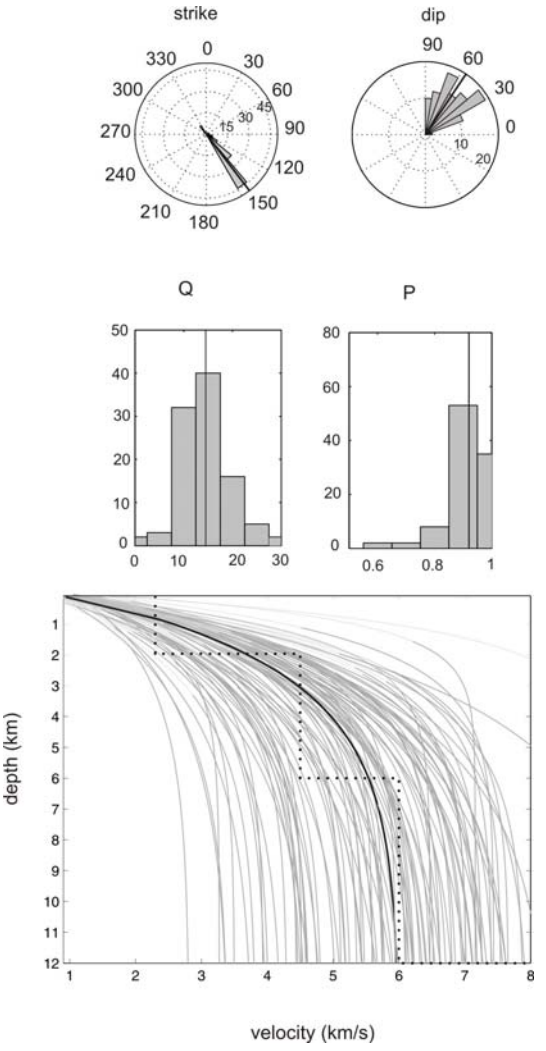

Figure 12. Results of the test on the effect of the choice of master event for cluster 5. (top) Histograms of strikes, dip angles, Q and planarities for random variations of the velocity model parameters. The black lines indicate the values obtained using our smoothed velocity model. (bottom) Original velocity model (black dotted line), smoothed velocity model (black solid line) and random velocity models used in the test (gray lines).

most important factors are related to the quality of the spatial location of the hypocenters. These include: (1) the effect of the velocity model used to represent the medium; (2) the uncertainty in the estimate of the apparent slowness vector of the master event; and (3) the choice of a master event within each cluster.

We began by testing the effect of the velocity model in the geometry of the fracture planes calculated. We generated 100 velocity models using random variations of the three parameters A,B,C that define the model. These values were obtained from normal distributions centered at the values of the parameters in the original model. The standard deviations were fixed to 25% of the central values. For each of these models we calculated the precise relative locations and the best-fit plane.

Although the original velocity model changes significantly during the above process (Figure 12), the geometry of the best-fit plane is relatively stable. The parameters that define the plane stay around the parameters obtained in the original model. For example, Figure 12a shows the distributions of strike, dip, Q, and P obtained for cluster 5. The dispersion of the results is larger for the dip angle than for the strike. The depth of the hypocenters is more sensitive to the velocity variations in the model.

The second factor that affects the results is the estimate of the absolute apparent slowness vector of the master event. We generated random distributions of azimuth and apparent slowness of the master event. We used normal distributions centered at the azimuth and apparent slowness obtained using the ZLCC method. The standard deviations were obtained from the size of the 90% uncertainty area on the apparent slowness plane. Figure 13 shows a summary of the results.

For variations in the azimuth of the master event, we found a marked stability in the strike and dip of the planes. This result was anticipated, since a change in the propagation azimuth implies a rotation of the hypocenters around the array, without any change in their relative positions. In a laterally homogeneous model, a rotation does not modify the angle θ between the strike of the best-fit plane and the line joining the array center and the master hypocenter. The dip angle is independent of the azimuth, while the variations in strike are related to the variations introduced in the absolute azimuth of the master event.

The variations in the apparent slowness of the master event also produced a high stability in the strikes, but there was more dispersion in the dip

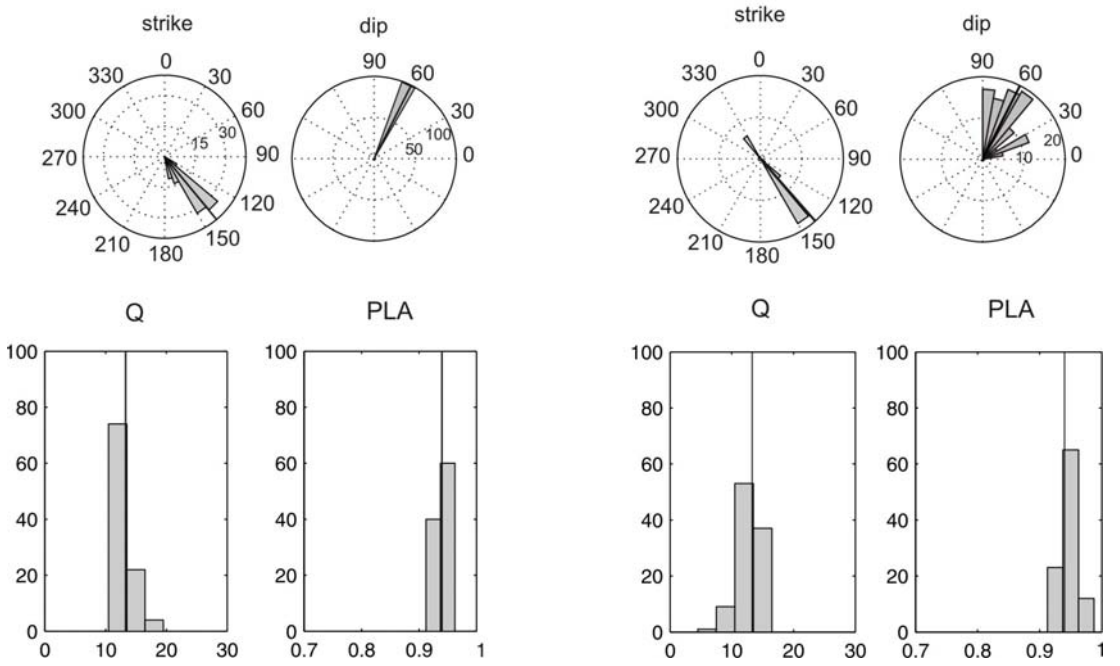

Figure 13. Results of the test on the effect of the estimate of the apparent slowness vector of the master event on the plane geometry for cluster 5. (a) Histograms of strikes, dip angles, Q and planarities of the best-fit plane for random variations of the azimuth of the master event. (b) Histograms of strikes, dip angles, Q, and planarities of the best-fit plane for random variations of the apparent slowness of the master event. In (a) and (b), the black lines indicate the values obtained using the apparent slowness and propagation azimuth of the master event estimated with the ZLCC method.

angles. A change in the absolute slowness yielded a change in the depth of the hypocenters and therefore a change in the inclination of the best-fit plane. However, the strike was stable, which suggests that the estimate is robust.

Both for variations of the azimuth and the apparent slowness of the master event, the values Q and P defining the quality of the fits are similar to those obtained in the fit of the original hypocenter distributions. These results indicate that the hypocenter distributions maintain planar structures for variations of the absolute apparent slowness vectors of the master events within their uncertainties.

The third factor is the selection of a master event. Almendros et al. (2004) demonstrated that the relative apparent slowness vectors are independent of the choice of master event. However, the absolute apparent slowness vectors of the cluster members (obtained by adding the absolute apparent slowness vector of the corresponding master event) do depend on the choice of master event. In our case, the differences are not significant, since the estimates of apparent slownesses and azimuths obtained with the ZLCC method for each cluster range within relatively narrow margins. For example, for cluster 5 the maximum difference of azimuths among cluster members is about 10º, and the maximum difference of slowness is about 0.05 s/km. These values are the same size as the 90% uncertainty regions associated with the ZLCC estimates. Therefore, the selection of a different master event is equivalent to an error in the estimate of the apparent slowness vector of the master event. And we have already tested that the solutions are stable.

In any case, it is important to select events with a good signal-to-noise ratio and a large maximum average correlation with the ZLCC me-

thod. The absolute location of the master event should be as accurate as possible, since we use it to position the other cluster members and to interpret the relative positions of the different clusters selected.

We calculate the θ angle to characterize the relative position of the best-fit plane and the array. We observe that for some clusters the S-P delays are practically the same for all the cluster members. In this case, all earthquakes would be at the same distance from the array. The fit would yield a plane with θ=90º regardless of the estimates of the relative apparent slowness vectors. In our results, there were five planes with θ angles between 80 and 100º that could be in that situation. But the fact that we found other orientations indicates that the relative locations obtained from the RelSE method are crucial to the definition of a plane. In any case, we performed a test to investigate the geometry and quality of a fit based on random locations. We generated hypocenter distributions based on random values of the relative apparent slowness vectors and S-P measures. We used normal distributions centered in the values of the master event, with standard deviations given by the maximum dispersion of the parameters within each cluster. Figure 14 shows the results obtained for two clusters. The cluster with a θ angle other than 90º does not show any agreement with the parameters derived from the random test. The cluster with a θ angle near 90º does show a strike perpendicular to the back-azimuth of the master. However, the fits of the random hypocenters do

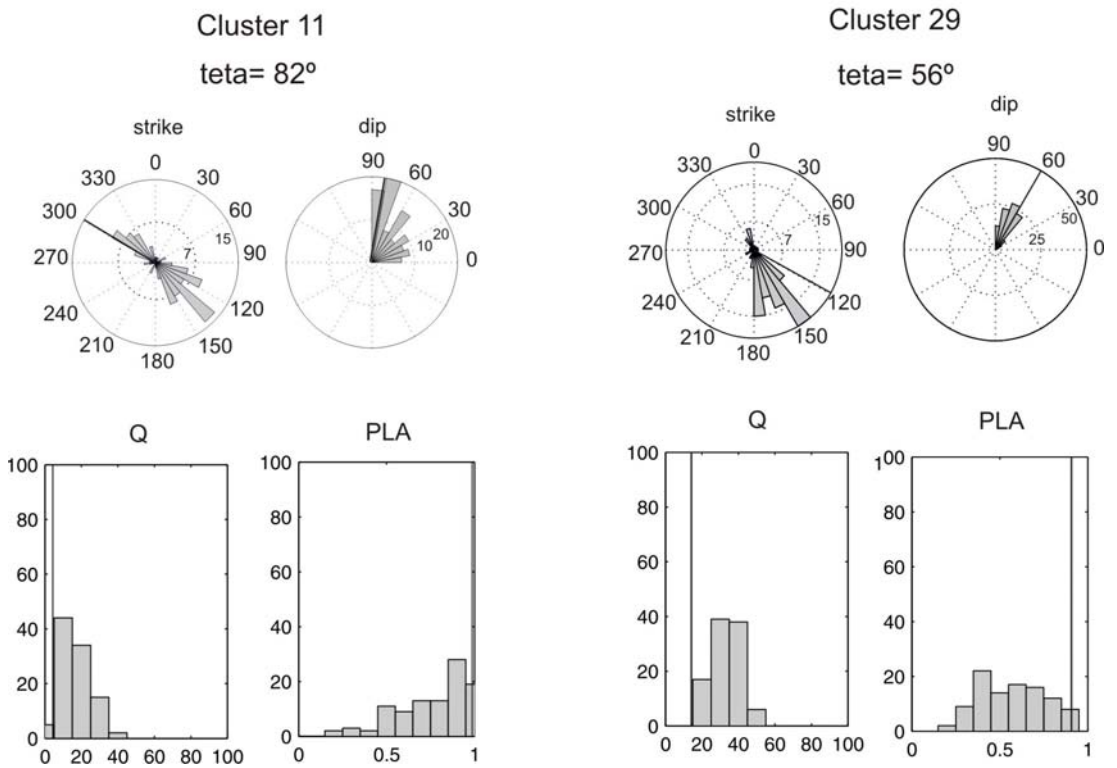

Figure 14. Results of the test on the reliability of those plane solutions that are perpendicular to the array-hypocenter direction. The different panels show histograms of strikes, dip angles, Q and planarities for random variations of relative apparent slowness vectors and S-P times within limits obtained from clusters 11 (left) and 29 (right). The black lines indicate the values corresponding to our best-fit plane

not have the quality achieved by the real data. They show lower P and higher Q compared with our results for the cluster. Again, this demonstrates that a precise estimate of the relative apparent slowness vectors is essential for the characterization of the fracture planes.

Interpretation of the results

The final results of our fracture characterization procedure show that the majority of the planes have strikes in the 120-140ºN direction (NW-SE). These trends coincide with some of the major fault systems in the island described by other authors. For example, Rey et al. (1995) presented three fault systems: 160-170ºN right-lateral strike-slip faults, 45-60ºN normal faults and 115-120ºN normal faults in the SW of the island. Martí et al. (1996) also describes three fault systems that cross the island NE-SW, NW-SE and N-S. The most relevant seems to be the NE-SW system (Smellie et al. 1988). González-Casado et al. (1999) also set out three main systems of microfractures: NE-SW, E-W and NW-SE, with dips greater than 60º and related to the NW-SE extension of the Bransfield Strait. These same authors state that the faults with NW-SE direction are transfer faults from the NE-SW systems. Smellie and López-Martínez (2000) made a geomorphological map of Deception Island in which normal NW-SE faults appear in our study area. Paredes et al. (2006) presented a morphoalignment map that showed the directions of the fractures in the island. They summarized all the work to date and combined it with a morphometric analysis of the digital elevation model, to create a synthesis map of the traces of faults. The preferred directions were NE-SW, N-S and NNW-SSE.

The predominant NW-SE direction found in our results coincides with some alignments reported by these authors. The directions of the other strikes are between 190 and 240°N, which also coincide with alignments described previously (NS and NE-SW). The dips of the planes, mostly sub-vertical, are consistent with the characteristics of the fault systems that are expected in an extensional area (González-Casado et al. 1999).

Both the distribution of the epicenters found by Ibáñez et al. (2003b) and our initial relocations shown in Figure 6 show two preferred alignments in directions NE-SW and NEE-SWW. These directions do not match the directions obtained from the geometry of the rupture planes of the series (Figure 11). The consequence is that the interpretation of epicentral maps in terms of fracture alignments can be severely biased, since we have no information about the real directions of rupture. The local tectonic regime can only be addressed using information on the source mechanisms, or at least with the definition of rupture planes using precise relative locations.

We found 16 fracture planes in the Fumarole Bay area. We were unable to investigate other areas of the island, since all the selected families occur in this area. However, Ibáñez et al. (2003b) showed that the accumulation of epicenters in the vicinity of the array is an apparent effect due to the low magnitude of the events and the high attenuation of the medium under Port Foster (Vila et al. 1995; Martínez-Arévalo et al. 2003). It is likely that there are distributions of similar fractures in the area N of Port Foster, where some of the more distant earthquakes in the series are located (Figure 2).

To some extent, one could interpret that the directions obtained from the planes are distributed parallel and perpendicular to the edge of the caldera in the Fumaroles area. This could suggest the presence of ring-fracture systems rela-ted to the formation of a caldera collapse. How-ever, the stability of the orientations of the planes (Figure 11) suggests a close relationship with the regional tectonics, as has been suggested by other authors (Martí et al., 1996; Rey et al., 1995; González-Casado et al., 1999).

The ruptures of the planes identified in our analyses could be a consequence of regional tectonics, volcanic activity, or a mixture of both. Ibáñez et al. (2003b) rule out the first two hypotheses, since they do not fit their results. These authors suggest that the most likely explanation for the origin of the series is the development of a magmatic intrusion that produced a change in the local stress field but did not reach the surface.

Studies of deformation of Deception Island suggest that there are two main directions of deformation related to the regional tectonics and volcanic activity of Deception Island (Fernández-Ros et al. 2007). After the 1999 crisis there was a change in the movement of the island. It changed from an extension and elevation of the entire island to a compressive process of subsi-

dence in the N and NW areas (Berrocoso et al. 2008). The work of Caselli et al. (2004) on the geochemistry of gases in the Fumarole Bay area after the 1999 crisis shows an increased SO_2 flux. This increase appears to be related to the intrusion of dykes into surface layers. This resulted in the emergence of native sulfur deposits and iron sulfides in thin layers in the fumarolic system. These works highlight the relationship between a volcanic reactivation and the emergence of swarms of VT earthquakes in 1999.

What seems clear is that a reactivation of the magma chamber of Deception Island would trigger an imbalance in the area. This may be the cause of the 1999 series of VT earthquakes. Seismic tomography has imaged a shallow magma chamber at Deception Island volcano (Zandomenegui et al. 2009; Ben-Zvi, et al. 2009). This chamber is situated at a depth of about 2-4 km under the inner bay of Deception, slightly shifted toward the W, elongated NW-SE direction. Deformation studies have situated the center of the superficial deformation produced after the 1999 crisis in the bay off Obsidianas Beach (Berrocoso et al. 2008). This area coincides with the position of the magma chamber established by seismic tomography studies. This fact indicates that the activation of the chamber was the origin of the series. Seismic tomography also indicates low velocities to a depth of 2 km in the Fumarole Bay area, suggesting a highly fractured medium, which supports our results. The fractures involved in the series are situated in or within the limits of the magma chamber. This should be an area of high-temperature rocks, which should show a somewhat ductile behavior, thus preventing the occurrence of VT earthquakes. However, VT earthquakes are commonly found within low-velocity bodies in volcanoes (Dawson et al. 1999, Waite et al., 2009), which indicates that the medium is rigid enough to produce earthquakes. The vicinity of the magma chamber could explain why we detected VT activity and hybrid events (i.e. presence of fluids) in the same place. The presence of magmatic fluids would increase the pore pressure, resulting in an increase of the normal stress acting on the fault plane. This facilitates the rupture processes responsible of the VT earthquakes. In any case, the faults should be consistent with the framework of the regional tectonics affecting the volcanic evolution of Deception Island.

9. Conclusions

We have developed a method to investigate the geometry of the fractures involved in a series of VT earthquakes recorded by a seismic array. The method exploits the similarity of the waveforms that appear in the seismic series to perform accurate estimates of the apparent slowness vector and the difference of S-P times. With these estimates, we obtain precise relative locations that indicate the orientation of the fracture.

Although the method for characterization of fracture planes through relative locations using seismic networks is widespread, this is the first time that results of equivalent quality are achieved using data recorded by a seismic array. The sensitivity of the method is very high, to the extent that it is able to discern small differences in the waveforms within a family of earthquakes and separate the events spatially. In two cases this has enabled us to identify two fracture planes within the same family.

To check the stability of our method for characterization of fractures we have carried out a series of tests. We have investigated the effect of the selection of the velocity model that is used to locate the earthquakes, the uncertainty in the estimation of the apparent slowness vector of the master event, and the choice of master event among the members of each cluster. The results show that the estimate of the strike is very robust in all cases, while the dip is more influenced by the characteristics of the model and the value of the apparent slowness of the master.

The fracture planes obtained in this work reveal the presence of active faults in the Fumarole Bay area. The strikes clearly show that most of the planes have a NW-SE trend while a few run NE-SW. These strikes are coincident with fracturing directions listed in other works about the island. The dips are mostly sub-vertical, which is consistent with the existence of normal faults related to the extension of the Bransfield. The geometry and position of these planes show that the 1999 series was influenced by regional tectonics, although the origin of the destabilization of the system is related to the reactivation of a shallow magma chamber.

We have created an analysis tool that can be easily applied in those volcanoes where arrays are used as recording media. The method provides the basis to determine rupture planes of the

VT events and obtain information on the local tectonic regime using only a seismic array. The simplicity of array logistics, easy maintenance, etc, compared to the deployment of a seismic network, and the equivalence of the quality of the results, means that the methodology should have successful applications in volcanic areas.

Acknowledgements. This work has been partly supported by Projects ANT-1111, TOMODEC, POL2006-08663, and CGL2008-01660 of the Spanish Ministry of Science and Innovation. We thank all the participants in the 1998-1999 seismic survey.

References

Almendros, J., Ibáñez, J.M., Alguacil, G., Del Pezzo, E., Ortiz, R., 1997. Array tracking of the volcanic tremor source at Deception Island, Antarctica. *Geophys. Res. Lett.,* **24,** 3069-3072.

Almendros, J., Ibáñez, J.M., Alguacil, G., Del Pezzo, E., 1999. Array analysis using circular wavefront geometry: An application to locate the nearby seismo-volcanic source. *Geophys. J. Int.*, **136,** 159-170.

Almendros, J., Ibáñez, J.M., Alguacil, G., Morales, J., Del Pezzo, E., La Rocca, M., Ortiz, R., Araña, V., Blanco, M.J. 2000. A double seismic antenna experiment at teide Volcano: Existence of local seismicity and lack of evidences of volcanic tremor. *J. Volcanol. Geotherm. Res.* **103,** 439-462.

Almendros, J., Chouet, B., Dawson, P., 2001a. Spatial extent of a hydrothermal system at Kilauea Volcano, Hawaii, determined from array analyses of shallow long-period seismicity: 1.Method, *J. Geophys. Res.,* **106** (B7), 13,565-13,580.

Almendros, J., Chouet, B., Dawson, P., 2001b. Spatial extent of a hydrothermal system at Kilauea Volcano, Hawaii, determined from array analyses of shallow long-period seismicity: 2. Results, *J. Geophys. Res.,* **106** (B7), 13,581-13,597.

Almendros, J., Carmona, E., Ibáñez, J.M., 2004. Precise determination of the relative wave propagation parameters of similar events using a small aperture seismic array. *J. Geophys. Res.,* 109, B11308, doi:10.1029/2003JB002930.

Almendros, J., Ibáñez, J.M., Carmona, E., Zandomenegui, D., 2007. Array analyses of volcanic earthquakes and tremor recorded at Las Cañadas caldera (Tenerife Island, Spain) during the 2004 seismic activation of Teide volcano. *J. Volcanol. Geotherm. Res.,* **160,** 285-299.

Alparone, S., Gambino, S., 2003. High precision locations of multiplets on south-eastern flank of Mt. Etna (Italy), reconstruction of fault plane geometry. *Phys. Earth Planet. Int.,* **135**, 281-289.

Aster, R.C., Scott, J., 1993. Comprehensive characterization of waveform similarity in microearthquake data sets. *Bull. Seismol. Soc. Am.,* **83,** 1307-1314.

Baker, P.E., McReath, I., Harvey, M.R., Roobol M.J., Davis, T.G., 1975. The Geology of the South Shetland Islands: V. Volcanic evolution of Deception Island, *British Antarctic Survey Scientific Reports,* **78**, 81.

Barclay, A.H., Wilcock, W.S.D., Ibáñez, J.M., 2009. Bathymetric constraints on the tectonic and volcanic evolution of Deception Island Volcano, South Shetland Islands. *Antarctic Science,* **21** (2), 153-167.

Baraldo A., Rinaldi, C.A., 2000. Stratigraphy and structure of Deception Island, south Shetland Island, Antarctica. *J. South Am. Sciences.* **13,** 785-796.

Battaglia, J., Thurber, C.H., Got, J., Rowe, C.A., White, R.A., 2004. Precise relocation of earthquakes following the 15 June 1991 eruption of Mount Pinatubo (Philippines). *J. Geophys. Res.,* **109,** doi:10.1029/2003JB002959.

Battaglia, J., Aki, K., Ferrazzini, V., 2005. Location of tremor sources and estimation of lava using tremor source amplitude on the Piton de la Fournaise volcano: 1. Location of tremor sources. *J. Volc. Geoth. Res.,* **147,** 268-290.

Ben-Zvi, T., Wilcock, W.S.D., Barclay, A., Zandomenegui, D., Ibáñez, J.M., Almendros, J., 2009. The P-wave velocity structure of Deception Island, Antartica, from two-dimensional seismic tomography. *J. Volc. Geoth. Res.,* **180,** 67-80.

Berrocoso, M., Fernández-Ros, A., Ramírez, M.A., Salamanca, J.M., Torrecillas, C., Pérez-Peña, A., Páez, R., García-García, A., Jiménez-Teja, Y., García-García, F., Soto, R., Gárate, J., Martín-Dávila, J., Sánchez-Arzola, A., de Gil, A., Fernández-Prada, J.A., Jigena, B., 2008. *Geodetic and Geophysical Observations in Antarctica,* A. Capra, R. Dietrich (eds.), 97-123.

Brancato, A., Gresta, S., 2003. High precision relocation of microearthquakes at Mt. Etna (1991-1993 eruption onset), a tool for better understanding the volcano seismicity. *J. Volcanol. Geotherm. Res.* **124.** 219-239.

Carmona, E., Martini, F., Ibáñez, J.M., 2007. Families of events and seismic velocity changes during the 1998–99 seismic series at Deception Island volcano. Eos Trans. AGU 88 (52) Fall Meet. Suppl.

Carmona, E., Stich, D., Saccorotti, G., Ibáñez, J.M., 2009. Multiplet focal mechanisms from polarities and relative locations: The Iznajar swarm in Southern Spain. *Bull. Seismol. Soc. Am.* In press.

Caselli, A. T., Santos-Afonso, M., Agusto, M. R., 2004. Gases fumarólicos de la isla Decepción (Shetlands del Sur, Antártida): variaciones químicas y depósitos vinculados a la crisis sísmica de 1999, *Rev Asoc. Geol. Arg.*, *59*, 291-302.

Chouet, B., 1996. Long-Period volcano seismicity: Its source and use in eruption monitoring, *Nature*, **380**, 309-316.

Chouet, B., Saccorotti, G., Martini, M., Dawson, P., De Luca, G., Milana, G., Scarpa, R., 1997. Source and path effects in the wave fields of tremor and explosions at Stromboli Volcano, Italy, *J. Geophys. Res.,* **102,** 15129-15150.

Dawson, P.B., Chouet, B.A., Okubo, P.B., Villaseñor, A., Benz, H.A., 1999. Three-dimensional velocity structure of the Kilauea caldera, Hawaii. *Geophys. Res. Lett.,* **26,** 2805-2808.

Deichmann, N., García-Fernández, M., 1992. Rupture geometry from high-precision relative hypocenter locations of microearthquake clusters. *Geophys. J. Int.* **110**, pp. 501–517.

Del Pezzo, E., La Rocca, M., Ibanez, J.M., 1997. Observations of high-frequency scattered waves using dense arrays at Teide volcano, *Bull. Seism. Soc. Am.,* **87**, 1637-1647.

Fernandez-Ibáñez, F., Pérez-López, R., Martínez-Díaz, J.J., Paredes, C., Giner-Robles, J.L., Caselli, A., Ibáñez, J.M., 2005. Costa Recta Beach, Deception Island, West

Antartica: a retreated scarp of a submarine fault? *Antartic Science,* **17,** 418-426.

Fernández Ros, A., Berrocoso, M., Ramírez, M.E., 2007, Volcanic deformation models for Decption Island (South Shetland Islands, Antartica). *USGS* OF-2007-1047, Extended Abstract 094.

Frankel, A., Hough, S., Friberg, P., Busby, R., 1991. Observations of Loma Prieta aftershocks from a dense array in Sunnyvale, California. *Bull. Seism. Soc. Am.* **81,** 1900-1922.

Fremont, M.J., Malone, S.D., 1987. High precision relative locations of earthquakes at Mount St. Helens, Washington. *J. Geophys. Res.* **92**,. 10223–10236.

Geller, R.J., Mueller, C.S., 1980, Four similar earthquakes in Central California. *Geophys. Res. Lett,* **7,** 821-824.

Gillard, D., Rubin, A.M., Okubo, P., 1996. Highly concentrated seismicity caused by deformation of Kilauea's deep magma system. *Nature,* **384,** 343-346.

González-Casado, J.M., López-Martínez, J., Giner, J., Durán, J.J., Gumiel, P., 1999. Análisis de la microfracturación en la isla Decepción, Antártida occidental. *Geogaceta,* **26,** 27-30.

González-Ferrán, O., Katsui, Y., 1970. Estudio integral del volcanismo cenozoico superior de las Islas Shetland del Sur, Antartica. *Instituto Antártico Chileno Ser. Cient.,* **1,** 123-174.

Havskov J., Peña, J.A., Ibáñez, J.M., Ottemöller, L., Martínez-Arévalo, C., 2003. Magnitude scales for very local earthquakes. Application for Deception Island volcano (Antarctica). *J. Volc. Geoth. Res.,* **128**, 115-133.

Hensch, M., Riedel, C, Reinhardt, J., Dahm, T., 2008. Hypocenter migration of fluid-induced earthquake swarms in the Tjörnes Fracture Zone (North Iceland). *Tectonophysics,* **447,** 80-94.

Ibáñez, J.M., Morales, J., Alguacil, G., Almendros, J., Ortiz, R., Del Pezzo, E., 1997. Intermediate-focus earthquakes under South Shetland Islands (Antarctica), **24,** *Geophys. Res. Lett.,* 531-534.

Ibáñez, J.M., Del Pezzo, E., Almendros, J., La Rocca, M., Alguacil, G., Ortiz, R., García, A., 2000. Seismovolcanic signals at Deception Island volcano, Antarctica: wavefield analysis and source modeling, *J. Geophys. Res.* **105,** 13,905–13,931.

Ibáñez, J.M., Almendros, J., Carmona, E., Martínez-Arévalo, C., Abril, M., 2003a. The recent seismo-volcanic activity at Deception Island volcano. *Deep-Sea Res. II,* **50**, 1611-1629.

Ibáñez, J.M., Carmona, E., Almendros, J., Saccorotti, G., Del Pezzo, E., Abril M., Ortiz, R., 2003b. The 1998-1999 seismic series at Deception Island volcano, Antarctica, *J. Volcan. Geotherm. Res.,* **128,** 65-88.

Ibáñez, J.M., Del Pezzo, E., Bengoa, C., Caselli, A., Badi, G., Almendros, J., 2008. Volcanic tremor and local earthquakes at Copahue volcanic complex, Southern Andes, Argentina. *J. Volcan. Geotherm. Res.,* **174,** 284-294.

Jones, J.P., Thurber, C.H., Lutter, W.J. 2001. High-precision location of pre-eruption seismicity at Mount Pinatubo, Philippines, 30 May-3 June, 1991. *Phys. Earth Planet. Int.,* **123,** 21-232.

La Rocca, M., Petrosino, S., Saccorotti, G., Simini, M., Ibáñez, J.M., Almendros, J., Del Pezzo, E., 2000. Location of the source and shallow velocity model deduced from the explosion quakes recorded by two seismic antennas at Stromboli Volcano. *Phys. Chem. Earth,* **25**, 731-735.

La Rocca, M., Saccorotti, G., Del Pezzo, E., Ibáñez, J.M., 2004. Probabilistic source location of explosion quakes at Stromboli volcano estimated with double array data. *J. Volcan. Geotherm. Res.,* **131,** 123-142.

La Rocca, M., Galluzzo, D., Malone, S., McCausland, W., Saccorotti, G., Del Pezzo, E., 2008. Testing Small-Aperture Array Analysis on Well-Located Earthquakes, and Application to the Location of Deep Tremor. *Bull. Seismol. Soc. Am.,* **98,** No.2, 620-635.

Luzón, F., Almendros, J., García-Jerez, A., 2009. Shallow structure of Deception Island volcano, Antarctica, using the two station spatial autocorrelation method on a dense set of seismic arrays. *Submitted to Geophysical Journal International.*

Maestro, A., Somoza, L., Rey, J., Martínez-Frías, J., López-Martínez, J., 2007. Active tectonics, fault patterns, and stress field of Deception Island: A response to oblique convergence between the Pacific and Antarctic plates. *J. South Am. Earth Sciences,* **23,** 256-268.

Martí, J., Vila, J., Rey, J., 1996. Deception Island (Bransfield Strait, Antarctica): an example of volcanic caldera developed by extensional tectonics. *J. Geological. Soc. London.***110,** 253-265.

Martínez-Arévalo, C., Bianco, F., Ibáñez, J.M., Del Pezzo, E., 2003. Shallow seismic attenuation and shear-wave splitting in the short period range of Deception island volcano (Antarctica). *J. Volcan. Geotherm. Res.,* **128**, 89-113.

Martínez-Arévalo, C., Mancilla, F., Almendros, J., Aznarte, J.L., Alguacil, G., 2009. Preliminary results of receiver function analyses at three sites across the Bransfield Strait. Antarctica, Geophysical Research Abstract, Vol. 11, EGU2009-13362-1, EGU General Assembly 2009.

Martini, F., Bean, C., Saccorotti, G., Viveiros, F., Wallenstein, N., 2009. Seasonal cycles of seismic velocity variations detected using coda wave interferometry at Fogo volcano, Azores, during 2003-2004. *J. Volcan. Geotherm. Res.,* **181,** 231-46.

Massa, M., Eva, E., Spallarossa, D., Eva, C., 2006. Detection of earthquake clusters on the basis of waveform similarity, an application in the monferrato region (Piedmont, Italy). *J. Seism.,* **10,** 1-22.

Maurer, H., Deichmann, N., 1995. Microearthquake cluster detection based on waveform similarities, with an application to the western Swiss Alps. *Geophys. J. Int.* **123**, pp. 588-600.

Metaxian, J.P., Lesage, P. Dorel, J., 1997. Permanent tremor of Masaya volcano, Nicaragua: wave field analysis and source location. *J. Geophys. Res.* ,**102,** 22529-22545.

Metaxian, J.P., Lesage, P., Valette, B., 2002. Locating sources of volcanic tremor and emergent events by seismic triangulation: Application to Arenal volcano, Costa Rica. *J. Geophys. Res. Solid Earth.* **107**, doi:10.1029/2001JB000559.

Mora, M.M., Lesage, P., Valette, B., Alvarado, G.E., Leandro, C., Métaxian, J.P., Dorel, J., 2006. Shallow velocity structure and seismic site effects at Arenal volcano, Costa rica. *J. Volcan. Geotherm. Res.,* **152,** 121-139.

Musumeci, C., Gresta, S., Malone, D., 2002. Magma system recharge of Mount St. Helens from precise relative hypocenter location microearthquakes. *J. Geophys. Res.,* **107,** doi: 10.1029/2001JB000629.

Ocaña, E., Stich, D., Carmona, E., Vidal, F., Bretón, M., Navarro, M., García-Jerez, A., 2008. Spatial analysis of

the La Paca, SE Spain, 2005 seismic series through the relative location of multiplets and principal component analysis. *Phys. Earth Planet. Intern.,* **166,** 117-127.

Ortiz, R., Garcia, A., Aparicio, A., Blanco, I., Felpeto, A., Del Rey, R., Villegas, M.T., Ibáñez, J.M., Morales, J., Del Pezzo, E., Olmedillas, J.C., Atiz, M., Vila, J., ramos, M., Viramonte, J.G., Risso, C., Caselli, A., 1997. Monitoring of the volcanic activity of Deception Island, South Shetland island, Antarctica (1986-1995). *The Antarctic Region: geological Evolution and Process.* 1071-1076.

Palo, M., Ibáñez, J.M., Cisneros, M., Bretón, M., Del Pezzo, E., Ocaña, E., Orozco-Rojas, J., Posadas, A.M., 2009. Analysis of the seismic wavefield properties of volcanic explosions at Volcán de Colima, México: insights into the source mechanism. *Geophys. J. Int.,* 2009, **177,** 1383-1398.

Pandolfi, D., Bean, C.J., Saccorotti, G., 2006. Coda wave interferometric detection of seismic velocity changes associated with the 1999 M=3.6 event at Mt. Vesuvius. *Geophys. Res. Lett.,* **33,** doi: 10.1029/2005GL025355.

Paredes, C., Pérez-López, R., Giner-Robles, J.L., De la Vega, R., García-García, A., Gumiel, P., 2006. Distribución especial y zonificación tectónica de los morfolineamientos en la Isla Decepción (Shetland del Sur, Antártida). *Geogaceta.* **39,** 75-78.

Pelayo, A.M., Wiens, D.A., 1989. Seismotectonics and relative plate motions in the Scotia Sea region, *Journal of Geophysical Research,* **94** (B6), 7293-7320.

Poupinet, G., Ellsworth, W.L., Frechet, J., 1984. Monitoring velocity variations in the crust using earthquakes doublets: an application to the Calaveras fault, California. *J. Geophys. Res.* **89**, pp. 5719–5731.

Press, W.H., Flannery, B.P., Teukolsky, S.A., Vetterling, W.T., 1989. Numerical recipes (Fortran version). Cambridge University Press, Cambridge.

Ratdomopurbo, A., Poupinet, G., 1995. Monitoring a temporal change of seismicity velocity in a volcano, application to the 1992 eruption of Mt. Merapi (Indonesia). *Geophys. Res. Lett.,* **22,** 775-778.

Rey, J., Somoza, L., Martínez-Frías, J., 1995. Tectonic, volcanic, and hydrothermal event sequence on Deception Island (Antarctica). *Geo-Marine Lett.,* **15,** 1-8.

Robertson Maurice, S.D., Wiens D.A., Shore P.J., Vera E., Dorman L.M. (2003). Seismicity and tectonics of the South Shetland Islands and Bransfield Strait from a regional broadband seismograph deployment.., *J. Geophys. Res.,* **108,** 10.029/2003JB002416.

Ruiz, M., Gaspà, O., Gallart, J., Díaz, J., Pulgar, J.A., García-Sansegundo, J., López-Fernández, C., Gonzalez-Cortina, J.M., 2006. Aftershocks series monitoring of the September 18, 2004 M=4.6 earthquake at the western Pyrenees: A case of reservoir-triggered seismicity? *Tectonophysics,* **424,** 223-243.

Saccorotti, G., Almendros, J., Carmona, E., Ibáñez, J.M., Del Pezzo, E., 2001a. Slowness anomalies from two dense seismic arrays at Deception Island Volcano, Antarctica. *Bull. Seismol. Soc. Am.,* **91,** 561-571.

Saccorotti, G., Maresca, R., Del Pezzo, E., 2001b. Array analyses of seismic noise at Mt. Vesuvius Volcano, Italy. *J. Volcan. Geotherm. Res.*, **110,** 79-100.

Saccorotti, G., Carmona, E., Ibáñez, J.M., Del Pezzo, E., 2002. Spatial characterization of Agrón, southern Spain, 1988-1989 seismic series. *Phys. Earth Planet. Intern.,* **129,** 13-29.

Saccorotti, G., Zuccarello, L., Del Pezzo, E., Ibañez, J.M., Gresta, S., 2004. Quantitative analysis of the tremor wavefield at Etna Volcano, Italy. *J. Volcan. Geotherm. Res.,* **136**, 223-245.

Scarfì, L. Langer, H., Gresta, S., 2003. High-precision relative locations of two microearthquakes clusters in Southeastern Sicily, Italy. *Bull. Seism. Soc. Am.,* **93,** 1479-1497.

Shearer, P.M., Hardebeck, J.L., Astiz, L., Richards-Dinger, K.,B., 2003. Analysis of similar event clusters in aftershocks of the 1994 Northridge, California, earthquake. *J. Geophys. Res.,* **108,** doi:10.1029/2001/JB000685.

Shelly, D.R., Ellsworth, W.L., Ryberg, T., Haberland, C., Fuis, G.S., Murphy, J., Nadeau, R.M., Bürgmann, R., 2009. Precise location of Andreas Fault tremors near Cholame, California using seismometer clusters: Slip on the deep extension of the fault?. *Geophys. Res. Lett.,* **36,** doi: 10.1029/2008GL036367.

Smellie, J.L., 1988. Recent observations on the volcanic history of Deception Island, South Shetland Islands. *Br. Antarct. Surv. Bull.,* **81,** 83-85.

Smellie, J.L., López-Martínez, J., 2000. Geological map of Deception Island. BAS GEOMAP Series, Sheet 6-A. 1:25,000. British Antarctic Survey, Cambridge.

Snieder, R., Hagerty, M., 2004. Monitoring change in volcanic interiors using coda wave interferometry: Application to Arenal Volcano, Costa Rica. *Geophys. Res. Lett.,* **31,** doi: 10.1029/2004GL019670.

Stich, D., Alguacil, G., Morales, J., 2001. The relative location of multiplets in the vicinity of the Western Almeria (southern Spain) earthquake series of 1993–94. *Geophys. J. Int.*, **146,** 801-812.

Tsujiura, M., 1983. Characteristics frequencies for earthquake families and their tectonic implications, evidences from earthquake swarm in the Kanto District, Japan. *Pure Appl. Geophys.,* **4,** 573-600.

Vila, J., Martí, J., Ortiz, R., García, A., Correig, A. M., 1992, Volcanic tremors at Deception Island (South Shetland Islands, Antarctica). *J. Volcanol. Geotherm. Res.,* **53,** 89-102.

Vila, J., Correig, A.M., Martí, J. 1995. Attenuation and source parameters at Deception Island (South Shetland Islands, Antarctica). *Pageoph.* **144,** 229-250.

Waite, G.P., Moran, S.C., 2009, Vp Structure of Mount St. Helens, Washington, USA, imaged with local earthquake tomography, *J. Volcanol. Geotherm. Res.,* **182,** 113-122.

Zandomenegui, D., Barclay, A., Almendros, J., Ibáñez, J.M., Wilcock, W.S.D., Ben-Zvi, T., 2009. The crustal structure of Deception Island Volcano from P-wave seismic tomography: tectonic and volcanic implications. *J. Geophys. Res.* 114, B06310, doi:10.1029/2008JB006119

TERCERA PARTE

Conclusiones

1. Caracterización de sistemas de fractura en la Cuenca de Granada
2. Caracterización de sistemas de fractura en la Isla Decepción
3. Conclusiones generales
4. Trabajos futuros

Conclusiones

En este capítulo se enumeran de manera resumida los principales resultados e interpretaciones de esta memoria de Tesis junto con algunos trabajos futuros.

1. Caracterización de sistemas de fractura en la Cuenca de Granada.

Se ha utilizado como herramienta para la caracterización de los sistemas de fractura en dos zonas de la Cuenca de Granada, el análisis de dos series de terremotos que tuvieron lugar en Agrón en 1988-1989 e Iznájar en 1998. Estas dos series proporcionaron el suficiente número de terremotos como para poder aplicar las técnicas de localización relativa con evento maestro. Estas localizaciones precisas permitieron junto con los mecanismos focales de algunos de los eventos de los multipletes caracterizar algunos de los planos de fractura de las series.

Para la serie de Agrón las conclusiones más relevantes han sido las siguientes:

- El primer análisis de relocalización indicaba dos alineamientos epicentrales aproximadamente NE-SO y unas profundidades comprendidas entre 1-25km

- La relocalización probabilística permitió definir mejor los rangos de profundidad para dos conjuntos de terremotos de 6-8 y 10-15 km y vagamente muestra los dos alineamientos NE-SO de la relocalización preliminar.

- Se aplicó el método de las componentes principales espacial al conjunto de terremotos relocalizados permitiendo identificar cinco posibles alineamientos de los cuales solamente uno se corresponde con la alineación epicentral preliminar.

- Se han obtenido un total de cinco familias con más de tres terremotos con formas de onda similares con un coeficiente de correlación de 0.9.

- A partir de las localizaciones relativas, se han obtenido dos planos N-S, uno E-O, uno NE-SO y otro NO-SE.

- La geometría de los planos obtenidos combinando la localización relativa, las componentes principales y los mecanismos focales de los cinco multipletes, revelan la complejidad existente en el pequeño volumen hipocentral. Se han obtenido dos soluciones de falla normal con direcciones NO-SE, y ENE- OSO y una tercera solución de salto en dirección sinistra con dirección N-S. Las localizaciones relativas y los mecanismos focales coincidieron con tres de los cinco planos obtenidos por las componentes principales del análisis preliminar.

- Tanto el plano NO-SE como uno de los dos planos conjugados del mecanismo del terremoto principal coinciden con la extensión regional ENE-OSO que actúa en el área. Sin embargo, los esfuerzos locales que actúan en la Cuenca de Granada parecen estar caracterizados por una naturaleza alargada del elipsoide de esfuerzos, con el eje σ_1 inclinado hacia el SO y los componentes σ_2 y σ_3 casi idénticos. Esta configuración del estado de esfuerzos local podría conducir a la reactivación de planos de falla preexistentes, como por ejemplo los planos de los multipletes II y III con dirección NE-SO.

- La proximidad de los distintos planos de falla encontrados pone de manifiesto la fragmentación significativa de la corteza superior en bloques tectónicos pequeños de 2-4 km. Esta conclusión coincide con lo propuesto por otros autores para la sismicidad occidental de Almería. Este grado de fragmentación explicaría la compleja redistribución del esfuerzo de cizalla después de cada evento, lo que provocaría la reactivación de planos de falla orientados de forma diferente a la esperada en el campo de esfuerzos regional.

Para la serie de Iznájar, las conclusiones son las siguientes:

- La localización preliminar de la serie indica una tendencia E-O cuando se ha representado la distribución epicentral, debido principalmente a la asimetría de los errores de localización producida por el emplazamiento de la serie, desplazada al O de la red sísmica.

- Se han podido obtener un total de 154 familias con 74 dobletes, 34 tripletes y 46 multipletes entre 4 y 26 terremotos. Este volumen de datos supone el 32% del total de la serie. Para el análisis de localización relativa se han empleado 13 de estas familias por el número adecuado de terremotos y su calidad en la forma de onda obteniendo 14 planos (un plano más por el desdoblamiento en dos planos de una de las familias).

- De los catorce planos de ajuste con la localización relativa, nueve se han podido combinar con los mecanismos focales para obtener la dinámica de la fuente (azimut del plano, buzamiento, ángulo de deslizamiento,…). Las soluciones de estos planos de falla han sido seis fallas de salto en dirección sinistras con azimut N-S y tres fallas normales con direcciones desde NO-SE a NNE-SSE.

- La familia que se ha podido desdoblar en dos planos paralelos se han obtenido dos de las fallas de salto en dirección. El hecho de que estos dos planos se encuentren a tan solo 230 m, indica el alto grado de fracturación en el que se encuentra el volumen de la fuente.

- Los tensores momento calculados no coinciden del todo con los resultados de la localización relativa pero su rango de confianza incluyen las fallas de salto en dirección N-S, con lo que podríamos identificar uno de los planos nodales N-S de los tensores momento como el plano de falla activo.

- Los mecanismos de falla dominantes en la serie son de salto en dirección sinistra. Pero la presencia de estas fallas junto con fallas de componente normal sugiere la permutación de los ejes principales mayores y medios del esfuerzo. Esta coexistencia de dos tipos de fallas implican que pueden actuar entre sí para compensar el desplazamiento diferencial entre fallas adyacentes.

- El predominio de fallas de salto en dirección hace que la actividad de la serie de Iznájar sea diferente de la sismicidad asociada a la Cuenda de Granada, donde dominan los mecanismos de falla normal y extensión ENE-

OSO. Sin embargo, la profundidad de la serie de Iznájar y las fallas bajo la Cuenca de Granada son similares y se concentran entre 9 y 16 km de profundidad.

- Debido a las pequeñas dimensiones de las fallas involucradas en los terremotos de pequeña magnitud del enjambre de Iznájar, no podemos especular sobre la importancia de estas fallas en relación con los esfuerzos de la tectónica regional, pero en cualquier caso, nuestros resultados ponen de relieve la alta heterogeneidad de la deformación tectónica en la Cordillera Bética, donde la sismotectónica a diferente escala puede ser controlada por fallas que interaccionan entre sí.

2. Caracterización de sistemas de fracturas en la isla Decepción.

Se han caracterizado las estructuras implicadas en la serie de 1999 de la isla Decepción, una zona volcánica activa situada en las Islas Shetland del Sur (Antártida). Para ello, hemos elaborado un método de localización relativa precisa para aplicarlo a terremotos registrados con antenas sísmicas, aprovechando la similitud de la forma de onda. El método parte de estimar de forma precisa el vector lentitud aparente relativo de los eventos de una misma familia respecto de su evento maestro con el método RelSE que hemos diseñado. Esto permite localizar espacialmente los eventos y en algunos casos, ajustar los hipocentros a un plano de ruptura. El análisis de la serie con la localización de los eventos volcánicos y volcano-tectónicos y la estimación de la energía, junto con la información proporcionada por la geometría de las fracturas con la localización precisa relativa, ha permitido establecer una hipótesis sobre el origen de la serie volcano-tectónica.

Algunas de las conclusiones de esta parte del trabajo han sido las siguientes:

- Las localizaciones de los eventos de la serie ponen de manifiesto la presencia de eventos de largo periodo (LP), tremor volcánico, terremotos volcano-tectónicos (VT) y eventos híbridos. El origen de las señales volcánicas (LP y tremor) está al O y S de la antena sísmica. Para los eventos volcanotectónicos (VT) e híbridos, su área fuente está localizada al NE en la bahía de Fumarolas, entre 1 y 4 km de distancia epicentral. Esto indica que el origen de la sismicidad LP no es el mismo que los eventos volcanotectónicos y que tendrían origen hidrotermal.

- El mapa epicentral preliminar muestra dos posibles alineamientos con direcciones N45ºE y N80ºE. Pero la incertidumbre de estas localizaciones no permite llegar a una conclusión sobre la geometría de las fracturas.

- Los híbridos fueron detectados cuando los hipocentros de los terremotos VT comenzaron a emigrar hacia abajo. La ocurrencia de híbridos durante de la serie sísmica en el mismo área que los VT es confirmación de la presencia de fluidos en el área fuente. Estos eventos son evidencia de que los fluidos están presentes en los sistemas de fractura.

- La mayoría de los terremotos VT se han producido con pequeñas caídas de esfuerzos (menos de 4 bares) en fracturas con un radio medio de cerca de 50 m. Este hecho se puede explicar por la lubricación de las microfallas debido a la presurización de los fluidos. El aumento de la presión de poro en la corteza superficial que cubre el sistema magmático habría podido inducir la activación repetida de la red de fracturas.

- Se han encontrado 48 familias, de las que 19 son dobletes, 9 son tripletes y 20 multipletes con 4 o más eventos con un alto grado de similitud de la forma de onda (~ 0.9 de correlación).

- De las 17 familias con cinco o más eventos, se han podido ajustar a un plano de ruptura 14 de ellas, obteniendo alta calidad de ajuste en la mayoría de ellas.

- En dos familias el método ha sido capaz de separar en dos subplanos los hipocentros para alcanzar un mejor ajuste. Esta separación se ha podido comprobar a posteriori con las leves diferencias de las formas de onda (sobre todo la onda S) entre estos dos grupos. Al final, contando con estos dos planos se ha conseguido la caracterización de 16 planos de fractura.

- Los azimutes de los planos varían entre N119ºE y N38ºO, pero la mayoría tiene dirección NO-SE. Los buzamientos varían entre 41 y 86º, la mayoría de ellos subverticales. Estos azimutes coinciden con algunos alineamientos descritos en otros trabajos. Los alineamientos encontrados en el análisis preliminar no coinciden con estas direcciones, lo que pone de manifiesto de nuevo que para interpretar las posibles estructuras es necesario hacerlo a través de las técnicas de localización relativa o el análisis de mecanismos de la fuente de los terremotos implicados.

- La activación de estos planos de ruptura bien podría deberse a factores puramente de tectónica regional, puramente volcánicos, o una mezcla de ambos.

  - Se puede excluir la primera hipótesis por porque la actividad sísmica se restringe a la bahía interna y no hay un número anómalo de terremotos fuera de la isla.

  - La segunda hipótesis también la descartamos. Si los fluidos magmáticos estuvieran implicados directamente deberíamos haber observado una migración ascendente de los hipocentros, siguiendo la migración ascendente del magma. Por el contrario, observamos una migración hacia abajo de los hipocentros. La presencia del magma en bajas profundidades y la presión relativamente baja es acompañada generalmente por gas, que produce la sismicidad de eventos LP y del tremor. El hecho de que no coinciden el área de la fuente de los eventos LP y la región hipocentral de los terremotos implica que no hay magma superficial en ningún momento durante la serie.

  - La hipótesis por la que nos decantamos es la inyección profunda de magma que desestabiliza el sistema de fracturas y que éstas a su vez se rigen por la tectónica regional de la zona. Cuando la tensión alcanza un valor umbral, los procesos de fractura comienzan, siguiendo zonas preexistentes de debilidad. La ausencia de una evidencia visible de una erupción y el bajo nivel de actividad de terremotos observados después de 1999 nos hace pensar que la inyección del magma paró antes de alcanzar la superficie.

3. Conclusiones generales

El análisis de estas tres series pone de manifiesto varias conclusiones en común:

- Las tres series tienen aspectos comunes. Son series localizadas en un área reducida de apenas unos km^2, magnitudes pequeñas, y en el caso de la serie de Iznájar y Decepción con un elevado número de terremotos, registradas con estaciones de corto periodo y para las tres series aparecen alineamientos en el mapa epicentral preliminar. Estas características comunes facilitan algunas de las técnicas empeladas que como se ha visto en esta memoria de Tesis han sido también las mismas.

- Queda demostrada la importancia del estudio sismotectónico de las series o enjambres sísmicos para la caracterización de los sistemas de fractura. Incluso para series como es el caso de la de Agrón con un número pequeño de terremotos (125 localizados) y de magnitudes bajas como el caso de la serie de Iznájar y Decepción.

- Cuando se trabaja con redes, el hecho de colocar estaciones portátiles de 3 componentes en la misma área hipocentral, en el momento de la ocurrencia de los terremotos ha permitido, sobre todo en el caso de la serie de Iznájar, poder precisar mejor la localización hipocentral, sobre todo la profundidad.

- Las estructuras sismogenéticas implicadas en las tres series no han coincidido del todo con los alineamientos epicentrales aparentes que se observan en la localización preliminar. Por tanto una correcta interpretación de la distribución de hipocentros en términos de fracturas debe basarse necesariamente en localizaciones precisas.

- Del mismo modo, los sistemas de fractura encontrados no coinciden del todo con las direcciones que se esperan a partir de la dinámica regional.

  - Las fallas implicadas en la generación las series de Agrón e Iznájar tienen direcciones variadas que no siguen la tectónica regional de la Cuenca de Granada. Esto probablemente se deba al hecho de que los terremotos tienen poca energía, y de hecho el terremoto de mayor magnitud de la serie de Agrón sí coincide con la tectónica regional. Esta diversidad de fallas, con distintos tipos de mecanismos, coexistiendo fallas de salto en dirección y fallas normales, pone de manifiesto el elevado grado de fracturación en el que se encuentra la Cuenca de Granada. Este tipo de fracturación sugiere para las dos series la fracturación de la corteza superior en bloques tectónicos pequeños que se activan con la desestabilización del sistema.

  - La mayoría de los planos obtenidos para la serie de Decepción tienen dirección predominante NO-SE y no coinciden con los sistemas de alineamientos más importantes, y en particular con la dirección NE-SO del Rift del Bransfield. Sin embargo coinciden con otros sistemas menores descritos en otros trabajos.

- Estos resultados ponen de manifiesto que la aplicación de técnicas de localización precisa para el estudio de series sísmicas es fundamental para

obtener información sobre las fracturas implicadas y así interpretarlas en el marco de la tectónica local y regional.

- El estudio de las series de Agrón e Iznájar permite entender mejor por qué ocurren enjambres sísmicos en la Cuenca de Granada y zonas aledañas y su relación con el riesgo sísmico. Si no hay grandes evidencias de sistemas de fallas dominantes y si junto a un esfuerzo vertical dominante aparecen actuaciones de esfuerzos horizontales secundarios, entones la posibilidad de tener un gran terremoto es menor. La actuación de los esfuerzos secundarios permite liberar energía en forma de enjambres sísmicos de forma progresiva.

- En el caso de la serie de Decepción, el estudio de la sismotectónica de la Isla a través de la serie de 1999 aporta nuevos resultados de una reactivación del volcán después de la última erupción de 1970 y de la anterior serie de 1992. Teniendo en cuenta la presencia de bases antárticas y de turismo, es fundamental conocer de qué forma actúa el volcán para evaluar el riesgo volcánico.

- Aunque el método de caracterización de planos de fractura mediante la localización relativa utilizando redes sísmicas está muy extendido, esta es la primera vez que se consiguen localizaciones relativas precisas utilizando datos registrados por una antena sísmica. La sensibilidad del método es muy elevada, hasta el punto de que es capaz de discernir las pequeñas diferencias en las formas de onda dentro de una familia de terremotos y separarlos espacialmente.

- Una aportación importante de este estudio estriba en la creación de un método que permite primero la estimación precisa relativa del vector lentitud aparente de terremotos con similar forma de onda registrados con antenas sísmicas, y segundo localizar de forma precisa los terremotos y ajustar a un plano los hipocentros. Esto permite investigar la geometría de los planos de fractura en series de terremotos registrados por una antena sísmica.

- A diferencia del método de localización relativa con redes sísmicas, muy utilizado, el método de localización relativa de terremotos registrados en antenas sísmicas es novedoso y por tanto necesita de unas pruebas de robustez y calidad.

- Se han realizado unos test de control de calidad de esta metodología para comprobar con datos sintéticos (1) la resolución del método RelSE modificando la relación señal ruido, (2) el efecto de la apertura de la antena

sísmica y (3) cómo afecta a la distribución de los vectores lentitud aparente la elección del evento maestro.

- También se ha comprobado con datos reales como le afectan a los resultados tres factores: (1) la influencia del modelo de velocidad empleado para representar el medio; (2) la incertidumbre de la estimación del vector lentitud aparente del evento maestro; y (3) la elección del evento maestro dentro de cada familia. El resultado ha sido una alta estabilidad de los resultados, en especial del azimut del plano. Algo más dependiente de estos factores es el buzamiento del plano, que queda determinado con mayor incertidumbre.

4. Trabajos Futuros

Viendo la facilidad con que la Cuenca de Granada genera series o enjambres sísmicos y aprovechando la instalación de instrumentación en el Sur de la Península con la incorporación de sensores de banda ancha, estamos en disposición de estudiar y analizar el resto de series que aunque son pequeñas en número, no lo son en importancia por la zona a las que representan y lo recientes de las mismas. Por ejemplo podemos citar las dos series de Loja (2000, 2003), las dos series de Alhama-Zafarraya (2001, 2009) y la más reciente al Sur de la capital de Granada (2009) (Figura 1). Estas series podrían suministrar más información de la sismotectónica local de las zonas implicadas.

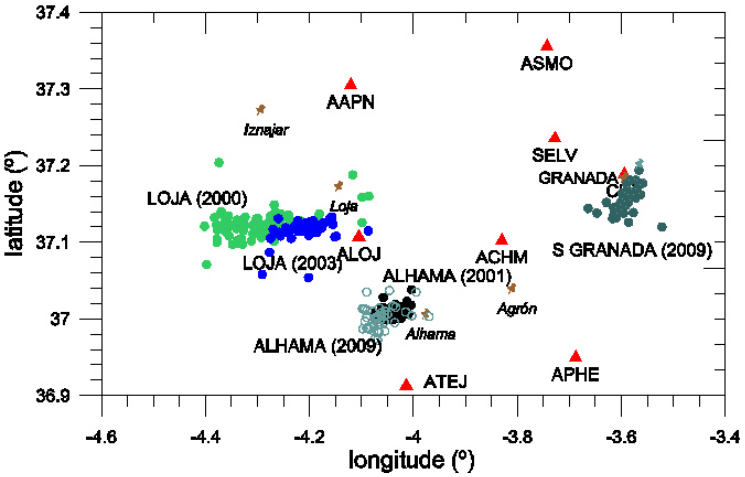

Figura 1. Series recientes de la Cuenca de Granada y zonas vecinas desde el año 2000 hasta la actualidad. Con distintos círculos de colores muestran las series. Los triángulos rojos son las estaciones permanentes de la RSA.

Además esta metodología está en disposición de ser utilizada en otros volcanes activos (Colima, Arenal, Copahue, Teide, Vesubio,…) donde en estos momentos se monitorea o se planea monitorear con antenas sísmicas (Figura 2).

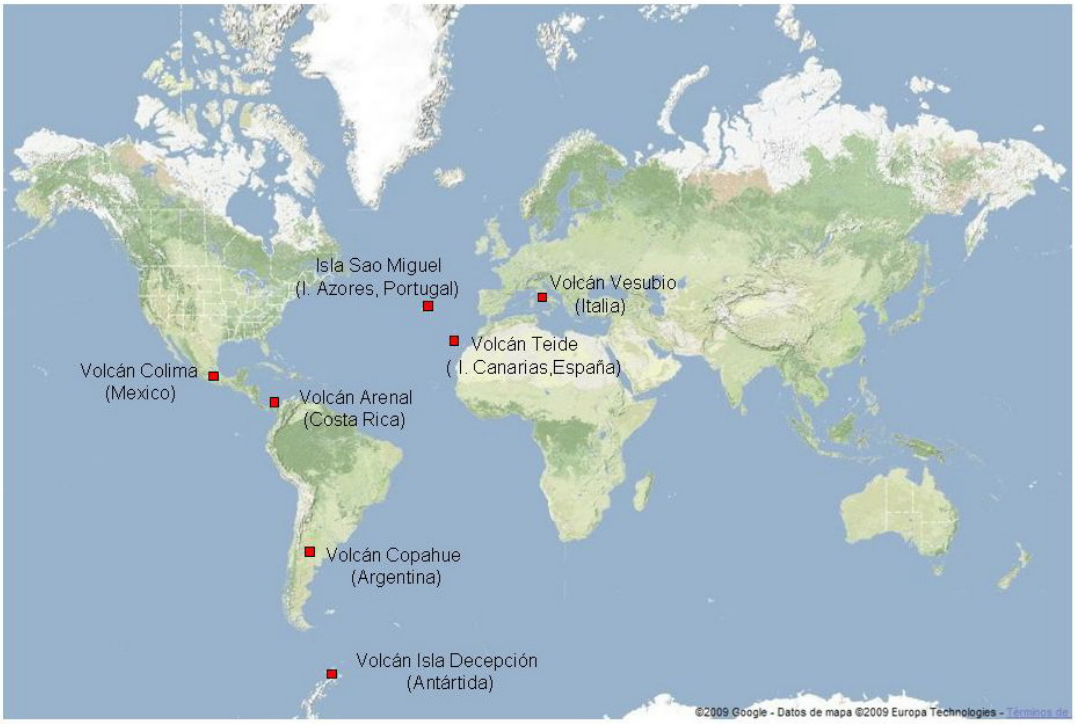

Figura 2. Mapa mundi con algunos volcanes donde se podrían aplicar las técnicas de localización precisa relativa con antenas sísmicas.

En el caso de zonas volcánicas y aprovechando la ventaja de utilizar antenas sísmicas para detectar y caracterizar frentes de ondas que atraviesan la antena, el método podría abarcar todo el sismograma incluyendo la coda. Teniendo esto en mente, podemos aventurar interesantes aplicaciones del método para estudiar el "scattering" sísmico y la generación de la coda.

ANEXOS

ANEXO I

VI. Slowness anomalies from two dense seismic arrays at Deception Island Volcano, Antarctica

ANEXO II

VII. The recent seismo-volcanic activity at Deception Island volcano

VI. Slowness anomalies from two dense seismic arrays at Deception Island Volcano, Antarctica.

Bulletin of the Seismological Society of America, 91, 3, pp. 561–571, June 2001

Slowness Anomalies from Two Dense Seismic Arrays at Deception Island Volcano, Antarctica

by G. Saccorotti, J. Almendros, E. Carmona, J. M. Ibáñez, and E. Del Pezzo

Abstract In this article, we analyze the data collected by two short-period seismic arrays deployed at Deception volcano, Southern Shetland Islands, Antarctica. The field survey was conducted during the 1998–1999 austral summer and was aimed at a quantitative assessment of the complex wave fields associated with the magmatic and hydrothermal activity of the volcano. The two arrays had apertures of 320 m and 240 m and were separated by a distance of about 3 km. During the experiment, the arrays recorded several regional earthquakes related to the dynamics of the Bransfield Strait and adjoining areas and local volcano–tectonic earthquakes. Seismograms of earthquakes recorded at regional distances reveal a marked difference in the apparent velocities measured at the two array sites. We investigate the causes and implications of these anomalies by first comparing the effectiveness of estimating the horizontal slowness vector using three different techniques: the multiple signal classification (MUSIC) approach, the zero-lag cross correlation (ZLC) method, and plane-wave fitting to *P*-wave arrival times. While each technique provides the same horizontal slowness vector as the most likely estimates, the plane-wave fitting is associated with the most robust definition of measurement uncertainties. We then investigate the dispersive properties of Rayleigh waves in the 1–8 Hz frequency band at both arrays and invert the two dispersion curves for a shallow velocity structure. The results indicate a marked difference in the seismic velocities for the shallower 200 m beneath the two sites. This may be reconciled with the observed wave vector anomalies by assuming the existence of a sharp lateral velocity heterogeneity, the effect of which would be to bend downward rays impinging at the northernmost array. The reliability of this hypothesis is verified by computing finite-difference wave fronts in a 2D heterogeneous medium. Based on the morpho-structural characteristics of the volcano, the inferred velocity discontinuity maybe associated with the ring-fracture system bordering the collapsed caldera structure that extends over the inner part of the island.

Introduction

Deception Island (62°59′ S, 60°41′ W), located northwest of the Antarctic Peninsula, is the main active volcano of the marginal trench of the Bransfield strait (Fig. 1a). Its main volcano–tectonic feature is the large (8 × 12 km), ellipsoid-like depression flooded by the sea (Fig. 1b), which has been interpreted as a caldera (Baker *et al.,* 1975). Most of the recent volcanic activity has occurred in the close neighborhood of the rims of this depression.

The first digital seismic observations at Deception Island date back to 1986, and through 1993 the measurements have been limited to sparse networks of a few stations. These earlier experiments allowed for seismic-based monitoring of volcanic activity (Ortiz *et al.,* 1997) and for investigations about the location and temporal recurrence of local earthquakes (Correig *et al.,* 1997). Since 1994 the island has been monitored during the austral summers using a dense, small-aperture array located in the close neighborhood of the Spanish Antarctic Base Gabriel De Castilla (see Fig. 1b). These observations allowed for detailed investigations about the spatial distribution of regional earthquakes (Ibañez *et al.,* 1997) and offered new glimpses for interpreting the source processes of the local seismicity related to magmatic and hydrothermal activity (Alguacil *et al.,* 1999; Almendros *et al.,* 1997, 1999; Ibañez *et al.,* 2000). The intriguing results obtained from these latter studies also suggested the need for extending dense-array observations to other sectors of the island, with special reference to the northern inner shore of the caldera, where the most recent eruptive activity oc-

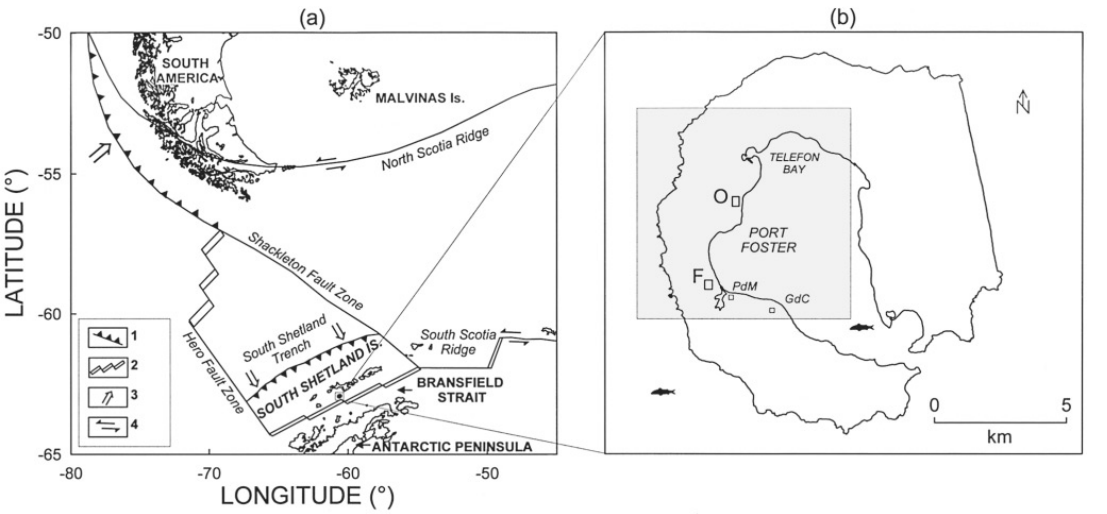

Figure 1. (a) Schematic tectonic map of the South Shetland Islands and Bransfield Strait between South America and the Antarctic Peninsula (modified from Grad *et al.,* 1997). (1) Subduction trench; (2) divergent plate boundary, ridge and transform faults; (3) direction of subduction; (4) relative motion at the plate boundary. (b) Sketch map of Deception Island with location of Spanish Base Gabriel de Castilla (GdC) and the Argentinian Base Primero de Mayo (PdM). Gray boxes mark the location of the arrays deployed during the austral summer 1998–1999; the two labels O and F indicate the Obsidiana and Fumarola sites, respectively. Telefon Bay is the site where the most recent (1967–1970) eruption activity occurred. The shaded rectangle marks the area depicted in Figure 7.

curred. This goal was attained with the 1998–99 survey, during which two seismic arrays were deployed at distances of about 2 and 5 km from the western edge of the eruptive fissure where the 1967–1970 eruptions originated (Fig. 1b).

The main advantage offered by seismic arrays over the classical distributed networks is that the joint estimate of slowness vector at the two arrays allows for source location, even for signals (such as volcanic tremor and long-period events) for which the identification of the arrival times of distinct body wave phases is generally impossible. These location procedures are based on the premise that arrays can accurately determine the direction and incidence of incoming seismic energy; the source of seismic waves is then determined by projecting back along this direction. The accuracy of any such location, therefore, will depend upon the nature of local heterogeneity between the source and receiver, inasmuch as such heterogeneity will cause seismic rays to deviate from their predicted paths. Hence, the usefulness of an array in this type of application will depend upon an ability to characterize and correct for these effects.

In this article, we present evidence for a marked slowness anomaly observed by the 1998–1999 array deployments. Although we hypothesize this anomaly to be related to the Deception caldera collapse, thorough modeling of the complete data sets of slowness and azimuth information from local seismicity is reserved for a subsequent article.

This work is structured into five sections: (1) description of the array deployments and the collected data set; (2) comparison and discussion of three different approaches for estimating the horizontal slowness vector from array data; (3) observations of significant *P*-wave slowness (~0.3 sec/km) and azimuth (up to 100°) anomalies from a selection of eight regional earthquakes; (4) investigation of the shallow velocity structure beneath the two arrays using the dispersion properties of Rayleigh waves as inferred from application of Aki's (1957) correlation method; and (5) discussion of the two velocity models and slowness anomalies in the framework of the volcano–tectonic feature of the island.

Array Setup and Instrumentation

The selection of the sites for the installation of the two arrays was mostly constrained by the rough topography and the accessibility for array maintenance and data retrieval. The first array was installed at the Obsidianas beach, about 2 km SSE of the craters formed during the 1967–1970 activity (see Fig. 1b). This array consisted of 14 stations deployed along two concentric semicircles with radii of 160 and 80 m, respectively (Fig. 2a). Stations at the external and internal semicircle were spaced by angular intervals of about 26° and 45°, respectively, with respect to the hub of the array. The station at the hub of the array was equipped with

a three-component, L-15 Mark Products sensor. All other stations were equipped with vertical-component, L-15 Mark Products sensors, with a natural frequency of 4.5 Hz. Electronic extensions allowed all the sensors to achieve a flat response curve in the 1–50 Hz frequency interval (Del Pezzo *et al.,* 1997).

The second array was deployed atop an alluvial fan in close proximity to the Fumarolas Bay fumarole system, approximately 500 m NW of the Argentinian base Primero de Mayo (Fig. 1b). This array had an aperture of 240 m with stations located along two semicircles, one of radius 120 m and the other of radius 60 m (Fig. 2b). The angular spacing between stations of the outer semicircle was 45° and was 60° for the inner semicircle. This array was equipped with three Mark Products L-4 three-component sensors having a natural frequency of 1 Hz, and with seven Mark Products L-15 vertical sensors having the same characteristics of those previously described for the Obsidianas array. Sensor positioning at both arrays was determined using the Global Positioning System (GPS), which allowed for a precision in the measurement of relative sensor position of about 1 cm. Recording at each array was performed via two eight-channel, PC-based digital recorders with a dynamic range of 16 bits, recording data at 200 samples/sec/channel. Absolute timing at each recorder was achieved via synchronization with the GPS time code. The instruments recorded in trigger mode from 9 December 1998, through 25 February 1999. In addition, 150-sec-long sections of background noise were periodically collected at both the arrays. The Fumarolas and Obsidianas arrays are hereinafter referred to as the F and O deployments, respectively.

Data Description and Analysis

The data set recorded by the array deployments includes a variety of seismic signals that were classified according to their shape, magnitude, and frequency content. These include noise samples, icequakes, local and regional earthquakes, tremor, and long-period signals. A review of the recent seismic activity at Deception volcano may be found in Ibañez *et al.* (2000).

During the field experiment, we routinely analyzed the array data using the zero-lag cross correlation (ZLC) technique (Frankel *et al.,* 1991; Del Pezzo *et al.,* 1997) in order to quickly retrieve qualitative information about the source backazimuth and depth. Comparison of the results obtained at the two arrays showed that, for a given phase of the same event, the ray parameters estimated at the O array were systematically higher than those observed at the F site. This observation could be explained in terms of different epicentral distances; however, the same discrepancies were observed also for regional events, for which the distances to the source are much greater than the spacing between the two arrays. This implies that no significant difference in the horizontal slowness should be observed at the two sites, if a laterally homogeneous propagation medium is assumed.

In the following, we analyze a set of eight regional ($t_s - t_p > 4$ sec) earthquakes recorded at both the arrays (see Table 1) and discuss the resolution and uncertainties of three different approaches for estimating the direction and apparent velocity with which seismic waves propagate across the antennas. We then use the results of the array analyses to quantify the slowness anomalies.

The earthquakes we consider were recorded by both the arrays between 16 December 1998 and 6 February 1999 (Table 1). Considering the range of observed epicentral distances and source backazimuths (see later in this section), the origin of this seismicity is probably related to the slow underthrusting of oceanic crust at the South Shetland Trench (Grad *et al.,* 1997) (see Fig. 1a). All the events are characterized by excellent signal-to-noise ratios, which allow for minimum uncertainty in the picking of both *P* and *S* waves (Fig. 3a).

Three distinct approaches are commonly used to estimate slowness and azimuth from an array of sensors: (1) time- or frequency-domain wave field decomposition techniques; (2) plane-wave fitting to first arrivals, and (3) particle motion analyses. We discarded the latter one for two rea-

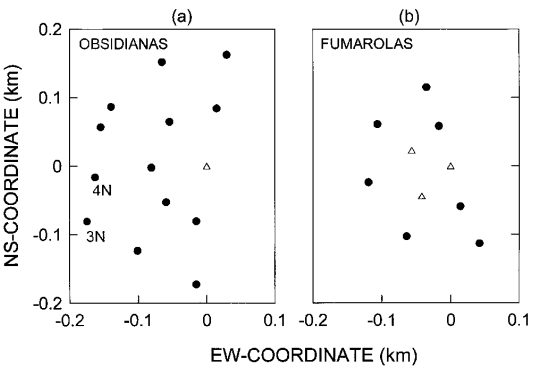

Figure 2. Configuration of the arrays deployed at (a) Obsidianas and (b) Fumarolas sites. Solid dots mark vertical component sensors, triangles indicate three-component stations.

Table 1
Description of the Earthquakes Used in This Study

Event ID	Date (mm-dd-yyyy)	Time at Start of Record (F-array, GMT)	T_s–T_p: O array (sec)	T_s–T_p: F array (sec)
3500250	12-16-1998	02:50:46	7.3	6.5
3582201	12-24-1998	22:01:58	8.4	7.8
3641216	12-30-1998	12:16:49	6.7	6.7
0031812	01-03-1999	18:12:17	11.5	11.3
0210853	01-21-1999	08:53:52	5.1	4.7
0270655	01-27-1999	06:55:20	11.6	11.6
0331550	02-02-1999	15:50:20	4.3	4.1
0370028	02-06-1999	00:28:46	11.4	11.6

sons. The first is that we observed the *P* waves to impinge at the F array almost vertically, thus making the estimate of the azimuth of the principal axis of the polarization ellipsoid extremely difficult (see Figs. 3c, d). The second is associated with the reduced number of three-component stations, which prevented us from using multiple-station averaging techniques (e.g., Jurkevics, 1988) aimed at smoothing the effects induced on particle motion by local heterogeneities beneath the array.

Among the numerous methods for decomposing the elastic-wave field observed by an array of sensors into a linear combination of plane waves, we select and compare the performance from application of (1) the multiple signal classification (MUSIC) technique (Goldstein and Archuleta, 1987, 1991) and (2) the ZLC technique (Frankel *et al.,* 1991; Del Pezzo *et al.,* 1997). In testing these techniques, we consider the first arrival of the event 3500250 as recorded at the O array. The results from this procedure are displayed in Figure 4, where the slowness spectra obtained from application of these techniques are compared to those derived from the plane-wave fitting to first arrivals, or the beamforming method. The slownesses estimated from application of these three approaches are basically the same and indicate a *P* wave propagating to an azimuth of about N80°W and ray parameter of about 0.5 sec/km. Nevertheless, two reasons make us favor the plane-wave fitting approach. The first is that both the ZLC and MUSIC methods are applied over a window of signal, thus inviting the undesired possibility of extending the analysis over multiple, delayed arrivals following the first *P*-wave pulse. The second is that neither of these techniques provides a quantitative assessment of the errors associated with the estimate of the slowness vector, a topic that becomes crucial once measurements from two distinct arrays are compared.

Conversely, the plane-wave fitting allows for a robust estimate of the uncertainties associated with the inversion procedure: the two components of the *P*-wave slowness vector are in fact expressed through a probability density function $P(\mathbf{S})$, which is obtained from the maximum-likelihood expression (Menke, 1989):

$$P(\mathbf{S}) = K \cdot \exp\left[-0.5 \sum_{i=1}^{N} (t_i - \mathbf{S}\cdot\mathbf{x}_i)^2/(\sigma_M^2 + \sigma_{D_i}^2)\right] \quad (1)$$

where the $\mathbf{x}i$ are the coordinates of the N array stations with respect to a reference sensor, and t_i and $\sigma_{D_i}^2$ are the arrival times and picking errors at the different array elements, respectively. σ_M^2 is the error in the prediction of travel times at the array sensors associated with local velocity heterogeneities beneath the array, and K is a normalization factor.

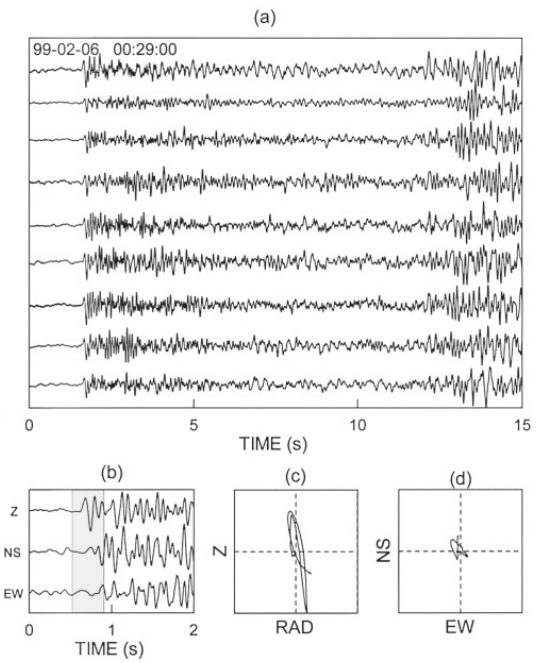

Figure 3. (a) Ground velocity recordings of the event 0370028 (see Table I in text) from the vertical sensors of the F array. Seismograms are arranged in no particular order. Date and time at the start of the recordings are indicated at the upper left. (b) Three-component seismograms from station F1, located at the hub of the F array. Traces have been band-pass filtered in the 1–10 Hz frequency band using a 5-poles, 0-phase-shift Butterworth filter. The shaded area marks the interval selected for the particle motion analyses depicted in (c) and (d). (c),(d): *P*-wave particle motion plots projected on the radial–vertical (c) and horizontal (d) planes, respectively.

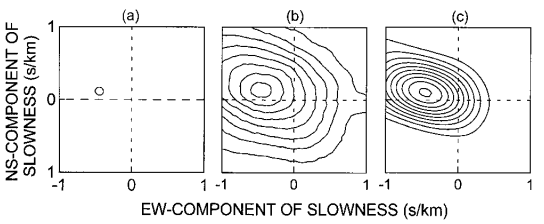

Figure 4. *P*-wave slowness spectra for the event 3582201 as recorded at the O array. The different spectra have been derived from application to the *P*-wave pulse recorded at the array of (a) the plane-wave fitting to *P*-wave arrival times, (b) the ZLC technique, and (c) the MUSIC method. The outer contour line of the spectrum in (a) marks the 90% confidence interval in the estimate of the two components of the slowness vector. The two spectra in (b) and (c) have been calculated over a 1.28-sec-long window encompassing the *P*-wave and in the 1–10 Hz frequency band. In all the three maps, the component of slowness have been reversed in sign, so that the peaks indicate source backazimuth.

The search for the signal slowness is conducted by maximizing equation (1), which is solved numerically by performing a grid search over a range of trial slownesses **S**, for which the predicted travel times at the different sensors are calculated.

Figure 5 shows the results of the plane-wave fitting analysis for the eight earthquakes recorded at the O and F arrays. Given the extreme precision with which it was possible to pick the *P*-wave onset, as well as the reduced aperture of the arrays, the calculation is made by setting the parameters σ_D and σ_M of equation (1) equal to 0.005 sec (1 time sample) and 0.01 sec, respectively. In these maps, the *P*-wave slownesses are represented by the 90% confidence bounds in the estimate of equation (1), and the (x, y) components of vector slowness are taken relative to a Cartesian system oriented E-W–N-S. As in Figure 4, the representation has been made by reversing the sign of the two components of vector slowness so that the peak values of the maps display source backazimuth. For all the cases taken into account, we note a systematic difference among the slownesses observed at the two array sites. Since these differences are significatively greater than the error bounds on the measurement procedures, we conclude that the two arrays measure two different portions of a deformed wave front. This observation is discussed in the last section, with reference to the morpho-structural features of the island.

Shallow Velocity Models

The shallow velocity structures beneath the two antennas are evaluated from the dispersive properties of the surface waves composing the noise wave field. We measure phase velocities of Rayleigh waves using the spatiotemporal correlation technique designed by Aki (1957) for the analysis of stationary stochastic wave fields. Assuming that the noise represents the sum of horizontally propagating waves with the same phase velocity for a given frequency and that the waves propagating in different directions are statistically independent, Aki's method provides a relation between the spectrum of the waves in time and their spectrum in space.

In the following, we first review the spatial correlation representing the vertical component of the two-dimensional wavefield, and follow with the data analyses and interpretation. Finally, a surface velocity structure is derived for beneath the two different arrays.

Aki's correlation method is introduced by first defining a spatial correlation function, $\phi(r, \varphi)$, as

$$\phi(r, \varphi) = \langle u(x, y, t)u(x + r\cos\varphi, y + r\sin\varphi, t)\rangle \quad (2)$$

where $u(x, y, t)$ is the ground velocity observed at point (x, y) and time t; r is the station separation; φ is the station azimuth measured counterclockwise from the x (E–W) axes, and $\langle\ \rangle$ denotes the ensemble (time) average. The azimuthal average of this function is given by

$$\bar{\phi}(r) = \frac{1}{\pi}\int_0^{\pi} \phi(r, \varphi)d\varphi. \quad (3)$$

For the vertical component, the power spectrum, $P(\omega)$, can be related to $\bar{\phi}(r)$ via J_0, the zeroth-order Bessel function:

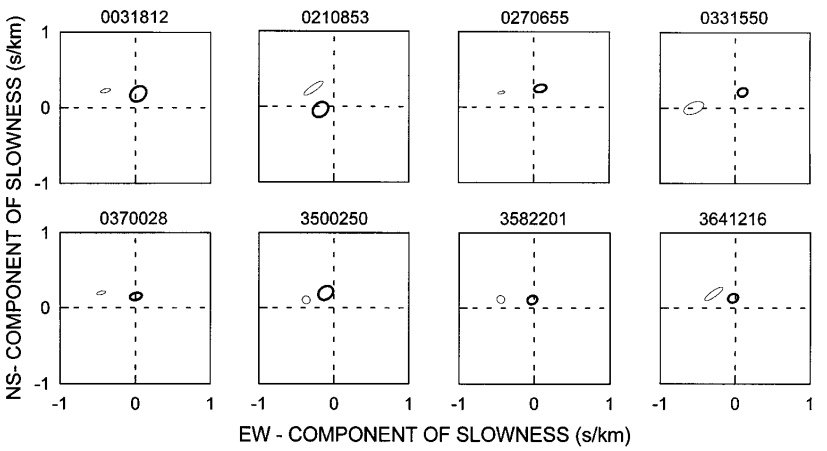

Figure 5. Slowness spectra evaluated at the F (bold lines) and O (thin lines) arrays from plane-wave fitting to *P*-wave arrival times for the eight earthquakes listed in Table I. In all the maps, the contour bounds the 90% confidence interval in the estimate of the slowness vector. The event IDs are reported at the top of each plot. As in Figure 4, the two Cartesian components of vector slowness have been reversed in sign, so that the peaks of the spectra indicate source backazimuth.

$$\bar{\phi}(r) = \frac{1}{\pi} \int_0^\infty P(\omega) J_0 \left(\frac{\omega}{c(\omega)} r \right) d\omega \quad (4)$$

where ω is the angular frequency and $c(\omega)$ is the frequency-dependent phase velocity. Filtering the waves through a narrowband filter centered at frequency ω_0 simplifies equation (4) to

$$\bar{\phi}(r, \omega_0) = P(\omega_0) J_0 \left(\frac{\omega_0}{c(\omega_0)} r \right). \quad (5)$$

Then, introducing a normalized correlation coefficient as

$$\rho(r, \omega_0, \varphi) = \frac{\phi(r, \omega_0, \varphi)}{\phi(0, \omega_0, \varphi)}, \quad (6)$$

we obtain its azimuthal average as

$$\rho(r, \omega_0) = J_0 \left(\frac{\omega_0}{c(\omega_0)} r \right). \quad (7)$$

Thus, phase velocity can be estimated from measurements of correlation functions for vertical motion from a semicircular array. Equation (7) is valid for the vertical component of motion, which consists of *P–SV* motion. Assuming that ambient noise is composed mainly of surface waves, the results from application of these equations can be interpreted as an estimate of Rayleigh wave phase velocities. This technique has been used by Ferrazini *et al.* (1991) to study the characteristics of shallow tremor and gas-piston events at Puu Oo crater, Hawaii; by Métaxian *et al.* (1997) to analyze the wave field properties of permanent tremor at Masaya volcano, Nicaragua, and by Chouet *et al.* (1998) to infer a shallow velocity structure at Stromboli volcano, Italy.

In our analyses, we first select 120-sec-long time series of background noise recorded at all the stations of the arrays. The seismograms from each station of the array are then Fourier transformed, and the complex spectrum is windowed using a 0.5-Hz-width cosine-taper function. We then calculate the inverse Fourier transform and, once back in the time domain, estimate the ZLC coefficient of the signal from the station located at the hub of the array and the stations located at the two semicircles. The frequency-dependent correlation coefficients thus obtained are finally averaged among stations located at the same distance from the hub of the array. This procedure is then repeated by shifting the frequency window with 0.25-Hz steps, in the 0.5–8 Hz interval. To improve the significance of the estimates, we processed six different noise windows, recorded between 10–17 December for the O array and 15–27 December for the F array, and separately averaged the results obtained at the two sites.

The frequency dependence of the azimuthally averaged correlation coefficient for the internal and external semicircles of the O and F arrays, respectively, are shown in Figure 6a. The inferred stationarity of the wave field over the time period spanned by our data windows is verified through the similarity of the correlation functions evaluated for the different intervals. In analyzing data from the external semicircle of the O array ($r = 160$ m), we omitted station 3N (see Fig. 2a), whose distance from the hub of the array was significantly different from the average distances of the other stations.

We then derive the frequencies corresponding to the maxima, minima and zero crossings of the average of the correlation functions shown in Figure 6a. These values are set equal to the corresponding arguments of the zeroth order Bessel function of equation (7), eventually deriving values of the frequency-dependent phase velocity $c(\omega)$. Following the procedures described in Ferrazzini *et al.* (1991) and Chouet *et al.* (1998), we evaluate the errors on such estimates to be about 10%. This procedure gives a more conservative evaluation of the uncertainties as if we had considered the sample standard deviation of the correlation coefficients calculated over the different recordings. The results from this procedure are depicted in Figure 6b, where the dispersion characteristics at the two arrays are shown. These two different data sets are then least-square fitted by a relationship of the form (Chouet *et al.,* 1998):

$$c(f) = A \cdot f^{-a} \cdot e^{bf} \quad (8)$$

where f is the frequency in Hz ($f = \frac{\omega}{2\pi}$) and A, a, and b are constants. For the O site, $A = 0.4$, $a = 0.86$, and $b = 0.13$; for the F site, $A = 2.8$, $a = 2.4$ and $b = 0.35$.

These dispersion functions are then inverted for the corresponding velocity structures under the assumption that those dispersions represent the fundamental modes of Rayleigh waves. Our search for structural models that produce phase velocities compatible with the experimental dispersions is conducted using both a trial-and-error approach and an inversion procedure based on the computer codes developed by Hermann (1987). For each array site, we first considered a simple model consisting of a single layer underlain by a homogeneous half-space. The thicknesses of the surficial layers are selected according to the minimum wavelength of Rayleigh waves observed at each site; the velocities of the top layer and the half-space are adjusted to fit the low- and high-frequency limits in the distribution of experimental data. We then fit the curvature of the dispersion data by gradually increasing the number of layers in the model and proceed changing layer thicknesses and velocities until the fit is considered satisfactory. This structure is then used as a starting model for the inversion procedure, which is iterated until the rms between the observed and predicted dispersion curves is smaller than a given threshold, set equal to 0.05. The velocity models at the two array sites resulting from this procedure are illustrated in Figure 6c, while in Figure 6b the dispersion curves for Rayleigh waves pre-

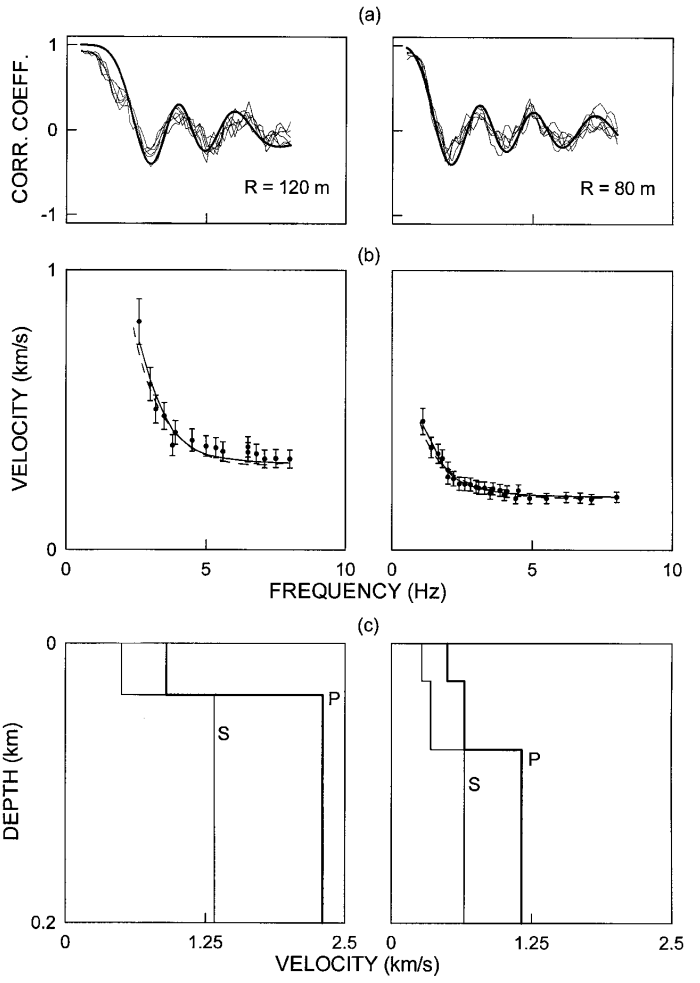

Figure 6. (a) Azimuthally averaged correlation functions for the outer semicircle of the Fumarolas array (left), and the inner semicircle of the Obsidianas array (right). The thick line represents the zeroth-order Bessel function derived from substitution of the dispersion relationship expressed through equation (5) to the phase velocity terms at the right-hand side of equation (4). (b) Phase velocities as a function of frequency for the P–SV component of motion derived at the F (left) and O (right) arrays. Dots represent velocities derived from reading of the zero-crossing, maxima and minima of the average of the correlation functions shown in (a). Dashed lines represent the dispersion functions derived from fitting equation (8) to the velocity data. These functions have been used for deriving the velocity models shown in (c). Dispersion functions predicted from these models are represented by the continuous lines. (c) *P*- (bold lines) and *S*- (thin lines) velocity structures for the F (left) and O (right) sites, derived from inversion of the Rayleigh waves dispersion data depicted in (b).

dicted from these structures are compared to the experimental phase velocities.

The F array is characterized by a ~40-m-thick surficial layer, whose *S*- and *P*-wave velocities are 0.5 and 0.9 km/sec respectively. These values are compatible with the sediments of the talus resulting from erosion of the caldera rim over which that array was deployed. The half-space underneath the shallowest layer is characterized by *S*- and *P*-wave velocities of about 1.3 and 2.3 km/sec respectively, in agreement with the larger scale crustal model derived by Grad *et al.* (1993) from analysis of refraction and wide-angle reflection data.

The two shallower layers at the O site are characterized by *S*- and *P*-wave velocities ranging in the 0.27–0.35 and 0.5–0.65 km/sec intervals, respectively. The half-space at that site depicts *S*- and *P*-wave velocities of 0.65 and 1.2 km/sec, respectively. These velocities are thus roughly half of those derived for the same range of depth at the F site.

The differences among the two sites for the shallower layers can be easily interpreted in light of the surface geology: the O array was in fact deployed onto a sandy epiclastic deposit of marine origin, whose shear modulus is expected to be significatively lower than that of the consolidated sediments beneath the F array.

More difficult is interpreting the differences observed at greater depths. Based on considerations about the penetration depths of the high-frequency surface waves used to derive the models, we estimate the validity of our measurements to extend down to depths of about 150–200 m. This thickness is obviously too great to be attributed solely to the sandy deposits without invoking any kind of structural control on the sedimentary processes. This evidence will serve

us to better interpret the slowness anomaly in the framework of the structural evolution of the volcano.

Discussion and Conclusions

In this article, we analyze ray parameters and backazimuths for a set of eight regional earthquakes recorded by a double-array deployment at Deception Island volcano, Southern Shetland Islands, Antarctica. Results from our measurements indicate that the *P*-wave pulse from the same earthquake is observed at the two sites with a significant difference in the apparent (horizontal) slowness. For most of the cases we analyzed, the source-to-receiver distance is much greater than the separation between the two arrays, thus implying that the slowness discrepancies cannot be attributed to different epicentral distances. We must therefore hypothesize that seismic rays traveling to the two arrays sample portions of the crust characterized by different seismic velocities. Two reasons constrain this lateral velocity discontinuity to be located in close proximity of one of the two arrays. The first is that vector slowness data are most sensitive to velocity structure near the receiver (see Figure 1 by Hu *et al.,* 1994); the second, is that this discontinuity has to be sampled selectively by only one of the two rays: this occurs if the two rays are separated by a sufficient distance, a condition that is achieved only in the terminal part of the ray paths.

A major question remains with regard to the location and extent of such heterogeneity. A difference between the present work and similar studies done in the past (e.g., Steck and Prothero, 1993; Lin and Roecker, 1996) is that for the earthquakes we analyze, no independent locations are available: to our knowledge, the eight events we considered were not recorded by any other seismic network. This means that the slowness data at our arrays cannot be compared to any prediction derived from an independent knowledge of the source location. Thus, the slowness anomalies we refer to must be analyzed as relative anomalies between a pair of observations, rather than discrepancies with respect to values predicted for a given hypocenter and velocity structure. In the previous analysis, we implicitly assumed the F array to be unaffected by slowness anomaly. This choice was motivated by the fact that the ray parameters we observed at that particular site were compatible with *P*-wave propagation from distant sources. In fact, the ray parameter observed by an array is constant throughout the ray path and corresponds to the inverse of the seismic velocity at the turning point of the ray. In the case of the O array, this would imply that P waves propagating from sources as far as 80–100 km would sample layers with velocities not exceeding 2 km/sec, which is obviously unrealistic. Taken together, these considerations seem to indicate that the velocity heterogeneity is located in close proximity to the O array and that its geometry and extent must be able to cause a downward bending of seismic rays impinging at that particular site from a range of backazimuths spanning the NW quadrant (see Fig. 5). To that purpose, a vertical or quasi-vertical impedance contrast could represent a reasonable interpretation: rays traveling through the higher-velocity region would be severely bent downward as they transmit across the interface to the low-velocity region.

From correlation analysis of selected records of seismic noise, we calculated the dispersive properties of Rayleigh waves, from which a shallow velocity model at the two array sites was obtained. The shallow velocity model derived for the F site is compatible with the regional crustal structure, except for the shallowest, 40-m-thick low-velocity layer. The concordance between the shallow velocity structure at the F site and the larger scale, regional model lends additional support to the idea that the anomalous ray propagation only affects the O array. Conversely, this latter site is characterized by a shallow velocity structure whose *P*-wave velocity is about one-half of that inferred for the F site. As indicated by the right bottom panel of Figure 6, the low-velocity zone beneath the O array appears to extend to a depth of at least 150 m. It is quite unlikely that the lens of loose epiclastic deposits, where that array was deployed, reaches such a thickness. Therefore, the low-velocity zone evidenced by our measurements has to be related to some structural depression successively filled by volcanoclastic and/or sedimentary deposits.

These observations and this hypothesis may be collected into a coherent picture, once one considers the structural and volcanological features of the island. Figure 7a reports a shaded relief map of the N–NW sector of the volcano encompassing the F and O sites. The principal morpho-structural characteristic is represented by the large ellipsoid-like depression (caldera), whose rims are crossed by faults dislocating the entire structure in discontinuous blocks (De Rosa *et al.,* 1995). However, geomorphological considerations (G. Ventura, personal comm., 1999) suggest that the caldera walls suffered major erosion, thus implying that the present-day caldera rims are displaced outward with respect to the fracture systems along which the collapse occurred.

The inner (submerged) part of the caldera is filled by loose sedimentary and volcanoclastic deposits, whose *P*-wave velocities range between 0.5 km/sec for the shallowest 20 m, to 1.4 km/sec for an underlaying layer that extends down to a depth of about 500–600 m, as indicated by a refraction survey conducted by Ortiz *et al.* (1989). These velocities are thus compatible with those obtained in the present study from Rayleigh wave dispersion data at the O site. The most recent eruptive activity (e.g., 1967 and 1970 eruptions) is located on a system of discontinuities trending NE–SW, which are very probably associated with the structures along which the inner part of the volcano collapsed. Moreover, data from a recent bathymetric survey (DECVOL Team, personal comm., 2000) indicate that a 200-m-high, NNW–SSE-oriented fault scarp is located a few hundreds of meter offshore the F site.

Taken together, these considerations allow us to estimate an approximate distance of about 1 km between the

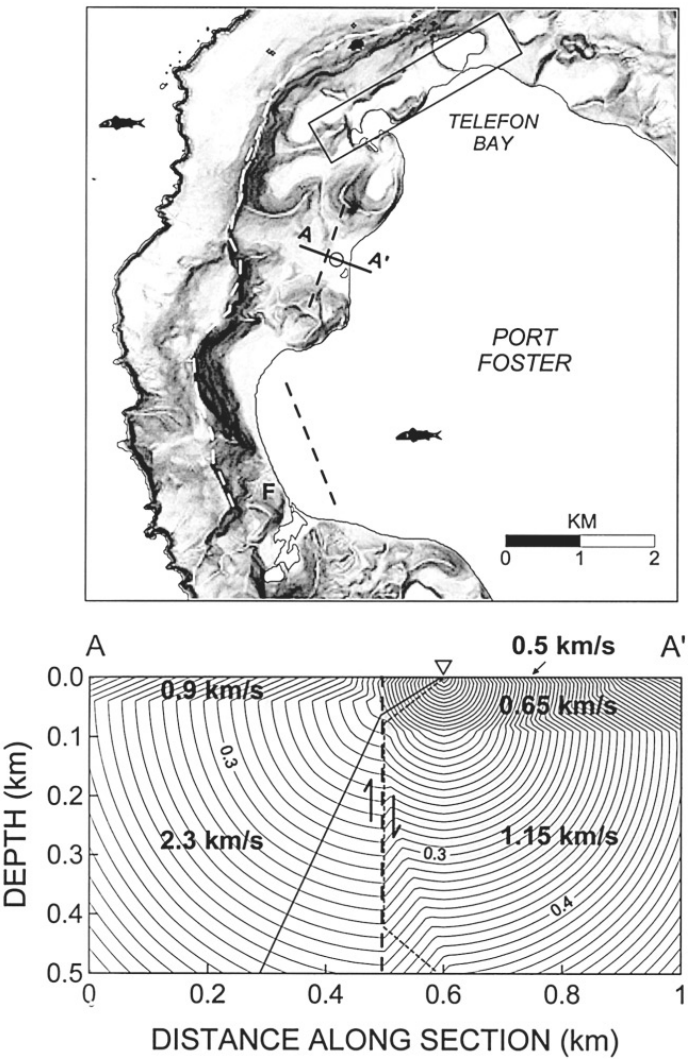

Figure 7. (a) Shaded relief map of the area encompassing the O and F arrays. This area corresponds to the rectangle in Figure 1a. The white dashed line onshore corresponds to the rim of the caldera. The rectangle at Telefon Bay bounds the region where the 1967–1970 phreato-magmatic and strombolian eruptions occurred. The dashed line offshore the F site marks the approximate position of a fault scarp imaged by a recent bathymetric survey. The A–A′ line marks the profile through which passes the cross-section depicted in (b). This line bisects the inferred fault associated to the caldera collapse (dashed line). The location of the hub of the array is marked by a circle. (b) Schematic model of the cross-section along profile A–A′ shown in (a). The triangle at the top of the map indicates the location of the array. *P*-wave velocities are indicated by different shading and bold numbers. Contour lines corresponds to the isochrones (wave fronts) for a source located at the hub of the array. Contour interval is 0.01 sec. The bold black line indicate a seismic ray impinging at the discontinuity with an incidence angle of about 30°. Note the deflection of the ray after having passed through the velocity interface. The dotted line indicates a ray coming from SE and refracted at the discontinuity. In that case, the backazimuth observed at the array points to a direction which is opposite to that of the source.

present-day caldera rims and the main fracture system along which the collapse occurred. According to this picture, and remembering the concordance of the velocity models at the F and O sites with the regional and inner caldera structures, respectively, we may conclude that the F array was deployed over the body of the old volcano edifice, while the O array was deployed over the collapsed part of the caldera successively filled by volcanoclastic and marine deposits. The F and O arrays would thus be located west and east, respectively, of the fracture system associated with the caldera formation.

To verify whether this hypothesis is compatible with the observed slowness anomalies, we examine the geometry of seismic rays propagating in a 2D, heterogeneous medium. Using the finite-difference approach of Podvin and Lecomte (1991), we use travel-time reciprocity and calculate the wave fronts of seismic waves that emanate from a source located at the O array and propagate through a laterally heterogeneous structure. The results from this simulation are illustrated in Figure 7b, where a vertical section orthogonal to the inferred fault trace is displayed. The trace of the fault is taken to be at a distance of about 1 km from the caldera rim and parallel to it. The velocity structures west and east of the fault are assumed to be those previously inferred for the F and O site, respectively. The figure clearly shows that, for a wide range of incidence angles (say, from 90° to 45°), wave

fronts impinging at the O array are severely bent downward by the subvertical interface, with a net decrease of the apparent velocity as the waves impinge at the surface. It must be stressed that the observations discussed thus far are not sufficient to definitively validate the proposed model. The lack of additional recordings of regional earthquakes spanning a wider range of backazimuths hinders the possibility of ruling out other effects, as for instance a strong diffraction west of the O array. However, three considerations lend support to our model. The first is the dependence of the observed slowness anomalies on the inferred source backazimuth. If the anomalies were due to the radiation from a strong, near-receiver diffractor, then the O array should always measure the backazimuth to this latter one, independently of the backazimuth to the primary source. Conversely, as displayed in Figure 5, the magnitude of the anomaly appears to be strongly dependent on the inferred source backazimuth. The second is the ability of the model to reconcile the observations with the surface geological features and seismic velocity distributions. The third, is related to the data of local earthquakes that occurred from late December 1998 through February 1999 below Port Foster (see Fig. 7a), 1–4 km NE of the F array. For these events, we observed the same backazimuth discrepancies among the two arrays as those previously observed for regional sources (Fig. 8). If the anomalous slowness of first arrivals observed at the O array for regional sources located north-northwest of the island were due to a diffractor, than that anomaly shouldn't be observed in the case of local earthquakes originating SSE of the same array. In light of the model proposed in Figure 7b, the persistency of the anomaly for these latter sources could be representative of head waves that travel along the vertical discontinuity and then turn back toward the array as they impinge at the free surface (dotted line in Fig. 7b). More quantitative constraints about the nature of the inferred velocity discontinuity and its spatial setting imply the need for a detailed analysis of the data set from local seismicity, which in turn requires the joint inversion of slowness measurements for both source location and 3D velocity structure. Such a complex process (called *polarization tomography* after Hu *et al.,* 1994) is an effort that goes beyond the purpose of the present article and is reserved for a subsequent study.

A major lesson is taken from the present work. Over the past 15 years, array techniques have progressively become more popular among seismologists faced with the analysis and interpretation of signals associated with volcanic activity (e.g., Goldstein and Chouet, 1994; Chouet *et al.,* 1997; Del Pezzo *et al.,* 1997, and references therein). Multichannel methods have been demonstrated to be a powerful tool for quantifying the kinematic properties of the complex wave fields observed in active volcanic environments, such as volcanic tremor, long-period events, and signals associated with mechanism of degassing in open vents. However, volcanic edifices are characterized by extremely complex tectonic features, resulting from the superposition of regional stresses and local, heterogeneous stress fields. The distribution of seismic velocities reflects these complexities, and variations of several tenths of a percent in both compressional and shear velocities are common over distance scales on the order of a few hundred meters. Any source localization procedure, based on the back propagation of seismic rays through a more or less defined velocity structure, should therefore account for these heterogeneities and their spatial distribution.

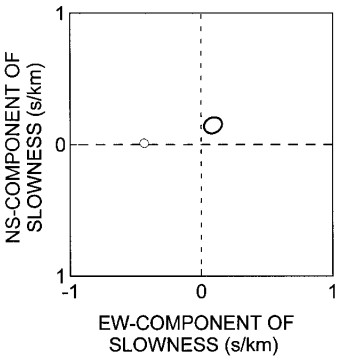

Figure 8. Slowness spectra evaluated at the F (bold line) and O (thin line) arrays for a local earthquake that occurred on 30 December 1998, at 14:54 UTC. The estimated S–P times are about 0.7 sec and 1.1 sec at the F and O array, respectively. As in Figures 4 and 5, contouring bounds the 90% confidence level in the estimate of slowness vector, whose Cartesian components have been reversed in sign so that the spectra indicate source backazimuth.

Acknowledgments

Thoughtful comments from Rick Aster, Mike Hagerty, and an anonymous reviewer greatly helped in improving the quality of the manuscript. The scientific expedition at Deception Island was supported through the project CICYT-ANT98-111 under the Spanish Antarctic Research Program. This work could not have been possible without the logistic and technical assistance of the military staff of the Gabriel de Castilla base. Jaime Potti, Ana de Leon, Juanto Fargallo, Mariano Rodriguez-Arias, and Fernando Calexico are gratefully acknowledged for their friendship and moral support. Tony Lomax made available, through the Internet, Podvin and Lecomte's finite-difference code for calculation of travel times. Guido Ventura provided precious suggestions while attempting to interpret the morpho-structural characteristic of Deception Volcano.

References

Alguacil, G., J. Almendros, E. Del Pezzo, A. Garcia, J. M. Ibáñez, M. La Rocca, J. Morales, and R. Ortiz (1999). Observations of volcanic earthquake and tremor at Deception Island, Antarctica, *Ann. Geofis.* **42,** 417–436.

Almendros, J., J. M. Ibáñez, G. Alguacil, E. Del Pezzo, and R. Ortiz (1997). Array tracking of the volcanic tremor source at Deception Island, Antarctica, *Geophys. Res. Lett.* **24,** 3069–3072.

Almendros, J., J. M. Ibáñez, G. Alguacil, and E. Del Pezzo (1999). Array analysis using circular wave-front geometry: an application to locate the nearby seismovolcanic source, *Geophys. J.* **136,** 159–170.

Aki, K. (1957). Space and time spectra of stationary stochastic waves with special reference to microtremors, *Bull. Earthquake Res. Inst. Tokyo Univ.* **25,** 415–457.

Baker, P., M. Phil, M. Mc Reath, M. Henry, M. Roobal, and T. Davies (1975). The geology of the South Shetland Islands, V: Volcanic evolution of Deception Island, *Brit. Ant. Survey. Scient. Rep.* No. 78, 81 pp.

Chouet, B. A., G. Saccorotti, M. Martini, P. B. Dawson, G. Milana, G. De Luca, and R. Scarpa, (1997). Source and path effects in the wavefields of tremor and explosions at Stromboli volcano, Italy, *J. Geophys. Res.* **102,** 15129–15150.

Chouet, B., G. De Luca, G. Milana, P. B. Dawson, M. Martini, and R. Scarpa (1998). Shallow velocity structure of Stromboli volcano, Italy, derived from small-aperture array measurements of strombolian tremor, *Bull. Seism. Soc. Am.* **88,** 653–666.

Correig, A. M., M. Urquizu, J. Vila, and J. Marti, (1997). Analysis of the temporal occurrence of seismicity at Deception Island (Antarctica): A nonlinear approach, *PAGEOPH* **149,** 553–574.

De Rosa, R., R. Mazzuoli, R. H. Omarini, G. Ventura, and J. G. Viramonte (1995). A volcanological model for the Historical Eruptions at Deception Island (Bransfield Strait, Antarctica), *Terra Antarctica* **2,** 131–165.

Del Pezzo, E., M. La Rocca, and J. M. Ibáñez (1997). Observations of high-frequency scattered waves using dense arrays at Teide volcano, *Bull. Seism. Soc. Am.* **87,** 1637–1647.

Ferrazzini, V., K. Aki, and B. A. Chouet (1991). Characteristics of seismic waves composing hawaiian volcanic tremor and gas-piston events observed by a near-source array, *J. Geophys. Res.* **96,** 6199–6209.

Frankel, A., S. Hough, P. Friberg, and R. Busby (1991). Observations of Loma Prieta aftershocks from a dense array in Sunnyvale, California, *Bull. Seism. Soc. Am.* **81,** 1900–1922.

Goldstein, P., and R. J. Archuleta (1987). Array analysis of seismic signals, *Geophys. Res. Lett.* **14,** 13–16.

Goldstein, P., and R. J. Archuleta (1991). Deterministic frequency–wavenumber techniques and direct measurements of rupture propagation during earthquakes using a dense array—theory and methods. *J. Geophys. Res.* **97,** 6173–6185.

Goldstein, P., and B. A. Chouet (1994). Array measurements and modeling of a source of shallow volcanic tremor at Kilauea Volcano, Hawaii, *J. Geophys. Res.* **99,** 2637–2652.

Grad, M., Guterch A., and T. Janik (1993). Seismic structure of the litosphere across the zone of subducted Drake plate under the Antarctic plate, West Antarctica, *Geophys. J.* **115,** 586–600.

Grad, M., Shiobara H., Janik T., Guterch A., and H. Shimamura (1997). Crustal model of the Bransfield Rift, West Antarctica, from detailed OBS refraction experiments, *Geophys. J.* **130,** 506–518.

Herrmann, R. B. (1987). *Computer Programs in Earthquake Seismology, Volume 2: Surface Waves Programs,* User's Guide, Department of Earth and Atmospheric Science, St. Louis University, St. Louis, Missouri.

Hu, G., W. Menke, and C. Powell (1994). Polarization tomography for P-wave velocity structure in southern California, *J. Geophys. Res.* **99,** 15245–15256.

Ibáñez, J. M., J. Morales, G. Alguacil, J. Almendros, R. Ortiz, and E. Del Pezzo (1997). Intermediate-focus earthquakes under South Shetland Islands (Antarctica), *Geophys. Res. Lett.* **24,** 531–534.

Ibáñez, J. M., E. Del Pezzo, J. Almendros, M. La Rocca, G. Alguacil, R. Ortiz, and A. Garcia (2000). Seismovolcanic signals at Deception Island volcano, Antarctica: wavefield analysis and source modeling, *J. Geophys. Res.* **105,** 13,905–13,931.

Jurkevics, A. (1988). Polarization analysis of three-component array data, *Bull. Seism. Soc. Am.* **78,** 1725–1743.

Lin, C. H., and S. W. Roecker (1996). *P*-wave backazimuth anomalies observed by a small-aperture seismic array at Pinyon Flat, Southern California: implications for structure and source location, *Bull. Seism. Soc. Am.* **86,** 470–476.

Menke, W. (1989). Geophysical Data Analysis: Discrete Inverse Theory, Academic Press, Inc., New York, 262 pp.

Métaxian, J. P., P. Lesage, and J. Dorel (1997). Permanent tremor of Masaya volcano, Nicaragua: wave field analysis and source location, *J. Geophys. Res.* **102,** 22529–22545.

Ortiz, R., R. Baloix, and E. Carreno (1989). Interpretation preliminar de un ensayo de perfil sismico de refraccion en Port Foster (Isla Decepcion), Presented at the 3rd Spanish Symposium of Antarctic Studies, Madrid, 3–9 September, 1989.

Ortiz, R., A. García, A. Aparicio, I. Blanco, A. Felpeto, R. del Rey, M. Villegas, J. M. Ibáñez, J. Morales, E. Del Pezzo, J. C. Olmedillas, M. Astiz, J. Vila, M. Ramos, J. G. Viramonte, C. Risso, and A. Caselli (1997). Monitoring of the volcanic activity of Deception Island, South Shetland Islands, Antarctica (1986–1995), in *The Antarctic Region: Geological Evolution and Processes,* C. A. Ricci (Editor), Terra Antarctica Publishers, Siena, Italy, 1071–1076.

Podvin, P., and I. Lecomte (1991). Finite difference computation of traveltimes in very contrasted velocity models: a massively parallel approach and its associated tools, *Geophys. J.* **105,** 271–284.

Steck, L. K., and W. A. Prothero Jr. (1993). Observations of direct *P*-wave slowness and azimuth anomalies for teleseisms recorded in Long Valley caldera, California, *Bull. Seism. Soc. Am.* **5,** 1391–1419.

Osservatorio Vesuviano
Via Diocleziano 328, 80124 Napoli, Italy
gilberto@ov.ingv.it
(G.S., E.D.P.)

Instituto Andaluz de Geofisica
Universidad de Granada
Campus Universitario de Cartuja
18071 Granada, Spain
ibanez@iag.ugr.es; ecarmona@iag.ugr.es.
(J.A., E.C., J.M.I.)

Manuscript received 31 May 2000.

VII. The recent seismo-volcanic activity at Deception Island volcano

PERGAMON

Deep-Sea Research II 50 (2003) 1611–1629

DEEP-SEA RESEARCH
PART II

www.elsevier.com/locate/dsr2

The recent seismo-volcanic activity at Deception Island volcano

Jesús M. Ibáñez*, Javier Almendros, Enrique Carmona, Carmen Martínez-Arévalo, Miguel Abril

Instituto Andaluz de Geofísica, Campus de Cartuja s/n, Universidad de Granada, 18071 Granada, Spain

Received 14 October 2002; received in revised form 10 December 2002; accepted 13 December 2002

Abstract

This paper reviews the recent seismic studies carried out at Deception Island, South Shetland Islands, Antarctica, which was monitored by the Argentinean and Spanish Antarctic Programs since 1986. Several types of seismic network have been deployed temporarily during each Antarctic summer. These networks have consisted of a variety of instruments, including radio-telemetered stations, autonomous digital seismic stations, broadband seismometers, and seismic arrays. We have identified two main types of seismic signals generated by the volcano, namely pure seismo-volcanic signals, such as volcanic tremor and long-period (LP) events, and volcano-tectonic (VT) earthquakes. Their temporal distributions are far from homogeneous. Volcanic tremors and LP events usually occur in seismic swarms lasting from a few hours to some days. The number of LP events in these swarms is highly variable, from a background level of less than 30/day to a peak activity of about 100 events/h. The occurrence of VT earthquakes is even more irregular. Most VT earthquakes at Deception Island have been recorded during two intense seismic crises, in 1992 and 1999, respectively. Some of these VT earthquakes were large enough to be felt by researchers working on the island. Analyses of both types of seismic events have allowed us to derive source locations, establish seismic source models, analyze seismic attenuation, calculate the energy and stress drop of the seismic sources, and relate the occurrence of seismicity to the volcanic activity. Pure seismo-volcanic signals are modelled as the consequence of hydrothermal interactions between a shallow aquifer and deeper hot materials, resulting in the resonance of fluid-filled fractures. VT earthquakes constitute the brittle response to changes in the distribution of stress in the volcanic edifice. The two VT seismic series are probably related to uplift episodes due to deep injections of magma that did not reach the surface. This evidence, however, indicates the high potential for future volcanic eruptions at Deception Island.

Contents

*Corresponding author. Tel.: +34-958-248910; fax: +34-958-160907.
E-mail address: ibanez@iag.ugr.es (J.M. Ibáñez).

0967-0645/03/$ - see front matter
doi:10.1016/S0967-0645(03)00082-1

1. Introduction

Deception Island is a volcanic island located at 62°59′S and 60°41′W in the South Shetland Islands region (Fig. 1). It constitutes a back-arc stratovolcano with a basal diameter of ~30 km. The volcano rises ~1400 m from the seafloor to a maximum height of 540 m above sea level. The 15-km-diameter island is horseshoe-shaped and displays a flooded caldera (Port Foster) with dimensions of about 6 × 10 km and maximum depth of 190 m. The caldera wall is breached by a 500-m-wide passage named Neptune's Bellows. Glaciers cover almost half of the island, mainly on Mount Pond and Mount Kirkwood in the east and south, respectively.

The geodynamic setting of the Deception Island region is characterized by interactions among small tectonic units. The Drake microplate (Fig. 1) represents the remnants of a subduction that once extended beneath the western margin of the Antarctic Peninsula. This subduction process finished progressively from southwest to northeast, but a slow subduction activity at the South Shetland Trench, northwest of the South Shetland Islands, still continues (e.g., Barker, 1982; Pelayo and Wiens, 1989; Kim et al., 1995; Lawver et al., 1995; Robertson et al., 2001).

The Bransfield Strait is a consequence of the rifting and separation between the South Shetland microplate and the Antarctic Peninsula. There are three active extensional basins that show evidence of volcanism and normal faulting. The axis of the central basin is marked by a series of seamounts between Deception and Bridgeman Islands, many of which have recently been active (Gracia et al., 1996; Lawver et al., 1996; Gracia et al., 1997). However, the crustal thickness of 12–30 km is consistent with extrusion through rifted continental crust rather than seafloor spreading (Bialas et al., 1990; Grad et al., 1992; Barker and Austin, 1994; Grad et al., 1997; Janik, 1997; Barker and Austin, 1998; Prieto et al., 1998; Barker et al., 2001). Based on the seismicity and volcano spatial distribution, Barker and Austin (1998) have suggested south-westward propagation of the Bransfield Rift. The NW-SE extension of ~10 mm/yr has been attributed to rollback of the subducted slab (Barker and Austin, 1998; Dietrich et al., 2001).

The seismicity in Bransfield Strait has characteristics of rift extension, subduction, and volcanism. Virtually all earthquakes in the region are either shallow (<40 km depth) and consistent with rifting, or deep and consistent with subduction of the Drake plate (Pelayo and Wiens, 1989; Ibáñez et al., 1997). Many of the shallow earthquakes tend to cluster near volcanoes, indicating a likely volcanic or volcano-tectonic origin (Pelayo and Wiens, 1989; Robertson et al., 2001). Seismic activity is specially pronounced at Deception Island volcano (Pelayo and Wiens, 1989; Lee et al., 1998; Robertson et al., 2001).

Most rocks on Deception Island have been classified relative to the undated caldera-forming eruption (Martí and Baraldo, 1990). All exposed

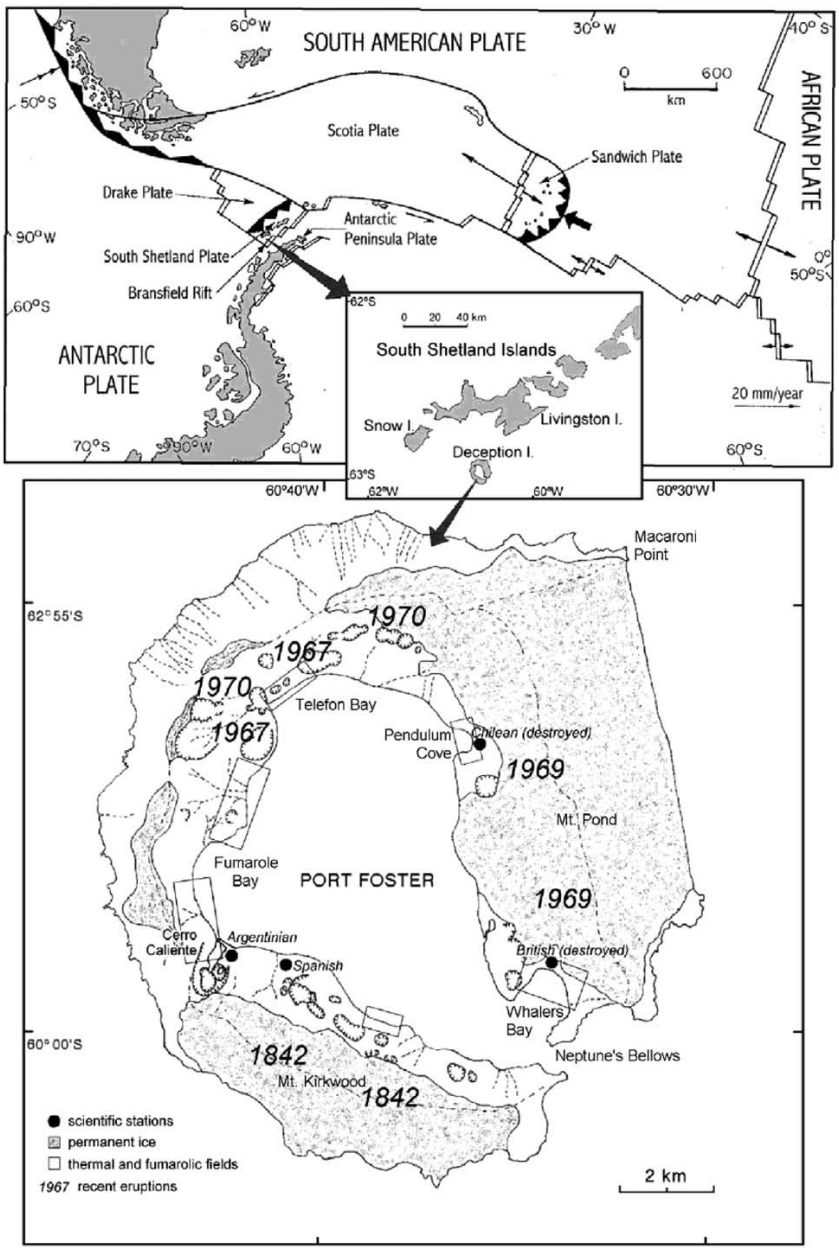

Fig. 1. Location of Deception Island in the South Shetland Islands region and map of Deception Island showing the main volcanological features.

rocks have normal magnetic polarity, indicating that they are younger than 700 ka; the oldest dated age of the pre-caldera deposits is 200 ka (Keller et al., 1991). The standard sequence has been developed by Birkemajer (1992), and correlated with shallow-penetration seismic reflection sections in Port Foster by Rey et al. (1997). The pre-caldera rocks are exposed on sea cliffs and parts of the caldera wall, and are composed of tuffs and agglomerates with interspersed lava flows and scoria horizons. The post-caldera deposits include basaltic lavas and scoria at higher elevations and pyroclastic cones around Port Foster where the magma interacted with seawater. It is generally accepted that the post-caldera deposits have been controlled by the ring-fracture system, with most eruptions occurring near the margins of the caldera (Baker et al., 1969; Smellie, 1990).

The caldera at Deception Island volcano has been traditionally described as a classic example of collapse caldera that formed about a ring fracture following one or more voluminous eruptions of andesitic magma (Baker et al., 1975; Smellie, 1988). However, there are other models of caldera formation, for example the incremental growth in response to a series of moderate-sized eruptions (e.g., Walker, 1984). On the basis of the structural data and other lines of evidence, Rey et al. (1995) and Martí et al. (1996) argue that the Deception Island caldera is a tectonic depression that was formed progressively by passive normal faulting along sets of nearly orthogonal normal faults that cut across the island and follow the regional trends. Structural mapping and shallow-penetration seismic reflection studies within Port Foster show that the architecture of Deception Island is controlled by three major fault systems (Rey et al., 1997). The first one is a NE–SW striking system that is consistent with the regional extensional regime of Bransfield Strait and controlled the vent alignment during the 1967 and 1970 eruptions. Several faults in this system cut across the caldera. A second system strikes at $\sim 120^{\circ}$N, defines the caldera wall near Mount Kirkwood in the south, and parallels an axis of submarine volcanic cones in the southern part of Port Foster. A third system strikes at $\sim 170^{\circ}$N, and includes the Macaroni fault that forms an 8 km length of the island's NE coastline. In support of this model, Rey et al. (1995) and Martí et al. (1996) note the absence of circular sections of the postulated ring fault and radial dikes and fractures within the caldera. They infer that nearly all the post-caldera eruptions have been located on linear faults, some of which lie outside the hypothetical ring fault, while others cut the caldera. One implication of their model is that the caldera may be underlain by much less extensive and perhaps discontinuous magma reservoirs whose position is controlled by the location of faults.

Deception Island is the most active volcano of the South Shetland Islands region, having erupted at least 6 times since it was first visited 160 years ago. All historical eruptions have been relatively small in volume. They have occurred at locations near the coast of the inner bay, all around the caldera (Fig. 1). Some of the eruptive episodes have included simultaneous eruptions of chemically distinct lavas from multiple vents (Newhall and Dzurisin, 1988). The first report of an eruption at Deception Island dates back to 1842, when a "wall of fire" was observed by whaling ships, related to a set of craters that formed below Mt. Kirkwood in the southwest part of the island (Roobol, 1973). From ice records at surrounding islands, explosive eruptions are inferred to have occurred in 1912 and 1917 (Orheim, 1972). The ice record in James Ross Island, 200 km from Deception (Aristarain and Delmas, 1998), suggests that an important eruption occurred in the 19th century. This eruption may have been the largest one on the island in the last 350 years. Three eruptions between 1967 and 1970 were observed directly and are well documented. In December 1967, two vents developed simultaneously at sites located ~ 2 km apart. One of them was a submarine eruption that gave birth to a new island in Telefon Bay, while the other occurred inland, between Telefon Bay and Pendulum Cove. A second eruption occurred in February 1969, when fissures opened in the ice on the west-facing slopes of Mt. Pond, accompanied by pyroclastic emissions. The last eruption took place in August 1970, when additional activity along the northern edge of Telefon Bay formed a chain of new craters and modified the coast line.

The chemical differences observed between the lavas suggest that the eruptions were fed by small isolated magma reservoirs (Roobol, 1979). Likewise, the synchronicity of some historical eruptions and the fact that they occurred throughout the caldera are most easily explained if the volcanic activity resulted from small magma bodies that rose up from a large magma chamber extended across the whole caldera. Leaks of silicic magma along ring fractures have preceded some large caldera-forming eruptions (e.g., Bacon, 1985), and one could speculate that the recent activity at Deception Island may be a long-term precursor of a larger eruption. The most accepted interpretation, however, assumes that Deception Island is presently in an early stage of the infilling of the caldera by small-volume eruptions (Roobol, 1982).

Evidences for present-day volcanic activity at Deception Island include fumaroles and hydrothermal activity (Fig. 1), resurgence of the floor of Port Foster, and seismicity. Fumaroles and hot springs with temperatures up to 110°C encircle Port Foster, while hydrothermal vents have been reported outside the island (Smellie, 1990). The analysis of repeated bathymetric surveys of Port Foster obtained between 1949 and 1993 allowed Cooper et al. (1998) to identify three regions that are shallowing at rates of up to 0.5 m/yr. High rates of shallowing in near-shore regions to the north of Fumarole Bay and in Telefon Bay could be entirely due to sedimentation, but a region of rapid shallowing in NE Port Foster is attributed to volcanic resurgence. Uplift has continued more recently in this area, with 5 m measured between 1990 and 1999. This region lies within an EW-trending belt of earthquake epicenters across Port Foster (Vila et al., 1992; Ibáñez et al., 2003), displays high seismic attenuation in the shallowmost crust (Vila et al., 1995), and is site of magnetic and gravity anomalies (Ortiz et al., 1992).

2. Seismicity of Deception Island

Based on the experience from the successive field surveys carried out at Deception Island volcano, the local seismicity has been classified in two main groups: volcano-tectonic (VT) earthquakes and long-period (LP) seismicity (which includes LP events and volcanic tremor). A third group of seismo-volcanic events are named hybrids, since they share characteristics from both of the main groups.

VT earthquakes are local earthquakes generated within the volcanic edifice. At Deception Island, for example, they usually display $S-P$ times smaller than 3–4 s. VT earthquakes are dominated by a double-couple mechanism, and often characterized by impulsive P-wave onsets and clear S arrivals. The spectral content is broad, with significant energy up to 30 Hz. In Fig. 2 we plot three examples of different types of tectonic earthquakes recorded at Deception Island. Note the clear differences in the temporal and spectral signatures. The hypocenters of VT earthquakes are not homogeneously distributed at Deception Island. For example, Vila et al. (1992, 1995) provided a map of the seismicity for the 1986–1991 period showing epicenters located all over the island; Ibáñez et al. (2000) located earthquakes recorded during the period 1994–1998 along a NE–SW fracture system near the Spanish base; and finally Ibáñez et al. (2003) located the epicenters of VT earthquakes belonging to the 1999 series, which were confined mostly to Port Foster. VT earthquakes at Deception Island are usually shallow, low-magnitude events. However, some earthquakes with magnitude greater than 3.5 have been recorded, and there is evidence of the occurrence of larger earthquakes near Deception Island, with magnitudes greater than 5.0 (Pelayo and Wiens, 1989). The source of the VT earthquakes is associated to the brittle failure of parts of the volcanic edifice in response to changes in the distribution of local or regional stresses. Stresses may change for example due to interactions of water with hot materials (Vila et al., 1995; Correig et al., 1997) or to the effects of shallow magma injections (Ortiz et al., 1997; Ibáñez et al., 2003).

LP seismicity is characterized by a quasi-monochromatic spectral content. The most frequent type of LP seismicity at Deception Island are the LP events, which constitute signals with a spindle-shaped envelope and durations smaller

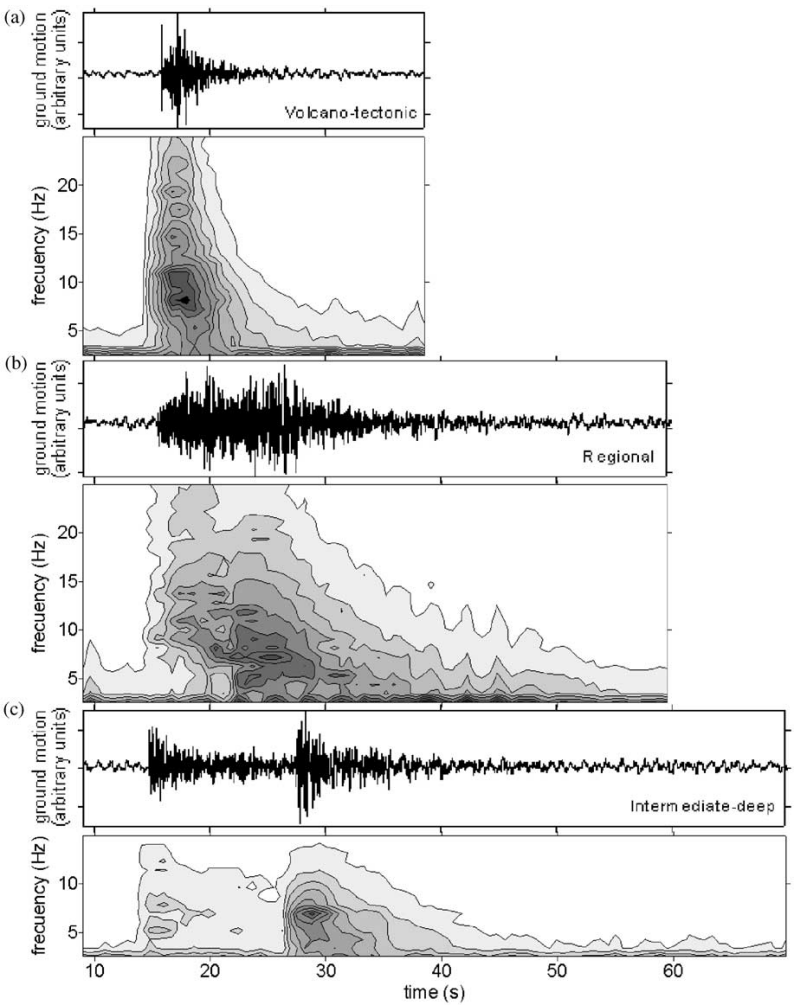

Fig. 2. Example of vertical-component velocity seismograms and array-averaged spectrograms for (a) a VT earthquake; (b) a regional earthquake; and (c) an intermediate-deep earthquake. All these signals have been recorded at Deception Island volcano. Spectrograms are obtained by dividing the seismograms into overlapping 2.56-s windows and averaging over the whole seismic array.

than 60 s. In some cases, a high-frequency phase precedes these events. In Fig. 3 we show examples of three types of LP events with different spectral content and duration. The location of the source of these pure volcanic signals has been derived from seismic antenna analyses (Almendros et al., 1997, 1999). Alguacil et al. (1999) and Ibáñez et al. (2000) have identified two different types of spectral behavior in the low-frequency band of these signals. The most common corresponds to a series of non-regularly spaced peaks, while the second shows regularly spaced harmonics of a fundamental peak. In the first group two subsets are differentiated by the frequency of the main

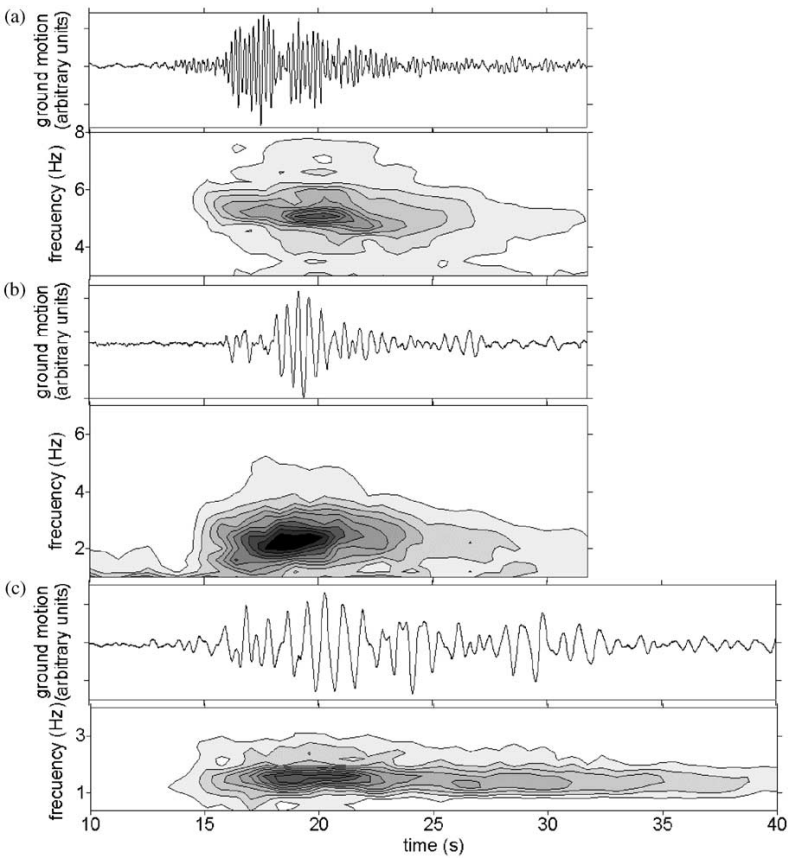

Fig. 3. Example of vertical-component velocity seismograms and array-averaged spectrograms for LP events recorded at Deception Island, with frequency contents centered at (a) 5 Hz; (b) 2.5 Hz; and (c) 1.5 Hz.

peak. The source processes that generate the LP seismicity involve a volumetric component due to the resonance of fluid-filled cavities (Chouet, 1996).

Volcanic tremor is a monochromatic signal with duration longer than that observed for LP events. Episodes of tremor that last from minutes to several hours and days have been observed at Deception Island volcano. In Fig. 4 we show a 3-h sample of volcanic tremor. Models of tremor generation are based on degassing, fluctuations of the gas, resonance of conduits, etc (e.g. Chouet, 1992; Julian, 1994). Those models considering the resonance of open conduits have been complicated by introducing different geometries of the resonance system. Although they are enough to explain some tremor signals, in other cases the geometrical considerations need to be completed by including in the tremor models data about the reology of the fluids and their dynamics (Chouet, 1996). Some results, which integrate observations of tremor and LP, show evidences that both type of events share similar source regions and processes (Almendros et al., 1997, 2001). Tremor and LP events are supposed to be different manifestations of the same process. An LP event is the

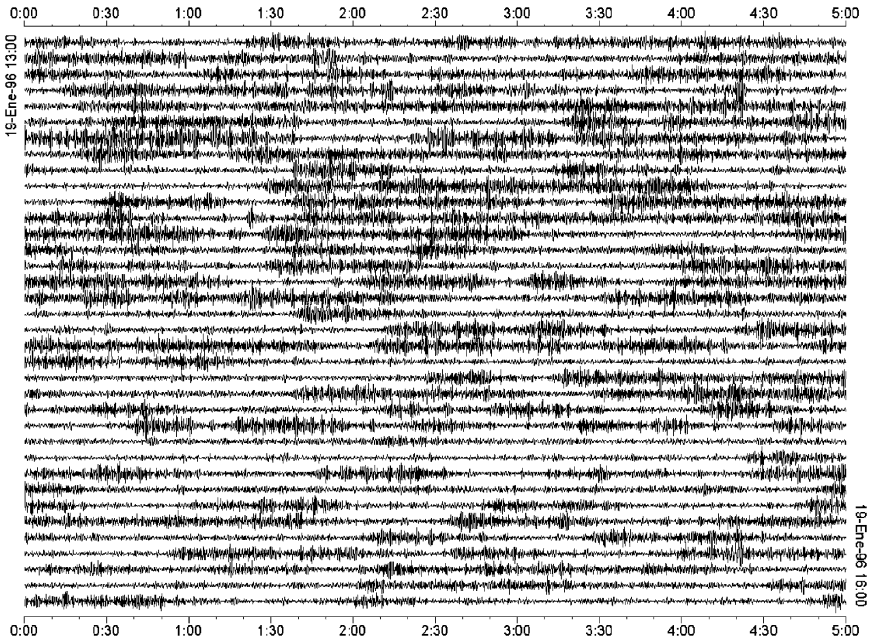

Fig. 4. Example of vertical-component velocity seismogram corresponding to continuous recording of 3 h of volcanic tremor at Deception Island volcano.

response to a sudden pressure transient within a fluid-filled crack, while tremor is the response to continuous fluctuations of pressure.

Hybrid events are signals that contain both double-couple and volumetric components. They are characterized by an initial high-frequency phase similar to a VT earthquake, followed by a monochromatic signal similar to those shown by the LP events (Fig. 5). In some cases, LP events with an energetic initial high-frequency onset could be confused with hybrids. While the low-frequency signature is originated in both cases by the resonance of a fluid-filled cavity, in the case of hybrid events the initial pressure step that triggers the resonance is caused by a brittle failure process. Recently, Ibáñez et al. (2003) have distinguished in Deception Island signals that might be interpreted as hybrids. They have found a few VT earthquakes that are closely followed by LP events. Both parts of the signals share a similar source region. This region coincides with an area of VT earthquake generation, which constitutes our only clue as to the hybrid character of the signals. In reality, only a detailed analysis of the source mechanisms using a network with appropriate coverage could settle the question of whether these signals are LP events or hybrids.

3. Review of recent seismic studies

3.1. History of seismic monitoring at Deception Island

The seismic monitoring of Deception Island volcano began in the 1950s when a seismometer was deployed at the Argentinean base. Data from this station were recorded continuously on smoked paper drum until the end of the 1960s when the series of eruptions that took place in the island forced the evacuation of the bases. Seismic records obtained during this period show the frequent

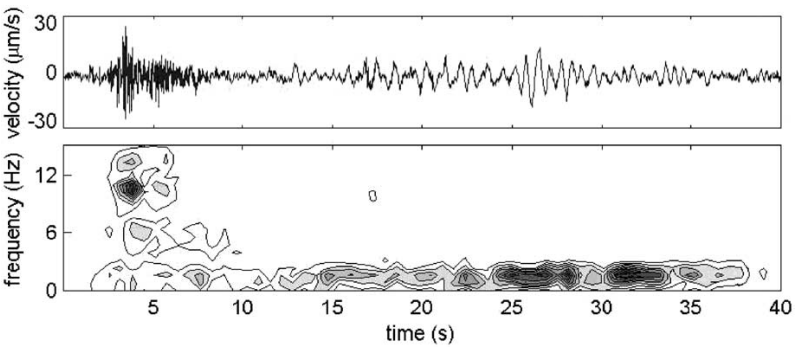

Fig. 5. Example of vertical-component velocity seismogram and array-averaged spectrogram for a signal interpreted as a hybrid event (Ibáñez et al., 2003).

occurrence of local seismicity, including VT earthquakes, LP events, and episodes of volcanic tremor. The rate of occurrence of seismic events increased just before each of the 1967–1970 eruptions, which emphasizes the usefulness of seismic monitoring as a forecasting tool at Deception Island. Regional and teleseismic earthquakes also were detected, but due to the lack of adequate coverage only earthquakes with magnitude 5 or above could be located.

From 1970 to 1986 there are no seismic records from Deception Island. In 1986 the monitoring of the seismic activity was re-established through summer field surveys carried out by Argentinean and Spanish researchers, with the result of a temporary control of the seismic activity of the volcano (Fig. 6). Several types of seismic deployments have been used (Fig. 3). Between 1986 and 1988 a vertical short-period seismic station recording on a thermal paper drum was used, at a location near the Argentinean base. Between 1989 and 1991, seismic data were recorded by a network composed of five short-period seismic stations with radio telemetry. In this period, several VT earthquakes and a few volcanic tremor episodes were recorded. Vila et al. (1992, 1995) and Correig et al. (1997) studied this seismic activity and provided the first epicentral map of the VT activity of Deception Island volcano. These authors also proposed a model of the occurrence of the activity based on the degasification of an aquifer in contact with deep hot materials. In average, the energy of the tectonic and volcanic quakes recorded between 1986 and 1991 was quite low.

This situation changed in January 1992, when an important increase in the number and magnitude of the seismic events was detected (Ortiz et al., 1997). More than 750 VT earthquakes were recorded in less than 2 months. Some of these earthquakes and even a few episodes of volcanic tremor were felt. During this survey the only available seismic instrument was a three-component short-period seismometer deployed near the Argentinean base. Although the epicentral area of the recorded activity could not be determined accurately, indirect evidence shows that the source area was probably located under Port Foster, just 2–3 km from the shoreline. Observations of small gravity irregularities and magnetic anomalies correlated with the successive seismic swarms suggest that a magmatic injection took place during this increase of seismic activity (Ortiz et al., 1992, 1997; García et al., 1997). However, it had not enough energy to reach the surface. Changes in fumarolic emissions and a possible deformation process near the Argentinean base support the hypothesis of magmatic injection. The seismic and gravimetric evidences of this activity started to decline in February 1992.

During the 1992–1993 and 1993–1994 field surveys new seismic stations were deployed near

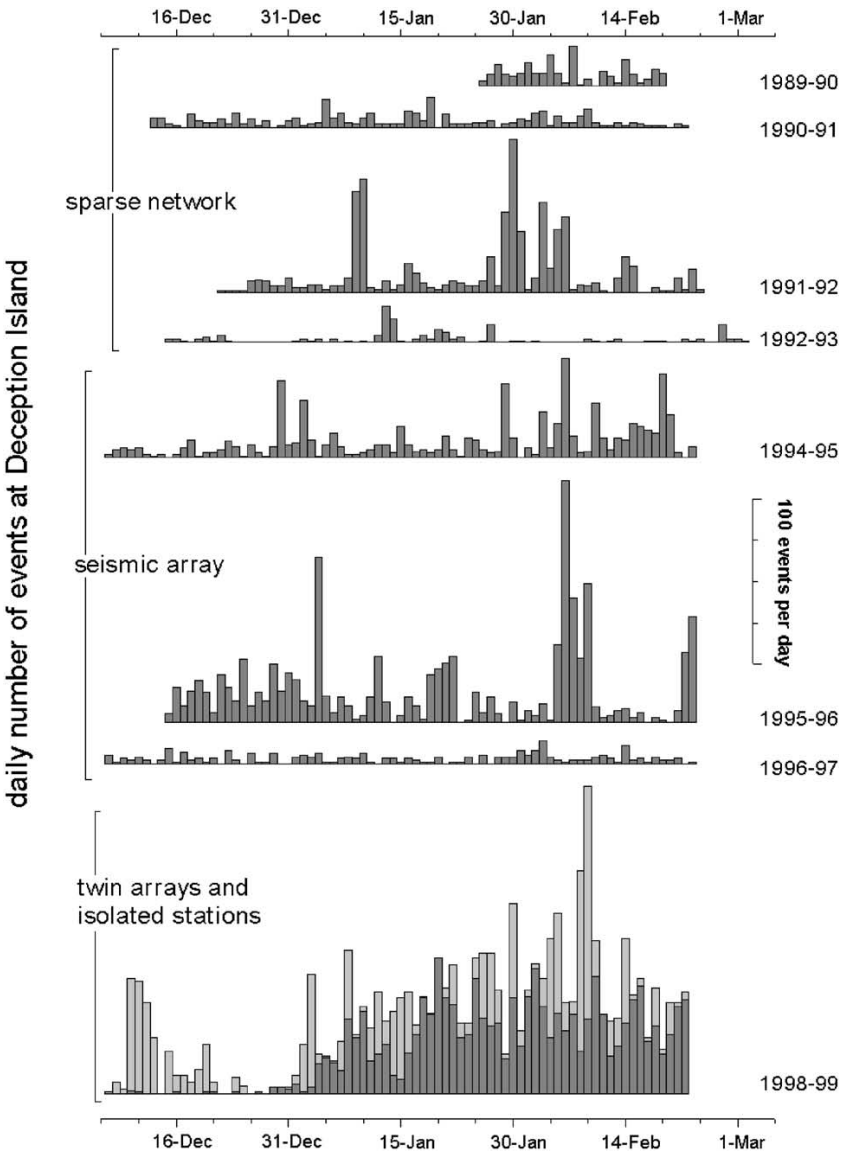

Fig. 6. Histogram of the daily number of seismo-volcanic earthquakes recorded at Deception Island during the summer field surveys in the period 1989–1999, with the exception of the 1997–1998 survey. In the 1998–1999 survey we show separately the VT earthquakes (dark gray) and LP events (light gray).

the Argentinean and Spanish bases to study the continuity of the seismic swarm of January 1992, although the activity had decreased to the pre-1992 level (Fig. 6). However, a change in the characteristics of the seismic activity was observed. Starting on December 1992, the number of VT

earthquakes clearly decreased, while the number of LP events and tremor increased (Felpeto et al., 1994). Since the seismic stations deployed on the island were powerless to locate or analyze the LP seismicity, the objectives of the seismic experiments were modified and the use of seismic antennas was introduced.

3.2. Seismic antenna surveys

The increasing contribution of LP events and tremor to the overall seismicity of Deception Island volcano motivated the introduction of seismic antennas. Seismic antennas allow complete analyses of the seismic wavefield and are able to provide useful information about the nature of LP events and volcanic tremors. In 1994, a small-aperture seismic antenna was set up near the Spanish Base "Gabriel de Castilla" to track the seismo-volcanic sources. This antenna was deployed again for the summer field surveys between 1995 and 1997. Preliminary reports obtained from analyses of the array data (Alguacil et al., 1999) confirmed the existence of VT earthquakes, LP events, and sustained tremors near the array site, in an area south of Cerro Caliente (see Fig. 1). Ibáñez et al. (1997) reported the presence of intermediate depth (30–120 km) and shallow earthquakes (0–30 km) in the area. Almendros et al. (1997) showed that some volcanic tremor episodes were generated by the multiple occurrence of low-energy LP events. Almendros et al. (1999) introduced a modification of the zero-lag cross-correlation technique taking into account the circular geometry of the incoming wave fronts. Using this technique, the epicentral locations of a subset of LP events were estimated to be close to the antenna, at distances of a few hundred meters southwest of the array site.

In 1998, two semi-circular seismic antennas were deployed along the inner coast of the western side of Deception Island (Fig. 7), at a distance of about 2 km. The objective of the two-antenna deployment was the investigation of the shallow velocity structures under the arrays and the use of a joint location method to improve the location capabilities of the antennas. The presence of the seismic antennas has allowed for the analysis of the LP seismicity generated in different regions of the island. Moreover, the source locations of several hundreds of VT earthquakes recorded in January and February 1999 were estimated using an inverse ray-tracing procedure (Ibáñez et al., 2003).

3.3. Seismic attenuation studies

Martínez-Arévalo et al. (2003) studied the seismic attenuation in the short-distance and high-frequency range using *P*, *S*, and coda waves. They applied different techniques, including both frequency-dependent and frequency-independent methods such as broadening of the pulse for direct *P*- and *S*-waves, coda normalization for *S*-waves, single back-scattering for coda waves, and the spectral method. The results show that Q values are significantly smaller, for the entire frequency range analyzed (6–30 Hz), than those found in other volcanic and tectonic areas. The attenuation for *P*-waves is greater than for *S*-waves in the frequency-independent methods, with a Q_β/Q_P ratio that ranges between 1.9 and 3.2. Q factors obtained for *S*-waves show clear differences depending on the method used. The coda normalization method has supplied significantly higher Q values (Q_d) than the other two methods (Q_β). This discrepancy is due to the fact that coda normalization and single back-scattering methods eliminate the contribution of the near-surface attenuation. Comparing Q_β and Q_d, the near-surface attenuation under the recording site, Q_κ, was estimated. Q_d displays an anomalous frequency dependence, with a minimum value at 21 Hz. This pattern was interpreted as the effect of strong scattering of the seismic waves in the source area. Q_c values clearly depend upon frequency and lapse time. The lapse time dependence could be interpreted as a depth dependence of the seismic attenuation in Deception Island volcano. Separating the contribution of intrinsic and scattering attenuation, Martínez-Arévalo et al. (2003) found that the scattering attenuation is predominant over the intrinsic effects. All these observations suggest a highly heterogeneous structure for Deception

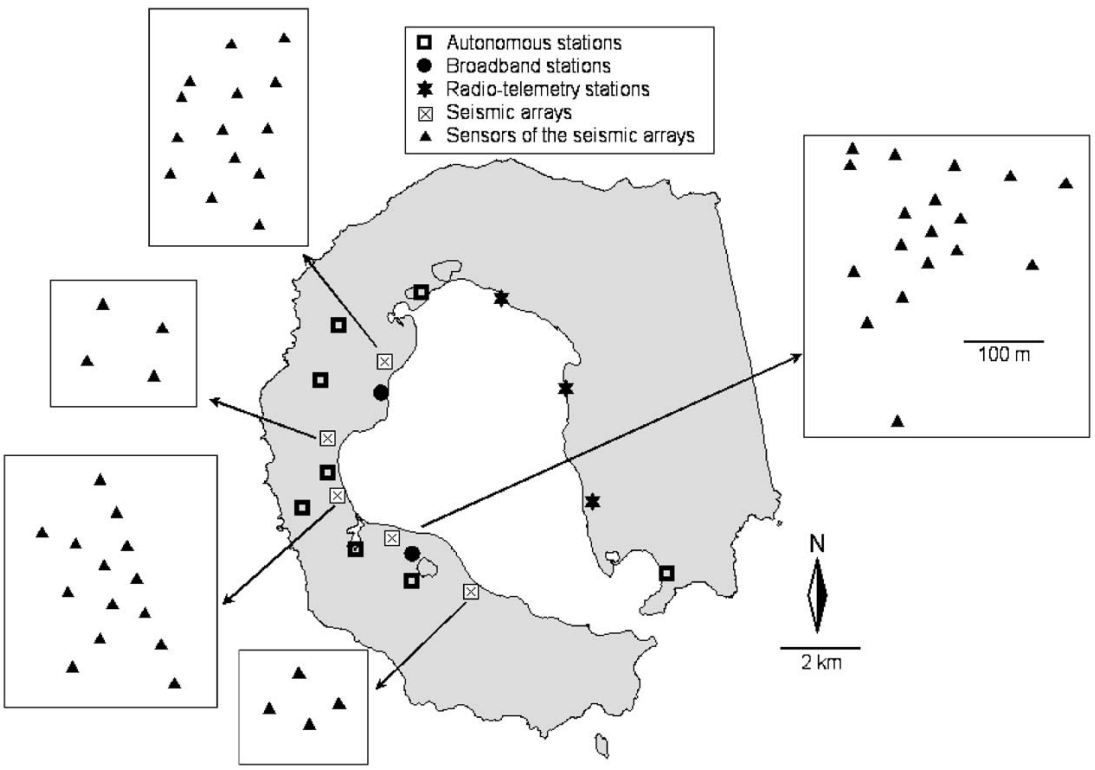

Fig. 7. Map of Deception Island volcano showing the position of the seismic stations and antennas deployed during the different seismic experiments carried out since 1994.

Island volcano. Similar observations were done by Havskov et al. (2003) using different techniques.

4. The 1999 seismic crisis

The seismic crisis that occurred in January–February 1999 represents a good example of the intense seismic swarms that occasionally shake Deception Island volcano. During the month of December 1998 only a few events were recorded (8 VT earthquakes), a rate similar to that reported by Ibáñez et al. (2000) for previous years. However, this trend was suddenly modified on January 1, 1999, when the number of local earthquakes suddenly increased (Fig. 8). The seismic swarm reached its maximum daily number of events on January 20, with the occurrence of 80 VT earthquakes. When the field survey finished, the seismic activity was still high, more than 50 earthquakes/day. At the bottom of Fig. 8 we show a histogram of the local earthquakes recorded by a seismic station deployed at the Spanish Base, which continued its operations for up to 2 months after the main field survey ended. We can infer from this figure that, although in March the activity was decreasing, at the end of this month there was a new increase. During the summer period more than 3000 earthquakes were detected and 863 have been analyzed. Several earthquakes had magnitude-momentum greater than 2.5. At least two of them were felt by the staff working on the island,

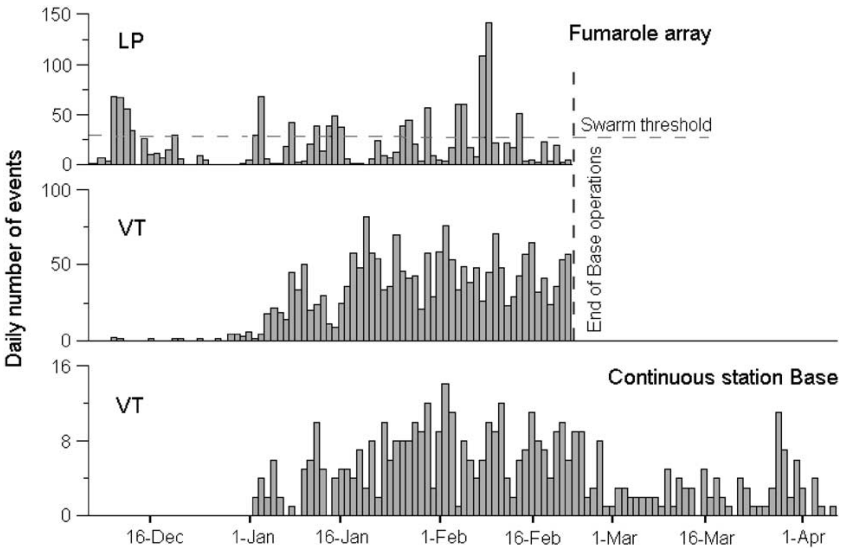

Fig. 8. Histograms of the daily number of LP events (top) and VT earthquakes (middle) detected during the 1999 crisis by the Fumarole seismic antenna, and VT earthquakes recorded by the continuous station at the Spanish Base between December 1998 and April 1999 (bottom).

one of them at the beginning of the series, on January 11, and the second in January 20, with magnitudes of 2.9 and 3.4, respectively. Both events represent a qualitative change in the seismic pattern, because since the 1991–1992 crisis no earthquakes of this magnitude had been reported (Ortiz et al., 1997). LP seismicity appeared in swarms that lasted a few days and alternated with rest periods of several days. A total of 1800 LP events were recorded, with peak activity reaching about 150 events/day. Using a lower limit of 30 events/day to define an LP swarm (Ibáñez et al., 2000), there were nine swarms distributed randomly throughout the recording period (Fig. 8). This pattern coincides with that previously observed for the LP seismicity (see Fig. 6), and therefore the LP activity in 1998–1999 was considered normal for the area.

Hypocenters of the VT earthquakes and hybrids were determined using the apparent slowness, back-azimuth, and $S-P$ time to perform an inverse ray-tracing source location (Ibáñez et al., 2003). The $S-P$ time fixes the distance to the source; the back-azimuth is the direction to the epicenter; and the apparent slowness provides the incidence angle. The hypocentral distribution (Fig. 9) indicates that the seismicity is clustered at a focal depth of $\sim$2 km near the Fumarole array and mostly toward the northeast. More than 90% of the events are clustered in a volume of around 10 km^3. However, deeper and more distant events also were found, with focal depths reaching 10 km and epicentral distances up to 18 km. The main cluster has two denser regions (see the dashed lines in Fig. 9). The first one extends about 3 km in a direction of about 45°N, with focal depths between 1 and 4 km. The second is longer but more diffuse, and extends toward 80°N. Most part of the seismicity is located within the inner bay of Deception Island and apparently dips at an angle of about 45°. Hybrid event locations coincide with the cloud of VT earthquakes. Most of them are contained in the branch of seismicity extending toward 80°N.

The VT earthquakes analyzed span a magnitude range from −0.8 to 3.4. These magnitudes allow us to track the energetic evolution of the seismic series, as well as estimate the cumulative seismic

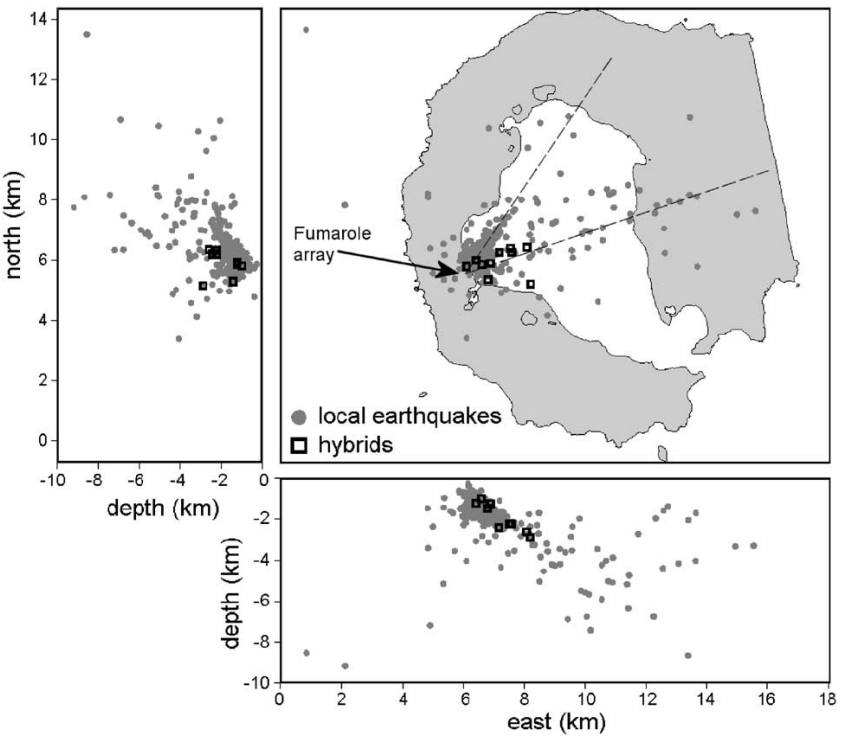

Fig. 9. Hypocentral locations of the VT earthquakes (dots) and hybrid events (squares) recorded by the Fumarole Bay seismic antenna during the 1999 crisis (from Ibáñez et al., 2003). The dashed lines represent the alignment of epicenters along preferred directions.

moment. Except for the two larger earthquakes mentioned above, the energy release is more or less steady in time. The distribution of magnitudes is nearly the same throughout the series. The stress drop of the VT earthquakes, derived from the magnitude analysis, is very low. More than 95% of the stress drop values are concentrated between 0.1 and 4 bar. Corner frequencies range from 40 Hz for the smallest events to 6 Hz for the largest ones (these values do not include those events that saturated the records). Using Brune's model (Brune, 1970) we found that the source dimensions range from 10 m up to 200 m, with an average of 50 m. Using Madariaga's model (Madariaga, 1977) the dimensions obtained are smaller, and range from 5 to 120 m, with an average of 30 m. In any case, the estimates of the source dimensions indicate clearly the small size of the fractures involved in the generation of earthquakes during the seismic series. These tiny fractures are primarily concentrated in a small focal volume, inside of which we have detected hundreds of events.

5. Source models

In this section, we will describe the models generally assumed to explain the origin of the LP seismicity and the generation of VT earthquakes at Deception Island. We also will explain the reason for their occurrence in swarm-type sequences.

5.1. Model for pure volcanic signals

The conceptual model proposed by Ibáñez et al. (2000) to explain the origin of the pure volcanic

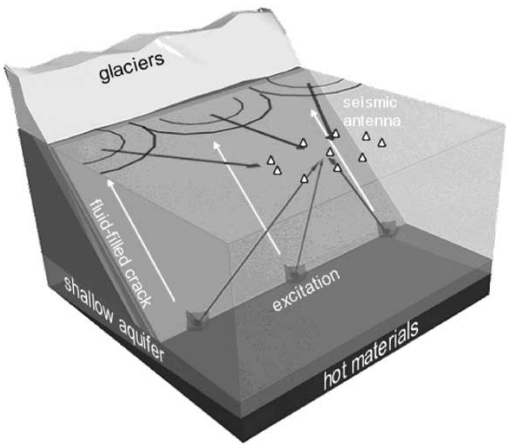

Fig. 10. Sketch of the seismic source model proposed by Ibáñez et al. (2000) to explain the origin of the LP seismicity at Deception Island volcano (see text for explanations).

signals (Fig. 10) can be summarized as follows: a sudden pressure step occurring at depth in a fluid-filled crack puts the crack itself in auto-oscillation. This pressure step may be caused for example by a sudden phase change of the hydrothermal fluids. A two- or three-dimensional source model is necessary to explain the spectral characteristics of the acoustic resonance. The high-frequency waves are produced by the phase change occurring at some position along the lower edge of the crack. The low-frequency waves are generated by the resonance of the whole crack and therefore propagate with similar back-azimuths, depending on the spatial orientation of the crack. The complex low-frequency wave pattern is due to the mixed contribution of P, SV, and SH waves radiated by the source (according to the model developed by Chouet, 1986, 1988, 1992) and to the generation of surface waves in the multiple-layered structure of the island, composed of frozen soil and different volcanic layers. This model could provide a unique source mechanism for LP events and volcanic tremors. The different spectra can be associated with different crack dimensions and properties. Assuming the model developed by Chouet (1992), the different energy of the initial high-frequency wave trains of the signals is explained by differences in the source time function of the pressure pulse that triggers the oscillation of the fluid-filled crack. When the rise time is sharp, we observe the highest energy of the high-frequency waves. A smooth source time function will reduce the high-frequency contribution to the spectrum. When the pressure step appears isolated, the duration of the resulting signal is short and produces an LP event. In the case of continuous or multiple activation of the source, the resulting signal may last for minutes or hours, producing volcanic tremor. Note that some of the seismo-volcanic events recorded at Deception Island during the 1994–1997 period were classified as hybrids (Ibáñez et al., 2000) based on their spectral properties; however, they may not represent true hybrids as described for example by Lahr et al. (1994) for Redoubt volcano. They can be explained by the same source mechanism described above, and therefore may be better considered as LP events with an energetic high-frequency onset. Finally, we must point out that the conceptual model of single crack in Fig. 10 is an over-simplification. In reality, the source may be composed of a complex crack system with different sizes and orientations.

Due to its characteristic spectral properties, the quasi-monochromatic tremor may be explained by a different mechanism, consisting of the resonance of a pipe-like conduit (Chouet, 1985). The signals show spectral peaks that are overtones of a fundamental frequency. This spectral pattern reveals that one dimension of the source is dominant over the other two, and therefore an organ pipe source model would be adequate to explain the spectral features of the tremor.

5.2. VT earthquake source model

To understand a fracture process involving low stress drop, small fault dimensions, and occurrence of multiplets, as observed in Deception Island, Ibáñez et al. (2003) invoked the role of the fluids. In this framework the release of seismic energy is associated with lubrication of a pre-existing zone of weakness. Lubrication reduces the friction coefficient and decreases the effective normal stress over the fault surface. This can in turn trigger the

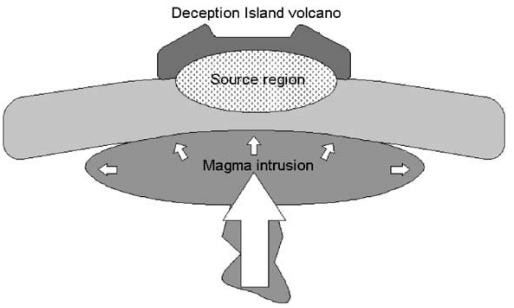

Fig. 11. Sketch of the deep magma intrusion model proposed by Ibáñez et al. (2003) for the origin of the 1999 VT series at Deception Island volcano (see text for explanations).

earthquake. Ibáñez et al. (2003) proposed a possible scenario that explained the origin of the seismic crisis based on the volcanic nature of Deception Island. The seismic series was caused by stress generated by the uplift of the source area in response to the injection of magma at depth (Fig. 11). The presence of a magma reservoir in the northeast area of Port Foster has been suggested by several authors (Blanco, 1997; García et al., 1997). An increase of pressure within the magma reservoir, or the upward displacement of magma, disturbs the stress field in the region over the reservoir. When the stress reaches a threshold value, fracture processes begin, following pre-existing zones of weakness. The absence of visible evidence of a subsequent eruption and the lower level of earthquake activity observed since 1999 imply that the injection of magma stopped before reaching of the surface. The uplift hypothesis is compatible with the majority of the geophysical observations. The small size of the fractures involved is explained by lubrication of the microfaults due to pressurized fluids. The increase of pore pressure in the very shallow crust overlying the magmatic system could have induced the repeated activation of the fracture network. The presence of fluids in the source area not only expedites the fracture processes, but also explains the origin of the hybrids. Their low-frequency segments are produced by resonances of fluid-filled cracks. The fluid involved in the lubrication of the microfaults and the generation of hybrid events is probably not magmatic, but water embedded in the geological structure. Martini and Giannini (1988) reported the existence of a shallow aquifer near the epicentral area, and a deeper aquifer may be present as well (Martini and Casselli, pers. comm.).

6. Conclusions

The data obtained since 1986 during several seismic field surveys at Deception Island demonstrate that this is a seismically active volcano. Both LP seismicity and VT earthquakes have been recorded and analyzed, leading to knowledge of different aspects of the volcano. The present paper describes this seismicity and proposes models that may realistically explain the release of seismic energy within the volcano.

The most intense seismic activity at Deception Island occurred during the seismic crises of 1992 and 1999. This means that in about 15 years of seismic monitoring, two intense volcanic crises have been observed. If we take into account that there are no permanent stations on the island, and seismic measurements can be performed only during 3 months/yr (from December to February), then similar periods of intense seismic activity might be occurring more often than what has been detected so far. Deception Island, therefore, seems to be a very active volcano, at least from a seismological point of view, although no eruption has been reported since 1970. Given the frequent presence of scientific teams, and also thousands of tourists (especially during the summer season), greater efforts should be put into seismic and geophysical monitoring of Deception Island in order to reduce the risk associated with volcanic hazards.

Acknowledgements

This work was partially supported by projects ANT98-1111, REN-2000-2897, EU project e-Ruption EVR1-2001-00024, and REN-2001-3833. We thank five anonymous reviewers and the

editors of this special volume. Their reviews helped to improve significantly this manuscript.

References

Alguacil, G., Almendros, J., Del Pezzo, E., García, A., Ibáñez, J.M., La Rocca, M., Morales, J., Ortiz, R., 1999. Observations of volcanic earthquakes and tremor at Deception Island, Antarctica. Annali di Geofisica 42, 417–436.

Almendros, J., Ibáñez, J.M., Alguacil, G., Del Pezzo, E., Ortiz, R., 1997. Array tracking of the volcanic tremor source at Deception Island, Antarctica. Geophysical Research Letters 24, 3069–3072.

Almendros, J., Ibáñez, J.M., Alguacil, G., Del Pezzo, E., 1999. Array analysis using circular wave-front geometry: an application to locate the nearby seismo-volcanic source. Geophysical Journal International 136, 159–170.

Almendros, J., Chouet, B., Dawson, P., 2001. Spatial extent of a hydrothermal system at Kilauea volcano, Hawaii, determined from array analyses of shallow long-period seismicity, 2. Results. Journal of Geophysical Research 106, 12318–12330.

Aristarain, A.J., Delmas, R.J., 1998. Ice record of a large eruption of Deception Island volcano (Antarctica) in the XVIIth century. Journal of Volcanology and Geothermal Research 80, 17–25.

Bacon, C.R., 1985. Implications of silicic vent patterns for the presence of large crustal magma chambers. Journal of Geophysical Research 90, 11243–11252.

Baker, P.E., Davis, T.G., Roobol, M.J., 1969. Volcanic activity at Deception Island in 1967 and 1969. Nature 224, 553–560.

Baker, P.E., McReath, I., Harvey, M.R., Roobol, M.J., Davis, T.G., 1975. The Geology of the South Shetland Islands: V. Volcanic evolution of Deception Island. British Antarctic Survey Scientific Reports 78, 81pp.

Barker, P.F., 1982. The Cenozoic subduction history of the Pacific margin of the Antarctic Peninsula: ridge crest-trench interactions. Journal of the Geological Society of London 139, 787–801.

Barker, D.H., Austin, J.A., 1994. Crustal diapirism in Bransfield Strait, West Antarctica: evidence for distributed extension in marginal-basin formation. Geology 22, 657–660.

Barker, D.H., Austin, J.A., 1998. Rift propagation, detachment faulting, and associated magmatism in Bransfield Strait, Antarctic Peninsula. Journal of Geophysical Research 103, 24017–24043.

Barker, D.H., Christeson, G.L., Austin, J.A., 2001. Crustal structure of an active backarc basin at the rift-drift transition: Bransfield Strait, Antarctica. EOS Transaction of the AGU Fall Meeting Supplement 82(47), pp. F1244 (abstract).

Bialas, J., Meissner, R., Miller, H., Fluh, E., Parker, T., Henriet, J.P., Hedrich, K., Heuverswyn, E.V., Jokat, W., Wever, T., 1990. Preliminary results of seismic reflection investigations and associated geophysical studies in the area of the Antarctic Peninsula. Antarctic Science 2, 223–234.

Birkemajer, K., 1992. Volcanic succession at Deception Island, West Antarctica: a revised lithostratigraphic standard. Studia Geological Polonica 101, 27–82.

Blanco, I., 1997. Análisis e interpretación de las anomalías magnéticas de tres calderas volcánicas: Decepción (Shetland del Sur, Antátida), Furnas (San Miguel, Azores) y las Cañadas del Teide (Tenerife, Canarias). Ph.D. Thesis, Universidad Complutense de Madrid, 250pp.

Brune, J.N., 1970. Tectonic stress and the spectra of seismic shear waves. Journal of Geophysical Research 89, 1132–1146.

Chouet, B., 1985. Excitation of a buried magmatic pipe: a seismic source model for volcanic tremor. Journal of Geophysical Research 90, 1881–1893.

Chouet, B., 1986. Dynamics of a fluid-driven crack in three dimensions by the finite difference method. Journal of Geophysical Research 91, 13967–13992.

Chouet, B., 1988. Resonance of a fluid-driven crack: radiation properties and implications for the source of long-period events and harmonic tremor. Journal of Geophysical Research 93, 4375–4400.

Chouet, B., 1992. A seismic model for the source of long-period events and harmonic tremor. In: Aki, K., Gasparini, P., Scarpa, R. (Eds.), Volcanic Seismology (IAVCEI Proceedings in Volcanology 3). Springer, Berlin, pp. 133–156.

Chouet, B., 1996. Long-period volcano seismicity: its source and use in eruption forecasting. Nature 380, 309–316.

Cooper, A.P.R., Smellie, J.L., Maylin, J., 1998. Evidence for shallowing and uplift from bathymetric records of Deception Island, Antarctica. Antarctic Science 10, 455–461.

Correig, A.M., Urquizu, M., Vila, J., Martí, J., 1997. Analysis of the occurrence of seismicity at Deception Island (Antarctica): a nonlinear approach. Pure and Applied Geophysics 149, 553–574.

Dietrich, R., Dach, R., Engelhardt, G., Ihde, J., Korth, W., Kutterer, H.J., others, 2001. ITRF coordinates and plate velocities from repeated GPS campaigns in Antarctica—an analysis based on different individual solutions. Journal of Geodesy 74, 756–766.

Felpeto, A., Blanco, I., Del Rey, R., Morales, J., 1994. Estudios de eventos de baja frecuencia registrados en Isla Decepción (in Spanish). In: Cacho, J., Serrat, D. (Eds.), Actas del V Simposio de Estudios Antárticos, CICYT, Barcelona pp. 147–154.

García, A., Blanco, I., Torta, J.M., Astiz, M., Ibáñez, J.M., Ortiz, R., 1997. A search for the volcanomagnetic signal at Deception volcano (South Shetland Islands, Antarctica). Annali di Geofisica 40, 319–327.

Gracia, E., Canals, M., Farran, M.L., Prieto, M.J., Sorribas, J., 1996. Morphostructure and evolution of the Central and Eastern Bransfield basins (NW Antarctic Peninsula). Marine Geophysical Researches 18, 429–448.

Gracia, E., Canals, M., Farran, M.L., Sorribas, J., Pallas, R., 1997. Central and Eastern Bransfield basins (Antarctica)

from high-resolution swath-bathymetry data. Antarctic Science 9, 168–180.

Grad, M., Guterch, A., Sroda, P., 1992. Upper crustal structure of Deception Island area, Bransfield Strait, West Antarctica. Antarctic Science 4, 469–476.

Grad, M., Shiobara, H., Janik, T., Guterch, A., Shimamura, H., 1997. Crustal model of Bransfield Rift, West Antarctica, from detailed OBS refraction experiments. Geophysical Journal International 130, 506–518.

Havskov, J., Peña, J.A., Ibáñez, J.M., Ottemöller, L., Martinez-Arévalo, C., 2003. Magnitude scales for very local earthquakes: application to Deception Island volcano (Antarctica). Journal of Volcanology and Geothermal Research, in press.

Ibáñez, J.M., Morales, J., Alguacil, G., Almendros, J., Ortiz, R., Del Pezzo, E., 1997. Intermediate focus earthquakes under South Shetland Islands (Antarctica). Geophysical Research Letters 24, 531–534.

Ibáñez, J.M., Del Pezzo, E., Almendros, J., La Rocca, M., Alguacil, G., Ortiz, R., García, A., 2000. Seismovolcanic signals at Deception Island volcano, Antarctica: wave field analysis and source modeling. Journal of Geophysical Research 105, 13905–13931.

Ibáñez, J.M., Carmona, E., Almendros, J., Saccorotti, G., Del Pezzo, E., Abril, M., Ortiz, R., 2003. The 1998–1999 seismic series at Deception Island volcano, Antarctica. Journal of Volcanology and Geothermal Research, in press.

Janik, T., 1997. Seismic crustal structure of the Bransfield Strait, West Antarctica. Polish Polar Research 18, 171–225.

Julian, B.R., 1994. Volcanic tremor: nonlinear excitation by fluid flow. Journal of Geophysical Research 99, 11859–11877.

Keller, R.A., Fisk, M.R., White, W.M., 1991. Geochemistry of quaternary volcanism in the Bransfield Strait and South Shetland Islands: preliminary results. Antarctic Journal of the United States 26, 132–133.

Kim, Y., Kim, H.-S., Larter, R.D., Camerlenghi, A., Gamboa, L.A., Rudowski, S., 1995. Tectonic deformation in the upper crust and sediments at the South Shetland Trench. In: Cooper, A.K., Barker, P.F., Brancolini, G. (Eds.), Geology and Seismic Stratigraphy of the Antarctic Margin. Antarctic Research Series 68, American Geophysical Union, Washington, DC, pp. 157–166.

Lahr, J., Chouet, B., Stephens, C., Power, J., Page, R., 1994. Earthquake classification, location and error analysis in a volcanic environment: implications for the magmatic system of the 1989–1990 eruptions at Redoubt volcano, Alaska. Journal of Volcanology and Geothermal Research 62, 137–151.

Lawver, L.A., Keller, R.A., Fisk, M.R., Strelin, J.A., 1995. Bransfield Strait, Antarctic Peninsula: active extension behind a dead arc. In: Taylor, B. (Ed.), Backarc Basins: Tectonics and Magmatism. Plenum Press, New York, pp. 315–342.

Lawver, L.A., Sloan, B.J., Barker, D.H., Ghidella, M., Von Herzen, R.P., Keller, R.A., Klinkhammer, G.P., Chin, C.S., 1996. Distributed, active extension in Bransfield Basin, Antarctic Peninsula: evidence from multibeam bathymetry. GSA Today 13, 2–6.

Lee, D.K., Kim, Y.D., Nam, S.H., Jin, Y.K., 1998. Local seismic activity monitored at King Sejong Station, Antarctica. Polar Geoscience 11, 76–89.

Madariaga, R., 1977. High-frequency radiation from crack (stress drop) models of earthquakes faulting. Geophysical Journal of Royal Astronomical Society 51, 625–652.

Martí, J., Baraldo, A., 1990. Pre-caldera pyroclastic deposits of Deception Island (South Shetland Islands). Antarctic Science 2, 345–352.

Martí, J., Vila, J., Rey, J., 1996. Deception Island (Bransfield Strait, Antarctica): an example of volcanic caldera developed by extensional tectonics. In: McGuire, W., Jones, A., Neuberg, J. (Eds.), Volcano Instability on the Earth and other Planets, Vol. 110. Geological Society Special Publication 110, London, pp. 253–265.

Martínez-Arévalo, C., Bianco, F., Ibáñez, J.M., Del Pezzo, E., 2003. Shallow seismic attenuation in the short period range of Deception Island volcano (Antarctica). Journal of Volcanology and Geothermal Research, in press.

Martini, M., Giannini, L., 1988. Deception Island (South Shetlands): an area of active volcanism in Antarctica. Memorie della Societa Geologica Italiana 43, 117–122.

Newhall, C.G., Dzurisin, D., 1988. Deception Island. In: Historical unrest at large calderas of the world. US Geological Survey Bulletin 1855, pp. 1013–1019.

Orheim, O., 1972. Volcanic activity on Deception Island, South Shetland Islands. In: Adie, R.J. (Ed.), Antarctic Geology and Geophysics. Universitetsforlaget, Oslo, pp. 117–120.

Ortiz, R., Vila, J., García, A., Camacho, A.G., Díez, J.L., Aparicio, A., Soto, R., Viramonte, J.G., Risso, C., Menegatti, N., Petrinovic, I., 1992. Geophysical features of Deception Island. In: Yoshida, Y., Kaminamura, K., Shiraishi, K. (Eds.), Recent Progress in Antarctic Earth Science. Terrapub, Tokyo, pp. 443–448.

Ortiz, R., García, A., Aparicio, A., Blanco, I., Felpeto, A., Del Rey, R., Villegas, M., Ibáñez, J.M., Morales, J., Del Pezzo, E., Olmedillas, J.C., Astiz, M., Vila, J., Ramos, M., Viramonte, J.G., Risso, C., Caselli, A., 1997. Monitoring of the volcanic activity of Deception Island, South Shetland Islands, Antarctica (1986–1995). In: Ricci, C.A. (Ed.) The Antarctic Region: Geological Evolution and Processes, Terra Antartica Publication, Siena, pp. 1071–1076.

Pelayo, A.M., Wiens, D.A., 1989. Seismotectonics and relative plate motions in the Scotia Sea region. Journal of Geophysical Research 94, 7293–7320.

Prieto, M.J., Canals, M., Ercilla, G., de Batist, M., 1998. Structure and geodynamic evolution of the Central Bransfield Basin (NW Antarctica) from seismic reflection data. Marine Geology 149, 17–38.

Rey, J., Somoza, L., Martínez-Frías, J., 1995. Tectonic, volcanic, and hydrothermal event sequence on Deception Island (Antarctica). Geo-Marine Letters 15, 1–8.

Rey, J., Somoza, L., Martínez-Frías, J., Benito, R., Martín-Alfageme, S., 1997. Deception Island (Antarctica): a new target for exploration of Fe–Mn mineralization? In:

Nicholson, K., Hein, J.R., Buhn, B., Dasgupta, S. (Eds.), Manganese Mineralization: Geochemistry and Mineralogy of Terrestrial and Marine Deposits, Geological Society Special Publication 119, London, pp. 239–251.

Robertson, S.D., Wiens, D.A., Dorman, L.M., Shore, P.J., Vera, E., 2001. Seismicity and tectonics of the South Shetland Islands region from a combined land-sea seismograph deployment. EOS Transaction of the AGU Fall Meeting Supplement 82(47), pp. F818 (abstract).

Roobol, M.J., 1973. Historic volcanic activity at Deception Island. British Antarctic Survey Bulletin 32, 23–30.

Roobol, M.J., 1979. A model for the eruptive mechanism of Deception Island from 1820 to 1970. British Antarctic Survey Bulletin 49, 137–156.

Roobol, M.J., 1982. The volcanic hazard at Deception Island, South Shetland Islands. British Antarctic Survey Bulletin 51, 237–245.

Smellie, J.L., 1988. Recent observations on the volcanic history of Deception Island, South Shetland Islands. British Antarctic Survey Bulletin 81, 83–85.

Smellie, J.L., 1990. Deception Island. In: LeMasurier, W.E., Thomson, J.W. (Eds.), Volcanoes of the Antarctic Plate and Southern Oceans. American Geophysical Union, Washington, DC, pp. 316–321.

Vila, J., Martí, J., Ortiz, R., García, A., Correig, A.M., 1992. Volcanic tremors at Deception Island (South Shetland Islands, Antarctica). Journal of Volcanology and Geothermal Research 53, 89–102.

Vila, J., Correig, A.M., Martí, J., 1995. Attenuation and source parameters at Deception Island (South Shetland Islands, Antarctica). Pure and Applied Geophysics 144, 229–250.

Walker, G.P., 1984. Downsag calderas, ring faults, caldera sizes, and incremental caldera growth. Journal of Geophysical Research 89, 8407–8416.